

AD-A255 005



2

MENTATION PAGE

Form Approved
OMB No. 0704-0188

1a. SECURITY CLASSIFICATION UNCLASSIFIED			1b. RESTRICTIVE MARKINGS		
2a. SECURITY CLASSIFICATION AUTHORITY			3. DISTRIBUTION/AVAILABILITY OF REPORT Approved for Public Release; Distribution Unlimited		
2b. DECLASSIFICATION/DOWNGRADING SCHEDULE AUG 17 1992			4. PERFORMING ORGANIZATION REPORT NUMBER		
5. MONITORING ORGANIZATION REPORT NUMBER(S) AFOSR-TR- 82 0180			6a. NAME OF PERFORMING ORGANIZATION Massachusetts Institute of Technology		
6b. OFFICE SYMBOL (If applicable)			7a. NAME OF MONITORING ORGANIZATION AFOSR/NA		
6c. ADDRESS (City, State, and ZIP Code) 77 Massachusetts Ave., Cambridge, MA02139			7b. ADDRESS (City, State, and ZIP Code) Bldg. 410 Bolling AFB, DC 20332-6448		
8a. NAME OF FUNDING/SPONSORING ORGANIZATION AFOSR			8b. OFFICE SYMBOL (If applicable) NA		
9. PROCUREMENT INSTRUMENT IDENTIFICATION NUMBER AFOSR-89-0060			10. SOURCE OF FUNDING NUMBERS		
8c. ADDRESS (City, State, and ZIP Code) Bldg. 410 Bolling AFB, DC 20332-6448			PROGRAM ELEMENT NO. 6.1102F	PROJECT NO. 2302	TASK NO. C1
11. TITLE (Include Security Classification) (U) INTERPRETATION OF IN SITU TESTING OF COHESIVE SOILS USING RATIONAL METHODS					
12. PERSONAL AUTHOR(S) Whittle, Andrew J., Aubeny, Charles P. & Ladd, Charles C.					
13a. TYPE OF REPORT FINAL		13b. TIME COVERED FROM Oct 15 88 TO Oct 15 91		14. DATE OF REPORT (Year, Month, Day) 92-07-06	
				15. PAGE COUNT 434	
16. SUPPLEMENTARY NOTATION					
17. COSATI CODES			18. SUBJECT TERMS (Continue on reverse if necessary and identify by block number)		
FIELD	GROUP	SUB-GROUP	In situ testing, cohesive soils, piezocone, dilatometer, pressuremeter, Strain Path Method, soil models		
19. ABSTRACT (Continue on reverse if necessary and identify by block number)					
<p>This research uses theoretical analyses to investigate the fundamental mechanisms controlling the performance of common in-situ penetration tests which are used to estimate the engineering properties of cohesive soils. The mechanics of penetration processes are modelled using the Strain Path Method together with generalized effective stress soil models. The analytical predictions provide a rational basis for establishing how soil properties are related to in-situ measurements. The predictions are evaluated by comparison with field data from well documented test sites. Results of this research show the following: 1) The cone resistance and excess pore pressures measured on the face of the cone during piezocone penetration are the most reliable measurements for estimating changes in undrained shear strength within a given clay deposit. 2) There is no rational basis for correlations between dilatometer contact pressures and in-situ K_0-stresses, undrained shear strength or preconsolidation pressure. 3) Model predictions provide a reliable basis for estimating the horizontal coefficient of permeability for normally and lightly overconsolidated clays ($OCR \leq 4$) using measurements of pore pressure dissipation on the shaft of the piezocone. 4) Installation disturbance affects significantly the interpretation of undrained shear strength in pressuremeter expansion tests. The analyses show that undrained shear strength can be estimated more reliably from measurements during the contraction phase of the pressuremeter test.</p>					
20. DISTRIBUTION/AVAILABILITY OF ABSTRACT <input checked="" type="checkbox"/> UNCLASSIFIED/UNLIMITED <input type="checkbox"/> SAME AS RPT <input type="checkbox"/> DTIC USERS			21. ABSTRACT SECURITY CLASSIFICATION UNCLASSIFIED		
22a. NAME OF RESPONSIBLE INDIVIDUAL Major Martin D. Lewis			22b. TELEPHONE (Include Area Code) (202) 767-6963		22c. OFFICE SYMBOL AFOSR/NA

EXECUTIVE SUMMARY

This research uses theoretical analyses to investigate the fundamental mechanisms controlling the performance of common in-situ penetration tests (piezocone, pressuremeter, dilatometer, field vane etc.) which are used to estimate the engineering properties of cohesive soils. The mechanics of penetration processes are modelled using the Strain Path Method together with two generalized effective stress soil models (Appendix A) 1) Modified Cam Clay (MCC), and 2) MIT-E3. The well known MCC model describes the idealized critical state framework of clay behavior and provides a base case for interpreting the analyses. MIT-E3 is a more complex elasto-plastic soil model which provides reliable predictions of the non-linear, inelastic and anisotropic effective stress-strain properties of K_0 -consolidated clays. The analytical predictions provide a rational basis for establishing how soil properties are related to in-situ measurements. The predictions are evaluated by comparison with field data from well documented test sites. The principal accomplishments of the research include the following:

1. The development and evaluation of reliable numerical methods for estimating pore pressure distributions around penetrometers using the Strain Path Method. In the proposed method (Chapter 2), equilibrium conditions are satisfied by numerical solution of a Poisson equation using finite element methods. Additional modification of the formulation is introduced to maintain vertical equilibrium at locations ahead of the tip of the penetrometer. The proposed formulation avoids arbitrary assumptions regarding the path of integration and is particularly suitable for penetrometers with non-axisymmetric geometries. It is used throughout this research to estimate distributions of excess pore pressures for piezocone penetrometers, the Marchetti dilatometer, earth pressure cells and the field vane.
2. Comprehensive strain path analyses have been used to predict the stresses and pore pressures during steady piezocone penetration (Chapter 3) in normally and lightly overconsolidated clays ($OCR \leq 4$). The analyses have evaluate the effects of tip geometry, soil modelling and stress history of the soil on piezocone measurements during steady penetration.
 - The results show that the net tip resistance can be correlated linearly with the undrained shear strength (in a triaxial compression mode of shearing) through a cone resistance factor, N_{KT} . However, the predictions of tip resistance are also affected by other soil properties including non-linear stress-strain behavior and post-peak strain softening. Although the factor N_{KT} is not a universal constant for all clays, the cone resistance is the most reliable measurement for estimating changes in undrained shear strength within a given soil deposit. However, in

220000 92-22712


435P8

practice, measurements of piezocone tip resistance can be unreliable due to large excess pore pressures which act on the base of the cone. This research identifies the need to refine the design of the piezocone in order to eliminate this source of error.

- Excess pore pressures measured by porous filters located either at the tip or on the face of the cone are also well correlated to the undrained shear strength and preconsolidation pressures in the soil. Pore pressures measured at the base of the cone or at locations along the shaft of the piezocone are much less sensitive to changes in undrained shear strength and hence, are less reliable measurements from which to estimate the undrained shear strength.
 - Comparisons of analytical predictions with field data from piezocone tests in Boston Blue Clay at two sites have shown that the analytical predictions can describe accurately trends in the measured data, although the analytical solutions generally underpredict the measured excess pore pressures.
3. The mechanics of flat plate penetration have been evaluated using the Strain Path Method (Appendix C, Annual Technical Report 1991). Soil deformations and strains are estimated from potential flow theory using fundamental analytical solutions for a finite length line source in a uniform flow. There are two geometric properties which control the mechanics of plate penetration: a) the aspect ratio, B/w , (i.e., the ratio of the length to width of the plate), and b) the equivalent radius, R_{eq} , which is a measure of the volume of soil displaced by the penetrometer. The equivalent radius controls the lateral extent of disturbance caused by the plate installation (e.g., at locations far from the surface of the penetrometer, soil strains and displacements depend only on the volume of soil displaced). The aspect ratio controls the distribution of stresses and pore pressures in the soil around the penetrometer. The magnitudes of effective stresses and excess pore pressures acting at the center of the plate are similar to predictions presented previously for axisymmetric penetrometers and are not significantly affected by the aspect ratio of the plate (for the aspect ratios considered in this study; $6.8 \leq B/w \leq 32.5$) Excess pore pressures acting at the edge of the plate are typically 20-25% smaller than at the center of the plate. Dissipation of excess pore pressures measured at the center of plate penetrometers are controlled by the equivalent radius of the penetrometer.
 4. Comprehensive Strain Path analyses have been performed in order to evaluate measurements of dilatometer contact pressures, p_0 , (Chapter 4) for normally and lightly overconsolidated clays ($OCR \leq 4$). The analyses show that the stresses acting on the dilatometer membrane are not uniform, due to the proximity of the membrane to the tip of the penetrometer. A systematic study of the predicted contact pressure has found that there are no simple linear correlations between the p_0 and the undrained shear strength or preconsolidation pressure of the soil. Furthermore, the predictions show that even when

pore pressures are measured on the dilatometer membrane (as proposed by a number of authors) there is still no simple interpretation of engineering properties from contact conditions. Thus, the analyses imply serious limitations of existing empirical correlations which relate in-situ K_0 stresses, undrained shear strength and preconsolidation pressure to the dilatometer contact pressures. A direct comparison of analytical predictions with measured data in Boston Blue Clay confirms that stress history cannot be reliably estimated from the contact pressure. Further studies of data from seven well documented test sites has shown that dilatometer contact pressures exhibit significant scatter and that site specific correlations for estimating the preconsolidation pressure vary significantly for different types of clay.

5. Predictions of pore pressure dissipation after piezocone penetration are widely used to estimate consolidation and/or permeability characteristics of clay layers. Existing methods of interpreting the measured data are based either on simplified theories for estimating penetration pore pressures, or from analyses which assume there is no coupling between pore pressure changes and displacements in the soil. Chapter 5 presents complete numerical predictions of non-linear, coupled consolidation around penetrometers installed in normally and lightly overconsolidated clays ($OCR \leq 4$) using: a) initial conditions predicted by Strain Path analyses; and b) non-linear stress-strain behavior using generalized effective stress soil models (MCC and MIT-E3). The solutions provide complete predictions of pore pressure and effective stress changes during consolidation. Porous filters located on the shaft of the piezocone are not affected significantly by non-linear coupling with stress changes in the soil and provide the most reliable measurements for estimating permeability. Detailed comparisons with shaft dissipation measurements in Boston Blue Clay and kaolin (from calibration chamber tests) show that the analyses can predict permeability to within a factor of 2.
6. Pressuremeter tests were analyzed in order to assess how the computed undrained shear strength is affected by installation disturbance in normally and lightly overconsolidated clays ($OCR \leq 4$). Chapter 6 describes Strain Path analyses which simulate the installation of three types of pressuremeter: 1) self-boring (SBPM), 2) push-in (i.e., open-ended cross-section, PIPM), and 3) full displacement (i.e., solid section, FDPM) devices. In all cases, the undrained shear strength is estimated from the pressuremeter expansion curve after installation. Further studies have also been performed to evaluate methods for interpreting undrained shear strength from measurements during the membrane contraction phase:
- The predictions show that displacement pressuremeter expansion tests (i.e., FDPM, PIPM) tend to underestimate the true undrained shear strength of the soil (i.e., in the ideal cavity expansion mode of shearing). The installation disturbance also

A-1

introduces significant non-linearity in the predicted expansion curve such that the interpretation of maximum shear resistance is highly dependent on the strain level.

- Undrained shear strengths computed for self-boring pressuremeter (SBPM) expansion tests depend on the rate at which soil is extracted during the penetration process. Self-boring pressuremeter tests can: a) underestimate the in-situ strength if the soil extraction rate is low (installation disturbance is similar to a displacement pressuremeter); or b) overestimate the in-situ strength when the soil extraction causes a reduction in the total lateral stress in the surrounding soil. The predictions show that SBPM tests can overestimate the undrained shear strength by up to 35% in these analyses.
- The undrained shear strength computed from membrane contraction is in good agreement with the in-situ shear strength of the soil and is not affected significantly by installation disturbance in either displacement or self-boring pressuremeter tests. This result suggests that contraction measurements provide a more reliable basis for estimating undrained shear strength than the conventional data obtained during membrane expansion.

The Strain Path analyses are qualitatively in good agreement with data reported in the literature for different types of pressuremeter. However, there has been no systematic field study of disturbance effects caused by pressuremeter installation. Field data in Boston Blue Clay show that pressuremeter strengths are more consistently estimated from contraction measurements. However, the interpreted shear strengths were higher than reference properties measured in laboratory tests. Further studies are required to evaluate contraction measurements at other sites.

7. Predictions of disturbances caused by field vane installation have been established from Strain Path analyses (Annual Technical Report, 1991). In contrast to existing hypotheses, the analyses show that disturbance of the stress and pore pressures fields is not limited to the soil immediately adjacent to the blades of the vane. Large excess pore pressures are predicted at points along the potential failure surface, and significant reductions in effective stresses occur for sensitive clays. Preliminary calculations of pore pressure dissipation show that there is little dissipation of the installation pore pressures during a typical rest period of 5 mins prior to vane rotation. However, almost complete dissipation occurs within 1 to 5 hours after vane insertion. Further studies are required to evaluate the importance of these factors on the undrained shear strength interpreted during vane rotation.

FOREWORD

This report describes the research results obtained in a three year project entitled 'Interpretation of in-situ testing of cohesive soils using rational methods' which was supported by the Air Force Office of Scientific Research through grant AFOSR-89-0060. The work was initiated in October 1988 under the supervision of Professors Charles C. Ladd, Mohsen M. Baligh and Andrew J. Whittle in the Civil and Environmental Engineering Department of the Massachusetts Institute of Technology.

The project has supported the following graduate student theses:

1. Williamson, Anne "Use of a panel method to predict disturbance due to penetrometer installation in clays," MS Thesis, August 1989.
2. Rafalovich, Alexander "The mechanics of plate installation in clays," MS Thesis, June 1991.
3. Elghaib, Majid "Prediction and interpretation of piezocone data during undrained, drained and partially drained penetration," PhD Thesis, July 1989 (Partial support).
4. Aubeny, Charles "Rational interpretation of in-situ testing in cohesive soils," PhD Thesis May 1992.
5. Sheahan, Thomas "An experimental study of the time-dependent undrained shear behavior of resedimented clay using automated stress path triaxial equipment," PhD Thesis, August 1991 (Partial Support).

Michael Geer has also contributed to the project as a Research Assistant (June 1991 - January 1992) working on the consolidation around penetrometers.

The research findings from the first two years of the project were summarized in a comprehensive Annual Technical Report (November 1991) submitted to the AFOSR which is now published as an MIT Research Report:

Whittle, A.J., Aubeny, C.P., Rafalovich, A., Ladd, C.C. & Baligh, M.M. (1991)
 "Predictions and Interpretation of In-situ Penetration Tests in Cohesive Soils,"
 Research Report R91-01, MIT Department of Civil Engineering.

Additional findings from the third year of the project will be published shortly in a companion volume:

Whittle, A.J., Aubeny, C.P., Ladd, C.C. & Geer, M. (1992) "Interpretation of in-situ tests after installation in clays" Research Report R92-21, MIT Department of Civil Engineering.

In addition to these reports the following papers have already been published from this work:

1. A.J. Whittle, C.P. Aubeny (1991) "Pore pressure fields around piezocone penetrometers installed in clays," Proceedings International Association for Computer Methods and

- Advances in Geomechanics (IACMAG'91), Cairns, Vol. 1, pp. 285-292.
2. Whittle A.J. & Aubeny, C.P. (1991) "Pore pressure fields around piezocone penetrometers installed in clays," Proceedings International Association for Computer Methods and Advances in Geomechanics (IACMAG'91), Cairns, Vol. 1, pp. 285-293.
 3. A.J. Whittle (1992) "Constitutive modelling for deep penetration problems in clays," Proceedings Third International Conference on Computational Plasticity, Barcelona, Vol. 1, pp. 883-895.
 4. A.J. Whittle & C.P. Aubeny (1992) "The effects of installation disturbance on interpretation of in-situ tests in clays," Proceedings Wroth Memorial Symposium, University of Oxford, U.K.

Several additional journal papers are currently in preparation.

This research has benefited significantly from a parallel program of laboratory and in-situ testing performed in Boston Blue Clay at a site in South Boston. This work was carried out in cooperation with Haley and Aldrich Inc. and funded by Bechtel/Parsons Brinckerhoff. Additional data was provided by Steven Saye (WCC), Dr Suzanne Lacasse (NGI) and Dr Gilliane Sills (University of Oxford).

The authors would like to thank the technical monitors of this project, Lt Col. Steven Boyce and Major Martin Lewis for their support of this research work.

Table of Contents

Executive Summary	i
Foreword	v
Table of Contents	vii
List of Tables	x
List of Figures	xii
1. Introduction	1
2. Penetration Pore Pressures from the Strain Path Method	7
2.1 Introduction	7
2.2 Background	7
2.3 Equilibrium Correction	13
2.4 Proposed Poisson Formulation	14
2.5 The Modified Poisson Formulation	17
2.6 Formulation for Three Dimensional Geometries	19
2.6.1 Formulation in the $y=0$ Plane	20
2.6.2 Formulation in $z=\text{const.}$ Planes	22
2.7 Conclusions	24
3. Piezocone Penetration	38
3.1 Introduction	38
3.2 Background	39
3.2.1 Cone Design and Testing Procedures	39
3.2.2 Interpretation of Engineering Properties of Clays	42
3.3 Analytical Predictions	48
3.3.1 Introduction	48
3.3.2 Effect of Tip Shape	49
3.3.3 Effect of Stress History	53
3.3.4 Effect of Soil Model	54
3.3.5 Discussion and Summary	55
3.4 Interpretation of Engineering Properties from Predictions	56
3.4.1 Undrained Shear Strength	57
3.4.2 Stress History	58
3.5 Comparisons with Measured Data	59
3.5.1 Measurements in Boston Blue Clay	59
3.5.2 Review of Field Data at Selected Sites	62
3.5.3 Calibration Chamber Data	64

3.6 Summary and Conclusions	66
4. Marchetti Dilatometer Penetration	122
4.1 Introduction	122
4.2 Interpretation of Contact Pressure, p_0	123
4.3 Predictions of Disturbance due to Dilatometer Installation	125
4.3.1 The Dilatometer Geometry	125
4.3.2 Distribution of Effective Stresses and Pore Pressures Acting around the Dilatometer	126
4.3.3 Evaluation of Contact Pressure from Analytical Solutions	128
4.3.4 Analytical Predictions of Dilatometer Membrane Conditions	129
4.3.5 Comparisons with Full Displacement Pressuremeters	133
4.4 Comparisons with Measured Dilatometer Data	134
4.4.1 Contact Pressure, p_0	134
4.4.2 Comparisons to Axisymmetric Measurements	139
4.5 Summary and Conclusions	140
5. Consolidation around Penetrometers	174
5.1 Introduction	174
5.2 Background	175
5.2.1 Uncoupled Analyses	175
5.2.2 Engineering Properties from Measured Data	177
5.2.3 Non-Linear Consolidation Analyses	178
5.2.4 Evaluation of Non-Linear Consolidation Analyses	180
5.3 Two Dimensional Non-Linear Consolidation	181
5.4 Predictions	184
5.4.1 Base Case Analysis	185
5.4.2 MIT-E3 Predictions	186
5.5 Comparisons with Measured Data	189
5.5.1 Field Measurements in BBC	189
5.5.2 Calibration Chamber Data	190
5.6 Summary and Conclusions	191
6. Pressuremeter Testing	236
6.1 Introduction	236
6.2 Background	237
6.2.1 Equipment and Procedures	237
6.2.2 Pressuremeter Test Interpretation	239
6.2.3 Influence of Finite Membrane Length	246
6.2.4 Field Experience	247

6.3 The Ideal Pressuremeter Shear Mode	250
6.4 Predictions of Pressuremeter Tests with Installation Disturbance	252
6.4.1 Analytical Framework	252
6.4.2 Interpretation of Predictions	253
6.4.3 Displacement Pressuremeter Predictions	254
6.4.4 Predictions for Self-Boring Pressuremeters	262
6.4.5 Finite Membrane Length Effects	265
6.5 Field Measurements in Boston Blue Clay	266
6.6 Conclusions and Summary	270
7. Summary, Conclusions, and Recommendations	336
7.1 Excess Pore Pressures during Penetration	336
7.2 The Piezocone	337
7.3 The Dilatometer	339
7.4 Pore Pressure Dissipation around Penetrometers	340
7.5 Pressuremeters	341
7.6 Recommendations	343
References	345
Appendix A. Generalized Effective Stress Soil Models	361
A.1 Introduction	361
A.2 Modified Cam Clay Formulation	361
A.3 MIT-E3 Model Formulation	363
Appendix B. Isoparametric Interpolation Functions	375
Appendix C. The Simple Plate	379
C.1 Introduction	379
C.2 The Simple Plate	379
Appendix D. Deformations, Strains, and Stresses during Self-Boring Penetration	405
D.1 Introduction	405
D.2 Deformation Grids and Penetrometer Geometry	405
D.3 Strains	406
D.4 Stresses and Pore Pressures	407

LIST OF TABLES

- 2.1 Pore Pressures Predicted Around a Plate by Different Equilibrium Equations
- 3.1 Input Material Properties Used by the MCC Model
- 3.2 Input Material Properties Used by the MIT-E3 Model
- 3.3 Comparison of Tip Resistance Predictions Using the Strain Path Method
- 3.4 Predictions of Piezocone Measurements for K_0 -Consolidated BBC
- 3.5 Dimensionless Ratios for Predicting Undrained Shear Strength
- 3.6 Dimensionless Ratios for Predicting Preconsolidation Pressure
- 3.7 Soil Properties at Six Test Sites
- 4.1 Predictions at Center of Dilatometer Membrane
- 4.2a Predictions of DMT Membrane Stresses Normalized by c_{uTC}
for K_0 -consolidated BBC
- 4.2b Predictions of DMT Membrane Stresses Normalized by σ'_p
for K_0 -consolidated BBC
- 4.3 Predictions at Center of Membrane of Full Displacement Pressuremeter
- 4.4 Comparison of Predicted DMT Contact Pressures to FDPMT lift-off
Pressure and CPTU Base Pore Pressures
- 5.1 Estimation of Soil Properties from Dissipation Tests
- 5.2 Summary of Previous Consolidation Predictions
- 5.3a Horizontal Consolidation Coefficient Values from Dissipation Tests
Using Levadoux and Baligh (1980) Theory Compared to
Reference Values (after Lacasse and Lunne, 1982)
- 5.3b Horizontal Consolidation Coefficient Values Computed from
Dissipation Test Data from Different Stone Locations -
Rio de Janeiro (after Sills et al., 1988)
- 6.1a Self-Boring Pressuremeters Characteristics
- 6.1b Typical SBPM Test Procedures
- 6.2 Summary of Methods for Estimating In Situ Horizontal
Stress from Self-Boring Pressuremeter Expansion Curves
- 6.3 Data Summary at Six Pressuremeter Sites
- 6.4 SBPMT Strength Estimates
- 6.5 Undrained Shear Strength Ratios for Boston Blue Clay at OCR's 1 and 4

6.6 Displacement Pressuremeters - No Drainage of Installation Pore Pressures:

- a) Installation Conditions
- b) c_u/σ'_{v0} from Predicted Pressuremeter Curves
- c) Limit Pressures

6.7 Displacement Pressuremeters - Full Drainage of Installation Pore Pressures

- a) Installation Conditions
- b) c_u/σ'_{v0} from Predicted Pressuremeter Curves
- c) Limit Pressures

6.8 Self-Boring Pressuremeters

- a) Installation Conditions
- b) c_u/σ'_{v0} from Predicted Pressuremeter Curves
- c) Limit Pressures

6.9a. Undrained Shear Strength from SBPMT Expansion Curves in BBC at South Boston Site (based on SBPMT expansion curves from Benoît, 1991)

6.9b. Undrained Shear Strength from SBPMT Contraction Curves in BBC at South Boston Site (based on SBPMT expansion curves from Benoît, 1991)

6.10 Relationship Between Undrained Shear Strength from SBPMT Expansion Curves and Contact Pressure in BBC at South Boston Site (based on SBPMT expansion curves from Benoît, 1991)

A.1 Transformed Stress Measures (Kavvadas, 1982)

B.1 Interpolation Functions and Their Derivatives for a Nine-Node Isoparametric Element

B.2 Interpolation Functions and Their Derivatives for a Four-Node Isoparametric Element

C.1 Fundamental Analytical Solutions Used in the Strain Path Method

D.1a Initial Radii of Stagnation Lines for Various Sink Strengths during Self-Boring Penetration, $B/t=12$

D.2b Penetrometer Characteristics for Various Sink Strengths during Self-Boring Penetration, $B/t=12$

LIST OF FIGURES

- 2.1 Flow Chart of Strain Path Method (Baligh, 1985a)
- 2.2 Strain Paths During Simple Pile Penetration (Baligh, 1985b)
- 2.3. Excess Pore Pressures Around Cones Predicted by Different Equilibrium Equations Using MCC Soil Model for K_0 -Normally Consolidated BBC:
a) 18° Cone, b) 60° Cone
- 2.4 Relative Contribution of Vertical Equilibrium Equation During Cone Penetration,
a) 18° Cone, b) 60° Cone
- 2.5 Excess Pore Pressures Around Cones Predicted by Modified Poisson Solution Using MCC Soil Model for K_0 -Normally Consolidated BBC:
a) 18° Cone, b) 60° Cone
- 2.6 Definition of Coordinate Frame for Plate Penetration Problems
- 2.7 Excess Pore Pressures at Plate Center by Different Equilibrium Equations
- 2.8 Comparison of Simple Plate, $B/w=6.8$, and Simple Pile Excess Pore Pressures:
a) Along Centerline and Plate Boundary, b) Lateral Distribution far above Tip
- 2.9 Pore Pressures in Horizontal Plane Far Above Tip for Simple Plate, $B/w=32.5$:
a) x -Direction Integration, b) y -Direction Integration, c) Poisson Solution
- 2.10 Dissipation of Excess Pore Pressures for Different Initial Conditions at Plate Center
- 2.11 Comparison of Excess Pore Pressures Predicted in $z/w=200$ and in $y/w=0$ Planes Using Proposed Poisson Formulations
- 3.1a Typical Electrical Cone (Schaap and Zindberg, 1982)
- 3.1b Pore Pressure Probes (Torstensson, 1975; Wissa, 1975)
- 3.2 Examples of Piezocones Jamiolkowski (1985)
- 3.3 Pore Pressure Filter Designs for Piezocone
- 3.4a Unequal Surface Areas of Cones (Battaglio and Maniscaldo, 1983)
- 3.4b Unequal Surface Areas of Cones (Nyirenda & Sills, 1989)
- 3.5 Cone Resistance Factor, N_k
- 3.6 Pore Pressure Factor, $N_{\Delta u}$ (Campanella and Robertson, 1988)
- 3.7 Relationships between Tip Resistance, q_T and Measured Pore Pressures (Mayne et al., 1990)
- 3.8a Evaluation of B_q Parameter with OCR (Jamiolkowski et al., 1985)
- 3.8b Evaluation of B_q Parameter with OCR (Robertson et al., 1989)
- 3.9a Correlation between Net Tip Resistance and OCR (Mayne, 1987)
- 3.9b Correlation between Piezocone Pore Pressures and OCR (Mayne, 1986)

- 3.10a Conceptual Distribution of Pore Pressure around Piezocone
(Robertson et al., 1986)
- 3.10b Correlation of Pore Pressure Difference with OCR (Sully et al., 1988)
- 3.11a Correlation of Pore Pressure Ratio with OCR (Robertson et al., 1989)
- 3.11b Correlation of Pore Pressure Ratio with OCR (Mayne et al., 1990)
- 3.12a Stress Paths of Idealized Soil Elements at Cone Tip (Konrad and Law, 1987)
- 3.12b OCR from Vertical Yield Stress (Konrad and Law, 1987)
- 3.12c Comparison between B_q and σ'_{yc}/σ'_p Relationships with OCR
(Konrad and Law, 1987)
- 3.13 Effect of Tip Shape on Predictions of Effective Stresses and Pore Pressures:
 - a) σ'_π/σ'_{v0}
 - b) σ'/σ'_{v0}
 - c) $(\sigma'_\pi - \sigma'_{\theta\theta})/2\sigma'_{v0}$
 - d) $(u-u_0)/\sigma'_{v0}$
- 3.14 Summary of Effect of Tip Shape on Distributions of Excess Pore Pressures
- 3.15 Effect of Overconsolidation Ratio on Predictions of Effective Stresses
and Pore Pressures:
 - a) σ'_π/σ'_{v0}
 - b) σ'/σ'_{v0}
 - c) $(\sigma'_\pi - \sigma'_{\theta\theta})/2\sigma'_{v0}$
 - d) $(u-u_0)/\sigma'_{v0}$
- 3.16 Predictions of Effective Stresses and Pore Pressures using the MIT-E3 Model:
 - a) σ'_π/σ'_{v0}
 - b) σ'/σ'_{v0}
 - c) $(\sigma'_\pi - \sigma'_{\theta\theta})/2\sigma'_{v0}$
 - d) $(u-u_0)/\sigma'_{v0}$
- 3.17 Effect of Soil Model on Distributions of Excess Pore Pressures
- 3.18 Location of Piezocone Pore Pressure Elements for Simple Pile and 60° Cone
- 3.19a Index Properties and Stress History, Saugus Test Site (Morrison, 1984)
- 3.19b Index Properties and Stress History, South Boston Test Site (Ladd, 1990)
- 3.20 Comparison of Predictions and Measured Data for Net Tip Resistance in BBC
- 3.21 Comparison of Predictions and Measured Data for Excess Pore Pressures in BBC
- 3.22 Comparison of Predictions and Measured Data for the Effective
Tip Resistance in BBC
- 3.23 Comparison of Predictions and Measurements for the B_q Ratio in BBC
- 3.24 Comparison of Predictions to Piezocone Measurements at Six Sites:

- a) $(q_t - \sigma_{v0}) / \sigma'_{v0}$
 - b) $(u_1 - u_0) / \sigma'_{v0}$
 - c) $(u_2 - u_0) / \sigma'_{v0}$
 - d) $(u_1 - u_0) / (q_t - \sigma_{v0})$
 - e) $(u_2 - u_0) / (q_t - \sigma_{v0})$
 - f) $(u_2 - u_0) / (u_1 - u_0)$
- 3.25 Pore Pressures Measured at Four Locations during Piezocone Penetration at the Inchinnan Site (Sills et al., 1988)
- 3.26 Comparison of Piezocone Measurements in Resedimented Kaolin to MIT-E3 Predictions for BBC (May, 1987; Nyirenda, 1989)
- 3.27 Comparison of Measured Pore Pressure Fields in Resedimented Kaolin to MIT-E3 Predictions for BBC (May, 1987)
- 4.1 Geometry of the Marchetti Dilatometer
- 4.2 Empirical Correlations Between Overconsolidation Ratio and Dilatometer Contact Pressure, p_0
- 4.3 Geometry of Simple Plate Used to Simulate Dilatometer
- 4.4 Comparisons of Simple Pile Solution to 180° Cone Solution
- 4.5a Simple Pile and Simple Plate Stress and Pore Pressure Contours: σ'_r / σ'_{v0}
- 4.5b Simple Pile and Simple Plate Stress and Pore Pressure Contours: $\Delta u_s / \sigma'_{v0}$
- 4.5c Simple Pile and Simple Plate Stress and Pore Pressure Contours: $(\sigma'_r - \sigma'_{\theta\theta}) / 2\sigma'_{v0}$
- 4.5d Simple Pile and Simple Plate Stress and Pore Pressure Contours: $\Delta u / \sigma'_{v0}$
- 4.6 Stress and Pore Pressure Distribution Along Dilatometer Membrane:
- a) $y=0$ Plane, b) $z/w=200$ Plane
- 4.7 Summary of DMT and FDPMT Predictions and Correlations
- 4.8 Full Displacement Pressuremeters: a) Briaud and Shields (1979),
b) Withers et al. (1986)
- 4.9 Index Properties and Stress Histories at Reference Sites
- 4.10 Predicted versus Measured K_D -OCR Correlation at South Boston Site
- 4.11 Correlation of Dilatometer Index, K_D , with OCR for Six Well-Documented Sites
- 4.12 Correlation of Dilatometer Index, K_D , with OCR, Summary
- 4.13a DMT versus Reference σ'_p Profiles at the South Boston Site (Ladd, 1990)
- 4.13b DMT versus Reference σ'_p Profiles at the Florence Lake Site
(Whittle et al., 1989)
- 4.13c DMT versus Reference σ'_p Profiles in the New Jersey Varved Clay
(Whittle et al., 1989)
- 4.14 Comparison of DMT Contact Pressure, p_0 , to FDPMT

- Lift-off Pressure, p_i (Luttenegger and Blanchard, 1990)
- 4.15a Comparison of Dilatometer Contact Pressure and Cone Base Pore Pressure
 - 4.15b Comparison of Dilatometer Contact Pressure and Cone Tip Pore Pressure
 - 5.1 Pore Pressure Dissipation around Cone Penetrometers from Uncoupled Consolidation Analyses (Levadoux and Baligh, 1986)
 - 5.2 Pore Pressure Dissipation around 60° Cone Penetrometer from Uncoupled Linear Analysis - Installation Conditions from SPM Using EPP Soil Model (Teh, 1987)
 - 5.3 Evaluation of Linear Uncoupled Dissipation Predictions for 60° Conical Probe in Lower BBC ($OCR < 2$) (after Levadoux and Baligh, 1986)
 - 5.4 Comparison of Predicted and Measured Coefficients in Boston Blue Clay (after Levadoux and Baligh, 1986)
 - 5.5 Normalized Theoretical and Driving Excess Pore Pressure (after Sills et al., 1988)
 - 5.6 Influence of Stress History on Dissipation Curves Far above Tip Predicted by MIT-E3 Model (after Whittle, 1987)
 - 5.7 Influence of Soil Model on Consolidation Predictions
 - 5.8a Comparison of MIT-E3 Predictions of Radial Stress at End of Consolidation with PLS Cell Measurements for Lower BBC, Saugus Site (after Whittle, 1987)
 - 5.8b Comparison of MIT-E3 Predictions of Total Radial Stress Decay with PLS Cell Measurements for Lower BBC, Saugus Site (after Whittle, 1987)
 - 5.9 Reference Permeability Profile in BBC at the Saugus Site (after Morrison, 1984)
 - 5.10a Boundary Conditions and Typical Finite Element Mesh for Non-Linear, Coupled Consolidation Analysis Around Simple Pile
 - 5.10b Effect of Mesh Refinement on Uncoupled Solutions - MCC, BBC, $OCR=1$ Installation Conditions
 - 5.11a Stress Conditions along Simple Pile Following Equilibration by Shear Distortion - MCC, BBC, $OCR=1$
 - 5.11b Radial Distribution of Stresses Far above Simple Pile Tip Following Equilibration by Shear Distortion - MCC, BBC, $OCR=1$
 - 5.12 Predicted Tip and Shaft Stress Histories for Different Equilibration Methods - MCC, BBC, $OCR=1$
 - 5.13a Setup Stresses along Simple Pile Boundary for Different Equilibration Methods - MCC, BBC, $OCR=1$
 - 5.13b Radial Distribution of Setup Stresses Far above Simple Pile Tip for Different Equilibration Methods - MCC, BBC, $OCR=1$
 - 5.14 Contours of Consolidation Stresses Predicted from Non-Linear, Coupled Solutions Using the MCC Soil Model with BBC Parameters: $OCR=1$

- 5.15 Contours of Excess Pore Pressures at Selected Times Predicted from Non-Linear, Coupled Solutions Using the MCC Soil Model with BBC Parameters: OCR=1
- 5.16 The Effect of Non-linear Coupling on Pore Pressure Dissipation Curves
- 5.17 Time History of Radial Stresses on Simple Pile Shaft ($z/R=30$) Predicted from Non-Linear, Coupled Solutions Using the MIT-E3 Soil Model
- 5.18 Time History of Vertical Stresses at Simple Pile Tip Predicted from Non-Linear, Coupled Solutions Using the MIT-E3 Soil Model
- 5.19 Contours of Consolidation Stresses Predicted from Non-Linear, Coupled Solutions Using the MIT-E3 Soil Model with BBC Parameters:
- a) Radial Effective Stress σ'_r/σ'_{v0}
 - b) Mean Effective Stress, σ'/σ'_{v0}
 - c) Cavity Shear Stress, q_h/σ'_{v0}
 - d) Meridional Shear Stress, $\sigma'_{rz}/\sigma'_{v0}$
- 5.20 Contours of Excess Pore Pressures at Selected Times Predicted from Non-Linear, Coupled Solutions Using the MIT-E3 Soil Model with BBC Parameters:
- a) OCR=1
 - b) OCR=2
 - c) OCR=4
- 5.21 Distribution of Consolidation Effective Stresses on Simple Pile Boundary Predicted from Non-Linear, Coupled Solutions Using the MIT-E3 Soil Model
- a) OCR=1
 - b) OCR=2
 - c) OCR=4
- 5.22 The Effect of Filter Location on Pore Pressure Dissipation Curves (Non-linear, Coupled Analysis)
- 5.23a The Effect of Stress History on Pore Pressure Dissipation Curves - Shaft Pore Pressures (Non-linear, Coupled Analysis)
- 5.23b The Effect of Stress History on Pore Pressure Dissipation Curves - Base Pore Pressures (Non-linear, Coupled Analysis)
- 5.23c The Effect of Stress History on Pore Pressure Dissipation Curves - Tip Pore Pressures (Non-linear, Coupled Analysis)
- 5.24 Comparison of MIT-E3 Predictions to Field Measurements of Shaft Pore Pressures
- 5.25 Comparison of MIT-E3 Predictions to Field Measurements of Tip Pore Pressures
- 5.26 Permeability of Resedimented Speswhite Kaolin (Al-Tabaa and Wood, 1987)

- 5.27 Comparison of MIT-E3 Predictions to Consolidation Chamber Test Measurements of Shaft Dissipation in Resedimented Kaolin (data from Nyirenda, 1989)
- 5.28 Comparison of MIT-E3 Predictions to Consolidation Chamber Test Measurements of Tip Dissipation Measurements in Resedimented Kaolin (data from Nyirenda, 1989)
- 6.1 Full-Displacement Pressuremeter Characteristics
- 6.2 Push-in Pressuremeter Characteristics
- 6.3 Self-Boring Pressuremeters: a) Camkometer; b) PAFSOR
- 6.4 Cavity Expansion Definitions: a) Expansion of a Cavity; b) Contraction of a Cavity
- 6.5 Undrained Strength from Pressuremeter Curve, Denby and Clough (1980) (from Ghionna et al., 1982)
- 6.6 Conceptual Model for Disturbance (Baguelin, 1978): a) Assumed Effects of Disturbance; b) Apparent Stress-Strain Curve
- 6.7 Methods of Estimating In Situ Horizontal Stress from SBPM Data, Lacasse and Lunne (1982): a) Inspection; b) Initial Excess Pore Pressure; c) Modified Lift-off; d) Log (Strain); f) Graphical Iteration; g) Hyperbolic-Plastic Model; h) Double Zero Shift; i) Origin Adjustment
- 6.8 SBPM Contact Pressure versus Estimated Undrained Shear Strength (Ghionna et al., 1982)
- 6.9 Influence of SBPM Test Procedures (Benoît and Clough, 1986): a) In Situ Horizontal Stress; b) Undrained Shear Strength; c) Effect of Membrane Expansion Rate
- 6.10 Strength Estimates from Pressuremeter Tests (Lacasse and Lunne, 1990): a) Onsoy; b) Haga
- 6.11 Model Predictions of Boston Blue Clay Behavior in a Pressuremeter Shear Mode: a) MIT-E3; b) MCC
- 6.12 Element Stress and Strain History in the Directional Shear Cell (DSC) Test (Germaine, 1982)
- 6.13 Comparison of Model Predictions and Measured Data for Stress-Strain Behavior of BBC at OCR=1 and 4 in the Isotropic (x-z) Plane
- 6.14 Contours of Octahedral Shear Strain, E, During Displacement Pressuremeter Installation
- 6.15 MIT-E3 Predictions of Displacement Pressuremeter Excess Pore Pressures and Stresses Immediately after Installation and at the End of Consolidation
- 6.16 Influence of Disturbance on Stress-Strain Behavior in a Pressuremeter Shearing Mode - No Dissipation of Installation Pore Pressures:

- a) Stress-Strain Behavior; b) Radial Distribution of Available Shear Strength
- 6.17 MIT-E3 Predictions of Total Radial Stress and Pore Pressure During Pressuremeter Expansion and Contraction In Normally Consolidated BBC- No Dissipation of Installation Pore Pressures
- 6.18 Predicted Expansion and Contraction Curves in Normally Consolidated BBC- No Dissipation of Installation Pore Pressures
- 6.19 Influence of Stress History on Disturbed Stress-Strain Behavior in a Pressuremeter Shearing Mode - No Dissipation of Installation Pore Pressures -OCR=2:
 - a) Stress-Strain Behavior; b) Radial Distribution of Available Shear Strength
- 6.20 Influence of Stress History on Disturbed Stress-Strain Behavior in a Pressuremeter Shearing Mode - No Dissipation of Installation Pore Pressures -OCR=4:
 - a) Stress-Strain Behavior; b) Radial Distribution of Available Shear Strength
- 6.21 Influence of Stress History on Total Radial Stress and Pore Pressure During Pressuremeter Expansion and Contraction - No Dissipation of Installation Pore Pressures:
 - a) OCR=2
 - b) OCR=4
- 6.22 Influence of Stress History on Predicted Expansion and Contraction Curves - No Dissipation of Installation Pore Pressure:
 - a) OCR=2
 - b) OCR=4
- 6.23 Influence of Stress History on Strength Estimates from Predicted Expansion and Contraction Curves - No Dissipation of Installation Pore Pressures
- 6.24 Influence of Disturbance on Stress-Strain Behavior- Full Dissipation of Installation Pore Pressure:
 - a) Effect of B/t Ratio
 - b) Effect of OCR
- 6.25 MIT-E3 Predictions of Total Radial Stress and Pore Pressure During Pressuremeter Expansion and Contraction - Full Dissipation of Installation Pore Pressures:
 - a) OCR=1
 - b) OCR=2
 - c) OCR=4
- 6.26 Predicted Expansion and Contraction Curves - Full Dissipation of Installation Pore Pressure:
 - a) OCR=1
 - b) OCR=2
 - c) OCR=4

- 6.27 Influence of Stress History on Strength Estimates from Predicted Expansion and Contraction Curves - Full Dissipation of Installation Pore Pressures
- 6.28 Contours of Octahedral Shear Strain During Self-Boring Penetration:
 - a) Push-in Pressuremeter; b) Ideal Self-Boring Pressuremeter
- 6.29 MIT-E3 Predictions of Total Radial Stress and Pore Pressure During Self-Boring Pressuremeter Expansion and Contraction in Normally Consolidated Boston Blue Clay
- 6.30 MIT-E3 Predictions of Self-Boring Pressuremeter Expansion and Contraction Curves in Normally Consolidated Boston Blue Clay
- 6.31 Influence of Stress History on Total Radial Stress and Pore Pressure During Self-Boring Pressuremeter Expansion and Contraction :
 - a) OCR=2
 - b) OCR=4
- 6.32 Influence of Stress History on Predicted Self-Boring Pressuremeter Expansion and Contraction Curves:
 - a) OCR=2
 - b) OCR=4
- 6.33 Influence of Stress History on Strength Estimates from Predicted Self-Boring Pressuremeter Expansion and Contraction Curves
- 6.34a Finite Element Mesh and Boundary Conditions Used for Analysis of Finite Membrane Length Effects
- 6.34b Influence of Finite Membrane Length on Predicted Pressuremeter Expansion Curves
- 6.35 Modified Camkometer Used in South Boston Pressuremeter Special Test Program (after Benoît, 1991)
- 6.36 Comparison of Predictions to Pressuremeter Measurements from South Boston Site:
 - a) OCR=1
 - b) OCR=4
- A.1 The Modified Cam Clay Model
- A.2 Conceptual Model of Unload-Reload Used by MIT-E3 for Hydrostatic Compression (Whittle, 1990)
- A.3 Yield and Failure Surface for Normally Consolidated Clay (Whittle, 1990)
- B.1 Isoparametric Element Definition Sketch
- C.1 Deformations fields for a) Spherical Cavity Expansion, and
 - b) Simple Pile (Baligh ; 1985b)
- C.2 Deformation paths for the Simple Pile (Baligh, 1985b)
- C.3 Coordinate system for the semi-infinite line source

- C.4 Source strength used for the semi-infinite line source
- C.5a Predicted deformation pattern around a simple plate, $B/w=6.8$
- C.5b Predicted deformation pattern around a simple plate, $B/w=20$
- C.5c Predicted deformation pattern around a simple plate, $B/w=32.5$
- C.6a Octahedral shear strain contours around simple plate, $B/w=6.8$
- C.6b Octahedral shear strain contours around simple plate, $B/w=20$
- C.6c Octahedral shear strain contours around simple plate, $B/w=32.5$
- C.7 Octahedral shear strain around simple plate
- C.8 Octahedral shear strain around simple with R_{eq} normalization
- C.9a Strain paths around soil elements Simple Plate in the $y/w = 0$ plane, $B/w=6.8$
- C.9b Strain paths around soil elements Simple Plate in the $y/w = 0$ plane, $B/w=20$
- C.9c Strain paths around soil elements Simple Plate in the $y/w = 0$ plane, $B/w=32.5$
- C.10 Example strain paths for soil elements around Simple Plate, $B/w = 6.8$,
with $y_0/w=6.8$
- D.1 Deformation Grids during Self-boring Penetration, $B/t=12$: a) $f=0$, b) $f=1$
- D.2 Strain Paths during Self-Boring Penetration, $B/t=12$:
 - a) E_1 versus E_2
 - b) E_3 versus E_2
- D.3 Lateral Distribution of Stresses and Pore Pressures far above Penetrometer
Tip during Self-Boring Penetration:
 - a) MCC
 - b) MIT-E3

1. INTRODUCTION

The primary aims of geotechnical exploration programs are a) to determine the location and general nature of the soil strata and b) to estimate the relevant engineering properties (strength, permeability, etc.). These are typically achieved using a combination of field and laboratory tests.

Laboratory investigations can range from simple index tests on highly disturbed samples to measurement of engineering properties under well controlled test conditions on 'undisturbed' specimens obtained using sophisticated sampling techniques. The latter tests are designed with well-defined boundary and drainage conditions to simplify interpretation of engineering properties. However, obtaining high quality 'undisturbed' samples and performing sophisticated tests can be time consuming and expensive. A second disadvantage of laboratory tests is that the small sample sizes required often do not permit an accurate picture of the effects of macrostructure; e.g., the effects of fissures or layering. A final disadvantage with laboratory testing is the difficulty in assessing the effects of sample disturbance. This problem has been widely recognized in the geotechnical profession and has led to the development of improved sampling techniques (block samples, foil sampler, etc.) as well as to the development of laboratory procedures which attempt to compensate for sample disturbance (Bjerrum, 1972; Ladd and Foott, 1974).

The above deficiencies associated with laboratory testing have given impetus for the development of in situ testing¹ for defining subsurface stratigraphy and engineering properties. In situ tests offer a number of advantages (Jamiolkowski et al., 1985) including:

1. They can be carried out in deposits where sampling is difficult (cohesionless soils) or laboratory testing is unreliable (soils with intense macro-fabrics such as highly layered or fissured soils).
2. Soils are tested in their natural environment, offering the possibility of measuring the in-situ stress state directly.
3. A larger volume of soil is tested than in most laboratory tests, hence in situ tests can more accurately reflect the effects of macro-fabric.

However, these tests suffer from a number of inherent limitations:

1. The boundary conditions are generally poorly defined (in terms of stresses and strains).

¹In situ' measurements can refer to both direct sensing devices such as cone penetrometers and plate load tests as well as remote sensing using geophysical techniques. This report considers only direct sensing devices.

2. The drainage conditions cannot be controlled and are often unknown. Thus it is difficult to estimate soil properties (e.g., shear strength) which depend upon effective stresses acting on the soil skeleton.
3. The modes of shearing are generally different from those imposed in standard types of laboratory tests.
4. The strain fields are generally non-uniform, and the strain rates are often much higher than those applied in laboratory tests or anticipated in the prototype problem.
5. With the exception of the Standard Penetration Test (SPT), the soil is not directly observed in the tests.
6. The mechanical installation of in-situ test devices in the ground inevitably causes disturbance of the surrounding soil. For devices such as the piezocone, measurements of tip resistance and excess pore pressure are manifestations of stress changes induced in the soil by the installation process. Qualitatively similar disturbances can be expected from other "displacement" penetrometers including earth pressure cells, field vanes, the Marchetti dilatometer, the Iowa stepped blade, the push-in pressuremeter, etc. In contrast, the design of the self-boring pressuremeter (SBPM; e.g.; Wroth and Hughes, 1973) attempts to minimize disturbance by removing soil in order to accommodate the volume of the device.

These limitations have often led to an empirical interpretation of in situ tests measurements, in which in situ test measurements are correlated to 'known' reference soil parameters. The Marchetti dilatometer (Marchetti, 1980; Chapter 4) is an example of an in situ test which is currently interpreted based on purely empirical correlations. This approach suffers from the following limitations:

1. The reference soil parameters may be unreliable. This is particularly the case when dealing with the in situ horizontal stress state, σ_{h0} , for which it is very difficult to provide satisfactory estimates by means of either field or laboratory tests.
2. Without a fundamental understanding of the factors which control in situ test measurements, it is difficult to determine which parameters have the most influence on test measurements; i.e., which soil parameters for which reliable correlations can be developed.

These above-mentioned limitations have provided a motivation for a rational interpretation of test results. This approach starts by performing the inverse of the interpretation process; i.e., a given in situ test measurement is predicted based on a known set of soil parameters. Ideally, the number of test measurements will balance the number of soil parameters affecting those measurements, and the inverse process of interpretation can proceed uniquely. In practice, however, due to the complex behavior of soil, the number

of soil parameters will exceed the number of test measurements. Thus, the primary aims of rational interpretation can be restated as follows:

1. To identify which soil parameter(s) have a predominating influence on test measurements; i.e., to determine which soil parameters can most reliably be estimated from measurements. The number of independent parameters estimated cannot exceed the number of independent measurements.
2. To establish the degree of reliability that can be expected when estimating the magnitude of a soil parameter from test measurements.

Additional objectives of a rational interpretation of in-situ tests include gaining an improved understanding of other factors on test measurements, such as: a) the effect of porous filter location in piezocone design, b) the effect of device geometry (flat plate versus axisymmetric), and c) to compare the effects of installation disturbance for different modes of installation (e.g.; displacement versus self-boring pressuremeter tests).

A rational approach to in situ test interpretation requires an analytical framework for relating soil properties to measurements. Analytical methods are required to model three aspects of in situ tests: 1) deep penetration (for prediction of installation measurements as well as for providing initial conditions for subsequent testing activities), 2) consolidation around a penetrometer following device installation, and 3) undrained shearing following device installation. The analyses described in this report use the Strain Path Method (Baligh, 1985a, 1986a, b) to simulate mechanisms of undrained steady penetration in clays. Soil behavior is modelled using generalized effective stress models including Modified Cam Clay (Roscoe and Burland, 1968) and MIT-E3 (Whittle, 1987) which describe the stress-strain-strength response throughout the tests. Post-installation test procedures are modelled using non-linear finite element methods².

In principle, analysis of deep penetration can be achieved numerically by finite element solutions. However, due to the high gradients near the penetrometers and the fine resolutions needed, realistic solutions that will help develop a basic understanding of disturbance are beyond the reach of existing computers. Approximate solutions for deep penetration in saturated clays have included bearing capacity methods (Meyerhof, 1961; Durgunoglu and Mitchell, 1975), cavity expansion methods (Bishop et al., 1945; Randolph et al., 1979), finite element analysis of loading of a pre-bored hole (deBorst and Vermeer, 1982) and the Strain Path Method (SPM; Baligh, 1985). Bearing capacity methods are unsuitable for the current work due to the following limitations: 1) the rigid-plastic assumption does not permit any account to be given to the energy absorbed in

²Using the commercially available finite element code ABAQUS which incorporates the generalized effective stress soil models (Hashash, 1992).

elastic straining, and 2) the deformational response of the soil is not considered, 3) the solutions are based on approximate collapse mechanisms which do not simulate accurately the steady deep penetration process. Cavity expansion solutions assume one-dimensional radial displacements in the soil and do not account for the path dependent nature of soil behavior (Baligh, 1986 a,b). Previous studies have shown the limitations of cavity expansion methods in predicting effective stresses around piezocones (Levadoux and Baigh, 1980) and pile shafts (Kavvas, 1982; Whittle, 1987). Finite element analysis of the loading of a pre-bored hole (e.g.; deBorst and Vermeer, 1982) provides solutions which satisfy both the field equations and the material constitutive law. However, the analyses use unrealistic initial conditions and require large displacements to achieve steady conditions.

The Strain Path Method (Baligh, 1985a) is an approximate method, which is based on the assumption, that due to the severe kinematic constraints involved in deep penetration problems, the strain fields are independent of the shearing resistance of the soil. This method has the advantage over cavity expansion methods that the two- (or three-) dimensional nature of deep penetration can be modelled. Using the Strain Path Method, excess pore pressures during penetration are obtained by integrating the equations of static equilibrium using the predicted fields of effective stresses. Due to the analytical approximations in the SPM, the equilibrium conditions are not satisfied uniquely, and the excess pore pressures are found to be integration path dependent (Levadoux and Baligh, 1980). In previous studies, excess pore pressures ahead of the penetrometer tip were estimated from vertical equilibrium conditions (Elghaib, 1989), while conditions around the shaft of long axisymmetric penetrometers were found from radial equilibrium (Levadoux and Baligh, 1980; Whittle, 1987). This preferential selection of integration path cannot be used reliably to establish the distribution of excess pore pressures around a penetrometer. Chapter 2 describes a robust numerical method which solves the equilibrium conditions in the form of a single Poisson equation. This method ameliorates the path dependence of pore pressures and provides a rational method for estimating pore pressures around penetrometers of general shape.

Although simple models of soil behavior provide useful physical insights into the underlying mechanics of deep penetration in clays (e.g.; Baligh, 1986a; Teh and Houlsby, 1989), more comprehensive constitutive equations are necessary in order to achieve reliable predictions of effective stresses and pore pressures during installation and subsequent test procedures. The analyses in this research use two particular effective stress models to describe clay behavior:

1. Modified Cam Clay (MCC; Roscoe and Burland, 1968) is the most widely used effective stress model in geotechnical analysis (e.g.; Gens and Potts, 1988). The model formulation uses the incremental theory of rate independent elasto-plasticity and is characterized by an isotropic yield functions, associated plastic flow, and density hardening. The version of the model used in this study uses a von Mises generalization of the yield surface.
2. MIT-E3 (Whittle, 1990, 1992) is a significantly more complex elasto-plastic model which describes many aspects of rate-independent behavior of K_0 -consolidated clays, which exhibit normalized behavior, including: a) small-strain non-linearity, b) anisotropic stress-strain-strength; c) hysteretic and inelastic behavior due to cyclic loading.

This report presents predictions of in-situ measurements for tests performed in K_0 -consolidated Boston Blue Clay (with $1 \leq OCR \leq 4$). Whittle (1987, 1990) has described the selection of model input parameters for this material and has presented a detailed evaluation of model predictive capabilities with extensive laboratory test data.

Chapter 3 reviews existing empirical correlations for undrained shear strength and stress history from piezocone measurements of tip resistance and excess pore pressures during steady penetration. Strain Path predictions of effective stresses and excess pore pressures are then obtained for piezocone tests performed in Boston Blue Clay ($1 \leq OCR \leq 4$), as described by the MCC and MIT-E3 soil models. These predictions extend earlier analyses presented by Baligh and Levadoux (1980) and provide a more comprehensive study of the effects of soil properties and stress history on penetration measurements. The predictions are evaluated through direct comparison with field measurements in Boston Blue Clay at the Saugus and South Boston sites (Baligh and Levadoux, 1980; Ladd, 1991). Further comparisons with data from other well-documented sites give an indication of the variability of piezocone measurements in other clay deposits. The predictions also provide a basis for evaluating the relative reliability of correlations between penetration measurements and engineering measurements.

Chapter 4 applies a similar methodology to assess the contact pressure measurements obtained using the flat-plate dilatometer (Marchetti, 1980). Strain Path predictions are modelled using "simple plate" geometries (Whittle et al. 1991; Rafalovich, 1991). The chapter presents complete predictions of effective stresses and excess pore pressures around the dilatometer, from which the lateral contact pressures are computed. The analyses show the effects of soil properties and stress history on the predicted contact pressures, which are then used to evaluate empirical correlations for in-situ lateral pressures (K_0), stress history, and undrained shear strength. The results also a) provide valuable

insight into the influence of the location of the dilatometer membrane on the measured data, and b) enable dilatometer measurements to be compared with lateral stress data obtained around the shaft of axisymmetric penetrometers. Measurements from South Boston (Ladd, 1991) and a number of well-documented sites are used to evaluate the predictions.

Chapter 5 uses the penetration predictions of soil stresses and excess pore pressures as initial conditions for analyzing the consolidation process which occurs when piezocone penetration is interrupted. Finite element analyses (using the ABAQUS program) solve the two-dimensional, coupled flow and deformation in the soil with non-linear stress-strain behavior described consistently by generalized effective stress soil models (MCC and MIT-E3). *The chapter presents complete predictions of excess pore pressure dissipation and effective stress changes for piezocone dissipation test performed in Boston Blue Clay with $1 \leq OCR \leq 4$.* The results compare dissipation behavior for porous filters at different locations around the penetrometer. The solutions are then used to interpret the coefficient of permeability from field measurements around the piezocone (Levadoux and Baligh, 1986b) and the piezo-lateral stress cell (Morrison, 1984) at the Saugus test site. Further comparisons are presented for laboratory calibration chamber measurements in kaolin (Nyirenda, 1989). These results provide the basis for assessing whether permeability can be estimated reliably from piezocone dissipation measurements.

Cylindrical cavity expansion theory provides a sound theoretical framework for predicting and interpreting the undrained shear strength of clays from pressuremeter expansion curves. However, extensive experience has shown that disturbance caused by device installation can affect significantly the interpreted undrained shear strength. Chapter 6 applies Strain Path analyses to predict the soil stresses and excess pore pressures generated by device installation of displacement (full-displacement and push-in geometries) and self-boring pressuremeters in Boston Blue Clay. These installation disturbances represent initial conditions for prediction of the undrained pressuremeter test. Undrained shear strengths are then derived from predicted pressuremeter measurements and compared to the real soil behavior. The analyses investigate the effects of: a) installation method, b) dissipation of excess pore pressures prior to membrane expansion, c) stress history, d) the use of the pressuremeter expansion versus contraction curve for estimating undrained shear strength, and f) finite membrane length effects. Predicted pressuremeter measurements are compared directly to self-boring pressuremeter test measurements in Boston Blue Clay from the South Boston site.

2. PENETRATION PORE PRESSURES FROM STRAIN PATH METHOD

2.1 INTRODUCTION

The undrained penetration of intrusive test devices (e.g. piezocone, field vane, dilatometer, etc.) in low permeability clay deposits leads to the development of excess pore pressures in the soil. For normally and moderately overconsolidated clays, these pore pressures are large and dominate other soil stresses and hence hold the key to the understanding of penetration mechanisms (Baligh, 1986b). Reliable analytical predictions of penetration pore pressures are essential if engineering properties of soils are to be interpreted rationally from in-situ measurements, both during penetration and in subsequent activities such as dissipation and holding tests, membrane expansion, vane rotation, etc.

Using the Strain Path Method (SPM), the effective (or deviatoric) stresses around a penetrometer are determined from the strain paths of soil elements using an appropriate soil model. The pore pressures can then be estimated by integrating the equilibrium equations from the known field of effective (or deviatoric) stresses. Due to the approximate nature of the strain and stress fields computed from the SPM, equilibrium will not be satisfied uniquely. This chapter discusses the implementation of a method which gives an 'averaged' pore pressure field obtained by solving the complete set of equilibrium equations in the form of a Poisson solution.

The method outlined in this chapter has two advantages: 1) it is rational and minimizes the need for subjective judgement to estimate the distribution of pore pressures; and 2) it can be used for penetrometers of general shape, and hence can be used to unify the interpretation of installation disturbance for different types of in-situ tests used in geotechnical practice, including axisymmetric and flat plate penetrometers.

2.2 BACKGROUND

Deep penetration problems are commonly modelled as the undrained expansion of spherical or cylindrical cavities. For cylindrical cavity expansion (Soderberg, 1962; Butterfield and Bannerjee, 1970; and Randolph et al., 1978), the soil is assumed to deform under plane strain and axisymmetric conditions, and displacements occur only in the radial direction. In this case the strain components can be obtained solely by the kinematics of

deformation and are given by:

$$\epsilon_{rr} = \frac{1}{2} \ln \left[1 + \left(\frac{R}{r_0} \right)^2 \right]; \quad \epsilon_{\theta\theta} = -\epsilon_{rr}; \quad \epsilon_{zz} = \epsilon_{rz} = 0 \quad (2.1)$$

Stresses in the soil mass can then be estimated from the known strain field using an appropriate constitutive model.

Baligh (1975, 1984) suggests that the Cavity Expansion Method (CEM) is too simplistic to describe the two-dimensional nature of the problem. Baligh (1985a, 1986a, b) also proposed the Strain Path Method (SPM), which provides a general analytical framework for describing the mechanics of quasi-static, steady, undrained deep penetration in saturated clay. The method assumes that, due to the severe kinematic constraints in deep penetration problems, deformations and strains are essentially independent of the shearing resistance of the soil, and can be estimated with reasonable accuracy based only on kinematic considerations and boundary conditions. By considering the two-dimensional deformations of soil elements, SPM analyses provide a more realistic framework for describing the mechanics of deep penetration problems than one-dimensional (cylindrical or spherical) cavity expansion methods, and can account properly for the effects of non-linear and inelastic soil behavior. On the other hand, the assumptions of strain-controlled behavior used in the Strain Path Method greatly simplify the problem of steady deep penetration and avoid the complexity of large scale numerical (finite element) analyses.

The analysis of steady deep penetration problems using the Strain Path Method (Baligh, 1985a, 1986a, b) includes the following steps (Figure 2.1):

- Step 1. Soil deformations are considered in terms of the steady flow of soil around a static penetrometer. Approximate velocity fields are estimated from potential theory (i.e., treating the soil as an incompressible, inviscid and irrotational fluid) and are differentiated with respect to the spatial coordinates in order to obtain strain rates ($\dot{\epsilon}_{ij}$). For the case of a penetrometer generated by a point source of incompressible material in a uniform flow field (the simple pile), solutions can be obtained in closed form (Baligh, 1985b; Teh & Houlsby, 1989). More complex geometries require numerical methods such as the methods of sources and sinks (Weinstein, 1948; Rouse, 1959) or boundary element methods (Williamson, 1989).
- Step 2. Integration of the strain rates along the streamlines defines the strain paths (histories) for individual soil elements moving around the penetrometer. Baligh (1985b) shows that soil elements are subject to complex histories of straining

involving reversals of individual strain components, as illustrated in Figure 2.2, which shows the strain paths in the triaxial compression (E_1), the pressuremeter (E_2), and the simple shear (E_3) shearing modes during simple penetration, where E_1 , E_2 , and E_3 are defined in the figure. In this case both the E_1 and E_3 components experience reversals, while E_2 increases monotonically. SPM predictions by Levadoux and Baligh (1980) showed that during penetration of 18° and 60° cones reversal of the E_2 component also occur. It can also be seen from this figure that the absence of a particular deformation mode at the end of penetration does not imply that the soil element did experience that deformation mode during penetration.

Step 3. Stress fields around the penetrometer estimated from the strain paths using either a) an effective stress approach in which the effective stresses, σ'_{ij} , are determined using a generalized effective stress soil model to characterize the constitutive behavior of the soil; or b) a total stress approach in which the deviatoric stresses, s_{ij} , and the shear-induced pore pressures, Δu_s , are determined separately using two constitutive models of soil behavior (Levadoux and Baligh, 1980; Baligh, 1985c, 1986a, b). The effective stress approach has the advantage that the same model can be used to study the consolidation process after installation. Input parameters for models (for both effective stress analysis and total stress analysis) include initial total stresses and pore pressures in the ground (σ_{ij}^0, u_0), together with (model specific) material properties. Baligh (1986a,b) shows that ahead of the penetrometer tip the soil is loaded primarily in a triaxial compression mode with no strain reversals; consequently, the predicted stress components, s_{ij} , are not sensitive to inelastic effects. By contrast, soil elements located near the penetrometer boundary above the tip have experienced extensive reversals of individual strain components and are therefore most sensitive to inelastic effects. Predictions in this region therefore require more realistic soil models incorporating the effects of anisotropy and strain softening. Previous studies (Baligh, 1986b; Whittle & Baligh, 1990) have shown that realistic predictions of effective stresses acting at the indenter-soil interface can be achieved using comprehensive soil models (Whittle, 1987, 1990) which incorporate strain softening, small strain non-linearity and anisotropic properties of clay.

Step 4. Baligh (1985a) shows that, since the effects of gravity on stress changes in deep foundation problems are negligible, the equilibrium equations in a cartesian frame

can be expressed in terms of total stresses as:

$$\frac{\partial \sigma_{ij}}{\partial x_j} = 0 \quad (2.2)$$

in which $x_i (=x_1, x_2, x_3)$ are the coordinates of a material point and repeated indices imply summation over 1, 2, and 3. By invoking the effective stress principle, $\sigma_{ij} = \sigma'_{ij} + \delta_{ij} u$,¹ he shows that

$$\frac{\partial u}{\partial x_i} = - \frac{\partial \sigma'_{ij}}{\partial x_j} = g_i \quad (2.3)$$

Alternatively, from a known field of deviatoric stresses, the changes in mean total stress, $\Delta \sigma$, is determined from:

$$\frac{\partial \sigma}{\partial x_j} = - \frac{\partial s_{ij}}{\partial x_j} \quad (2.4)$$

whereupon, the excess pore pressure can be computed from:

$$\Delta u = \Delta \sigma + \Delta u_s \quad (2.5)$$

For axisymmetric problems, the equilibrium equations in terms of effective stresses can be expressed in a cylindrical coordinate frame as:

$$- \frac{\partial u}{\partial r} = - g_r = \frac{\partial \sigma'_{rr}}{\partial r} + \frac{\partial \sigma'_{rz}}{\partial z} + \frac{\sigma'_{rr} - \sigma'_{\theta\theta}}{r} \quad (2.6a)$$

$$- \frac{\partial u}{\partial z} = - g_z = \frac{\partial \sigma'_{zz}}{\partial z} + \frac{\partial \sigma'_{rz}}{\partial r} + \frac{\sigma'_{rz}}{r} \quad (2.6b)$$

¹ where δ_{ij} is the Kronecker defined by:

$$\delta_{ij} = \begin{cases} 1 & i=j \\ 0 & i \neq j \end{cases}$$

In principle, the pore pressures can be calculated by integrating in either the radial or vertical (z) direction (using the known distributions g_r , g_z , respectively). If the stress fields are exact, the predicted pore pressure will be independent of the path of integration and the stress gradients will satisfy the relation:

$$\frac{\partial g_r}{\partial z} = \frac{\partial g_z}{\partial r} \quad (2.7)$$

This condition is only satisfied if the strain paths are compatible with the model used to determine the stresses. However, from step 1, the strains are approximated using potential flow theory and are not compatible with the soil model used in step 3.

Figure 2.3 illustrates the potential differences in predictions of pore pressures that can arise by satisfying equilibrium in different directions. The figure shows the distribution of excess pore pressures, $(u-u_0)/\sigma'_{v0}$, at points along the surface of 18 and 60° cone penetrometers and at vertical locations ahead of the penetrometer tip. The initial fields of effective stresses were predicted using the Modified Cam Clay soil model (MCC; Roscoe & Burland, 1968) with material properties selected to represent the behavior of K_0 -normally consolidated Boston Blue Clay (Whittle, 1987). This model has the advantage that it is formulated in terms of effective stresses; and it is isotropic and has a well defined critical state condition, so it can be readily interpreted. Unless otherwise stated, this case is used in subsequent analyses illustrated in this chapter. The results show the following:

1. For both the 18° and 60° cones the Poisson solution approximately coincides with the radial integration solution ($\Delta u^r = \int g_r dr$).
2. In the vicinity of the 60° cone, the Poisson solution tends to be between the vertical ($\Delta u^z = \int g_z dz$) and radial equilibrium solutions. At the tip the Poisson solution is 20% greater than the radial integration solution and 20% less than the vertical integration solution. Ahead of the tip the Poisson solution closely matches the radial integration solution and substantially underpredicts the vertical integration solution.
3. For the 18° cone the Poisson solution is much closer to the radial integration solution and near the tip predicts a much lower (40-50%) pore pressure than the vertical integration solution.
4. The vertical equilibrium equation suggests that apex angle has little effect on pore pressures near the tip.

Non-uniqueness of pore pressure (or octahedral stress) fields was first observed by Levadoux and Baligh (1980) by integrating the equilibrium equations along isochrones and streamlines, where isochrones are lines describing the deformed geometry of originally horizontal lines in the soil and streamlines correspond to orthogonal lines of the deformed mesh of soil. Their results for isochronic and streamline integration showed differences similar to those shown in Figure 2.3 for vertical and radial integration. They attributed the differences, in large part, to unrealistic predictions in σ'_{rz} , which contributes significantly to equilibrium in the vertical direction. Subsequent fields of pore pressure reported by Levadoux and Baligh (1980) were based on isochronic integration only.

The nature of the uncertainty in σ'_{rz} predictions and its impact on vertical integration solutions are illustrated by considering region far above the penetrometer tip, where $\partial\sigma'_{ij}/\partial z = 0$. In this case Equation 2.6b reduces to

$$-\frac{\partial u}{\partial z} = -g_z = \frac{\partial \sigma'_{rz}}{\partial r} + \frac{\sigma'_{rz}}{r} \quad (2.8)$$

For a steady condition ($\partial u/\partial z = 0$), $\partial \sigma'_{rz}/\partial r$ must equal $-\sigma'_{rz}/r$; however, SPM predictions (Levadoux, 1980) of σ'_{rz} indicate both $\partial \sigma'_{rz}/\partial r$ and σ'_{rz}/r to be positive near the penetrometer boundary far above the tip. This implies that pore pressures will decrease indefinitely in the vertical direction far above the penetrometer tip. This unreasonable result shows that vertical integration solutions are unreliable above the cone tip.

To mitigate discrepancies between vertical and radial integration solutions, Chin (1986) integrated the equilibrium equations in a polar direction (the ϕ -direction) in spherical coordinates, using deviatoric stress fields based an elastic-perfectly-plastic soil model. His results showed that for $(z/R) > 0$ polar integration provides a smooth and continuous transition between the vertical and radial integration. But far above the tip, polar integration did not match the steady-state radial integration solutions and should therefore be considered unreliable.

Subsequent studies have shown that:

1. In the region ahead of the cone tip, since the soil is subject to triaxial compression modes of shearing only, Baligh (1986b) and Elghaib (1989) proposed that vertical equilibrium can reliably be used to estimate pore pressures at the tip of a piezocone.
2. Far behind the penetrometer tip, predictions of excess pore pressures can be obtained from radial equilibrium. Predicted stresses in this region are very susceptible to

inelastic effects (Baligh 1986a) due to reversal of individual strain components. Consequently, predicted pore pressures will be strongly influenced by complex aspects of soil behavior including anisotropy, strain softening and rate dependence.

2.3 EQUILIBRIUM CORRECTION

As discussed above, vertical equilibrium controls the pore pressures ahead of the cone tip, while radial equilibrium controls the shaft pore pressures on the shaft far above the tip. For other locations around the cone, the path dependence in the predicted pore pressures represents a major source of uncertainty in the analysis. Equilibrium imbalance can be dealt with by two possible approaches: a) applying corrections to the initial SPM stress and strain fields to reduce disequilibrium, or b) adoption of a scheme which satisfies the two equilibrium equations (equations 2.6a and b) predicted from the SPM in an 'average' sense.

Iterative schemes for correcting the equilibrium imbalance have been proposed by a number of authors (Baligh, 1985a; Teh, 1987). Teh (1987) proposed a number of iterative corrections including:

1. Newton-Raphson Correction.- Using an error term defined in terms of the curl of \mathbf{g} such that

$$\mathbf{H} = \nabla \times \mathbf{g} \quad (2.9)$$

the SPM stream functions ψ are successively corrected to approximately eliminate \mathbf{H} , using a Newton-Raphson iteration scheme. This scheme was found to converge very rapidly in regions where no plastic deformations occur, but convergence could not be achieved in regions of plastic deformation. Since realistic solutions for penetration must consider plastic deformations, this approach cannot provide useful corrections.

2. Finite Element Correction.- Using stress fields from SPM predictions, out-of-balance nodal forces are computed based on equilibrium equations. These out-of-balance forces are eliminated by incrementally applying equal but opposite nodal forces in a conventional finite element analysis. Convergence could not be achieved by this scheme. Teh (1987) attributed the lack of convergence to be due, in part, to numerical difficulties involved in interpolation of stresses from the SPM grid to the finite element

grid.

Another equilibrium correction approach has been to include the strain path solutions as initial conditions in a finite element analysis (Teh & Houlsby, 1989). In this method, the deviatoric stresses during an increment of penetration are computed based on a SPM solution. The out-of-balance forces occurring during this penetration increment are then computed based on equilibrium considerations. While holding the cone fixed, the initial SPM displacements are modified by incrementally applying nodal forces equal and opposite to the out-of-balance forces. This process is then repeated for the next increment of cone penetration. Some disadvantages to this approach include:

1. The large strains involved in this analysis require a large strain formulation, which increases the complexity of the analysis.
2. Computation of the out-of-balance forces requires an arbitrary selection regarding which equilibrium equation is correct (radial or vertical). In situations where vertical and radial equilibrium solutions differ significantly from one another, such an arbitrary selection can conceivably have a significant effect on the final result. The arbitrary selection of one equilibrium equation to be correct is particularly unattractive when the SPM is extended to penetrometers of general geometry (plates, vanes, etc.), as a different set of assumptions will be required for each different geometry that is analyzed.

2.4 PROPOSED POISSON FORMULATION

An alternative approach (Baligh, 1985a), which can ameliorate the difficulties associated with path dependent pore pressures, is to solve both equilibrium equations by taking the divergence of eqn. 2.3:

$$\nabla^2 u = - \nabla \cdot \mathbf{g} = - q \quad (2.10)$$

In this case the scalar pore pressure field is determined as the solution of a Poisson equation using standard finite element techniques. In general, Poisson pore pressure fields will not satisfy either equilibrium equation exactly. However, the Poisson solution does not rely upon an arbitrary selection of an integration path; it therefore provides a flexible method for extending SPM solutions to penetrometers of general shape.

The Poisson solution was first implemented by Chin and Whittle (1984) for simple pile penetration in a bilinear soil model. They reported results which were in reasonable agreement with radial integration solutions, except near at the tip and face of the pile. The inaccuracies near the tip were probably due to a) inaccuracies of the numerical differentiation in regions of high stress gradients, and b) an improperly formulated boundary condition at the indenter interface. Teh (1987) subsequently implemented a Poisson solution (also using a bilinear model) with a properly formulated boundary condition; however, his predicted distribution of mean stress ahead of the tip was much too low, being much less than his predicted mean stress distributions obtained by radial and vertical integration.

In principle, the flux term, q , is calculated by numerical differentiation (first and second derivatives) of the stress components from the strain path method. However, accurate numerical evaluation of second derivatives is very difficult to achieve, especially in regions of high stress gradients. Considerable simplifications in computing can be achieved using the divergence theorem to estimate an average flux within a given finite element:

$$\int_V q \, dV = \int_A \mathbf{g} \cdot \mathbf{n} \, dS \quad (2.11)$$

$$\bar{q} V = \sum_{i=1}^n (\mathbf{g} \cdot \mathbf{n})_i \Delta S_i \quad (2.12)$$

where; \bar{q} = average q within element

V = volume of element

\mathbf{g} = pore pressure gradient vector on side i
of the n -sided element

\mathbf{n} = unit vector normal to side i of the element

S_i = Surface area of side i of the element

The numerical procedure for evaluating derivatives of stress components (\mathbf{g}) is based on the construction of nine node isoparametric elements (Bathe, 1982), where three closely spaced streamlines are used to define a nine-node element around the point of interest. An isoparametric differentiation scheme permits data points from the streamlines (see Section

2.2, steps 2 and 3) to be used directly without intermediate interpolation onto a finite difference grid. A natural coordinate system (s,t) is introduced to enable standard isoparametric interpolation of the stress derivatives at the point (Bathe, 1982):

$$\frac{\partial \sigma'_{ij}}{\partial s} = \frac{\partial h_n}{\partial t} \sigma'_{ij}{}^n ; \quad \frac{\partial \sigma'_{ij}}{\partial t} = \frac{\partial h_n}{\partial t} \sigma'_{ij}{}^n \quad (2.13)$$

where h_n are the interpolation functions shown in Appendix B, and $\sigma'_{ij}{}^n$ are the effective stresses computed at the nodal points. The derivatives in the (r,z) coordinate frame are obtained through a Jacobian transformation:

$$\begin{pmatrix} \frac{\partial}{\partial r} \\ \frac{\partial}{\partial z} \end{pmatrix} = \begin{bmatrix} \frac{\partial r}{\partial s} & \frac{\partial z}{\partial s} \\ \frac{\partial r}{\partial t} & \frac{\partial z}{\partial t} \end{bmatrix} \begin{pmatrix} \frac{\partial}{\partial s} \\ \frac{\partial}{\partial t} \end{pmatrix} \quad (2.14)$$

Boundary conditions for the Poisson equation (locations A,B,C,D are shown schematically in fig. 2.3) include: 1) $\partial u / \partial r = 0$, due to symmetry, along the centreline (OD); 2) $u = 0$, along BCD (assuming soil behavior is linear far from the penetrometer); and 3) $\partial u / \partial z = 0$, to satisfy steady state conditions along AB. The most difficult boundary condition is that at the penetrometer boundary (OA), as it has no simple physical interpretation and there is no reason to assume that there are no pore pressure gradients normal to this boundary ($\partial u / \partial n \neq 0$). This boundary is treated in an approximate manner by computing the gradients adjacent to the indenter interface (g_r and g_z) and imposing the condition:

$$g_n = g_r n_r + g_z n_z \quad (2.15)$$

Poisson solutions for normalized excess pore pressure, $(u - u_0) / \sigma'_{v0}$, during 18° and 60° cone penetration in the K_0 -normally consolidated BBC described in section 2.2.1 are shown in figure 2.3. These solutions show:

1. At the base of the cones the normalized excess pore pressures predicted from the Poisson solutions are 10 to 20% greater than the those predicted from radial integration. As a steady state is approached, the Poisson solutions match the radial integration solutions.

2. The normalized excess pore pressure at the tip of the 60° cone predicted from the Poisson solution is approximately 25% less than that predicted by the vertical integration solution. On the centerline ahead of the cone tip the differences between the Poisson solution and the vertical integration solution become more significant.
3. The normalized excess pore pressure at the tip and on the face of the 18° cone predicted from the Poisson solution are essentially zero up to within $R/4$ ahead of the tip. This differs significantly from the vertical integration solution, which indicates substantial excess pore pressures to within $10R$ ahead of the tip.

These observations suggest the following conclusions:

1. Far above the cone tip, the Poisson solutions match the radial integration solutions. Since radial integration solutions are considered to be very reliable in this region, the Poisson solutions can accordingly be considered to be reliable in this area.
2. On the cone face and on the centerline ahead of the cone tip, the Poisson solutions differ substantially from the vertical integration solutions. The differences between the Poisson solutions and the vertical integration solutions increase with decreasing cone angle. The discrepancies between Poisson and vertical integration solutions ahead of the tip are serious for two reasons: a) the vertical equilibrium equation is considered to be reliable ahead of the tip, and b) the Poisson solutions imply that tip angle has a major influence on magnitudes of tip pore pressures, which is contrary to measured data (Levadoux and Baligh, 1980). Accordingly, the excess pore pressures on the cone face and ahead of the cone tip predicted from the Poisson solution cannot be considered reliable, particularly for sharp cone angles.

2.5 THE MODIFIED POISSON FORMULATION

Since the vertical equilibrium equation is considered to be more reliable ahead of the cone tip, the Poisson solutions described in the previous section can be improved by considering only the vertical equilibrium equation in the region ahead of the tip. If the pore pressure field u^z is computed based on vertical integration using Equation 2.6b, the flux term q based solely on vertical equilibrium can then be determined by computing the Laplacian of u^z

$$q = \nabla^2 u^z \quad (2.16)$$

For implementation in a finite element solution, the equivalent nodal loads corresponding to Equation 2.16 are required. These can be computed by a simple matrix multiplication

$$\{ q_e \} = [K] \{ u^z \} \quad (2.17)$$

where $[K]$ is the system conductivity matrix which is used in the solution of the Poisson equation.

To implement the modified Poisson solution, a rational means is required for identifying the extent of the zone ahead of the tip which is dominated by vertical equilibrium equation. To assess the contribution of the radial and vertical equilibrium equations to the total value of q defined in equation 2.10, the following scalar terms were defined

$$\text{Radial Equilibrium Contribution: } q^r = \frac{g_r}{r} + \frac{\partial g_r}{\partial r} \quad (2.18a)$$

$$\text{Vertical Equilibrium Contribution: } q^z = \frac{\partial g_z}{\partial z} \quad (2.18b)$$

where $q = q^r + q^z$. A simple measure of the relative contribution of the vertical equilibrium equation can be defined as:

$$R_z = q^z / (|q^z| + |q^r|) \quad (2.19)$$

When vertical equilibrium dominates R_z will be unity, and when radial equilibrium predominates, R_z will be zero. Contours of R_z for 18° and 60° cone penetration are shown in Figure 2.4. These results indicate three regions:

1. Below line OA the vertical equilibrium is dominant ($R_z \approx 1$); except near the tip ($z/R < 3$).
2. Above line OB radial equilibrium the radial equilibrium is dominant ($R_z \approx 0$).
3. The area between OA and OB is a transition region where both equilibrium equations influence the solution ($0 < R_z < 1$).

To eliminate the influence of the unreliable radial equilibrium equation near the face and tip of the cone, the following modified Poisson procedure was adopted:

1. Subdivide the problem into two regions, which are separated by a line OA.
2. In the upper region compute q based on both equilibrium equations using Equation 2.10.
3. In the lower region compute q based solely on the vertical equilibrium equation using Equation 2.16.

Modified Poisson solutions for 18° and 60° cone penetration in K_0 -normally consolidated BBC based on effective stress fields from the MCC soil model are shown in Figure 2.5. Comparison to the integration solutions described in Section 2.2 and the modified Poisson solution described in Section 2.5 indicates:

1. For both cone angles, the normalized excess pore pressure near the cone tip predicted from the modified Poisson solution matches the vertical integration solution to within 5%. On the centerline ahead of the cone tip the modified Poisson solution agrees very well with the vertical integration solution.
2. On the shaft above the base of the cone the modified Poisson solutions are quite similar to the Poisson solutions, with the normalized excess pore pressures predicted from the modified Poisson solutions being a maximum of 15% greater than those predicted from the Poisson solutions. Far above the cone tip ($z/R > 15-20$), the modified Poisson solutions closely match the radial integration solutions.

The modified Poisson solutions therefore agree with integration solutions in two important areas:

1. Ahead of the cone tip they agree with solutions based on the vertical equilibrium equation, which have proved reliable in past studies (Elghaib, 1989).
2. Far above the cone tip they agree with radial integration solutions, which are most reliable in the steady state region far above the cone tip.

2.6 THE POISSON SOLUTION FOR THREE-DIMENSIONAL GEOMETRIES

Plate penetration problems can be described in a three-dimensional cartesian frame as shown in Figure 2.6, where the z -direction is vertical, the y -direction is parallel to the major (wide) axis of the plate, and the x -direction is parallel to the minor (thin) axis of the plate. Strain and stress field predictions during plate penetration are discussed in detail in

Appendix C. In a three-dimensional cartesian frame the equilibrium equations are

$$-\frac{\partial u}{\partial x} = -g_x = \frac{\partial \sigma'_{xx}}{\partial x} + \frac{\partial \sigma'_{xy}}{\partial y} + \frac{\partial \sigma'_{xz}}{\partial z} \quad (2.20a)$$

$$-\frac{\partial u}{\partial y} = -g_y = \frac{\partial \sigma'_{xy}}{\partial x} + \frac{\partial \sigma'_{yy}}{\partial y} + \frac{\partial \sigma'_{yz}}{\partial z} \quad (2.20b)$$

$$-\frac{\partial u}{\partial z} = -g_z = \frac{\partial \sigma'_{xz}}{\partial x} + \frac{\partial \sigma'_{yz}}{\partial y} + \frac{\partial \sigma'_{zz}}{\partial z} \quad (2.20c)$$

In principle, Equations 2.20 can be substituted into Equation 2.12, and pore pressures can be determined as the solution of a Poisson equation in three dimensions; however, the complexity and cost of three-dimensional finite element analyses can be avoided by using simplified two-dimensional analyses in two orthogonal planes ; namely: a) the $y=0$ plane, and b) $z=\text{constant}$ planes. The $y=0$ plane corresponds to a vertical plane on the centerline of a blade penetrometer. Physical measurements are often made in this plane during plate penetration; for example, the center of the membrane of the dilatometer and the pore pressure filter in the piezoblade are located in this plane. Predictions in this plane are accordingly quite important for validation of predictions and for assessing the vertical variation in pore pressures and total stresses along the dilatometer membrane during penetration. Predictions in $z=\text{constant}$ (horizontal) planes are important for predicting the horizontal variation in pore pressures and total stresses along the blade; for example, in assessing the horizontal variation in total horizontal stress along the membrane of a dilatometer.

2.6.1 Formulation in the $y=0$ plane

In the $y=0$ plane, the two relevant equilibrium equations become equations 2.20a and c. Derivatives of stress components in the x and z directions can be computed numerically using Equations 2.13 and 2.14. The $y=0$ plane is a plane of anti-symmetry with respect to the σ_{xy} and σ_{yz} stress components, as demonstrated in Appendix C; therefore, the partial derivatives with respect to these stress components cannot be assumed to be zero and must be evaluated numerically. Partial derivatives of these stress components with respect to y at a point (x^*, z^*) can be evaluated by the following steps:

1. Compute the stresses along three streamlines whose initial positions far ahead of the tip are offset a distance Δy from the $y=0$ plane. Δy is selected to be equal to the initial streamline spacing within the $y=0$ plane. This is typically $\Delta y/w = \Delta x/w = 0.1$, where w =plate half-thickness.
2. Evaluate the stress components $(\sigma'_{ij})_{y=\Delta y}$ at x^*, z^* by interpolation.
3. Evaluate the partial derivative by a first order finite difference approximation

$$\frac{\partial \sigma'_{ij}}{\partial y} \approx \frac{(\sigma'_{ij})_{y=\Delta y} - (\sigma'_{ij})_{y=0}}{\Delta y} \quad (2.21)$$

With g_x and g_z thus evaluated, excess pore pressures in the $y=0$ plane can be predicted by direct integration of the equilibrium equations as discussed in section 2.2 or by the modified Poisson solution discussed in section 2.5. Figure 2.7 illustrates the potential differences in predictions of pore pressures that can arise amongst these three solutions. The figure shows the distribution of excess pore pressures, $(u-u_0)/\sigma'_{v0}$, at points along the surface and at vertical locations ahead of the tip of a simple plate penetrometer having an aspect ratio $B/w=6.8$; where B is the half-length and w is the half-thickness of the plate. The simple plate is the penetrometer geometry defined by a line source of incompressible material of length $2B$ in a uniform flow field. The geometry of the simple plate is described in detail in section 4.2. This aspect ratio corresponds to the aspect ratio of the Marchetti dilatometer described in Chapter 4. The results show the following:

1. At the tip of the plate, excess pore pressures predicted from the modified Poisson solution match the vertical solution to within 10%. On the centerline ahead of the tip the modified Poisson solution closely matches the vertical integration solution. The horizontal integration solution underpredicts the vertical integration solution by approximately 20% at the plate tip. The horizontal integration solution substantially underpredicts the vertical integration and modified Poisson solutions on the centerline ahead of the plate tip.
2. Far above the plate tip the Poisson solution matches the horizontal integration solution. The two solutions begin to converge at approximately $z/w=40-50$.
3. Above the plate tip, vertical equilibrium pressures, Δu^z , decrease rapidly and become unbounded (i.e. continue to decrease with distance along the penetrometer), while horizontal equilibrium pressures reach a steady state solution at $z/w=40-50$.

These observed trends are qualitatively quite similar to the trends observed for

axisymmetric penetrometers which were discussed in sections 2.2 and 2.5. A major difference is the distance above the tip at which a steady condition is achieved. This is due to the fact that the plate in this example displaces a larger volume of soil than the axisymmetric penetrometers discussed in sections 2.2 through 2.5; that is, the plate has a cross-sectional area far above the tip equal to $4Bw$, while the cone penetrometers have a cross-sectional area equal to πR^2 . This difference can be accounted for by normalizing the plate coordinates by an equivalent radius, R_{eq} , which is defined as

$$R_{eq} = \sqrt{\frac{4Bw}{\pi}} \quad (2.22)$$

Figure 2.8 shows predictions of excess pore pressure around a plate after normalizing the plate coordinates by R_{eq} . Figure 2.8a shows the predicted distribution in the $y=0$ plane on the plate boundary and on the centerline ahead of the plate tip, and Figure 2.8b shows the predicted lateral distribution of excess pore pressures far above the plate tip. Comparing the plate predictions to the predicted distribution of pore pressures during simple pile ($B/w=0$) penetration indicates:

1. The normalized distance above the penetrometer tip at which a steady state pore pressure distribution is reached is $10-20z/R_{eq}$ for both the simple pile and the simple plate.
2. The predicted pore pressures at the penetrometer tips for the two penetrometer shapes match to within 15%. The predicted pore pressure distributions ahead of the tip pore are also quite similar to one another.
3. The lateral distribution of pore pressure far above the penetrometer tip for the simple plate and simple pile match quite closely, with the predicted pore pressures at the penetrometer boundaries agreeing to within 3%.

These observations imply:

1. Penetrometer geometry (aspect ratio) has a relatively small influence on magnitudes of tip and shaft pore pressures.
2. The extent of the zone of disturbance is strongly influenced by the volume of soil displaced during penetration. Penetrometer geometry does not significantly alter the extent of the zone of disturbance.

2.6.2 Formulation in $z=\text{constant}$ planes

In a horizontal plane the relevant equilibrium equations are equations 2.20a and b. For the special case of a plane located far above the plate tip these equations reduce to

$$-\frac{\partial u}{\partial x} = -g_x = \frac{\partial \sigma'_{xx}}{\partial x} + \frac{\partial \sigma'_{xy}}{\partial y} \quad (2.23a)$$

$$-\frac{\partial u}{\partial y} = -g_y = \frac{\partial \sigma'_{xy}}{\partial x} + \frac{\partial \sigma'_{yy}}{\partial y} \quad (2.23b)$$

The derivatives of the stress components in Equations 2.23 were evaluated using a 4-node isoparametric interpolation scheme (Bathe, 1982), where four closely spaced streamlines are used to define an element around the point of interest. A description of numerical differentiation using isoparametric functions is contained in section 2.4, and a listing of isoparametric functions and their derivatives for four-node elements is contained in Appendix B.

Equations 2.23 can be substituted into Equation 2.12, and pore pressures can be determined as a solution of a Poisson equation in the x-y plane. Pore pressure contours during installation of a $B/w=32.5$ plate as computed by integration solutions and the Poisson equation are shown in Figure 2.9. This figure indicates significant (on the order of 25%) differences between the two integration solutions. It further shows that the Poisson solution generally provides an 'average' between the two integration solutions in the vicinity of the penetrometer; although, in the far field in the x-direction, the Poisson solution predicts a greater zone of disturbance than either the x- or y-integration solutions. Table 2.1 compares Poisson pore pressure predictions to integration solutions far above the plate tip (large z/w) at the plate center and at the edge of penetrometers having aspect ratios $B/w=6.8, 20$, and 32.5 . This table indicates that at the plate center the pore pressure predicted from the Poisson solution is intermediate between the two integration solutions. The predicted pore pressures at the edge of the plate also lie between the two integration solutions at the higher aspect ratios of 20 and 32.5. For $B/w=6.8$ the Poisson prediction is slightly lower (approximately 5-10%) than both integration solutions. In general, the Poisson solution appears to provide a reasonable 'average' of the two integration solutions at the penetrometer boundary for a wide range of aspect ratios.

Uncoupled dissipation (see Chapter 5) solutions at the plate center are shown in Figure 2.10. It can be seen that the dissipation solutions based on the pore pressure distribution predicted from the Poisson equation gives a reasonable average in all cases. The practical

implication of this result is that, although the Poisson installation pore pressures are not an 'average' of the two integration solutions at all points within the field (note the reference above to the zone of disturbance in the x-direction), the dissipation curves for Poisson pore pressures at the plate center nevertheless lie intermediate between the dissipation curves for the two integration solutions.

The Modified Poisson solutions presented in Section 2.6.1 were based on equilibrium in the x-z plane, while the Poisson solutions presented in this section are based on equilibrium in the x-y plane. To assess the consequences of the simplification of the analyses from a three-dimensional problem to a 2-dimensional problem within a particular plane of interest, these two solutions are compared to one another in Figure 2.11, which shows the predicted distributions of pore pressure along the x-axis (on the plate centerline) far above the tip of a simple plate having an aspect ratio $B/w=6.8$. This figure indicates that the pore pressure distributions along the x-axis are in good agreement, with the predicted excess pore pressures at the plate boundary agreeing to within 10%.

2.7 CONCLUSIONS

1. The Poisson solution provides a reliable means for predicting pore pressure distribution without requiring arbitrary assumptions regarding the path of integration. This makes the method particularly suitable for application to more complex penetrometer geometries such as the field vane, the dilatometer, spade cells, etc.
2. The Poisson solution was evaluated by comparing it to: a) the radial integration solution far above the tip, where radial integration provides the most reliable solution, and b) the vertical integration solution ahead of the tip, where vertical integration provides the most reliable solution. It was found that: a) far above the tip, the Poisson solution matches the reliable radial integration solution, and b) ahead of the tip, the Poisson solution seriously underpredicts the vertical integration solution.
3. The Modified Poisson solution, which a) considers only vertical equilibrium ahead of the tip (below line OA in Figure 2.4) and b) considers both equilibrium equations above line OA, provides excellent agreement with vertical integration solutions. Line OA in Figure 2.4 was established by assessing the relative contribution of the gradient terms g_r and g_z to the flux term q in the Poisson equation.
4. The modified Poisson formulation enforces the more reliable vertical equilibrium

equation ahead of the tip; therefore, in this study, it will be used to make predictions for the following types of penetration problems in which vertical equilibrium is important: 1) piezocone penetration, 2) the push-in pressuremeter test (based on open-ended pile solutions), and 3) the Marchetti dilatometer test (based on plate solutions in a vertical plane). Analysis of pore pressure distribution in horizontal planes far above the penetrometer tip do not involve the vertical equilibrium equation; therefore, the originally proposed Poisson formulation described in Section 2.4 should be implemented for such cases. In this study, such cases will include predictions of pore pressure distribution in horizontal planes around: 1) single plates, and 2) the field vane (i.e. superposition of two plates rotated at 90° .)

Table 2.1 Normalized excess pore pressure predicted around a simple plate by different equilibrium equations

(a) At plate center

Aspect ratio, B/w	x-integration	y-integration	Poisson
6.8	1.04	1.17	1.09
20	.91	1.20	1.04
32.5	.84	1.15	1.03

(b) At edge of plate

Aspect ratio, B/w	x-integration	y-integration	Poisson
6.8	.92	.96	.87
20	.68	.87	.71
32.5	.61	.83	.73

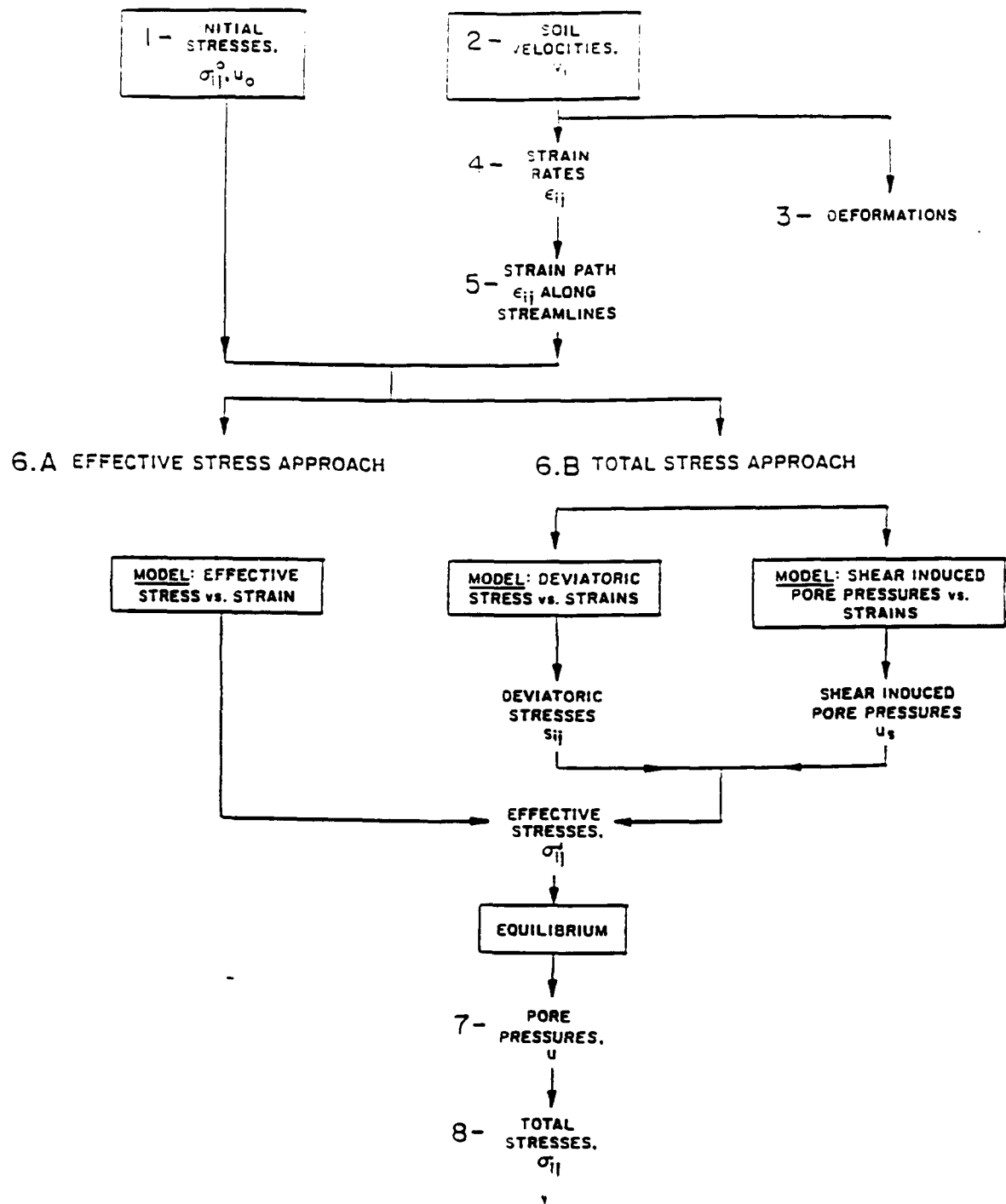


Fig. 2.1 The Strain Path Method (Baligh, 1985)

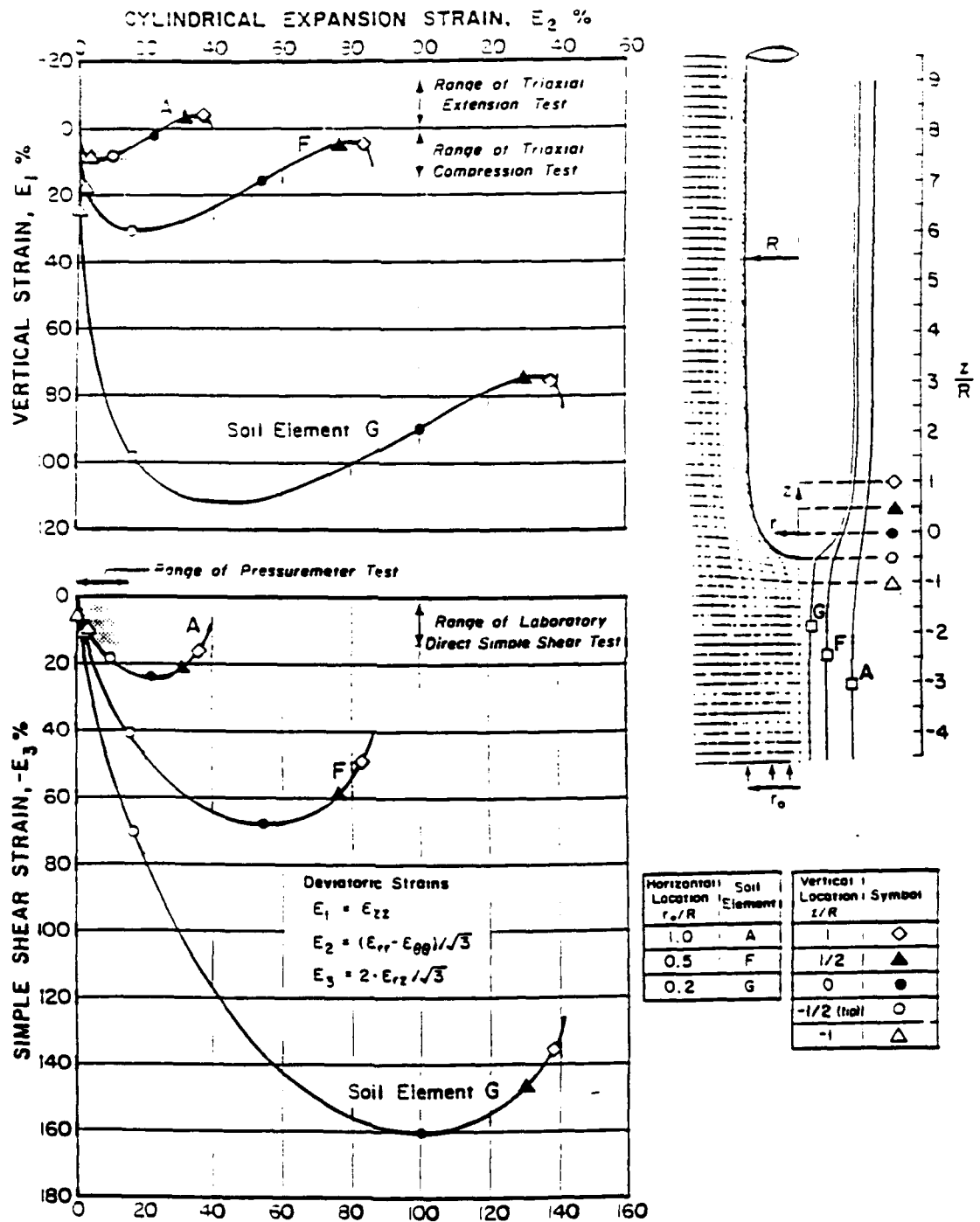


Figure 2.2 Strain Paths During Simple Pile Penetration (Baligh, 1985)

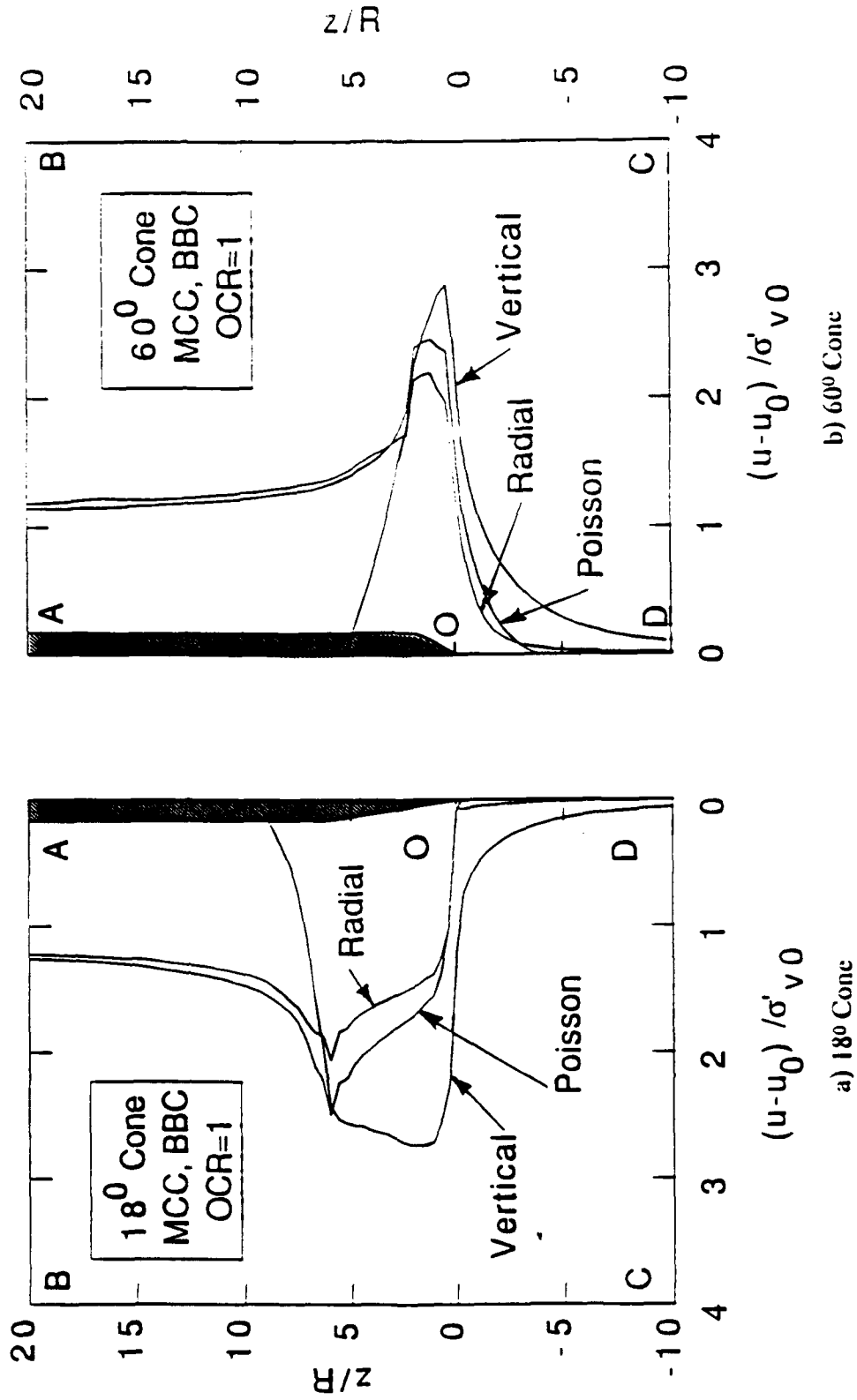


Figure 2.3. Excess Pore Pressures Around Cones Predicted by Different Equilibrium Equations Using MCC Soil Model for K_0 -Normally Consolidated BBC

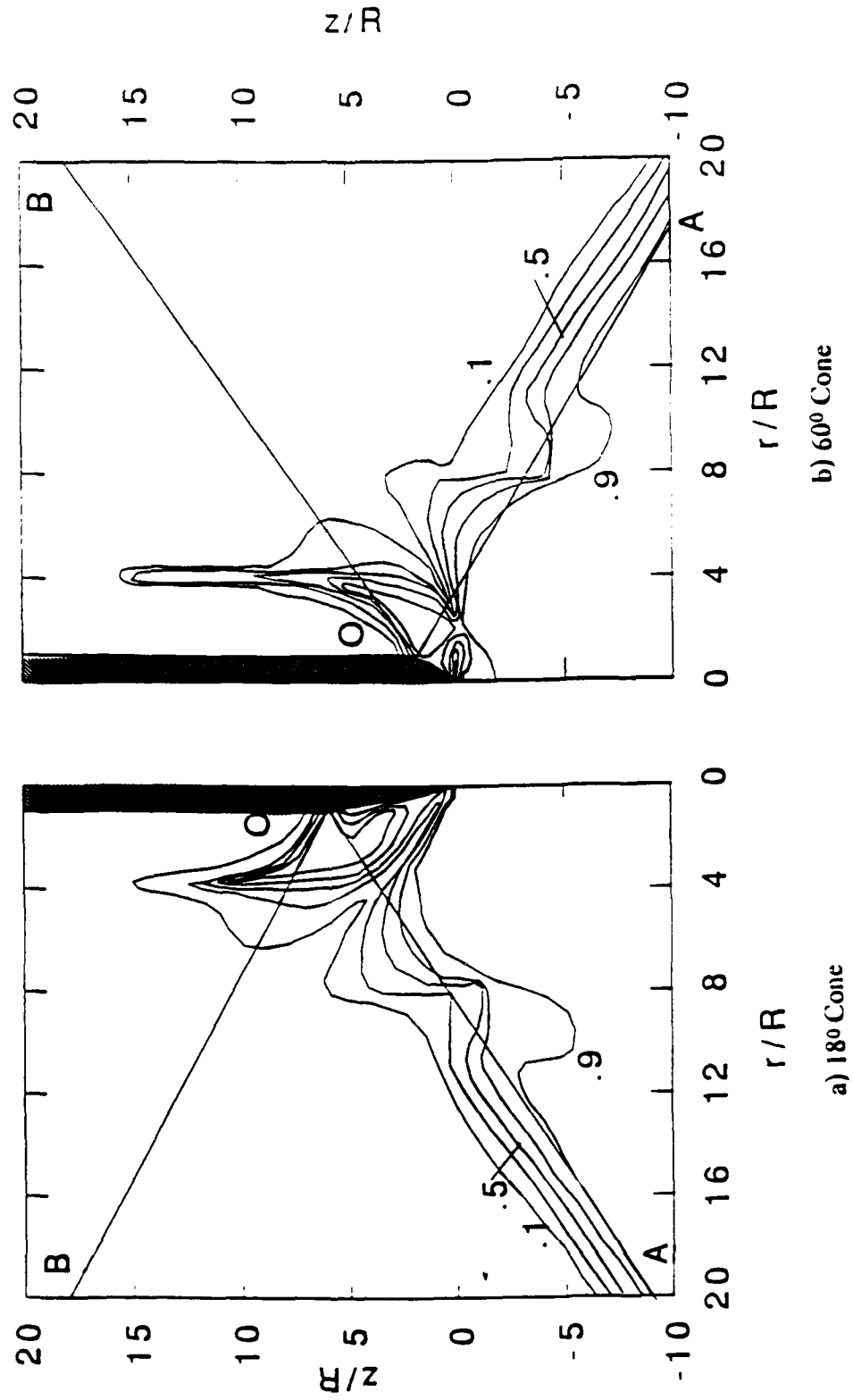


Figure 2.4 Relative Contribution of Vertical Equilibrium Equation During Cone Penetration

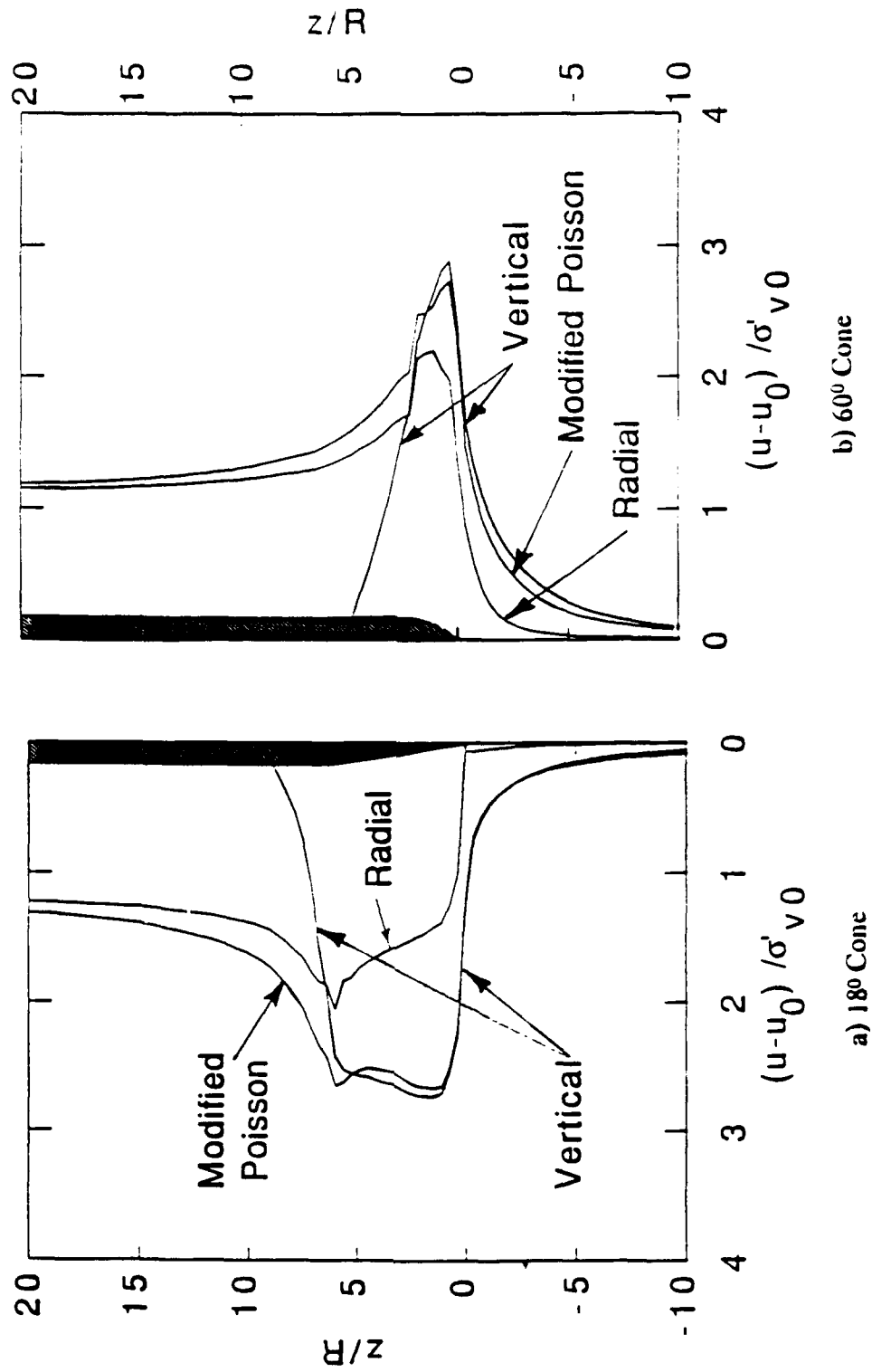


Figure 2.5 Excess Pore Pressures Around Cones Predicted by Modified Poisson Solution Using MCC Soil Model for K_0 -Normally Consolidated BBC

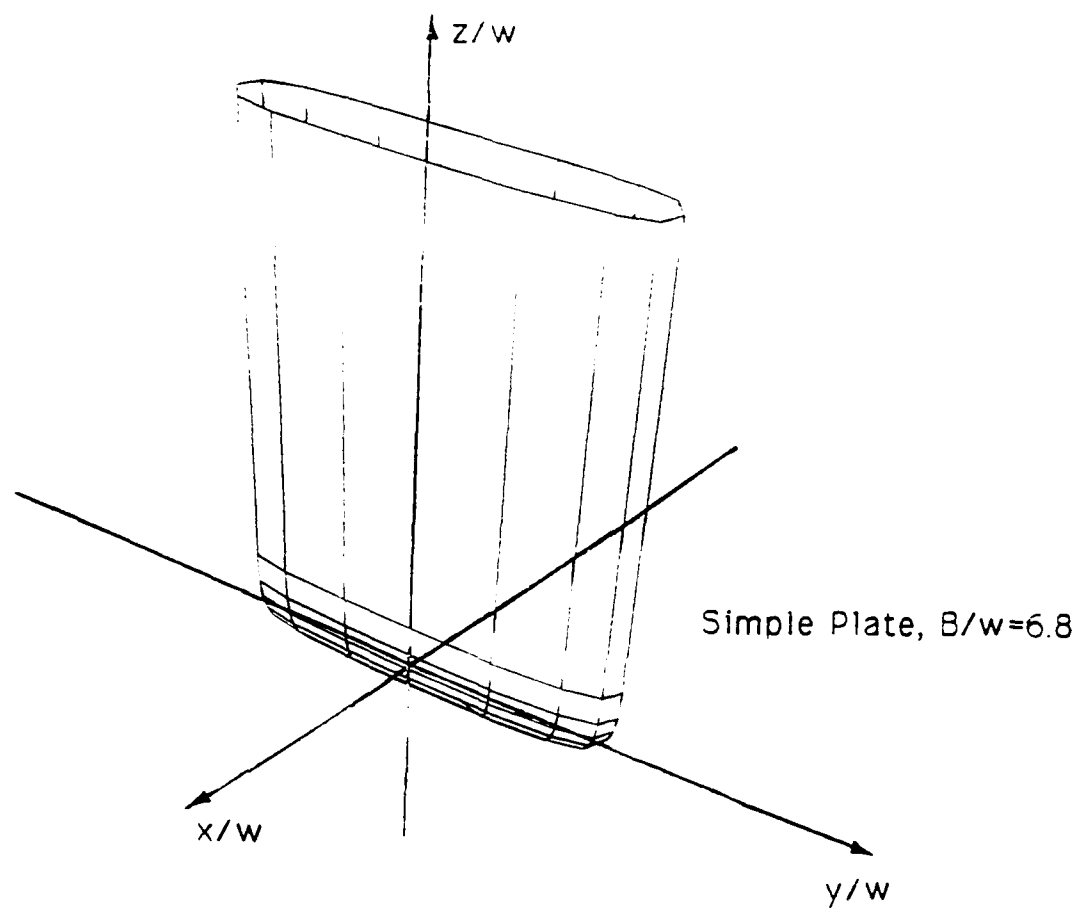


Figure 2.6 Definition of Coordinate Frame for Plate Penetration Problems

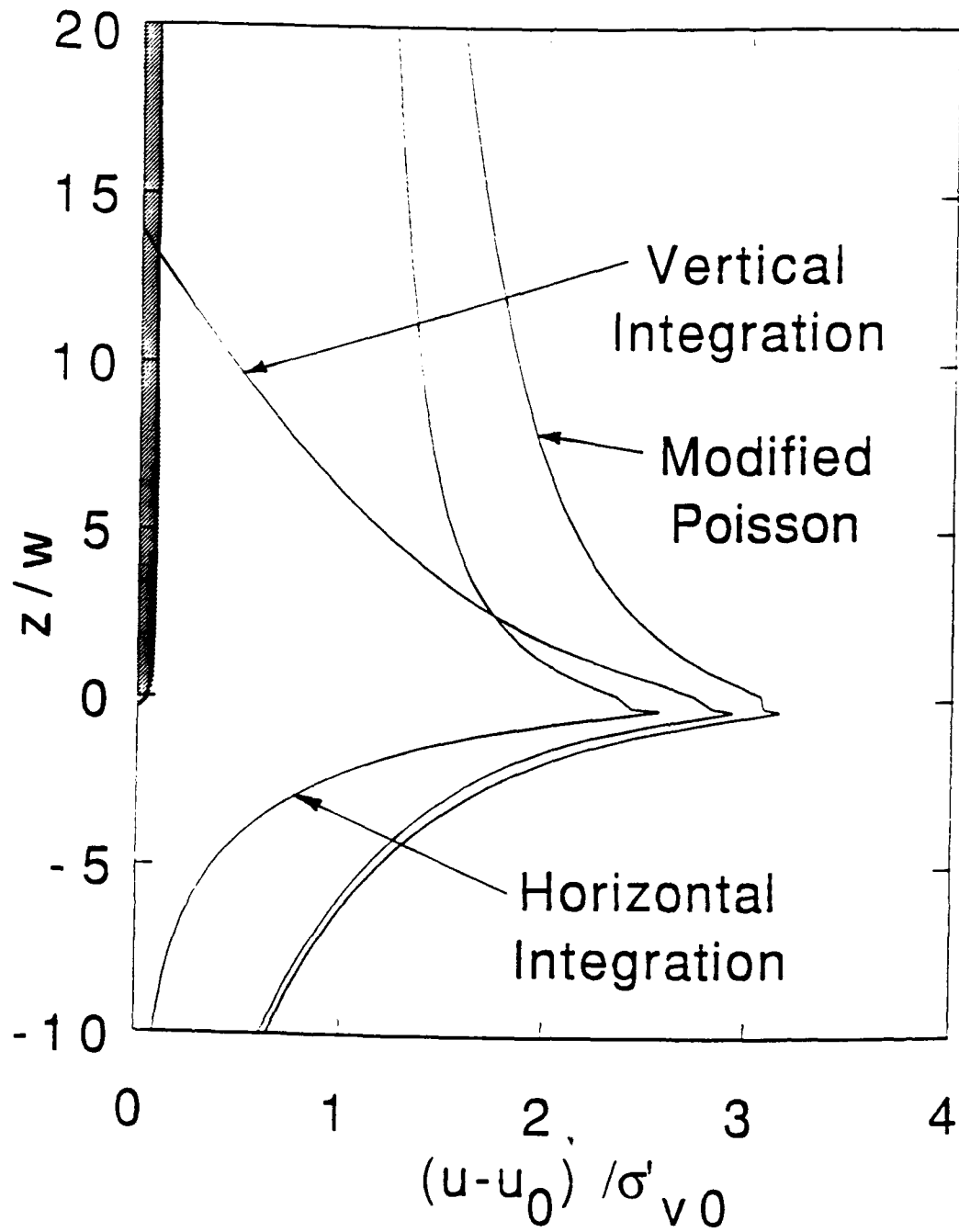
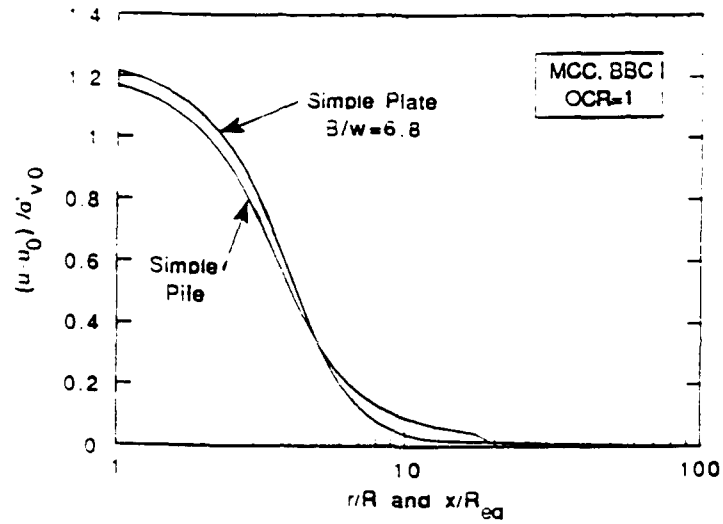
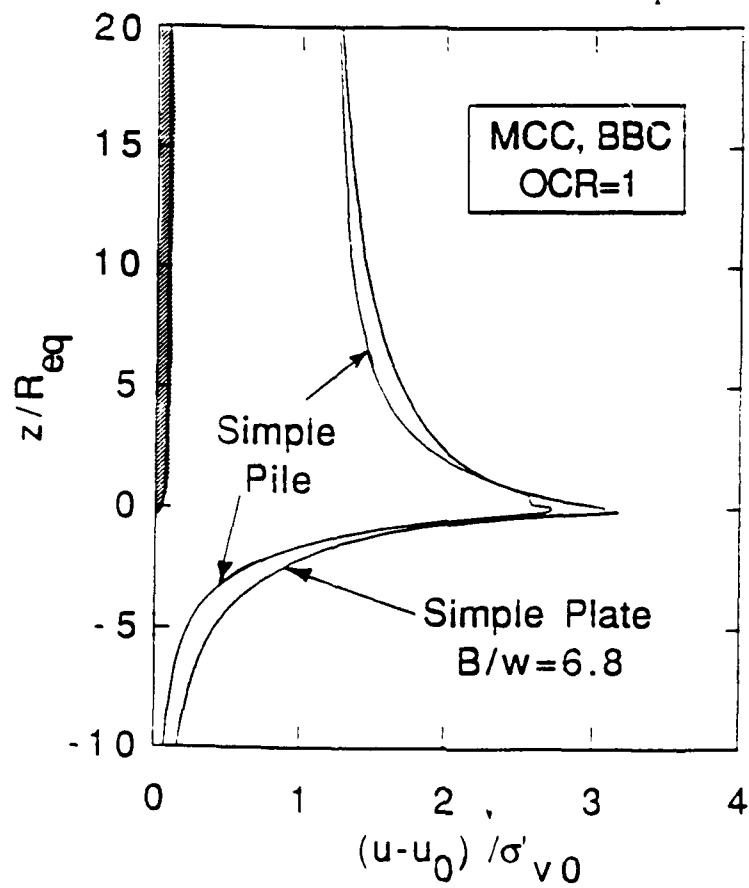


Figure 2.7 Excess Pore Pressures at Plate Center by Different Equilibrium Equations

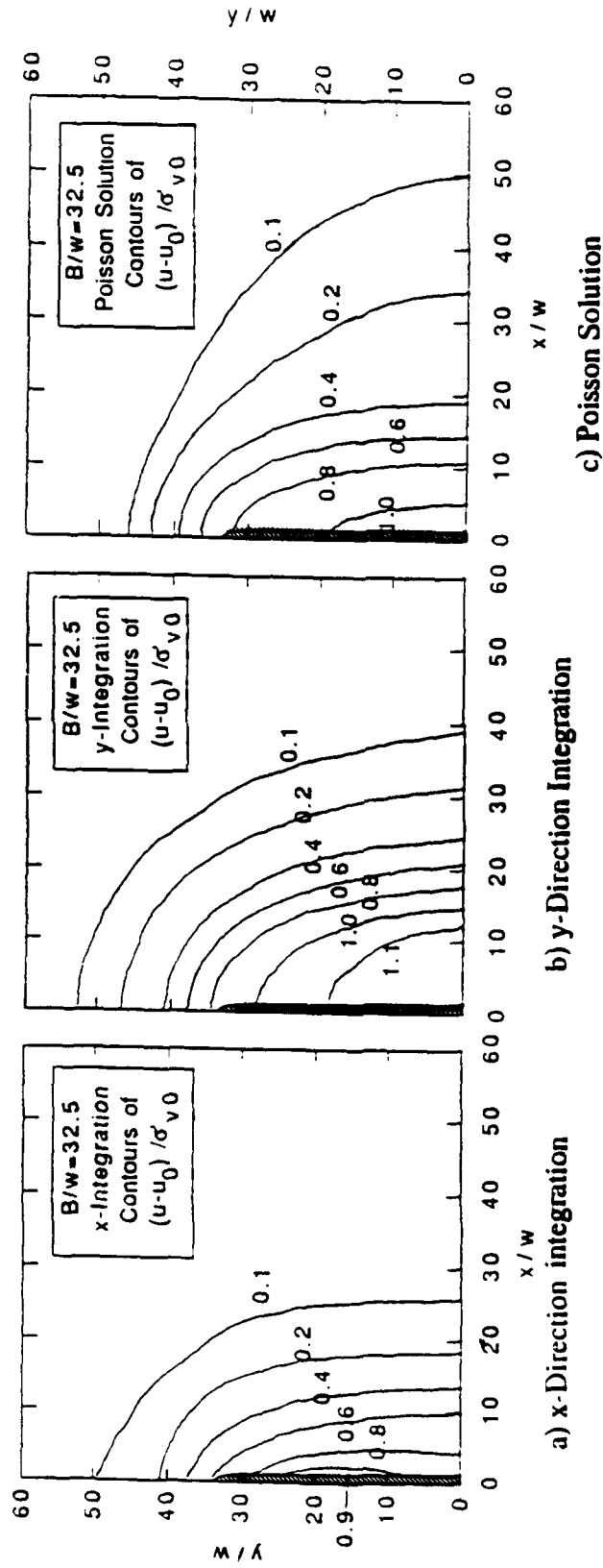


b) Lateral Distribution far above Tip



a) Along Centerline and Plate Boundary

Figure 2.8 Comparison of Simple Plate, $B/w=6.8$, and Simple Pile Excess Pore Pressures



2.9 Pore Pressures in Horizontal Plane Far Above Tip for Simple Plate, $B/w=32.5$

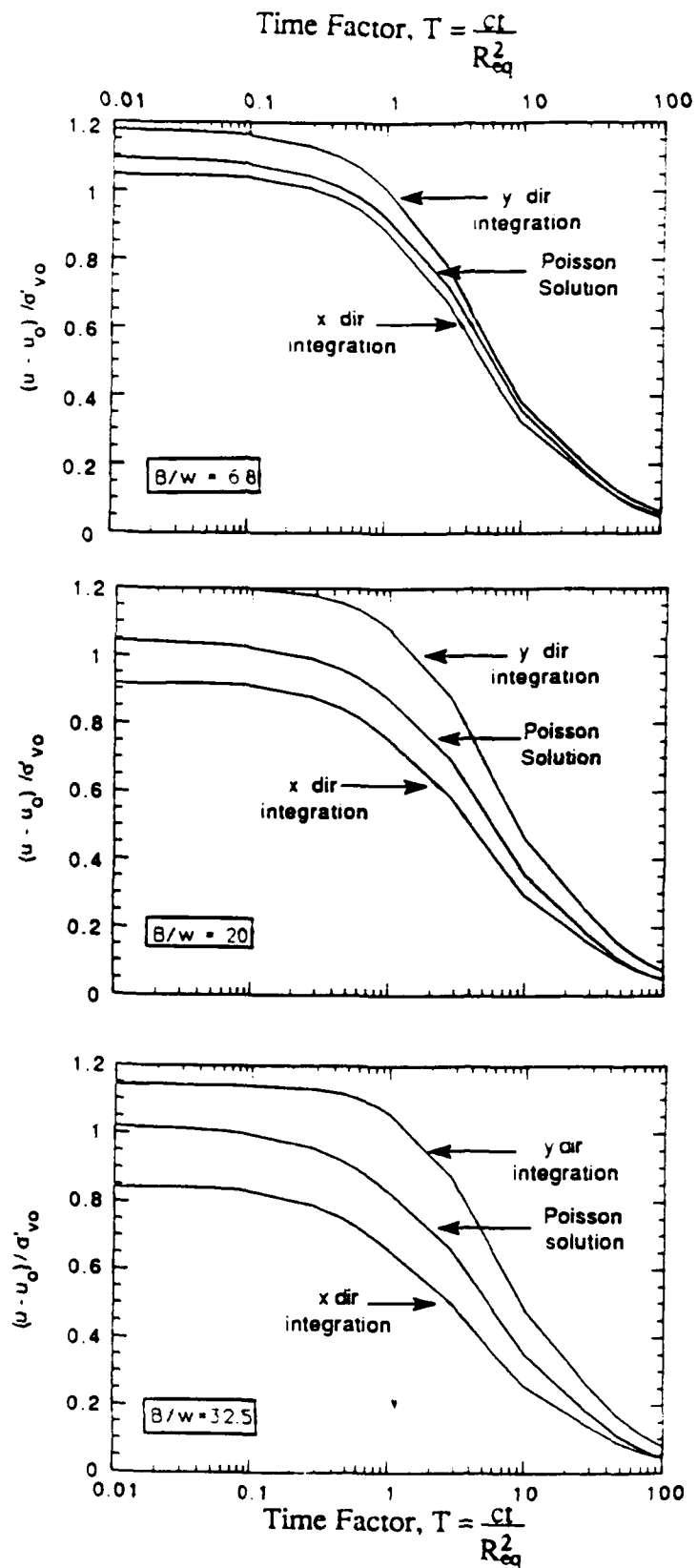


Figure 2.10 Dissipation of Excess Pore Pressures for Different Initial Conditions at Plate Center

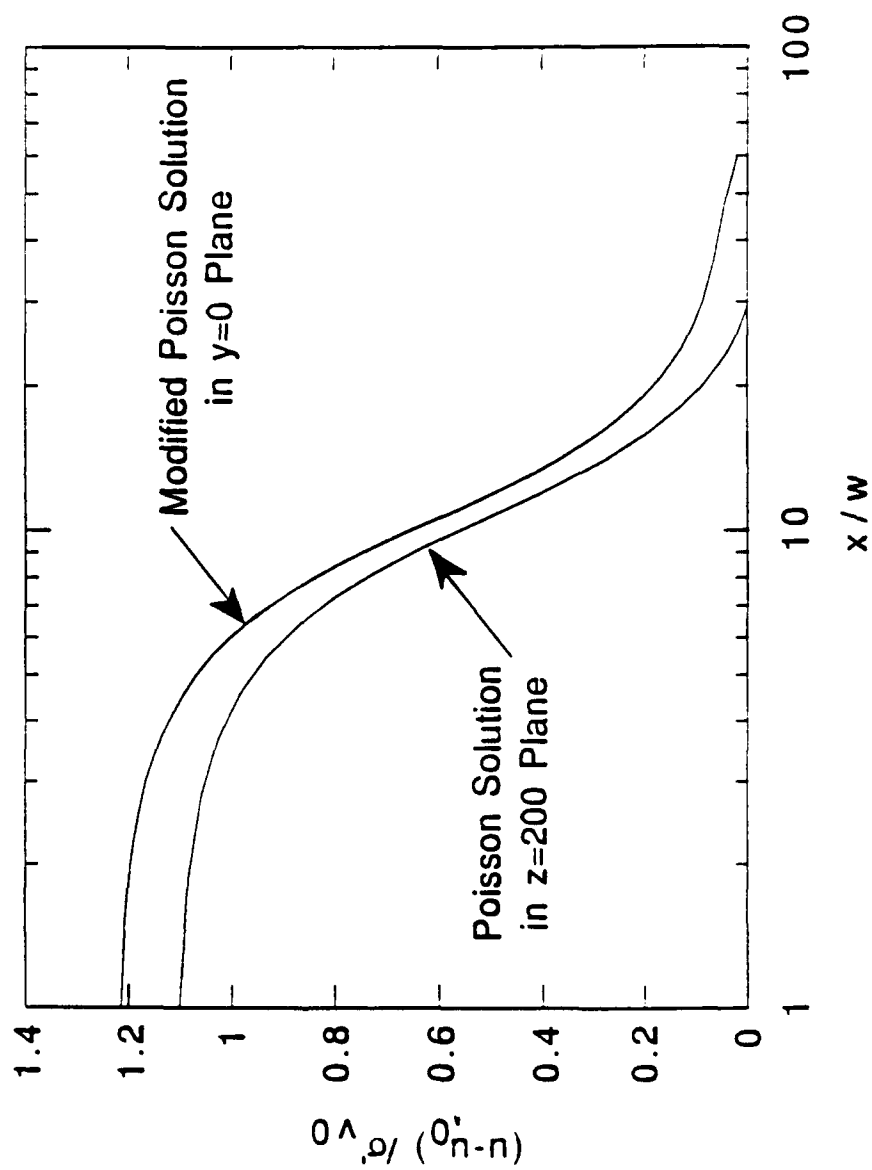


Figure 2.11 Comparison of Excess Pore Pressures Predicted in $z/w=200$ and in $y/w=0$ Planes Using Proposed Poisson Formulations

3. THE PIEZOCONE

3.1 INTRODUCTION

The piezocone penetrometer (CPTU; Janbu & Senneset, 1974; Baligh et al., 1981; DeRuiter, 1981) combines the measuring capabilities of: a) the electrical cone penetrometer (CPT; DeRuiter, 1971 Figure 3.1a), which provides continuous measurement of tip resistance, q_c , and local skin friction, f_s (acting along a friction sleeve); and b) the pore pressure probe (PPP, Figure 3.1b), which measures pore pressures, u , both during penetration and in subsequent dissipation tests (Wissa et al., 1975; Torstensson, 1975). The simultaneous measurement of pore pressure and tip resistance gives the piezocone unique capabilities for estimating soil stratification and spatial variability (Baligh et al., 1980; Jones et al., 1981; Campanella & Robertson, 1988). The test is also widely used to estimate engineering properties using various empirical correlations. In clays, measurements of tip resistance and pore pressures during penetration are correlated with undrained shear strength and stress history; while pore pressure dissipation data are used to estimate consolidation and permeability properties. This chapter focuses on the prediction and interpretation of engineering properties during cone penetration.

In previous studies, the Strain Path Method (SPM; Baligh & Levadoux, 1980; Baligh, 1985a, b) has provided a rational framework for predicting piezocone penetration in clays, and hence, establishing a basis for interpretation of the measured data. The previous studies have included the following:

1. Baligh and Levadoux (1980) presented predictions of the stresses and pore pressures around 60° and 18° cone penetrometers: shear stresses in the soil were obtained using a total stress, multi-surface plasticity model (MIT-T1), with input parameters selected for K_0 -normally consolidated Boston Blue Clay. Changes in mean total stress were estimated from radial equilibrium (c.f. section 2.2), while a separate model was introduced for shear induced pore pressures.
2. Baligh (1985a) obtained upper bound, closed form expressions for the penetration resistance of 'simple pile' geometry, q_{sp} , based on the energy required to achieve steady penetration. These studies showed that the undrained point resistance at a particular depth depends on a) the level of total confining stress (σ_0 , in-situ), b) the undrained shear strength of the clay, c) the shear strain at yield, and d) the shear stiffness at small strain levels. Preliminary comparisons of the predicted point

resistance indicated reasonable agreement with typical cone measurements; however, the analysis does not consider important aspects of soil behavior in the plastic region around the penetrometer and hence cannot be used for more detailed, site specific evaluations (Whittle et al., 1989).

3. Baligh (1986b) and Elghaib (1989)¹ have presented predictions of stress conditions at the tip of a 'simple pile' penetrometer² based on the strain history of soil elements along the centerline (ahead of the advancing penetrometer). For these assumptions, a simplified 'centerline analysis' was developed in order to predict the tip resistance and tip pore pressures during steady penetration, based on known soil properties. From these analyses, Elghaib (1989) has shown that the undrained shear strength, c_{uTC} (in triaxial compression) can be interpreted from measurements of either the tip resistance or tip pore pressures. The proposed interpretation method was shown to predict c_{uTC} to within $\pm 25\%$ using data from nine well documented sites.

This chapter presents comprehensive strain path predictions of effective stresses and pore pressures for piezocone penetration in normally and moderately overconsolidated clays ($OCR \leq 4$). The distributions of effective stresses are obtained from generalized soil models³ (MCC and MIT-E3); while excess pore pressures are found using the finite element solutions of the (modified) Poisson equation described in Chapter 2. A detailed interpretation of the predictions then provides a basis for establishing possible correlations between piezocone measurements and soil properties. The predictions are also compared directly with measured data from well documented sites in order to establish the capabilities and limitations of the strain path analyses.

3.2 BACKGROUND

3.2.1 Cone Design and Testing Procedures

The basic geometry of the standard electrical cone (Figure 3.1) comprises a penetrometer with 10 cm^2 base area (i.e., shaft radius, $R \approx 1.78 \text{ cm}$) and apex angle, $\delta = 60^\circ$. The friction sleeve is located immediately behind the cone and has a surface area $A_s = 150 \text{ cm}^2$. The cone is installed at a standardized penetration rate, $U \approx 2 \text{ cm/sec}$.

¹This work has been summarized in Whittle et al. (1989).

²In this case the tip resistance, $q_c = (\sigma_{zz})_{\text{tip}}$.

³These same effective stress soil models will also be used in subsequent analysis of pore pressure dissipation and membrane expansion procedures (e.g, Chapters 5 and 6, respectively).

Baligh (1985b) has presented preliminary analyses which show that for the standard penetration rate (i.e., $U/R=1.1 \text{ sec}^{-1}$):

1. In low permeability clays ($k < 10^{-7} \text{ cm/sec}$), there is effectively no migration of excess pore water pressure during steady cone penetration (i.e., penetration is undrained).
2. In clean sands (<10% by weight smaller than ASTM sieve no. 200) with permeability, $10^{-4} \leq k \leq 10^{-1} \text{ cm/sec}$, there is no measurable excess pore pressure during penetration due to the free migration of pore fluid (i.e., fully drained).
3. For intermediate classes of soils such as silt and 'dirty sands'⁴ (with $10^{-7} \leq k \leq 10^{-4} \text{ cm/sec}$) partial dissipation of excess pore pressures will occur during penetration.

Penetration of the cone is generally continuous over 1m intervals, separated by short delays ($\Delta t=15$ to 90 sec) during which the next push rod is assembled. These delays introduce small discontinuities in the tip and pore pressure profiles due to partial dissipation of pore pressures.

There is currently no standardized design for either the dimensions or location of the porous filter elements used to measure penetration pore pressures (Figure 3.2). However, most piezocones used in practice have a single porous element located either at the base or on the face of the cone (Figure 3.3). Baligh and Levadoux (1980) have shown both experimentally and theoretically (based on strain path analyses) that there are large spatial variations in the excess pore pressures which develop around the cone during steady penetration. Thus, variations in the location of porous elements have provided a major source of confusion in the interpretation of engineering properties using piezocone pore pressures. The debate over optimal filter location is still unresolved.

Baligh (1985c) concludes that pore pressure measurements at the cone tip are reliable and repeatable, and provide the most sensitive indicators of soil stratification. Based on strain path analyses, the tip pore pressures are controlled by a small number of soil properties (from centerline analyses; Elghaib, 1989; Whittle et al., 1989) and can be used to interpret undrained shear strength in clays. There are two main disadvantages of the tip location: a) the porous element is vulnerable to damage and abrasion; and b) the measured pore pressure response can be significantly affected by the compressibility of the filter element (Battaglio et al. 1986). Many authors now support the view that mid-cone filter locations are almost as reliable for profiling, but are less vulnerable to damage.

⁴i.e., high proportion of fine materials.

Tavenas et al. (1982) and Robertson and Campanella (1984) advocate the filter located at the base of the cone (especially for soil profiling). This location is very convenient for making essential corrections to the measured tip resistance (as discussed below). However, previous experimental and theoretical results have shown that there are large pore pressure gradients acting around the base of the cone⁵. Thus, the repeatability of base pore pressures is an important consideration in the piezocone design.

Wroth (1984) postulated that pore pressures measured at $z/R=5-6$ above the base of the cone provide the best indicator of stress history. This recommendation was based on the assumption that shear induced pore pressures contribute a significant percentage of the measured pore pressure around the shaft. In contrast, strain path analyses (Baligh, 1986b; Whittle, 1987) show that predictions of shaft pore pressures are strongly influenced by more complex aspects of soil behavior. Thus, it is difficult to establish how measured pore pressures are related to soil properties.

In addition to the problems created by non-standardization of piezocone geometry, there are also a number of hardware design issues which have an important influence on the measured/reported data.

1. Load cell resolution:

Almost all electrical cones are instrumented with a single load cell which can measure penetration resistance in soils ranging from very soft clays to very dense sands (i.e., $100 \leq q_c \leq 30,000$ kPa). Thus, it is clear that measurements in soft clays suffer from low resolution of the load cell readings which can have a very significant influence on the reliability of reported tip resistance. More sophisticated designs using two load cells with different ranges have been described by Ridgen et al. (1982) but are not common in practice.

2. Correction of tip resistance:

When a piezocone is subjected to hydrostatic pressure, a shift occurs in the zero reading of the load cell (and hence the implied tip resistance⁶, DeRuiter, 1981, 1982; Campanella et al., 1982). This is due to unequal areas on which the pore water pressure is acting around the cone (Figure 3.4a). Therefore the measured tip resistance, q_c , and the sleeve friction, f_s , do not measure the actual resistance offered by the surrounding soil. Correction of the tip resistance is difficult to achieve due to

⁵Particularly erratic measurements are obtained for highly overconsolidated clays; e.g., Powell & Uglov (1988).

⁶This also occurs in the load cell for the friction sleeve.

the non-uniformity of pore pressures acting around the cone in soil. Current correction procedures involve: a) estimating the 'apparent' area correction, $a = A_N/A_T$ (Figure 3.4a) for a given cone design, and b) adjusting the cone resistance reading from test data, q_c , using the penetration pore pressure measured at the base of the cone, u_b , (Figure 3.4a). Hence the corrected tip resistance is generally reported as:

$$q_T = q_c + (1-a) u_b \quad (3.1)$$

If pore pressures are not measured at the base of the cone, further empirical modification factors are required⁷. The correction factor can increase the reported tip resistance by up to 50% in soft clays.

It is important to note that the apparent area factor is also subject to potential errors. For example, Nyirenda and Sills (1989) have correctly demonstrated that $a \neq A_N/A_T$, but is controlled by the equilibration of forces acting on the cone as shown in Figure 3.4b. This figure indicates that the design of the friction sleeve and its O-ring seal can affect significantly the calculation of the correction factor. Thus, the most reliable method for correcting tip resistance is to calibrate the cone in a pressurized water chamber.⁸

3. Response of the porous elements

The reliability (accuracy and response rate) of the monitored pore pressures depends largely on the rigidity of the measuring system. In practice, this can be achieved by using a small volume for the measuring 'fluid' and by ensuring that the filter is fully de-aired. Filter materials should contain small pores ($\sim 2\mu\text{m}$ in diameter; Smits, 1982) to ensure that the filter can sustain external tension forces (i.e., due to negative pore pressures in the soil). Battaglio et al. (1986) have also shown that the compressibility of the filter element located at the tip of the cone can lead to erroneous pore pressures, especially in stiff clays. This problem can be circumvented by re-locating the filter onto the face of the cone.

3.2.2 Interpretation of Engineering Properties of Clays

There are numerous empirical correlations reported in the literature in which piezocone

⁷For example, Baligh et al. (1980) assume that $0.3 u_{tip} \approx (1-a)u_b$.

⁸Even this process may not account for compression of the friction sleeve which occurs in the soil.

penetration measurements (or ratios of measurements) are correlated with undrained shear strength and/or stress history of cohesive soils. The following paragraphs provide a brief summary of these existing correlations. (Note: estimation of consolidation parameters from pore pressure dissipation rates is covered in Chapter 5.)

3.2.2.1 Undrained Shear Strength

The undrained shear strength, c_u , is commonly estimated from the cone resistance, q_c , (or corrected cone resistance q_T , Equation 3.1) using the following equation:

$$c_u = \frac{q_c - \sigma_{v0}}{N_k} \quad \text{or} \quad c_u = \frac{q_T - \sigma_{v0}}{N_{kT}} \quad (3.2)$$

where σ_{v0} is the total overburden pressure, and N_k , N_{kT} are empirical cone factors.

A rational basis for Equation 3.2 is provided by Baligh (1986b), who shows that for simple pile penetration in an isotropically consolidated Prandtl-Reuss (elastic-perfectly plastic) material work considerations require:

$$c_u = \frac{q_{sp} - \sigma_0}{N_{sp}} \quad (3.3)$$

where q_{sp} = simple pile tip resistance

$$N_{sp} = \frac{\sqrt{3}}{4} \left[\log_e \left(\frac{3}{4} \right) - 2 - 4 \log_e (E_y) \right]$$

$$E_y = \text{Yield strain} = \frac{1}{\sqrt{6}} \frac{c_u}{G} \text{ for a P-R material}$$

Although it is based on a simplified penetrometer geometry and soil behavior, Equation 3.3 elucidates several fundamental aspects of deep penetration, namely:

1. Undrained shear strength is directly proportional to net tip resistance.
2. The tip resistance factor N_{sp} is a function of soil stress-strain behavior (i.e., the yield strain, E_y), which is a function of soil type and stress history.

The magnitudes of N_{kT} (or N_k) are backfigured by comparing cone resistance measurements (q_T or q_c) with some reference profile of undrained shear strength. For example, Baligh et al. (1980) report $N_k=10-20$ (Figure 3.5a) for uncorrected tip resistance, q_c , correlated with field vane strengths, μc_{uFV} (where μ is a 'standard' correction factor introduced by Bjerrum (1972) based on plasticity index, I_p). Aas et al.

(1986) report similar ranges for N_{kT} correlated with c_{uDSS} (i.e., undrained shear strength from laboratory direct simple shear tests⁹) based on data from five sites in Norway, with $1 \leq OCR \leq 8$. However, the same authors report much higher values of N_{kT} (up to 40) for overconsolidated clay when the net cone resistance ($q_T - \sigma_{v0}$) is normalized with the field vane strength (in this case the field vane strength has been corrected using a factor to account for anisotropy, μ_A ; Figure 3.5c). This discrepancy is loosely attributed to 'strain rate affects'. Other researchers (Kjekstad et al., 1978; Lunne et al., 1981, 1985; Thornburn et al., 1981; Rad & Lunne, 1988) report $N_{kT}=5-20$ using consolidated, undrained, triaxial compression data.

Undrained shear strength is also estimated from measured pore pressures using an empirical pore pressure factor, $N_{\Delta u}$:

$$c_u = \frac{u - u_0}{N_{\Delta u}} \quad (3.4)$$

where u is the pore pressure measured at some (fixed) reference location on the cone. A rational basis for relating tip pore pressure to undrained shear strength c_u is also provided by Baligh (1985c) who showed that for simple pile penetration in an isotropically consolidated Prandtl-Reuss material equilibrium considerations along the centerline require:

$$c_u = \frac{\Delta u - \Delta u_s}{N_\sigma} \quad (3.5)$$

$$\text{where } N_\sigma = \sqrt{3} \log_e \left[\frac{1}{3} + \frac{2}{3} \frac{1}{\sqrt{2} E_y} \right]$$

Δu_s = shear-induced pore pressure

Equation 3.5 implies the following:

1. Undrained shear strength c_u is proportional to the change in mean stress $\Delta\sigma$ ($=\Delta u - \Delta u_s$) during penetration rather than to Δu as assumed in Equation 3.4. Hence, Equation 3.4 is approximately valid only if the shear-induced pore pressure Δu_s is small relative to the change in mean stress $\Delta\sigma$.
2. The relationship between $\Delta\sigma$ and c_u is a function of stress-strain behavior of the soil (E_y) which is a function of soil type and stress history, hence a unique relationship for

⁹From Recompression type tests.

all soils and histories is not possible.

Lunne et al. (1985) report values $4 \leq N_{\Delta u} \leq 12$ from tests on North Sea clays with pore pressures measured at the base of the cone and undrained shear strength, c_{uTC} (from recompression CAUC tests). Campanella and Robertson (1988) have reported $0 \leq N_{\Delta u} \leq 20$ from test data in the Vancouver area. However, the authors do not specify the source/type of their reference c_u profile. Their results (Figure 3.6) also produce similar ranges of N_{kT} ($5 \leq N_{kT} \leq 17$) as reported previously by Baligh et al. (1980).

A third dimensionless cone factor, N_{ke} , was introduced by Seneset et al. (1982) using both tip resistance and pore pressure measurements:

$$c_u = \frac{q_T - u}{N_{ke}} \quad (3.6)$$

where u is the pore pressure measured at the base of the cone. The authors report values of $N_{ke} = 9 \pm 3$.

In concept, the difference ($q_T - u$) represents some measure of the effective stress acting in the soil close to the cone. In practice, calculated values of N_{ke} are likely to exhibit significant scatter, especially in soft clays where $q_T \approx u$, and where there are potentially large errors in the reported magnitude of q_T . Mayne et al. (1990) have recently compiled data from 83 sites in which they show that (for non-fissured clays), $u = 0.53q_T$ to $0.73q_T$ (for intact clays; Figs. 3.7a,b), where u is measured either on the face or at the base of the cone. These results suggest that $(q_T - u) = 0.27q_T$ to $0.47q_T$, and hence imply that c_u is proportional to the measured cone resistance q_T .

3.2.2.2 Stress History

The most widely used correlation for OCR is based on the ratio of excess pore pressure to net tip resistance, B_q , proposed by Seneset et al. (1982), and Jones and Rust (1982):

$$B_q = \frac{u - u_0}{q_T - \sigma_{v0}} \quad (3.7)$$

In the standard definition of B_q , u is measured at the base of the cone, while q_T is the

corrected tip resistance. Wroth (1984) attempts to rationalize the use of B_q by making the analogy between the shearing of the soil due to cone penetration and the failure of soil in laboratory shear tests using the following reasoning:

1. OCR is well correlated with the invariant pore pressure parameter, a_f measured at failure in laboratory undrained shear tests (Henkel, 1960)¹⁰, where:

$$a_f = (\Delta u - \Delta \sigma) / \Delta \tau = \Delta u_s / \Delta \tau \quad (3.8)$$

Δu_s is the shear induced pore pressure, $\Delta \sigma$ is the change in mean total stress, and $\Delta \tau$ is the change in octahedral shear stress.

2. For cone penetration, Wroth asserts that the maximum shear stress should be specified as a difference of two total stresses and hence advocates $(q_T - \sigma_{v0})$ to estimate undrained shear strength. He also speculates that $\Delta u_s / \Delta u$ reaches a maximum value at locations above the base of the cone.
3. The parameter B_q is then presented as a 'best available' ratio which is conceptually similar to a_f .

These arguments are, however, misleading for two main reasons: a) for $OCR \leq 4-8$, Baligh (1986b) shows that Δu_s is only a small proportion of the total excess pore pressure ($\Delta u_s / \Delta u \approx 20-30\%$); while b) $(q_T - \sigma_{v0})$ is controlled by the shear stress at failure (τ_f) and not by the change in shear stress ($\Delta \tau$).

Based on these arguments, there is not a strong fundamental basis for correlating B_q to OCR, and the published correlations should be regarded as purely empirical. Jamiolkowski et al. (1985) and Robertson et al. (1986, 1988) have evaluated B_q correlations from a number of sites (e.g. Figure 3.8¹¹) and concluded that the value of B_q reflects changes of OCR within a soil deposit (e.g. Figure 3.8a). However, due to differences in sensitivity and pre-consolidation mechanism, there is no unique relationship between B_q and changes in OCR.

Mayne (1986, 1987) has presented direct correlations for OCR using: a) net normalized tip resistance, $(q_c - \sigma_{v0}) / \sigma'_{v0}$ (uncorrected tip resistance; Figure 3.9a); and b)

¹⁰ a_f is a generalized version of the A parameter introduced by Skempton (1954) for triaxial shear tests.

¹¹The data in Figure 3.8b show that $0.3 \leq B_q \leq 1.0$. However, the same authors (Figure 3.6) report much higher B_q values (up to 1.6) in other published work from the same sites. Thus there appear to be discrepancies in the measured data reported in the literature.

normalized excess pore pressures, $(u-u_0)/\sigma'_{v0}$ (Figure 3.9b). Assuming that natural soils exhibit normalized shear strength properties¹² (as used in SHANSEP analysis, Ladd & Foott, 1974); or critical state soil mechanics, Schofield & Wroth, 1968), then:

$$\frac{q_T - \sigma'_{v0}}{\sigma'_{v0}} = a_1(\text{OCR})^m \quad (3.9a)$$

or

$$\frac{u - u_0}{\sigma'_{v0}} = a_2(\text{OCR})^m \quad (3.9b)$$

where a_1 , a_2 are empirical coefficients backfigured from test data and $m=0.8\pm0.05$ (Ladd, 1991).

However, Mayne (1987) implicitly assumes¹³ $m=1$ and reports $\kappa=1/a_1=0.2$ to 0.6 (Figure 3.9a). These results are consistent with previous correlations for undrained strength (i.e. using $a_1=N_{kt}S$ and $N_{kt}=5$ to 15 , and $S=(c_u/\sigma'_{vc})_{NC}=0.3$).

A third type of correlation proposed for OCR uses pore pressures measured concurrently at two locations on the cone. For example, Robertson et al. (1986) sketch 'conceptual' pore pressure distributions around the cone based on comparisons of data from two highly overconsolidated clays (London clay and Taranto clay) with typical results for a 'normally consolidated clay' (Figure 3.10a). These results prompted Sully et al. (1988) to correlate $(u_t - u_b)/u_0$ with OCR with surprising apparent success at low OCR¹⁴ (Figure 3.10b) and huge scatter at high OCR, while Robertson et al. (1989) have adopted u_t/u_b (Figure 3.11a) whose true scatter is revealed by Mayne et al. (1990) (Figure 3.11b).

Finally, Konrad and Law (1987) have presented a semi-empirical interpretation of tip resistance and tip pore pressures (based on similar concepts to the centerline analysis described by Whittle et al, 1989). Konrad and Law estimate that the vertical effective stress at yield, σ'_{yc} (i.e., the vertical stress at the elasto-plastic boundary) is identical to the vertical effective stress at the tip of the cone, $(\sigma'_v)_{tip}$ (Figure 3.12a). However, in order to use base pore pressures, u_b , to estimate σ'_{yc} , they introduce additional correction

¹²i.e. For normalized soil behaviour: $a_1=SN_{kt}$ and $a_2=SN_{\Delta u}$, where $S=(c_u/\sigma'_{vc})_{NC}$ is the undrained strength ratio of the normally consolidated clay.

¹³Absolute values of m are masked by the scatter in the empirical factors a_1 , a_2 .

¹⁴The source of the reported OCR values is not given.

factors to account for cone geometry and interface friction:

$$\sigma_{yc} = \frac{q_T - au_b}{1 + M \tan \phi' \cot \frac{\delta}{2}} \quad (3.10)$$

where ϕ' is the friction angle for shearing of normally consolidated clay at large strain levels, $\delta/2$ is the half apex angle, M is an interface friction factor and a is used to correct the base pore pressures (the authors propose $M=0.5$ to 1.0 and $a=1.0$ to 1.33 ; but actually use $M=1.0$, $a=1.0$). Finally, σ'_{yc} is correlated directly with σ'_p obtained from laboratory oedometer tests on five sensitive Canadian clays (Figure 3.12b). The results of the study (Figure 3.12c) show $0.8 \leq \sigma'_{yc}/\sigma'_p \leq 1.2$, for $1 \leq \text{OCR} \leq 5$. For a given site, the OCR can be estimated by iteration using the results from Figure 3.12b. Preliminary assessment of Equation 3.10 by Jamiolkowski et al. (1989) has been generally positive. However, the success of the method depends on the reliability of the measured values of q_T and u_b .

3.3. ANALYTICAL PREDICTIONS

3.3.1 Introduction

The previous sections have shown that there are currently a multiplicity of correlations to estimate undrained shear strength and stress history from piezocone measurements. It is believed that these divergent correlations and the resulting confusion reflect two problems. The first arises due to the lack of standardization of the piezocone design and testing techniques, which contributes to excessive scatter in reported tip resistance (i.e., measured versus corrected for unequal area effects) and penetration pore pressures (i.e., location and size of porous filters and their response times). The second problem is due to lack of understanding of the fundamental mechanics of piezocone penetration (i.e., which soil properties affect the measured response).

In previous analyses (using the Strain Path Method), Baligh (1986b), Elghaib (1989), and Whittle et al. (1989) have proposed that tip resistance and tip pore pressures can be used to estimate the undrained shear strength of clays. In this section, the analyses are extended to include detailed predictions of the stress and pore pressure distributions around a piezocone penetrometer as a function of overconsolidation ratio and of the soil

model used to represent clay behavior. The aims of the analysis are: a) to provide insight into possible relationships (and interrelationships) between piezocone measurements and soil properties (c_u , OCR); and, b) to evaluate more fully the assumptions used in previous centerline solutions. Predictions of effective stresses around the piezocone are achieved using two generalized effective stress soil models:

1. The Modified Cam Clay model (MCC; Roscoe & Burland, 1968) is used as a 'base case' against which the results of a more complex model (MIT-E3) can be compared. Table 3.1 summarizes the input parameters used by MCC and gives specific values to describe the behavior of K_0 -consolidated Boston Blue Clay (Whittle, 1987, 1990).
2. The MIT-E3 model (Whittle, 1987, 1990) was developed to describe more realistically the behavior of K_0 -normally and moderately overconsolidated ($OCR \leq 8$) clays observed in laboratory tests. The MIT-E3 model describes a) strain-softening of clays in undrained shearing, b) anisotropic stress-strain-strength, and c) small strain non-linearity for overconsolidated clays. Table 3.2 summarizes the input parameters used by the model together with selected values for Boston Blue Clay. Detailed evaluations of model predictions have been shown elsewhere (Whittle, 1992).

Finite element solutions of the modified Poisson formulation (Section 2.5) are used to obtain predictions of excess pore pressures around the penetrometers.

3.3.2 Effect of Tip Shape

The tip geometry of the standard piezocone has an apex angle, $2\delta=60^\circ$. This geometry was adopted to be consistent with earlier standards for the electrical cone (DeRuiter, 1971). However, apart from the early work at MIT (Baligh et al., 1980; Vivatrat, 1978), there have been no detailed studies to evaluate the effects of tip geometry on piezocone predictions.

In recent analytical work (Baligh, 1985b, 1986a,b; Elghaib, 1989) it has been assumed that the simple pile geometry can provide a good approximation for the standard 60° cone. A major advantage of this assumption is that the soil strains can be obtained in closed form (Baligh, 1985; Teh & Houlsby, 1989). Thus, numerical approximations¹⁵ can be avoided and higher accuracy achieved in the predictions of effective stresses and pore pressures.

Figures 3.13a to d compare strain path predictions of effective stresses and excess

¹⁵These include the method of 'sources and sinks' (Baligh and Levadoux, 1980), boundary element/panel methods (Williamson, 1989) or finite differences (Teh, 1987).

pore pressures for; a) simple pile, b) (standard) 60° cone, and c) the 18° cone¹⁶. The solutions are presented for a 'base case analysis' using the MCC model with input parameters corresponding to K_0 -normally consolidated BBC ($K_0 = 0.48$). The figures show the following:

1. Predictions of radial effective stress σ'_r/σ'_{v0} (Figure 3.13a) show similar patterns for all three tip geometries. There are large gradients of σ'_r/σ'_{v0} in the immediate vicinity of the tip ($\sigma'_r/\sigma'_{v0} \approx 0.2$ at the tip for all three shapes) and immediately above the base of the cone. The radial effective stress reaches a maximum value, $\sigma'_r/\sigma'_{v0} = 0.8$, and is almost constant along the upper face of the cone. Along the shaft, $\sigma'_r/\sigma'_{v0} \approx 0.2$ -0.3 for all three tip shapes¹⁷, and are significantly less than $K_0 = 0.48$ which exists far from the penetrometer.
2. For the selected base case analysis, changes in the mean effective stress¹⁸, σ'/σ'_{v0} , (Figure 3.13b) are controlled exclusively by the magnitude of the final octahedral shear strain due to the isotropic yield behavior of the MCC model¹⁹. As a result, there are no changes in the shear induced pore pressures predicted around the surface of the penetrometer for the three geometries considered.
3. The cavity shear stress $(\sigma'_r - \sigma'_{\theta\theta})/2\sigma'_{v0}$ (i.e., q_h , the maximum shear stress acting in a horizontal plane) (Figure 3.13c) reaches a maximum value ($q_h/\sigma'_{v0} \approx 0.3$) close to the base of the 60° cone and simple pile tip. However, for the 18° cone, maximum cavity shearing occurs over the full face of the cone. At locations above the base, $q_h/\sigma'_{v0} \approx 0$ for the simple pile, while $q_h/\sigma'_{v0} < 0$ for the 18° and 60° cones. By contrast, for expansion of a cylindrical cavity the MCC soil model predicts $q_h = 0.37$ at the boundary of the expanding cylinder. These reductions of q_h around the shaft during cone penetration can be attributed to the details of the strain paths. Differences in q_h predicted from one dimensional cavity expansion and SPM solutions illustrate the importance of realistically the two dimensional nature of deep penetration. It should be noted that the reductions in q_h around the shaft predicted from the MCC model are consistent with previous predictions made by Baligh (1986a) using the elastic-perfectly plastic soil model.

¹⁶The 18° cone was used extensively in field tests presented by Baligh et al. (1980). The standard dilatometer (Chapter 5) also has an apex angle $\delta = 18$ -20°.

¹⁷At locations close to the shaft, small differences in effective stresses (Fig. 3.13a) may be due to numerical errors associated with the 18° and 60° cones.

¹⁸The shear induced pore pressure, $\Delta u_s \equiv -\Delta\sigma'$.

¹⁹For the base case analysis, $\sigma'/\sigma'_{v0} = 0.653$ at K_0 conditions and 0.475 at critical state conditions.

4. Figure 3.13d shows that large excess pore pressures $(u-u_0)/\sigma'_{v0} > 2-3$ are predicted close to the tips of the penetrometers for all three geometries. For locations around the shaft (e.g., $z/R \approx 15-20$), the magnitude ($\Delta u/\sigma'_{v0} \approx 1.2$ at the shaft) and distribution of excess pore pressures are very similar and are not affected by tip geometry. For locations closer to the tip, there are very high gradients of excess pore pressures which make interpretation of the contours very difficult. However, it can be seen from the shape of the contours that the excess pore pressures are approximately constant between the tip of the penetrometer and the base of the cones. The distribution of excess pore pressures are very similar at all locations for the simple pile and 60° cones. For the 18° cone, however, the distribution of excess pore pressures is significantly different. These results imply that the simple pile solutions cannot be used to simulate conditions around the tip of a sharp cone.

Figure 3.14 compares in more detail the excess pore pressures predicted for the three geometries for three different stress histories ($OCR = 1, 2$, and 4). The excess pore pressures are reported at locations a) radially around the shaft of the penetrometers at steady state conditions (far above the tip of the penetrometer), and b) along the centerline (ahead of the tip) and surface of the three penetrometer geometries:

1. Distributions of excess pore pressure predicted for the simple pile and 60° cone geometries are very similar at all locations²⁰: the maximum excess pore pressures occur at the tip of the penetrometers and match to within 1% at all OCR's. These results show that prediction of standard piezocone tip pore pressures can be reliably estimated from simple pile solutions, and confirms the hypothesis used in the centerline analyses presented by Elghaib (1989).
2. There are small variations in excess pore pressures ($10\pm\%$) at locations around the face of the 60° cone and simple pile. Thus, the pore pressures measured by a filter located on the face of the standard piezocone should measure very similar pore pressures to one located exactly at the tip.
3. For the 60° cone, there are severe gradients of excess pore pressures predicted close to the base of the cone ($z/R \approx 1.7$). These effects become more pronounced as OCR increases. In contrast, for the simple pile, there is a more gradual decrease in excess pore pressures in this same region. This result indicates that pore pressures measured

²⁰Differences up to 15% reported around the shaft may be due, in part, to numerical errors for the 60° cone.

at or close to the base of a 60° cone can exhibit significant scatter depending on the exact location and size of the porous filter.

4. For the 18° cone, excess pore pressures are approximately constant over the face of the cone for $z/R \geq 1.5$ ($\Delta u_{\max}/\sigma'_{v0}$ occurs close to the base of the cone, $z/R \approx 6.3$) and are similar in magnitude to the maximum pore pressures predicted by the 60° cone and simple pile geometry. There are large gradients of excess pore pressures very close to the tip of the 18° cone ($0 \leq z/R \leq 1.5$). Thus, tip pore pressures (at $z/R = 0$) for the 18° cone will be less reliable than those measured on the face of the cone.

The results in figures 3.13 and 3.14 have shown the similarity of effective stresses and excess pore pressures for the simple pile and 60° cone geometries. Based on these predictions, it can be expected that the tip resistance²¹, q_c , will be similar for the two geometries:

$$q_c = \frac{1}{\pi R^2} \int (p_n \sin \delta + p_t \cos \delta) dA \quad (3.11)$$

where p_n , p_t are the normal and tangential (total) interface tractions acting around the penetrometer face; δ is the cone half-angle; and A is the surface area of the face.

The distributions of interface tractions are computed from the predicted effective stresses and pore pressures (e.g., Figure 3.13 for $OCR = 1$ case). Table 3.3 summarizes the normalized net cone resistance $(q_c - \sigma'_{v0})/\sigma'_{v0}$ for: a) the simple pile, b) the 60° cone penetrometer, and c) the centerline analyses, $q_c = (\sigma_{zz})_{\text{tip}}$, used by Elghaib (1989) (for a simple pile geometry). The results show that the tip resistance of the simple pile is typically 5 - 10 % larger than the tip resistance of the 60° cone. For the base case analyses, centerline solutions compute a tip resistance which is approximately the average of the simple pile and 60° cone values. These results show that the much simpler centerline approximation can be used to provide reasonable estimates of tip resistance. Comparison of computed tip resistance to total vertical stress for simple pile penetration in normally consolidated BBC using the more realistic MIT-E3 soil model (Table 3.3) supports this conclusion.

Based on the above comparisons, the simple pile geometry can be used reliably to

²¹Note: $q_c \equiv q_T$ in analytical predictions.

estimate the influence of soil properties on various parameters used to interpret CPTU data. Hence, the simple pile geometry is used throughout the remainder of this chapter.

3.3.3 Effect of Stress History

Figures 3.15a to d show predictions of the effective stresses and pore pressures around the simple pile for the base case analysis (MCC model, K_0 -consolidated BBC) at OCR's = 1, 2 and 4. The results show the following:

1. Excess pore pressures, $\Delta u/\sigma'_{v0}$ (Figure 3.15d), increase very significantly with OCR. At the tip of the simple pile, excess pore pressures increase from $\Delta u/\sigma'_{v0} = 2.7$ at OCR = 1, to 6.2 at OCR = 4²². More modest changes occur at locations around the pile shaft ($\Delta u/\sigma'_{v0} = 1.2$ at OCR = 1, to 2.3 at OCR = 4)²³. These results show clearly that pore pressure measurements $\Delta u/\sigma'_{v0}$ made at filter locations on the tip or face of the piezocone should be more sensitive to changes in OCR in a particular deposit than filters located on the shaft. More detailed study of the predictions in Figure 3.15d shows that as OCR increases the zone of disturbance (i.e. of excess pore pressures) decreases. This result can be attributed, in large part, to linear pre-yield behavior of the MCC model²⁴ for clay with OCR > 1.
2. Contours of radial effective stress, σ'_r/σ'_{v0} (Figure 3.15a) show spatial variations that are qualitatively similar for all OCR's. Maximum values of σ'_r/σ'_{v0} occur on the penetrometer at $z/R \approx 0$ to 0.5. For locations around the shaft (at $z/R > 10$), the radial effective stress is lower than K_0 at OCR=1 (i.e. $\sigma'_r/\sigma'_{v0} = 0.3$ vs. $K_0 = 0.48$), but is higher than K_0 at OCR = 4 (i.e. $\sigma'_r/\sigma'_{v0} = 1.1$ vs. $K_0 = 0.75$). It is also important to note that there are large variations in radial effective stresses in the region $0 \leq z/R \leq 7.5$ where the friction sleeve is located in standard cone designs. These results may account for some of the scatter observed in measurements of f_s .
3. Changes in mean effective stress (i.e., shear induced pore pressures) are related to the critical state conditions described by the MCC model. The magnitude of σ'/σ'_{v0} increases substantially with OCR, but is approximately constant at all locations around the simple pile as the large strains produce critical state conditions. Similarly, contours of cavity shear stress, q_h/σ'_{v0} (Figure 3.15c) are qualitatively similar for all OCR's.

²²There are also large increases in tip resistance as shown in Table 3.3.

²³Similar results are also obtained for 180° and 60° cones in Fig. 3.14.

²⁴i.e. for $E < E_y$, the yield strain, MCC predicts no excess pore pressures in the soil.

3.3.4 Effect of Soil Model

Whittle (1987, 1990) has shown that much more realistic predictions of the behavior of K_0 -consolidated BBC (with $1 \leq \text{OCR} \leq 8$) measured in laboratory tests can be achieved using the MIT-E3 soil model. Figures 3.16a to d show predictions of the effective stresses and excess pore pressures around the simple pile for OCR's = 1, 2 and 4. When compared with the predictions for the MCC model (Figure 3.15) the following effects of soil model can be observed:

1. At a given OCR, the MIT-E3 model predicts much lower values of radial effective stress, σ'_r/σ'_{v0} (Figure 3.16a) acting on the penetrometer than MCC. At OCR's = 1 and 2, $\sigma'_r/\sigma'_{v0} \leq 0.3$ at all locations around the simple pile. At OCR = 4, the pattern of radial effective stress contours is similar for both MIT-E3 and MCC soil models. These results are due primarily to strain-softening described by MIT-E3.
2. For MIT-E3, the mean effective stress, σ'/σ'_{v0} (Figure 3.16b) decreases from a maximum value at the tip of the pile, to a minimum value on the pile shaft. Hence, the maximum shear-induced pore pressures are along the pile shaft. These results reflect anisotropic and strain softening behavior of the MIT-E3 model²⁵. These predictions are significantly more complex than results from the MCC model for which 'critical state' conditions are uniquely defined (at a given OCR).
3. Distributions of cavity shear stress, q_h/σ'_{v0} (Figure 3.16c) predicted by MIT-E3 are qualitatively similar to results for the MCC model and reflect the strain history for the simple pile geometry. Differences in magnitudes of q_h/σ'_{v0} reflect anisotropic shear strength of MIT-E3 (i.e. for shearing in the $r-\theta$ plane). Along the shaft ($z/R \geq 5$), $q_h/\sigma'_{v0} \Rightarrow 0$ for both soil models and $1 \leq \text{OCR} \leq 4$. As noted earlier, magnitudes of q_h near the pile shaft are strongly influenced by strain reversals and inelastic behavior of the soil, and predictions based on the Prandtl-Reuss model presented by Baligh (1986a) indicated results similar to those obtained from the more complex MCC and MIT-E3 models.
4. For OCR's = 1 and 2, the MIT-E3 model predicts that maximum excess pore pressures (Figure 3.16d) occur at locations along the face of the cone (excess pore pressures on the face are up to 20% larger than tip pore pressures). These results are shown more clearly in Figure 3.17. The excess pore pressures around the face (-0.5

²⁵In this case, σ'/σ'_{v0} is no longer uniquely defined at critical state conditions. Similar results were also presented by Baligh and Levadoux (1980) for the anisotropic MIT-T1 total stress soil model.

$\leq z/R \leq 1.7$) are up to 30-40% lower for the MIT-E3 model as compared to MCC results at OCR=1 and 2. These differences are due primarily to strain softening and anisotropic behavior of MIT-E3, as described above²⁶. At locations far above the tip, however, the two soil models give very similar predictions of excess pore pressures acting on the shaft of the penetrometer. The MIT-E3 model also predicts a much larger zone of disturbance (excess pore pressure) around the penetrometer, due primarily to small strain non-linearity. At OCR = 4, the maximum excess pore pressures predicted by MIT-E3 are only 10% lower than those for the MCC model. In this case, strain softening effects are minimized and inelastic behavior occurs much closer to the pile; hence differences between the two soil models become less significant.

3.3.5 Discussion and Summary

The analytical predictions described in the previous sections provide a basis for evaluating which engineering properties of cohesive soils can be estimated from piezocone measurements and what interpretation techniques are best suited for making these estimates. Table 3.4 summarizes the analytical predictions of net tip resistance and excess pore pressures for K_0 -consolidated BBC using the two effective stress soil models (MCC and MIT-E3) at OCR's 1, 2 and 4. The assumptions used to construct this table are as follows:

1. The simple pile geometry can be used to simulate stresses and pore pressure distributions around a 60° cone penetrometer (Figure 3.18). Partial predictions for the 60° cone are included for comparison.
2. The (net) tip resistance is estimated by integrating the surface tractions from Equation 3.11.
3. Four representative locations of pore pressure filter are considered (u_1, u_2, u_3, u_4 ; Figure 3.18). It is assumed that the pore pressures measured at the tip or on the face of the cone are very similar in magnitude (u_1) and are equal to the maximum pore pressures predicted analytically.
4. The pore pressure, u_2 , is measured at $z/R = 1.73$ for both the simple pile and 60° cones. Table 3.4 compares simple pile and 60° cone predictions for $(u_2 - u_0)/\sigma'_{v0}$ using the MCC model. For the 60° cone, a range of values must be specified due to

²⁶The predictions shown in Fig. 3.16d also imply limitations in the centerline analyses which require further investigation.

the severe gradients of excess pore pressures in this region (Figure 3.14).

5. Pore pressure measurements u_3 and u_4 correspond to positions approximately at the top of the standard friction sleeve and at steady state conditions around the shaft, respectively.

Table 3.4 also summarizes ratios of the predicted measurements which have been used previously in empirical correlations (see Section 3.2.2).

3.4 INTERPRETATION OF ENGINEERING PROPERTIES FROM PREDICTIONS

In this section, the correlations between undrained shear strength and OCR are compared systematically with piezocone "measurements" based on the analytical predictions presented in Section 3.3.

Correlations can be classified according to: a) the functional relationship between the measurement and soil property of interest; and, b) the range of applicability of the correlation (range of measurements, soil properties and soil types). For an 'ideal' correlation, the measurement is directly proportional to the engineering property of interest and the correlation is universally applicable. Correlations of this type can be evaluated directly from the predictions in Table 3.4. However, the existence of more complex functional relationships between the measurement and the soil property can only be evaluated by comparing predictions directly with field data from well-documented sites (Section 3.5).

It is important to emphasize that the interpretations described in this section are based on the predictions in Table 3.4 and contain certain limitations: a) the analyses have been performed for one particular type of soil (BBC), with $1 \leq \text{OCR} \leq 4$; and b) predictions of pore pressures around the piezocone (and hence also the total stress such as the tip resistance q_t) using strain path analyses are obtained by approximate methods (Chapter 2). Differences in predictions from the two soil models can be attributed to complex aspects of soil behavior (e.g., strain softening, anisotropy, etc)²⁷, and provide initial insight into the effects of soil type on piezocone measurements²⁸.

²⁷However, both MCC and MIT-E3 assume normalized clay behavior and neither describes rate effects (creep or strain rate dependent properties).

²⁸Further studies are currently in progress to generate solutions for different types of soil having stress-strain characteristics quite different from BBC.

3.4.1 Undrained Shear Strength

From the results shown in Table 3.4, it can be seen that changes in the undrained strength ratio, c_{uTC}/σ'_{v0} , correlate most closely with the net tip resistance, $(q_t - \sigma_{v0})/\sigma'_{v0}$, and tip pore pressures, $(u_1 - u_0)/\sigma'_{v0}$. Excess pore pressures measured at other locations around the cone (u_2, u_3, u_4) are much less sensitive to changes in undrained shear strength. Table 3.5 summarizes the predicted ratios²⁹, $(q_t - \sigma_{v0})/c_{uTC} = N_k$; $(u_1 - u_0)/c_{uTC} = N_{\Delta u}^1$; and $(u_2 - u_0)/c_{uTC} = N_{\Delta u}^2$. For an ideal correlation, N_k (or $N_{\Delta u}^i$) should be constant for all OCR's for each soil model. The results show the following:

1. For the MCC model, $N_k = 7.75 \pm 0.25$, which is within the lower range of values quoted previously from empirical correlations (e.g., Rad & Lunne, 1988) and from the centerline analyses (Elghaib, 1989). The MIT-E3 model predicts much lower tip resistance factors; $N_k = 4.9 \pm 0.5$. Comparison of predicted tip resistance factors, N_k , at various OCR's indicates that differences between the two model predictions are greatest at lower OCR's (1 to 2) where strain softening is most significant. Therefore, differences in tip resistance N_k predicted from the two models can be attributed in part to strain softening (sensitive) behavior modelled by MIT-E3. However, since smaller but still significant differences between the model predictions also occur at OCR=4 (where strain softening is negligible), it must be concluded that other aspects of soil behavior (anisotropy, stress-strain behavior) which are modelled differently by the two models also have a significant influence of predicted tip resistance values. The predictions suggest that strain softening behavior tends to reduce tip resistance. These results are consistent with field data reported by Ladanyi and Eden (1969) and also with centerline analyses of Elghaib (1989)³⁰. Overall, the predictions in Table 3.5 suggest that undrained shear strength can be correlated directly with the net tip resistance ($q_t - \sigma_{v0}$) for a given soil. Thus, tip resistance measurements can be used to estimate variations in undrained shear strength within a particular soil deposit. However, the analytical predictions imply that the magnitudes of the undrained shear strength can be affected significantly by soil sensitivity.
2. The predicted tip pore pressure factors, $N_{\Delta u}^1$ (Table 3.5), are similar in magnitude for

²⁹ The notation $N_k, N_{\Delta u}^i$ ($i = 1, 2, \dots$) is consistent with previous empirical correlations, see Section 3.2.

³⁰ However, not all sensitive clays have unusually low tip resistance factors (Aas et al., 1986). This contradictory trend in the field data may be explained by the fact that other aspects of soil behavior (stress-strain behavior, strain rate effects) can also have a strong influence on tip resistance.

both MCC and MIT-E3 models³¹ ($N_{\Delta u}^1 = 7.2 \pm 1.2$ for MCC, $N_{\Delta u}^1 = 5.0 \pm 0.6$ for MIT-E3). Shear-induced pore pressures $\Delta u_s/\sigma'_{v0}$ predicted from both models comprise a relatively small portion of the total pore pressure $\Delta u/\sigma'_{v0}$; i.e., the MCC model predicts $\Delta u_s/\Delta u = +5$ and -11% at OCR's of 1 and 4, respectively; while the MIT-E3 model predicts $\Delta u_s/\Delta u = +17$ and -11% at OCR's of 1 and 4, respectively. This result confirms earlier observations (Baligh, 1986b) that shear induced pore pressures represent a small fraction of the excess pore pressures at the tip of the penetrometer; hence, the ratio $(u_1 - u_0)/(q_t - \sigma'_{v0})$ (Table 3.4) varies over a small range (1.05-0.8 for MCC and 1.2-1.03 for MIT-E3).

3. Excess pore pressures measured at the base of the cone ($u_2 - u_0$) are 10 to 40% smaller than tip pore pressures (Table 3.4). Direct correlations with undrained shear strength are significantly less reliable (e.g., $N_{\Delta u}^2 = 5.0 \pm 1.3$ for MCC model) than those predicted for tip pore pressures or net tip resistance.

Further direct correlations can be considered from differences in the measured tip resistance and pore pressures; $(q_t - u^i)/c_{uTC} = N_{ke}^i$ (following the notation of Seneset et al., 1982). In this case, results from the MCC model (Table 3.5) suggest that c_{uTC} can be estimated from either $N_{ke}^1 = 2.55 \pm 0.05$ or $N_{ke}^2 = 4.9 \pm 0.1$. However, these predictions can be directly linked to assumptions of critical state behavior in the MCC model. For MIT-E3, values of N_{ke}^i are more variable due to the anisotropic properties described in Section 3.3.4. However, N_{ke}^2 values have the same variation as $N_{\Delta u}^1$. Thus, if base pore pressures are measured, $(q_t - u_2)$ provides a somewhat better correlation for undrained shear strength than $(u_2 - u_0)$ according to the MIT-E3 predictions.

3.4.2 Stress History

Using similar reasoning to the previous section, ideal correlations would show that piezocone measurements are proportional to the preconsolidation pressure, σ'_p . In Table 3.6, the predicted piezocone measurements are normalized by σ'_p to form a set of dimensionless ratios (M_x^i , comparable to N_x^i developed in Table 3.5 for c_{uTC}). Inspection of these results shows the following:

1. Qualitatively, the results presented in Tables 3.5 and 3.6 are very similar. Hence, $(q_t -$

³¹The predictions show variation scatter in the $N_{\Delta u}^i$ values than in N_k . In practice, however, errors in correcting the tip resistance ($q_c \Rightarrow q_T$) may make u_1 a more reliable measurement.

- σ_{v0}) and $(u_1 - u_0)$ are the most reliable measurements to estimate σ'_p .
2. For a given piezocone measurement (e.g., tip pore pressures, u_1), there is a greater scatter in the corresponding dimensionless ratio for σ'_p than for c_{uTC} (i.e. there is more variation in $M_{\Delta u}^i$ than in $N_{\Delta u}^i$). Thus, for a given soil deposit, the piezocone is a more sensitive indicator of changes in undrained shear strength, c_{uTC} , than of changes in preconsolidation pressure, σ'_p ³². However, the use of ratios such as B_q , to estimate OCR, can only be considered by comparison with measured data, as discussed in the next section.
 3. Examination of MCC predictions of B_q values indicates this parameter to be relatively insensitive to changes in OCR, regardless of whether the pore pressure is measured at the tip or base of the cone, with B_q^1 decreasing by 20-30% and B_q^2 decreasing by 30-40% over as OCR increases from OCR=1 to 4. However, the MIT-E3 predictions show B_q^2 to be much more sensitive to changes in OCR than , with B_q^2 decreasing by 50-60% and B_q^1 by approximately 10% as OCR increases from 1 to 4.

3.5 COMPARISON WITH MEASURED DATA

3.5.1 Measurements in Boston Blue Clay

In this section, the analytical predictions of piezocone measurements (Table 3.4) are compared directly with field data for Boston Blue Clay from two separate sites. These comparisons: a) illustrate capabilities and limitations of the strain path analyses for predicting the tip resistance and pore pressure measured by a piezocone; and b) enable the correlations proposed in the previous section to be evaluated.

Piezocone data have been obtained at two test sites containing deep layers of relatively uniform BBC:

1. Station 246 of the I-95 test embankment in Saugus, Massachusetts. This site has been extensively studied in conjunction with the development of in-situ test devices (e.g., Vivatrat, 1978; Morrison, 1984). Extensive field and laboratory testing has been carried out at the site to establish stratigraphy and engineering properties of the site. Figure 3.19a shows the soil profile, index properties and stress history at the site. In situ overconsolidation ratios range from OCR = 7 at depth $d = 30$ ft. to OCR = 1.23 at $d = 120$ ft. Piezocone data at the site, reported by Morrison (1984), include a) the

³²This result could have been anticipated from the SHANSEP equation where c_u is proportional to $(OCR)^m$, and the fact that $m < 1$.

uncorrected tip resistance, q_c , and b) the tip pore pressures, u_1 . Tip resistance was corrected as recommended by Baligh et al. (1980):

$$q_T = q_c + 0.3 u_1 \quad (3.12)$$

The corrected tip resistance is presented in this section. Baligh et al. (1980) also report pore pressures at four filter locations around an 18° cone penetrometer. These data have been discussed by Whittle and Aubeny (1990) and are not considered further in this section.

2. South Boston Special Test Program for the Central Artery/Third Harbor Tunnel (CA/T) project. This site, located in South Boston immediately adjacent to the proposed route of a third harbor tunnel has been extensively studied by Haley and Aldrich, Inc. and by research at MIT³³. Figure 3.19b summarizes the index properties and stress history at the test site obtained from extensive oedometer and continuous loading consolidation tests. In-situ OCR's at the site range from OCR ≈ 5 at elevation³⁴ El. = 65 ft. to OCR = 1.1 at El. = -20 ft. The soil is significantly more sensitive below elevation, El. = 20 ft. Piezocone data were obtained at two locations and include: a) corrected tip resistance; and b) pore pressures at the base of the cone, u_2 .

Figure 3.20 compares analytical predictions of the net tip resistance with the measured data, $(q_T - \sigma_{v0})/\sigma'_{v0}$, at the two sites:

1. The reported measurements are average values recorded over 5 ft. intervals from the original penetration records. Error bars represent maximum and minimum measured data (over the same interval). Scatter in the overconsolidation ratio is based on the laboratory test data shown in Figure 3.19.
2. The analytical predictions are directly from Table 3.4. Input parameters for the MCC and MIT-E3 models (Tables 3.1 and 3.2, respectively) are based primarily on laboratory test data on resedimented BBC.
3. The most noticeable observation from Figure 3.20 is that the test data from the two sites are not consistent. The net tip resistance (at a given OCR) is significantly (30 - 50%) higher at the Saugus site than at South Boston. The source of these differences may be partly attributed to uncertainties in the 'true' tip resistance at the Saugus site.

³³This project is supported by a contract with Haley & Aldrich, Inc., Cambridge, MA.

³⁴Elevations in the figure are quoted with respect to the project datum, which equals NGVD plus 100ft.

Further investigation is required to establish other possible causes of this discrepancy.

4. The analytical predictions using the MCC model match the measured data very consistently (except at $OCR=4$) at the Saugus site, while MIT-E3 underpredicts the net tip resistance. At South Boston, good agreement is found using the MIT-E3 model, while MCC overpredicts the measured data. If both sets of measurements are reliable, then these trends suggest significant differences in normalized soil properties at the two sites (either sensitivity or stiffness). In both cases, the net tip resistance increases significantly with OCR as predicted from the strain path analyses.

Figure 3.21 compares the analytical predictions with the measured excess pore pressures at the two sites. At the Saugus site the MCC model gives excellent agreement with tip pore pressures $(u_1 - u_0)/\sigma'_{v0}$, while MIT-E3 underpredicts the measurements by up to 50% for $OCR \leq 2$. For $OCR < 2$, the measured data confirm the sensitivity of the tip pore pressures to changes in overconsolidation ratio, as predicted by the strain path analyses. The decrease in tip pore pressures with increasing OCR for $OCR > 2$ is not consistent with model predictions; However, as discussed in Section 3.5.2 the Saugus tip pore pressure measurements for $OCR > 2$ do not reflect typical trends. At South Boston, the base pore pressures show very little variation with OCR and hence confirm previous assessments that preconsolidation pressures cannot be reliably estimated from the $(u_2 - u_0)$ data. Analytical predictions for both soil models underpredict the measured data at $OCR \leq 2-3$.

The differences in tip resistance and piezocone pore pressures (i.e., $(q_T - u_1)/\sigma'_{v0}$ from Saugus and $(q_T - u_2)/\sigma'_{v0}$ from South Boston; Figure 3.22) both show well defined trends with OCR. Analytical predictions from the MCC model are in excellent agreement with the data at Saugus, but significantly overpredict the behavior measured at South Boston. In contrast, MIT-E3 gives better matching with South Boston data and does not describe correctly the trends measured at Saugus.

Finally, the ratios of excess pore pressure to net tip resistance are considered in Figure 3.23. The data from the Saugus site (B_q^1 ; using tip pore pressures) show a consistent decrease with OCR and range from $B_q^1 \approx 1.1$ at $OCR \approx 1.2$ to 0.7 at $OCR = 4$. Predictions using the MCC model again show excellent agreement with these data, while MIT-E3 gives a consistently higher value of B_q^1 . At South Boston, the B_q^2 ratio (this is the more common ratio presented in empirical correlations after Senneset et al., 1982) shows much larger changes with OCR, ranging from $B_q^2 = 1.7$ at $OCR = 1.1$, to 0.6 at $OCR \approx 5$. In this case the MCC model significantly underpredicts the measured ratio at $OCR < 4$.

However, MIT-E3 predicts higher values of B_q^2 and is more consistent with the trends in the measured data.

Overall, the results in Figure 3.23 are consistent with earlier observations that BBC at the South Boston site may exhibit significantly different normalized properties to the material underlying the Saugus site. It should be noted that the stress history at the Saugus site is less well defined (and possibly less reliable) than that at the South Boston site. In addition, the corrected tip resistances from the Saugus site are based on tip rather than base pore pressures, making them less reliable than the tip resistances from the South Boston site, which are corrected based on base pore pressure measurements. Consequently, the Saugus q_t -OCR correlations should be considered less reliable than the South Boston correlations, which may account for the differences in measured correlations obtained from the two sites. In particular, the clay at South Boston appears to be more sensitive at low OCR and is therefore better described by the MIT-E3 analyses.

3.5.2 Review of Field Data at Other Selected Sites

This section compares piezocone measurement predictions and measurements in BBC to measurements obtained from piezocone soundings in the four well-documented sites: 1) Amherst (Connecticut Valley Varved Clay), 2) Emmerstad, 3) Inchinnan, and 4) Onsøy. Pertinent data for these sites is summarized in Table 3.7. All soundings were obtained from 60° cones having cross-sectional area of 10 cm², except for the sounding at the Inchinnan site, which used both 5 cm² and 10 cm² cones. The cone used at the Inchinnan site was also equipped with four pore pressure filters, located on the cone face, base, and the middle and top of the friction sleeve.

Figures 3.24a to f compare the measured tip resistance, pore pressures and dimensionless ratios with the analytical predictions (for the BBC properties) at these sites. Figure 3.24a shows the net normalized tip resistance $(q_t - \sigma_{v0})/\sigma'_{v0}$ versus OCR:

1. For $1 \leq \text{OCR} \leq 3$, the Onsøy, Amherst, Saugus, and Emmerstad data fall into a relatively narrow band which defines the upper bound of the measured data. Above OCR=3, the Saugus data exhibits an anomalous trend of decreasing tip resistance with increasing OCR. The South Boston data defines the lower bound of the scatter band. At low OCR the Inchinnan data agree with the South Boston data, but at higher OCR they agree with the other four sites.
2. Both sets of model predictions lie within the scatter band of the measured data. The MIT-E3 predictions are in good agreement with the South Boston data, but represent a

lower bound of the data from these six sites. In contrast the MCC predictions correspond more closely with the data from the Saugus sites.

3. The width of the scatter band is such that at a given OCR the net normalized tip resistance varies by a factor of 2.

Plots of normalized tip or face excess pore pressures shown in Figure 3.24b and the net normalized base pore pressures in Figure 3.24c show:

1. There is a very large scatter in tip pore pressures measured at the six sites. At all sites, with the exception of Saugus, the tip/face excess pore pressures increase monotonically with increasing OCR. The width of the scatter band in Figure 3.24b is such that, at a given value of the OCR, the corresponding excess tip pore pressure can vary by a factor of 1.5 to 2.0.
2. The MIT-E3 predictions underestimate significantly the measured pore pressure, while MCC results are in good agreement with data reported from the Amherst site. Both sets of predictions underpredict the measured pore pressures at the Onsøy and Emmerstad sites.
3. Most of the measured data indicate relatively small changes in base excess pore pressures with increasing OCR (Figure 3.24c for the South Boston, Emmerstad, and Inchinnan sites). The Emmerstad site data shows an erratic pattern which shows sharp increases in shoulder pore pressures to approximately OCR=4 and much lower pore pressures at higher OCR's.
4. Model predictions underpredict the magnitudes of measured base pore pressures but show similar variations with OCR.

Plots of B_q^1 and B_q^2 versus OCR shown in Figures 3.24 d and e indicate:

1. Sensitivity to changes in OCR at low OCR (1 to 2) varies widely among soil types. Measurements at the Inchinnan site show B_q^1 values decreasing from 1.5-1.7 down to $B_q^1=1.2$ at OCR=2. In contrast, data from Onsøy and Amherst data are almost constant over the same range of stress history.
2. Except for the Inchinnan data B_q^1 shows little variation with OCR. This trend is consistent with model predictions.
3. Plots of B_q^2 versus OCR show that three of the sites have a well-defined trend of decreasing B_q^2 with increasing OCR³⁵.

³⁵The Onsøy data show little variation in B_q^2 with changing OCR; however, the variation in OCR at that site is relatively slight.

4. The width of the scatter band is such that for a given value of OCR B_q^2 varies by a factor of 2.
5. Model predictions are in overall good agreement with the Amherst, Saugus, South Boston, and Onsøy measurements.

Measurement of values of $\beta = (u_2 - u_0)/(u_1 - u_0)$ was possible at three sites (Figure 3.24f). This figure shows that β decreases slightly with OCR and is in good agreement with the model predictions.

For the purpose of developing site specific correlations of piezocone measurements to OCR, the predictions and measured data suggest that the reliability of the correlation factors should be ranked in the following order:

1. Tip pore pressure $(u_1 - u_0)/\sigma'_{v0}$ shows well-defined correlation with OCR, assuming the pore pressure measurements are reliable.
2. Net tip resistance $(q_t - \sigma'_{v0})/\sigma'_{v0}$ is in theory more sensitive to changes in OCR than tip pore pressure; however, current limitations in equipment design require a correction which reduces the reliability of this measurement.
3. B_q^2 shows better correlations to OCR than B_q^1 , although it is much less sensitive to changes in OCR than either the tip resistance or the tip pore pressure.
4. Excess pore pressures measured at the base of the cone $(u_2 - u_0)/\sigma'_{v0}$ appear unsuitable for estimating OCR due to the insensitivity of this parameter to changes in OCR, particularly for $OCR > 2$.
5. The β parameter generally shows little variation with changing OCR; hence, there appears to be little justification for using this parameter in correlations.

As stated earlier, soundings at the Inchinnan site included pore pressure measurements at four filter locations located at the tip (u_1), shoulder (u_2), middle of the friction sleeve (u_3), and top of the friction sleeve (u_4). Figure 3.25 compares MCC and MIT-E3 predictions (for cone penetration in BBC) to the Inchinnan measurements. This figure shows that both sets of predictions tend to underestimate the measurements by 30-40% at locations 1, 2, and 3 and by up to 20% at location 4.

3.5.3 Calibration Chamber Data

This section compares the results of penetration tests in laboratory calibration chambers performed at Oxford University to the predictions presented in Section 3.3.

Consolidation chamber tests have the following advantages over field measurements for validating predictions: 1) close control over stress state and stress history, 2) soil homogeneity, and 3) the capability for measuring pore pressures in the soil mass around the penetrometer during penetration. May (1987) performed piezocone penetration tests in normally consolidated Speswhite kaolin ($w_L=66\%$, $I_p=33\%$) in a laboratory consolidation chamber. Nyirenda (1989) extended this work to lightly overconsolidated kaolin with $1.6 \leq OCR \leq 9.1$. The kaolin specimens were prepared by consolidating from a slurry with initial water content, $w_c=120\%$, to maximum vertical stresses in the range 300-900 kPa.

Tests were performed using a 5 cm² penetrometer in a 1000mm diameter chamber and a 1 cm² penetrometer in a 580mm chamber. Thus the ratio of chamber radius to penetrometer radius $R_{cc}/R=40$ to 50 in these tests. Comparison of tip and pore pressure measurements obtained from 5 cm² and 10 cm² cones at the Inchinnan site showed that cone size has negligible influence on measurements (May, 1987). The 5 cm² piezocone was instrumented with filters located at the mid-face, base, and the middle and top of the friction sleeve ($z/R=0.87, 2.2, 7.3$ and 12.4 , respectively), while the miniature cones had a single filter, located at either the mid-face or the base of the cone. Tip resistance correction factors (Equation 3.1) were: $a=0.448$ for the 5 cm² cone, and $a=0.4464-0.4693$ for the 1 cm² cones³⁶.

Figure 3.26 compares consolidation chamber piezocone measurements for various OCR's with Strain Path predictions for BBC (Table 3.4):

1. The Strain Path predictions for the MCC and MIT-E3 models bound the measured net normalized tip resistances, $Q = (q_t - \sigma_{v0})/\sigma'_{v0}$, for $OCR \leq 4$.
2. For $OCR=1$ to 2, the MIT-E3 predictions overpredict B_q^2 by 5-50%, while the MCC predictions underpredict B_q^2 by 0-30%. For $OCR=2$ to 4 both sets of model predictions lie within the scatter band of the measured data.
3. Measured β values are in general agreement with MCC predictions, while MIT-E3 overpredicts β by 25% at $OCR \leq 2$.
4. Pore pressure measurements at the cone face exceed MIT-E3 predictions by 0-30%. MCC predictions exceed measurements by up to 60%.
5. Pore pressure predictions at the cone base, mid-sleeve, and top-sleeve, (u_2, u_3 , and u_4) from both models are in excellent agreement with the measured data.

Overall, given that the scatter in test data is of the same order of magnitude as the

³⁶These corrections were obtained by hydraulic chamber tests.

discrepancies between predictions and measurements, agreement between predictions and measurements appears to be quite good. Particularly remarkable is the excellent agreement between pore pressure predictions and measurements at the base and shaft of the cone. This last result is surprising in view of the fact that previous comparisons consistently show that Strain Path analyses underpredict significantly (by up to 50%) excess pore pressures in field tests (Section 3.5.1; Levadoux and Baligh, 1980). It should also be noted that the shaft excess pore pressures measured during penetration in chamber test soils, $\Delta u_4/\sigma'_{v0} = 1.2$, are significantly lower than typical values measured during penetration in field tests ($\Delta u_4/\sigma'_{v0} = 2.2-2.4$; Baligh, 1986b). This suggests that the structure of natural clays can have an important impact on penetration pore pressures (possibly related to properties of higher stiffness and greater sensitivity; Burland, 1990).

Contours of measured normalized excess pore pressure $(u-u_0)/\sigma'_{v0}$ obtained from chamber test data in normally consolidated kaolin are compared to MIT-E3 predictions for normally consolidated BBC in Figure 3.27. The internal pore pressures were measured using pore pressure probes which were inserted into the soil cake through ports in the side of the calibration chamber. This figure shows overall excellent agreement between predictions and measurements. If this figure is compared with the MCC predictions of excess pore in Figure 3.13, it can be seen that, although the MCC predictions tend to agree with MIT-E3 predictions at the shaft boundary, they do not provide realistic spatial distributions of excess pore pressure.

3.6 SUMMARY AND CONCLUSIONS

This chapter analyzes the measurements of tip resistance and excess pore pressures during steady piezocone penetration. A comprehensive series of Strain Path predictions for tests performed in BBC with $1 \leq OCR \leq 4$ were performed to assess the effects of: 1) tip shape (Figures 3.13 and 3.14), 2) stress history (Figure 3.15), and 3) soil model (Figures 3.16 and 3.17). The main results from these predictions can be summarized as follows:

1. Distributions of excess pore pressures around the 60° cone (standard piezocone) and the simple pile are very similar at all locations. The total vertical stress at the tip of a simple pile closely approximates the tip resistance of a 60° cone. These predictions: 1) justify the use of simple pile solutions to simulate penetration of the standard 60° cone; and 2) support the use of simple pile centerline solutions Elghaib (1989) to estimate

cone tip resistance.

2. Tip shape (based on comparisons of the simple pile, 60° and 18° cones) has minimal ($\pm 10\%$) effect of predicted excess pore pressures on the shaft of the cone.
3. The predicted variation in excess pore pressure along the cone face (60° and 18°) is minor ($\pm 10\%$); hence, locating a pore pressure sensing element anywhere on the cone face should yield similar measurements. Sharp pore pressure gradients are predicted at the cone base, indicating that pore pressure measurements will be sensitive to location of the pore pressure sensing element in this region.
4. Predicted tip and face excess pore pressures increase significantly with OCR (by a factor of 2.0 to 2.5 for an increase in OCR from 1 to 4), while the shaft and base excess pore pressures are less sensitive to changes in OCR. A practical implication of this set of predictions is that tip/face pore pressures measurements are more reliable indicators for profiling the stress history of a soil deposit.
5. Comparison of MCC and MIT-E3 predictions during simple penetration indicates that soil model has negligible influence on predictions of shaft excess pore pressures. This result is remarkable in view of the differences in the formulation of the two models. However, at the tip of the penetrometer, MIT-E3 predictions of excess pore pressures are significantly lower (up to 40%) than MCC predictions. This behavior can be explained in part by the strain softening behavior simulated by the MIT-E3 model.

A variety of predicted piezocone measurements and ratios of measurements were reviewed to assess their suitability for use as a basis for correlation to undrained shear strength, c_u , and stress history, OCR (Tables 3.3 and 3.4). The predictions indicated that the net tip resistance and the excess pore pressure at the cone tip are the most sensitive indicators of c_u and OCR.

Detailed analyses were performed to identify possible functional relationships between piezocone measurements and undrained shear strength, c_{uTC} (Table 3.5), and preconsolidation pressure, σ'_p (Table 3.6). This study showed that undrained shear strength c_{uTC} can be correlated to either net tip resistance or tip excess pore pressure by an approximately linear relationship.

The predicted measurements described above were compared to field measurements in Boston Blue Clay at a well-documented site in South Boston (Figures 3.20 through 3.23). The comparisons showed that MIT-E3 predictions of net tip resistance are in excellent agreement with measurements; however, the predictions of excess pore

pressures significantly underestimate (by up to 30%) measurements. Further comparisons with piezocone measurements in Boston Blue Clay at the Saugus site show significant discrepancies. This may be due to differences in test procedures (tip correction factors, etc.) or may indicate differences in soil properties at the two sites which require further validation.

Piezocone data at four additional well-documented sites reported in the literature were compiled and are summarized in Figure 3.24. Comparisons indicated significant scatter in the measurements indicating that piezocone measurements are significantly influenced by parameters other than OCR (e.g.; stress-strain behavior, sensitivity); hence, universal correlations applicable to all soil types are unlikely to be meaningful. Predictions and field measurements of various piezocone parameters indicate the order of reliability for profiling OCR should be ranked as follows: 1) net tip pore pressure $(u_1 - u_0)/\sigma'_{v0}$, 2) net tip resistance $(q_t - \sigma_{v0})/\sigma'_{v0}$, 3) $B_q^2 = (u_2 - u_0)/(q_t - \sigma_{v0})$, 4) $B_q^1 = (u_1 - u_0)/(q_t - \sigma_{v0})$. Excess pore pressures at the base of the cone, $(u_1 - u_0)/\sigma'_{v0}$, and the factor $\beta = (u_2 - u_0)/(u_1 - u_0)$ are relatively insensitive to changes in OCR, and are therefore not suitable indicators of stress history.

Calibration chamber test measurements of the distribution of excess pore pressures during cone penetration in resedimented kaolin are in excellent agreement with predictions obtained using Boston Blue Clay parameters, suggesting that Strain Path analyses are capable of making realistic predictions of disturbance effects for deep penetration in clays.

Test Type	Parameter/ Symbol	Physical contribution/ meaning	Boston Blue Clay
Oedometer or CRS	e_0	Void ratio at reference stress on virgin consolidation line	1.12
	λ	Compressibility of virgin normally consolidated clay	0.184
	κ	Compressibility of overconsolidated clay	0.034
Undrained Triaxial (OCR=1; CK ₀ UC)	ϕ'_{TC}	Critical state friction angle in triaxial compression	33.4°
K ₀ -oedometer or K ₀ -triaxial	2G/K	Ratio of elastic shear to bulk modulus (Poisson's ratio for initial unload)	1.05

Table 3.1 Input Material Properties used by the MCC Model

Test Type	Parameter/ Symbol	Physical contribution/ meaning	BBC	Empire Clay
Oedometer or CRS	e_0	Void ratio at reference stress on virgin consolidation line	1.12	1.26
	λ	Compressibility of virgin normally consolidated clay	0.184	0.274
	C	Non-linear volumetric swelling behaviour	22.0	24.0
	n		1.6	1.75
	h		0.2	0.2
K_0 -oedometer or	K_{0nc}	Irrecoverable plastic strain		
K_0 -triaxial	2G/K	K_0 for virgin normally consolidated clay	0.48	0.62
Undrained Triaxial Shear Tests: OCR=1; CK ₀ UC OCR=1; CK ₀ UE OCR=2; CK ₀ UC	ϕ'_{TC}	Ratio of elastic shear to bulk modulus	1.05	0.86
	ϕ'_{TE}	Critical state friction angles in triaxial compression and extension (large strain failure criterion)	33.4 ⁰	23.6 ⁰
	c	Undrained shear strength (geometry of bounding surf.)	45.90*	21.6 ⁰
	s_t	Amount of strain softening in undr. triax. comp.	0.86	0.75
	ω	Non-linearity at small strains in undrained shear	4.5	3.0
	γ	Shear induced pore pressure for OC clay	0.07	0.2
	κ_0	Small strain compressibility at load reversal**	0.5	0.5
Resonant Column	ψ_0	Rate of evolution of anisotropy	0.001	0.0035
Drained Triaxial			100.0	100.0

Table 3.2 Input Material Properties used by the MIT-E3 Model

* Value is based on data from Ladd & Varallyay (1965). More recent data suggest $\phi'_{TE}=40^0$

** Alternatively use field shear wave velocity test data

Predictions of Net Tip Resistance, $\frac{(q_t - \sigma_{v0})}{\sigma'_{v0}}$				
Soil Model	OCR	Simple Pile	60° Cone	Centerline Analysis
MCC	1.0	2.65	2.50	2.61
	2.0	4.77	4.44	4.66
	4.0	8.43	7.71	8.07
MIT-E3	1.0	1.40-1.60		1.66

* Effective stresses from MCC model for K_0 -consolidated BBC
 Pore pressures from modified Poisson formulation

Table 3.3 Comparison of tip resistance predictions using the Strain Path Method

Model	OCR	K ₀	Analytical Predictions of Piezocone Measurements					Predicted Ratios of Measurements		
			$\frac{q_t - \sigma_{v0}}{\sigma'_{v0}}$	$\frac{u_1 - u_0}{\sigma'_{v0}}$	$\frac{u_2 - u_0}{\sigma'_{v0}}$	$\frac{u_3 - u_0}{\sigma'_{v0}}$	$\frac{u_4 - u_0}{\sigma'_{v0}}$	$B_q^1 = \frac{u_1 - u_0}{q_t - \sigma_{v0}}$	$B_q^2 = \frac{u_2 - u_0}{q_t - \sigma_{v0}}$	$\beta = \frac{u_2 - u_0}{u_1 - u_0}$
MCC	1.0	0.48	2.5 - 2.6	2.7	2.0 (2.0 - 2.5)	1.4	1.3	1.04 - 1.08	0.77 - 0.80 (0.8 - 1.0)	0.74 (0.7 - 0.9)
	2.0	0.57	4.4 - 4.7	4.1	2.7 (2.8 - 3.6)	1.8	1.7	0.88 - 0.93	0.58 - 0.61 (0.6 - 0.8)	0.66 (0.7 - 0.9)
	4.0	0.75	7.7 - 8.1	6.2	3.9 (3.9 - 5.3)	2.4	2.3	0.77 - 0.81	0.48 - 0.51 (0.5 - 0.7)	0.62 (0.6 - 0.9)
MIT-E3	1.0	0.48	1.4 - 1.6	1.8	1.6	1.3	1.2	1.12 - 1.29	1.03 - 1.17	0.91
	2.0	0.57	2.3 - 2.5	2.5	2.1	1.6	1.5	1.0 - 1.08	0.85 - 0.93	0.85
	4.0	0.75	5.4 - 6.1	5.9	3.4	2.2	2.0	0.96 - 1.09	0.55 - 0.63	0.58

() Predicted values for 60° cone tip geometry

* See Figure 3.18 for locations of porous filter elements

Table 3.4 Predictions of piezocone (simple pile) measurements for K₀-consolidated BBC

Model	OCR	$\frac{c_{uTC}}{\sigma'_{vc}}$	K_0	$N_k = \frac{q_u - \sigma_{v0}}{c_{uTC}}$	$N_{\Delta u}^1 = \frac{u_1 - u_0}{c_{uTC}}$	$N_{\Delta u}^2 = \frac{u_2 - u_0}{c_{uTC}}$	$N_{ke}^1 = \frac{q_u - u_1}{c_{uTC}}$	$N_{ke}^2 = \frac{q_u - u_2}{c_{uTC}}$
MCC	1.0	0.32	0.48	8.0	8.4	6.3	2.6	1.8
	2.0	0.57	0.57	7.8	7.1	4.6	2.5	5.0
	4.0	1.05	0.75	7.5	5.9	3.7	2.6	4.8
Variation*				3%	17%	26%	2%	2%
MIT-E3	1.0	0.33	0.48	4.5	5.5	4.8	2.1	2.1
	2.0	0.54	0.57	4.4	4.4	3.7	1.7	2.1
	*4.0	1.05	0.75	5.4	5.6	3.3	0.8	3.1
Variation*				10%	12%	19%	45%	13%

* Variation = $\frac{\Delta x}{\hat{x}} \cdot 100\%$; where $\Delta x = x_{max} - x_{min}$ and $\hat{x} = \frac{x_{Min} + x_{Max}}{2}$

Table 3.5 Dimensionless ratios for predicting undrained shear strength (for simple pile)

Model	OCR	$\frac{e_{ult}}{\sigma'_{vc}}$	K_0	$M_k = \frac{q_t - \sigma_{v0}}{\sigma'_p}$	$M_{\Delta u}^1 = \frac{u_1 - u_0}{\sigma'_p}$	$M_{\Delta u}^2 = \frac{u_2 - u_0}{\sigma'_p}$	$M_{ke}^1 = \frac{q_t - u_1}{\sigma'_p}$	$M_{ke}^2 = \frac{q_t - u_2}{\sigma'_p}$
MCC	1.0	0.32	0.48	2.6	2.7	2.0	0.9	1.6
	2.0	0.57	0.57	2.3	2.1	1.4	0.7	1.4
	4.0	1.05	0.75	2.0	1.6	1.0	0.7	1.3
Variation*				13%	26%	33%	13%	10%
MIT-E3	1.0	0.33	0.48	1.5	1.8	1.6	0.7	0.9
	2.0	0.54	0.57	1.2	1.3	1.1	0.5	0.7
	4.0	1.05	0.75	1.4	1.5	0.9	0.2	0.8
Variation*				11%	16%	28%	56%	13%

* Variation = $\frac{\Delta x}{\hat{x}} \cdot 100\%$; where $\Delta x = x_{max} - x_{min}$ and $\hat{x} = \frac{x_{Min} + x_{Max}}{2}$

Table 3.6 Dimensionless ratios for predicting pre-consolidation pressure (for simple pile)

Site	South Boston	Saugus	Onsøy	Emmerstad	Amherst	Inchinnan
Reference	Ladd (1990)	Vivatrat (1978)	Lacasse et al. (1981)	Lacasse et al. (1985)	Vivatrat (1978)	Sills et al. (1988)
Test Depth	2-34	12-28	2-16m	3-8m	4-22	2-12m
Soil Type	CL	CL	CH	CL	Varved Clay ML, CL, CH	CL
Sensitivity		5-9	5-6	>60	5-7	**
OCR	1.1-6	1.1-4	1.3-15	2.4-7.3	1.3-5.5	1.1-2.6
PWP meas. Location*	2	1	1, 2	1, 2	1	1, 2, 3, 4

*See Figure 3.18 for filter location definition

**Sensitivity measurement not known, liquidity index $I_L=0.6-1.2$

Table 3.7 Soil Properties at Six Test Sites

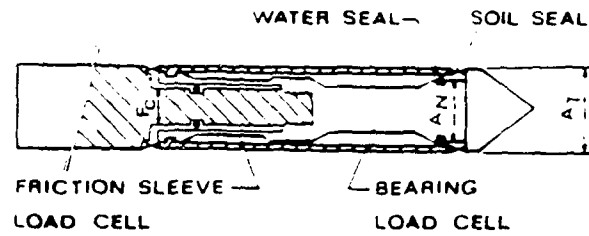


Figure 3.1a Typical Electrical Cone (Schaap and Zindberg, 1982)

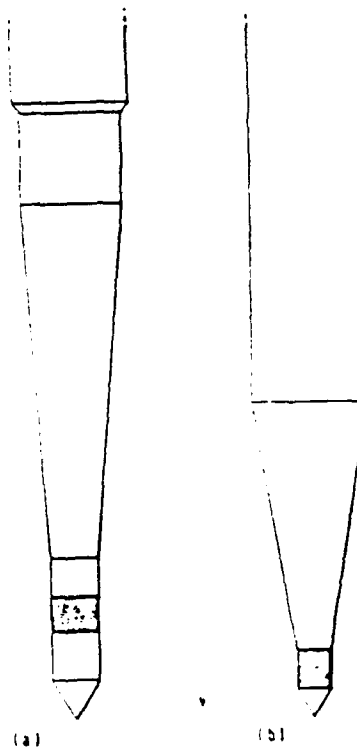


Figure 3.1b Pore pressure probes (Torstensson, 1975; Wissa, 1975)

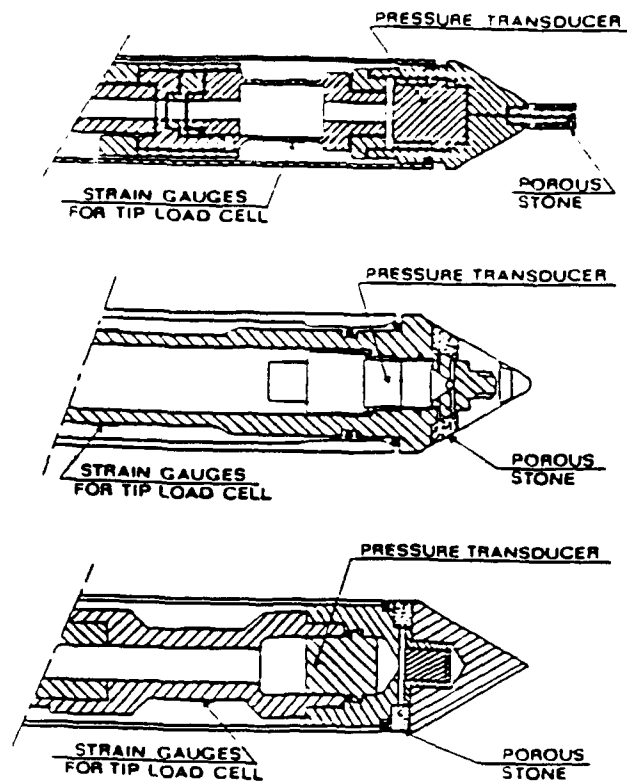


Figure 3.2 Examples of piezocones Jamiolkowski (1985)






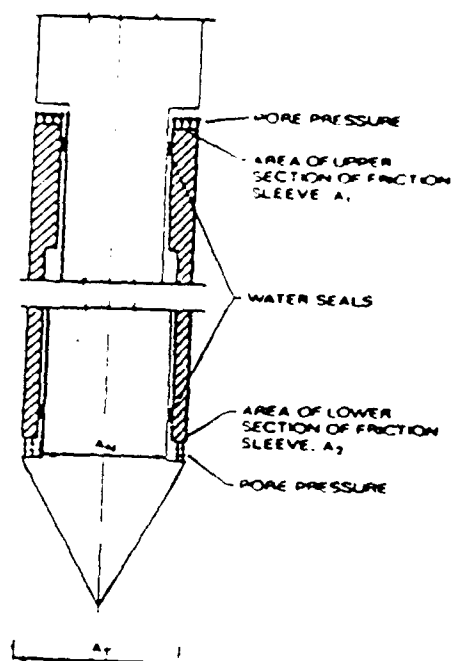
Filter Location	Filter Material	Filter Thickness (mm)	Reference
	Stainless Steel	1.28	Wissa (1975)
	Stone	7.0	Wissa (1975)
	Ceramic Stone	6.5 7.0	Zuidberg et al (1982) McClelland (1985)
	Stainless Steel Polyethylene Stainless Steel	2.5 5.0 4.0	Forstensson (1982) Campanella et al (1982) vd Berg (1982)
	Sintered Bronze		McClelland (1985)

Figure 3.3 Pore pressure filter designs for piezocone



NET AREA RATIO, $\alpha = \frac{A_2}{A_1}$

FRICTION SLEEVE UNEQUAL END AREA,
 $A_1 \neq A_2$

Figure 3.4a Unequal surface areas of cones (Battaglio and Maniscaldo, 1983)

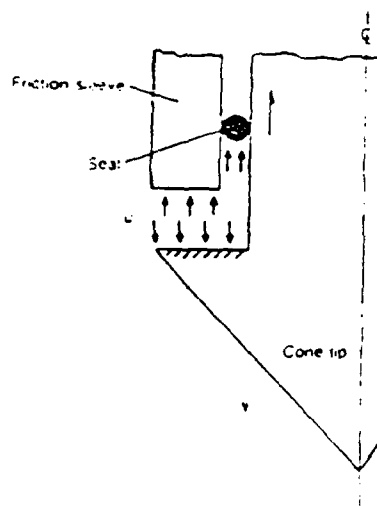
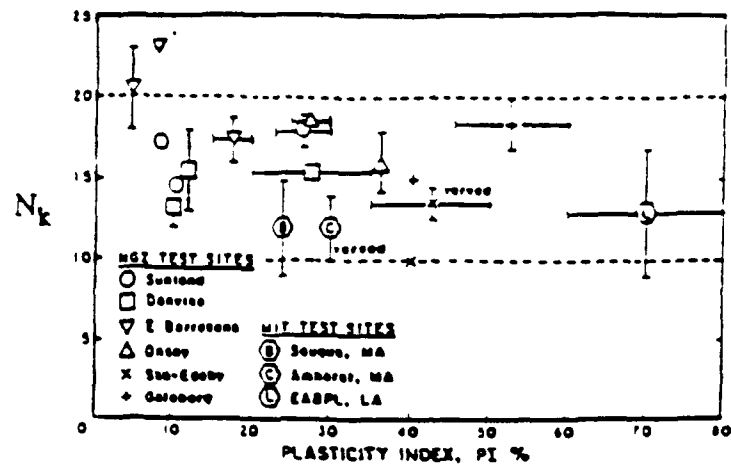
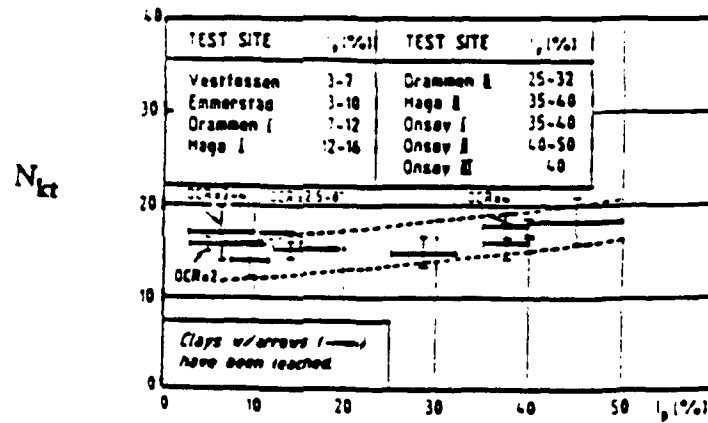


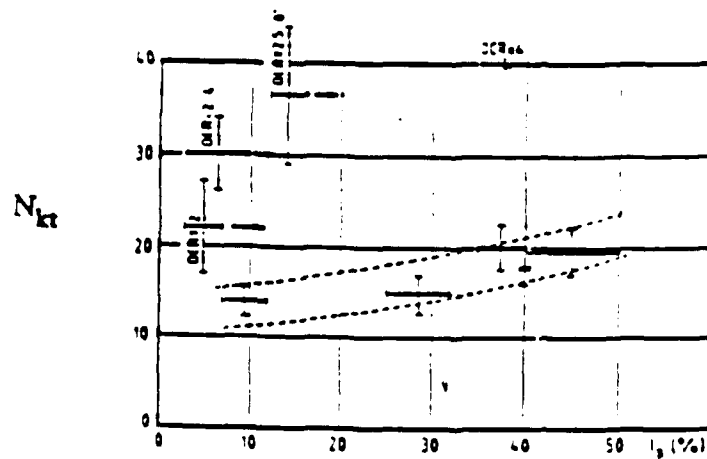
Figure 3.4b Unequal surface areas of cones (Sills et al., 1989)



a) $s_u = \mu s_u (FV)$ (From Baligh et al., 1980)

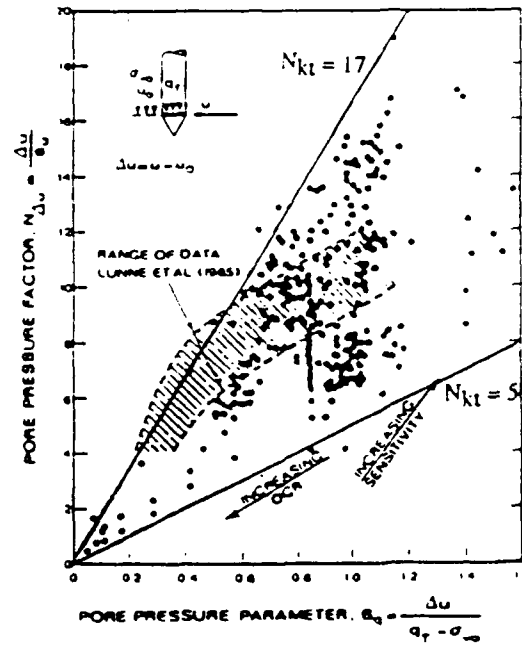


b) $s_u = s_u(LAB) = s_u(DSS)$ (From Aas et al., 1986)



c) $s_u = \mu_A s_u (FV)$ (From Aas et al., 1986)

Figure 3.5 Cone resistance factor, N_k



$N_{\Delta u}$ versus B_q (From Campanella and Robertson, 1988)

Figure 3.6 Pore pressure factor, $N_{\Delta u}$ (Campanella and Robertson, 1988)

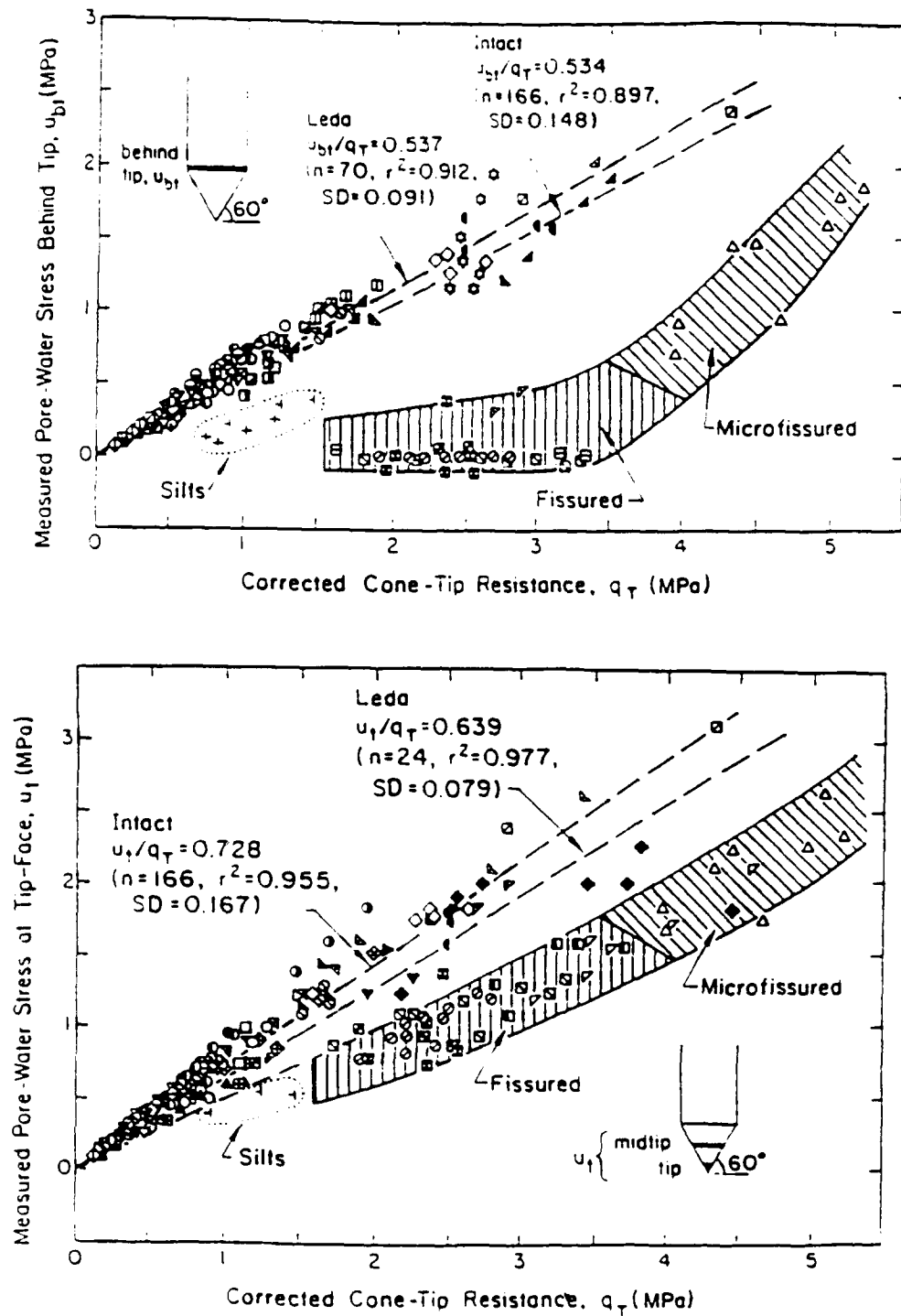
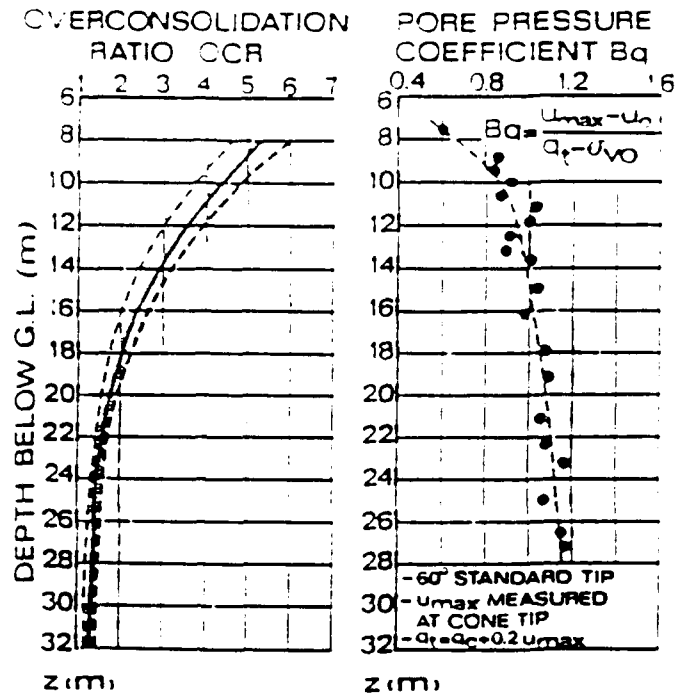
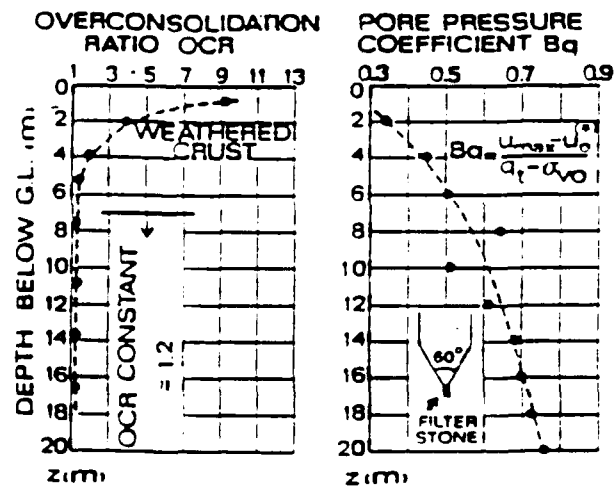


Figure 3.7 Relationships between tip resistance, q_T and measured pore pressures (Mayne et al., 1990)



a) BBC site



(*) THE WRITERS ARE NOT AWARE IF q_c USED HAS ALREADY BEEN CORRECTED FOR Δu EFFECT

b) Onsdly site

Figure 3.8a Evaluation of B_q parameter with OCR (Jamiolkowski et al., 1985)

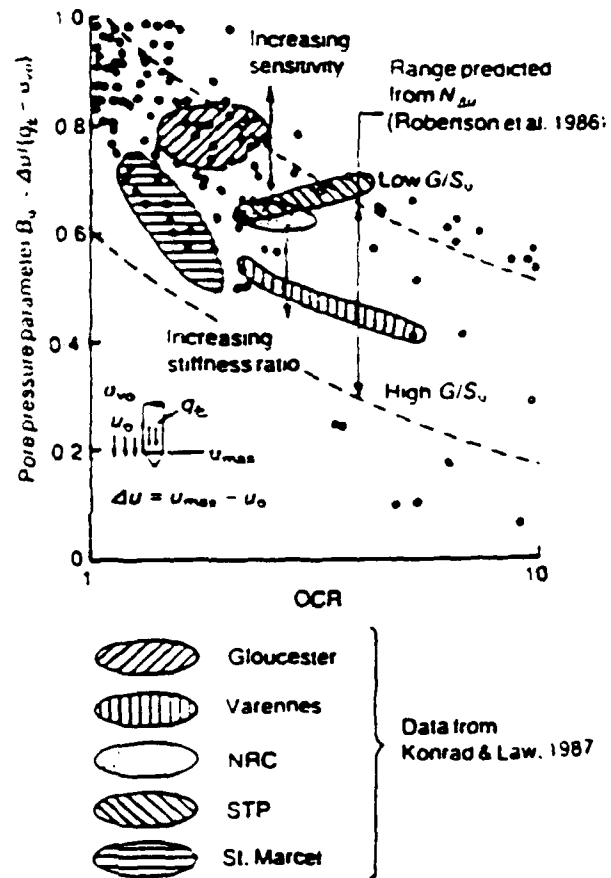


Figure 3.8b Evaluation of B_q parameter with OCR (Robertson et al., 1989)

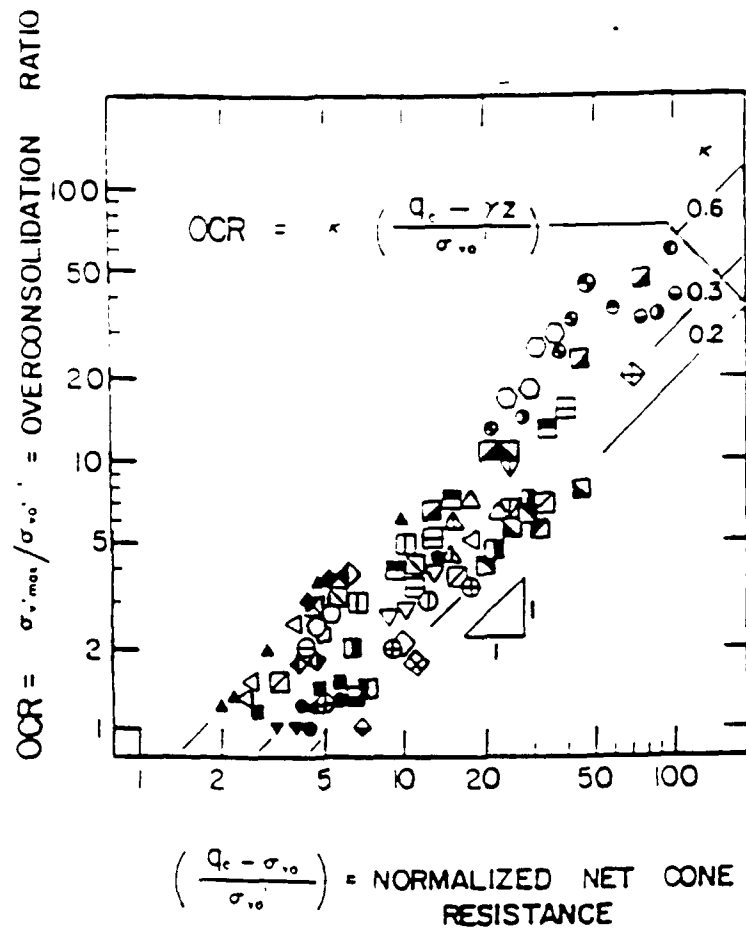


Figure 3.9a Correlation between net tip resistance and OCR (Mayne, 1987)

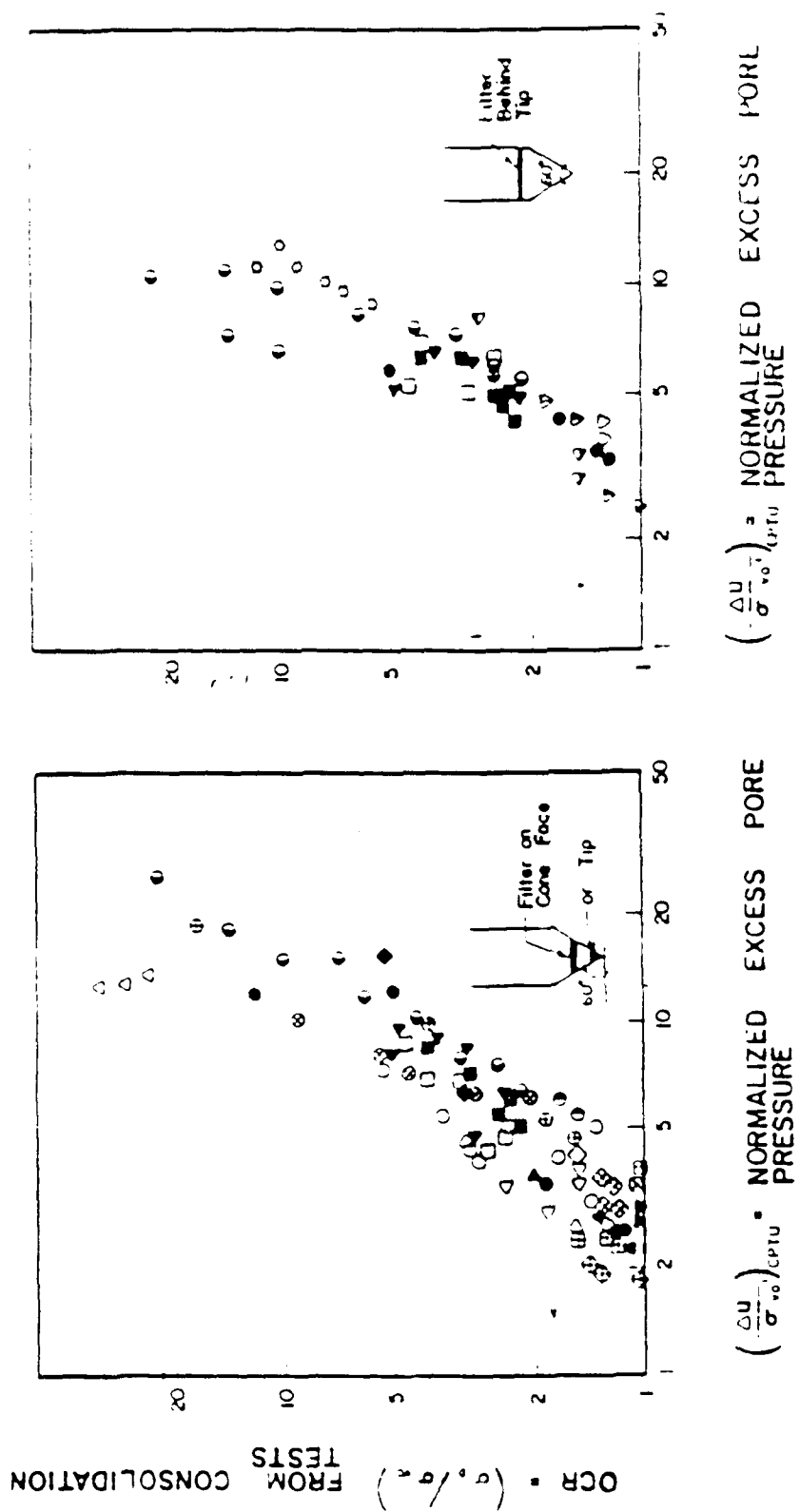


Figure 3.9b Correlation between piezocone pore pressures and OCR (Mayne, 1986)

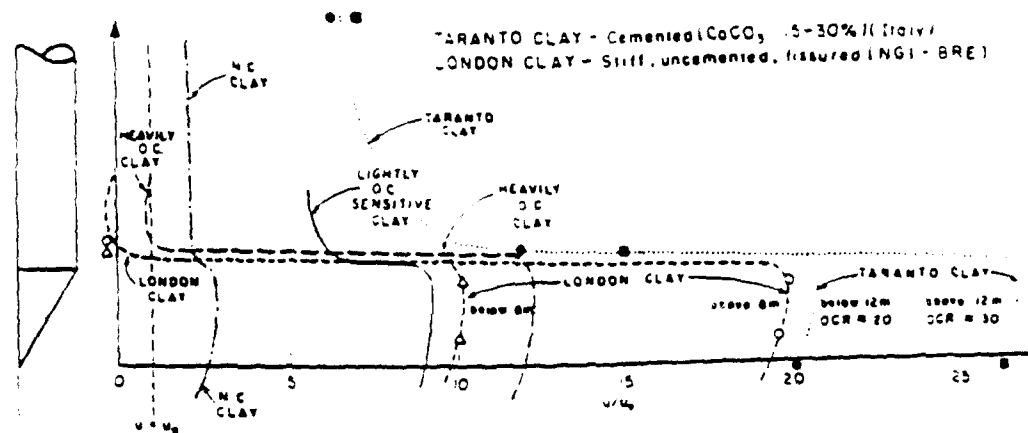


Figure 3.10a Conceptual distribution of pore pressure around piezocone (Robertson et al., 1986)

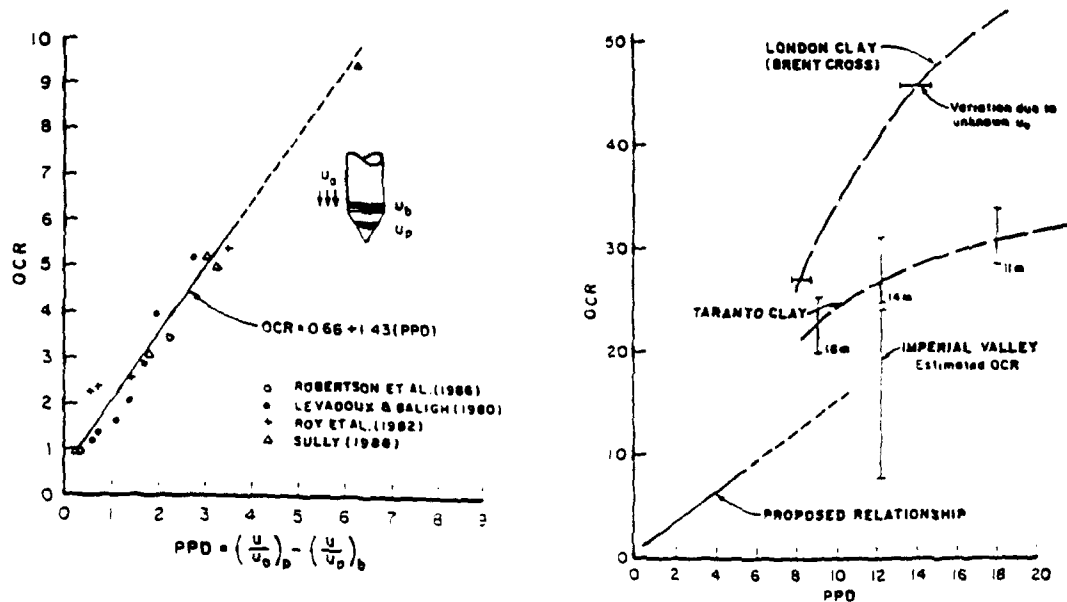


Figure 3.10b Correlation of pore pressure difference with OCR (Sully et al., 1988)

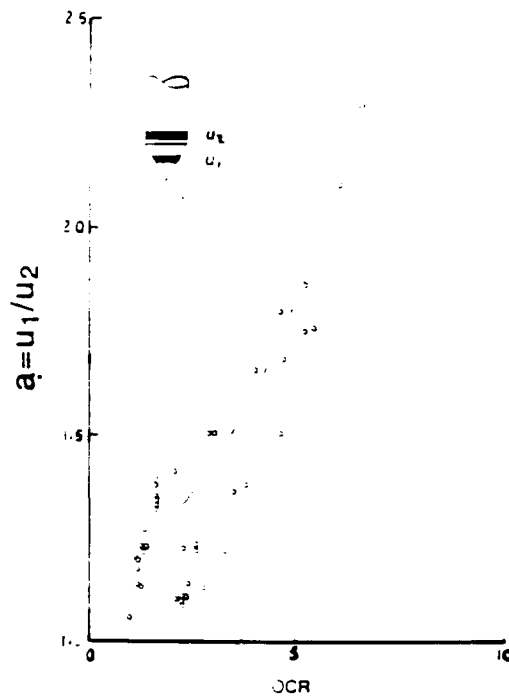


Figure 3.11a Correlation of pore pressure ratio with OCR (Robertson, 1989)

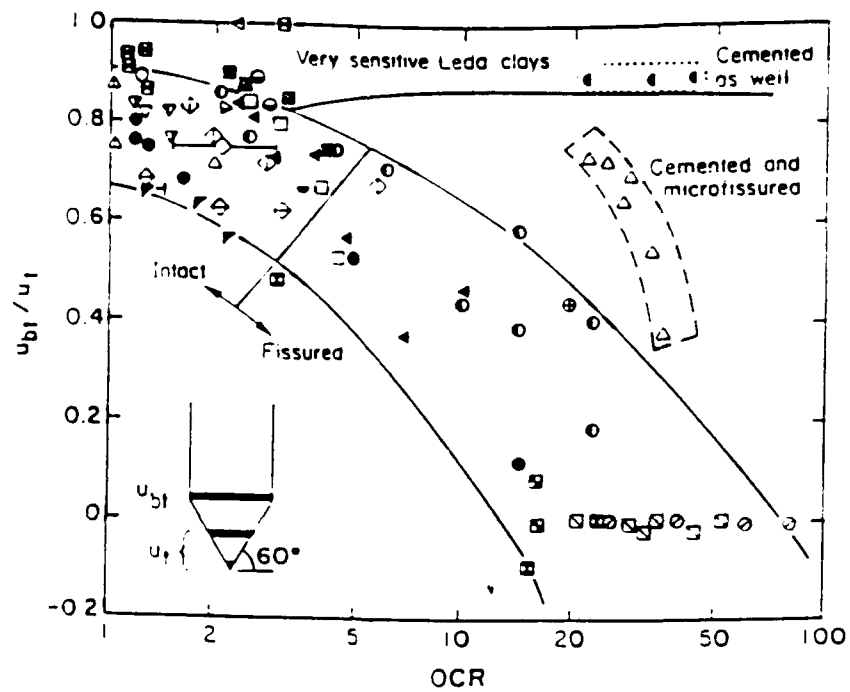


Figure 3.11b Correlation of pore pressure ratio with OCR (Mayne et al., 1990)

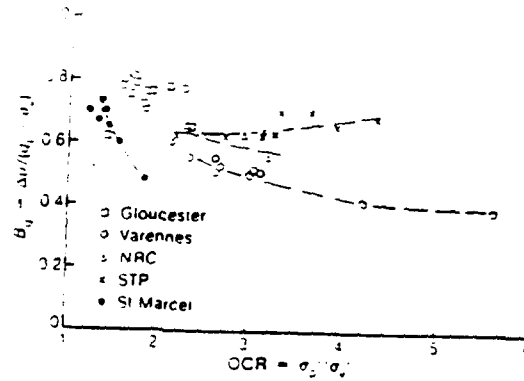


Figure 3.12b OCR from vertical yield stress (Konrad and Law, 1987)

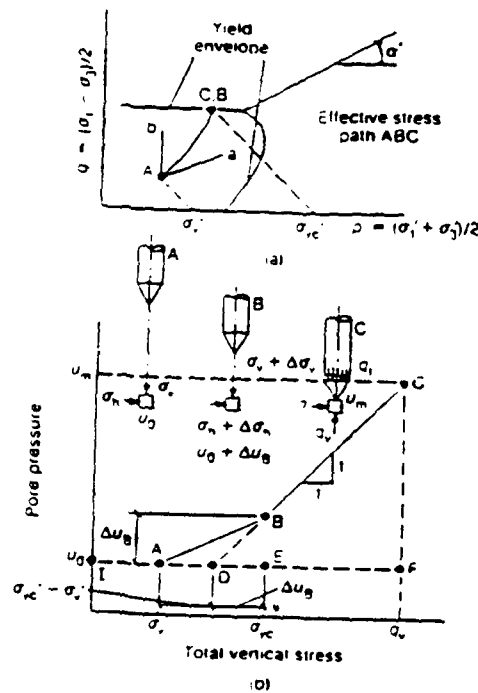


Figure 3.12a Stress paths of idealized soil elements at cone tip (Konrad and Law, 1987)

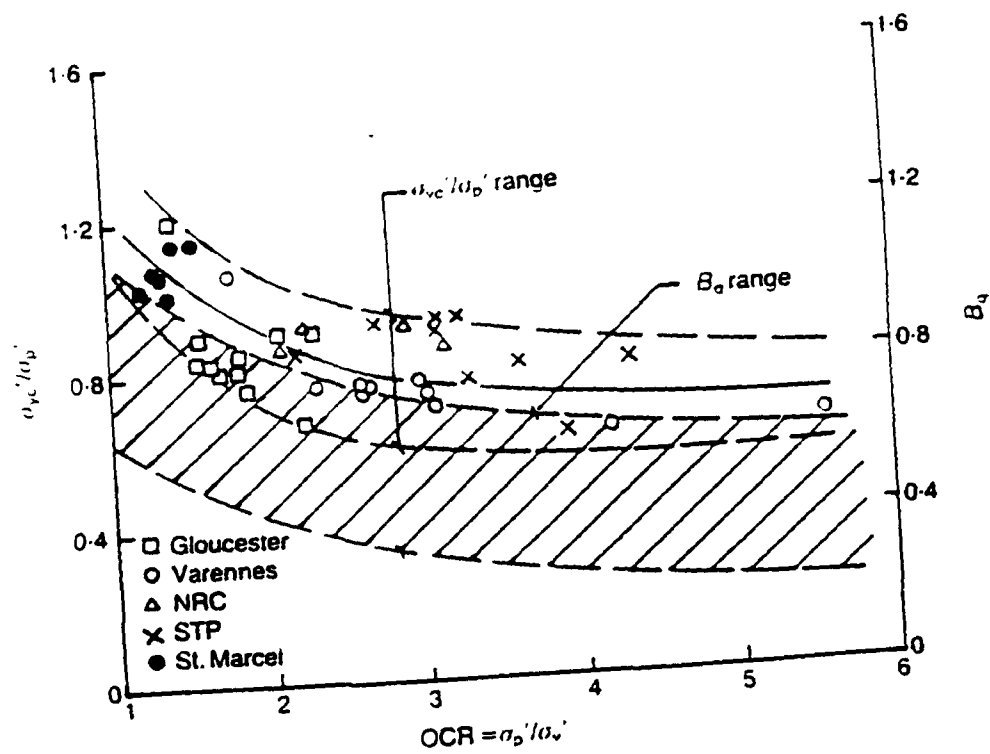


Figure 3.12c Comparison between B_q and σ'_{vc}/σ'_p relationships with OCR

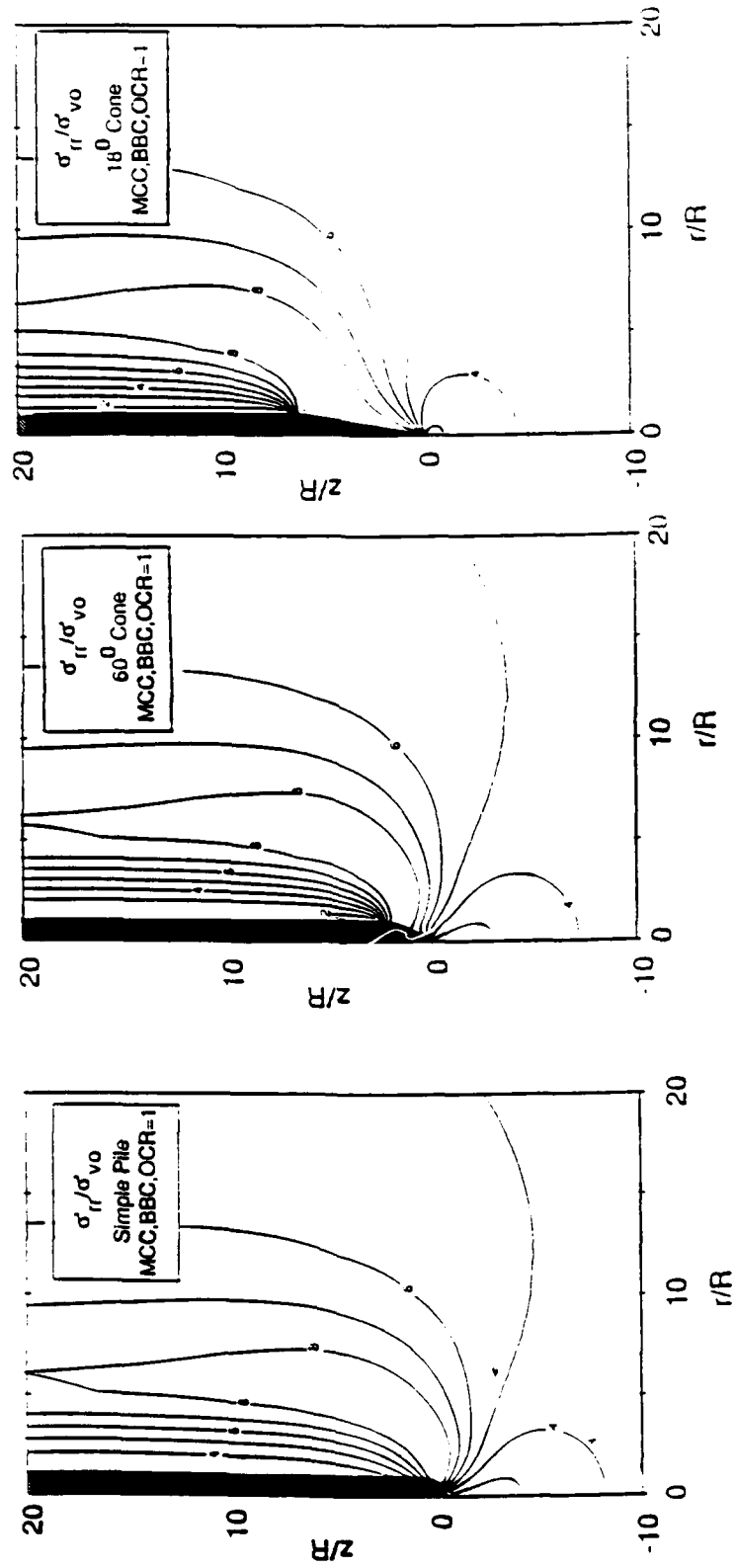


Figure 3.13 Effect of tip shape on predictions of effective stresses and pore pressures

a) $\sigma'_{rr}/\sigma'_{v0}$

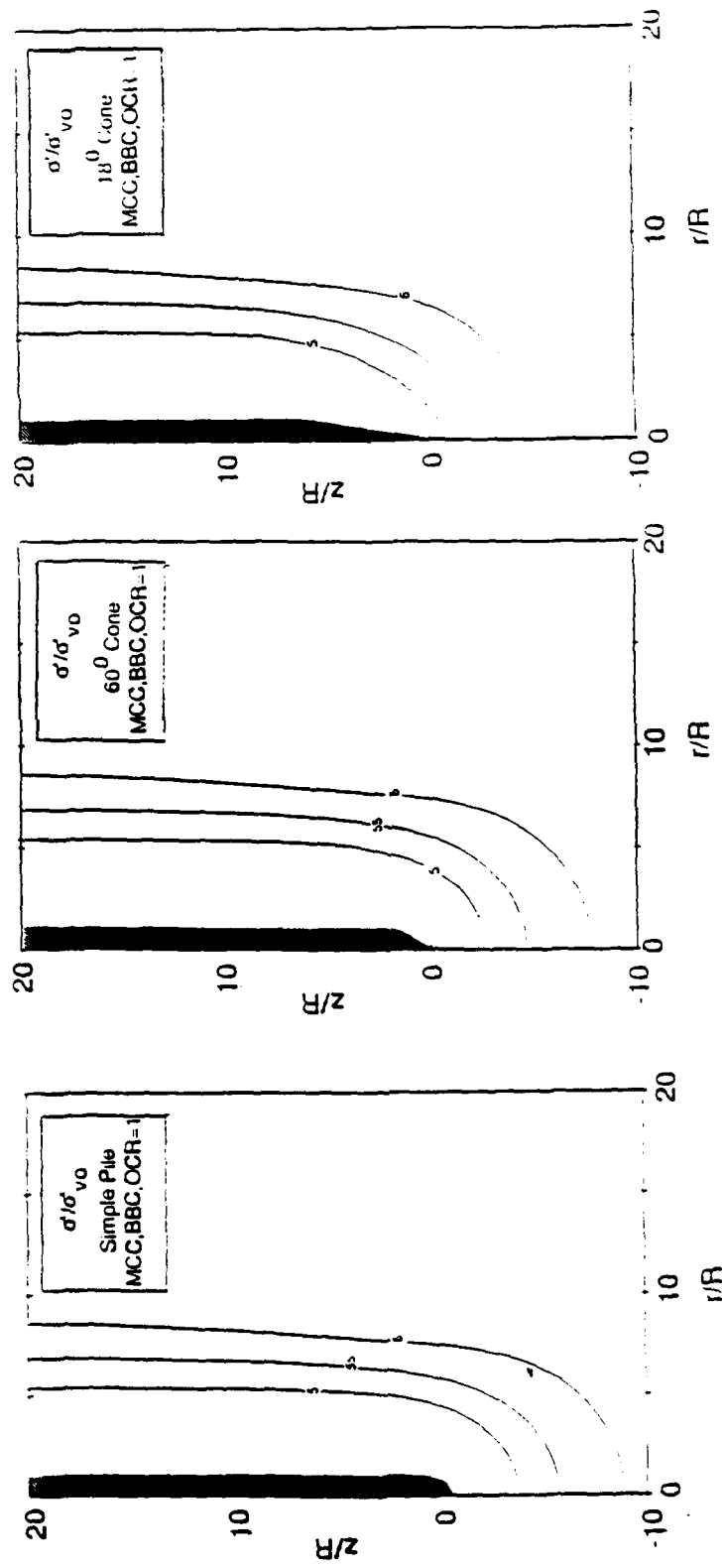


Figure 3.13 Effect of tip shape on predictions of effective stresses and pore pressures

(contd.) b) σ'/σ'_v0

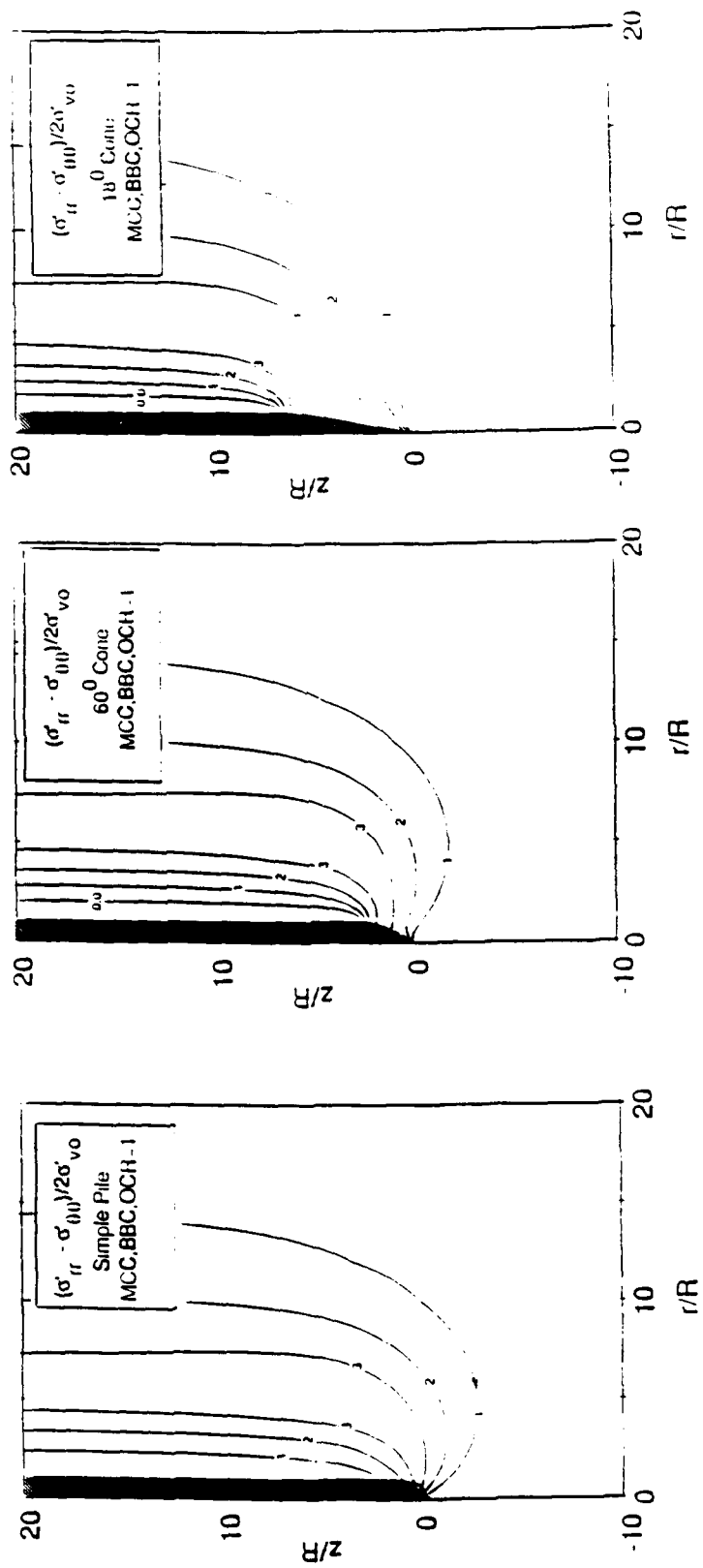


Figure 3.13 Effect of tip shape on predictions of effective stresses and pore pressures

(contd.) c) $(\sigma'_{rr} - \sigma'_{\theta\theta})/2\sigma'_{v0}$

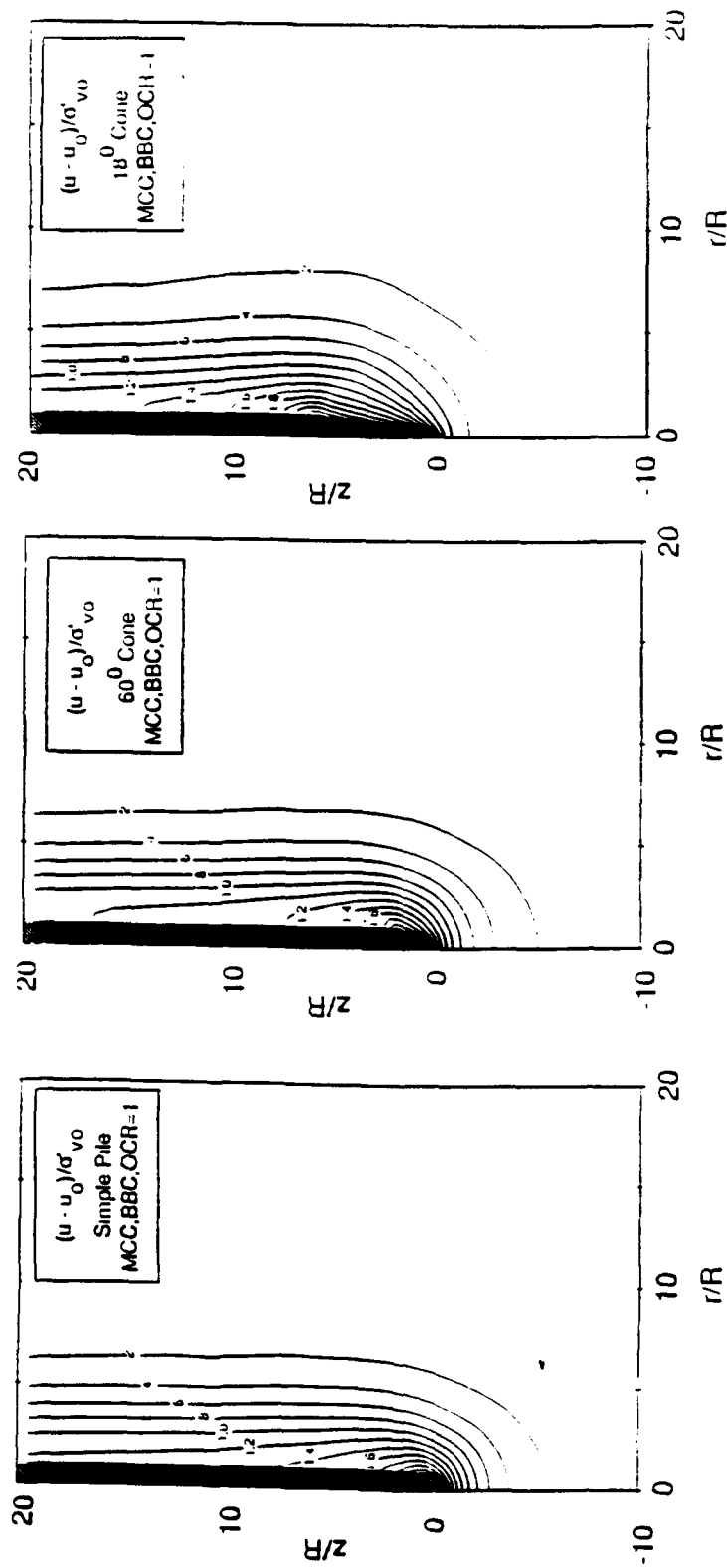


Figure 3.13 Effect of tip shape on predictions of effective stresses and pore pressures

(contd.) d) $(u - u_0)/\sigma'_{v0}$

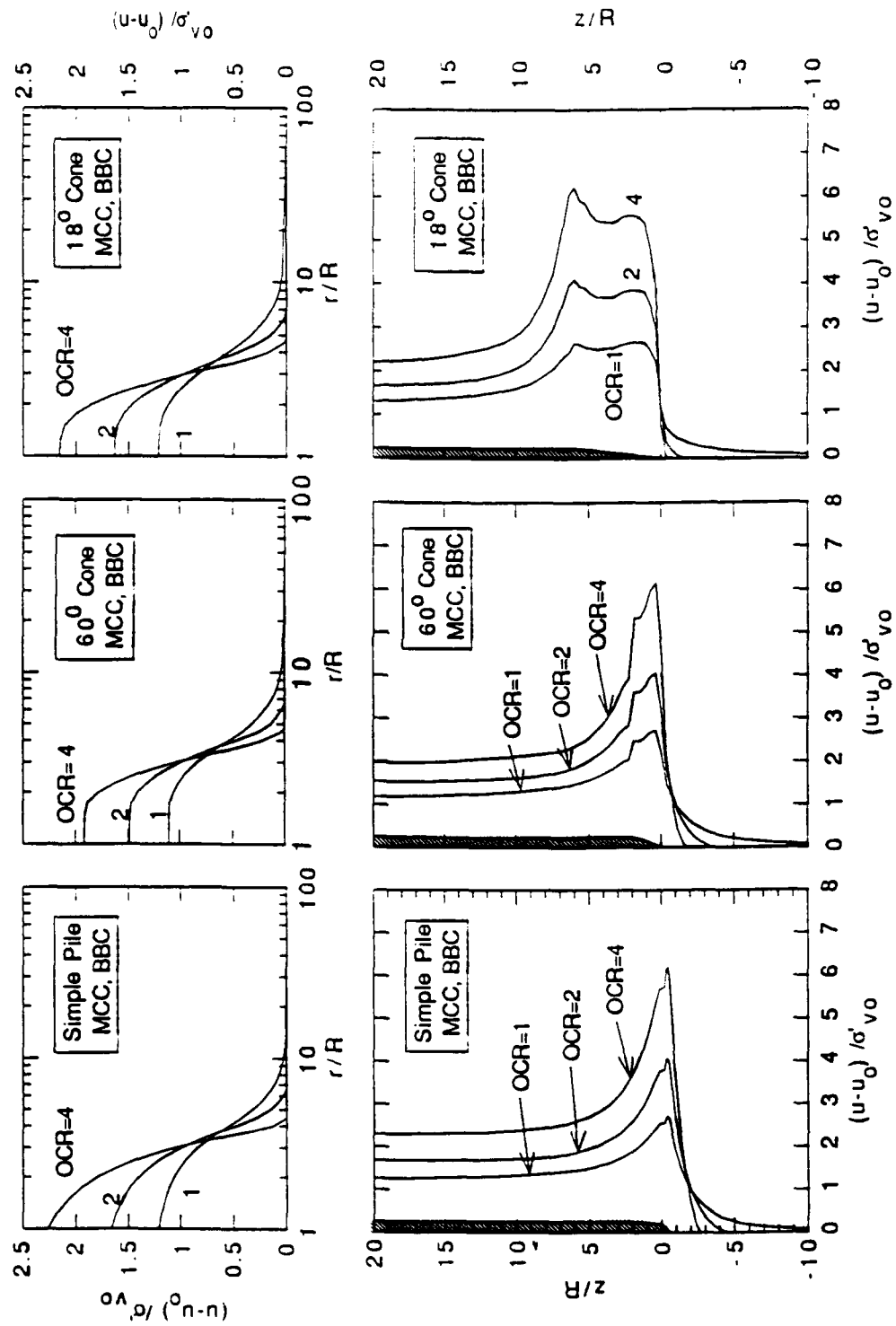


Figure 3.14 Summary of effect of tip shape on distributions of excess pore pressures

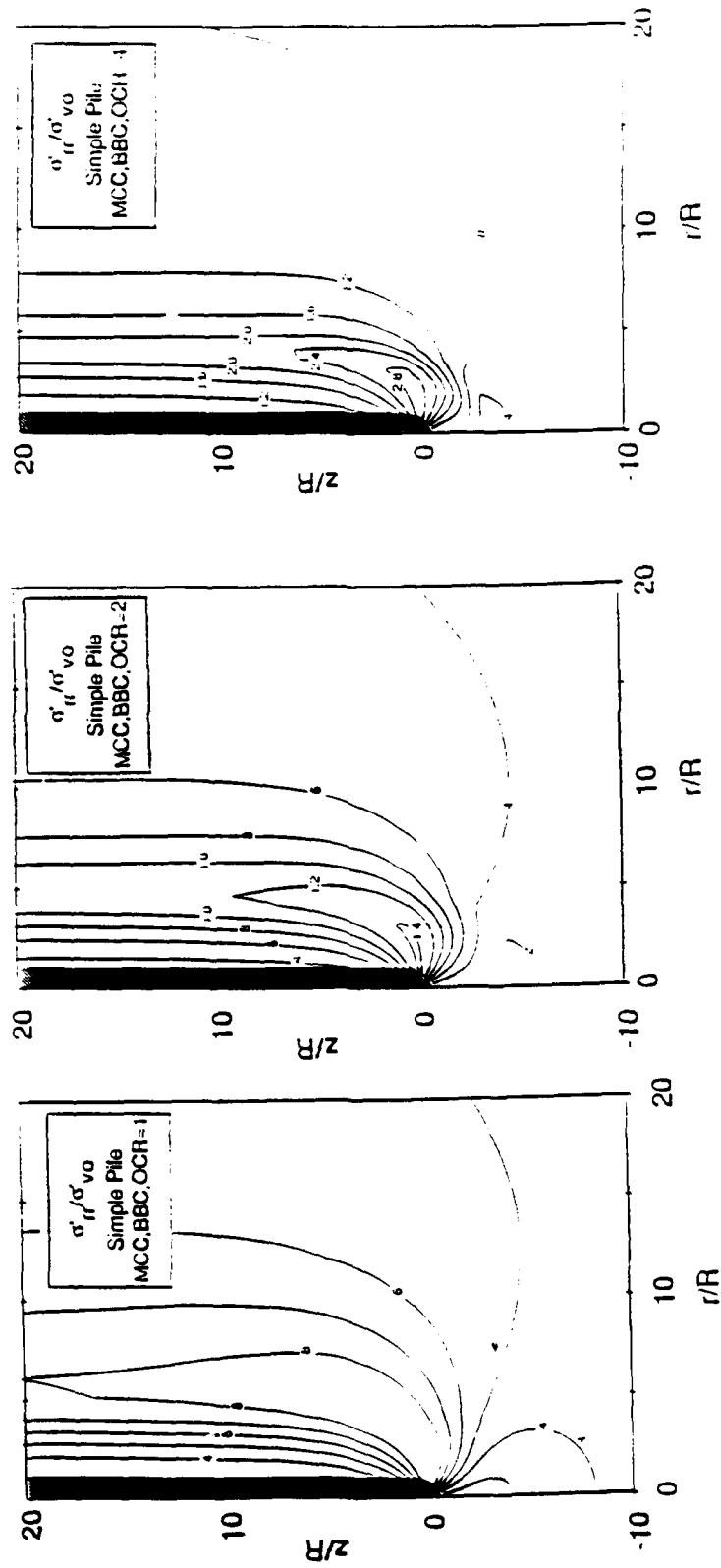


Figure 3.15 Effect of Overconsolidation ratio on predictions of effective stresses and pore

pressures a) σ'_r/σ'_{v0}

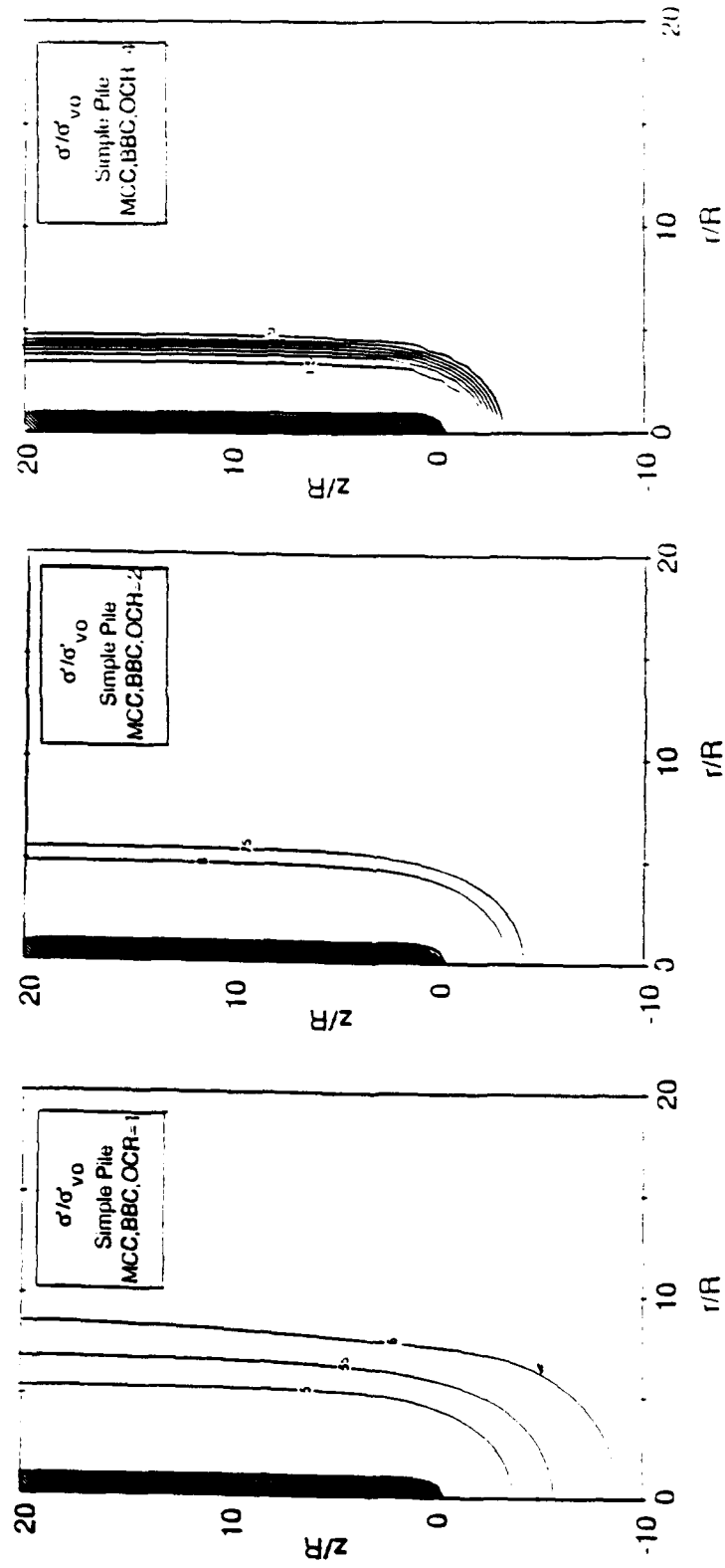


Figure 3.15 Effect of Overconsolidation ratio on predictions of effective stresses and pore pressures (contd.) b) σ'/σ'_{v0}

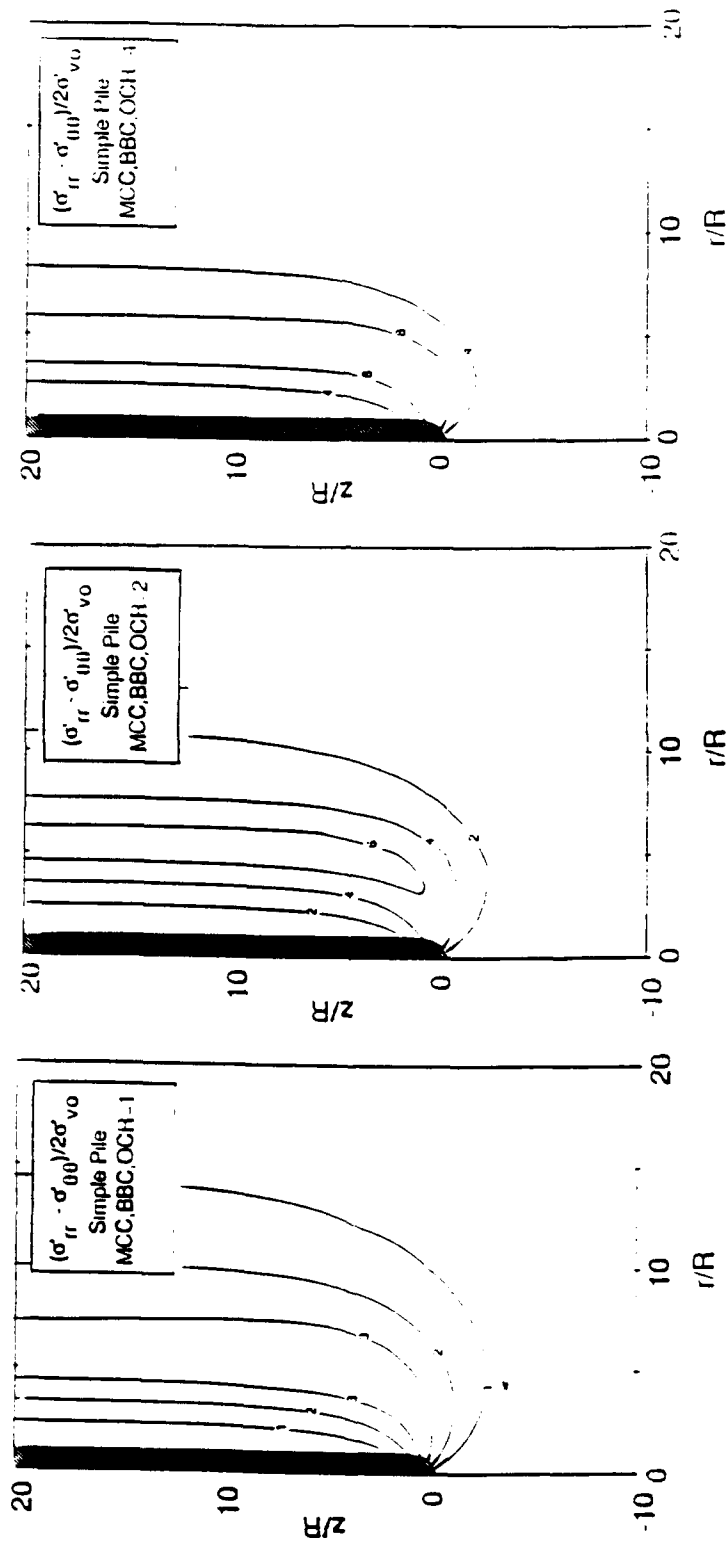


Figure 3.15 Effect of Overconsolidation ratio on predictions of effective stresses and pore pressures (contd.) c) $(\sigma'_{rr} - \sigma'_{\theta\theta})/2\sigma'_{v0}$

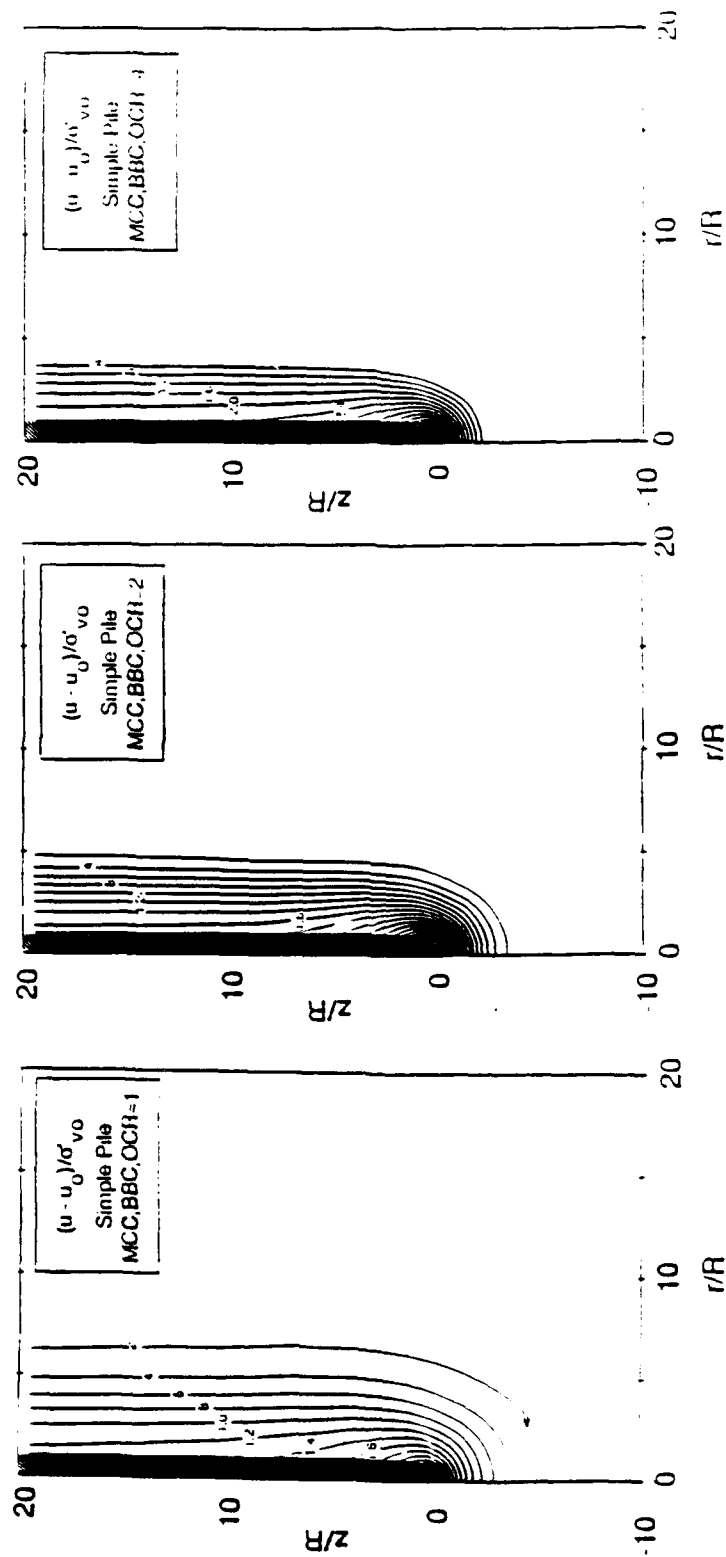


Figure 3.15 Effect of Overconsolidation ratio on predictions of effective stresses and pore pressures (contd.) d) $(u - u_0)/\sigma'_{v0}$

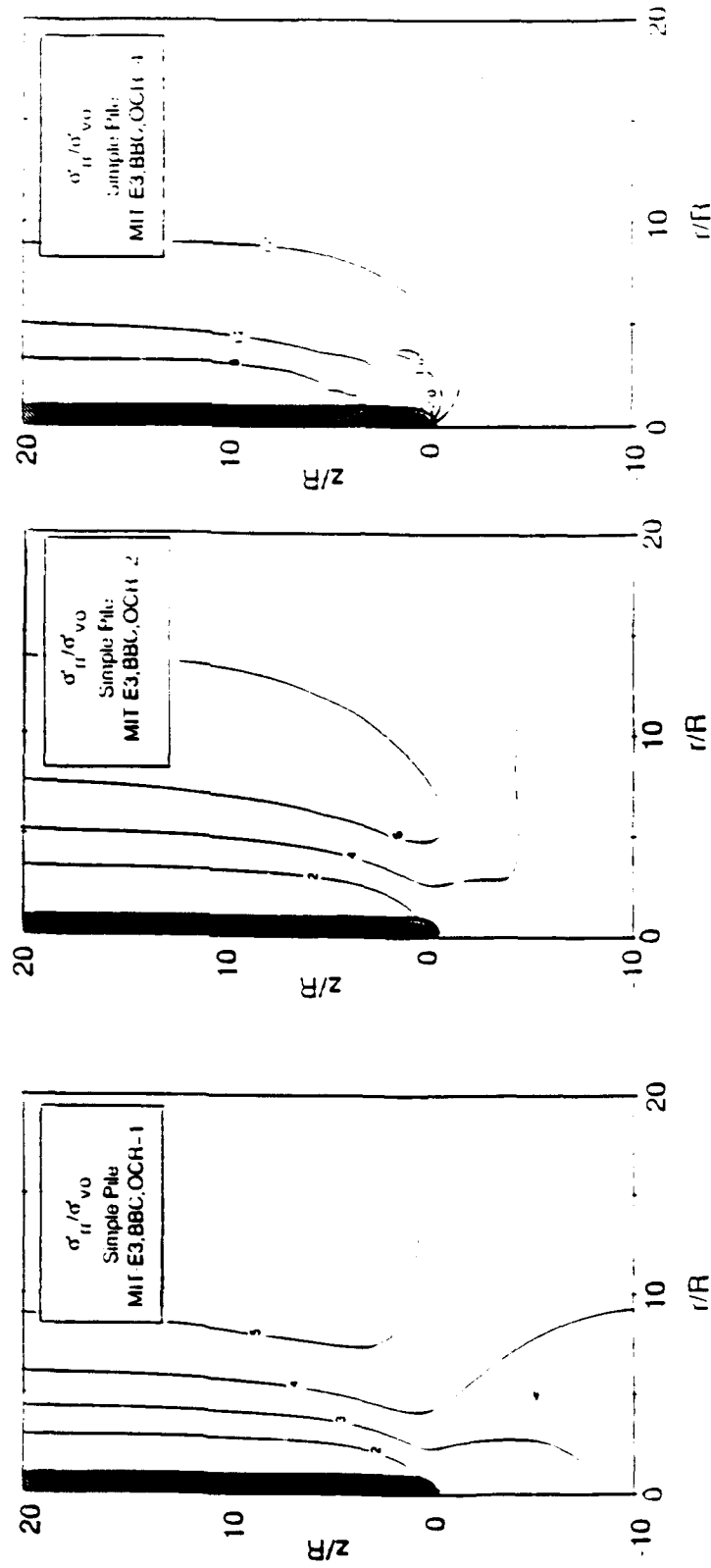


Figure 3.16 Predictions of effective stresses and pore pressures using the MIT-E3 model

a) σ'_r / σ'_{v0}

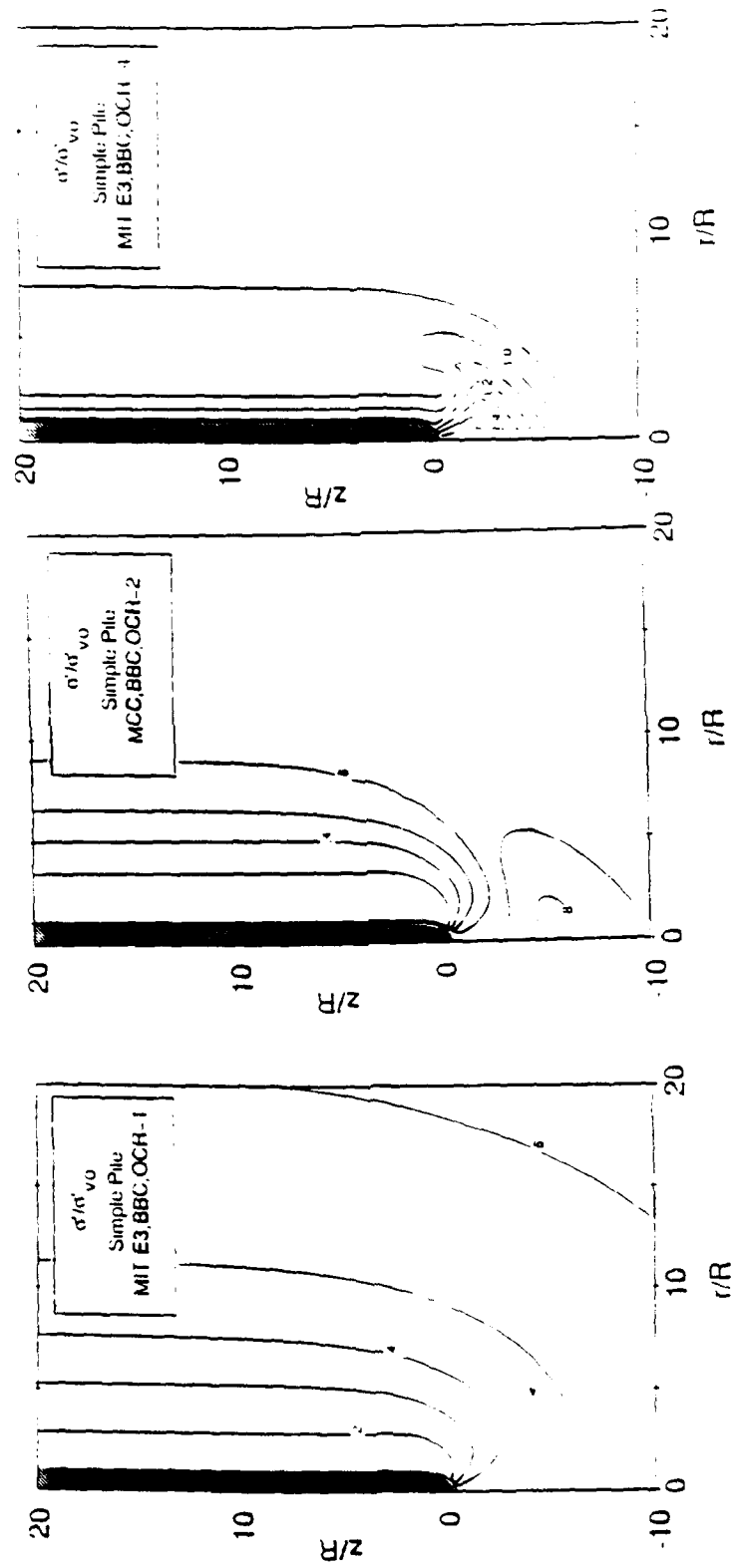


Figure 3.16 Predictions of effective stresses and pore pressures using the MIT-E3 model

(contd.) b) σ'/σ'_{v0}

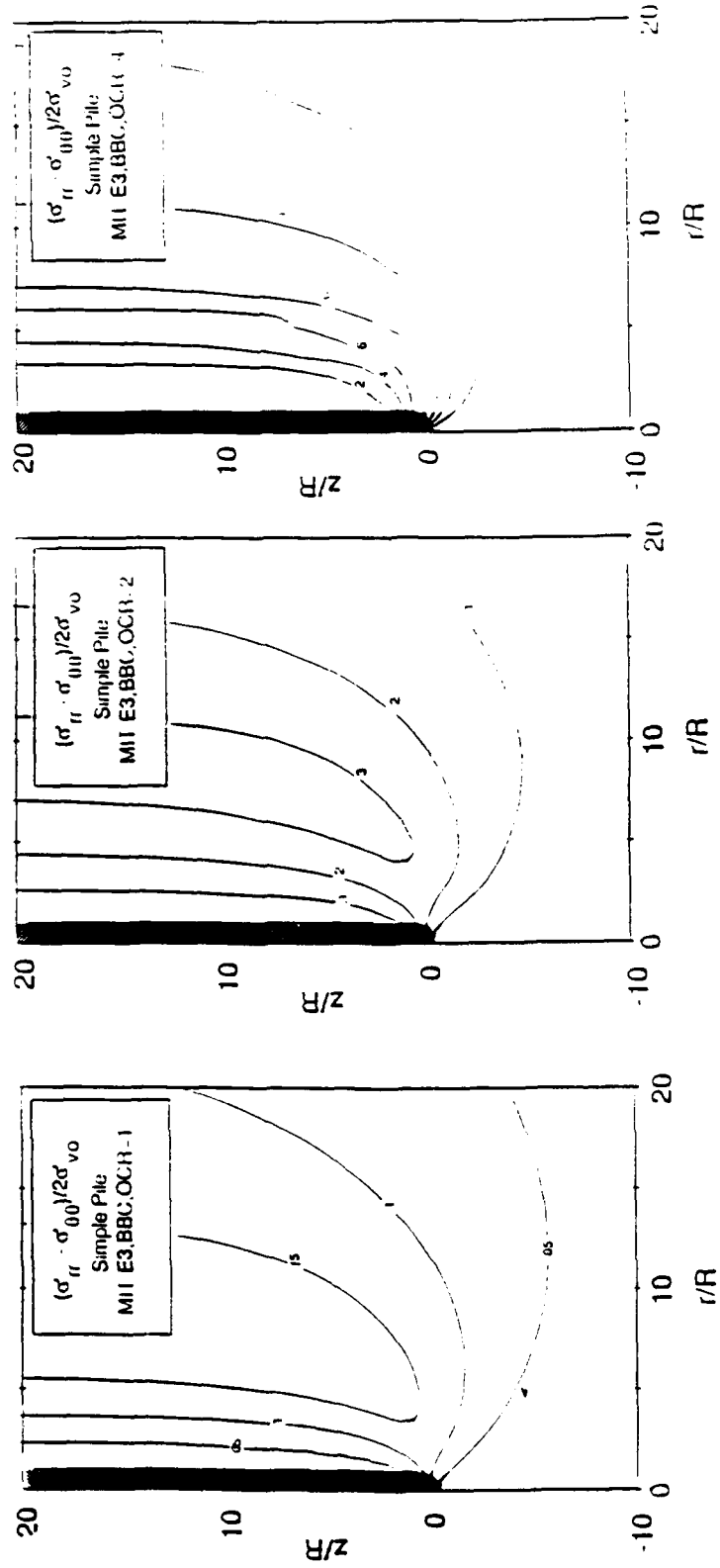


Figure 3.16 Predictions of effective stresses and pore pressures using the MIT-E3 model

(contd.) c) $(\sigma'_r - \sigma'_0)/2\sigma'_{v0}$

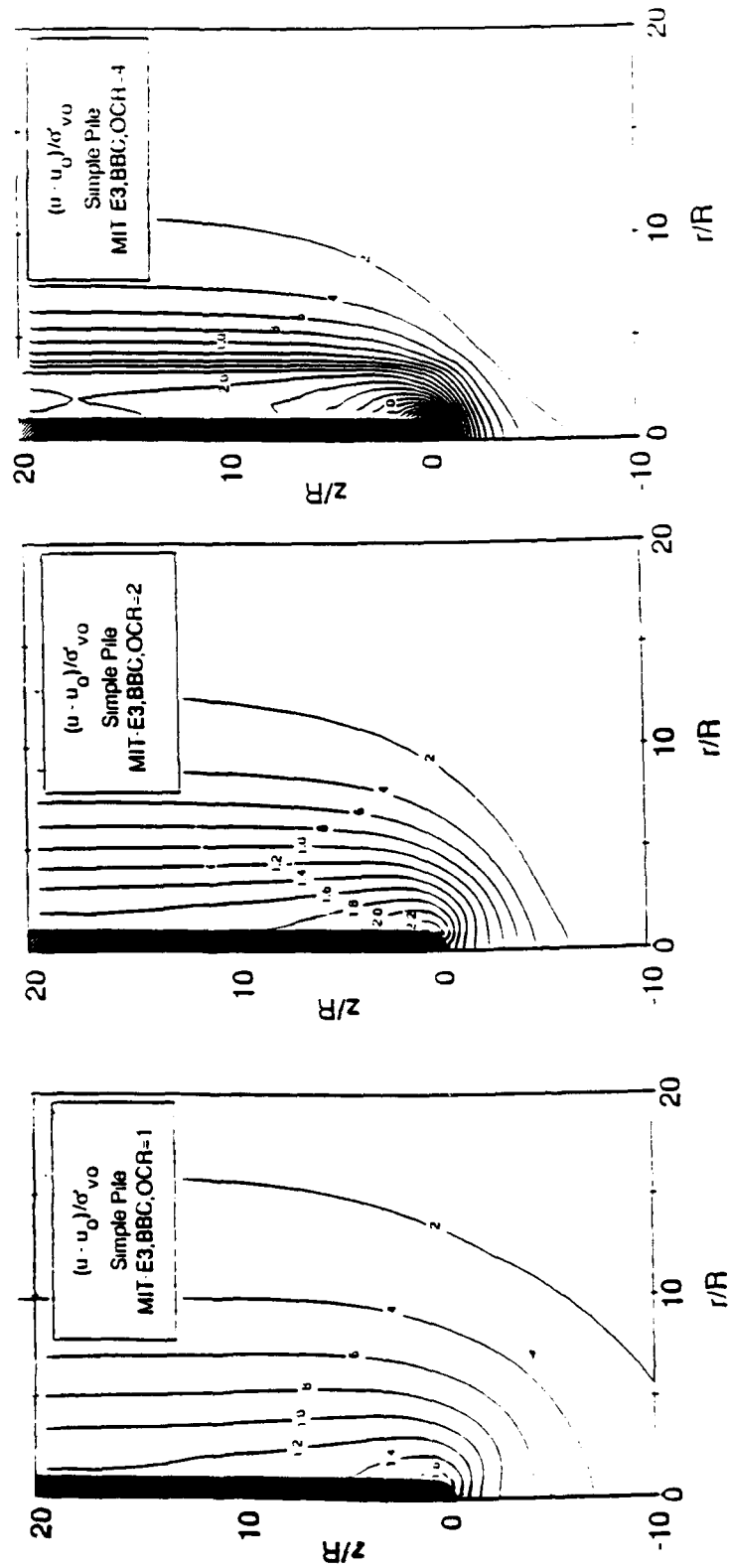


Figure 3.16 Predictions of effective stresses and pore pressures using the MIT-E3 model

(contd.) d) $(u - u_0)/\sigma'_{v0}$

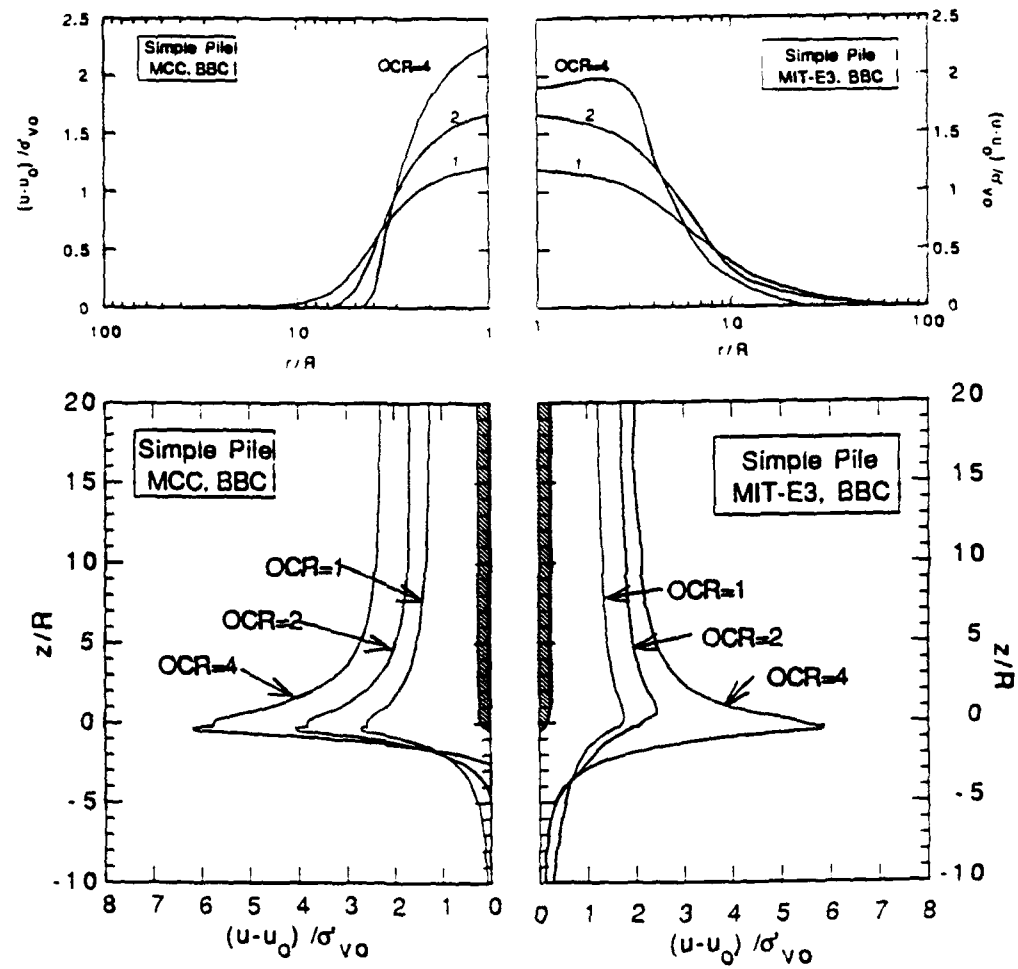


Figure 3.17 Effect of soil model on distributions of excess pore pressures

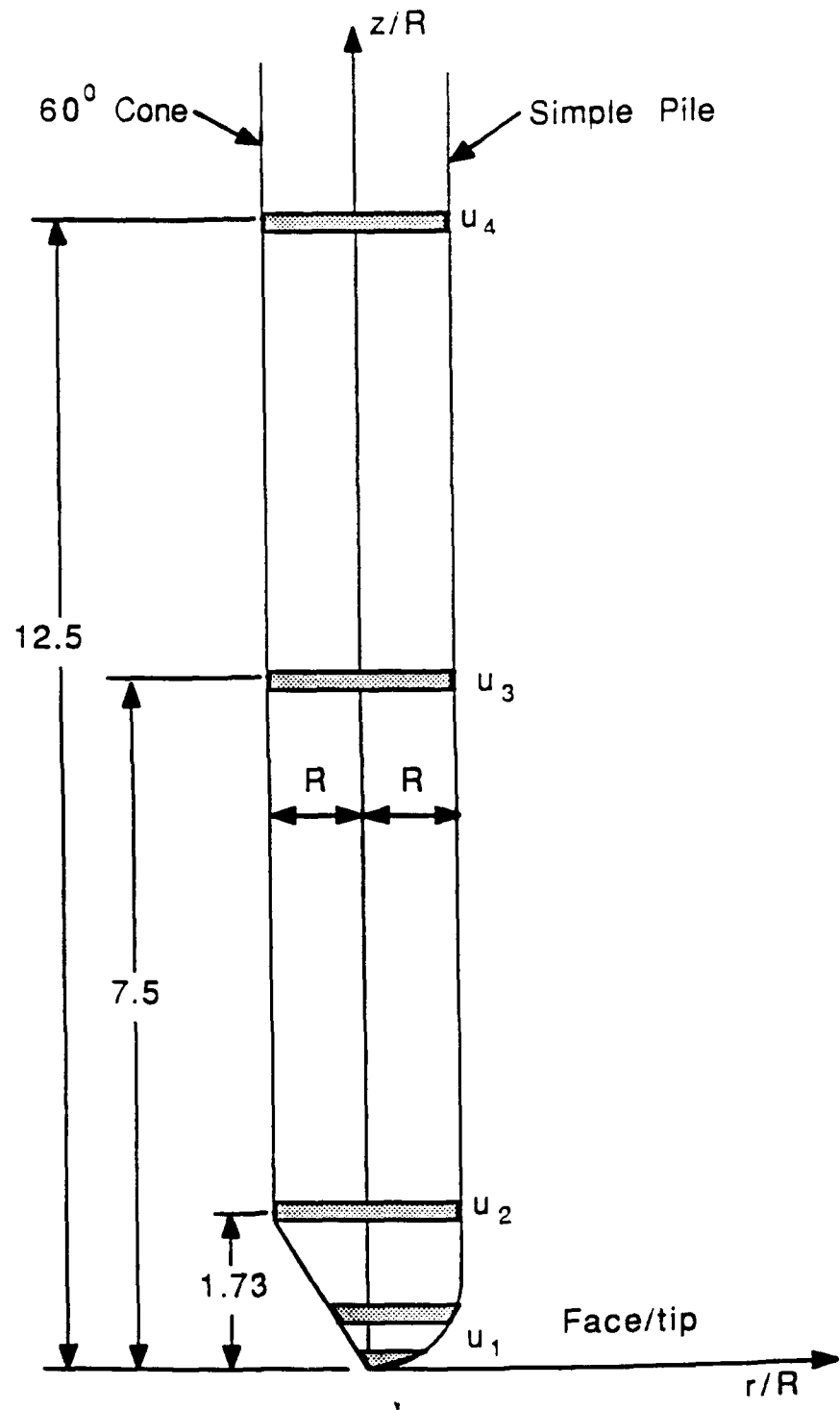


Figure 3.18 Definitions used to interpret predictions of piezocone pore pressures

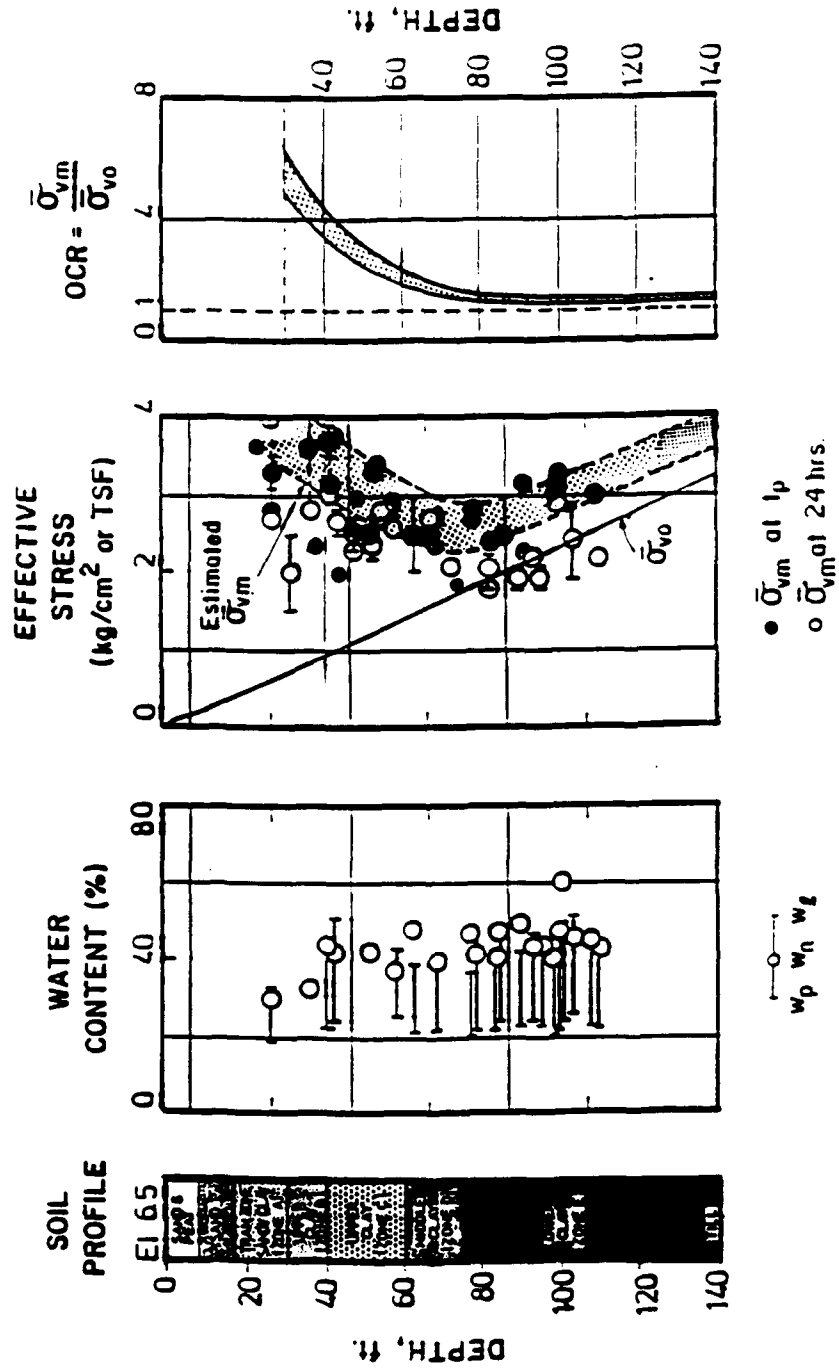
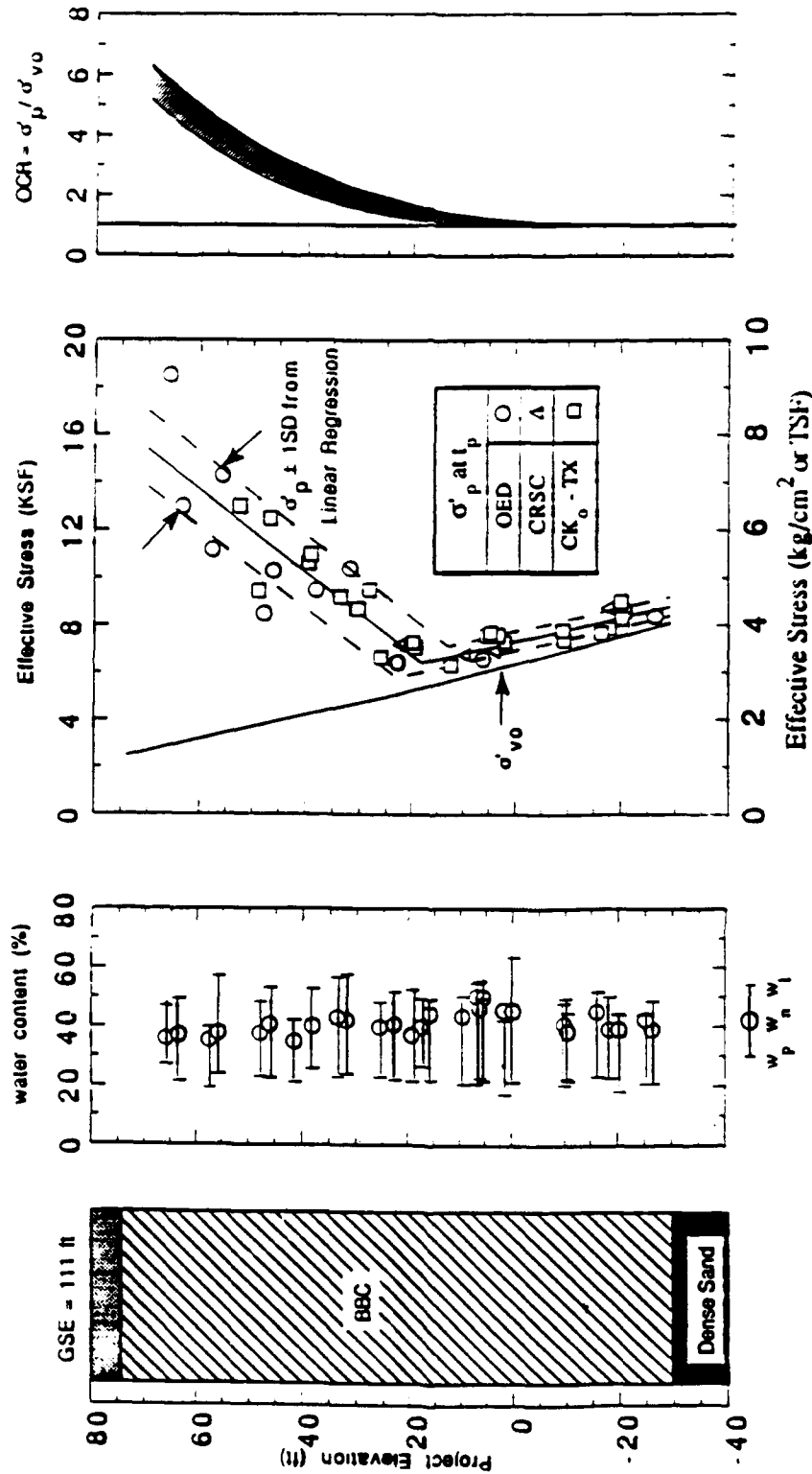


Figure 3.19a Index properties and stress history, Saugus test site (Morrison, 1984)



NOTE: Project Elevation = MSL + 100.0 ft.

PRELIMINARY UNPUBLISHED DATA
DO NOT USE OR COPY

Figure 3.19b Index properties and stress history, South Boston test site (Ladd, 1990)

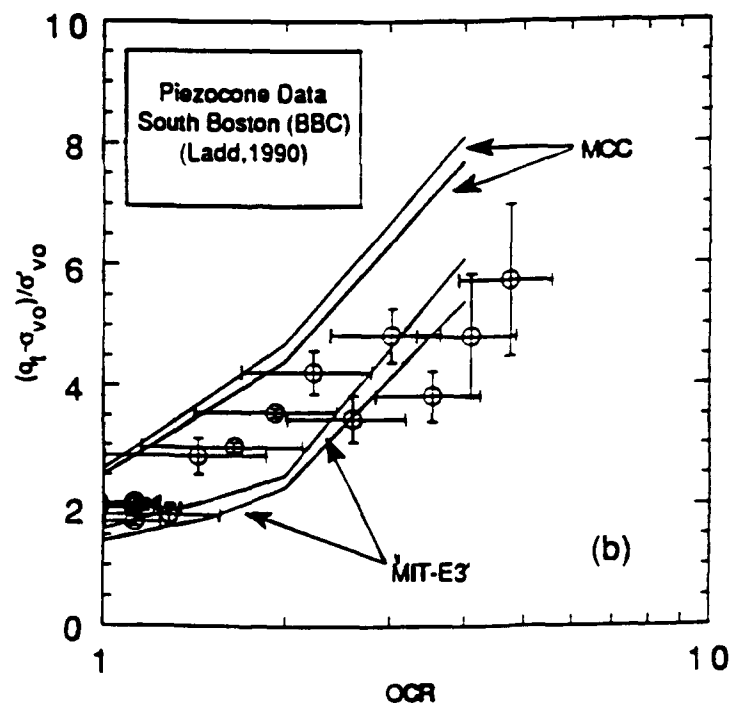
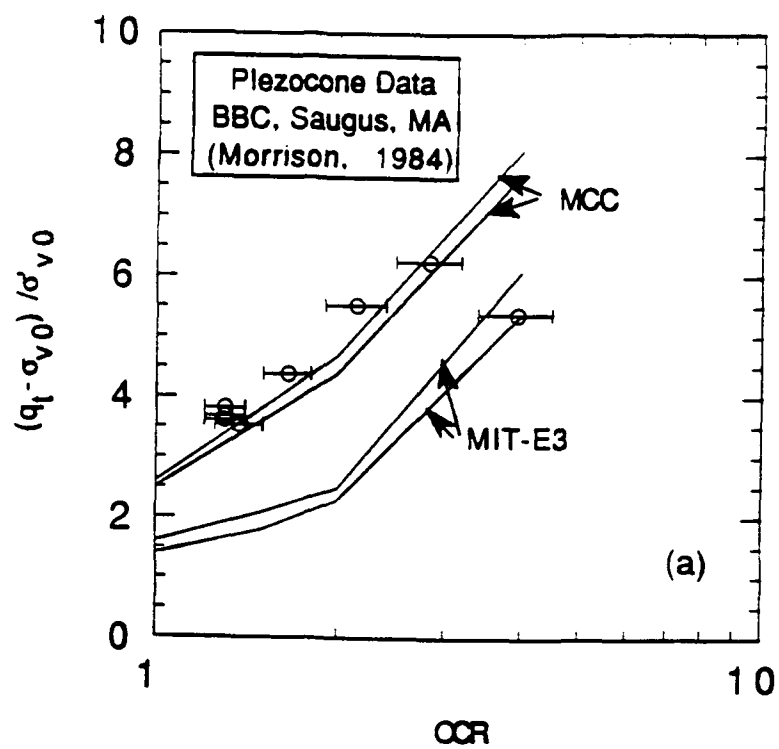


Figure 3.20 Comparison of predictions and measured data for net tip resistance in BBC

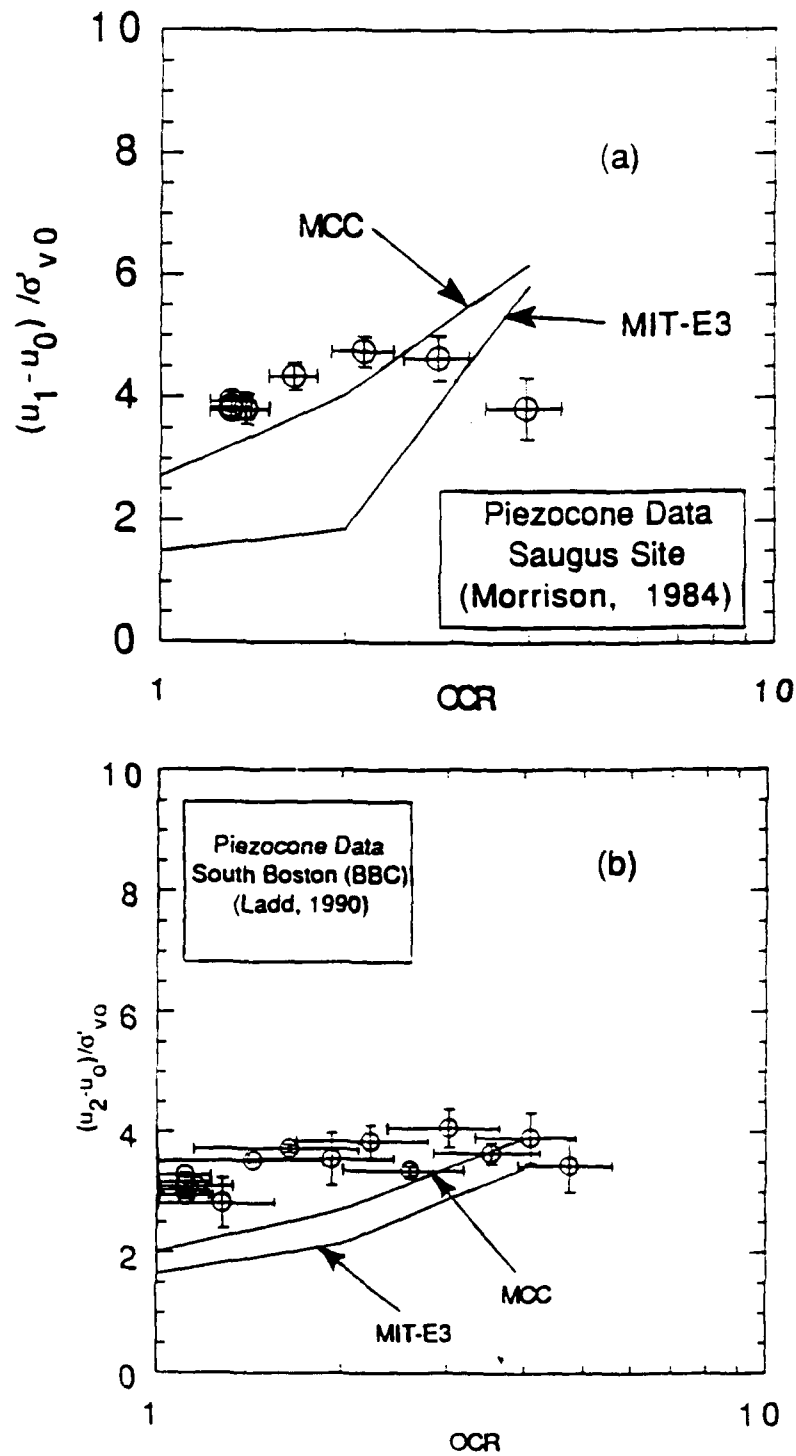


Figure 3.21 Comparison of predictions and measured data for excess pore pressures in BBC

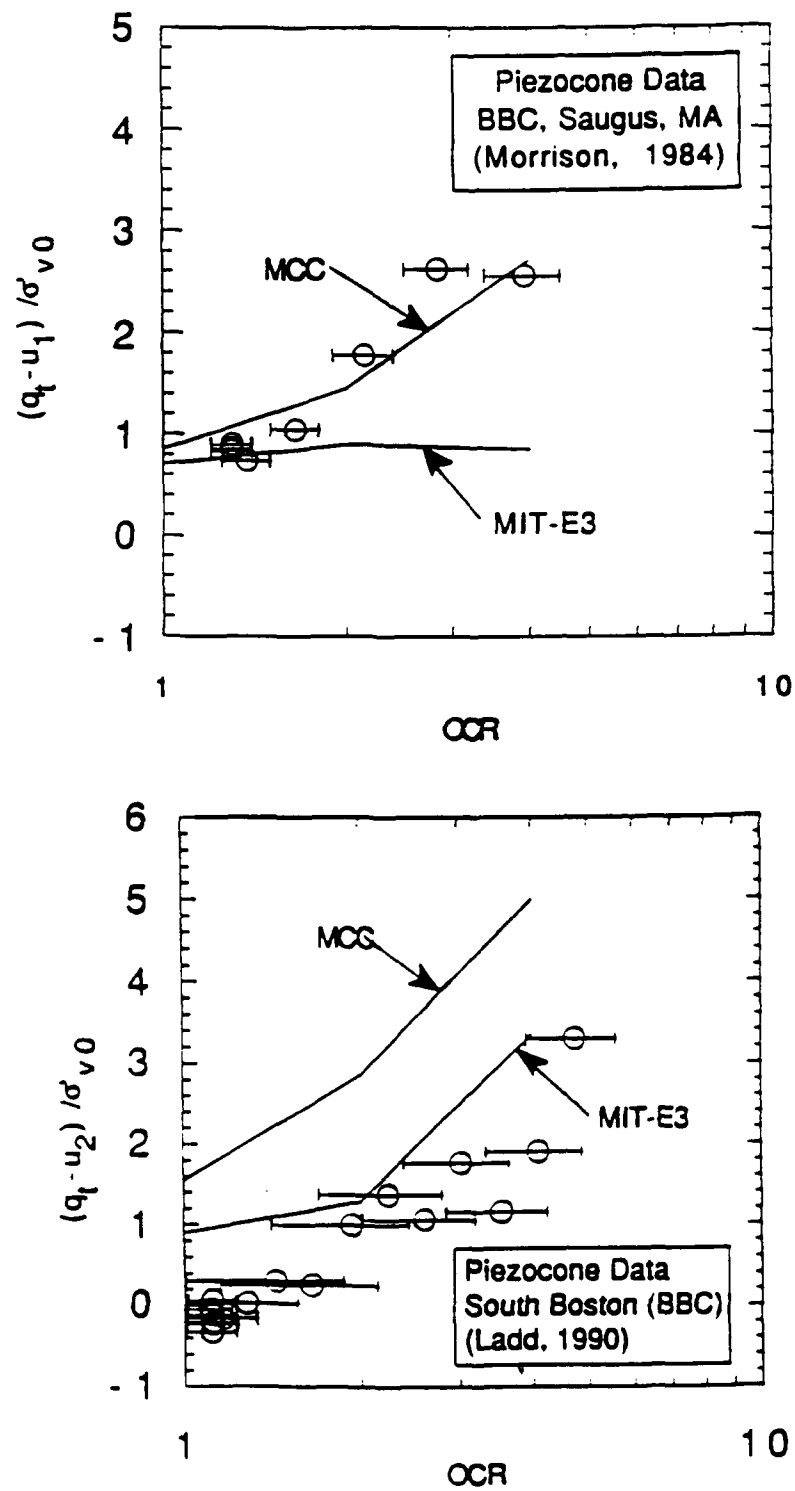


Figure 3.22 Comparison of predictions and measured data for the effective tip resistance in BBC

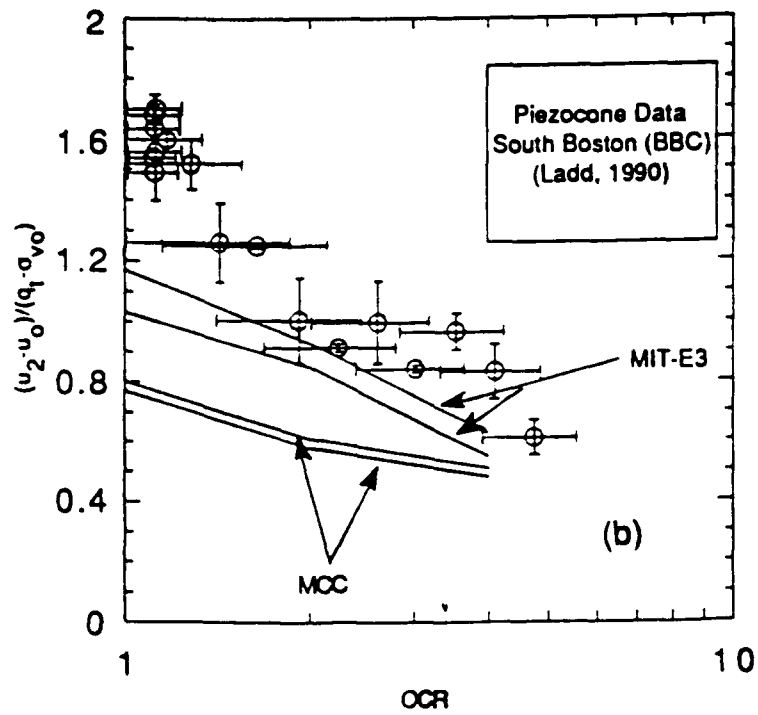
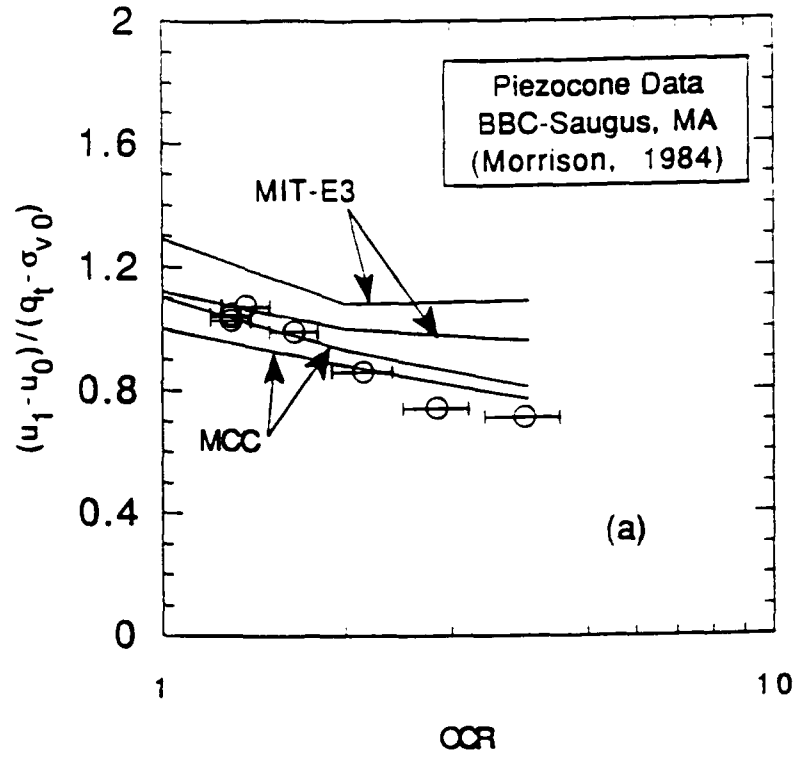
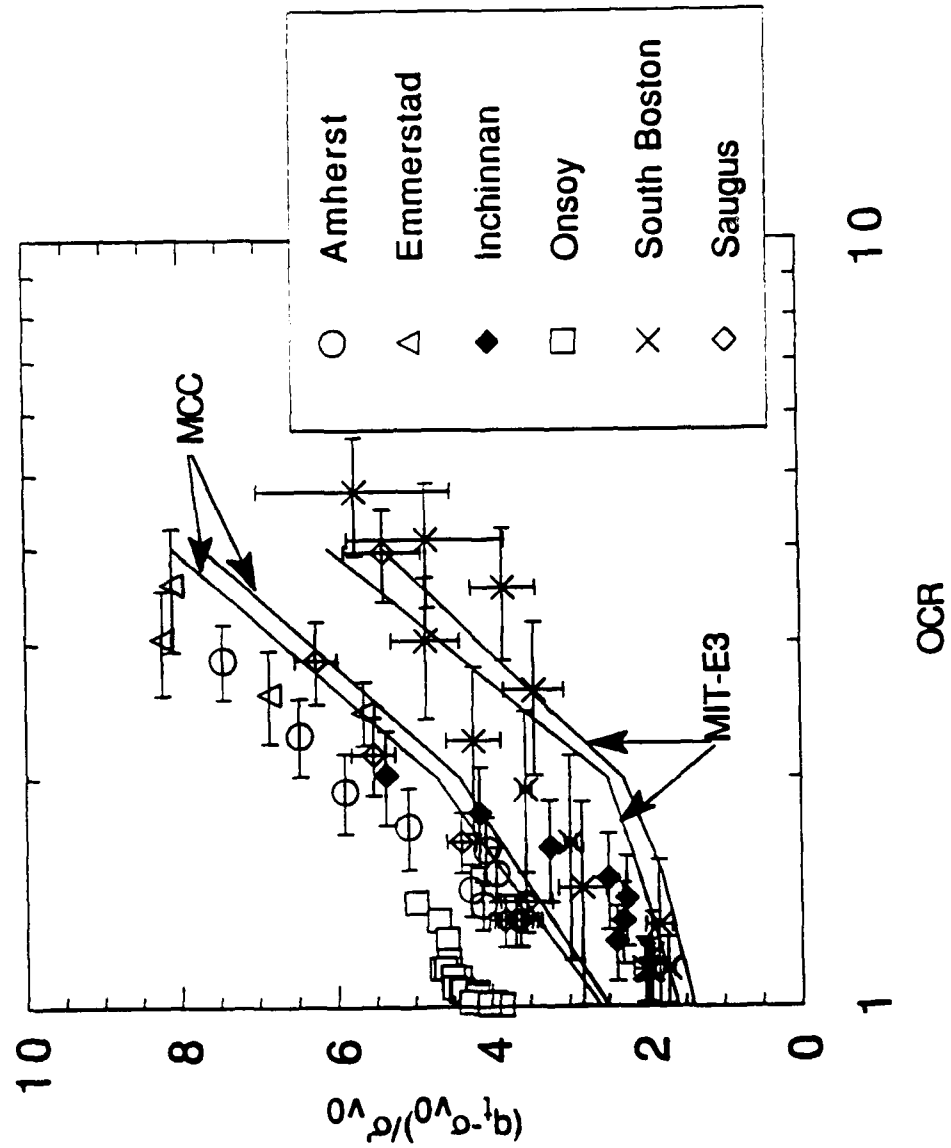
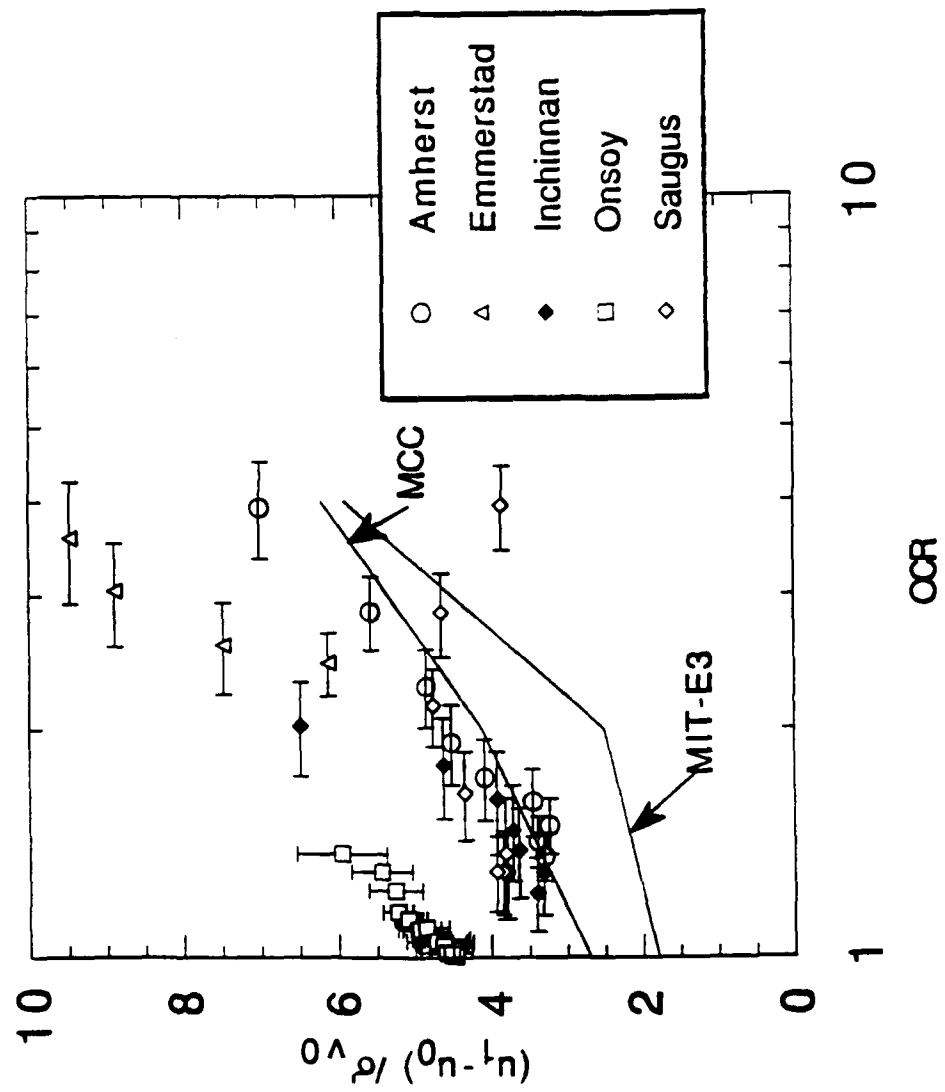


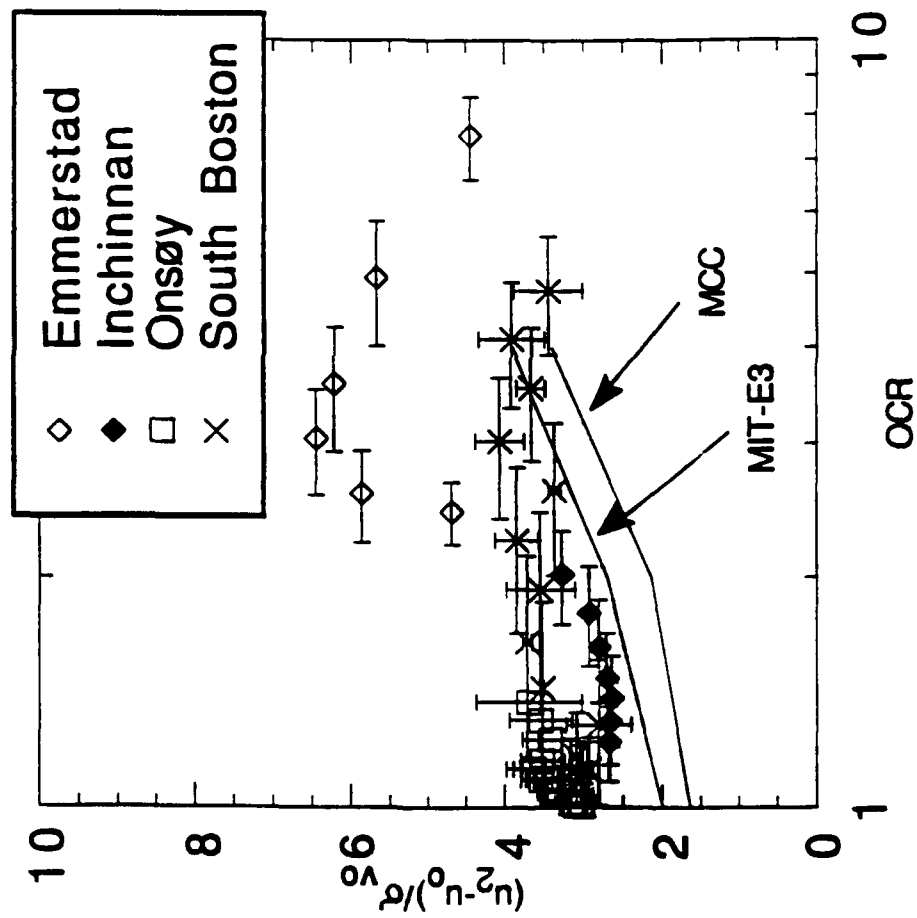
Figure 3.23 Comparison of predictions and measurements for the B_q ratio in BBC

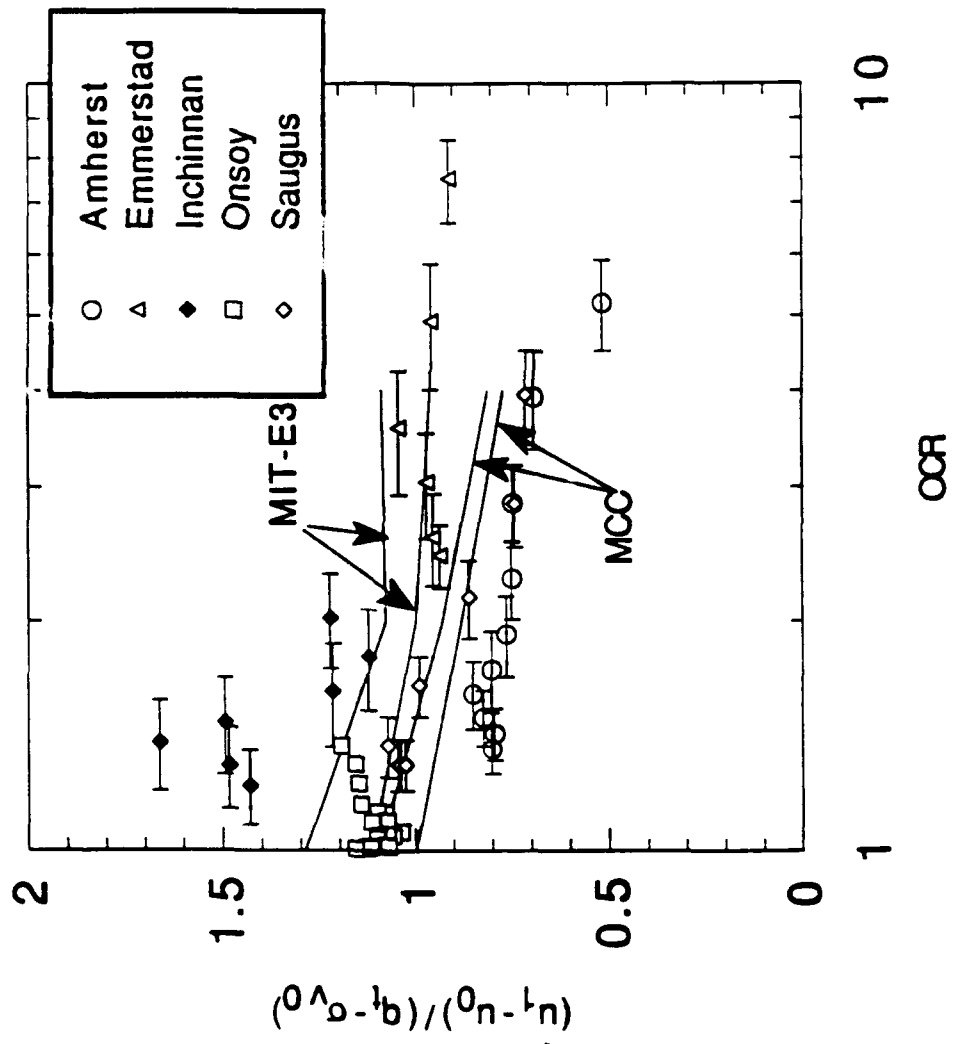


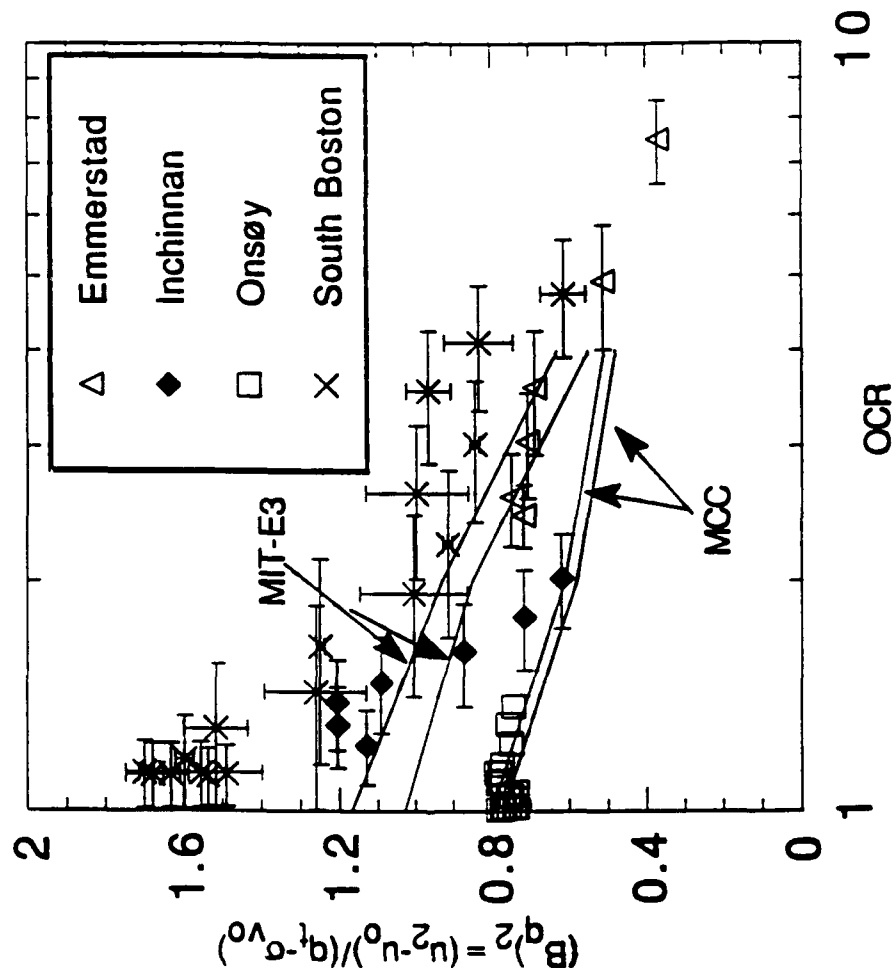
$$3.24a \quad (q_t - \sigma'_{v0}) / \sigma'_{v0}$$

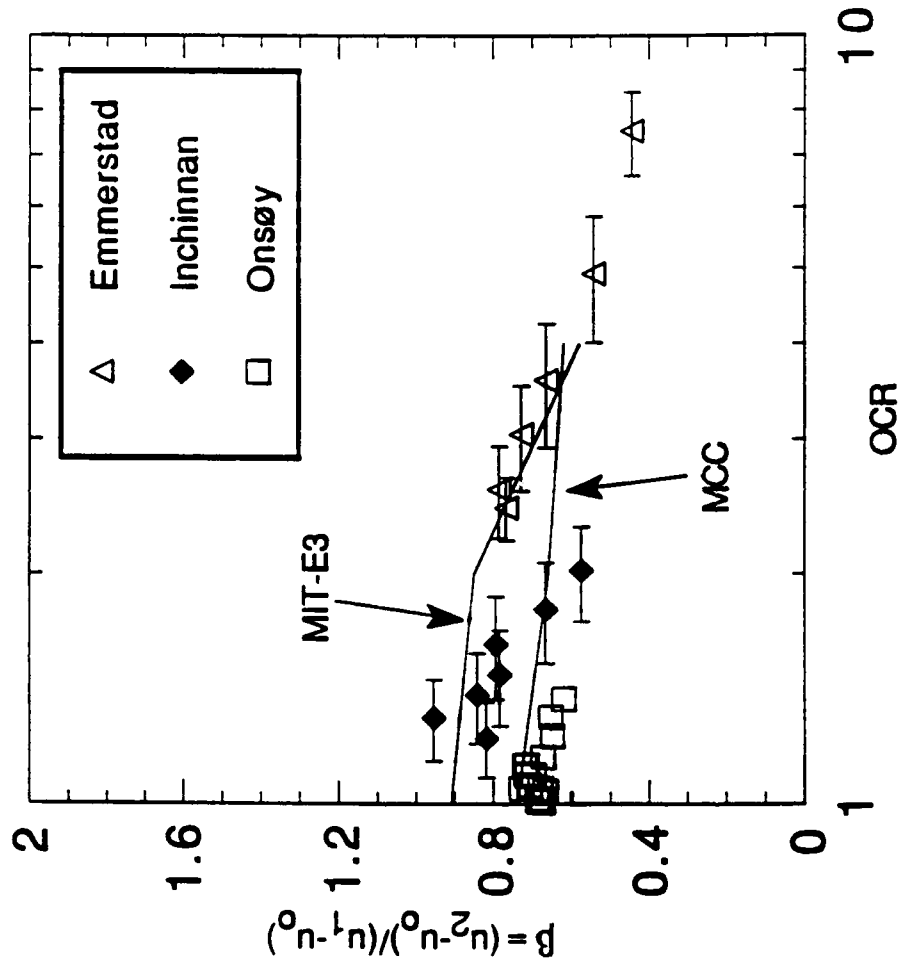
Figure 3.24 Comparison of predictions to piezocone measurements at six sites

Figure 3.24b $(u_1 - u_0) / \sigma'_v$

Figure 3.24c $(u_2 - u_0) / \sigma'_{v0}$

Figure 3.24d $(u_1 - u_0)/(\sigma_v - u_0)$

Figure 3.24e $(u_2 - u_0) / (q_t - \sigma_{v0})$

Figure 3.24f $(u_2 - u_0)/(u_1 - u_0)$

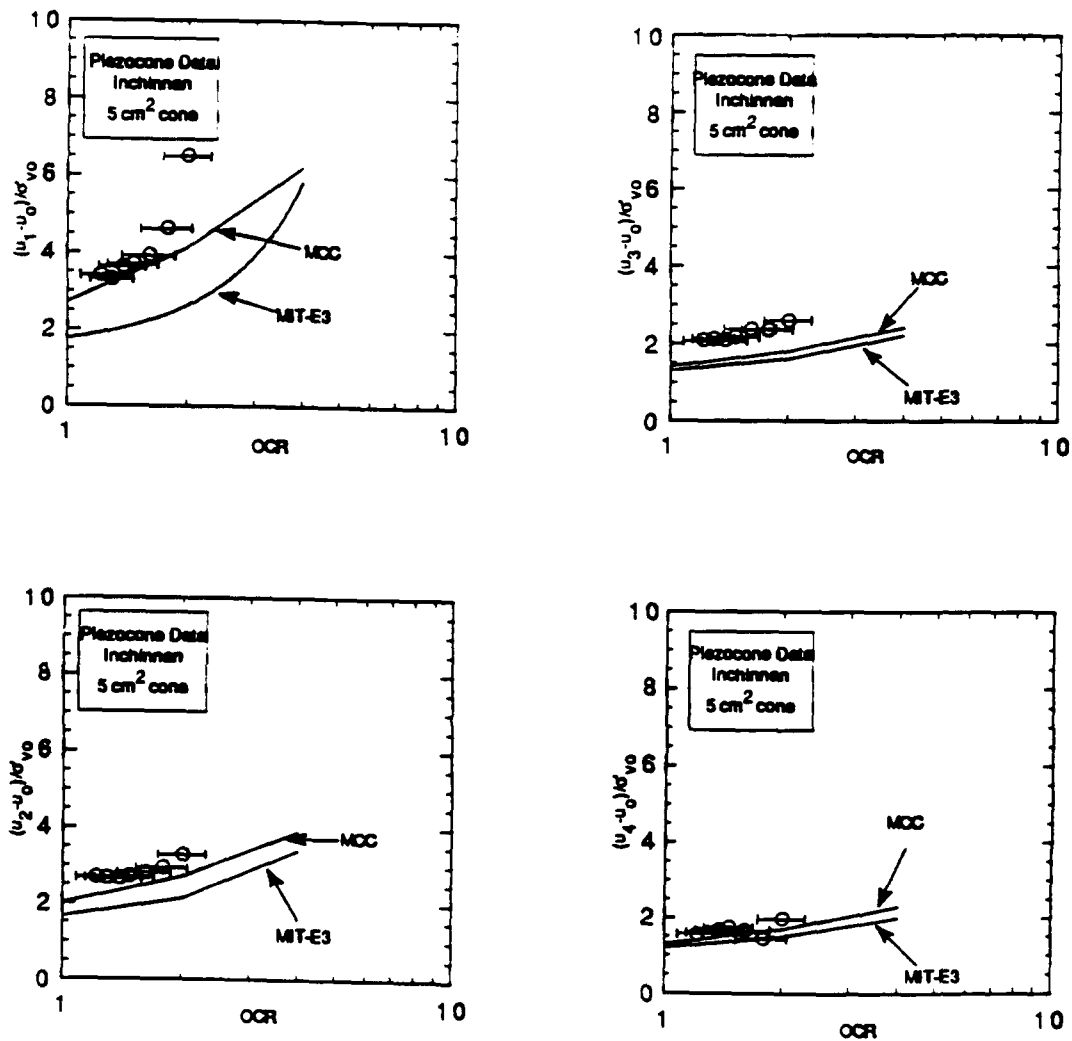


Figure 3.25 Pore pressures measured at four locations during piezocone penetration at the Inchinnan site (Sills et al., 1988)

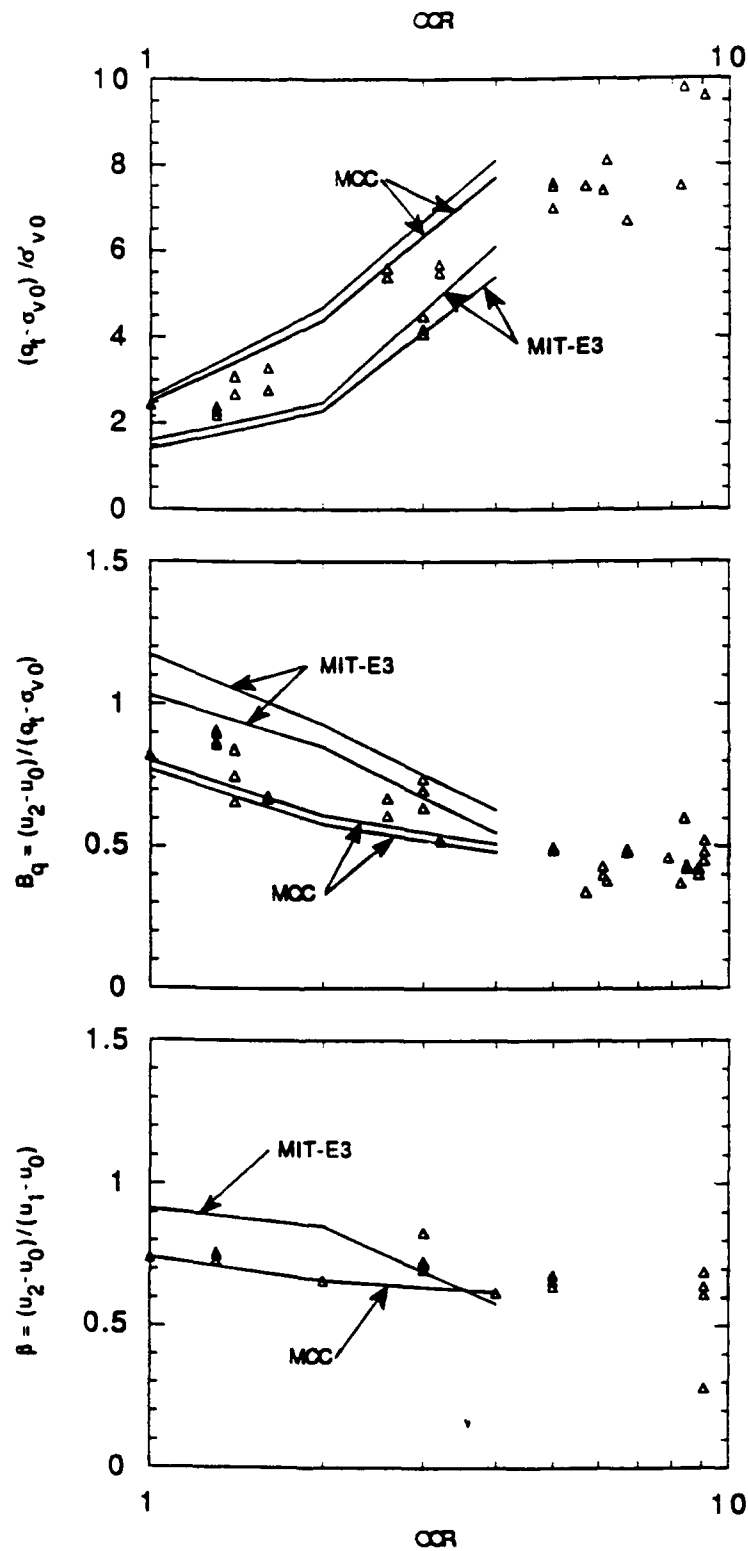


Figure 3.26 Comparison of Piezocone Measurements in Resedimented Kaolin to MIT-E3 Predictions for BBC (May, 1987; Nyirenda, 1989)

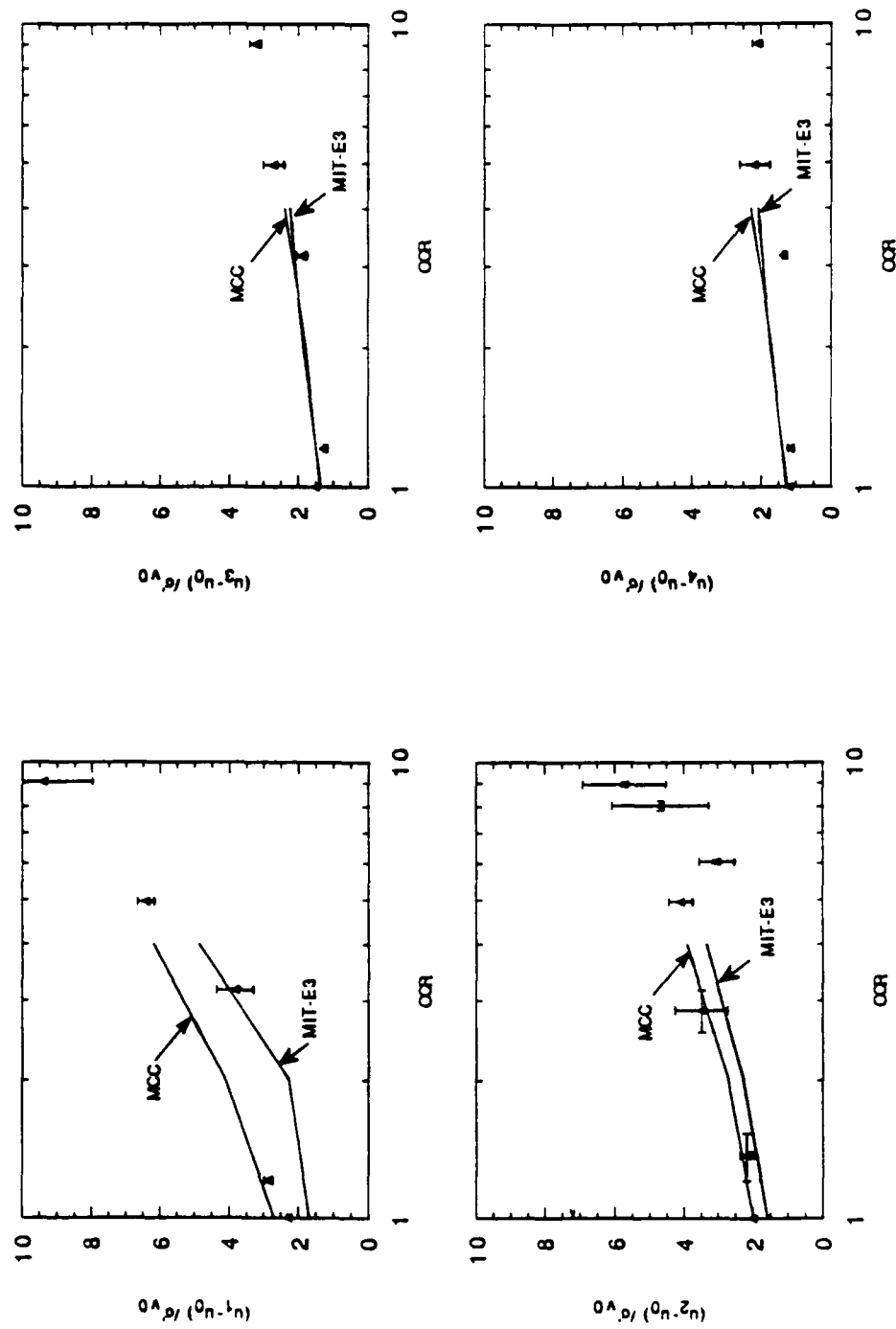


Figure 3.26 (cont.) Comparison of Piezocone Measurements in Resedimented Kaolin to

MIT-E3 Predictions for BBC (May, 1987; Nyirenda, 1989)

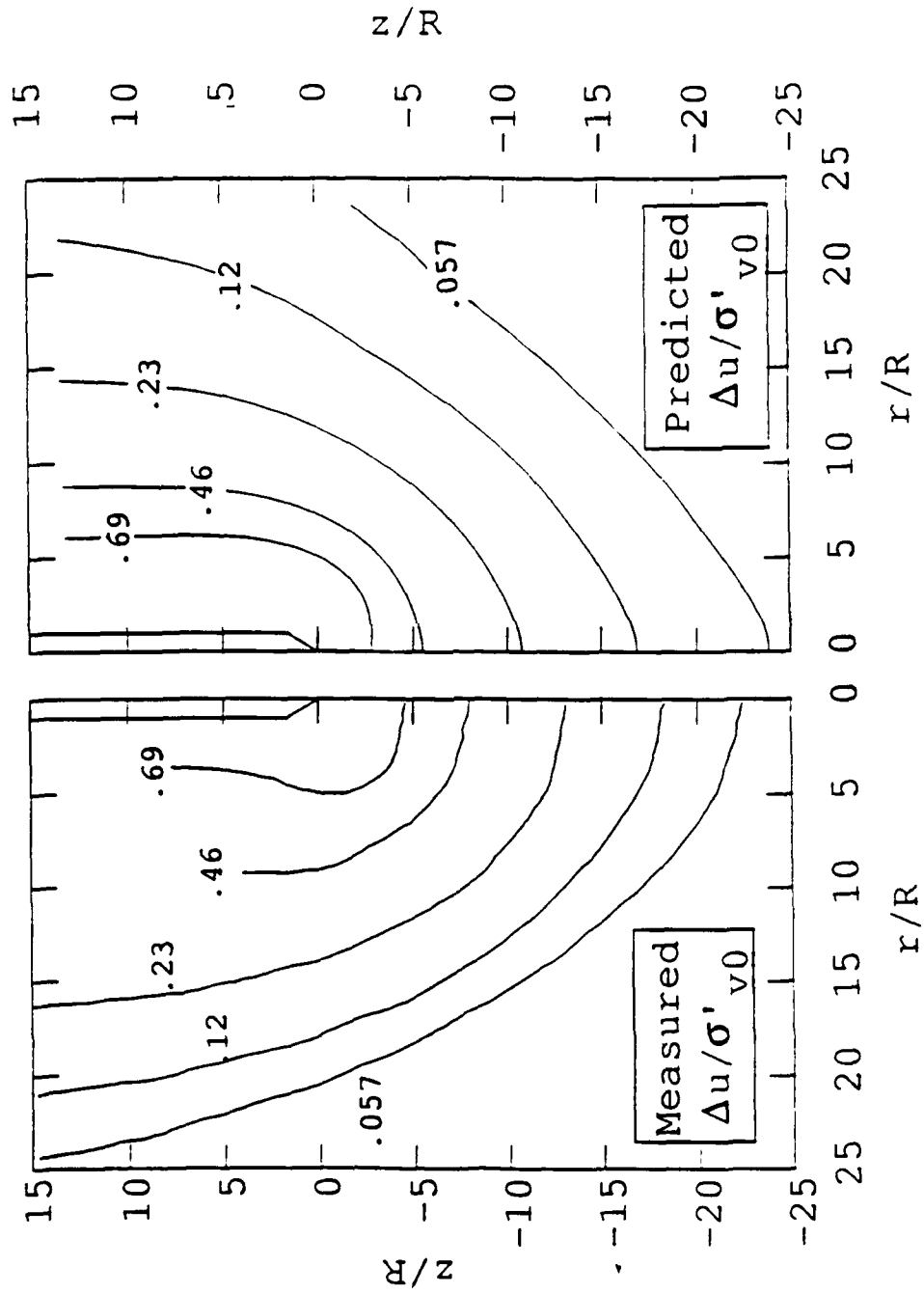


Figure 3.27 Comparison of Measured Pore Pressure Fields in Resedimented Kaolin to
MIT-E3 Predictions for BBC (May, 1987)

4. THE MARCHETTI DILATOMETER

4.1 INTRODUCTION

The flat plate dilatometer (Figure 4.1) was developed in Italy by Marchetti (1980) and introduced into the United States in 1982 (Schmertmann, 1982). It has gained considerable popularity due to its operational simplicity, repeatability of measurements and low cost. The device consists of a flat blade with overall thickness $2w=14\text{mm}$, aspect ratio $B/w=6.8$ ($2B=95\text{mm}$), and a cutting edge with apex angle $2\delta=18^\circ$. The dilatometer is instrumented with a flexible circular steel diaphragm to measure the lateral pressure. The diaphragm has a total surface area, $A_D \approx 2800\text{mm}^2$ (diameter $=60\text{mm}$.) The standard dilatometer (DMT) procedure involves the following steps (Schmertmann, 1986):

1. The blade is jacked vertically into the ground (at a steady rate of $U \approx 1\text{--}2\text{ cm/sec}$) over a standard interval ($10\text{--}20\text{cm}$)
2. Immediately on interruption of jacking, the internal pressure, p_0 , necessary to cause lift-off of the membrane is measured.
3. The membrane is then inflated to a prescribed displacement ($\Delta=1\text{mm}$), at which the pressure p_1 is recorded.
4. Membrane pressure is released prior to subsequent jacking and a closure pressure, p_2 , is obtained when the membrane recontacts the plane of the plate (Luttenegger and Kabir, 1988).

More elaborate procedures have recently been proposed, including a) measurement of $p(t)$ from holding tests (Marchetti et al., 1986; Robertson et al., 1988), and b) measurement of pore pressures in conjunction with the lateral stress diaphragm (Robertson et al., 1988, Boghrat, 1982).

In the original development of the dilatometer, Marchetti (1980) combined the measured pressures p_0 and p_1 with the known (estimated a priori) in situ pore pressure, u_0 , and effective overburden stress, σ'_{v0} , to form a set of these dimensionless indices:

$$I_D = \text{Material Index} = \frac{p_1 - p_0}{p_0 - u_0} \quad (4.1a)$$

$$K_D = \text{Horizontal Stress Index} = \frac{p_0 - u_0}{\sigma'_{v0}} \quad (4.1b)$$

$$E_D = \text{Dilatometer Modulus} = 34.7 (p_1 - p_0) \quad (4.1c)$$

Empirical correlations were then developed (Marchetti, 1980) to provide estimates of the following characteristics and properties:

1. From I_D , a soil classification that is 'closely related' to the prevailing grain size fraction.
2. From K_D , the in situ lateral stress ratio, $K_0 = \sigma'_{h0}/\sigma'_{v0}$, and $OCR = \sigma'_p/\sigma'_{v0}$ (for both granular and cohesive soils.) The undrained shear strength of cohesive soils is then estimated using the SHANSEP procedure relating c_u/σ'_{v0} to OCR (Ladd and Foott, 1974).
3. From E_D , (together with I_D and K_D), the 1-D constrained modulus, $M=1/m_v$, for both granular and cohesive soils.

It is apparent from the correlations that the contact pressure, p_0 , (used in K_D) is most important in estimating engineering properties of cohesive soils (K_0 , OCR, c_u .) This chapter describes the application of Strain Path analyses for predicting the dilatometer contact pressures, p_0 , in Boston Blue Clay. The Strain Path predictions are based on fundamental analytical solutions for a simple plate geometry (Whittle et al., 1991; Rafalovich, 1991) which are summarized in Appendix C. Using generalized effective stress models (MCC and MIT-E3), analytical predictions of K_D are then obtained using predefined input properties corresponding to K_0 -consolidated Boston Blue Clay (BBC) with $1 \leq OCR \leq 4$. The predictions are evaluated by comparison with measured data from a test site in South Boston at which the preconsolidation history has been determined from an extensive laboratory test program (Ladd, 1990). Further comparisons with data for a number of well-documented test sites suggest severe limitations of the K_D index for estimating OCR in soft clays. The analytical solutions provide a rational basis: a) for estimating the effects of membrane locations on the measurement of p_0 , b) for comparing p_0 with lateral stress measurements on axisymmetric devices such as full-displacement pressuremeter tests (Withers et al., 1986; Baguelin and Jezequel, 1983; Briaud and Shields, 1979), and c) for interpretation of test measurements.

4.2 INTERPRETATION OF CONTACT PRESSURE, p_0

Although dilatometer tests in saturated cohesive soils provide (empirical) estimates of several engineering parameters, most of the discussion in this chapter is related to the prediction of stress history ($OCR = \sigma'_p/\sigma'_{v0}$). The main reason for this is that the actual in situ OCR can usually be obtained quite reliably from laboratory oedometer or CRSC tests

(if performed on high quality samples). Hence, correlations between K_D index and OCR can be checked and directly compared with analytical predictions.

Marchetti (1980) originally used data from 9 test sites in Italy (Figure 4.2a) in order to develop the following correlation for OCR:

$$\text{OCR} = a K_D^m \quad (4.2)$$

where $a=0.34$ and $m=1.56$.

Subsequent work by Lacasse and Lunne (1982) and Powell and Uglow (1988) based on data from well documented sites in Norway and the U.K., respectively, show that the correlation originally proposed by Marchetti can underpredict or overpredict the actual OCR by a factor of 3-4. Figure 4.2b shows the correlation reported by Lacasse and Lunne (1982) based on data from seven well documented marine clay sites. From these results, the authors propose revised correlations for OCR using equation 4.2 with $a=0.225$ and $m=1.35$ to 1.67 . However, more detailed investigation of the data for Onsøy (Section 6.3, Whittle et al., 1989) has shown possible discrepancies in the reported correlations. Subsequently, Lunne et al. (1989) have presented separate correlations for 'young' and 'old' clays, Figure 4.2c, following the suggestion of Powell and Uglow (1988). Even with this subdivision, it is clear that there is a wide scatter in predictions of OCR from the K_D index.

Figure 4.2d shows the correlations presented by Powell et al. (1988) from four sites in the U.K. In this case, the correlations between the different sites are radically different from one another and do not match the correlations developed by Marchetti (1980). In large part, these differences might be explained by the types of clay at these sites:

1. Brent Cross (London Clay) and Madingley (Gault Clay) are sites with ancient clays which have been heavily overconsolidated. Preconsolidation pressures, σ'_p , are very difficult to estimate from oedometer tests (e.g. Bond, 1990). For example, at Brent Cross, Jardine and Bond (1990) report $\text{OCR}=20$ to $70+$ from oedometer tests, while geological history suggests $\text{OCR}=10-20$ (Burland, 1990).
2. For the Cowden till similar difficulties may be associated with the deposition of the clay at low water content as a 'lodgement till' (Hight, 1983).
3. Finally the Grangemouth clay is a recent low plasticity alluvial clay of moderate sensitivity (Powell and Uglow, 1988) and similar to a number of clays considered by Marchetti (1980).
4. In addition, Section 6.3 of Whittle et al. (1989) have pointed out large discrepancies

between the c_u/σ'_{v0} values compared to the OCR values in of Figure 4.2d.

Finally, Mayne (1987), has used data from the 29 sites shown in Figure 4.2e in order to propose a much simpler correlation between preconsolidation pressure and p_0 :

$$\sigma'_p = \frac{p_0 - u_0}{\delta} \quad (4.3)$$

(i.e., $OCR = K_D/\delta$) where δ is a factor observed by Mayne to range from about 1 to 3.

More recently, Robertson et al. (1988) have shown that the 'closure pressure', p_2 , is approximately equal to the penetration pore pressure. Thus the difference, $(p_0 - p_2) \approx \sigma'_{xx}$, the lateral effective stress. Although this method has not been evaluated in detail, it is likely to give a large scatter in predicted OCR as the lateral effective stress is small compared to either p_0 or p_2 (i.e., it suffers the same limitations previously reported for the piezocone using $(q_t - u)$ (see Chapter 3)

4.3 PREDICTIONS OF STRESSES DUE TO DILATOMETER INSTALLATION

4.3.1 The Dilatometer Geometry

The standard (Marchetti) dilatometer (Figure 4.1) has an approximate aspect ratio $B/w=6.8$ (95mm/14mm) and a tip apex angle, $\delta=18-20^\circ$. Lateral stresses are measured in a 60mm diameter flexible steel membrane centered at a vertical location $z/w=13$ (90mm/7mm) above the tip of the blade. Accurate modeling of the surface geometry of the dilatometer can be achieved by numerical boundary element methods (panel methods). This approach was first proposed by Huang (1989) and has been investigated in detail by Williamson (1989) and Whittle et al. (1989). This latter study has shown that although the panel method can be used to model accurately the surface geometry, numerical accuracy of the strain paths is very difficult to achieve. Thus the results of panel method computations require careful evaluation in order to establish their reliability and accuracy for a given discretization of the surface. This limitations imposes severe restrictions on the practical use of the panel method for estimating stresses and pore pressures around the dilatometer.

In this work, the dilatometer geometry is approximated using a simple plate geometry (Whittle et al., 1991) of the same overall aspect ratio ($B/w=6.8$) as described in Appendix C. Figure 4.3 shows the simple plate geometry. Differences in geometry between the simple plate and the dilatometer include:

1. The simple plate has a 'blunt' tip geometry as compared to the sharp apex angle ($\delta \approx 18-20^\circ$) of the dilatometer.
2. The simple plate has smooth curved edges in the horizontal plane, while the dilatometer is square cut.
3. The dilatometer extends to a finite vertical elevation $z/w=34$, while the simple plate is infinite in vertical extent.

The approximations of tip geometry have been studied in detail for axisymmetric cone penetrometers in Chapter 3. These results have shown that the stresses and pore pressures above the base of the conical tip are very similar for the simple pile, 18° and 60° cones and good matching of the solutions can then be achieved by adjusting the reference vertical location of the simple pile with respect to the location of tip of the 18° cone. Figure 4.4 shows that if a point source is located at the elevation of the base of the cone (i.e., at $z/R \approx 6.5$ as shown in Figure 4.4) the corresponding simple pile solution matches closely the 18° cone solution for all locations above the base of the cone. This result suggests that reliable predictions of the stresses and pore pressures on the dilatometer membrane can be achieved using the simple plate solution ($B/w=6.8$) with the source at the elevation of the base of the 20° dilatometer tip ($z/w=5.7$). In this case the center of the membrane on a standard dilatometer will be located at $z/w=7.2$. Note that the dilatometer has an equivalent radius R_{eq}^1 of 20.5mm; therefore, the normalized equivalent diameter of the DMT membrane shown in Figure 4.4 is $60/20.5 \approx 2.93$. The normalized dimensions of the $B/w=6.8$ plate therefore become:

$$\text{Normalized half-thickness of plate} = w/R_{eq} = 1/2.93 = 0.34$$

$$\text{Normalized half-width of plate} = B/R_{eq} = 2.3$$

4.3.2 Distribution of Stresses and Pore Pressures Acting around the Dilatometer

Figure 4.5 (a, b, c, and d) presents a complete picture of the stresses (σ'_{rr} , σ'_r , q_h^2) and excess pore pressures (Δu) generated around the simple plate dilatometer during

¹ $R_{eq} = (4Bw/\pi)^{1/2}$

²The cavity shear stress is defined as the maximum shear stress acting in a horizontal plane (x,y); i.e.

$$q_h = \sqrt{(\sigma_{xx} - \sigma_{yy})^2 - \sigma_{xy}^2}$$

installation. The results correspond to the 'base case' analysis (presented in previous chapters) using the Modified Cam Clay model with input parameters selected to characterize K_0 -normally consolidated Boston Blue Clay. The figures show contours of stresses in two planes; a) the vertical center plane through the dilatometer membrane, and b) the horizontal plane corresponding to the steady state stress field far above the tip of the penetrometer ($z/w=200$). Excess pore pressures ($\Delta u/\sigma'_{v0}$, Figure 4.5d) are obtained from finite element solutions of the modified Poisson equation, as described in Chapter 2. All dimensions are normalized by the equivalent radius of the dilatometer, R_{eq} (Appendix C), in order to compare with predictions for an axisymmetric penetrometer (simple pile). The location of an equivalent membrane (i.e., of same diameter and center) is also marked on the axisymmetric penetrometer in Figures 4.5a to d. By coincidence, this membrane is at an elevation comparable to the friction sleeve on standard piezocones (Chapter 3).

Overall, it can be seen that the magnitudes and distributions of the effective stresses and excess pore pressures are very similar for both penetrometer geometries and have the following characteristics:

1. Excess pore pressures (Figure 4.5d) achieve maximum values at or close to the penetrometer tip ($\Delta u_{tip}/\sigma'_{v0} \approx 3$). At locations far above the tip of the penetrometer, the excess pore pressures are $\Delta u/\sigma'_{v0} \approx 1.0$ to 1.2 or about 0.3 to 0.4 times the tip pore pressures. The region of excess pore pressures extends to lateral distances $x/R_{eq} \approx 10$ - 20 and is controlled by the elastic shear modulus G , (Baligh, 1986a, Whittle, 1987) used in the MCC model.
2. Above $z/R_{eq} \approx 5$ the lateral effective stress $\sigma'_{xx}/\sigma'_{v0}$ ($\sigma'_{rr}/\sigma'_{v0}$ for the axisymmetric case) is approximately constant and equal to 0.2 to 0.3 (Figure 4.5a). The lateral stress acting on the interface is smaller than the free field K_0 stress condition due to principal stress rotations described in the Strain Path Method (Whittle and Baligh, 1990).
3. Cavity shear stresses q_h/σ'_{v0} (Figure 4.5c) are zero in the far field (since $\sigma'_{xx} = \sigma'_{yy} = \sigma'_{ho}$), increase to a maximum slightly above 0.3 at $x/R_{eq} \approx 5$, and then decrease to less than 0.05 at the indenter interface.
4. Changes in the mean effective stress, $\Delta\sigma' = -\Delta u_s$, (Figure 4.5b) are small and reflect the description of 'critical state' conditions (σ'_f/σ'_{v0} is uniquely defined at large strains for all modes of shearing) used in the MCC model.

Apart from the overall similarities, a more detailed comparison of the stresses in the vicinity of the dilatometer membrane shows:

1. Excess pore pressures acting at the dilatometer boundary vary by up to 30% along the membrane ($\Delta u/\sigma'_{v0} \approx 1.8-2.4$ also shown in Figure 4.5d). Similar magnitudes ($\Delta u/\sigma'_{v0} \approx 1.6-2.2$) are predicted at the same locations on the axisymmetric penetrometer.
2. The lateral effective stresses acting at the center of the dilatometer membrane, $\sigma'_{xx}/\sigma'_{v0} = 0.21$, is significantly smaller than that for the equivalent axisymmetric membrane ($\sigma'_{\pi}/\sigma'_{v0} = \sigma'_{xx}/\sigma'_{v0} = 0.6$ at the membrane center $z/R_{eq} = 2.45$).
3. The effective stresses, $\sigma'_{xx}/\sigma'_{v0} = 0.21$ (see also Figure 4.6), are much smaller than the excess pore pressures at all locations around the membrane. Thus measurements of total lateral pressures obtained using the standard dilatometer are controlled by excess pore pressures, as observed by Lutenegger (1988) and Robertson et al. (1988).

4.3.3 Evaluation of Contact Pressure from Analytical Solutions

In general, the net contact pressure, $p_0 - u_0$, measured by the dilatometer can be equated with the net average total normal stress acting on the membrane:

$$(p_0 - u_0) = (\sigma_{xx} - u_0)_{avg} = \frac{\int (\sigma_{xx} - u_0) dA}{A} \quad (4.4)$$

In principle, predictions of $p_0 - u_0$ require a complete knowledge of the three-dimensional effective stress fields around the dilatometer to estimate pore pressures from equilibrium. Figure 4.6 shows the distributions on lateral stresses and pore pressures calculated along the vertical centerline ($y/w=0$) of the device and at steady state ($z/w=200$) for the horizontal centerline of the membrane. From these results, it can be seen that:

1. The lateral pressures are almost constant across the width of the ('equivalent') membrane (Figure 4.6b), with variations in horizontal effective stresses and pore pressures being less than 5%.
2. In the vertical plane (Figure 4.6a), there is a fairly significant (25%) decrease in net total lateral stress ($\sigma_{xx} - u_0$) moving from the bottom to the top of the membrane. Horizontal effective stresses are very nearly constant with respect to the vertical coordinate. The fact that pore pressure, and hence total stress, vary significantly along the membrane is a potential source of scatter in DMT correlations.

Based on the results in Figure 4.6, the dilatometer contact pressure can be calculated assuming no variation in σ_{xx} in the y-direction (at any given z) as follows:

$$(p_0 - u_0) = \frac{\int_{z_1}^{z_2} (\sigma_{xx} - u_0) 2 \sqrt{r_m^2 - (z - z_c)^2} dz}{\pi r_m^2} \quad (4.5)$$

where r_m is the membrane radius and z_c is the elevation of the membrane center.

Application of Equation 4.5 to the results in Figure 4.6 gives $K_D = (p_0 - u_0) / \sigma'_{v0} = 2.23$, which is essentially equal to the lateral stress acting at the center of the membrane is $(p_0 - u_0) / \sigma'_{v0} = 2.21$. This result suggests that the contact pressure can be estimated reliably from the total lateral stress computed at the center of the membrane.

4.3.4 Analytical Predictions of Dilatometer Membrane Conditions

This section presents predictions of total lateral stress and pore pressure conditions at the center of a dilatometer membrane immediately following undrained penetration. As tentatively concluded in the preceding section, the total lateral stress at the center of the DMT membrane closely approximates the contact pressure, p_0 , measured in the standard dilatometer test. While not a standard DMT measurement, predictions of pore pressures at the center of the membrane are also considered in this section in order to assess whether installation pore pressures can be used to improve the interpretation of dilatometer test results. Such pore pressure measurements could be obtained directly from a filter located at the center of the membrane as described by Robertson et al. (1988). Based on the assumptions described in previous sections, Table 4.1 (see also Figure 4.7) presents a summary of analytical predictions for plate dilatometer contact pressures. The table shows results for two soil models (MCC and MIT-E3) with input parameters selected for Boston Blue Clay with OCR's of 1, 2, and 4 (c.f., results for the piezocone in Chapter 3).

The aim of these predictions is to address the following questions regarding interpretation of DMT measurements in cohesive soils:

1. Which soil parameter(s) is being measured (i.e., which soil parameter provides the most suitable basis for correlation with DMT results?). While many soil parameters will undoubtedly affect a DMT measurement, the aim is to identify one which has a dominating role and hence can be used as a basis for correlations. Soil parameters

which will be considered in this section are a) OCR (σ'_p/σ'_{v0}) because it controls the undrained behavior of cohesive soils, and b) undrained shear strength c_u because it has been shown to provide a reliable basis for correlation in other penetration tests (e.g. the correlation between $(q_t - \sigma_{v0})$ and c_u in the piezocone test). Since c_u is dependent upon shearing mode, correlations should use a consistent reference shear strength (e.g., TC, DSS, or TE). In this section c_{uTC} will be used as the reference shear strength.

2. Which DMT measurement provides the most reliable basis for estimating soil properties? Consideration will first be given to the K_D parameter measured in the standard DMT, defined by equation 4.1b:

$$K_D = \frac{p_0 - u_0}{\sigma'_{v0}} \quad (4.1b)$$

If pore pressures are measured at the center of the membrane, a number of additional parameters may be considered as a means for estimating soil properties, which can include:

$$\frac{u - u_0}{\sigma'_{v0}} = \text{Normalized excess pore pressure}$$

$$\frac{p_0 - u}{\sigma'_{v0}} \approx \text{Normalized effective lateral stress}$$

$$\frac{u - u_0}{p_0 - u_0} \approx \text{Ratio of excess pore pressure to net lateral stress}$$

Finally, the normalized net change in horizontal total lateral stress

$$\frac{(p_0 - \sigma_{h0})}{\sigma'_{v0}}$$

at the membrane will be considered. Although this parameter would be of limited practical value, as σ_{h0} is generally unknown, it will be considered for the purpose of understanding the mechanics of plate penetration (i.e., do soil properties relate to total stresses acting on a penetrometers or to net stresses?).

3. How do DMT measurements vary with soil properties? The first type of relationship linking soil parameter (OCR, c_{uTC}) to DMT measurement (K_D , etc.) that will be considered is that of a direct proportion between soil parameter and DMT

measurement:

$$(\text{soil parameter}) = a \times (\text{DMT measurement}) \quad (4.6)$$

where 'a' is a constant. This type of relationship is desirable as it clearly relates soil parameter to measurement in a way that can be readily interpreted. Using MCC and MIT-E3 model predictions, a number of DMT measurements (K_D , pore pressure, etc.) will be used evaluated to determine whether they can be directly related (approximately) to either OCR or c_u .

If no direct relationships relating soil property to measurement can be identified, then more complex functions, such as a power function of the form proposed by Marchetti (1980) (see also equation 4.2):

$$(\text{Soil Property}) = a \times (\text{DMT measurement})^m \quad (4.7)$$

(where 'a' and 'm' are constants) must be considered.

4. What is the range of applicability of a correlation? This question can be considered in two parts: a) can correlations from one site be extrapolated to other sites (i.e., are reliable universal correlations possible for a wide range of soils?); and b) can meaningful site-specific correlations be developed (i.e., over what range of OCR and for what conditions of soil variability will a correlation be valid at a specific site?). These questions can be addressed by comparing model predictions to DMT measurements for different types of soils. This research only presents results for BBC. However, some tentative conclusions on the effect of soil properties can be made by comparing MCC (no strain softening) and MIT-E3 (moderate sensitivity) model predictions.

4.3.4.1 Correlation with Undrained Shear Strength, c_{uTC}

Table 4.2a shows predictions of DMT membrane pore pressures and stresses normalized by the undrained shear strength, c_{uTC} . This table indicates:

1. Predictions of $(u-u_0)/c_{uTC}$, $(p_0-u_0)/c_{uTC}$, and $(p_0-\sigma_{h0})/c_{uTC}$ based on both the MCC and MIT-E3 models all vary substantially (30-50%) as the OCR increases from 1 to 4; i.e. these ratios cannot be considered to be even approximately constant over the range of OCR considered. This result predicts that $(u-u_0)$, (p_0-u_0) , and $(p_0-\sigma_{h0})$ cannot be directly correlated to undrained shear strength, c_{uTC} , in a manner described by

equation 4.6.

2. The normalized effective lateral stresses acting on the membrane, σ'_{xx}/c_{uTC} , predicted from the MCC model are approximately constant with OCR; however, the MIT-E3 model shows this ratio to vary substantially with OCR (by a factor of 2.5). The different trends predicted from the two models can be attributed to the strain-softening behavior in the MIT-E3 model. In any event, this result predicts that for realistic conditions involving strain softening, effective lateral stresses, σ'_{xx} , cannot be reliably correlated the undrained shear strength, c_{uTC} in a manner described by equation 4.6.

While some authors (Lacasse and Lunne, 1988; Marchetti, 1980) propose more complex K_D - c_u correlations of the type described by equation 4.7, it appears preferable to correlate DMT measurements to OCR, because a) stress history profiles (from oedometer tests) can be more reliably defined than shear strength profiles, and b) shear strength is dependent upon shearing mode, which complicates correlations.

4.3.4.2 Correlations with Stress History, OCR

Table 4.2b shows MCC and MIT-E3 predictions of DMT membrane pore pressures and stresses normalized by preconsolidation pressure σ'_p . Again it can be seen that $(u-u_0)/\sigma'_p$, $(p_0-u_0)/\sigma'_p$, and $(p_0-\sigma_{h0})/\sigma'_p$, all vary substantially (by up to a factor of 2) with OCR. This implies that direct correlation (of the type defined by equation 4.6) between DMT membrane measurements and preconsolidation pressure cannot be considered even as an approximation.

The ratio of excess pore pressure to total stress, $(u-u_0)/(p_0-u_0)$, merits discussion since similar correlations to predict OCR have been proposed in the piezocone test (e.g., B_q , Senneset et al., 1982). The results in Table 4.1 show that both the MCC and the MIT-E3 models predict very little variation in this ratio with OCR, i.e., a slight decrease of only 5 to 10% as OCR increases from 1 to 4. The analyses therefore indicate that DMT measurements of $(u-u_0)/(p_0-u_0)$ cannot provide a reliable basis for correlations with OCR, especially given the likely scatter in actual DMT test data.

The above observations imply:

1. Simple linear correlations between DMT measurements and OCR do not appear feasible; therefore, there is no alternative to the empirical power function relationships (equations 4.2 and 4.7) proposed by Marchetti (1980).
2. Membrane pore pressure measurements will not simplify the interpretation of the dilatometer test; therefore, no compelling reason exists for abandoning the K_D

parameter in favor of pore pressure or effective stress measurements. However, pore pressure data might be useful for other purposes, such as for soil classification or for estimation of consolidation behavior.

Table 4.1 presents MCC and MIT-E3 model predictions of K_D versus OCR. These predictions suggest that, for a given set of soil parameters, a unique relationship exists between OCR and K_D . Therefore, a correlation of the type proposed by equation 4.2 is possible. Secondly, recalling that the MCC predictions represent an insensitive soil while the MIT-E3 predictions (both using BBC parameters) represent a moderately sensitive soil, it can be seen that the location and slope of the K_D -OCR curve in $\log(K_D)$ - $\log(OCR)$ space is sensitive to variations in soil sensitivity. This second conclusion should be considered tentative until model predictions with soil input parameters for a wider range of soil types are completed. The implications of these observations on practical use of the DMT are:

1. Site specific $\log(K_D)$ - $\log(OCR)$ correlations can probably be developed from DMT test in soils exhibiting a) normalized behavior (no cementation, etc.) and b) minimal variation in soil type. However, while model predictions show that for a given set of normalized soil properties K_D is not independent of OCR, the slope of the K_D -OCR curve is relatively small and hence of little practical value.
2. It is unlikely that a general, universal correlation between DMT K_D and OCR can be established. This conclusion is based on the apparent sensitivity of the location and trend of the K_D -OCR curve to variations in soil type. A corollary to this conclusion is that, at sites exhibiting substantial variations in soil type, even site specific correlations cannot be reliably established.

4.3.5 Comparisons with Full Displacement Pressuremeters

The full displacement pressuremeter test (FDPMT) combines a cone penetrometer with a pressuremeter. Devices described by Baguelin and Jézéquel (1983), Withers et al. (1986), and Briaud and Shields (1979) are shown in Figure 4.8. For the device described by Withers et al., the center of the expandable membrane is located a normalized vertical distance $z/R \approx 43$ above the cone tip, and has a length $L/R \approx 21$. As discussed in Chapter 2, a steady state condition occurs above $z/R \approx 15-20$ during cone penetration; therefore, the entire membrane can be considered to be located in the steady state zone. The initial total stress, p_i , measured in this test corresponds to the average total lateral stress acting on the membrane and is therefore analogous to the contact pressure, p_0 , measured in the

dilatometer test. Since the membrane is located entirely in the steady state zone, p_i can be taken to be equal to the steady state total lateral stress.

MCC and MIT-E3 predictions of $p_i (= \sigma_{\pi} - u_0)$ are shown in Table 4.3 (see also Figure 4.7). Comparison of these predictions with the dilatometer predictions in Table 4.4 indicate that MCC predictions of total lateral stress at the FDPMT membrane are 20-30% less than the DMT predictions. This can be largely attributed to the fact that the FDPMT membrane is located in the steady state zone, while the DMT membrane is located nearer to the tip. MIT-E3 predictions indicate the FDPMT p_i to be roughly 10-20% less than the corresponding DMT predictions. When comparing DMT contact pressure to CPTU base pore pressure, two offsetting effects must be considered: a) the DMT contact pressure is a total stress measurement which is slightly higher than the pore pressure in normally to moderately overconsolidated soils (by 4-18% according to predictions presented in Table 4.1), and b) the center of the DMT membrane is at a slightly higher equivalent elevation ($z/R_{eq}=2.45$) than that of the piezocone base ($z/R_{eq}=1.73$), and pore pressures and total stresses are slightly less at the higher elevation (6% less for the $B/w=6.8$ plate predictions shown in Figure 4.6 and 5-15% less for the cone predictions shown in Figure 3.17). Consequently DMT contact pressure measurements would be expected to be roughly equivalent to CPTU base pore pressure measurements.

4.4 COMPARISONS WITH MEASURED DILATOMETER DATA

4.4.1 Contact Pressure, p_0

In this section the model predictions presented in Section 4.3 are compared with measured data to determine:

1. The capabilities and limitations of the analytical predictions for describing: a) the magnitudes of K_D ; and b) variations in K_D with stress history.
2. The validity of the preliminary conclusions drawn in previous section: a) K_D cannot be linked to OCR by a simple direct proportion; b) well-defined trends can be established between K_D and OCR at sites exhibiting normalized behavior (no cementation, etc.) and minimal variability in soil type; c) a universal correlation relating K_D to OCR for all soils is not feasible; and d) at sites showing extensive soil variability or non-normalized behavior, even site-specific correlations cannot be reliably obtained.

Data from seven well-documented sites are reviewed to assess the relationship between

DMT K_D and OCR. The OCR profiles are based on either incremental oedometer or constant rate of strain consolidation (CRSC) tests. A description of the geotechnical characteristics of each of the seven sites is described below:

1. The Central Artery and Tunnel (CA/T) test site located in South Boston is described in detail by Ladd (1990). The soil profile (Figure 3.19b) from elevation 74ft to -29ft consists of Boston Blue Clay (Note: project El. 100 ft equals mean sea level). The deposit is a marine illitic clay of low to moderate sensitivity having a mean plasticity index of $28.7 \pm 5.2\%$ from El. 70 to 0 and $26.9 \pm 2.5\%$ from El. 0 to -30. From El. 70 to 0 the liquidity index increases from about 0.4 to about 0.8 ± 2 . The preconsolidation pressure decreases linearly with depth within the upper 55 ft of the deposit (OCR decreasing from 6.5 to 1.2), whereas the bottom 50 ft (below El. 20 ft) is only slightly overconsolidated ($OCR=1.15$) and behaves as a "structured" material.
2. The Potomac River Alluvium (Figure 4.9a) described by Mayne (1987) consists of 25m organic silty clay (OH) having an average liquid limit of 83% and an average plasticity index of 37%. Below a depth of 11 m the liquidity index generally ranges from 0.5 to 0.8. Above 11m, the liquidity index is highly variable, ranging from approximately 0.4 to 1.6. Oedometer data indicate a well-defined OCR profile with moderate scatter. The σ'_p profile is essentially linear with depth $\sigma'_p - \sigma'_{v0}$ being almost constant. Over most of the deposit there is a fairly uniform decrease in OCR, with $OCR \approx 2$ at $d=5m$ and $OCR \approx 1.4$ at $d=20m$.
3. The Porto Tolle site (figure 4.9b), located on the delta of the Po River, is described by Ghionna et al (1981) and Jamiolkowski et al. (1982). The CL-CH stratum of interest for the dilatometer evaluation is the soft silty clay between depths of 10 to 28m. This stratum contains frequent seams and lenses of fine silty sand which never exceed a few centimeters thickness. The liquid limit within the stratum is 52.3% with a standard deviation of 2.2, and the mean plasticity index is 30.5% with a standard deviation of 1.6%. The sensitivity measured from field vane tests ranges from 2 to 3. The entire stratum has a small, uniform OCR ranging from 1.2 to 1.3.
4. The Drammen site (Figure 4.9c) (Lacasse and Lunne, 1982) comprises a marine deposit of sand and clay (0-5m) overlying a 5m layer of plastic clay (5-10m) and 35m of lean clay (10-45m). In the plastic layer (5-10m) the liquid limit ranges from 50-70% and plasticity index ranges from 25-30%. The plasticity index in the lean clay layer (below 10m) ranges from 10-15%. The sensitivity (based on field vane data) ranges from 6-8 in the plastic clay layer and from 4-7 in the lean clay layer. The OCR

is relatively uniform in both layers, with an OCR from 1.3-1.5 in the plastic layer and from 1.1-1.2 in the lean clay layer.

5. The Onsøy site (Figure 4.9d) (Lacasse and Lunne, 1982) is a soft to medium marine clay deposit extending to a depth of 45m. Liquid limit and plasticity indices range from 55-75% and 20-35%, respectively. In the upper 2-6m the OCR decreases from 15 to 1.3. Below 6m the OCR is essentially constant at 1.3, and the sensitivity based on field vane data ranges from 5-6.
6. The Florence Lake deposit (Figure 4.9e) is an oxbow lake of the nearby Missouri River, consisting of plastic alluvial clay (Whittle et al., 1989.) The plasticity index increases with depth to approximately 60% at a depth of 20ft, and then decreases with depth to a value of about 25% at a depth of 40 ft. The liquidity index generally varies from 0.6-0.9 throughout the deposit, with no observable trend with depth. A reference σ'_p profile was established by a) oedometer tests, and b) back-calculation of σ'_p from field vane strength (Whittle, 1989). Reference σ'_p profiles from the two methods are also shown in Figure 4.9e. The data indicate an OCR profile with three zones: a) a normally consolidated zone below 20ft, b) a nearly constant preconsolidation pressure from 10-20ft, and c) a crust below the surface with scattered OCR's ranging from approximately 1.5-10. Sensitivity measured from field vane tests ranges from 3-4 at depths greater than 10ft.
7. The New Jersey Varved Clay site (Figure 4.9f) is described in detail by Whittle et al. (1989). Preconsolidation pressure data indicate a desiccation crust within the top 15-20ft and then a constant amount of preconsolidation ($\sigma'_p - \sigma'_{v0}$) within the lower 40ft.

For the purpose of establishing whether the model predictions portray realistically actual DMT behavior, MCC and MIT-E3 predictions of K_D for BBC are compared to DMT measurements taken from the Central Artery and Third Harbor Tunnel (CA/T) test site in South Boston (BBC), as presented in Figure 4.10. Error bars indicate the measured range in dilatometer measurements and the range of OCR estimated from laboratory or other field data (Ladd, 1990). The solid lines show the predictions at the center of the membrane, while the dashed lines show the predicted lateral stresses at the top and bottom of the membrane. This comparison shows that for $OCR > 2$ and for low OCR, the MCC and MIT-E3 predictions compare well to measured data. For $1.2 \leq OCR \leq 2$, the predictions do not match measurements with respect to either magnitudes or trend with varying OCR. Moreover, application of Marchetti's (1980) technique (Equation 4.2) to obtain OCR's from the measured K_D values predict a more or less

constant preconsolidation pressure within the upper 65 ft of clay, which contradicts the actual σ'_p profile (Figure 3.19b). Other interpretation techniques could not remove this serious discrepancy. Extensive consolidation and CK₀U shear data indicate that the clay at this site does not exhibit normalized behavior. For example, the consolidation tests show S-shaped virgin compression curves and the CK₀U tests show significant decrease in the normally consolidated undrained strength ratio, c_u/σ'_{v0} , with depth (Ladd, 1990). Such behavior cannot be modelled by either the MIT-E3 or MCC models, which no doubt contributes to the discrepancy between model predictions and measured K_D . Most importantly, neither the universal correlation proposed by Marchetti (1980) nor site-specific correlations can lead to reliable estimates of σ'_p at this site.

Plots of K_D versus OCR on a log-log scale for the remaining six sites are shown in Figure 4.11. From these plots it can be seen that:

1. At three sites, Onsøy, Potomac, and Florence Lake, the data show a clearly defined K_D -OCR (site-specific) relationship. In all three cases, the data show that for a given OCR, the scatter in K_D is less than 25%. Such trends are consistent with model predictions, indicating that reasonable site-specific trends are possible in deposits exhibiting minimal heterogeneity and (presumably) normalized behavior.
2. The Drammen data indicate a much wider scatter band. This could be linked to the heterogeneity of the deposit and supports the suggestion that the relationship of K_D versus OCR is heavily influenced by variations in normalized soil properties.
3. The New Jersey varved clay data shows K_D to be virtually independent of OCR for $OCR > 2$. This could be a consequence of the unique behavior of varved clays. Evaluation of these data in light of model predictions is not feasible, as neither model is capable of realistically simulating a varved clay. However, as discussed in Section 6.5.3 of Whittle et al. (1989), the DMT data completely "missed" the high preconsolidation within the upper desiccated crust of the deposit for reasons that still remain unknown.
4. All data sets indicate that a complex relationship exists between K_D and OCR; that is, K_D cannot be correlated (even approximately) to OCR by a simple direct proportion (note that a 1:1 slope on a log-log plot implies that a directly proportional relationship exists). This further reinforces the notion that K_D is related to OCR in a very complex manner that can only be treated within an empirical framework.

Finally all seven data sets are superimposed in Figure 4.12. This data shows that the width of the scatter band is such that for $1 < OCR < 1.5$, K_D can vary by a factor of 2. At

higher OCR the scatter is somewhat less, if the New Jersey varved clay data is discounted. Overall, the wide scatter band demonstrates that a universal K_D -OCR relationship cannot be established. Furthermore, at three of the sites (South Boston, Drammen, and the New Jersey Varved Clay) even site-specific K_D -OCR correlations could not be established.

Comparisons of the σ'_p estimated from the DMT test using the Marchetti (1980) correlation for the South Boston site (Ladd, 1990) and the Florence Lake and New Jersey Varved Clay sites (Whittle et al., 1989) are shown in Figures 4.13a, b, and c, respectively. Plotted values of σ'_p estimated from the DMT test represent the mean value over a 3-10 foot interval. Error bars shown for the South Boston data represent the standard deviation corresponding to the same interval. The best estimate and range of the reference σ'_p obtained from laboratory and field vane data is also shown. These comparisons show:

1. At the South Boston site (Figure 4.13a), the DMT σ'_p profile bears no relation to the reference profile. Between El. 20 and -15, the DMT indicates increasing $(\sigma'_p - \sigma'_{v0})$ with increasing elevation, while the reference profile shows $(\sigma'_p - \sigma'_{v0})$ to be approximately constant in this elevation range. In the desiccation crust above El. 20 the DMT profile indicates a trend of σ'_p being approximately constant or slightly decreasing with increasing elevation, which contrasts with the reference profile showing σ'_p to increase sharply with increasing elevation.. At this site the DMT is clearly provides poor estimates of σ'_p with regard to both magnitudes and to relative changes in σ'_p with depth.
2. DMT estimates of σ'_p at the Florence Lake (Figure 4.13b) site show good agreement with reference values between depths of 25 to 40 ft. In the desiccation crust from depths of 0 to 10 ft, agreement between DMT estimates and predictions is also good, although there is considerable scatter in the data. Between 10 and 25 ft the DMT overestimates σ'_p by up to 50%. Overall, the DMT gives reasonable estimates of σ'_p at this site.
3. In the New Jersey Varved Clay (Figure 4.13c), the DMT gives reliable estimates of σ'_p beneath the desiccation crust below El. -30. However, in the from El. -30 to -10, the DMT gives no indication at all of the highly precompressed desiccation crust. As with the South Boston site, the DMT cannot generally make reliable estimates of σ'_p magnitudes, nor does it adequately identify relative changes in σ'_p .

Overall, the data presented in Figure 4.13 suggests a variable performance of the DMT, with the DMT giving reasonable estimates at one site (Florence Lake) and

unreasonable estimates at two sites (South Boston, New Jersey). It should be noted that correlations between K_D and OCR as presented in Figures 4.11 and 4.12 can give misleading indications of DMT performance. For example, the K_D -OCR relationship measured at the South Boston site (Figure 4.11) indicates the Marchetti (1980) correlation to be reasonable, while Figure 13a shows the Marchetti (1980) correlation to be very unreliable. Therefore, evaluations of field performance should include both K_D -OCR correlations and comparisons between laboratory and DMT estimates of σ'_p .

4.4.2 Comparison to Axisymmetric Measurements

This section compares dilatometer contact pressures to axisymmetric penetrometer test measurements, including pore pressures measured by the piezocone (CPTU) and lift-off pressures measured by the full-displacement pressuremeter (FDPMT). The chief aim of this section is to validate the conclusions suggested from the MCC and MIT-E3 predictions for cone and plate penetration in BBC presented in Sections 3.3, 4.3.4, and 4.3.5 (summarized in Table 4.4) which indicated:

1. The DMT contact pressure p_0 is comparable to the full-displacement pressuremeter (FDPMT) lift-off pressure p_i with $p_0/p_i \approx 1.05-1.2$ over the range $1 \leq \text{OCR} \leq 4$. Higher values of this ratio correspond to higher values of OCR.
2. DMT contact pressure p_0 roughly compares with CPTU pore pressures measured at the cone base u_2 , with $u_2 \approx 0.9-1.1 p_0$ for soils in the range $1 \leq \text{OCR} \leq 4$. CPTU tip pore pressures u_1 exceed p_0 by 10-75% over the range $1 \leq \text{OCR} \leq 4$ with larger differences occurring at higher OCR's.

Luttenegger and Blanchard (1990) compared DMT contact pressure p_0 to FDPMT lift-off pressure p_i at eight sites as shown in Figure 4.14. The FDPMT device used in the study was designed by Briaud and Shields (1979) as described in Section 4.3.5 and illustrated in Figure 4.7a. The soils included sensitive marine clay in northern New York (SLS) and dense glacial till in central Iowa (AMES). The overall trend of the data is that of the DMT contact pressure being slightly greater than the FDPMT lift-off pressure. This trend generally conforms to the trend predicted from the model predictions also shown in this figure. As noted in Section 4.3.5, the small difference in the two measurements can be attributed to the fact that the FDPMT membrane is located at a greater equivalent distance above the penetrometer tip than the DMT membrane, consequently pore pressures and total horizontal stresses are lower. Overall, the data support the conclusion suggested from the predictions, which indicate that penetrometer geometry (cone versus plate) has

little effect on total horizontal stress measured at the penetrometer boundary.

Comparison of DMT horizontal stress index K_D to CPTU pore pressures measured at the shoulder and face of the cone are shown in Figures 4.15a and b, respectively. Comparison of K_D to CPTU shoulder pore pressures $\Delta u_2/\sigma'_{v0}$ at the South Boston site shows:

1. In the near normally consolidated soil ($OCR=1.1-1.2$), K_D is not unique, but varies from 2.0 to 2.8.
2. From $OCR=1.2$ to 4, the DMT K_D approximately matches the CPTU $\Delta u_2/\sigma'_{v0}$, compared to $\Delta u_2/\sigma'_{v0}=3.0$ measured by the piezocone.
3. Above $OCR=4$ $\Delta u_2/\sigma'_{v0}$ begins to remain approximately constant with increasing OCR, while K_D continues to increase.

Comparison of DMT K_D values to CPTU base pore pressures $\Delta u_2/\sigma'_{v0}$ measured at the Onsøy site also indicate K_D to be comparable to $\Delta u_2/\sigma'_{v0}$, although in this case $\Delta u_2/\sigma'_{v0}$ consistently exceeds K_D by 5-30%.

Comparison of CPTU face pore pressures $\Delta u_1/\sigma'_{v0}$ to DMT horizontal stress index K_D at the Onsøy site in Figure 4.15b shows that in the normally consolidated soil $\Delta u_1/\sigma'_{v0}$ exceeds K_D by 60%. Furthermore, with increasing OCR the CPTU face pore pressures increase much more rapidly than K_D . It should also be noted that Figure 3.24b shows the Onsøy tip pore pressures for $OCR < 1.5$ to be at the upper boundary of the data.

In conclusion, both predictions and field data indicate that a) DMT contact pressure, p_0 , is comparable to (usually slightly greater than) the FDPMT lift-off pressure, p_i ; b) DMT contact pressure, p_0 , is roughly equal to the pore pressure measured at the base of a piezocone, $\Delta u_2/\sigma'_{v0}$; and c) CPTU tip pore pressure, $\Delta u_1/\sigma'_{v0}$, is both greater (by up to 60%) than DMT contact pressure and more sensitive to changes in OCR.

4.5 SUMMARY AND CONCLUSIONS

This chapter presented strain path analyses of the DMT contact pressure, p_0 , for normally to lightly overconsolidated clays. The analyses show that:

1. Stresses acting on the DMT membrane are not uniform due to the proximity of the membrane to the penetrometer tip.
2. A systematic study of predictions showed no simple correlation between DMT contact pressure, p_0 , and either undrained shear strength, c_u , or preconsolidation pressure,

σ'_p . Predictions of pore pressures at the center of the DMT membrane also show that no simple correlation is possible between membrane stresses and pore pressures and soil properties.

3. Model predictions as well as field data indicate that the K_D -OCR correlation is sensitive to various soil properties (sensitivity, stress-strain behavior) besides preconsolidation pressure and strength; hence, a universal correlation as proposed by Marchetti (1980) is not feasible. Further, even site-specific correlations can be unreliable if the soil properties do not exhibit normalized behavior.
4. Model predictions as well as field data indicate that there is little fundamental difference between cone and plate (DMT) stress fields when dimensions are normalized by the equivalent radius of the plate, R_{eq} . Specifically, comparisons between DMT p_0 and axisymmetric measurements show: a) DMT p_0 is comparable (usually slightly less than) the FDPMT contact pressure; b) p_0 is roughly comparable to pore pressure measured at the base of the piezocone; and c) p_0 is substantially less than (up to 60%) the CPTU tip pore pressure and less sensitive to changes in OCR.

Soil Model	OCR	K_0	$\frac{c_{ATC}}{\sigma'_{v0}}$	$\frac{(u-u_0)}{\sigma'_{v0}}$	$\frac{\sigma'_{xz}}{\sigma'_{v0}}$	$\frac{(p_0-u_0)}{\sigma'_{v0}}$	$\frac{(u-u_0)}{u-u_0}$	$\frac{(p_0-\sigma_{H0})}{\sigma'_{v0}}$
MCC	1.0	0.48	0.32	2.0	0.21	2.2	0.91	1.7
	2.0	0.57	0.57	2.3	0.37	2.7	0.86	2.1
	4.0	0.75	1.05	3.3	0.66	3.9	0.83	3.2
MIT-E3	1.0	0.48	0.33	1.4	0.05	1.5	0.96	1.0
	2.0	0.57	0.54	2.2	0.11	2.3	0.95	1.8
	4.0	0.75	1.05	2.8	0.54	3.4	0.92	2.0

Table 4.1. Prediction at Center of Dilatometer Membrane (for Boston Blue Clay Properties)

Soil Model	OCR	K_0	$\frac{c_{uTC}}{\sigma'_{v0}}$	$\frac{(u-u_0)}{c_{uTC}}$	$\frac{\sigma'_{v0}}{c_{uTC}}$	$\frac{(p_0-u_0)}{c_{uTC}}$	$\frac{(p_0-\sigma'_{h0})}{c_{uTC}}$
MCC	1.0	0.48	0.32	6.3	0.7	6.9	5.4
	2.0	0.57	0.57	4.0	0.6	4.7	3.7
	4.0	0.75	1.05	3.1	0.6	3.7	3.0
Var.*				34%	8%	30%	29%
MIT-E3	1.0	0.48	0.33	4.3	0.2	4.5	3.0
	2.0	0.57	0.54	4.0	0.2	4.2	3.2
	4.0	0.75	1.05	2.7	0.5	3.2	1.9
Var.*				23%	43%	17%	22%

$$* \text{Variation} = \frac{\Delta x}{2\hat{x}} \cdot 100\% ; \Delta x = x_{\max} - x_{\min} \text{ and } \hat{x} = \frac{x_{\min} + x_{\max}}{2}$$

Table 4.2a Prediction of DMT membrane stresses normalized by c_{uTC} for K_0 -consolidated BBC

Soil Model	OCR	K_0	$\frac{c_{uTC}}{\sigma'_{v0}}$	$\frac{(u-u_0)}{\sigma'_p}$	$\frac{\sigma'_{xx}}{\sigma'_p}$	$\frac{(p_0-u_0)}{\sigma'_p}$	$\frac{(p_0-\sigma'_{h0})}{\sigma'_p}$
MCC	1.0	0.48	0.32	2.0	0.2	2.2	1.7
	2.0	0.57	0.57	1.2	0.2	1.4	1.1
	4.0	0.75	1.05	0.8	0.2	1.0	0.8
Var.*				43%	0%	38%	36%
MIT-E3	1.0	0.48	0.33	1.4	0.05	1.5	1.0
	2.0	0.57	0.54	1.1	0.06	1.2	0.9
	4.0	0.75	1.05	0.7	0.3	0.8	0.5
Var.*				33%	71%	30%	33%

$$* \text{Variation} = \frac{\Delta x}{2\hat{x}} \cdot 100\% ; \Delta x = x_{\max} - x_{\min} \text{ and } \hat{x} = \frac{x_{\min} + x_{\max}}{2}$$

Table 4.2b Prediction of DMT membrane stresses normalized by σ'_p for K_0 -consolidated BBC

Soil Model	OCR	K_0	$\frac{c_{dTC}}{\sigma'_{v0}}$	$\frac{(u-u_0)}{\sigma'_{v0}}$	$\frac{\sigma'_{xx}}{\sigma'_{v0}}$	$\frac{(p_i-u_0)}{\sigma'_{v0}}$	$\frac{(u-u_0)}{p_i-u_0}$	$\frac{(p_i-\sigma_{h0})}{\sigma'_{v0}}$
MCC	1.0	0.48	0.32	1.3	0.29	1.5	0.81	1.1
	2.0	0.57	0.57	1.7	0.53	2.2	0.76	1.6
	4.0	0.75	1.05	2.3	0.95	3.2	0.71	2.5
MIT-E3	1.0	0.48	0.33	1.2	0.12	1.4	0.91	0.86
	2.0	0.57	0.54	1.7	0.23	1.9	0.88	1.4
	4.0	0.75	1.05	2.0	0.70	2.7	0.74	1.9

Table 4.3 Prediction at Center of Membrane of Full-Displacement Pressuremeter, $z/R=20$

Soil Model	OCR	FDPMT $\frac{(p_i - u_0)}{\sigma'_{v0}}$	DMT $\frac{(p_0 - u_0)}{\sigma'_{v0}}$	CPTU $\frac{(u_2 - u_0)}{\sigma'_{v0}}$
MCC	1.0	1.5	2.2	2.0
	2.0	2.2	2.7	2.7
	4.0	3.2	3.9	3.9
MIT-E3	1.0	1.4	1.5	1.6
	2.0	1.9	2.3	2.1
	4.0	2.7	3.4	3.4

Table 4.4 Comparison of predicted DMT contact pressures to FDPMT lift-off pressure and CPTU base pore pressures

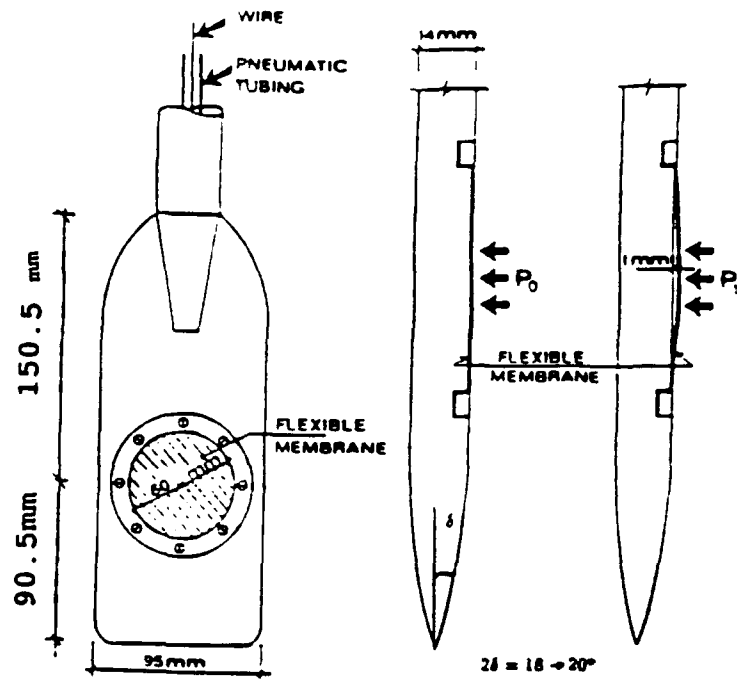
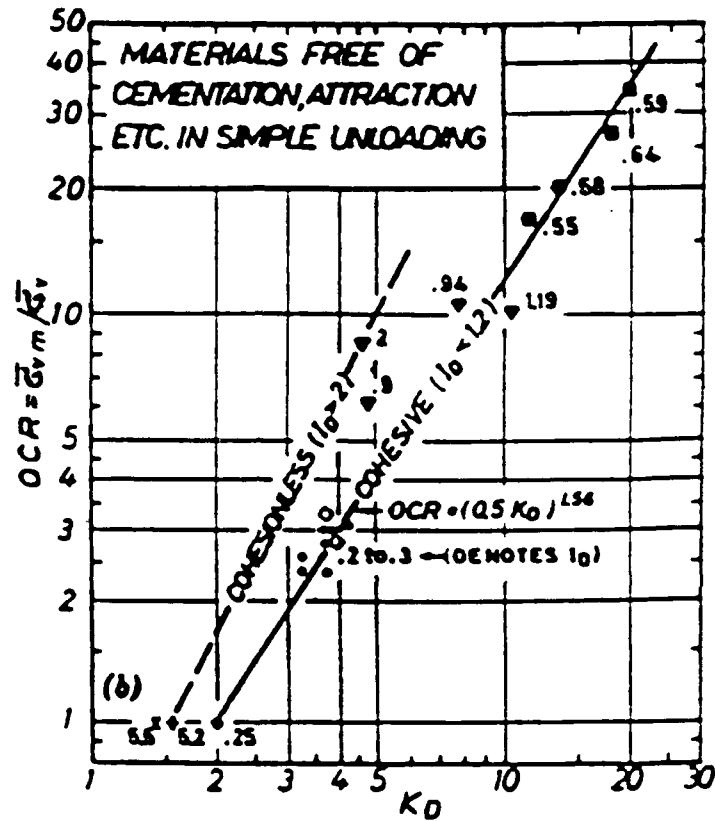
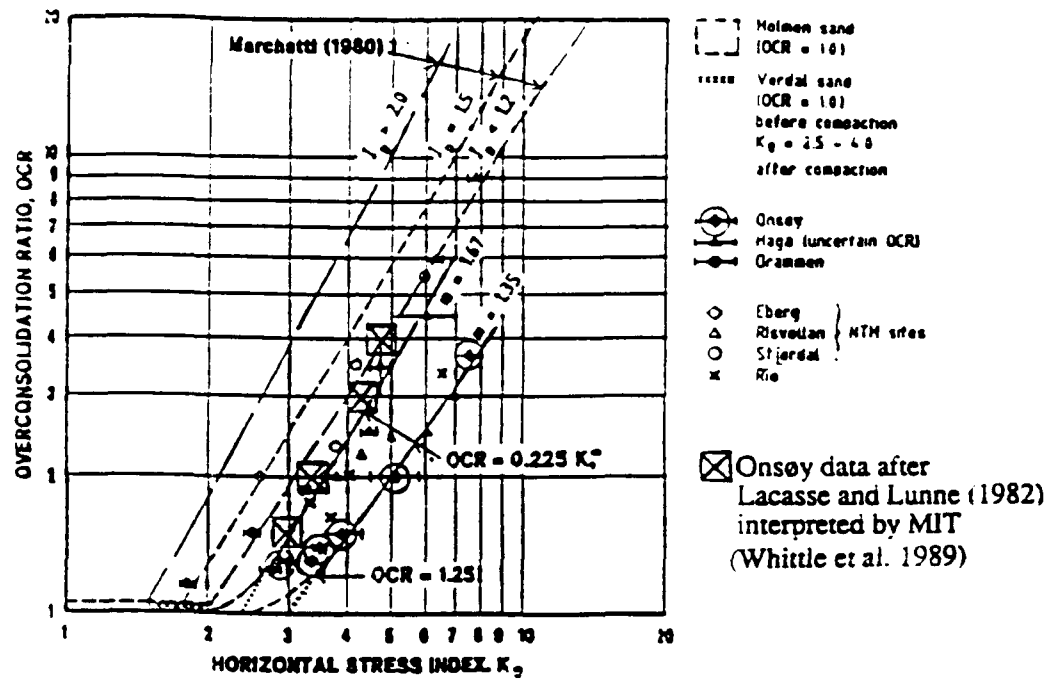


Figure 4.1 Geometry of the Marchetti Dilatometer

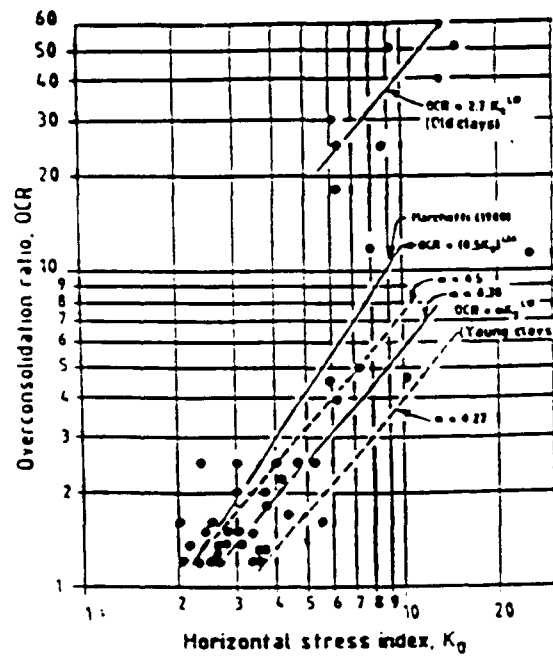


a) Marchetti (1980)

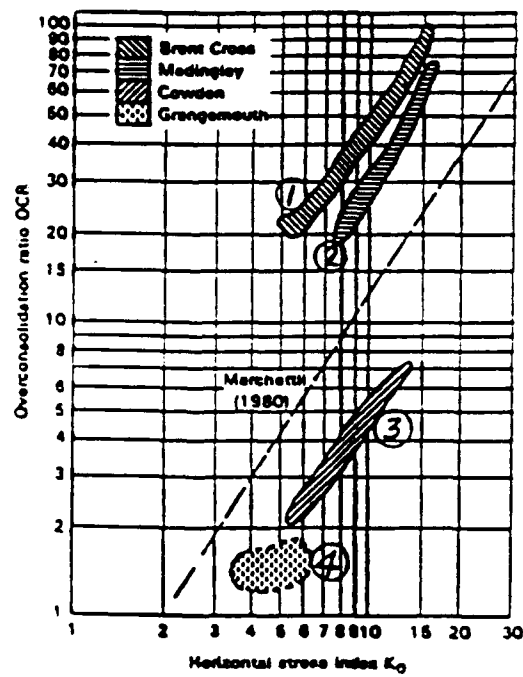
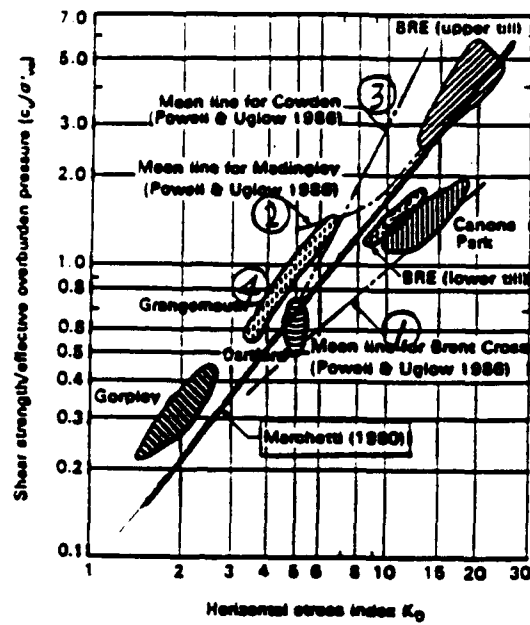
Figure 4.2 Empirical correlations between overconsolidation ratio and dilatometer contact pressure, p_0 : a) Marchetti (1980); b) Lacasse and Lunne (1982); c) Lunne et al. (1989); d) Powell and Uglow (1988); e) Mayne (1986)



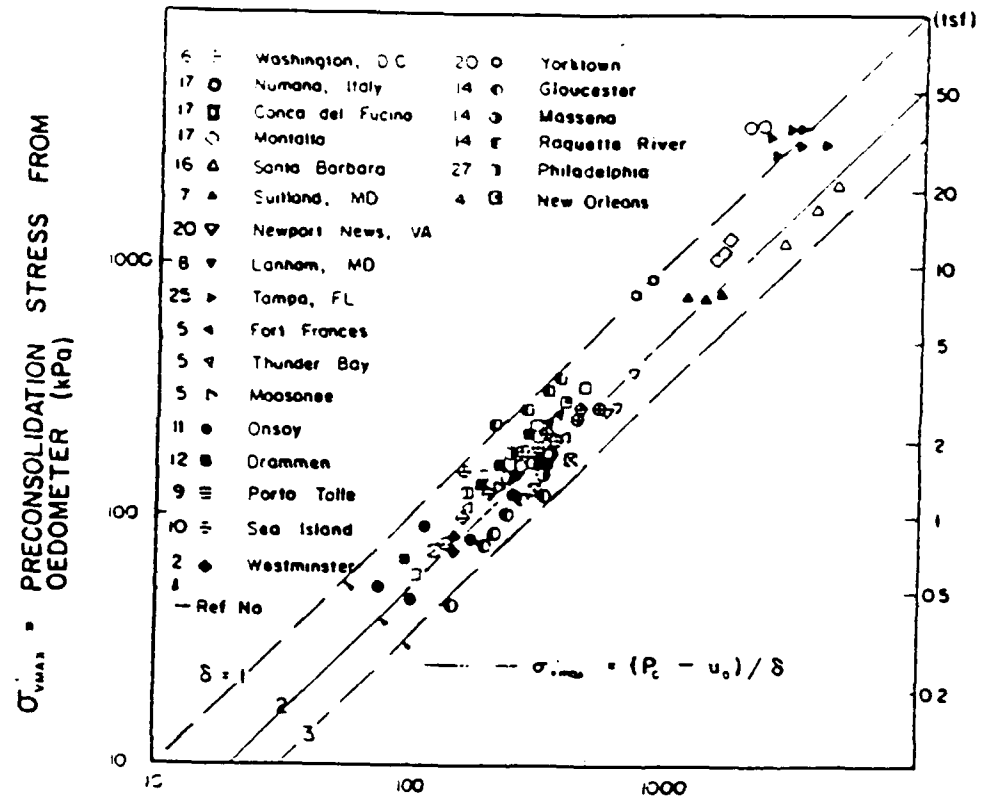
b) Lacasse and Lunne (1982)



c) Lunne et al. (1989)



d) Powell and Uglov (1988)



$P_0 - u_0$ = EFFECTIVE CONTACT PRESSURE
FROM DMT (kPa)

e) Mayne (1986)

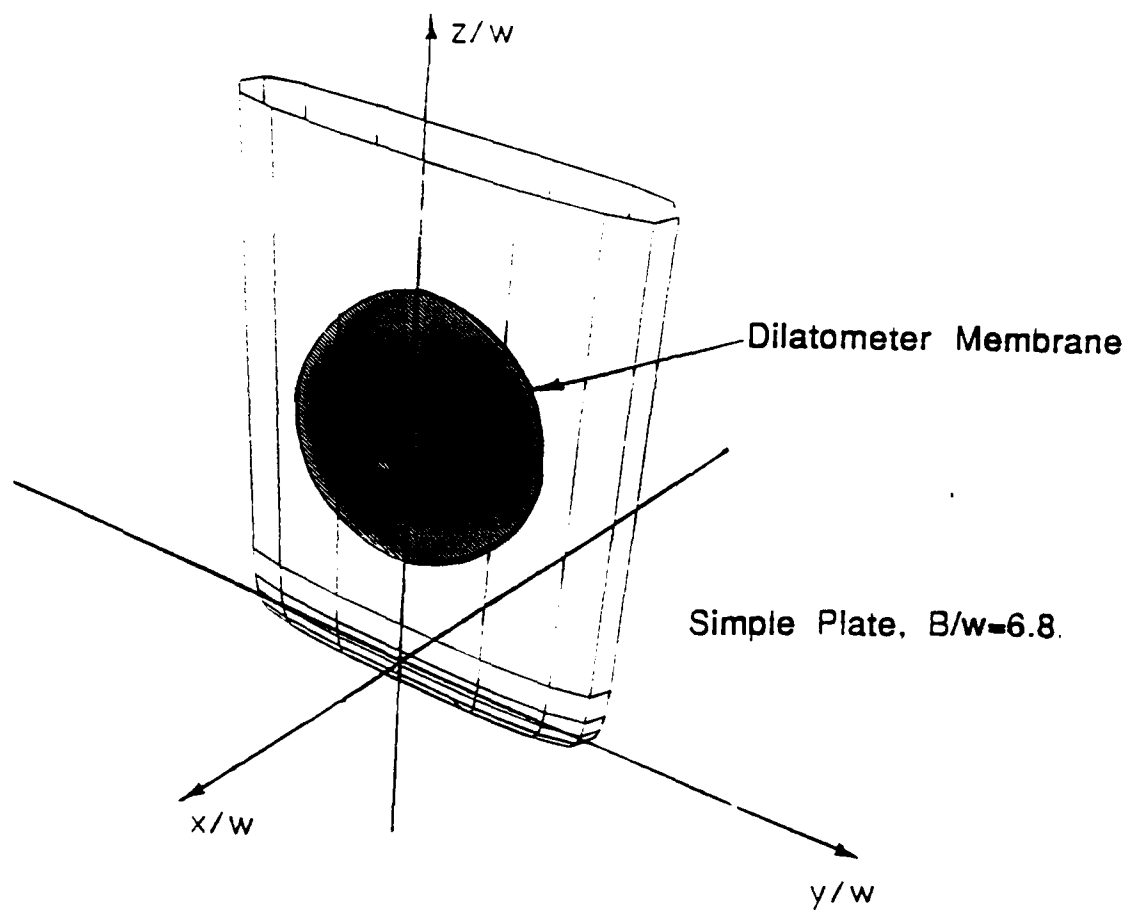


Figure 4.3 Geometry of Simple Plate Used to Simulate Dilatometer

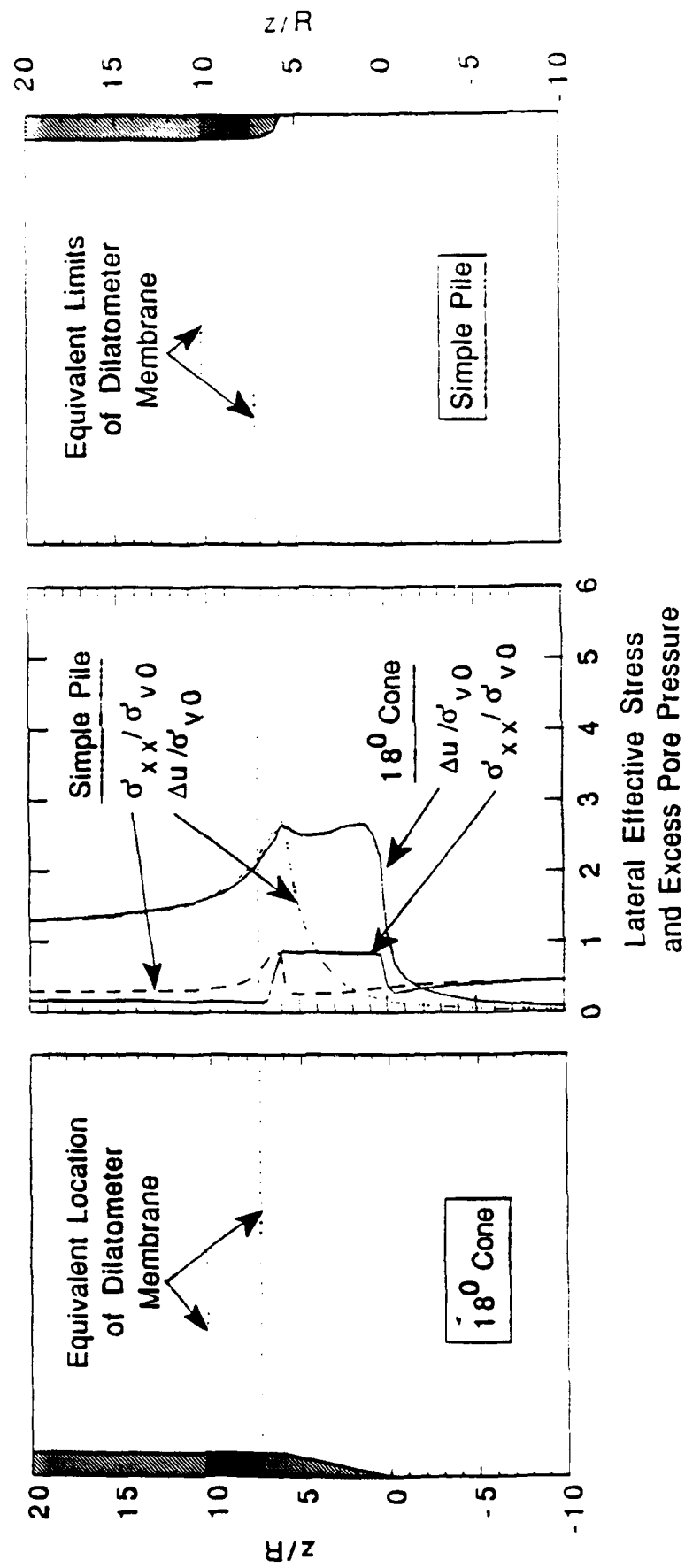


Figure 4.4 Comparisons of Simple Pile Solution to 180° Cone Solution

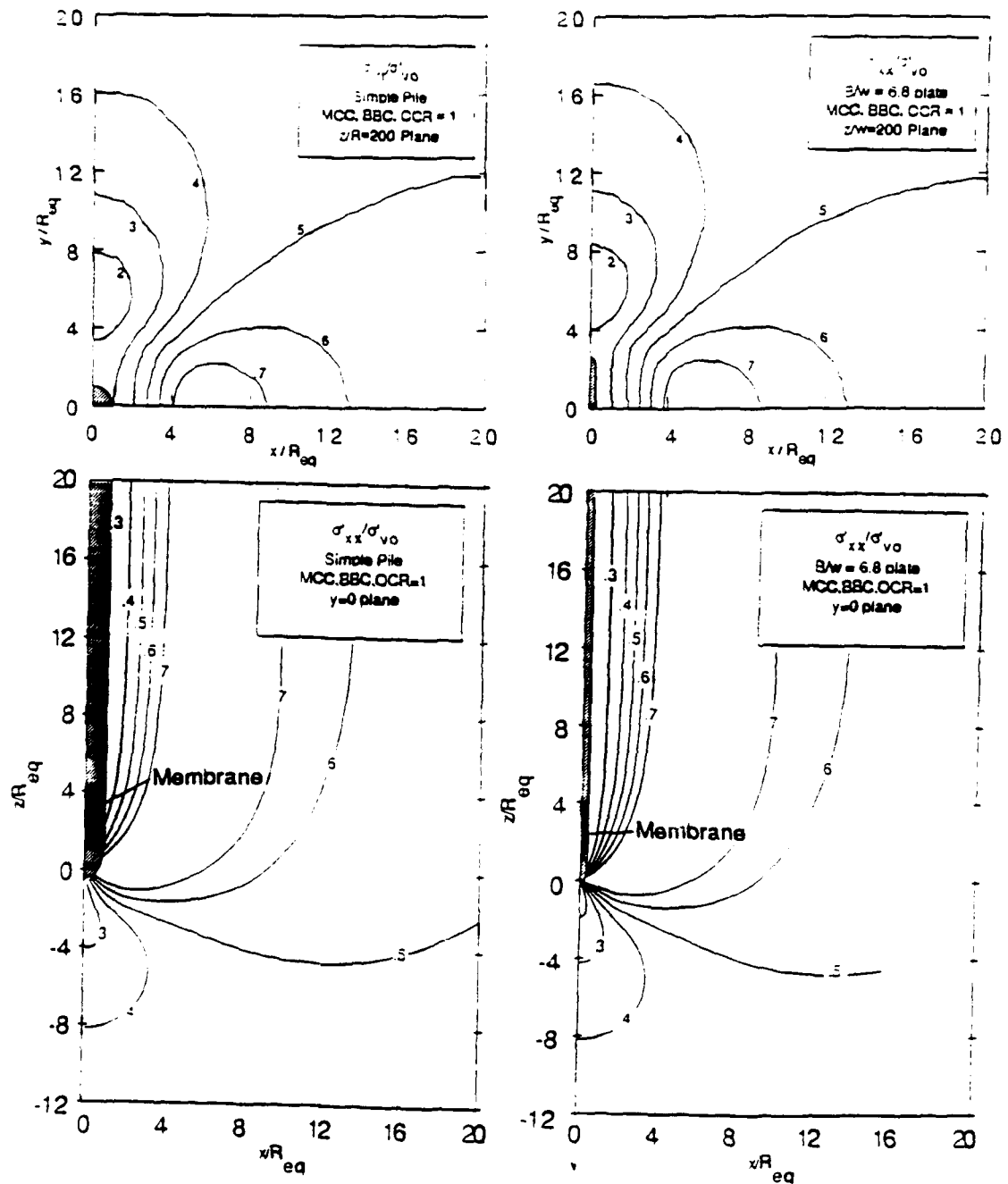


Figure 4.5 Simple Pile and Simple Plate Stress and Pore Pressure Contours

a) $\sigma'_{zz}/\sigma'_{v0}$

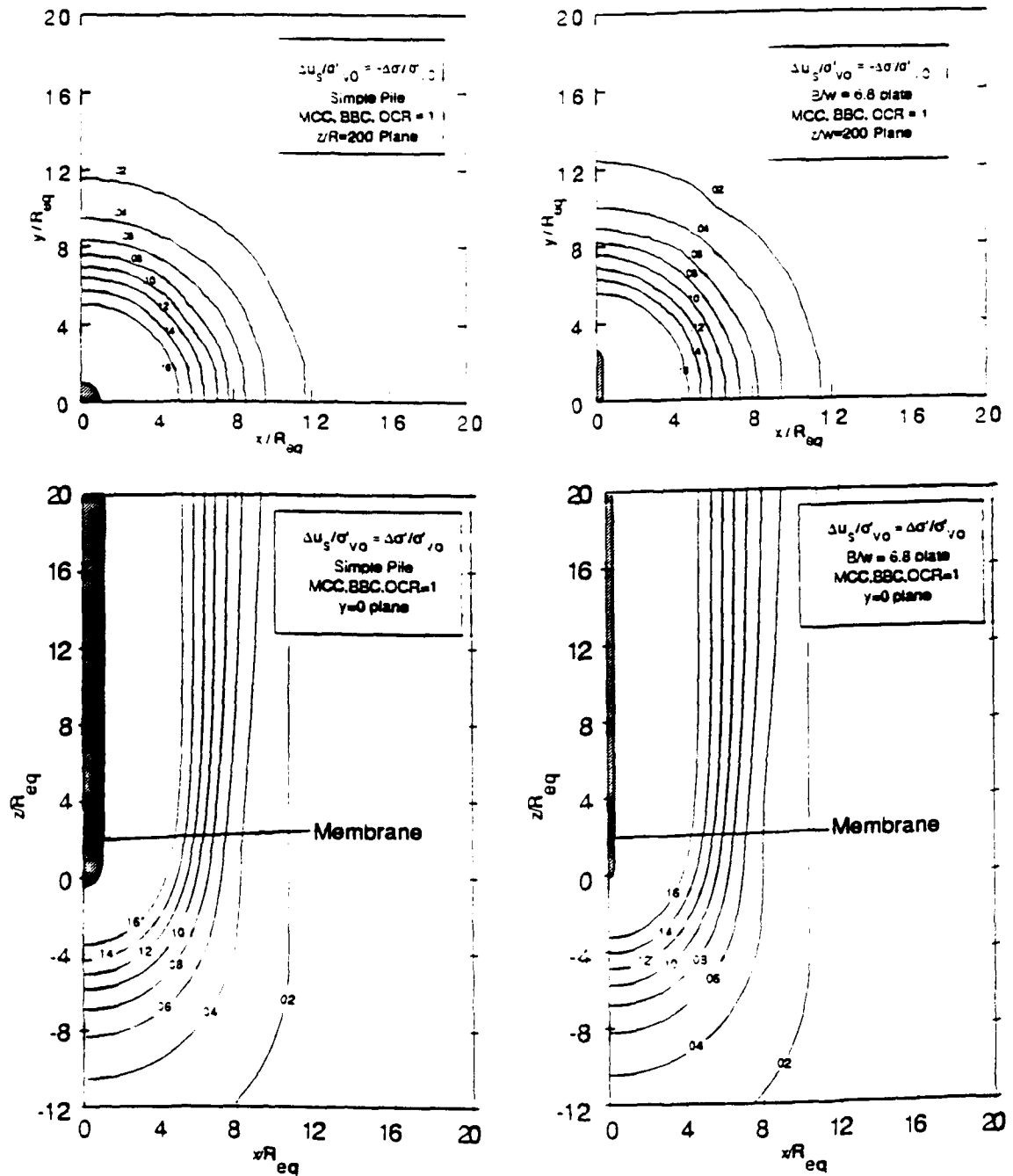


Figure 4.5 Simple Pile and Simple Plate Stress and Pore Pressure Contours
(contd.) b) $\Delta u_s / \sigma'_{v0}$

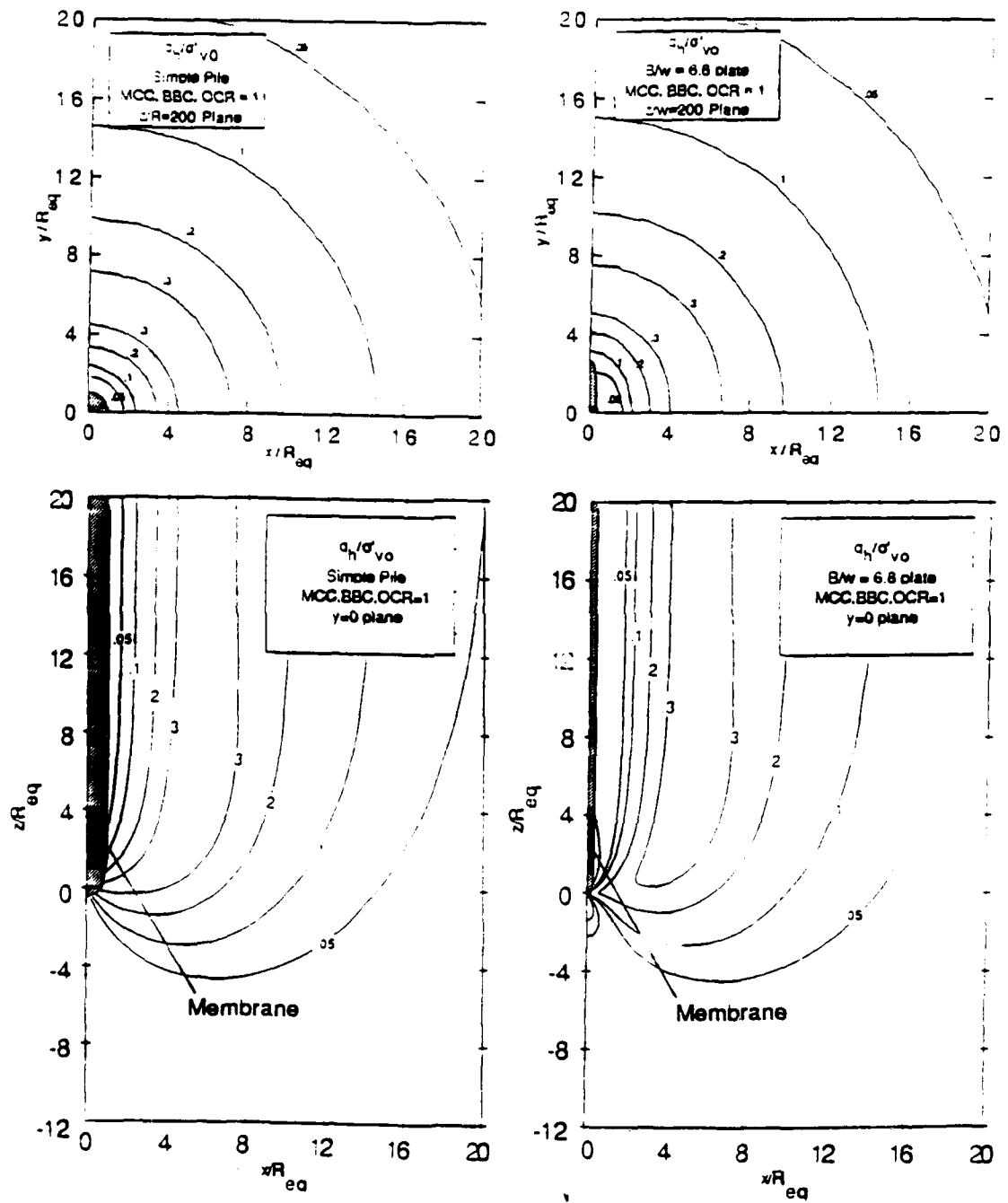


Figure 4.5 Simple Pile and Simple Plate Stress and Pore Pressure Contours
(contd.) c) $(\sigma_r - \sigma_{\theta\theta})/2\sigma'_v0$

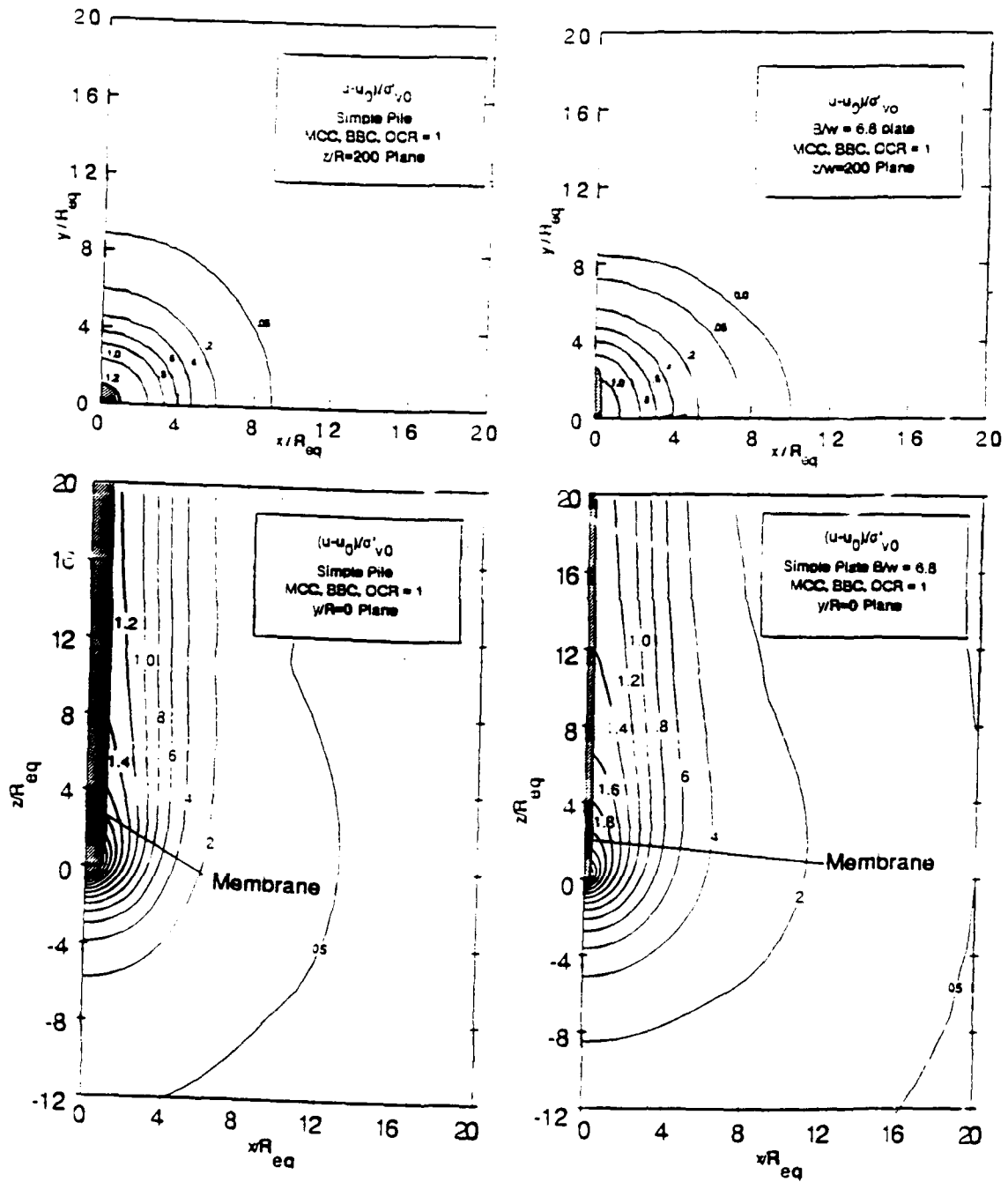


Figure 4.5 Simple Pile and Simple Plate Stress and Pore Pressure Contours
(contd.) d) $\Delta u/\sigma'_{v0}$

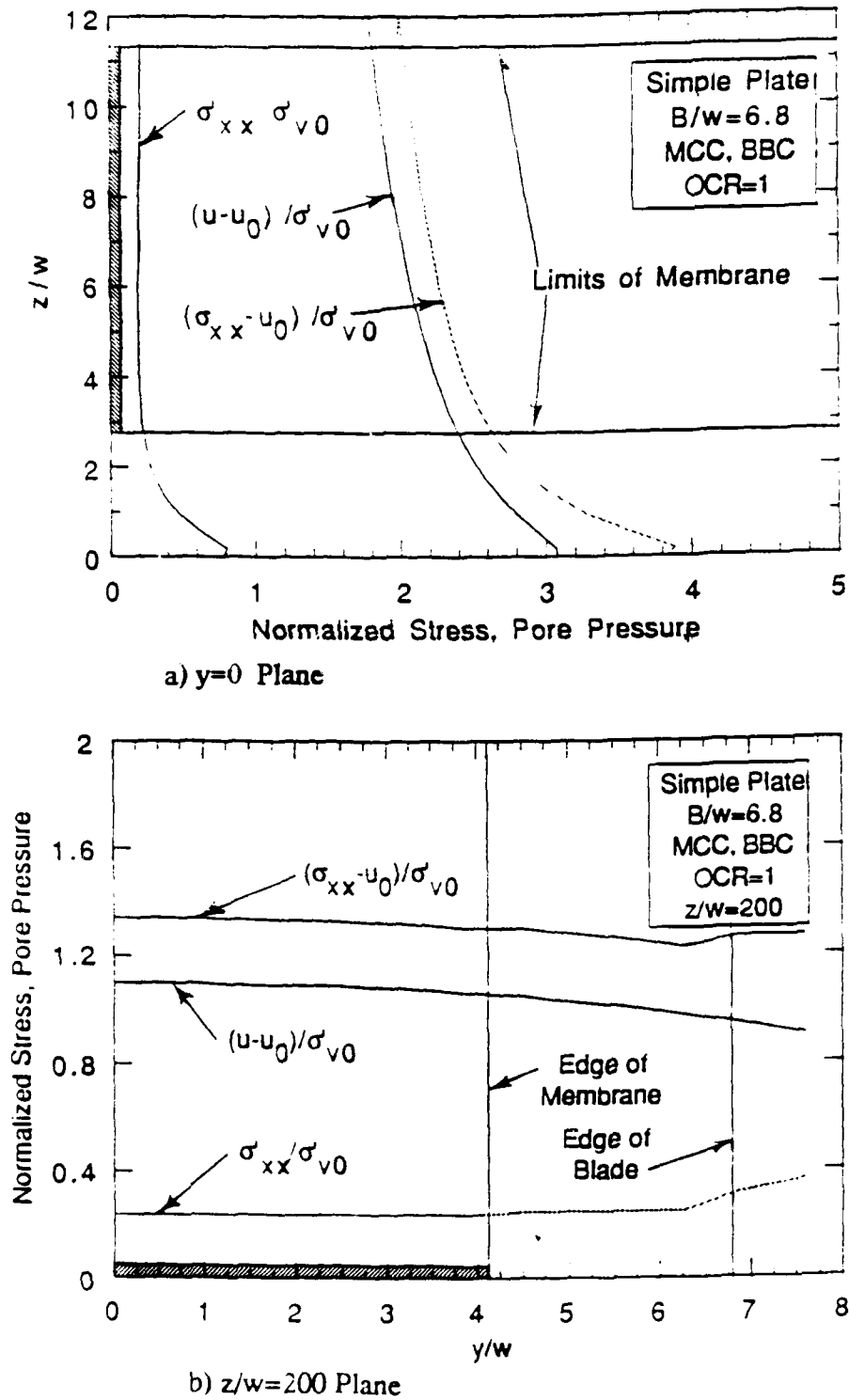


Figure 4.6 Stress and Pore Pressure Distribution Along Dilatometer Membrane

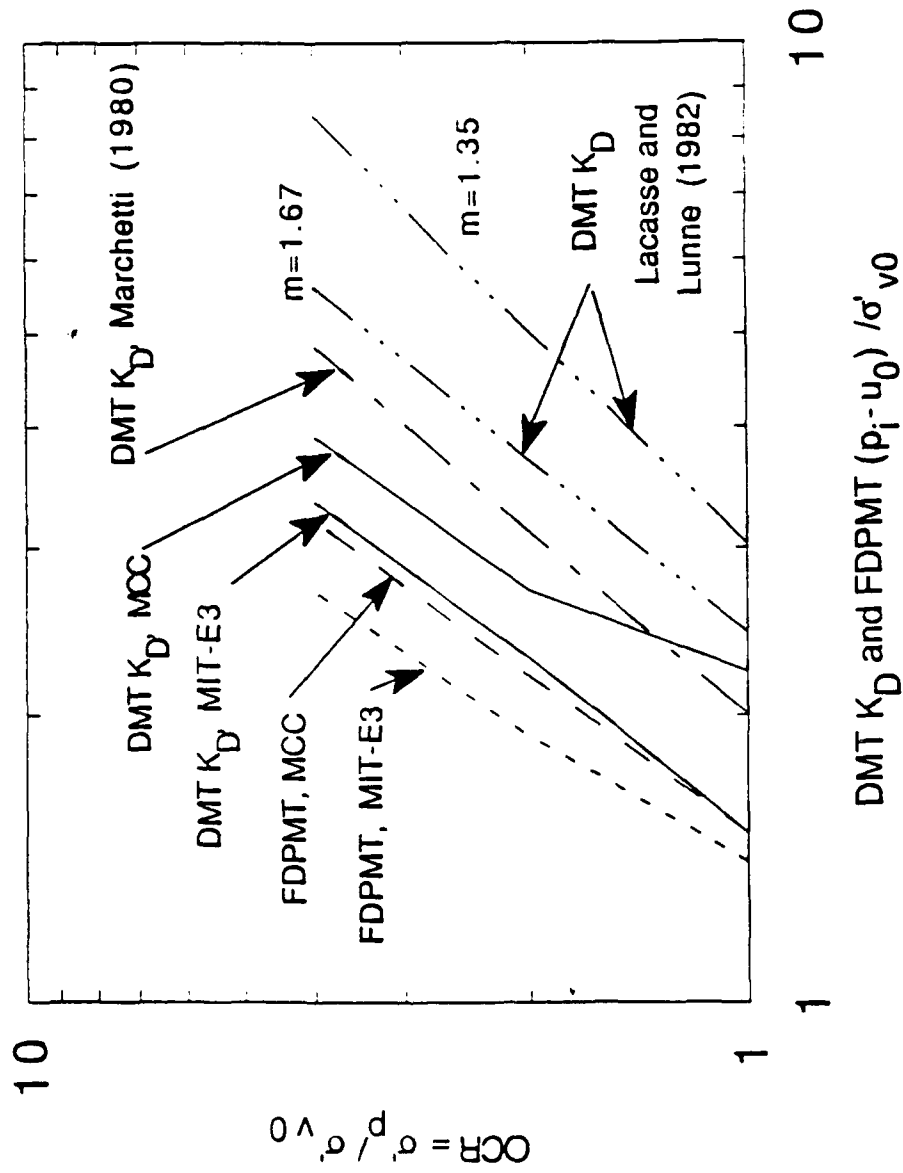
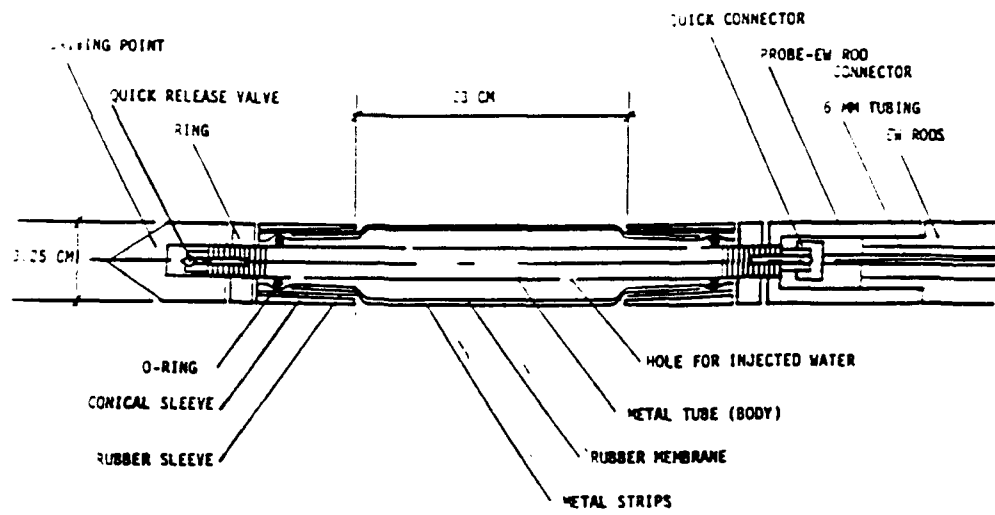
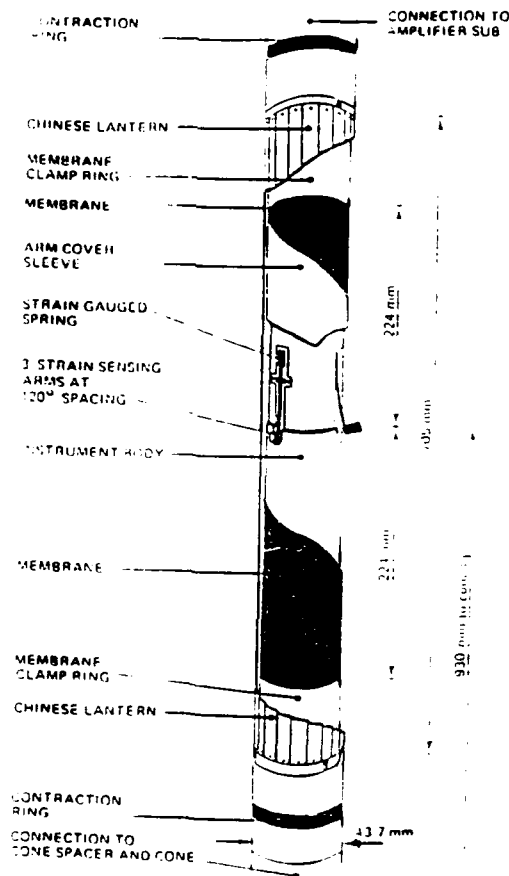


Figure 4.7 Summary of DMT and FDPMT Predictions and Correlations

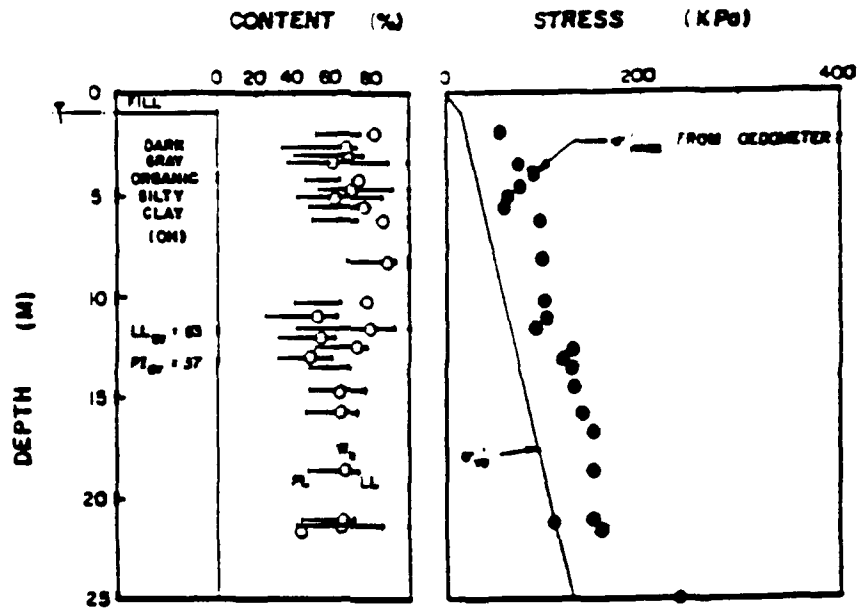


a) Briaud and Shields (1979)

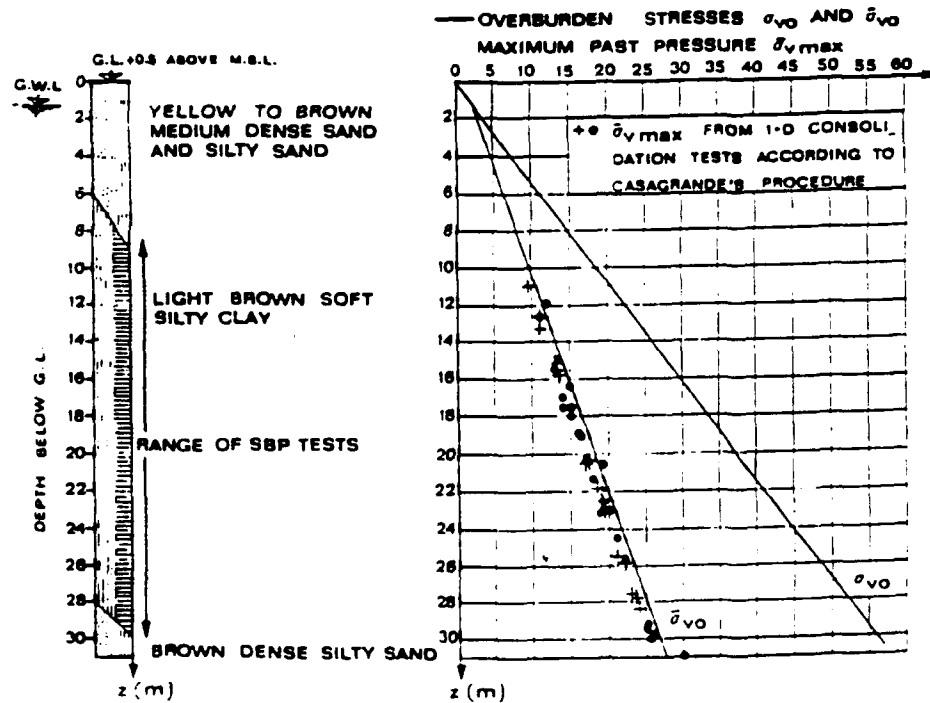


b) Withers et al. (1986)

Figure 4.8 Full Displacement Pressuremeters

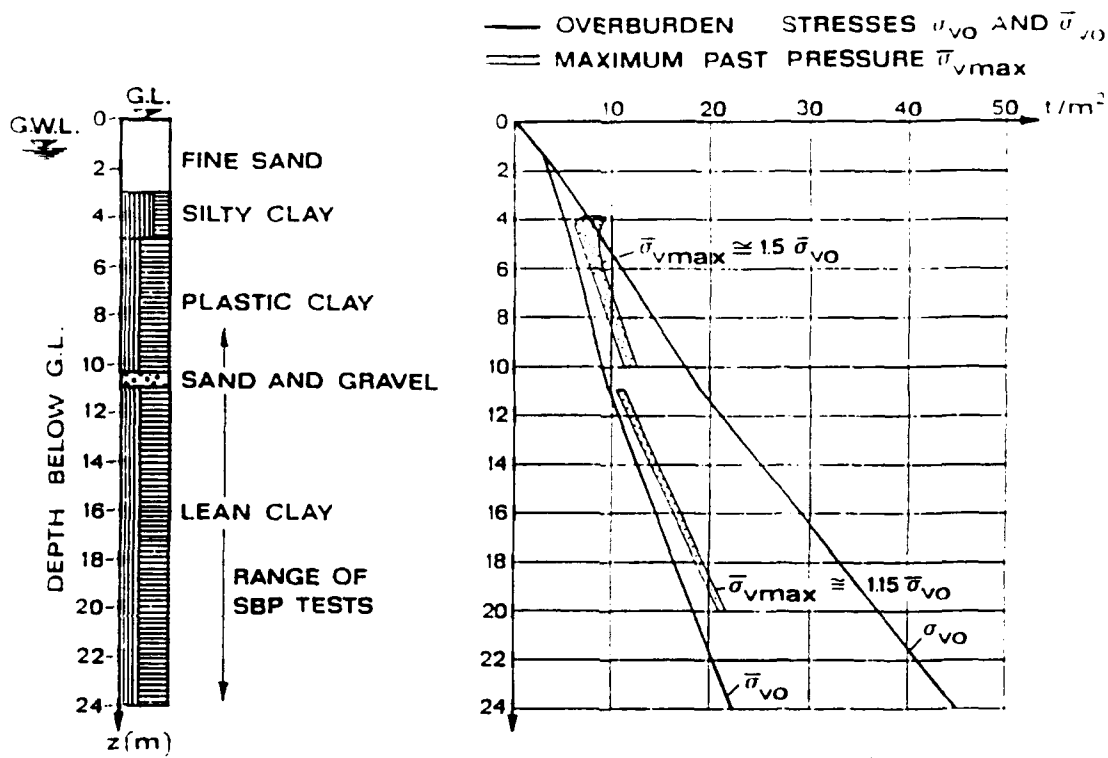


a) Potomac River Aluvium (Mayne, 1987)

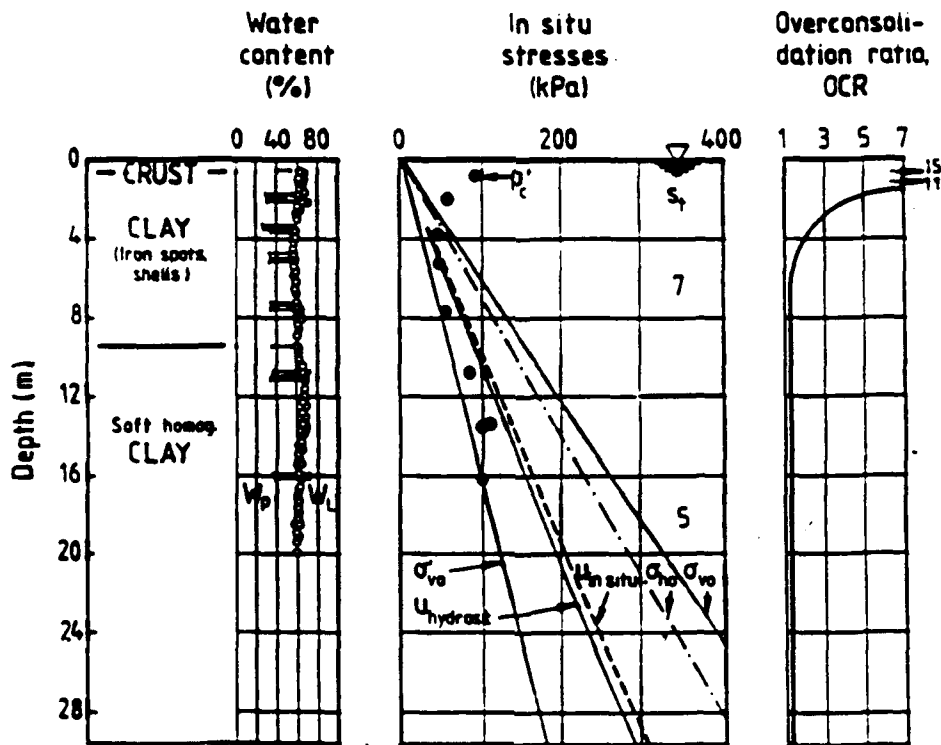


b) Porto Tolle (Ghionna et al., 1981)

Figure 4.9 Index Properties and Stress Histories at Reference Sites



c) Drammen (Lacasse and Lunne, 1982)



d) Onsoy (Lacasse and Lunne, 1982)

Figure 4.9 (contd.) Index Properties and Stress Histories at Reference Sites

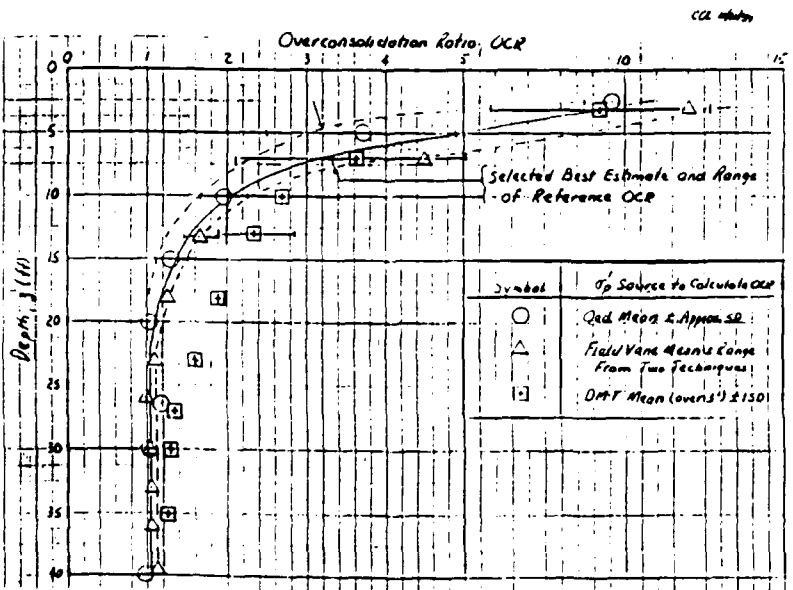
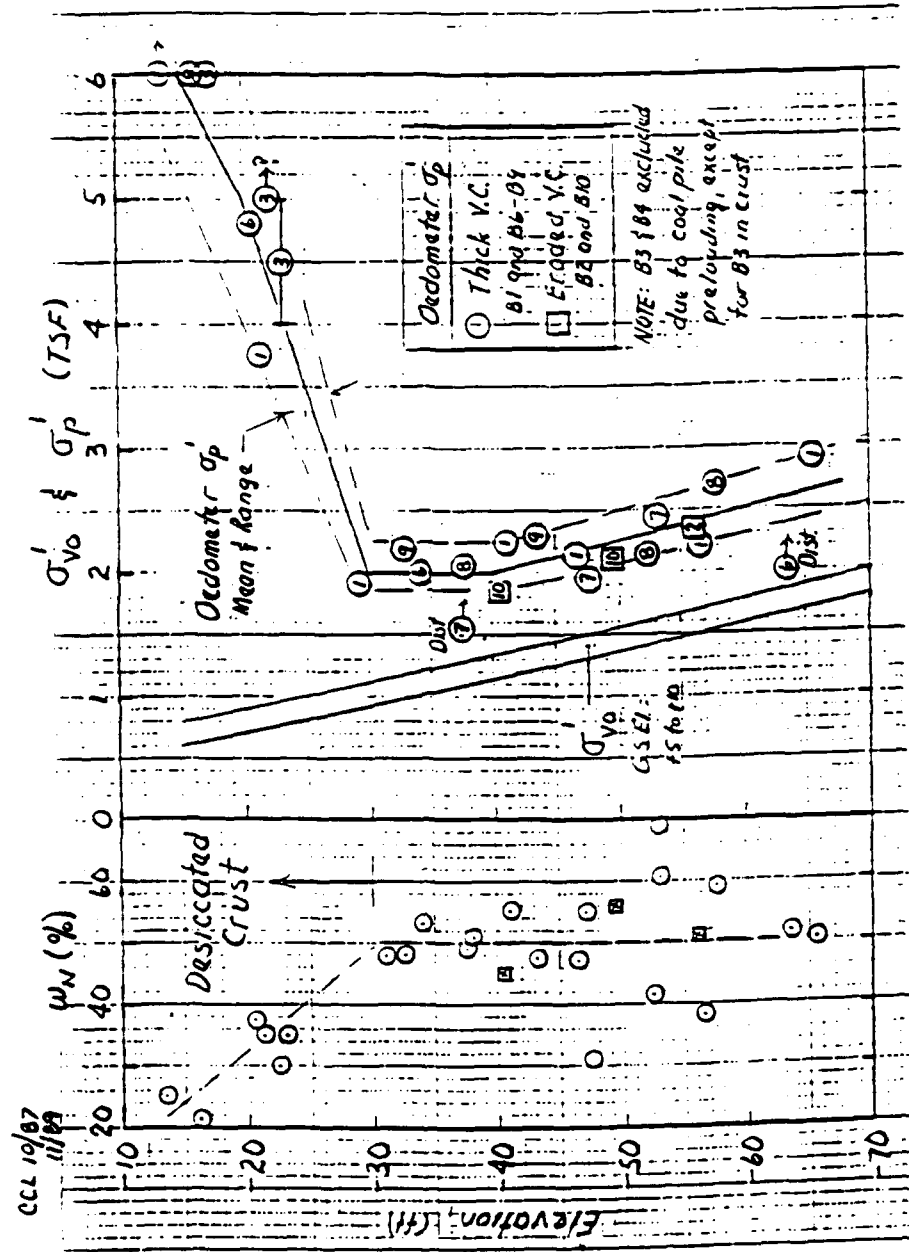


Figure 4.9 (contd.) Index Properties and Stress Histories at Reference Sites



f) New Jersey Varved Clay (Whittle et al., 1989)

Figure 4.9 (contd.) Index Properties and Stress Histories at Reference Sites

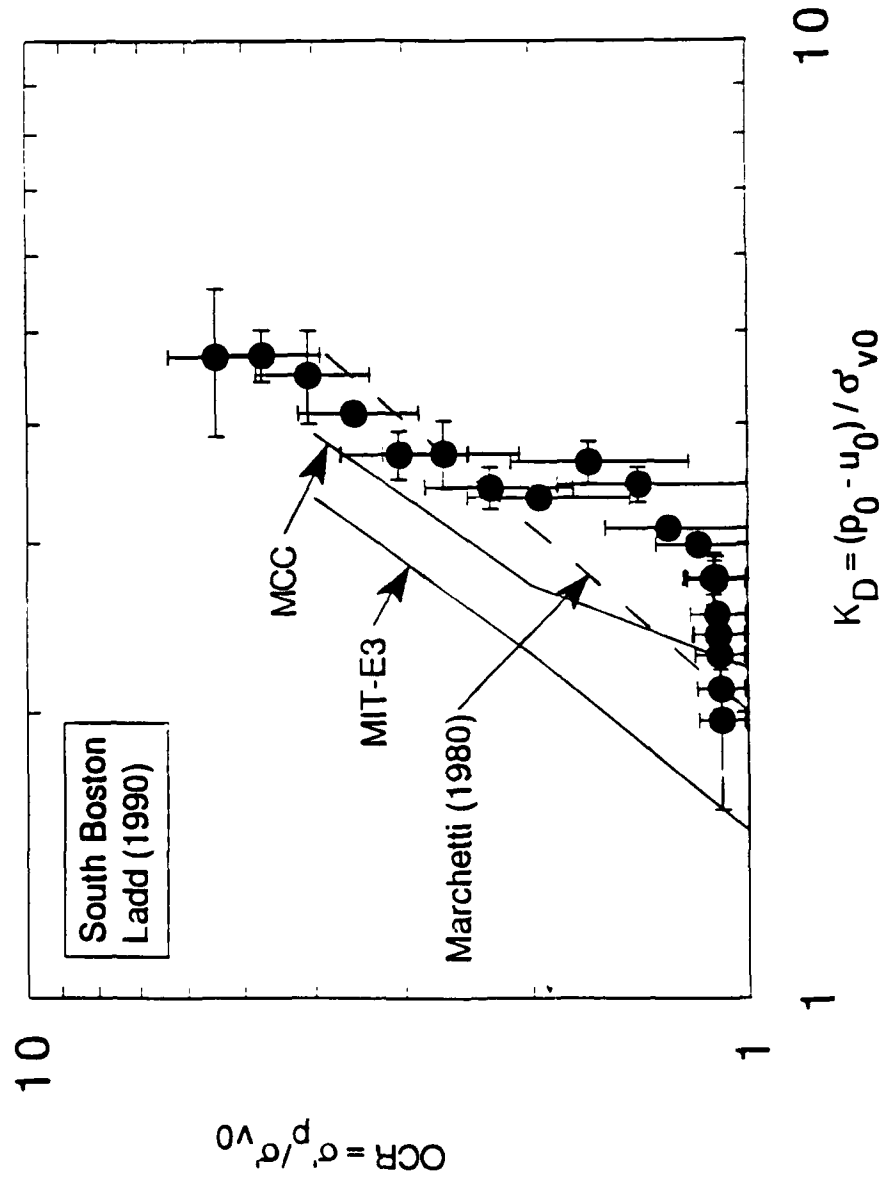


Figure 4.10 Predicted versus Measured K_D -OCR Correlation at South Boston Site

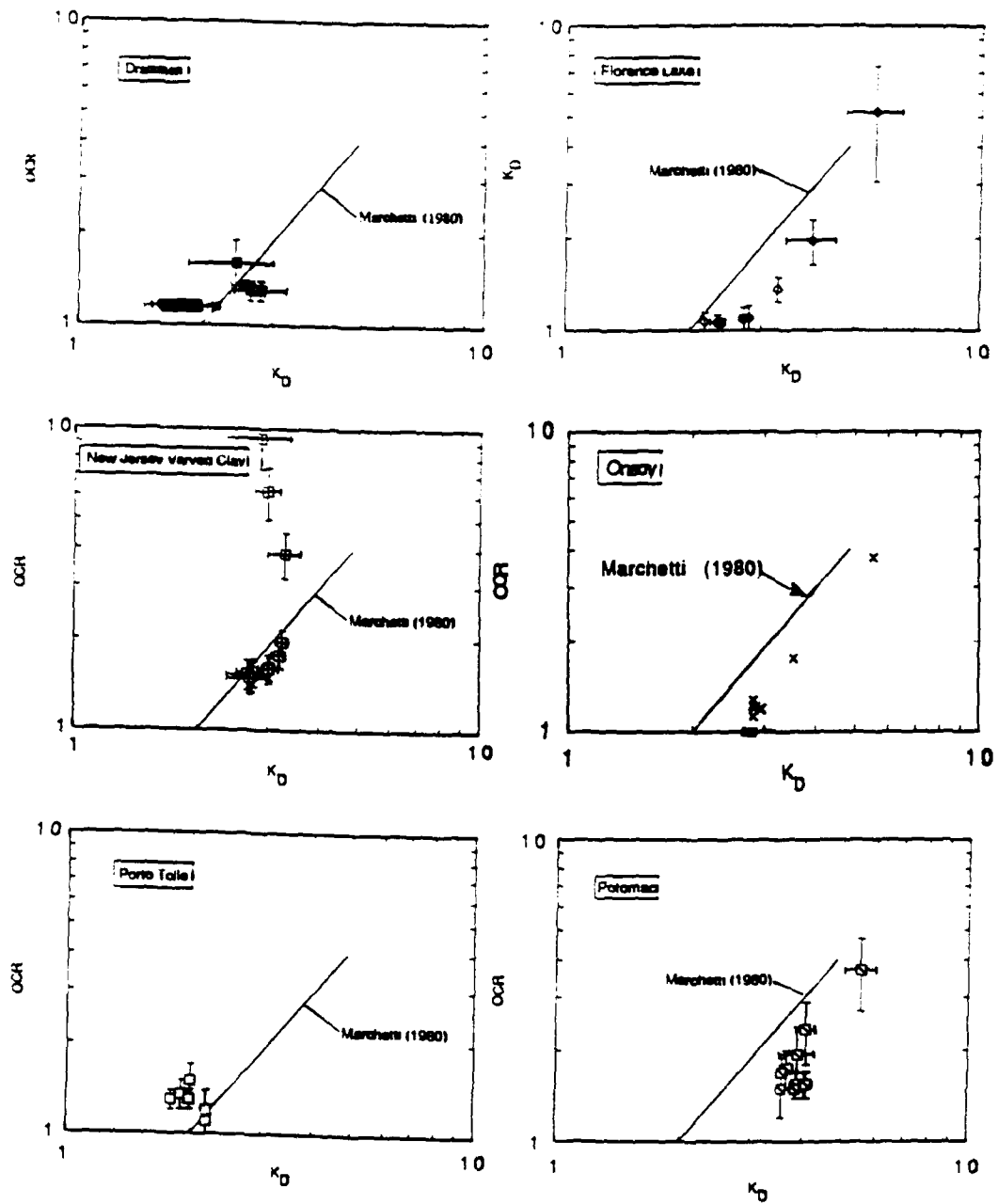
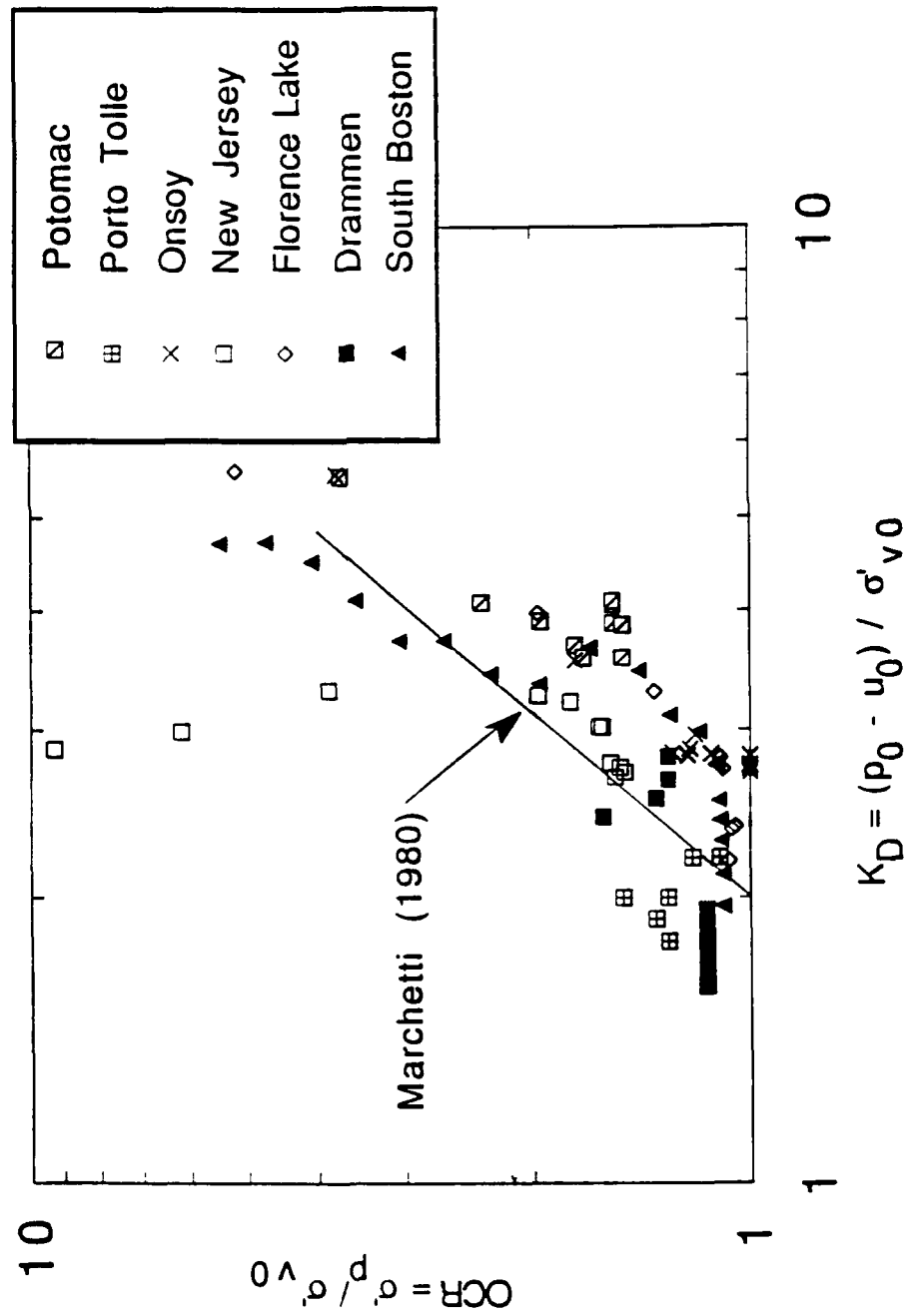
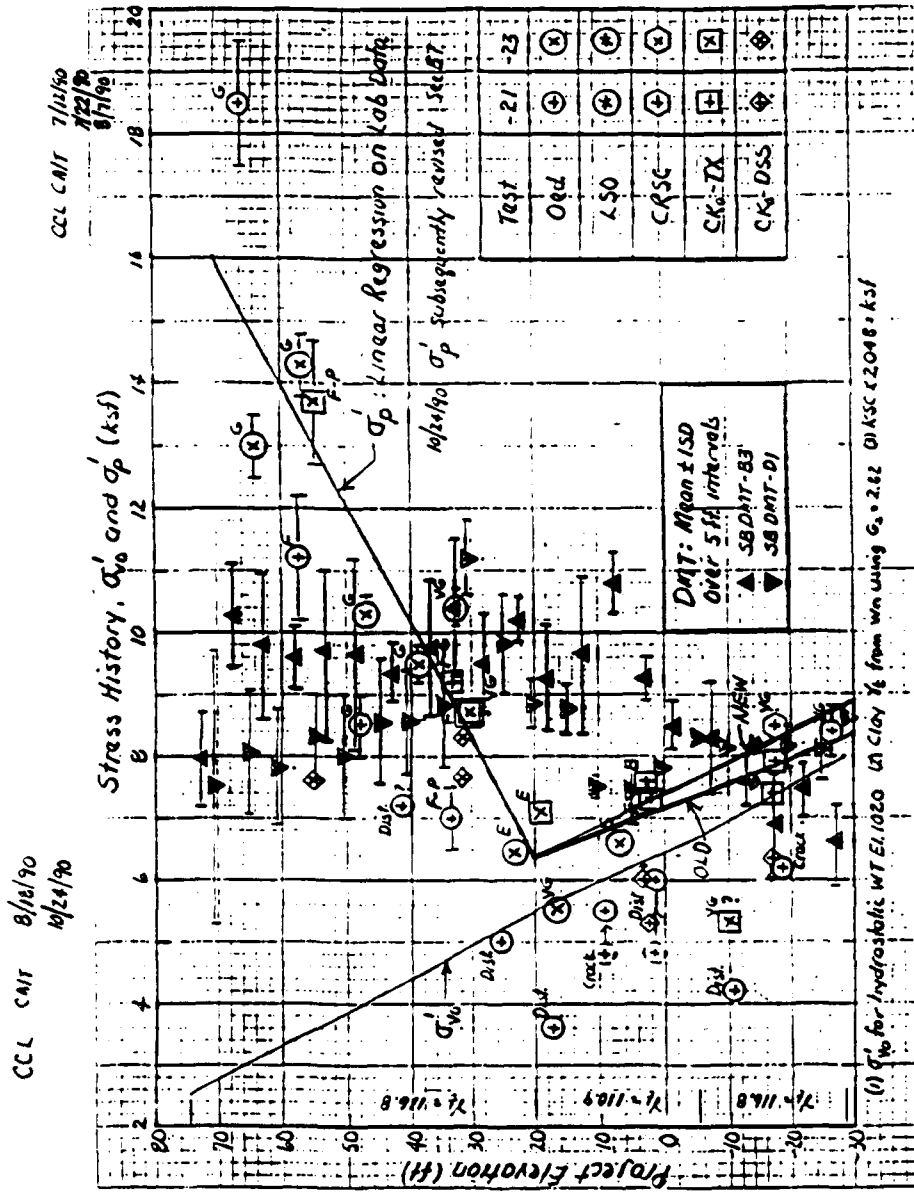


Figure 4.11 Correlation of Dilatometer Index, K_D , with OCR for Six Well-Documented Sites

Figure 4.12 Correlation of Dilatometer Index, K_D , with OCR, Summary

Figure 4.13a DMT versus Reference σ'_p Profiles at the South Boston Site (Ladd, 1990)

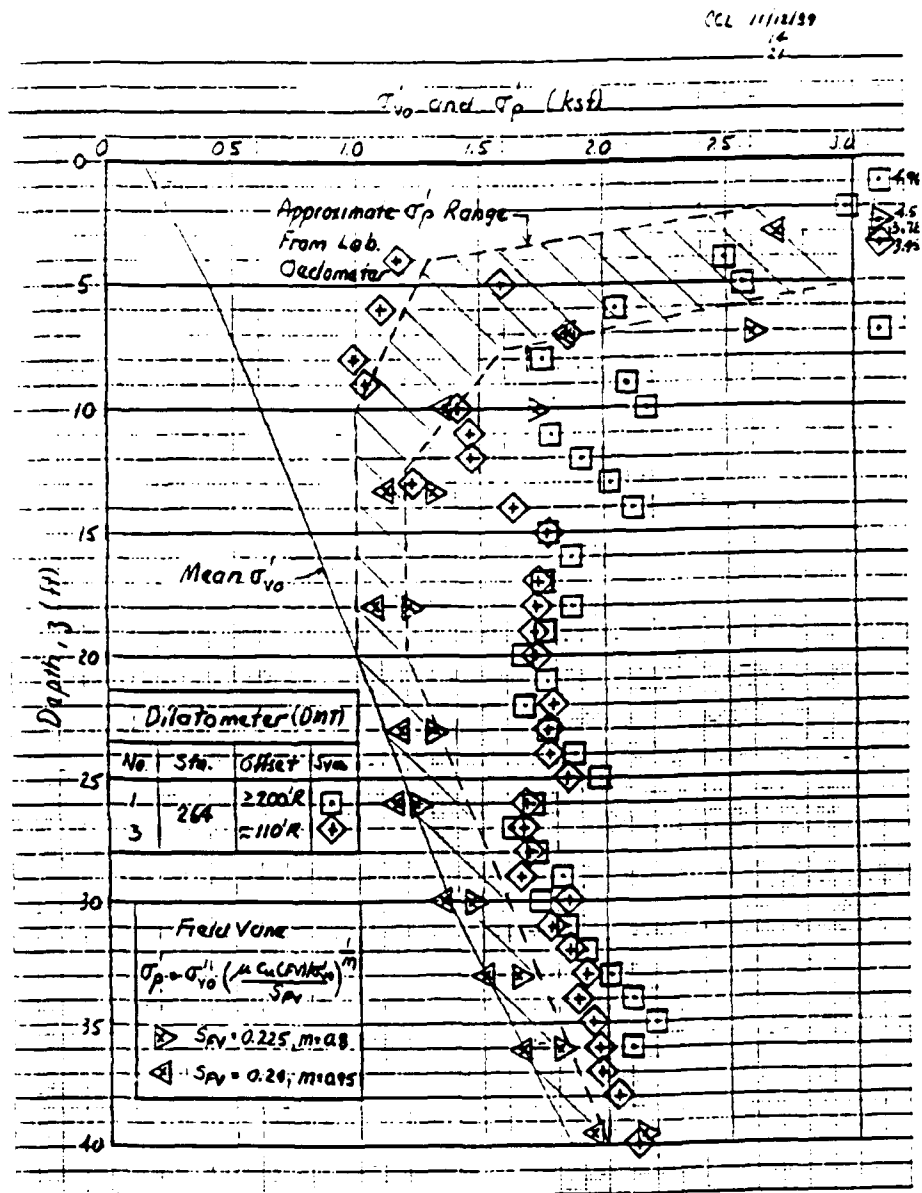


Figure 4.13b DMT versus Reference σ'_p Profiles at the Florence Lake Site (Whittle et al., 1989)

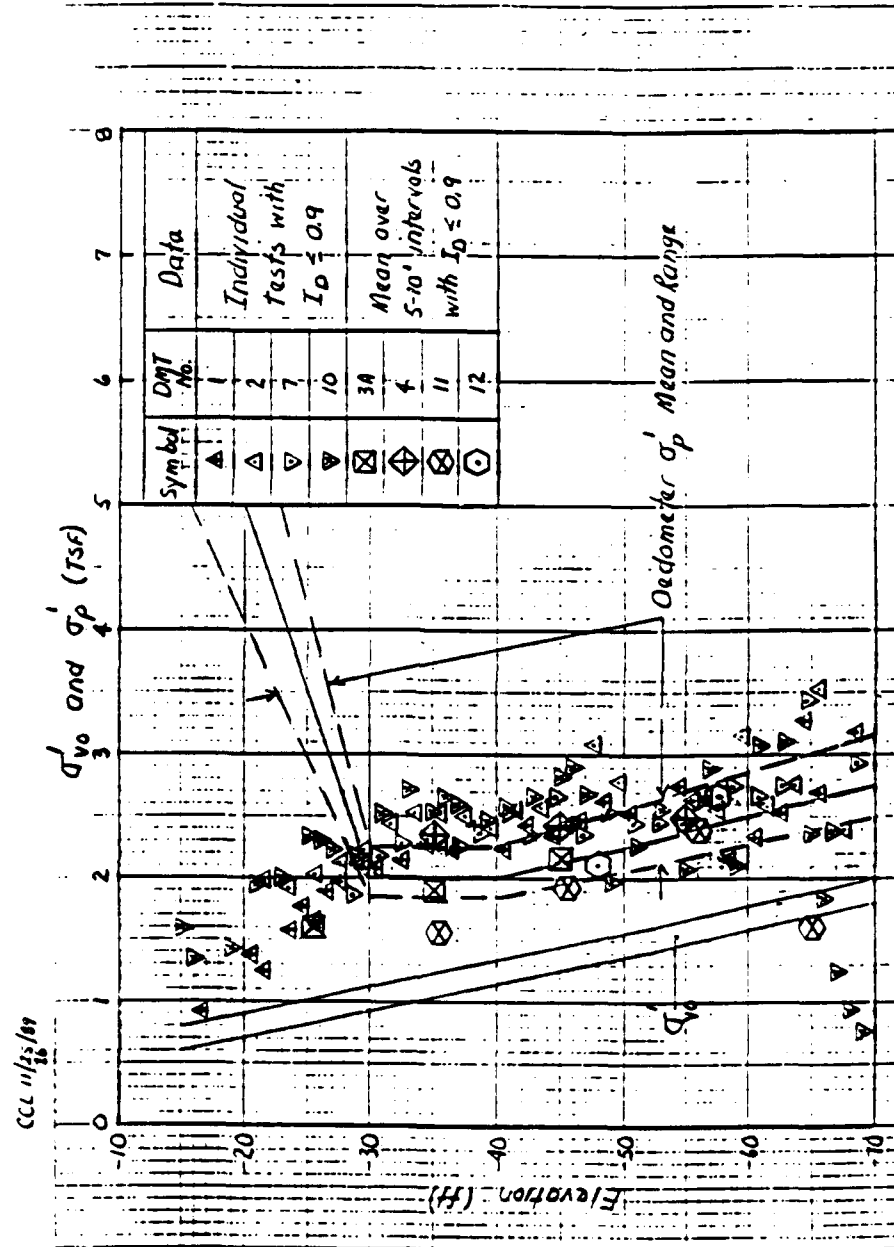


Figure 4.13c DMT versus Reference σ'_p Profiles in the New Jersey Varved Clay (Whittle et al., 1989)

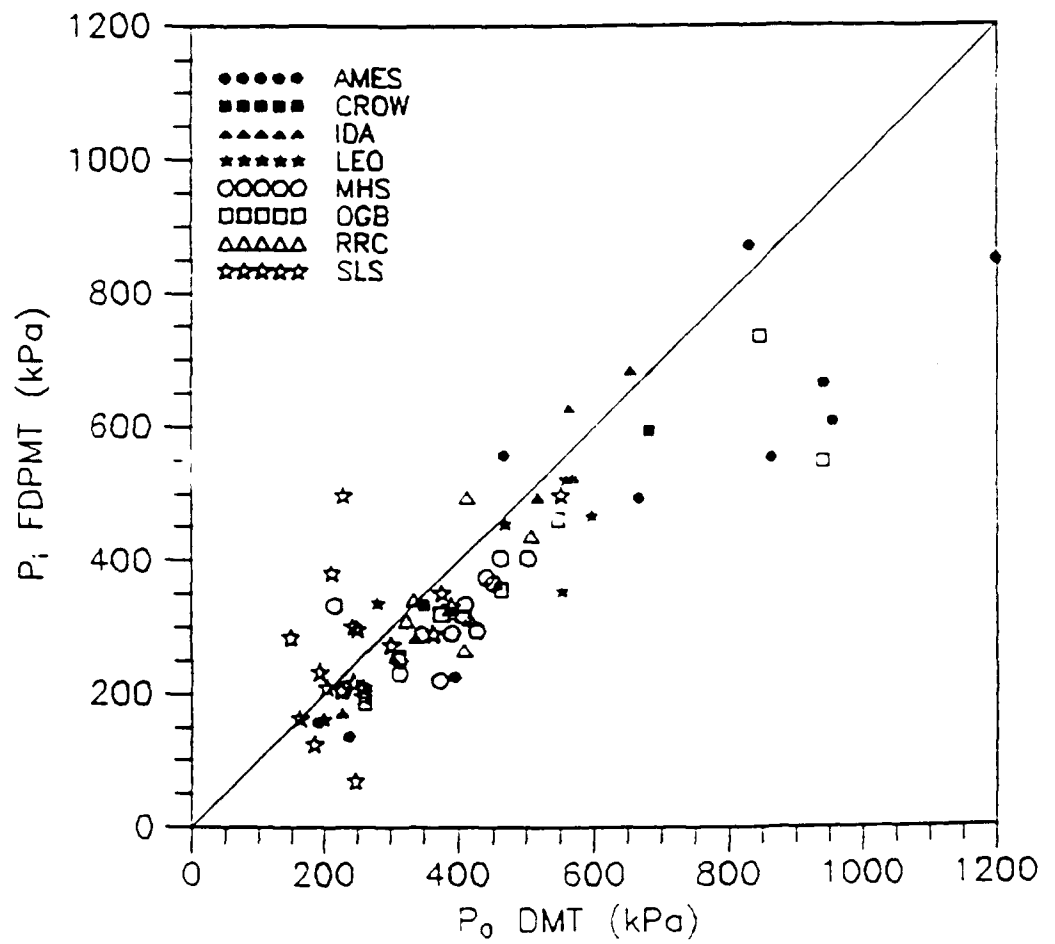


Figure 4.14 Comparison of DMT Contact Pressure, p_0 , to FDPMT Lift-off Pressure, p_i (Luttenegger and Blanchard, 1990)

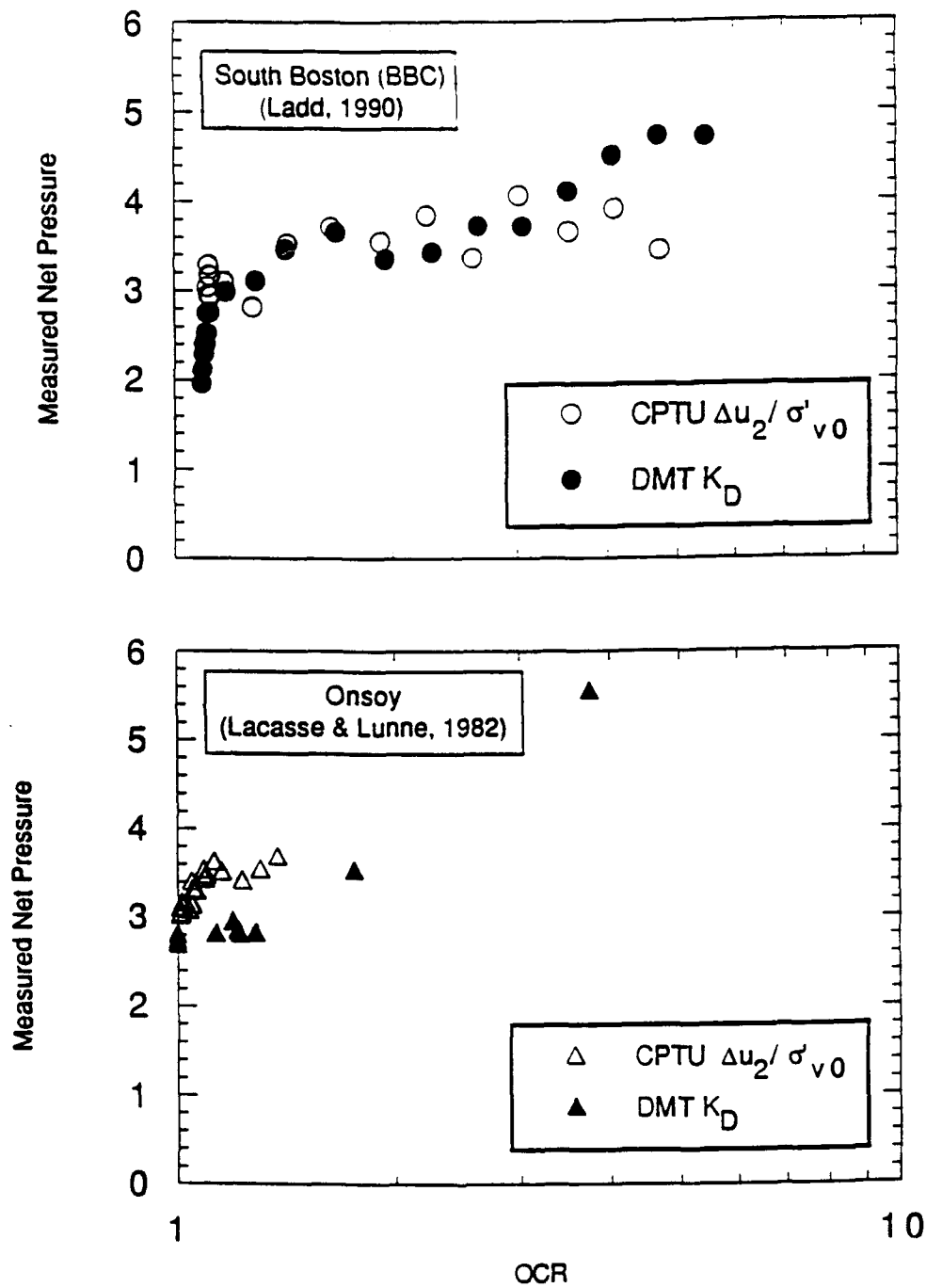


Figure 4.15a Comparison of Dilatometer Contact Pressure and Cone Base Pore Pressure

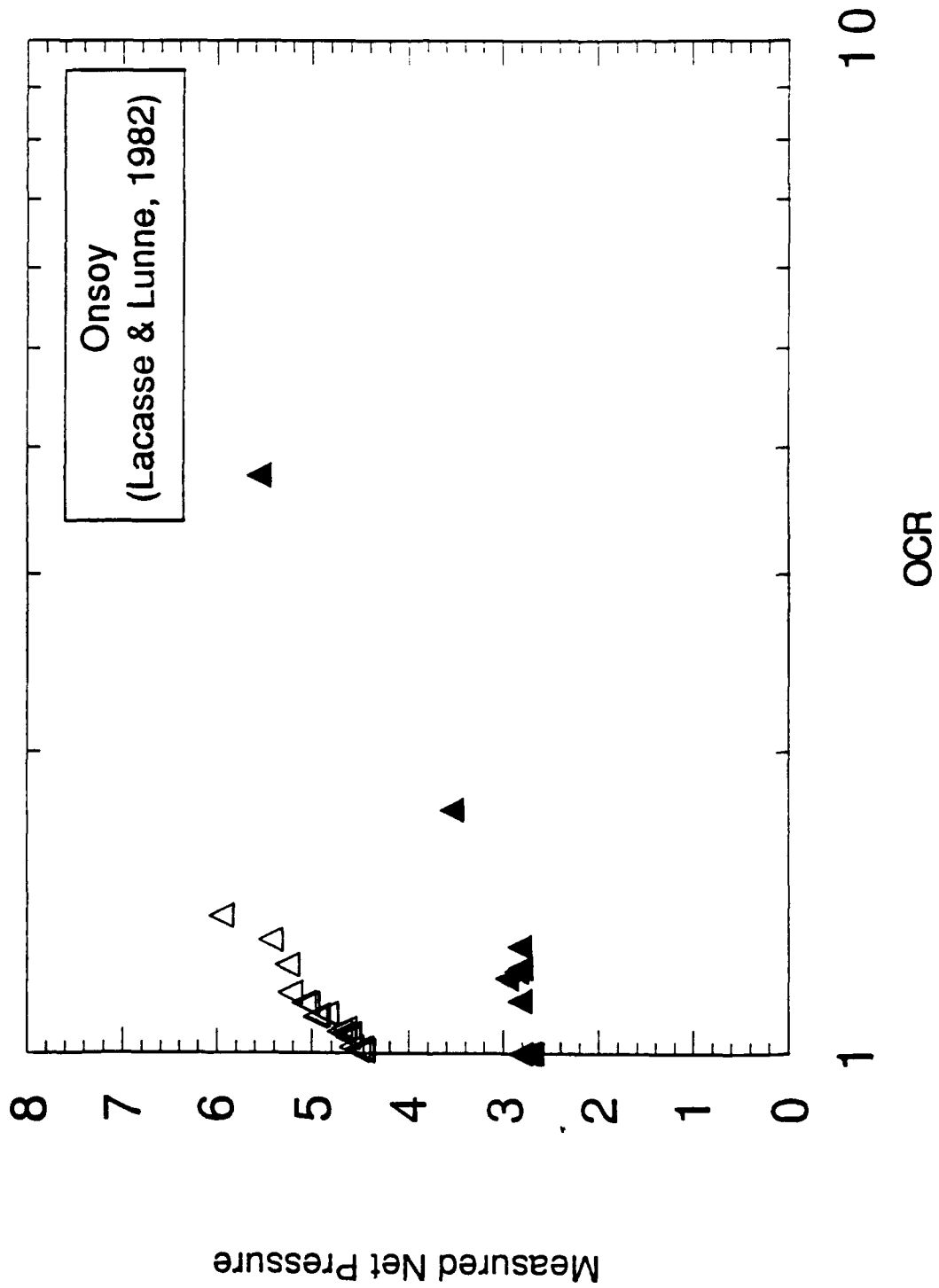


Figure 4.15b Comparison of Dilatometer Contact Pressure and Cone Tip Pore Pressure

5. PORE PRESSURE DISSIPATION AFTER PENETROMETER INSTALLATION

5.1 INTRODUCTION

The previous chapters (3 and 4) have described the effective stresses and excess pore pressures which develop during steady penetration of axisymmetric and plate-shaped penetrometers in low permeability clays. When the penetration process is interrupted, the excess pore pressures dissipate and there are concomitant changes in the effective stresses. Measurements of this consolidation process have two general applications: 1) the estimation of permeability and/or consolidation properties of the soil from pore pressure dissipation or total stress decay measurements (e.g.; Torstensson, 1975; Baligh and Levadoux, 1980); and 2) the estimation of the in-situ horizontal stress conditions σ_{h0} from lateral stress measurements at the end of consolidation (Tedd and Charles, 1981; Tavenas et al., 1975)¹. Table 5.1 summarizes the in-situ measurements which have been used for the above applications, including a) pore pressure measurements for axisymmetric penetrometers (piezoprobe, piezocone, push-in piezometers) and b) total horizontal stress measurements for flat blades (dilatometer, earth pressure cells).

There are many factors which complicate the theoretical interpretation of dissipation records:

1. There are significant uncertainties in the pore pressures, stresses and soil properties which are associated with the analysis of steady penetration. The results in Chapter 3 and 4 show large gradients of the field variables around the penetrometer during installation.
2. The consolidation analysis involves: a) coupling of total stresses and pore pressures with deformations and flow occurring in two dimensions²; and b) the soil properties are non-linear, anisotropic, and non-homogeneous.
3. The stress-strain response of the soil for conditions of partial drainage is non-linear and can be described reliably only through generalized effective stress models. Although the flow resistance of the clay can be modelled by Darcy's law, the permeability depends on the soil structure and void ratio.

Previous analyses of consolidation after penetrometer installation have (Table 5.2) adopted simplifying assumptions in estimating the initial (installation) conditions. For

¹The equilibration lateral stress σ'_{hc} is has direct applications in pile design (e.g.; Randolph, 1979; Whittle, 1987; Marchetti, et al., 1986)

²Three dimensions for plate-shaped penetrometers.

example, Torstensson (1975, 1977), and Randolph et al. (1979) use cavity expansion methods, which restrict subsequent dissipation analyses to one-dimensional conditions. Baligh and Levadoux (1980), and Teh and Houlsby (1989) use total stress soil models during installation. These models cannot reliably describe the effective stress changes during dissipation; and hence, the authors compute pore pressure dissipation solutions assuming no coupling³ between total stresses and pore pressures.

Kavvasdas (1982) and Whittle (1987) are the first two authors to perform non-linear, coupled consolidation analyses using generalized effective stress soil models with initial conditions obtained from two-dimensional Strain Path analyses. However, their analyses consider only radial consolidation, which is relevant to conditions around the shaft of a long pile. Direct comparisons with field data from an instrumented model pile shaft (the PLS cell; Morrison, 1984) has shown that the non-linear consolidation analyses can provide reliable predictions of both pore pressure dissipation and effective stress 'setup' during consolidation (Whittle, 1987).

This chapter reviews the interpretation of engineering properties from dissipation measurements based on previous analyses (Section 5.2). Section 5.3 then describes the procedures and assumptions used in the numerical analysis for coupled, non-linear consolidation analyses using the finite element code ABAQUS (HKS, 1989). Sections 5.4 and 5.5 describe the numerical predictions of pore pressure dissipation and stress changes around piezocone penetrometers in Boston Blue Clay. These calculations represent the first two-dimensional, non-linear analysis of coupled consolidation and provide new insights into the mechanisms and interpretation of these measurements. The analyses are compared with field measurements and data from large scale laboratory calibration chamber tests in Section 5.6.

5.2 BACKGROUND

5.2.1 Uncoupled Analyses

Baligh and Levadoux (1980) were the first investigators to present two-dimensional solutions for consolidation around a cone penetrometer. Installation conditions were analyzed using the Strain Path Method for 18 and 600 cone penetrometers installed in K_0 -normally consolidated Boston Blue Clay (BBC) described using the MIT-T1 total stress soil model (Levadoux, 1980), while excess pore pressures were estimated approximately

³Levadoux and Baligh (1986a) evaluate the effects on linear coupling during consolidation.

by integration along isochronous⁴ lines. Figure 5.1 summarizes the main findings of their study:

1. Dissipation results can be presented in a dimensionless format relating the normalized excess pore pressure, $\bar{U} = \Delta u / \Delta u_i$, where $\Delta u_i = (u_i - u_0)$ are the installation excess pore pressures, to the time factors, $T = ct/R^2$, where c is the isotropic, consolidation coefficient and R is the radius of the penetrometer.
2. Dissipation rates depend on the location of the porous filter and on cone geometry (Figure 5.1a, 5.1c). For a given value of \bar{U} , time factors can vary by up to two orders of magnitude depending on filter location. This result implies that one-dimensional solutions are not adequate for interpreting cone dissipation measurements. The dissipation rates around the penetrometer shaft (location 4, Figures 5.1a, c) are similar for both the 18 and 60° cone geometries.
3. For the standard 60° piezocone (Figure 5.1c) dissipation at the cone apex and mid-face are essentially identical, while consolidation at a point located along the shaft is substantially slower (up to 50 times). This result implies that reliable measurements at the shaft require much longer dissipation times.
4. Figure 5.1a also evaluates the effects of linear coupling on dissipation around an 18° cone penetrometer. These results show the coupling has a pronounced effect on predicted pore pressures located on the face and base of the cone, especially for small time factors, $T \leq 5$. Coupling has negligible effect on the predicted dissipation around the shaft. This is consistent with analyses by Sills (1975) who demonstrated that total stresses and pore pressures are decoupled for radial consolidation with an infinite drainage horizon.
5. The effects of cross-anisotropic, consolidation properties are reported in Figure 5.1b for an 18° cone penetrometer with $c_h = 10c_v$ (typical of a varved clay; Ladd, 1976). Soil anisotropy has a minor effect on the predicted dissipation behavior, when the time factor is defined in terms of the horizontal consolidation coefficient, c_h (i.e.; $T = c_h t / R^2$). This result implies that piezocone dissipation data are most closely related to the horizontal consolidation coefficient, c_h .

Teh (1987) presents similar results of uncoupled dissipation analyses (for a 60° cone penetrometer) with initial conditions from the Strain Path Method in conjunction with an elastic-perfectly plastic soil model (EPP, Table 5.2.) Solutions were generated for rigidity indices ($I_r = \sqrt{G/c_u} = 25$ to 500.) This study generalizes the effects of the initial pore

⁴Isochronous lines represent the distorted shape of an initially horizontal line (before penetration).

⁵Coupling effects are very pronounced at the apex; however, Levadoux and Baligh consider this solution to be uncertain due to numerical inaccuracies close to this singular point.

pressure distribution on subsequent dissipation curves. Figure 5.2 summarizes the predicted dissipation behavior for several filter locations. The results were presented using a modified time factor $T^* = \sqrt{I_r} c_h t / R^2$. The modified time factor, T^* , appears to give a useful normalization for filters located on the face and base of the cone, but is less reliable for interpreting results along the pile shaft.

5.2.2 Interpretation of Engineering Properties from Measured Data

It is not readily apparent which engineering properties of the clay can be estimated from dissipation measurements. Baligh and Levadoux (1980) compare predictions from the uncoupled analyses directly with measurements in BBC ($1 \leq \text{OCR} \leq 4$) at the I-90 test site in Saugus, Massachusetts (see Section 3.5 for details.) Measurements were obtained for porous filters located at the tip of a standard 600 cone penetrometer and at four positions (tip, face, base, and shaft at $z/R=16$) for an 180 cone. Figure 5.3 illustrates the procedure for relating the predictions and measurements for tests in the lower deposit of BBC (i.e.; at depths greater than 60ft, $\text{OCR} \leq 2$.) The predictions are matched to the experimental data⁶ by selecting appropriate values for the horizontal consolidation coefficient $c_h = 0.02$ to 0.04 cm²/sec. The derived (back-figured) c_h values are then compared with reference properties for BBC reported from laboratory CRSC tests (Germaine, 1978) and other related studies (Duncan, 1975; Bromwell and Lambe, 1968) in Figure 5.4. The authors note the following:

1. The back-figured $c_h(\text{cone})$ is in excellent agreement with c_v during swelling computed by Bromwell and Lambe (1975) and in good agreement with CRSC measurements for overconsolidated Boston Blue Clay. This supports the suggestion by Levadoux and Baligh (1986) that $c_h(\text{cone})$ approximates $c_v(\text{swelling})$ or $c_v(\text{OC})$ provided the soil does not exhibit significant anisotropy. The authors then propose simplified methods for estimating profiles of k_h and $c_v(\text{NC})$ from the $c_h(\text{cone})$ results.
2. Tip measurements show significant scatter for $\bar{U} \geq 0.6$, whereas shaft measurements show significant scatter only for $\bar{U} \geq 0.8$. Levadoux and Baligh (1986b) attribute this effect to a) the natural variation of soil properties within the deposit, and b) the fact that tip pore pressures are more sensitive to variations in soil properties than shaft pore pressures. Consolidation coefficients back-calculated at various degrees of consolidation demonstrate the consistency of the proposed interpretation method.
3. Dissipation occurs more rapidly at the tip than on the shaft and thus requires shorter dissipation test durations. However, due to the scatter in the tip measurements, a

⁶ Baligh and Levadoux (1980) report that the most reliable matching of predictions and measurements can be achieved for $0.4 \leq \Delta u / \Delta u_i \leq 0.6$.

greater degree of pore pressure dissipation is necessary to achieve reliability comparable with data obtained at the shaft.. Overall, Levadoux and Baligh (1986b) show that reliable interpretations of c_h can be obtained from tip measurements in approximately one-third of the time required for shaft measurements.

Lacasse and Lunne (1982) have applied the analytical predictions of Baligh and Levadoux (1980) to interpret dissipation measurements at the Onsøy and Drammen test sites in Norway (see Section 4.4). Table 5.3a summarizes the comparison between back-figured $c_h(\text{cone})$ values and reference $c_h(\text{lab})$ values from incremental oedometer tests for reloading of the soil from σ'_{v0} to σ'_p . The data indicate excellent agreement between laboratory and piezocone values of c_h and suggests that the dissipation curves presented by Levadoux and Baligh (1986) for normally consolidated BBC are applicable to measurements in other normally and lightly over-consolidated clays.

Sills et al. (1988) report piezocone dissipation pore pressure test measurements in highly plastic, sensitive Rio de Janeiro clay. The in-situ stress history ranges from $\text{OCR} > 4$ in the upper crust to 1.8-2.5 in the lower clay. Piezocone soundings were made using a 5 cm² cone with porous filters located at positions 1, 2, 3, and 4 (Figure 3.18). Figure 5.5 shows the pore pressures during steady penetration and immediately after penetration is interrupted. These measurements indicate that the tip pore pressures decrease significantly when penetration is interrupted, while on the shaft there is little or no difference between pressures during and after penetration. Subsequent calculations of the pore pressure ratio, \bar{U} , are based on the post-penetration measurements. Table 5.3b shows values of the horizontal consolidation coefficient, c_h , back-calculated using the method of Levadoux and Baligh (1986). These results indicate that 1) c_h back-calculated from dissipation curves at different locations can vary by a factor of 3, and 2) data from the filter located on the shaft consistently estimate higher c_h values than those from the face and shoulder.

5.2.3 Non-Linear Consolidation Analyses

Kavvasdas (1982) and Whittle (1987) have presented solutions for coupled, non-linear, radial consolidation around the shaft of an axisymmetric penetrometer. The initial excess pore pressures and stresses are estimated from Strain Path analyses in conjunction with generalized effective stress soil models (MCC, MIT-E1, and MIT-E3). The consolidation analyses were performed using the finite element program NON-CAP (Kavvasdas, 1982) which comprises a weighted residuals formulation of the incremental, poro-elastic consolidation theory of Biot (1935). The non-linear, effective stress-strain response of the soil is represented consistently by the same generalized effective stress soil models used

during installation, while flow is controlled by Darcy's law assuming homogeneous, constant permeability in the soil.

The non-linear analyses model changes in the effective stresses as well as the pore pressure dissipation. However, the assumption of a non-linear stress-strain response complicates significantly the interpretation of the results. Kavvadas (1982) and Whittle (1987) present their results using a dimensionless time factor, T , defined as:

$$T = \frac{k \sigma'_0 t}{\gamma_w R^2} \quad (5.1)$$

where σ'_0 is the initial mean effective stress in the ground, and k is the horizontal permeability of the soil⁷. The selection of this time factor is not unique, but is consistent with the assumption of normalized soil behavior used in the formulation of generalized effective stress soil models such as MCC and MIT-E3. Different authors, such as Tavenas et al. (1982) have argued that soil stress-strain behavior is most strongly influenced by the preconsolidation pressure, σ'_p , and thus recommended that time factors be defined in terms of σ'_p :

$$T = \frac{k \sigma'_p t}{\gamma_w R^2} \quad (5.2)$$

Figure 5.6 shows predictions of pore pressure dissipation from non-linear analysis of in BBC using the MIT-E3 model. The results show clearly the effect of the initial stress history on the predicted dissipation behavior (Figure 5.6a). However, when the time factor is modified using the preconsolidation pressure (σ'_p , Equation 5.2), variations in the dissipation response are reduced significantly. It is important to emphasize that these results are empirical interpretations of the analytical solutions similar to those proposed by Teh and Houlsby (1989).

Figure 5.7 illustrates the effects of soil modelling on the predictions of consolidation around the penetrometer shaft by comparing results from three K_0 -normally consolidated BBC analyses⁸ using: 1) the MIT-E3 model, 2) the MCC model, and 3) a linear-elastic model with the same initial stiffness properties assumed in the MCC model (Table 3.1; i.e.; $K=62.4\sigma'_0$ and $2G/K=1.05$) with the installation stresses and pore pressures determined using the MCC model. The results show the following:

1. The pore pressure dissipation predictions show time factors at a given degree of consolidation which vary by a factor of 3 or less. These results imply that pore pressure dissipation around the pile shaft is controlled primarily by the horizontal

⁷Note that it is equally valid to use σ'_{v0} in place of σ'_0 in Equation 5.1 as a more readily defined reference stress.

⁸The installation process is modelled using the Strain Path Method for all three cases.

permeability of the soil, while the effects of stress-strain non-linearity, anisotropy, etc. are less significant.

2. Effective stress changes at the penetrometer shaft (Figure 5.7c) are affected significantly by the modelling of soil behavior. Linear consolidation analyses predict $\Delta(\sigma_{\pi}-u_0)=0$ and thus, the dissipation of excess pore pressure is balanced by equal increases in radial effective stress. The effective stress ratio at the end of consolidation, $K_c=\sigma'_{\pi}/\sigma'_{v0}$, is then controlled by predictions of the installation pore pressures. In contrast, non-linear soil behavior (using either the MCC or MIT-E3 model) gives rise to a decay or release of total stresses which is most clearly illustrated by changes in the parameter $H=(\sigma_{\pi}-u_0)/(\sigma_{\pi}-u_0)$ (Figure 5.7a)⁹.

Predictions of K_c are important for evaluating equilibrium stress measurements from a variety of in-situ devices. The results in Figure 5.7c show that K_c values using MCC are significantly (by a factor of greater than 3) larger than those predicted using the MIT-E3 model. These results can only be evaluated through comparison with field measurements.

5.2.4 Evaluation of Non-Linear Consolidation Analyses

Whittle (1987) has evaluated predictions of non-linear consolidation through detailed comparisons with field measurements acting on a model pile shaft referred to as the Piezo-Lateral Stress cell (PLS; Morrison, 1984). Figure 5.8a compares numerical predictions with measurements of K_c versus depth at the Saugus test site. The results show:

1. The MIT-E3 model predictions generally match measurements within 10-20%. In contrast, the predictions of the MCC model for normally consolidated BBC shown in Figure 5.7 overestimate the measured K_c values in the lower clay by 100%.
2. Measurements of K_c are generally within 30-40% of the magnitudes of K_0 the values estimated from the laboratory test data presented by Morrison (1984).

These results imply that non-linear analyses using the Strain Path Method in conjunction with the MIT-E3 model can predict reliably the effective stresses on a pile shaft at the end of consolidation. Further comparisons with PLS measurements (Whittle and Baligh, 1990) have supported this conclusion.

Figure 5.8b matches MIT-E3 predictions with PLS measurements of pore pressures and total stresses using back-figured values of permeability ranging from $k=3.3-8.0(10)^{-8}$ cm/sec. Figure 5.9 shows that these permeability values are in reasonable agreement with properties measured in laboratory CRSC and constant head permeability tests.

⁹Azzouz et al. (1990) show even larger differences for installation conditions modelled using CEM and SPM analyses.

Overall, comparison of field data to predictions indicates that analyses based on 1) SPM installation predictions and 2) non-linear, consolidation analyses using the MIT-E3 soil model, provide reasonable estimates of both the time histories of stresses and pore pressures and the magnitudes of effective stresses at the end of consolidation.

5.3 TWO-DIMENSIONAL NON-LINEAR CONSOLIDATION

The previous sections have shown the capabilities of: a) uncoupled dissipation analysis for interpreting equivalent consolidation properties around penetrometers, and b) predictions of effective stresses and horizontal permeability from non-linear, radial consolidation analyses around the penetrometer shaft. This section describes numerical procedures used to compute two-dimensional, non-linear consolidation around a penetrometer.

Consolidation is analyzed in this chapter assuming:

1. The soil is fully saturated.
2. Soil deformations and fluid flow occur under quasi-static conditions.
3. Soil particles and the pore fluid are assumed to be incompressible.

The computations are performed using the finite element code ABAQUS (Hibbitt, Karlsson, and Sorenson; 1988). The relevant equations for coupled consolidation are based on a) equilibrium, which can be expressed in terms of the principle of virtual work:

$$\int_V \sigma : \delta \epsilon \, dV = \int_s \mathbf{t} \cdot \delta \mathbf{v} \, dS + \int_V \mathbf{f} \cdot \delta \mathbf{v} \, dV \quad (5.3)$$

where $d\mathbf{v}$ is a virtual velocity field, $d\epsilon$ is the virtual rate of deformation, σ is the true Cauchy stress, \mathbf{t} are the surface tractions per unit area, and \mathbf{f} are the body forces per unit volume; and b) continuity for fluid flow, which can be expressed as

$$\int_V \frac{d}{dt} \left(\rho_w \frac{dV_w}{dV} \right) dV + \int_s \rho_w \mathbf{n} \cdot \mathbf{v}_w \, dS = 0 \quad (5.4)$$

where V_w is the fluid volume within the control volume, V is the control volume, and ρ_w is the fluid density. Discretization and solution of these equations is discussed in the ABAQUS Theory Manual (HKS, 1988), and the implementation of the MIT-E3 soil model in the ABAQUS code is presented by Hashash (1992).

Figure 5.10a shows a finite element mesh consisting of 584 elements and 1773 nodes which was used for solving the two-dimensional, non-linear consolidation around a simple pile penetrometer. The analysis uses mixed elements with eight displacement nodes and four pore pressure corner nodes, which enable quadratic interpolation of displacements and linear interpolation of pore pressures. To evaluate the adequacy of the mesh in Figure 5.10a, linear uncoupled analyses were performed for the base case installation conditions (MCC, OCR=1) using a coarse mesh consisting of 584 and a fine mesh of 1561 elements. Figure 5.10b presents computed dissipation curves for points located on the shaft far above the tip ($z/R=30$) and at the simple pile tip:

1. For the point located on the shaft, the coarse mesh predictions are in good agreement with the fine mesh predictions.
2. For a point located at the tip, the discrepancy between the coarse and fine mesh predictions are more significant, particularly at early times ($\Delta u/\Delta u_i \geq 0.5$), where the mesh refinement can have an affect of up to one-half order of magnitude on time factor, T , corresponding to a given degree of consolidation, $\Delta u/\Delta u_i$.

This result suggests that the mesh in Figure 5.10a is adequate for shaft predictions, but some uncertainty will exist for predictions of tip measurements at early times¹⁰.

The selected boundary conditions during consolidation include the following considerations:

1. At locations around the pile shaft, there is radial dissipation of pore pressures and radial displacements in the soil (hence, $\partial u/\partial z=0$ and $w_z=0$ along BC). The upper boundary is located at $z/R=40$ for simple pile geometries. Similar conditions are imposed at $z/R=-40$ ahead of the pile tip along boundary ED.
2. Symmetry along the centerline requires $\partial u/\partial r=0$ and $w_r=0$ along OE.
3. On the far radial boundary, CD, the excess pore pressures $\Delta u=0$; and $\sigma_{rr}=\sigma_{h0}$ corresponding to the in-situ K_0 conditions prior to penetration.
4. The penetrometer surface represents an impermeable boundary ($\partial u/\partial n=0$ along OAB)¹¹. The analysis also assumes that the tip of the penetrometer (boundary OA) does not displace during consolidation, but does allow sliding along the shaft-soil interface (smooth shaft). This corresponds approximately to the case where displacements are locked at the tip of the penetrometer, which is one of several possible scenarios from standard piezocone testing procedures.

¹⁰These differences in numerical accuracy may explain, in large part, the results obtained previously by Baligh and Levadoux (1980) for linear coupling (Figure 5.1a).

¹¹The penetrometer is not modelled as a structural element in these calculations.

For non-linear problems, the basic tolerance measure for the solution used by the ABAQUS code is the residual of the force imbalance at the nodes¹², which is restricted to the range of 10^{-2} to 10^{-4} of the typical actual nodal value. For the MCC analyses, this guideline is generally followed. However, for MIT-E3 analyses, Hashash (1992) recommends a less stringent tolerance based on the maximum displacement residual between two successive iterations in the global Newton scheme¹³.

Due to the approximate nature of the Strain Path Method solution, the initial installation stress fields do not satisfy internal equilibrium, and are incompatible with the boundary conditions used in the consolidation analysis (Figure 5.10a). The incompatibility is most severe along boundaries AB and BC for which SPM solutions generally predict non-zero meridional shear stresses, σ_{rz} , in conflict with the assumption of zero tangential traction along these boundaries (Figure 5.10a). The equilibrium imbalance can be dealt with by two possible approaches:

1. Prior to consolidation, the initial Strain Path stresses and pore pressures as initial conditions are allowed to equilibrate with the boundary conditions shown in Figure 5.10a by shear distortion under conditions of no drainage. The equilibrated stress state then provides the initial conditions for subsequent consolidation analysis.
2. Apply external corrective nodal forces which are determined as follows:

$$\mathbf{R} = - \sum_{i,j} \alpha_{ij} t_{ij} \mathbf{B}_{ij}^T \boldsymbol{\sigma}_{ij} \det \mathbf{J}_{ij} \quad (5.5)$$

where the indices i, j refer to the integration sampling point

α_{ij} is the integration weight factor

t_{ij} is the element thickness

\mathbf{B}_{ij}^T is the strain-displacement transformation matrix

$\boldsymbol{\sigma}_{ij}$ are total stresses predicted from the SPM

\mathbf{J}_{ij} is the Jacobian matrix.

The nodal forces \mathbf{R} are applied at the the beginning of the analysis and maintained throughout consolidation. It should be noted that the corrective nodal forces will treat both the problem of inequilibrium and the problem of incompatibility of boundary conditions.

The following discussion (Figures 5.11 through 5.13) presents a comparison of results obtained from the above two approaches for the base case analysis of consolidation

¹²i.e.; ${}^n\mathbf{R} \cdot {}^n\mathbf{F}$, where ${}^n\mathbf{R}$ is the vector of applied nodal loads and ${}^n\mathbf{F}$ is the vector of nodal forces due to element stresses.

¹³For the analyses presented in this chapter, a maximum displacement residual $(\Delta w_i/R)=10^{-5}$ was used.

following simple pile penetration in K_0 -normally consolidated BBC using the MCC soil model.

Figures 5.11a, b show the effects of equilibration by undrained distortion on the initial stress field prior to consolidation for the base case analysis of simple pile penetration in K_0 -consolidated BBC using the MCC soil model. The figures show the following:

1. Undrained shear distortion causes reductions in excess pore pressures at locations close to the tip of the penetrometer and at vertical distances within $z/R=10$ of the upper boundary.
2. The changes in effective radial stress σ'_{rr} along the shaft during equilibration are relatively small, except within $z/R=10$ of the upper mesh boundary. This is due to the fact that SPM predicted stresses are not compatible with the imposed boundary condition along BC in which tangential boundary tractions are zero.

Figure 5.12 compares predictions of consolidation at the tip of the penetrometer and at a shaft element located $z/R=30$ for the base case analysis and using the equilibrium procedures of a) undrained shear distortion, and b) applied nodal forces:

1. At locations on the pile shaft ($z/R=30$) the equilibration procedure has little effect on the predicted consolidation behavior. The two solutions predict similar stresses and excess pore pressures throughout consolidation.
2. The equilibration method has an important effect on vertical stresses at the tip at early consolidation times ($T<0.1$). Undrained shear distortion does not provide realistic predictions of vertical stresses and excess pore pressures at these early times.
3. At the end of consolidation, the solutions for vertical stresses and excess pore pressures are within 10-15% of one another for both equilibration procedures.

The distribution of effective stresses along the shaft at the end of consolidation (Figure 5.13) shows:

1. Neither approach provides reliable predictions for within $z/R=10$ of the top boundary.
2. For $5 \leq z/R \leq 30$, the two solutions predict similar stress fields (within 10%).
3. Ahead of the penetrometer tip ($-5 \leq z/R \leq 5$) the maximum discrepancy between the two solutions is between 30-40%.

Based on the above comparisons it is apparent that both of the proposed methods give realistic solutions for stresses at the end of consolidation, although neither is completely reliable. However, the procedures with applied nodal forces gives more reasonable behavior at the penetrometer tip during early stages of consolidation. This method is used throughout subsequent computations.

5.4 PREDICTIONS

5.4.1 Base Case Analysis

Solutions for non-linear, coupled consolidation around a simple pile following penetration in K_0 -consolidated BBC, based on the MCC soil model are presented in Figures 5.14 and 5.15, which present selected stress components at the end of consolidation and excess pore pressures at selected times, respectively. These figures show that for $z/R > 10$ conditions are essentially uniform in the vertical direction. Figure 5.14c shows a net (locked-in) change in the cavity shear stress (q_h/σ'_{v0}) extending to a radial distance $r/R = 10-15$, while comparison to installation conditions (Figure 3.15c) indicates that the magnitudes of q_h/σ'_{v0} decrease by 30-40% during consolidation. Figure 5.14d shows the magnitudes of the meridional stresses at the end of consolidation to be significant, which can be due in part to the equilibrating nodal forces applied at the penetrometer boundary (Section 5.3). The contours of excess pore pressures at selected times (Figure 5.14) show a monotonic decrease in excess pore pressures along the penetrometer boundary throughout consolidation.

The effect of non-linear coupling was investigated for the base case condition; i.e., K_0 -consolidated BBC modelled by the MCC soil model and is illustrated in Figure 5.16. The shaft predictions show that the uncoupled pore pressure time history far above the tip can be matched to the non-linear coupled solution by using an equivalent stiffness $(K+4G/3)/\sigma'_0 = 45$ for the uncoupled solution¹⁴. This result is similar to that obtained by Kavvadas (1982), who showed that the shape of the pore pressure dissipation curve far above the cone tip is essentially unaffected by non-linear coupling and that uncoupled and non-linear coupled solutions can be matched by selection of an appropriate equivalent stiffness factor.

Uncoupled solutions at the cone base ($z/R = 2.3$) and using the same equivalent stiffness $(K+4G/3)/\sigma'_0 = 45$ which was used to match uncoupled and non-linear coupled solutions far above the cone tip show:

1. For the $z/R = 2.3$ location non-linear coupling also has negligible effect on the shape of the dissipation curve, and the uncoupled and non-linear coupled solutions can be matched by using the same equivalent stiffness factor which was used to match the two solutions far above the cone tip.
2. At the cone tip, non-linear coupling has a noticeable influence on the shape of the dissipation curve for $\bar{U} > 0.2$. For a given level of dissipation, \bar{U} , the time factor T corresponding to the two solutions can differ by a factor of up to 2.5.

¹⁴Note: The initial stiffness for the MCC model is $(K+4G/3)/\sigma'_0 = 106$.

5.4.2 MIT-E3 Predictions

This section presents two-dimensional solutions for non-linear, coupled consolidation around a simple pile following penetration in K_0 -consolidated BBC, based on the MIT-E3 soil model. Installation pore pressure and stress fields are obtained from the solutions presented in Chapter 3. Predictions are made to assess the effects of a) non-linear coupling, b) filter location, and c) stress history (OCR) on pore pressure time histories. Predictions are based on consolidation around a simple pile following penetration in K_0 -consolidated BBC for OCR=1, 2, and 4.

Figure 5.17 compares the consolidation behavior (radial total and effective stresses and excess pore pressures acting at a point on the shaft far above the penetrometer tip ($z/R=30$), with one-dimensional radial consolidation solutions from Whittle (1987):

1. The two solutions are in good agreement for consolidation in normally consolidated BBC (OCR=1, Figure 5.17a). The two-dimensional analyses predict slightly larger time factors for the same degree of excess pore pressure dissipation, while the final set-up stress, $K_c=0.42$ compared to $K_c=0.38$ reported previously from the one-dimensional solution.
2. At higher OCR (2 and 4) there are more significant discrepancies between one- and two-dimensional solutions. At OCR=2, the dissipation times are up to a factor of 2 larger for the two-dimensional analysis, while $K_c=0.83$ is 30% larger than that reported previously. In contrast, at OCR=4, the excess pore pressure dissipation is similar for both analyses, while the effective stress set-up is less for the two-dimensional computations, $K_c=1.52$, compared to $K_c=1.93$ from radial consolidation¹⁵.

Figure 5.18 presents predicted time histories of vertical stresses and excess pore pressures at the tip of the simple pile. These predictions show that excess pore pressures decrease monotonically at the tip, while there is a small set-up in vertical effective stress (20% increase in $\sigma'_{zz}/\sigma'_{v0}$ at all OCR's). At OCR=1 and 2 (Figures 5.18a, b) there is no computed change in effective vertical stress for time factors, $T<0.01$.

Figures 5.19a-d show contours of the stresses at the end of consolidation for OCR's 1, 2, and 4. The penetrometer installation causes a net (locked-in) change in the cavity shear stress q_h (Figure 5.19c) which extends around the pile shaft to a radial distance $r/R=5$ for consolidation at OCR=1 and 2; and to $r/R=20$ for OCR=4. The radial effective stress (σ'_r/σ'_{v0} ; Figure 5.19a) and mean effective stress (σ'/σ'_{v0} ; Figure 5.19b) show more

¹⁵These discrepancies in shaft predictions reflect both the effects of equilibration procedures and the numerical accuracy of the non-linear finite element analyses.

complex patterns of behavior, especially in the proximity of the tip ($z/R \leq 5$)¹⁶. This behavior reflects the tip boundary conditions assumed in the analysis. The analyses show small vertical variations in stress conditions at locations $z/R \geq 10$.

Excess pore pressures, $\Delta u/\sigma'_{v0}$, at selected time factors, $T (=k\sigma'_{0t}/\gamma_w R^2)$ during intermediate stages of consolidation (Figure 5.20) show a smooth monotonic decrease of excess pore pressures at all locations around the penetrometer surface. Thus, the solutions do not explain the increases in excess pore pressures reported from field measurements by a number of authors (e.g.; Azzouz and Baligh, 1984). The figures also mark the progress of the "dissipation front" within the soil. this boundary separates the inner zone of soil, where the excess pore pressures is decreasing ($\partial \Delta u / \partial t < 0$) from the outer zone which experiences an increase in Δu with time. Previous authors (Kavvasdas, 1982) have equated this front with the direction of loading in the soil (the inner zone representing "plastic" loading, while the outer zone exhibits unloading).

Figure 5.21 presents the distribution of effective stress components ($\sigma'_{rr}/\sigma'_{v0}$, $\sigma'_{zz}/\sigma'_{v0}$, and $\sigma'_{\theta\theta}/\sigma'_{v0}$) at the end of consolidation in a horizontal plane (i) far above the penetrometer tip ($z/R=30$) and (ii) along the centerline and penetrometer boundary. For all OCR's, the radial stress reaches a maximum at the pile shaft and decrease significantly (up to 50%) in the zone $1 \leq r/R \leq 5-20$. Predicted effective stresses along the penetrometer boundary show little vertical variations for $z/R \geq 5$. All stress components exhibit complex behavior in the vicinity of the penetrometer tip, which is influenced by the prescribed tip boundary conditions assumed in the analyses.

Figure 5.22 illustrates the effect of filter location on pore pressure dissipation curves for OCR=1, 2, and 4. The results are shown for filter locations on the shaft ($z/R=30$), at the base of the cone ($z/R=2.3$), and at the cone tip ($z/R=-0.5$):

1. Dissipation rates are 4-10 times faster for filters located at the cone tip, compared to those predicted on the shaft. This trend is in general agreement with the uncoupled solutions presented by Levadoux and Baligh (1986) (Section 5.2.1).
2. The stress history has a significant effect on relative dissipation rates at the tip and shaft. At OCR=1, differences in dissipation times are less than a factor of 4, while at OCR=4 time factors vary by a factor of 10.

The effect of stress history on dissipation curves is illustrated in Figure 5.23. This figure compares the dissipation curves using three different dimensionless time factors, defined in terms of the preconsolidation pressure, σ'_p , the in situ mean effective stress,

¹⁶This result confirms the difficulties of interpreting consolidation stresses acting at the tip of the penetrometer.

σ'_0 , and the in situ vertical effective stress, σ'_{v0} , respectively, for predictions at the tip, base, and shaft locations:

1. The dimensionless time factor defined using the preconsolidation pressure provides the most reliable method for unifying dissipation curves for different OCR's in clay. Dissipation predictions at the shaft and base of the cone give the time factor, $T=k\sigma'_p t/\gamma_w R^2$, which agree to within a factor of 2 at a given degree of consolidation, \bar{U} .
2. Tip dissipation curves (Figure 5.23c) show a much wider band of scatter for varying OCR than the shaft dissipation curves, regardless of how the time axis is scaled. Scaling using the preconsolidation pressure minimizes the differences. However, at early stages of consolidation ($\bar{U}>0.8$) time factors corresponding to a given \bar{U} for different OCR's can differ by an order of magnitude. At later stages ($0.8>\bar{U}>0.1$) these differences are less severe, with the time factor corresponding to a given \bar{u} for different OCR's differing by a factor of 5-6.

Overall, the predictions presented in this section have the following practical implications:

1. Differences in pore pressure dissipation curves due to variations in OCR are best minimized by using the time factor defined in terms of the preconsolidation pressure, σ'_p . This procedure is most effective for porous filters located on the shaft or at the base of the piezocone.
2. Predicted dissipation curves for filters located on the shaft show the least sensitivity to variations in OCR, and this filter location is therefore the most desirable from the standpoint of obtaining the most reliable determinations of permeability. However, the predictions also show that dissipation at this location is up to 10 times more slowly than that at the tip. Thus, holding tests can be performed more economically if the filter element is located on the cone tip/face rather than on the shaft.
3. If shaft measurements are used, permeability in normally to moderately overconsolidated ($1 \leq \text{OCR} \leq 4$) soil can theoretically be estimated to within a factor of 2. If tip measurements are used, the permeability can theoretically be estimated to within a factor of 5-6, provided the middle to later portions ($0.8 > \bar{u} > 0.1$) of the dissipation curve is used. These estimates are based solely on theoretical variations in dissipation curves due to variations in OCR and do not consider additional sources of scatter such as variations in soil type or measurement errors.
4. Non-linear coupling has negligible influence on the shape of dissipation curves, except in the vicinity of the cone tip. The predictions from non-linear consolidation analysis are qualitatively in agreement with simplified, uncoupled solutions presented by

Levadoux and Baligh (1986a). However, the non-linear analyses provide a direct basis for estimating the horizontal coefficient of permeability.

5.5 COMPARISON TO MEASURED DATA

5.5.1 Field Measurements in BBC

This section compares tip and shaft predictions of pore pressure dissipation curves to field measurements in BBC from the Saugus site. Detailed descriptions of the Saugus site are given by Vivatrat (1978) and Morrison (1984) and a summary is contained in Section 3.5.1. Levadoux and Baligh (1980) report measurements of tip pore pressure dissipation curves for a 600 cone; while, Morrison (1984) presents dissipation data measured by the piezo-lateral stress (PLS) cell. Reference values of vertical and horizontal permeabilities obtained from laboratory constant rate of strain consolidation (CRSC) and constant head permeability tests are shown in Figure 5.9. Comparisons of shaft and tip measurements to MIT-E3 predictions are shown in Figures 5.24 and 5.25. Figure 5.24a shows excess pore pressures measured by the PLS at 4 depths (with $1.2 \leq \text{OCR} \leq 4$). Installation excess pore pressures (i.e.; $\Delta u_i / \sigma'_{v0}$ at $t=0$) are also tabulated in the figure. The data are converted to a dimensionless format (\bar{U} vs. T ; Figure 5.24b) using a) preconsolidation pressures, σ'_p , reported by Vivatrat (1978), and horizontal coefficients of permeability, k_h , reported from laboratory constant head and CRS tests (Figure 5.9). Comparison of shaft (PLS) measurements to predictions (figure 5.24b) indicates:

1. Dissipation measurements in the range $\bar{U} \leq 0.6$ show minor scatter in lightly overconsolidated soil ($1 \leq \text{OCR} \leq 4$) and are in excellent agreement with predictions. At earlier dissipation times ($\bar{U} \geq 0.6$), the measurements show a greater degree of scatter (time factors T at $\bar{U}=0.9$ vary by more than a factor of 10).
2. No consistent trends can be discerned with respect to the relationship between OCR and the shape and location of the measured dissipation curve. This observation is in accordance with predictions which indicate that a single dissipation curve can be used to characterize dissipation measurements at all OCR's (for $1 \leq \text{OCR} \leq 4$), provided that the time factor is defined in terms of Equation 5.2.

Figure 5.25b repeats similar comparisons with high quality piezocone data reported by Baligh and Levadoux (1980) at six locations:

1. In the range $0.4 \leq \bar{U} \leq 0.6$, predictions agree with measurements to within a factor of 5. At earlier times, discrepancies between measurements and predictions become more significant, which reflects the greater uncertainty in tip predictions at early times.

2. The overall slope of the measured dissipation curves are flatter than the predicted curves. The measurements also show less scatter due to variations stress history than that indicated from the predictions.

Overall, the results in Figures 5.24 and 5.25 show that:

1. The predicted shaft dissipation curve is in good agreement with the measured data. The predictions: a) provide consistent estimates of permeability for $0.6 \geq \bar{U} \geq 0.2$ (i.e.; permeability estimates will be relatively insensitive to the degree of consolidation at which the estimate is made), and b) provide reasonable estimates of the magnitude of the horizontal coefficient of permeability, k_h . A single normalized dissipation curve can be used to interpret dissipation data in lightly overconsolidated BBC, provided that the time factor is defined by Equation 5.2.
2. The predictions of normalized dissipation (\bar{U} vs. T) tend to overestimate the in-situ permeability by roughly a factor of up to 5. Variations in OCR result in minor scatter in the measured normalized dissipation curve; hence, a single predicted curve can be used to interpret dissipation data in lightly overconsolidated ($1 \leq \text{OCR} \leq 4$) BBC. Tip data exhibit higher scatter at early times ($0.6 \geq \bar{U}$), indicating that the most reliable permeability estimates will be obtained in the range $0.6 \geq \bar{U} \geq 0.4$.

5.5.2 Calibration Chamber Data

This section compares the predictions presented in Section 5.4 from piezocone tests on kaolin in large-scale calibration chambers (Nyirenda, 1989). These tests are part of the same program described in Section 3.5.3. The test material is resedimented Speswhite kaolin (liquid limit, $w_L = 66\%$; and plastic limit, $w_p = 33\%$). All measurements were made using a 5 cm² piezocone (Section 3.5.3).

Reference permeabilities in the vertical and horizontal directions) for resedimented Speswhite kaolin are reported by Al-Tabaa and Wood (1987) from falling head tests. Figure 5.26a shows permeability measurements in normally consolidated kaolin for K_0 -normally consolidation of the soil from a slurry condition, while Figure 5.26b presents similar data in over-consolidated. The data show that the permeability is controlled by void ratio and is essentially independent of OCR. Horizontal permeabilities corresponding to the calibration chamber tests are summarized in Figure 5.27.

Figures 5.27 and 5.28 show dissipation curves for shaft (u_4) and tip (u_1) pore pressures, respectively. The error bars indicate uncertainties in the estimated permeability k and preconsolidation pressure σ'_p . The plots are presented in terms of the time factors, $T = k\sigma'_p t / \gamma_w R^2$ following the same format used in previous comparisons (Figure 5.24, 5.25):

1. The shaft dissipation measurements are in excellent agreement with predictions, especially within the range $0.6 \leq \bar{U} \leq 0.8$.
2. Tip measurements generally fall within the band of MIT-E3 predictions for BBC. The scatter in dissipation times due to variations in OCR is less than predicted by the analyses.

This data suggest that there is little practical difference in the reliability of tip and shaft measurements (i.e., the scatter in curves of different OCR's). In both cases less scatter (as a result of variations in OCR) occurs in the later $\bar{U} > 0.4$ portions of the curves. The data also suggest that predicted dissipation curves for BBC can be applicable to other soils for estimating permeability to within a factor of 3-5.

5.5 SUMMARY AND CONCLUSIONS

For consolidation around axisymmetric penetrometers, this chapter has assessed the effect of non-linear coupling, filter location, and stress history. Predictions and measurements suggest the following:

1. Non-linear coupling has negligible influence on the shape of shaft dissipation curves. It does have a noticeable influence on the shape of tip dissipation curves, with deviations between coupled and uncoupled permeability estimates being on the order of a factor of 2-3.
2. Predictions and measurements in both field and calibration chamber tests indicate that definition of a dimensionless time factor in terms of the preconsolidation pressure (Equation 5.2) best unifies dissipation data for tests conducted in soils of varying stress histories.
3. Comparison of tip and shaft predictions to field measurements in BBC are excellent agreement, indicating the general validity of the two-dimensional consolidation solutions. Predictions for BBC are also in excellent agreement measurements in kaolin, indicating that the predicted curves for BBC can be used for interpretation of dissipation data in other soils. The comparisons show that the predicted dissipation curves can provide reliable estimates of permeability to within 3-5 when data in the range $0.4 \leq \bar{U} \leq 0.6$ is used.

Table 5.1 Estimation of Soil Properties from Dissipation Tests

Penetrometer	Quantity Measured	Soil Property Estimated	Reference	Notes
Piezometer Probe	$u(t)$	c_h c_h	Tortenson (1975) Battaglio et al. (1981)	
Piezocene		c_h, k	Levadoux and Baligh (1986)	180° Tip - filter locations at tip, face, base & shaft; 600° Tip - filter locations at tip
	$u(t)$	c_h k c_h c_h	Lacasse and Lunne (1982) Tavenas et al. (1982) Senneset et al. (1988) Sills et al. (1988)	Filters @ cone base Filters @ cone base Filters @ Positions 1, 2, 3, & 4 (Fig 3.18)
Dilatometer	$P_0(t)^1$ $P_0(t)$ $P_2(t)^2$	c_h σ_{hc} c_h	Marchetti and Totani (1989) Marchetti et al. (1986) Robertson et al. (1988)	
Piezoblade	$u(t)$	c_h	Kabir & Luttenegger (1989)	Same dimensions as DMT, u measured @ middle of membrane
Push-in Piezometer	$u(t)$ $u(t)$	c_h, k c_h	Bennett et al. (1985) Foott et al. (1987)	50° Tip
Earth Pressure Cells	$P(t)$ $P(t)$ $P(t)$	K_0 K_0 K_0, k	Ladd et al. (1981) Tavenas et al. (1975) Tedd et al. (1981, 1990)	$B/w^3=12.6$; 20 & 400° tips $B/w=25$ $B/w=20$
Pressuremeter	Δu_{max}^4		Clark et al. (1979)	Camkometer (fig. 6.3a)

¹ P_0 =dilatometer contact pressure.² P_2 =dilatometer closure pressure.³ B/w =aspect ratio.⁴ Δu_{max} =membrane pore pressure after expansion to maximum strain.

Table 5.2 Summary of Previous Consolidation Predictions

Reference	Installation Conditions		Consolidation Analysis			Notes
	Installation Model	Soil Model	Type	Geometry	Soil Model	
Torstensson (1975, 1979)	CEM (spherical & cylindrical)	EPP	Uncoupled	1-D	—	Cylindrical: shaft PWP Spherical: tip PWP
Randolph et al. (1979)	CEM (cylindrical)	MCC	Non-linear, coupled	1-D	MCC k=constant	Shaft conditions: setup stresses and PWP
Baligh & Levadoux (1980)	SPM (180°, 60° cones)	MIT-T1 (BBC, OCR=1)	Uncoupled (anisotropic, isotropic)	2-D	—	PWP only, effects of: - cone shape - filter location
Baligh (1986a)			Linear coupled	2-D	Elastic	- anisotropy - linear coupling
Kavvas (1982)	SPM (simple pile, 60° cone)	MIT-E1; MIT-E3 (BBC, 1 ≤ OCR ≤ 8)	Non-linear, coupled	1-D	MIT-T1 MIT-E3 k=constant	Shaft conditions: set-up stresses and PWP Evaluation w/PLS data
Whittle (1987)						
Teh & Houlsby (1991)	SPM ¹ (60° cone)	EPP	Uncoupled	2-D	—	PWP only: Effect of G/c _u on time history
Aubeny (1992) (this thesis)	SPM ² (simple pile)	MCC; MIT-E3 (BBC; OCR ≤ 4)	Non-linear, coupled	2-D	MIT-E3 k=constant	Effect of: - Non-linear coupling in 2-D - OCR

¹Finite element equilibrium correction.²Pore pressures from Poisson solution.

Test Site	Depth (m)	OCR	c_h (cone) (m ² /yr)	c_h (lab) ¹ (m ² /yr)
Onsøy	11.5	1.3	32-60	30-47
	15.6	1.3	17-43	14-25
	18-20	1.3	18-28	14-25
Drammen	9.5	1.5	20-22	17-48
	12.5	1.15	33-64	59
	18.5-19.5	1.15	30-58	

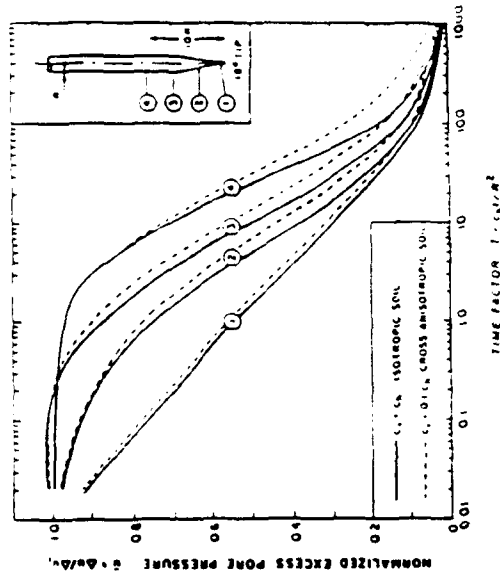
¹Incremental oedometer tests.

Table 5.3a Horizontal Consolidation Coefficient Values from Dissipation Tests Using Levadoux and Baligh (1980) Theory Compared to Reference Values (after Lacasse and Lunne, 1982)

Depth (m)	c_h (piezocone) ($\times 10^{-4}$ cm ² /sec)		
	Cone Face ¹ (1)	Base (2)	Shaft (4)
4.39	120	98	183
8.38	195	94	
4.22	167	152	310
8.22	132	92	
2.38	175	152	459
6.38	290	252	492
8.38	145	90	303

¹For filter locations see Figure 3.18.

Table 5.3b Horizontal Consolidation Coefficient Values Computed from Dissipation Test Data from Different Stone Locations - Rio de Janeiro Site (after Sills et al., 1988)

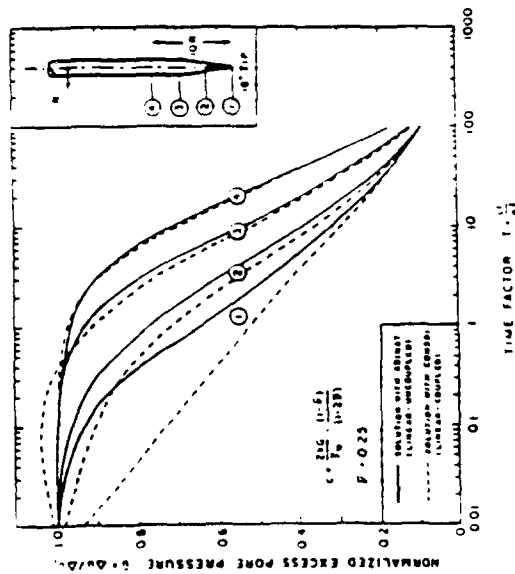


b) 18° Cone, Effect of Anisotropy

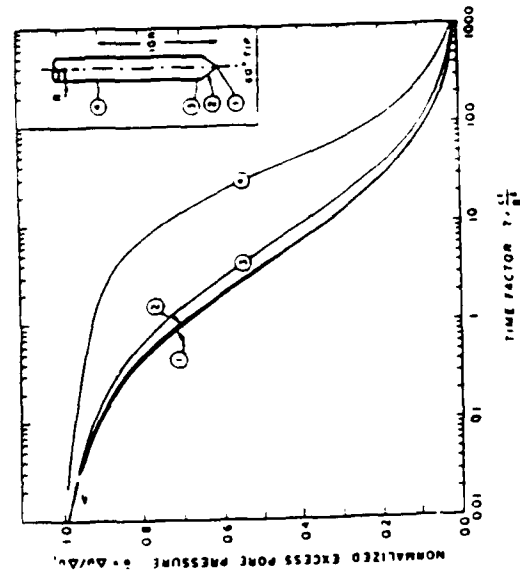
Initial Conditions
- SPM Installation predictions; PWP computed by integration along isochronous lines - MIT-711 soil model BBC, OCR=1 parameters

Uncoupled Analysis:

$$c_h \frac{\partial}{\partial r} \left(r \frac{\partial u}{\partial r} \right) + c_v \frac{\partial^2 u}{\partial z^2} = \frac{\partial u}{\partial t}$$

Isotropic: $c_h = c_v = c$ 

a) 18° Cone, Effect of Linear Coupling



c) 60° Cone, Effect of Filter Location

Figure 5.1 Pore Pressure Dissipation around Cone Penetrometers from Uncoupled Consolidation Analyses (Levadoux and Baligh, 1986)

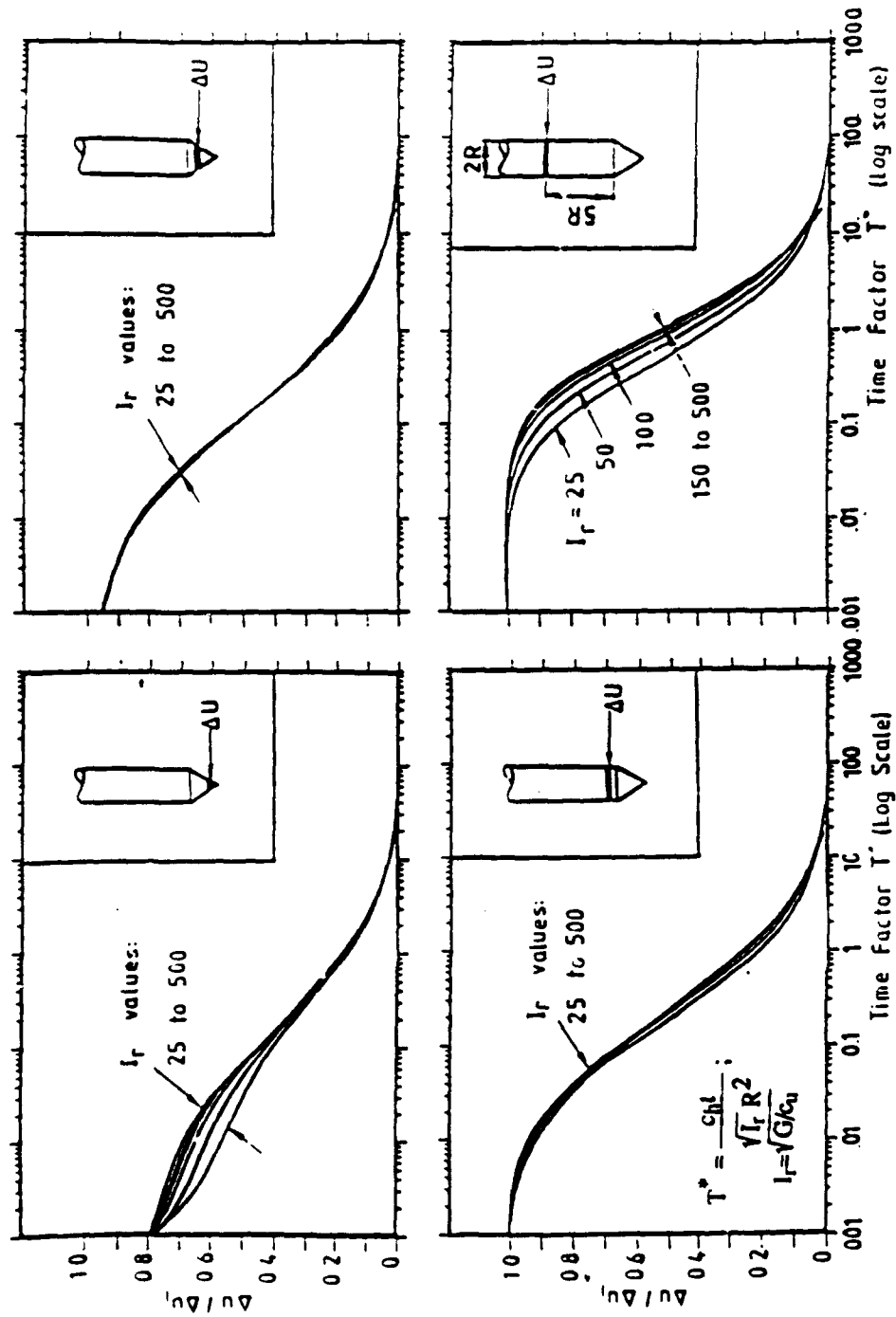


Figure 5.2 Pore Pressure Dissipation around 60° Cone Penetrometer from Uncoupled Consolidation Analyses - Installation Conditions from SPM using EPP Soil Model (Teh, 1987)

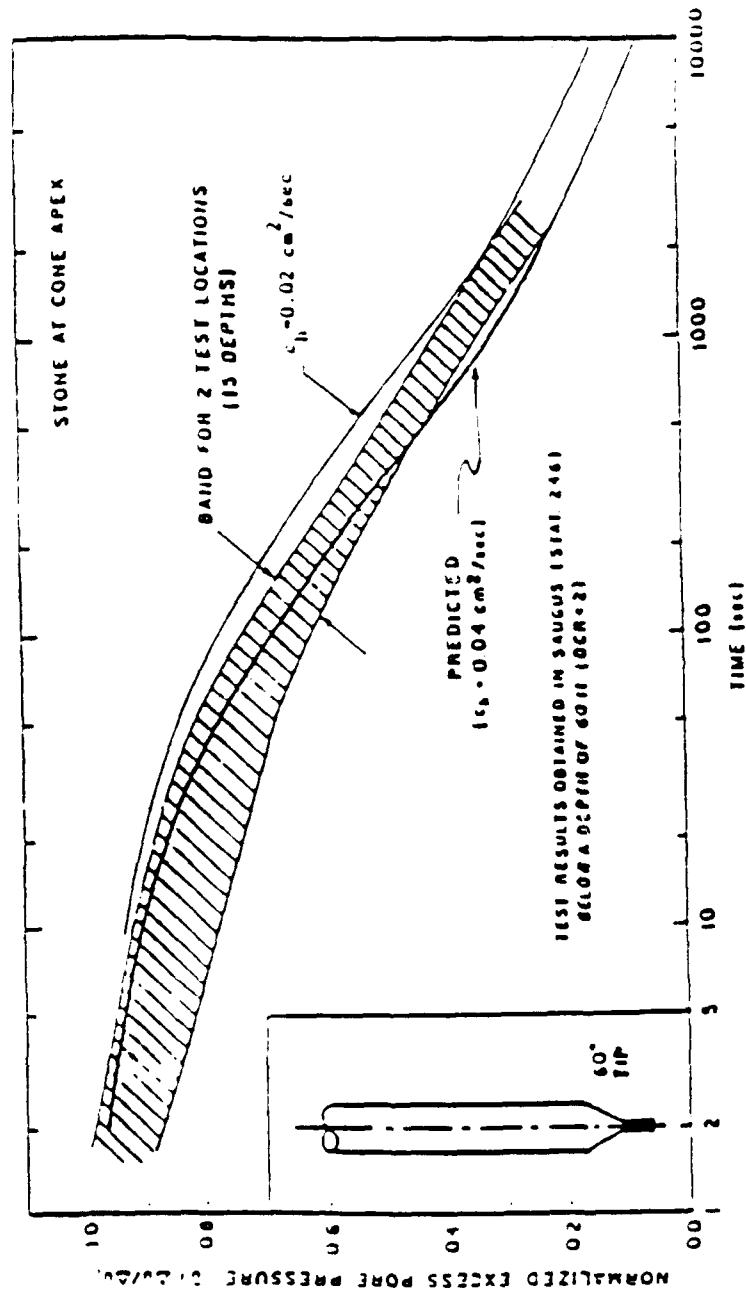


Figure 5.3 Evaluation of Linear Uncoupled Dissipation Predictions for 60° Conical Probe in Lower BBC (OCR < 2) (after Levadoux and Baligh, 1986)

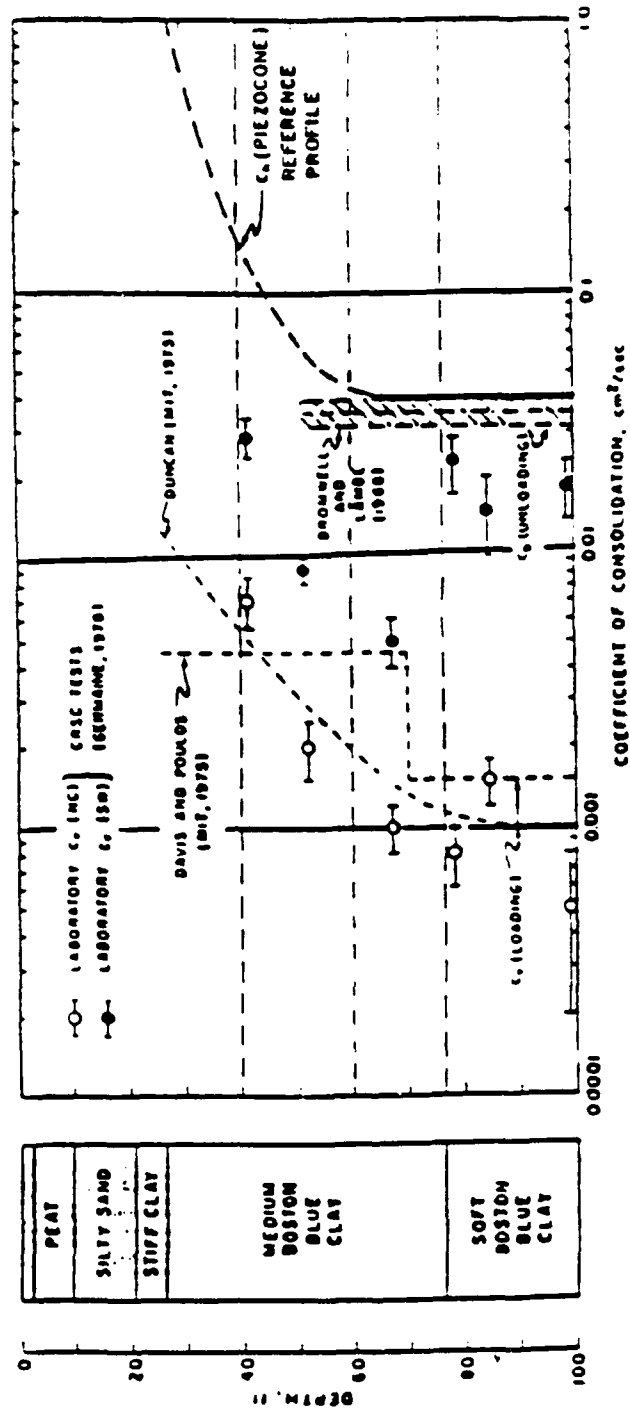


Figure 5.4 Comparison of Predicted and Measured Coefficients in Boston Blue Clay
(after Levadoux and Baligh, 1986)

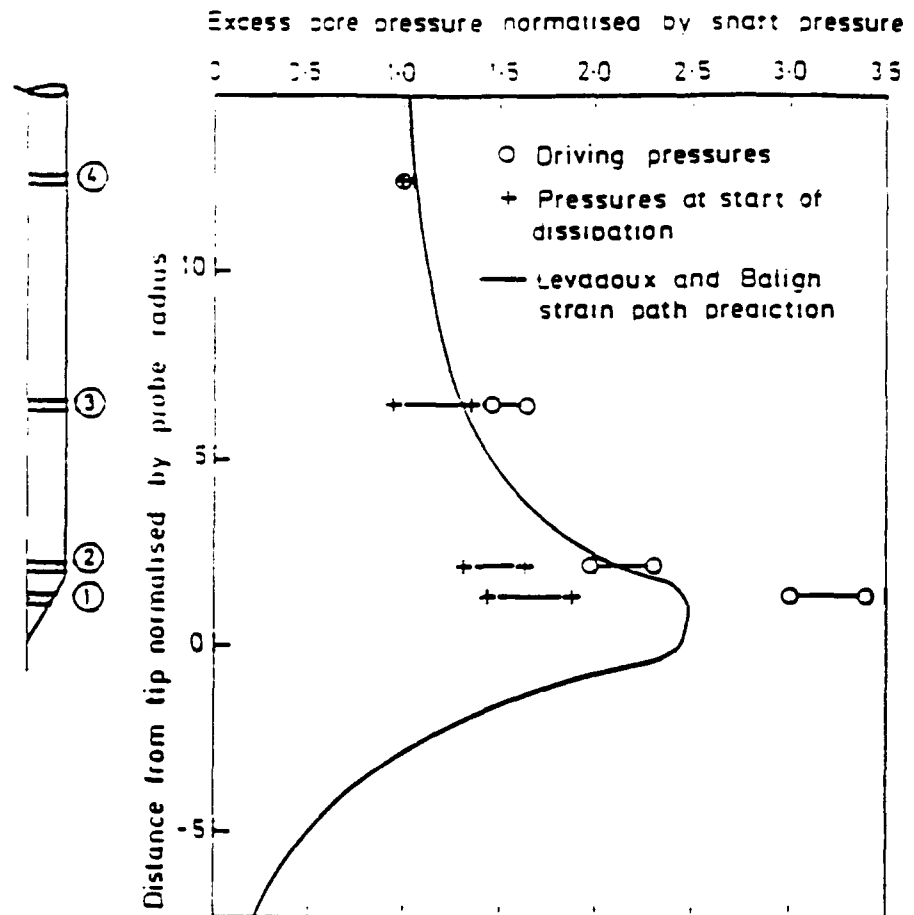


Figure 5.5 Normalized Theoretical and Driving Excess Pore Pressure
(after Sills et al., 1988)

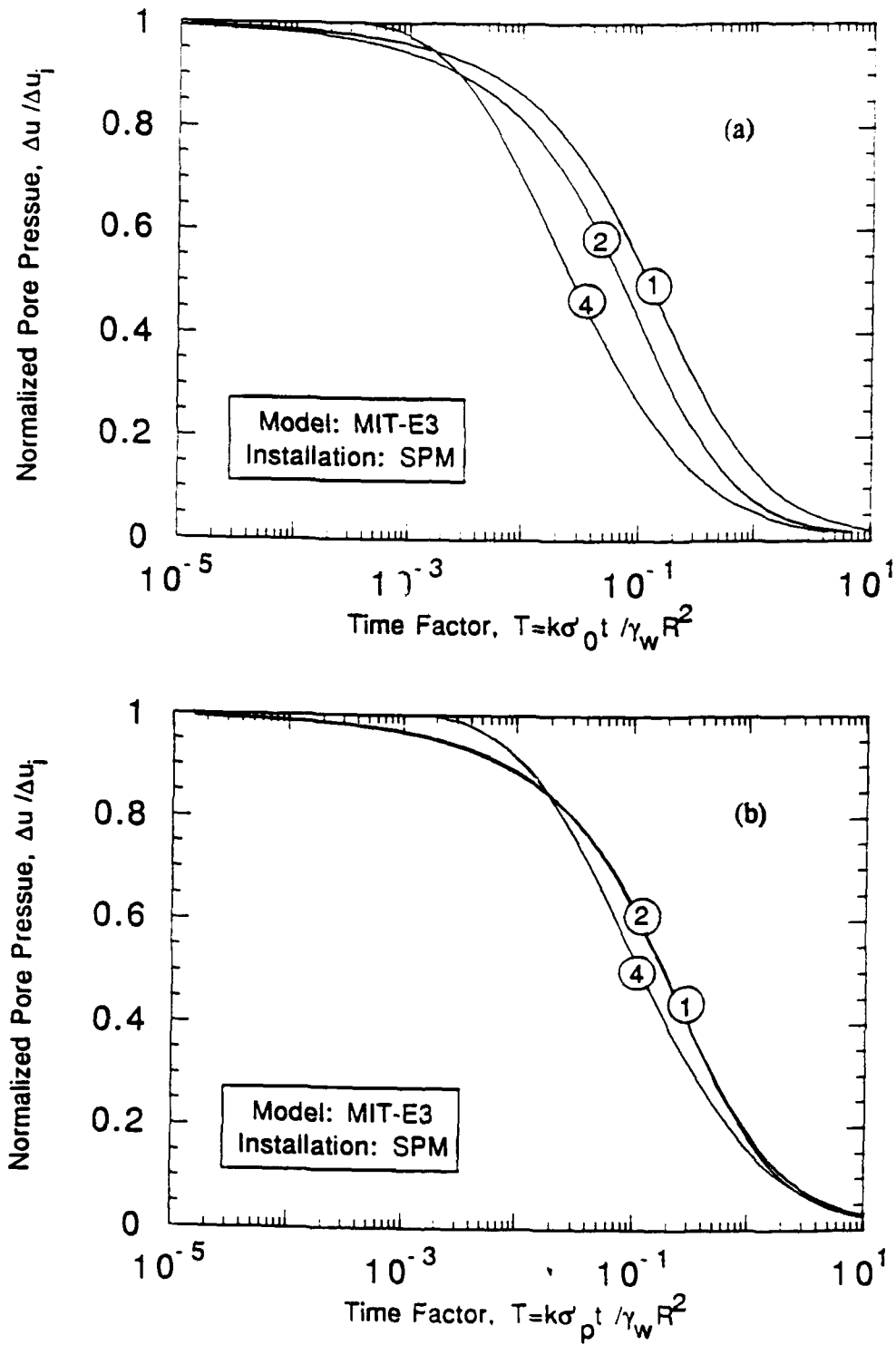


Figure 5.6 Influence of Stress History on Dissipation Curves Far above Tip Predicted by MIT-E3 Model (after Whittle, 1987)

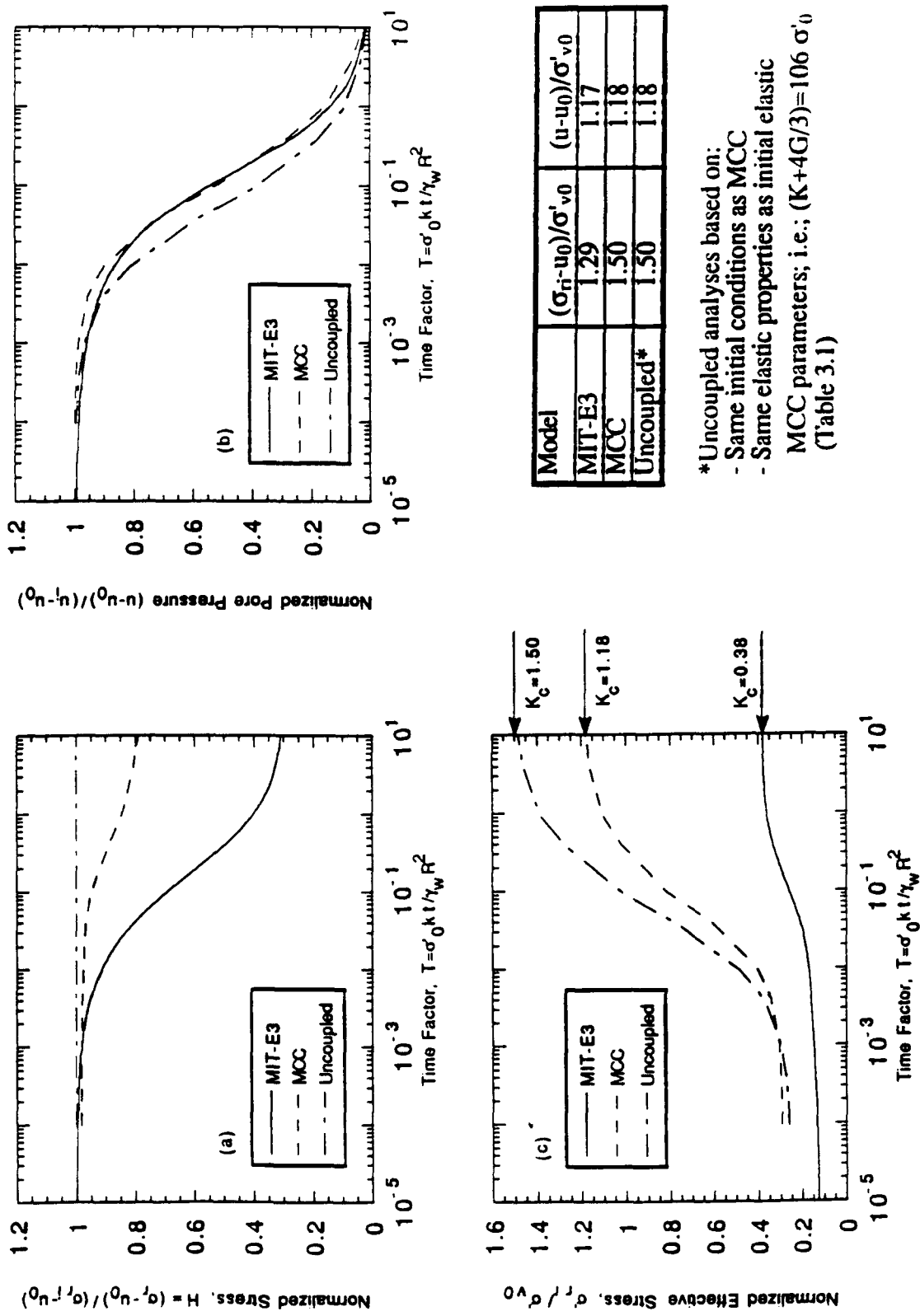


Figure 5.7 Influence of Soil Model on Consolidation Predictions

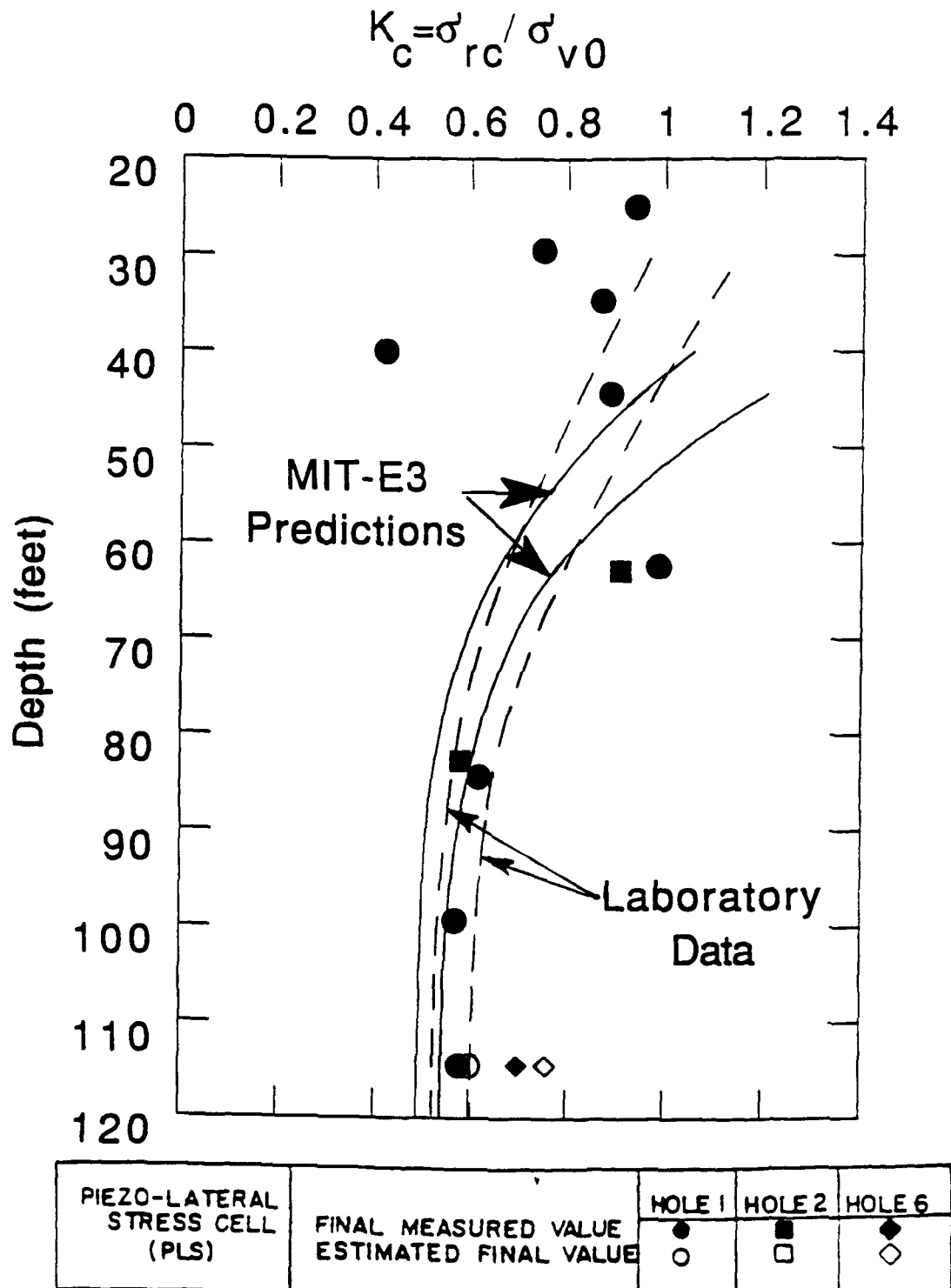


Figure 5.8a Comparison of MIT-E3 Predictions of Radial Stress at End of Consolidation with PLS Cell Measurements for Lower BBC, Saugus Site (after Whittle, 1987)

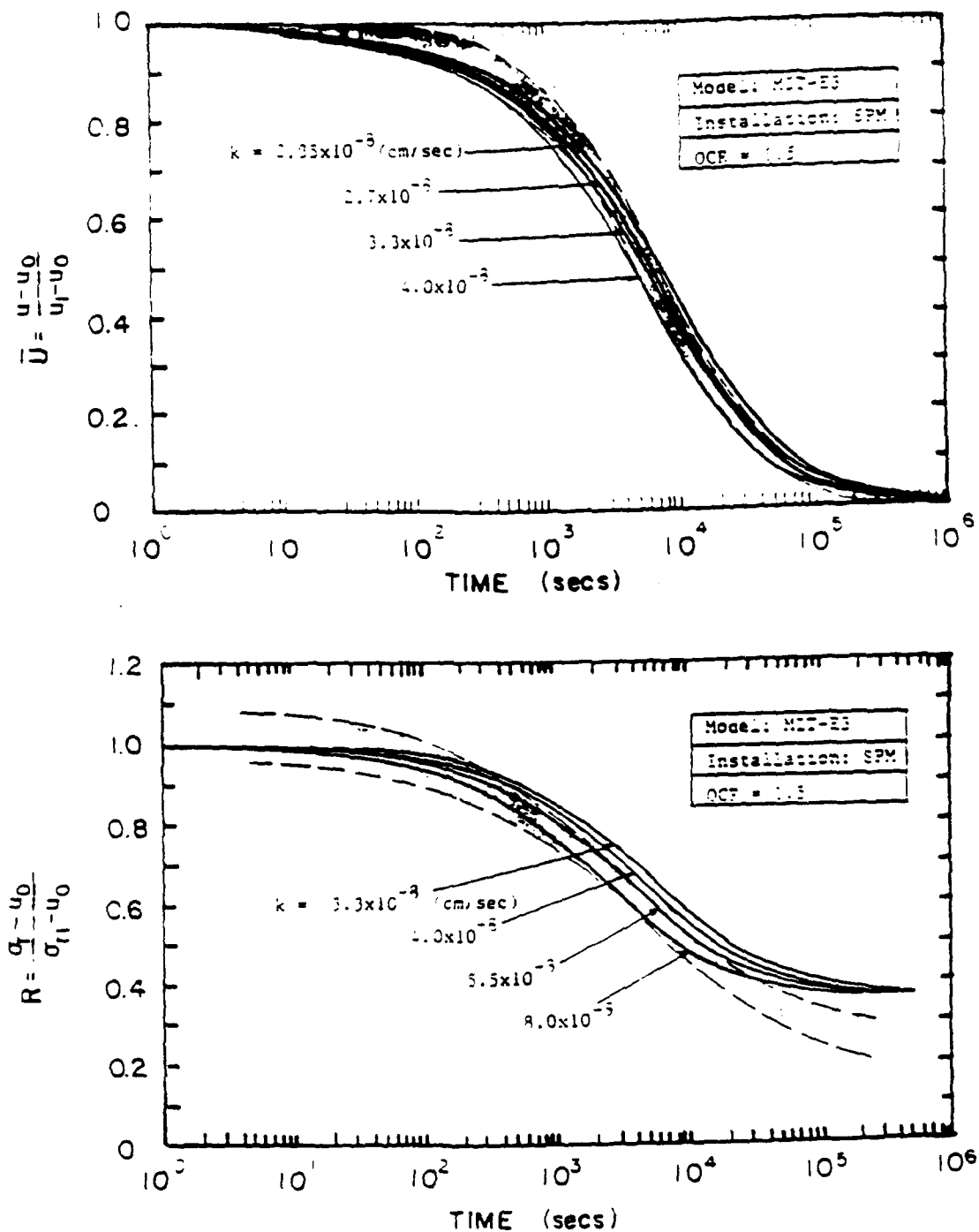


Figure 5.8b Comparison of MIT-E3 Predictions of Total Radial Stress Decay with PLS Cell Measurements for Lower BBC, Saugus Site (after Whittle, 1987)

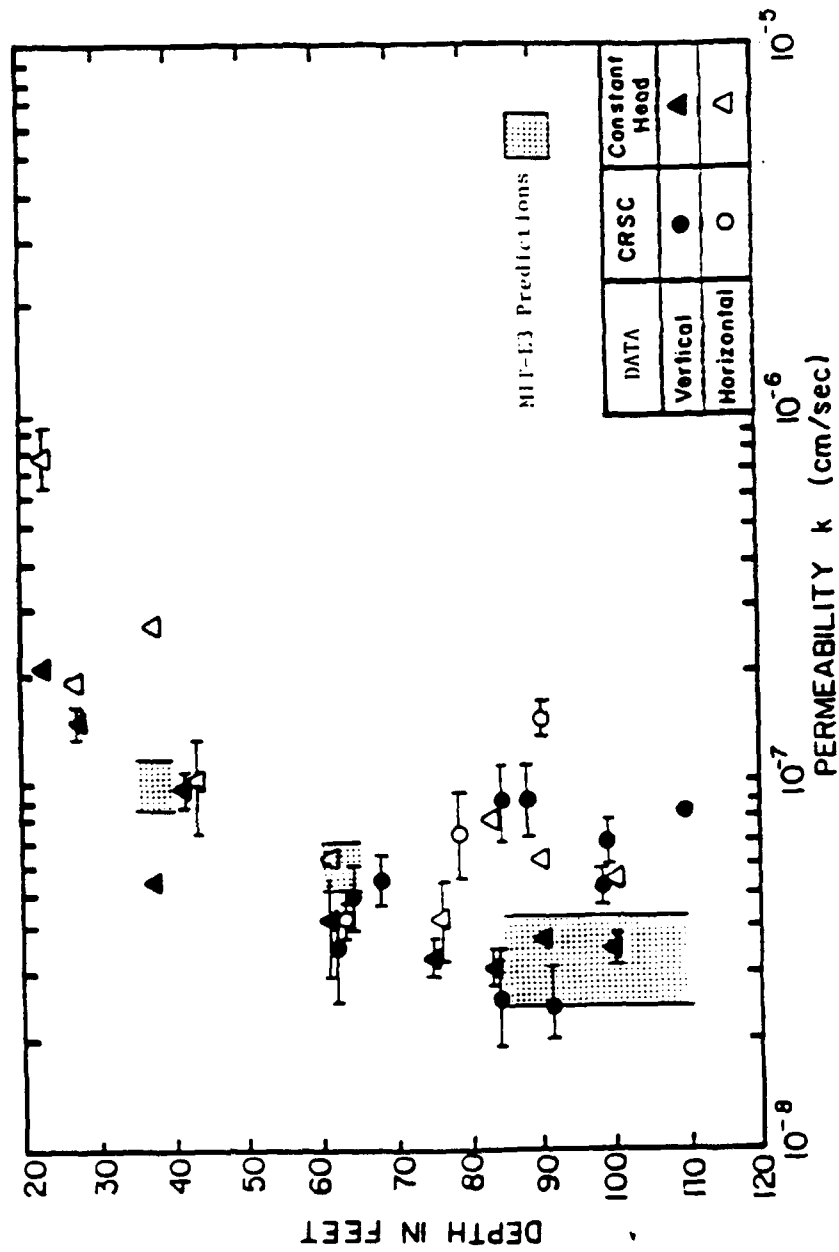


Figure 5.9 Reference Permeability Profile in BBC at the Saugus Site
(after Morrison, 1984)

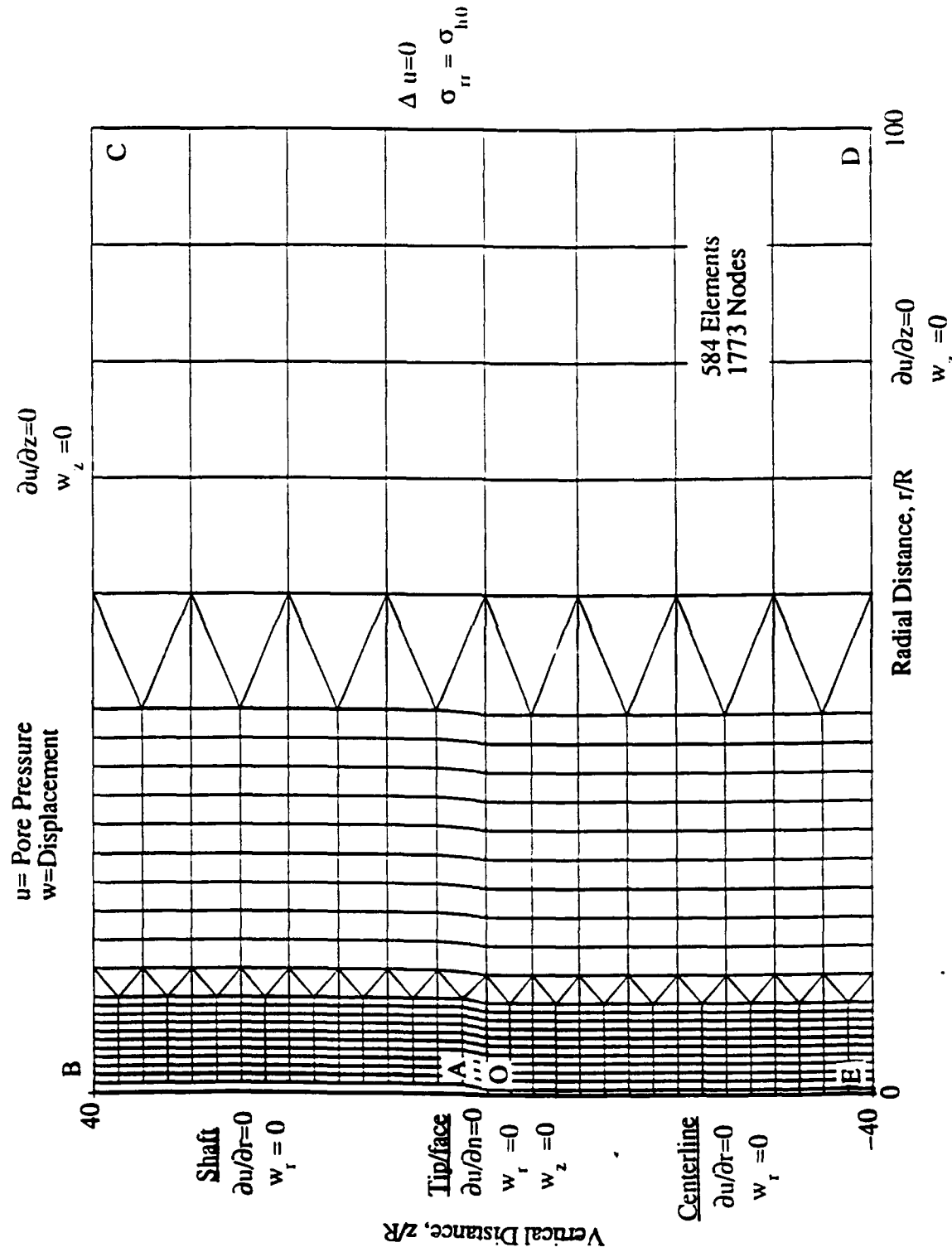


Figure 5.10a Boundary Conditions and Typical Finite Element Mesh for Non-Linear, Coupled Consolidation Analysis Around Simple Pile

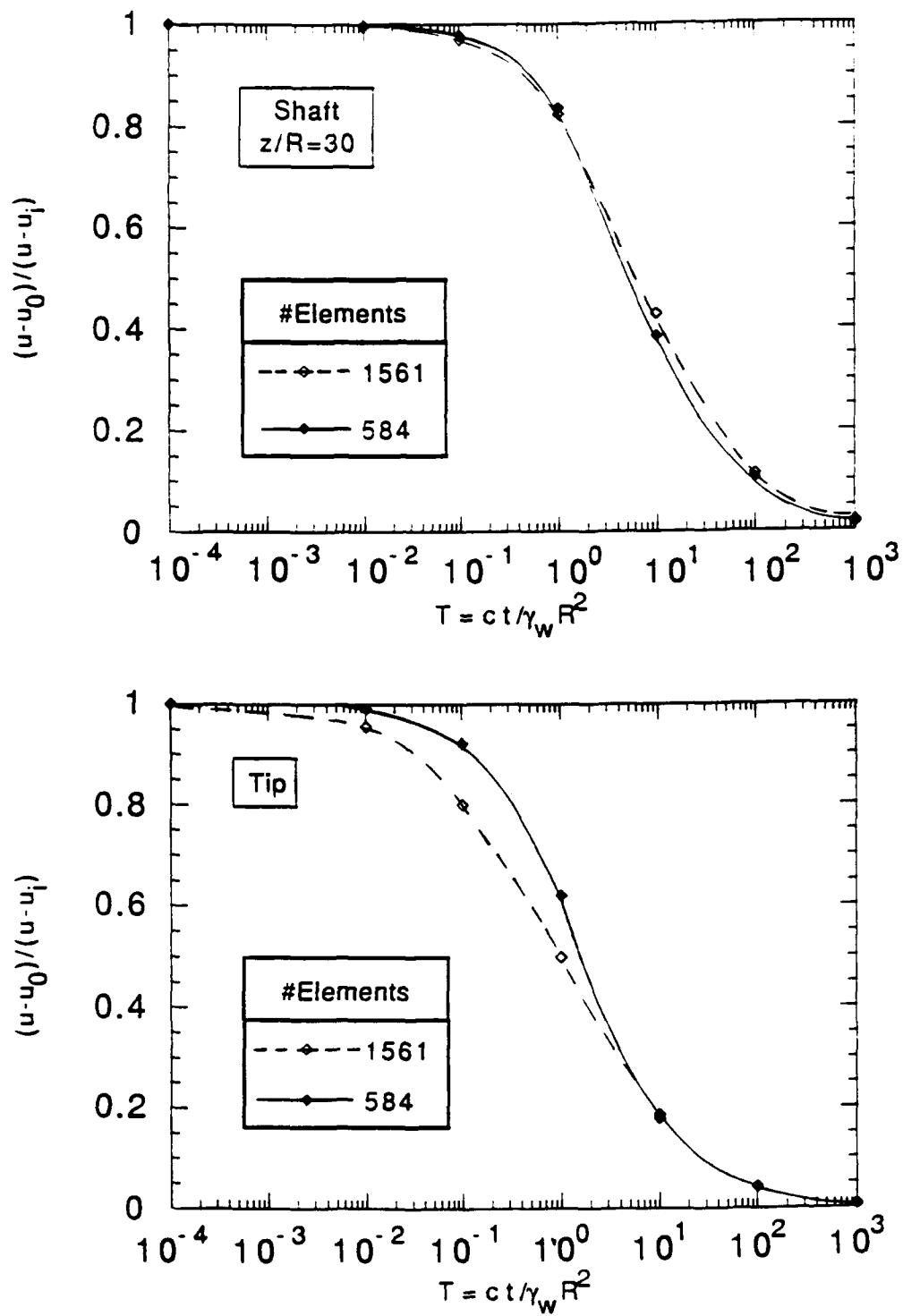


Figure 5.10b Effect of Mesh Refinement on Uncoupled Solutions - MCC, BBC, OCR=1 Installation Conditions

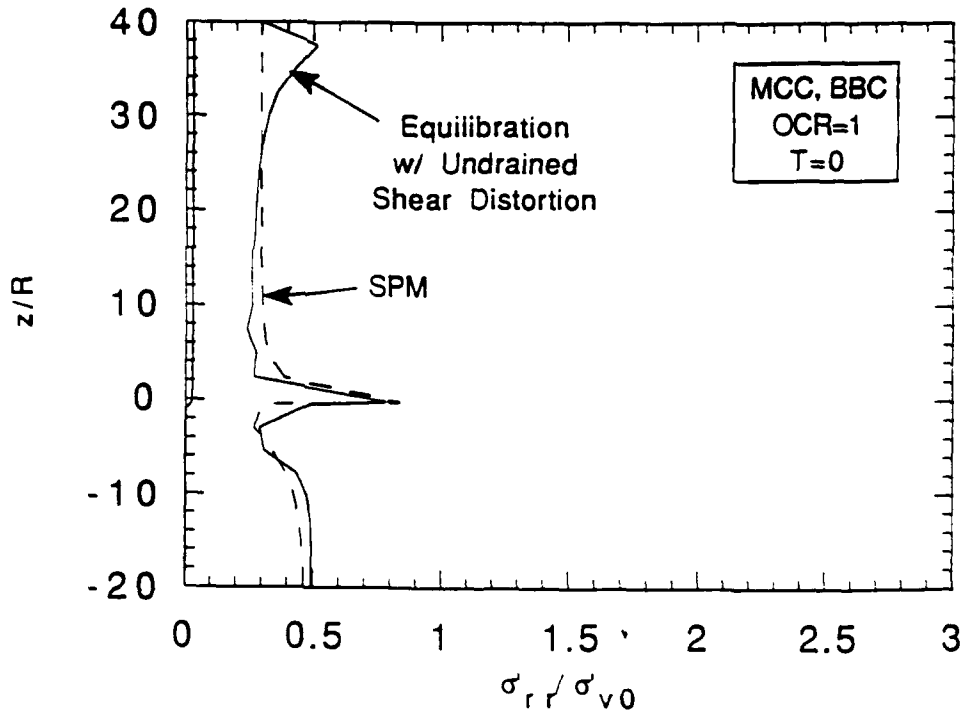
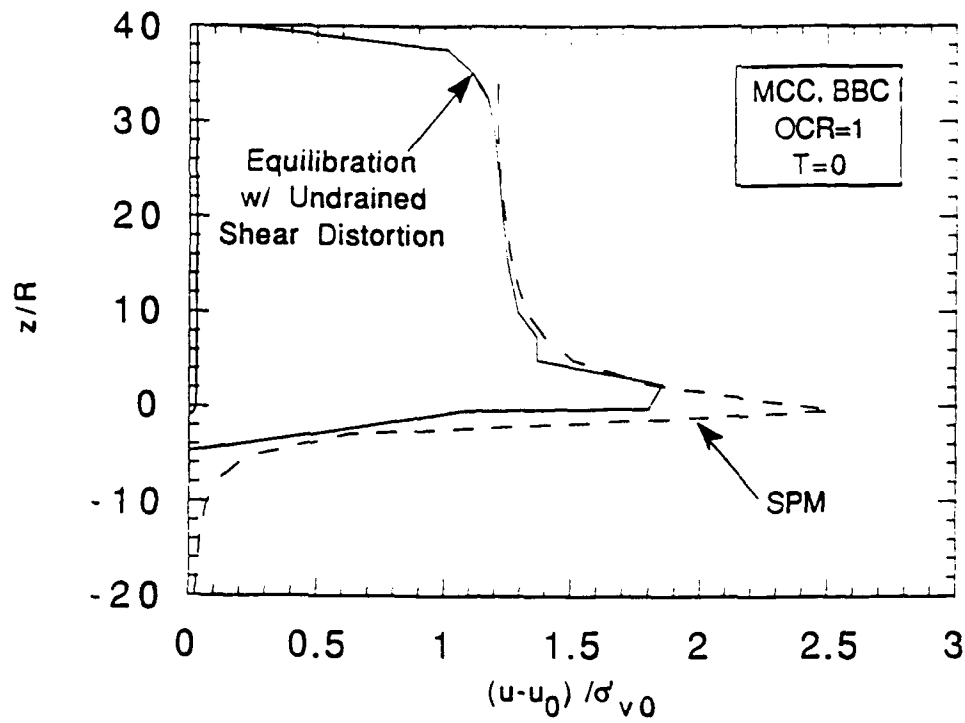


Figure 5.11a Stress Conditions along Simple Pile Following Equilibration by Shear Distortion - MCC, BBC, OCR=1

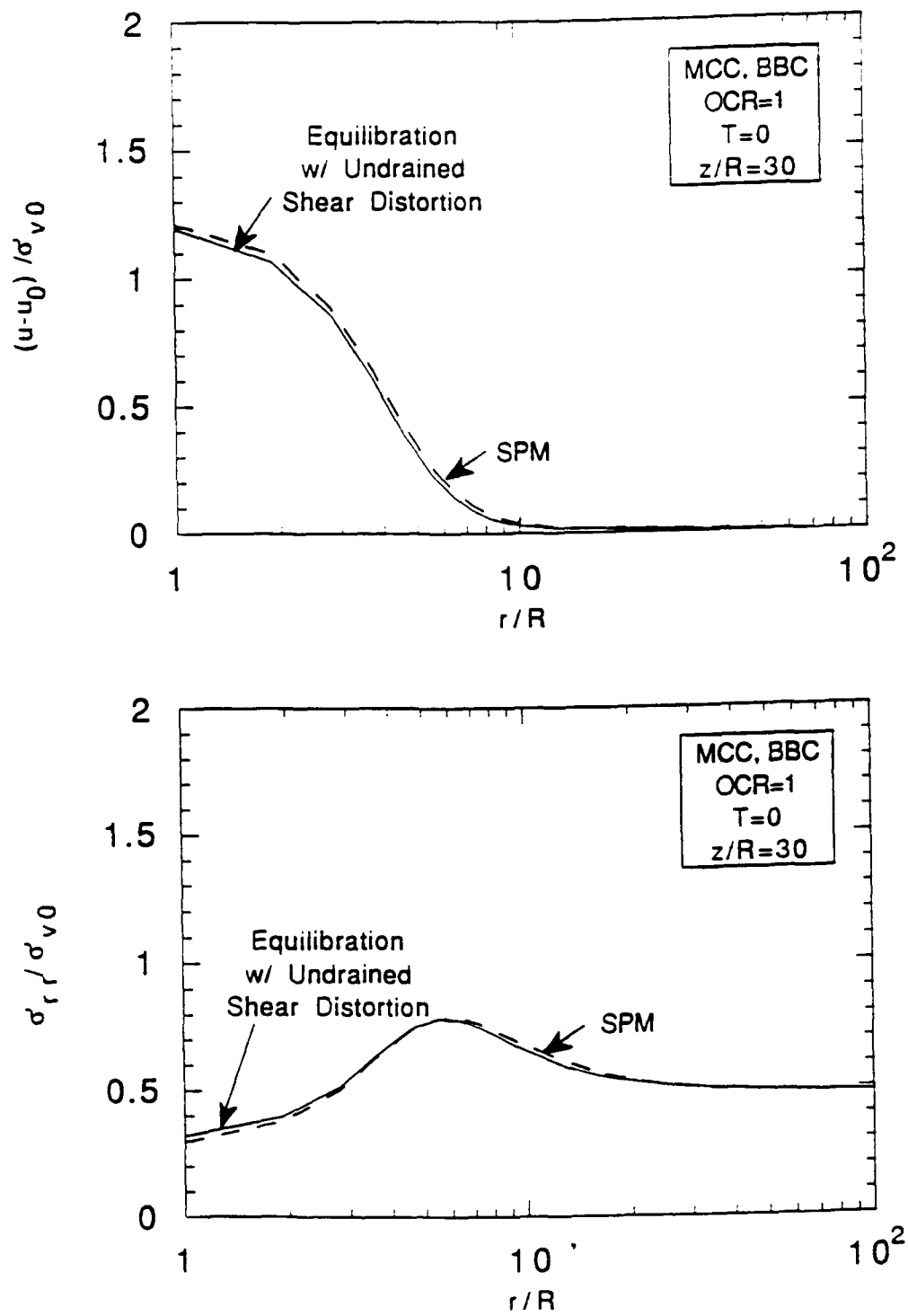


Figure 5.11b Radial Distribution of Stresses Far above Simple Pile Tip Following Equilibration by Shear Distortion - MCC, BBC, OCR=1

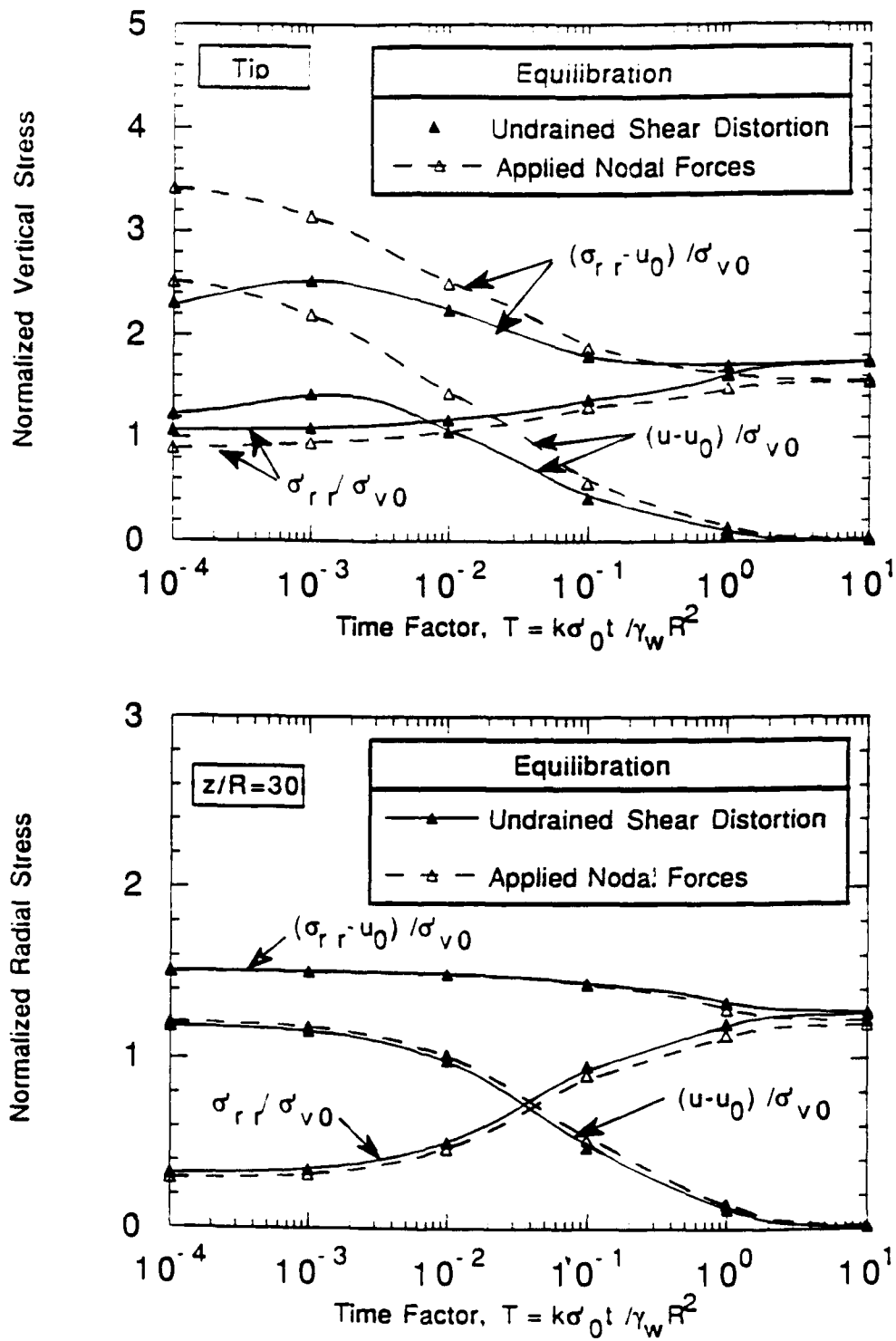


Figure 5.12 Predicted Tip and Shaft Stress Histories for Different Equilibration Methods - MCC, BBC, OCR=1

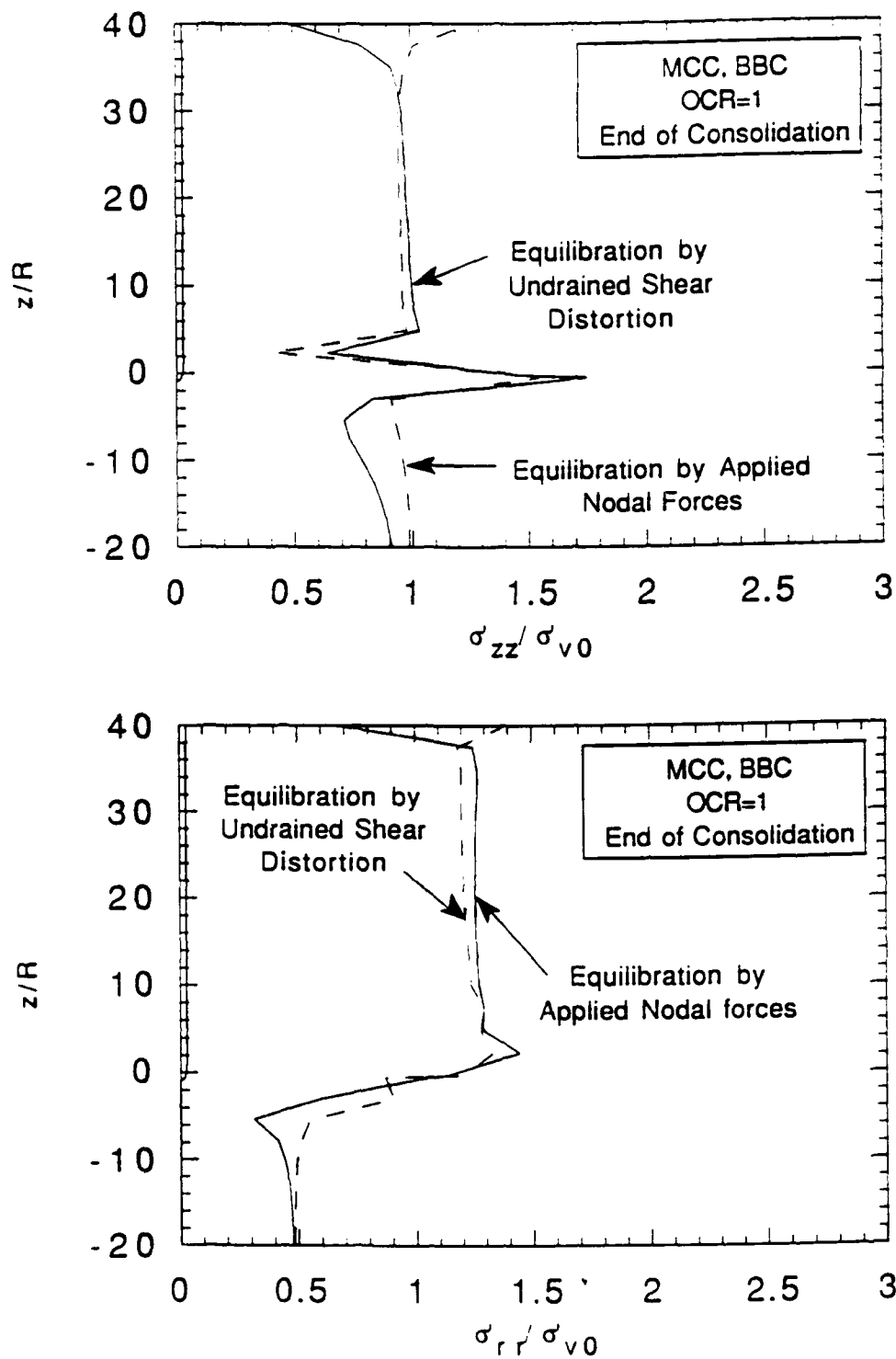


Figure 5.13a Setup Stresses along Simple Pile Boundary for Different Equilibration Methods - MCC, BBC, OCR=1

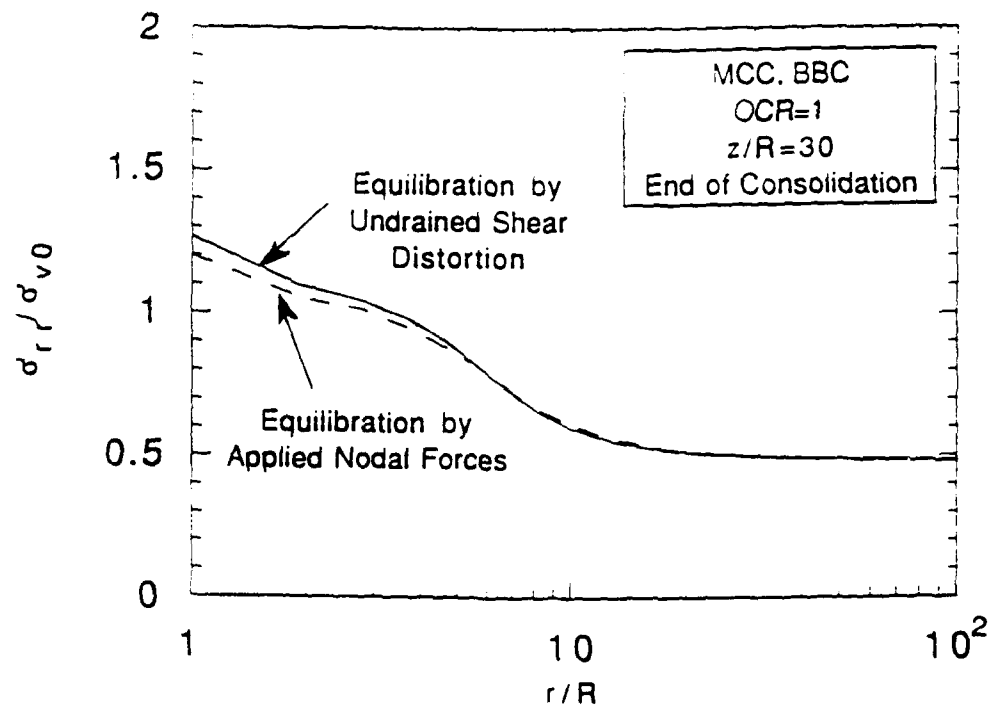


Figure 5.13b Radial Distribution of Setup Stresses Far above Simple Pile Tip for Different Equilibration Methods - MCC, BBC, OCR=1

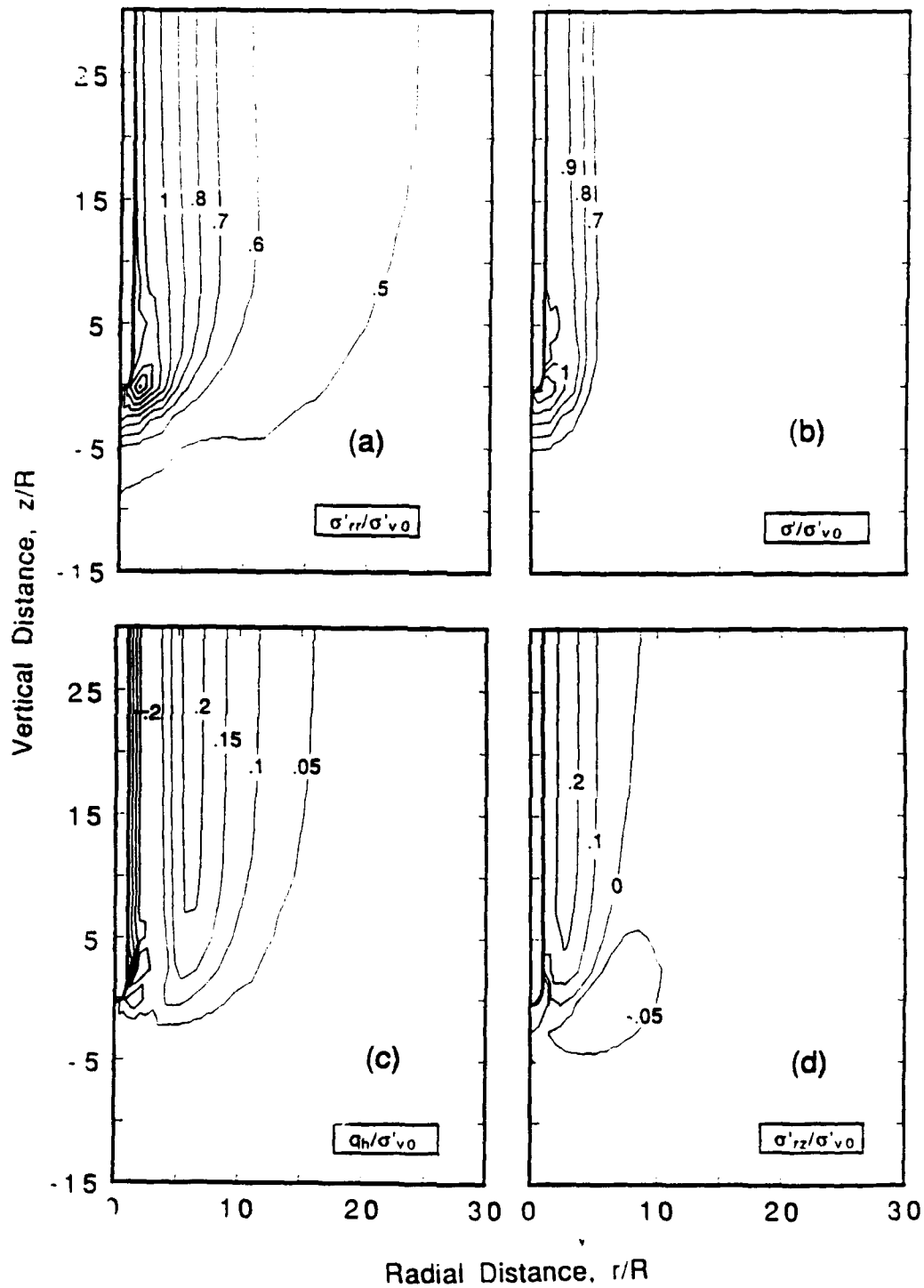


Figure 5.14 Contours of Consolidation Stresses Predicted from Non-Linear, Coupled Solutions Using the MCC Soil Model with BBC Parameters: OCR=1

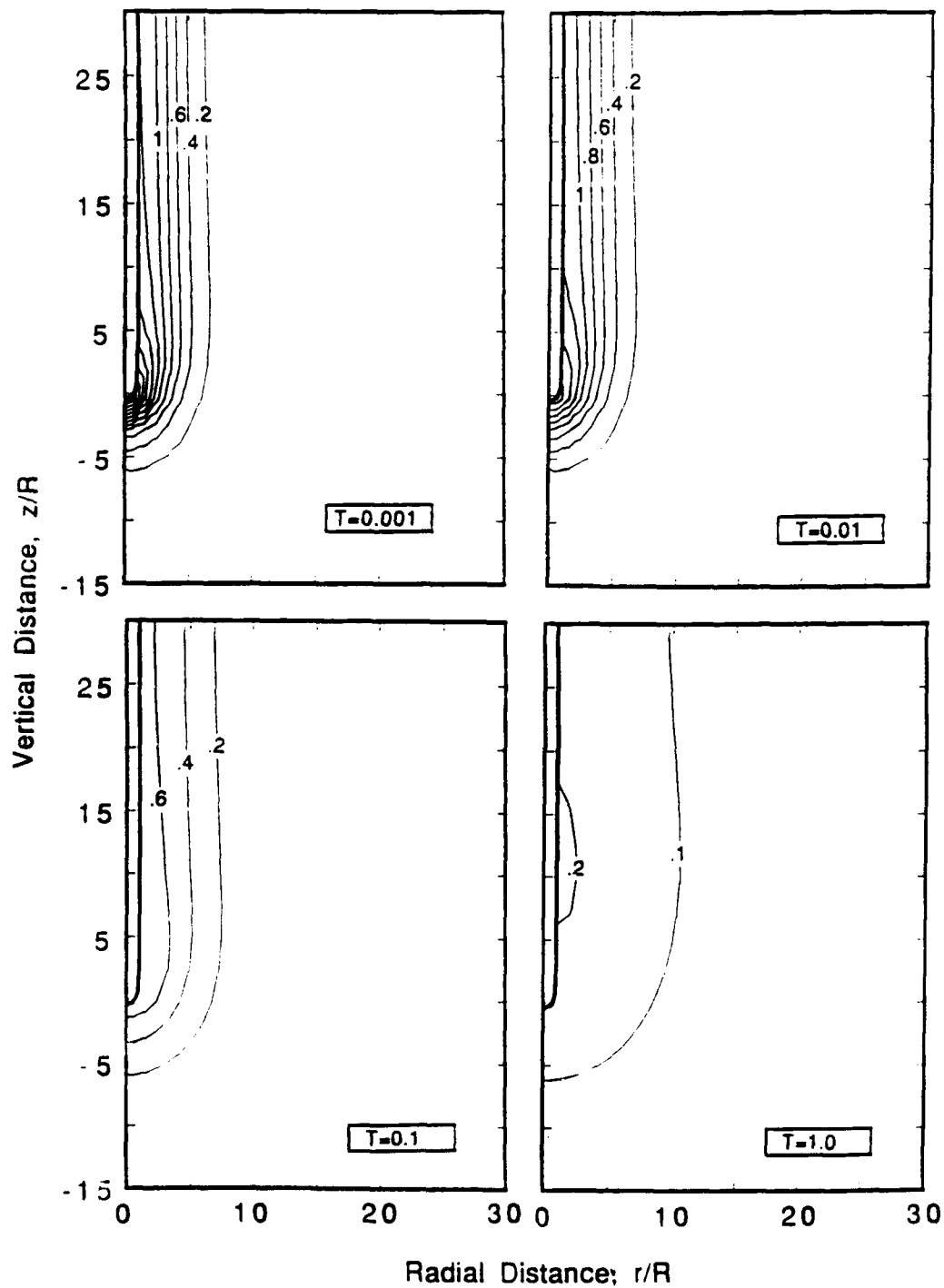


Figure 5.15 Contours of Excess Pore Pressures at Selected Times Predicted from Non-Linear, Coupled Solutions Using the MCC Soil Model with BBC Parameters: $OCR=1$

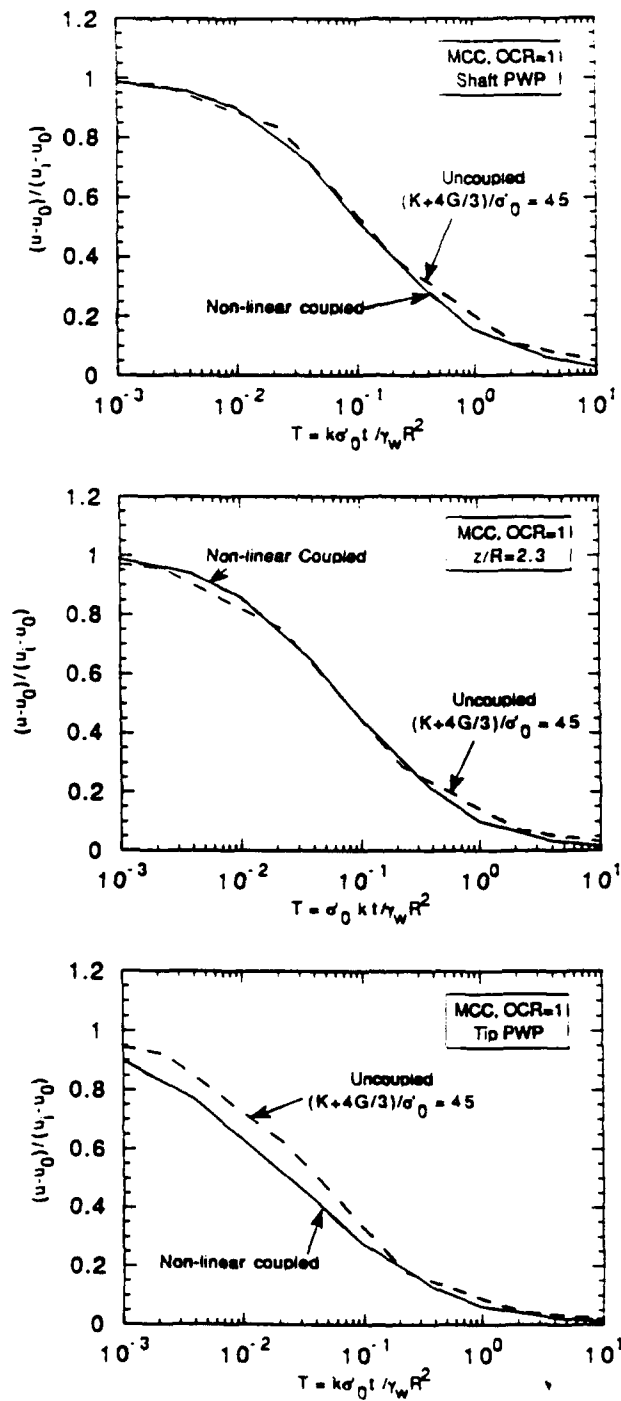


Figure 5.16 The Effect of Non-linear Coupling on Pore Pressure Dissipation Curves

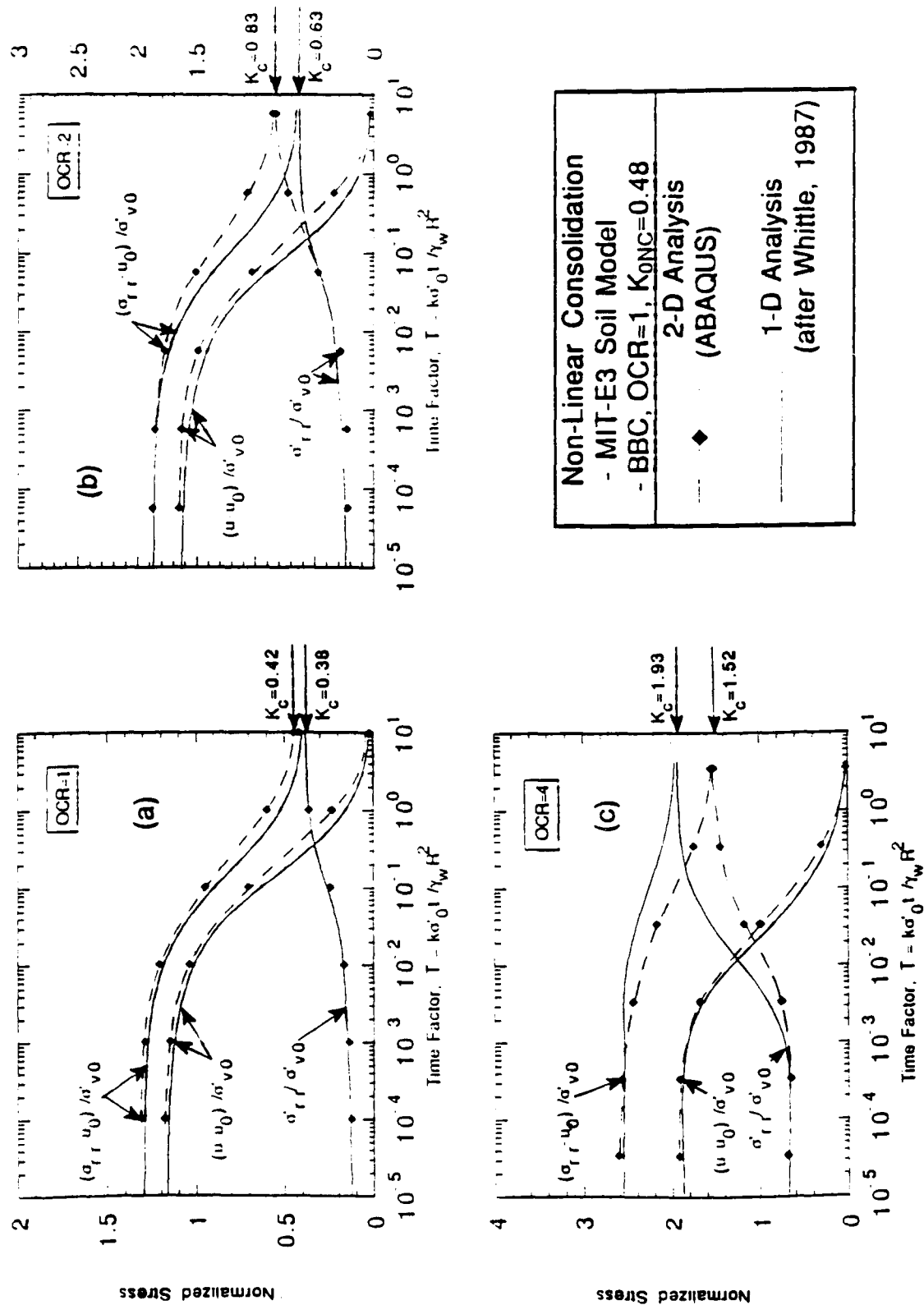


Figure 5.17 Time History of Radial Stresses on Simple Pile Shaft ($z/R=30$) Predicted from Non-Linear, Coupled Solutions Using the MIT-E3 Soil Model

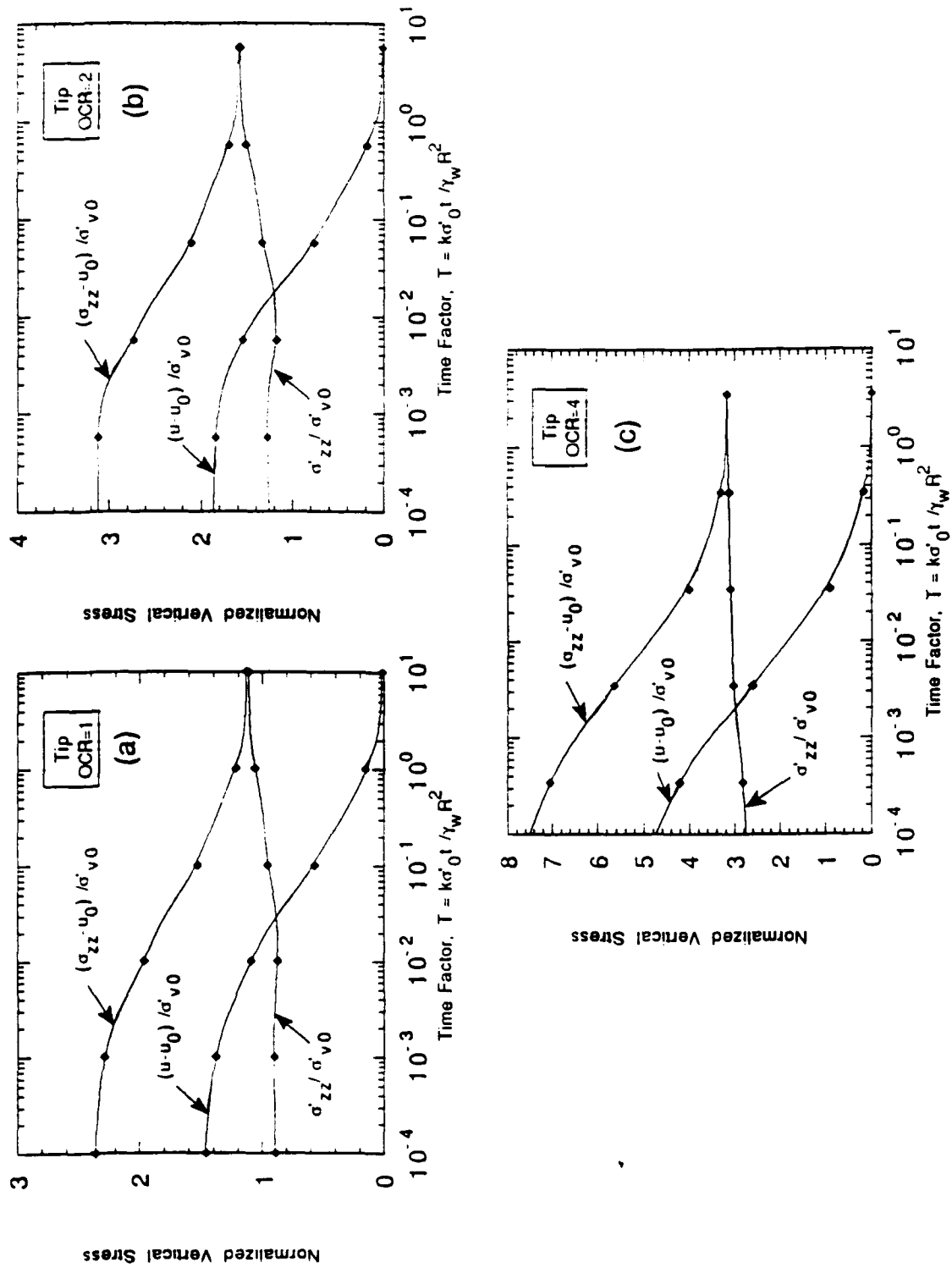


Figure 5.18 Time History of Vertical Stresses at Simple Pile Tip Predicted from Non-Linear, Coupled Solutions Using the MIT-E3 Soil Model

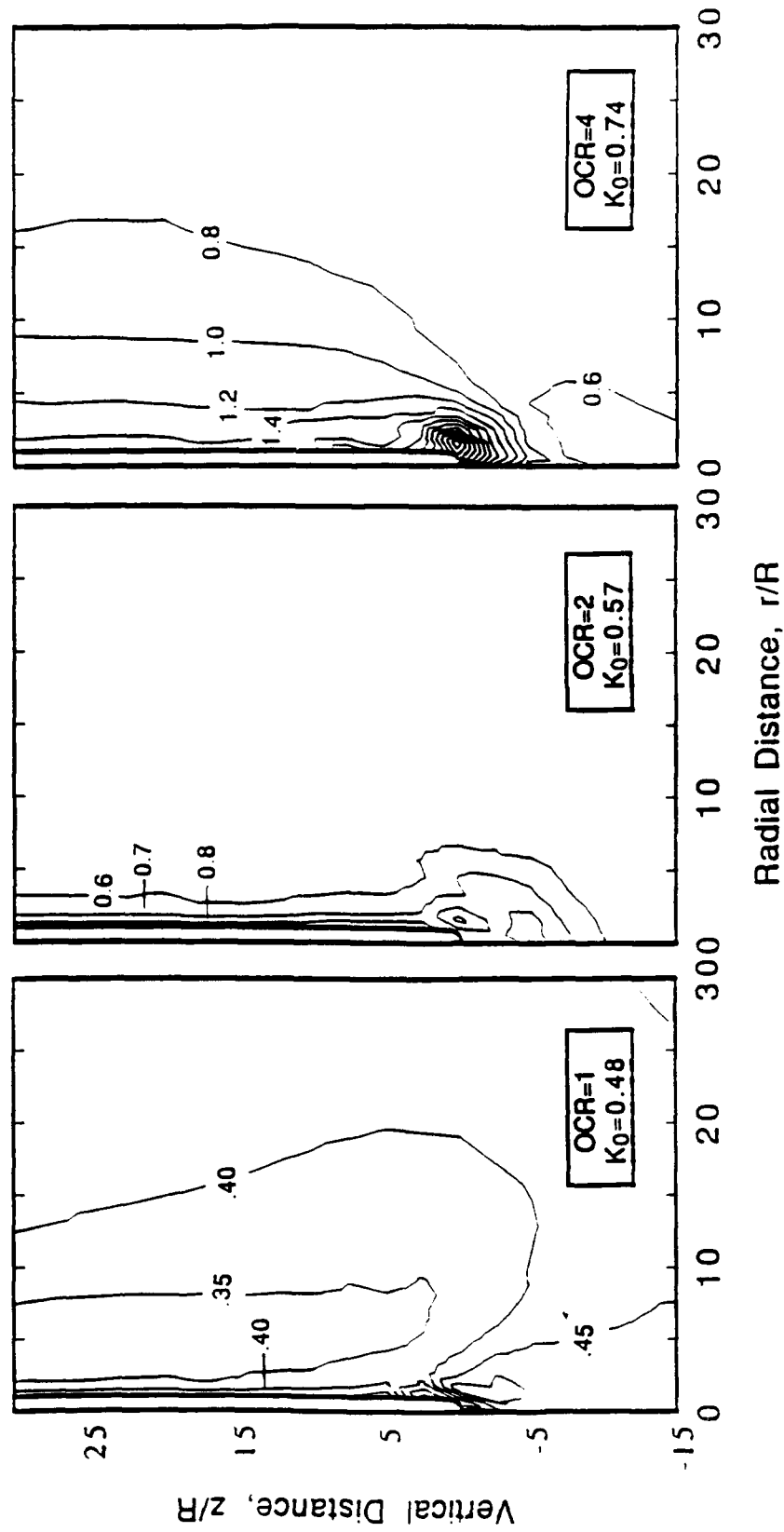


Figure 5.19 Contours of Consolidation Stresses Predicted from Non-Linear, Coupled Solutions Using the MIT-E3 Soil Model with BBC Parameters: a) Radial Effective Stress, σ'_r/σ'_{v0}

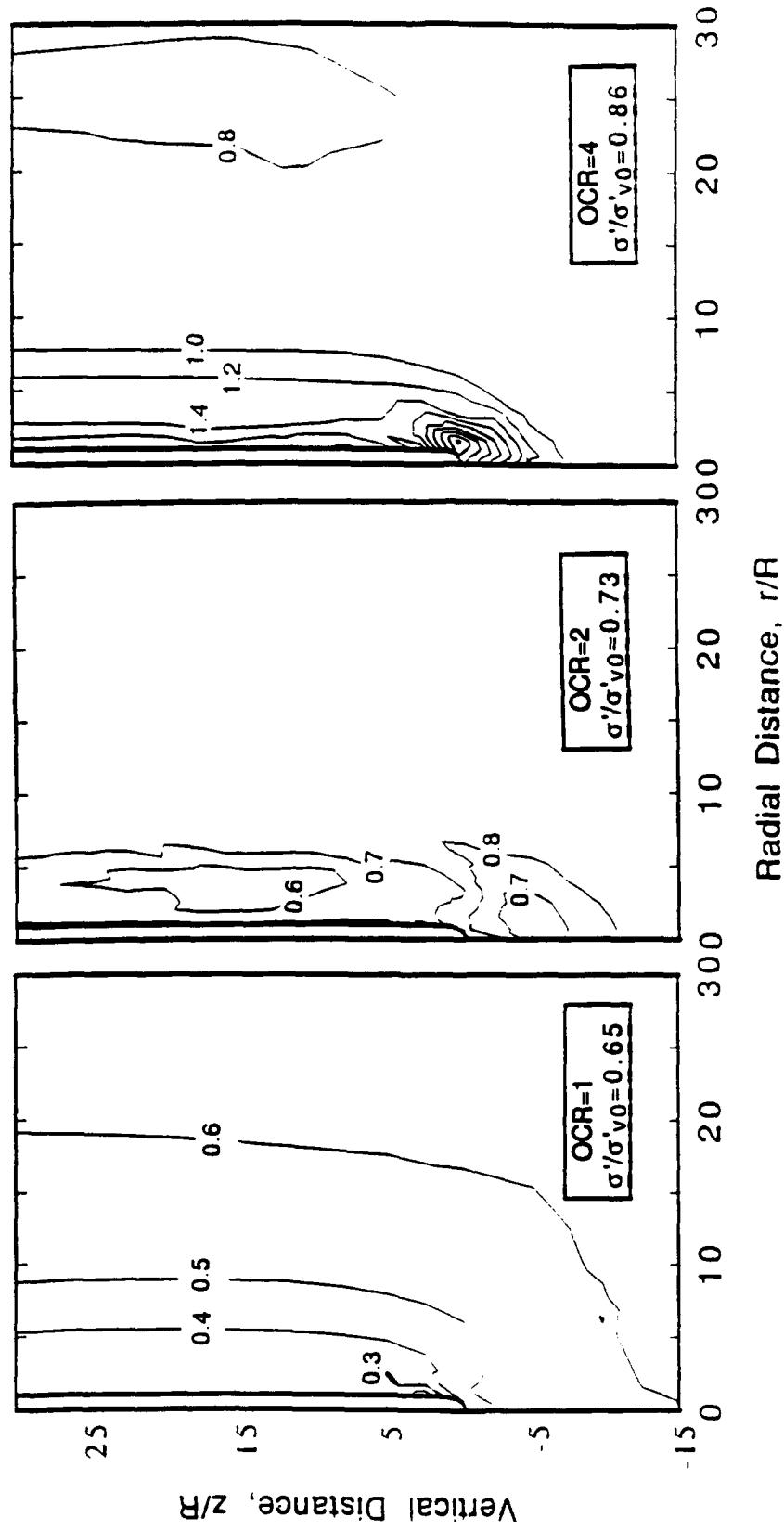


Figure 5.19 (contd.) Contours of Consolidation Stresses Predicted from Non-Linear, Coupled Solutions Using the MIT-E3 Soil Model with BBC Parameters: b) Mean Effective Stress, σ'/σ'_{v0}

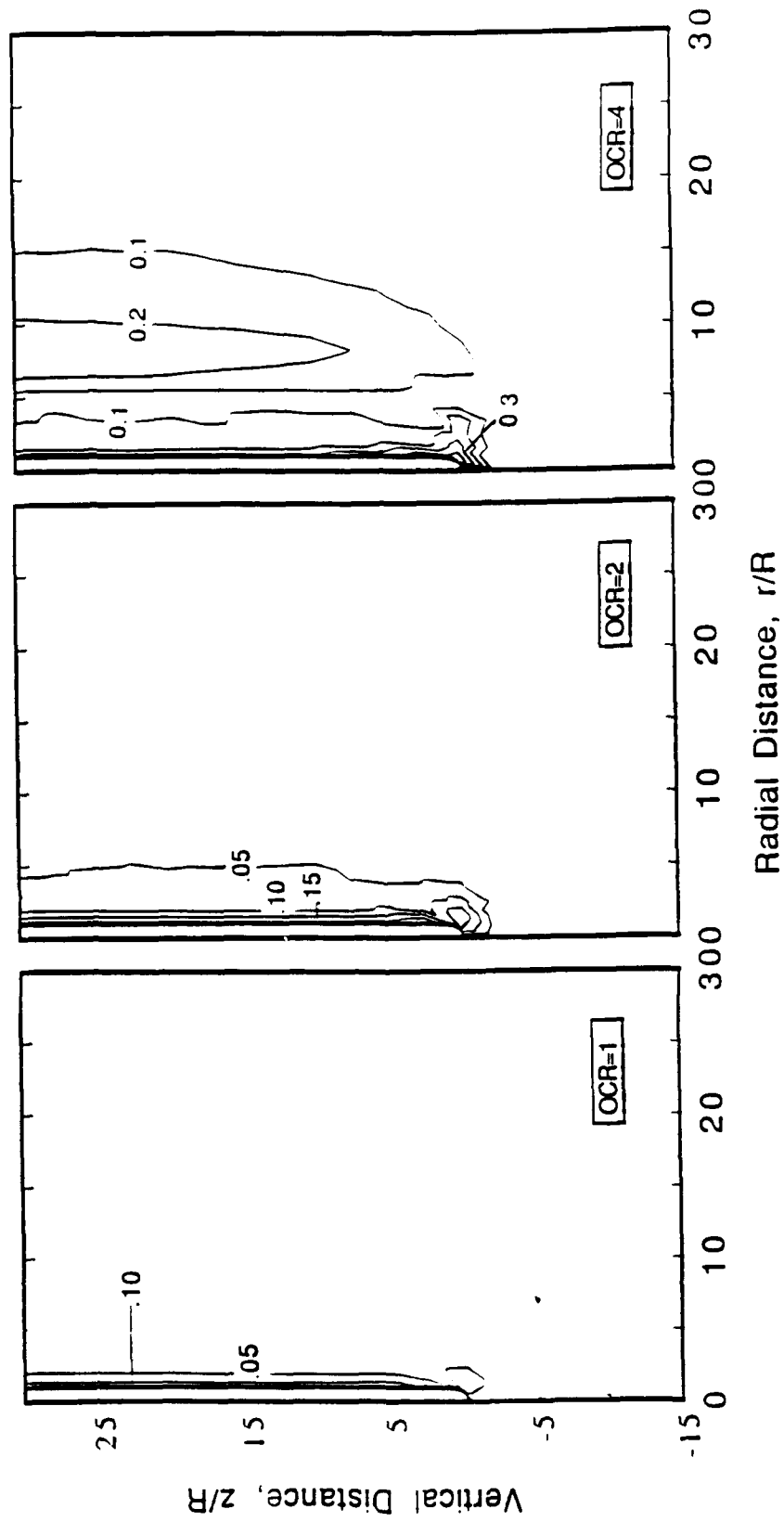


Figure 5.19 (contd.) Contours of Consolidation Stresses Predicted from Non-Linear, Coupled Solutions Using the MIT-E3 Soil Model with BBC Parameters: c) Cavity Shear Stress, $q(t)/\sigma'_{v(0)}$

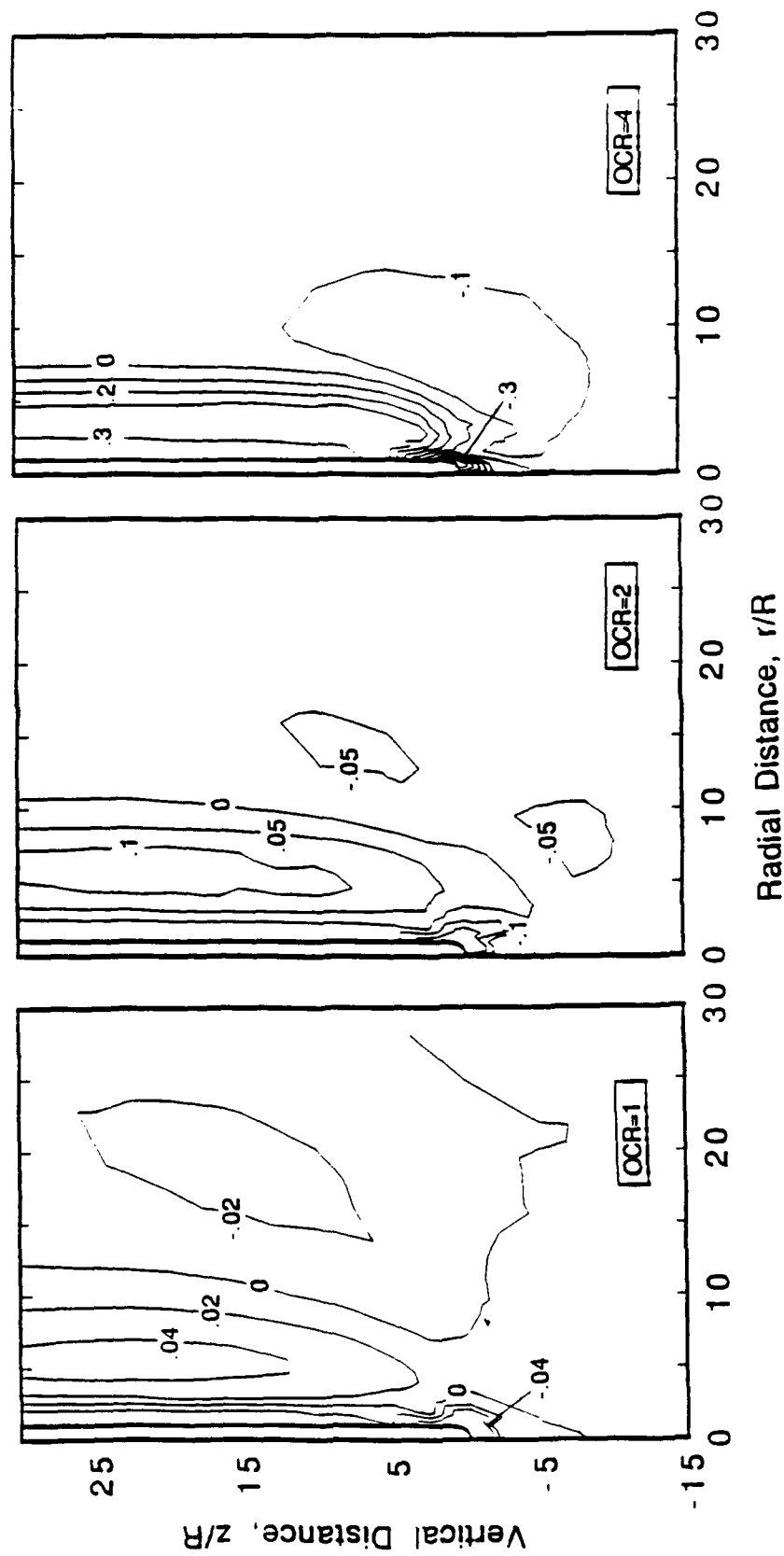


Figure 5.19 (contd.) Contours of Consolidation Stresses Predicted from Non-Linear, Coupled Solutions Using the MIT-E3 Soil Model with BBC Parameters: d) Meridional Shear Stress, $\sigma'_{rz}/\sigma'_{v0}$

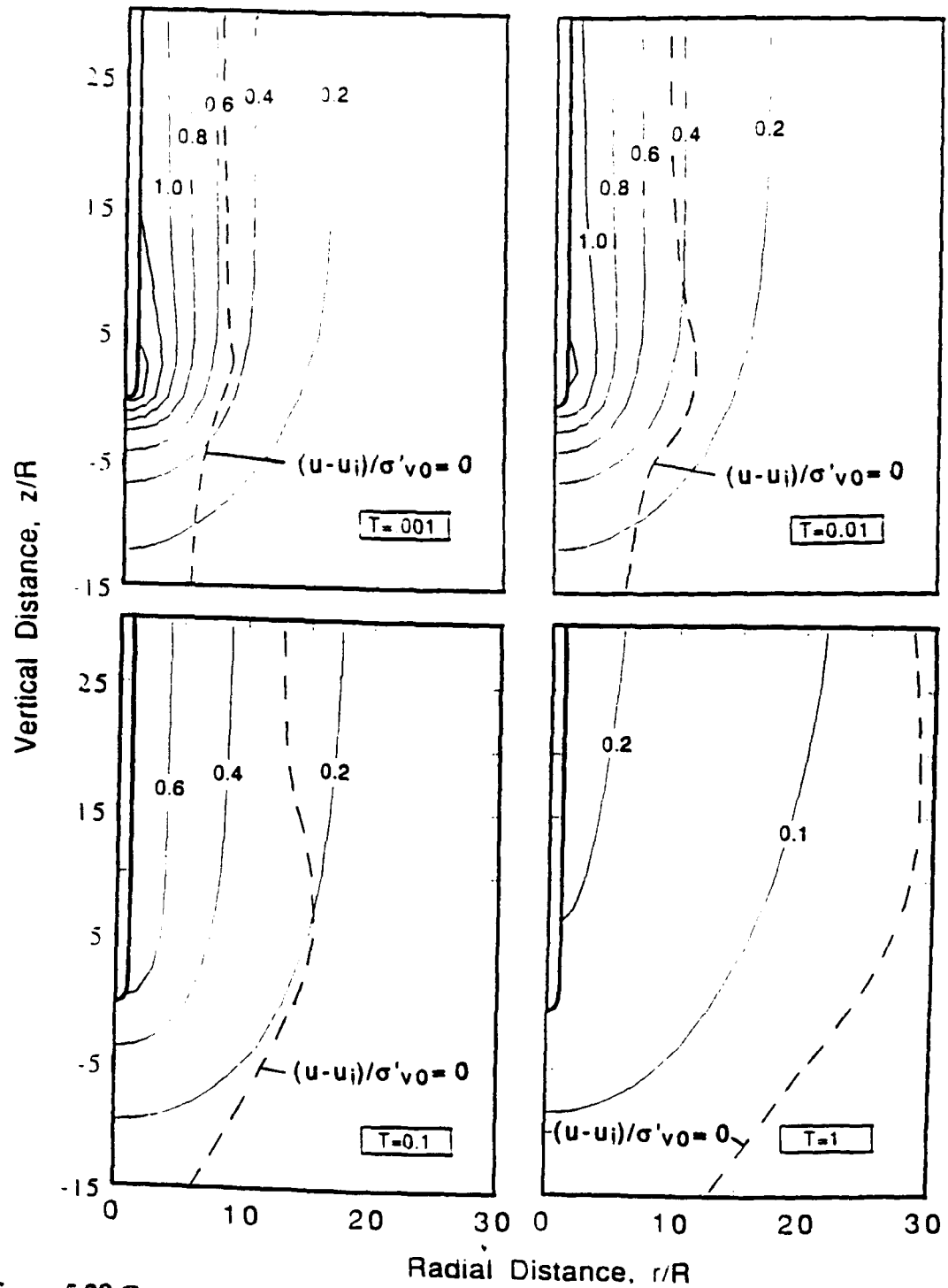


Figure 5.20 Contours of Excess Pore Pressures at Selected Times Predicted from Non-Linear, Coupled Solutions Using the MIT-E3 Soil Model with BBC Parameters: a) $\text{OCR}=1$

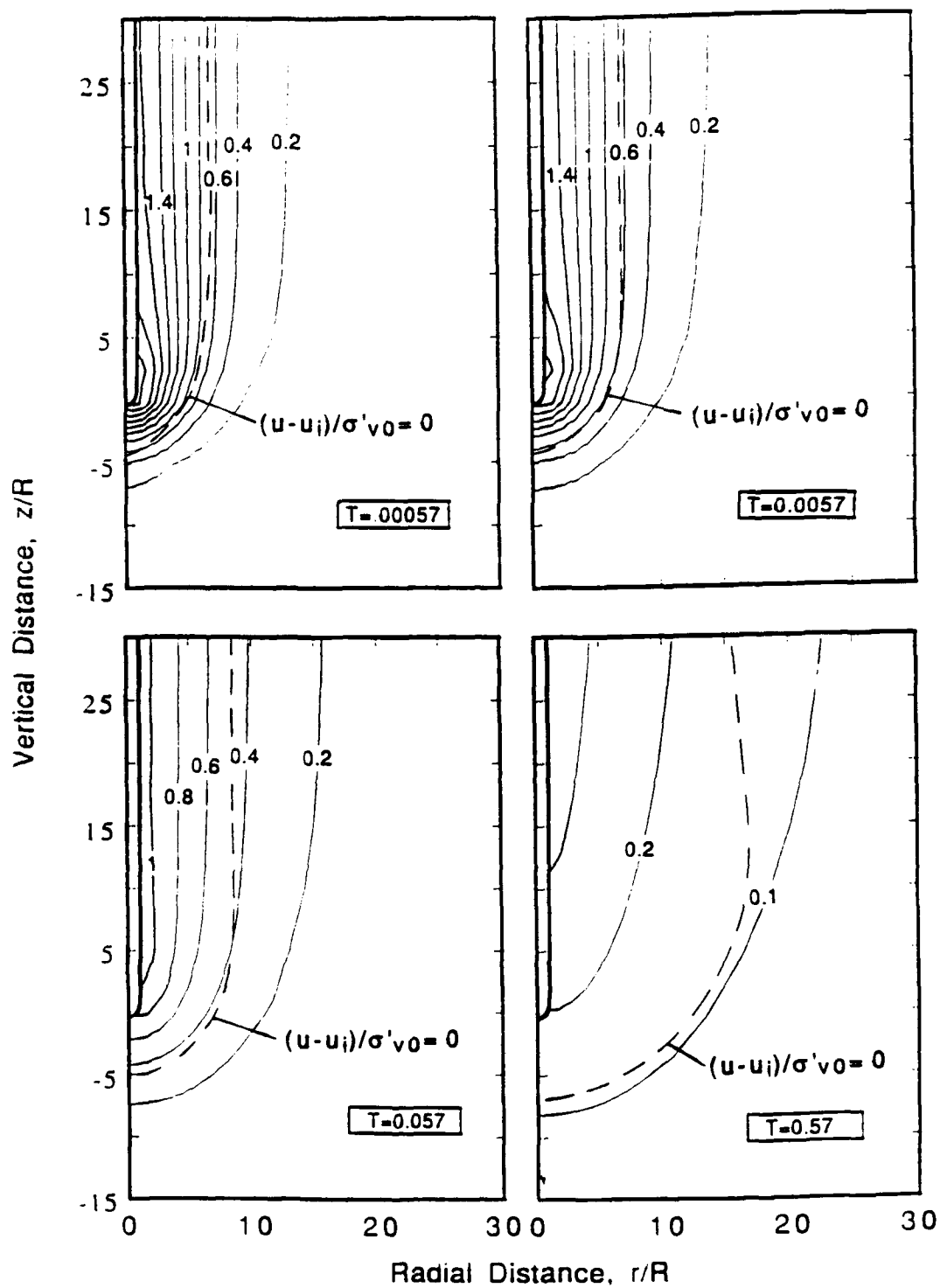


Figure 5.20 (contd.) Contours of Excess Pore Pressures at Selected Times Predicted from Non-Linear, Coupled Solutions Using the MIT-E3 Soil Model with BBC Parameters: b) OCR=2

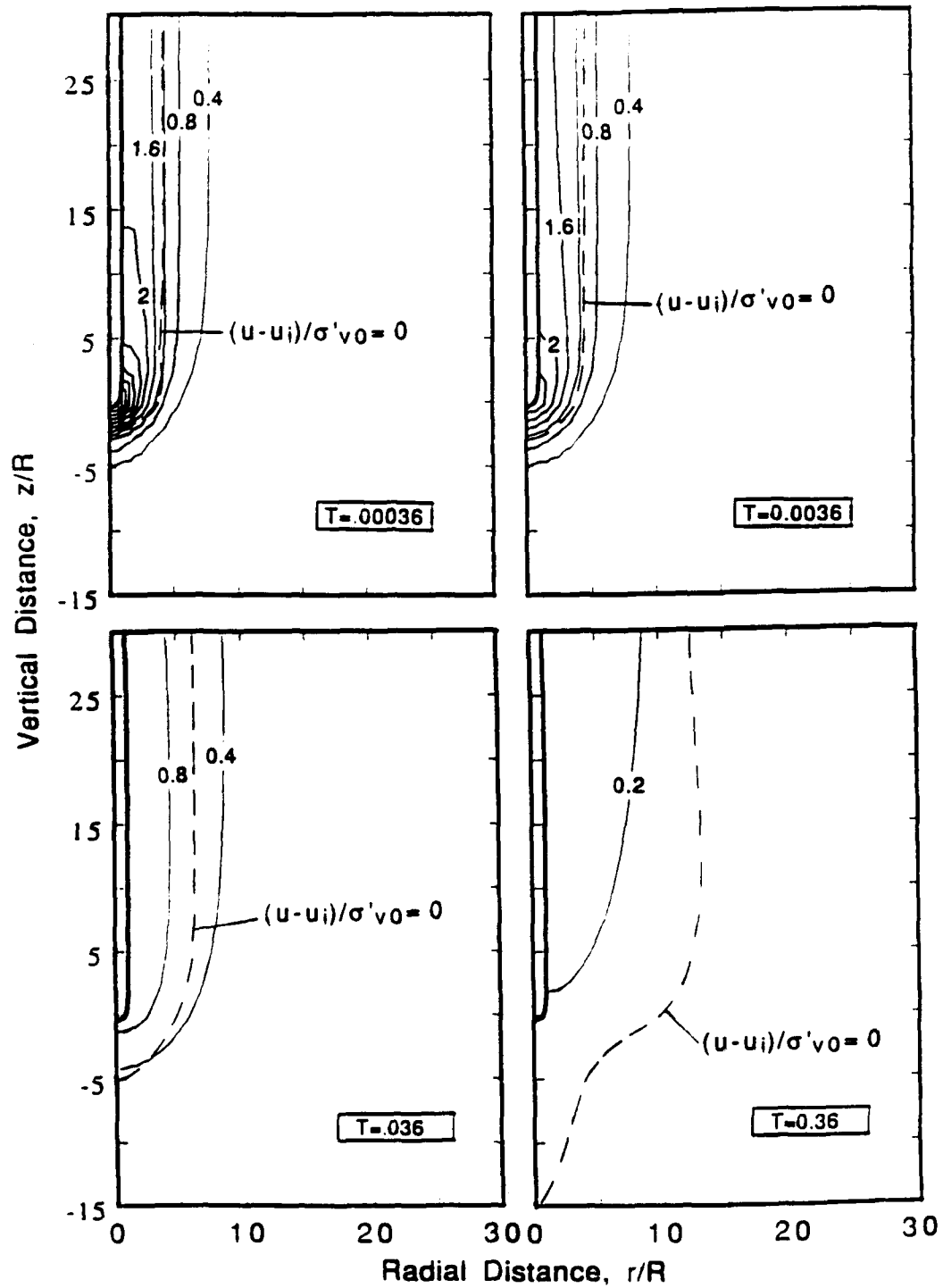


Figure 5.20 (contd.) Contours of Excess Pore Pressures at Selected Times Predicted from Non-Linear, Coupled Solutions Using the MIT-E3 Soil Model with BBC Parameters: c) $OCR=4$

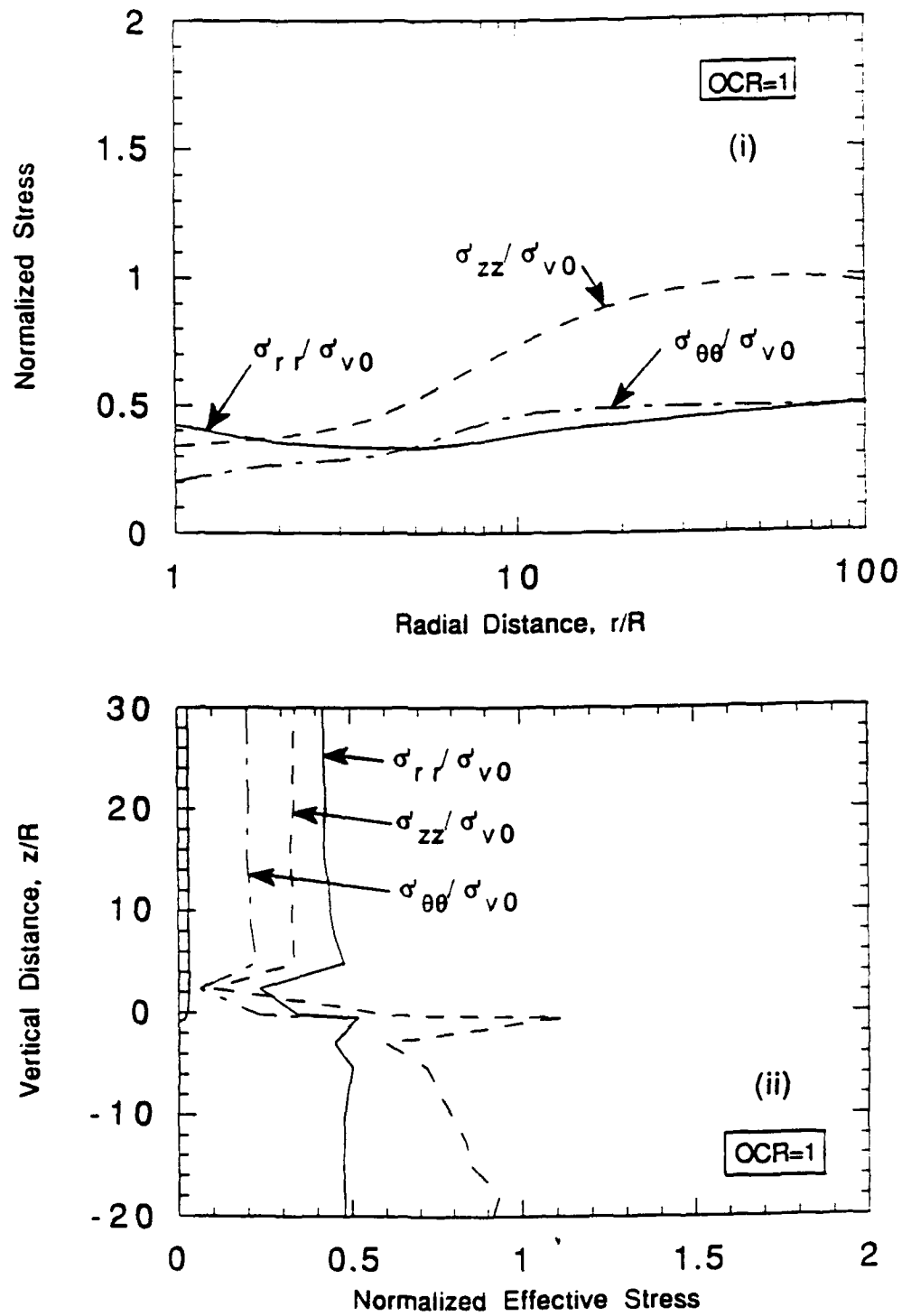


Figure 5.21 Distribution of Consolidation Effective Stresses on Simple Pile Boundary Predicted from Non-Linear, Coupled Solutions Using the MIT-E3 Soil Model: a) $OCR=1$

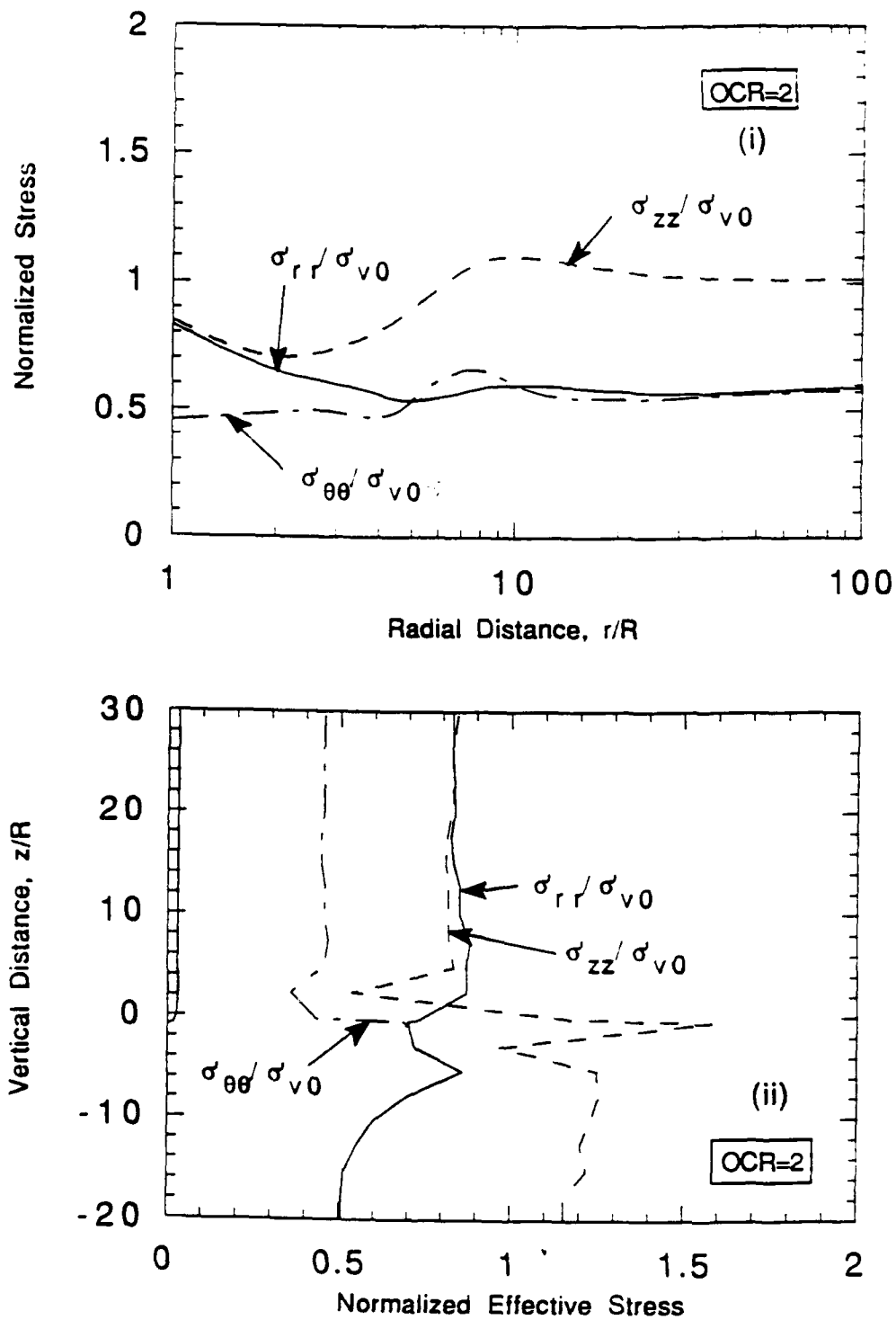


Figure 5.21 (contd.) Distribution of Consolidation Effective Stresses on Simple Pile Boundary Predicted from Non-Linear, Coupled Solutions Using the MIT-E3 Soil Model:
b) OCR=2

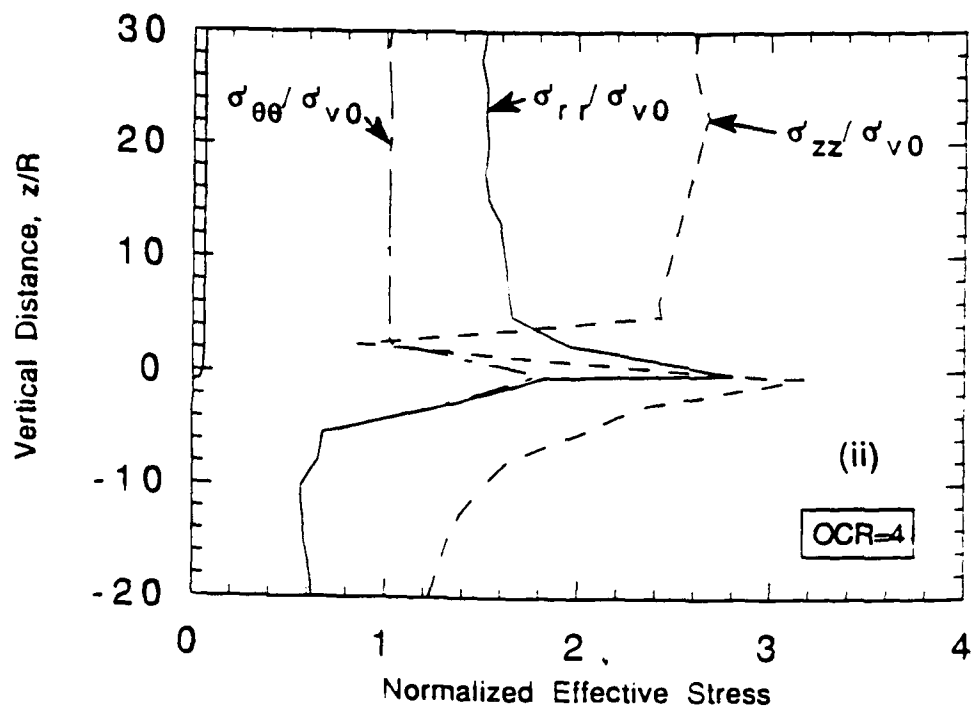
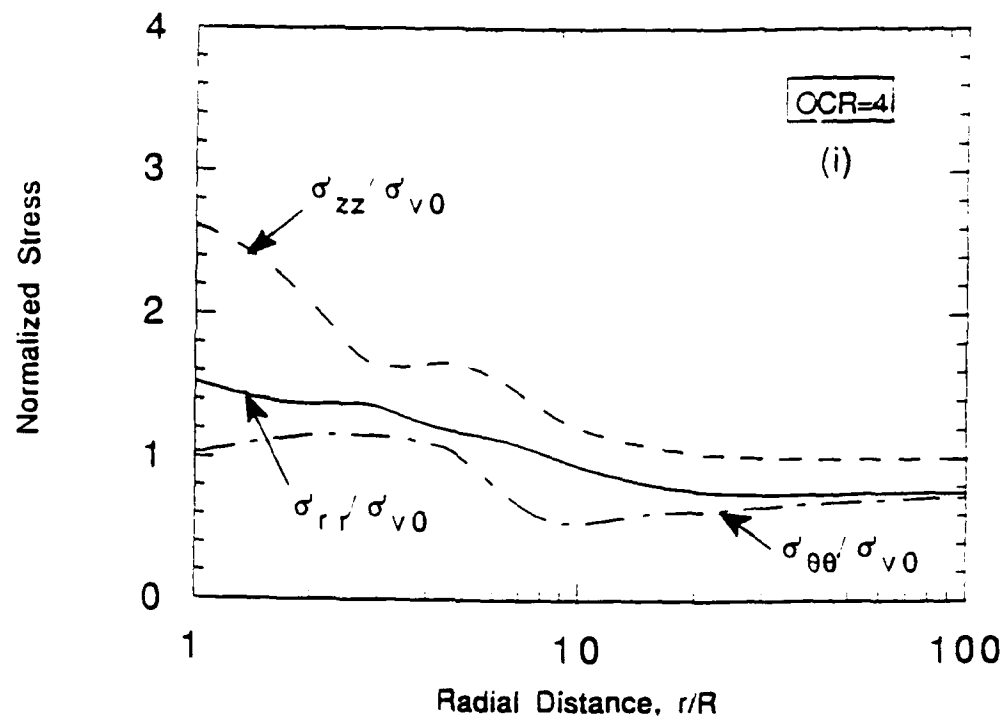


Figure 5.21 (contd.) Distribution of Consolidation Effective Stresses on Simple Pile Boundary Predicted from Non-Linear, Coupled Solutions Using the MIT-E3 Soil Model:
c) $OCR=4$

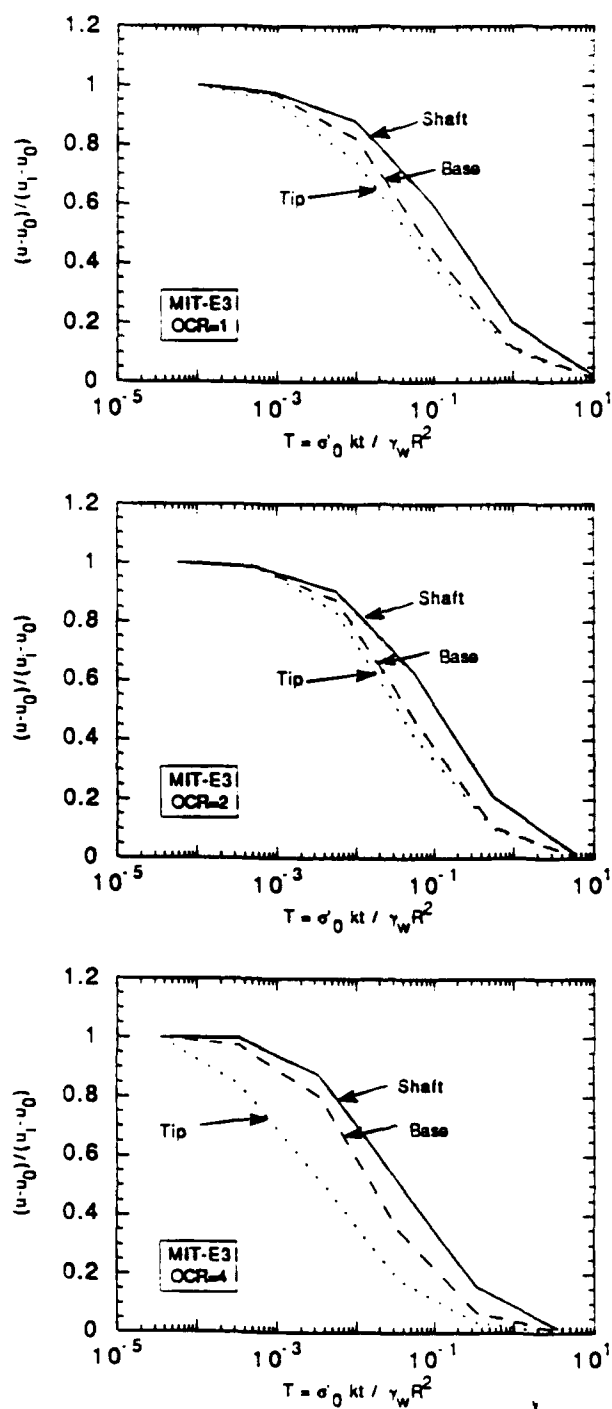


Figure 5.22 The Effect of Filter Location on Pore Pressure Dissipation Curves (Non-linear, Coupled Analysis)

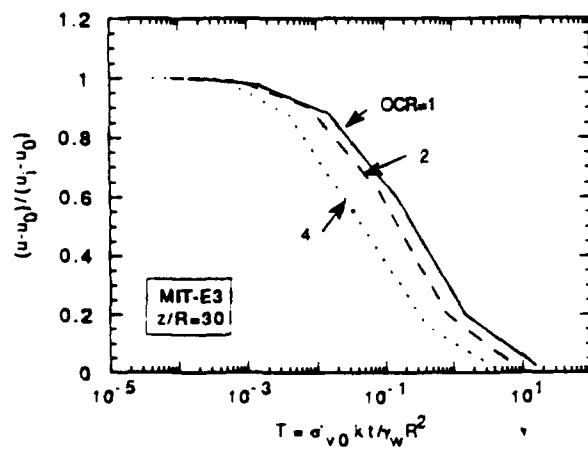
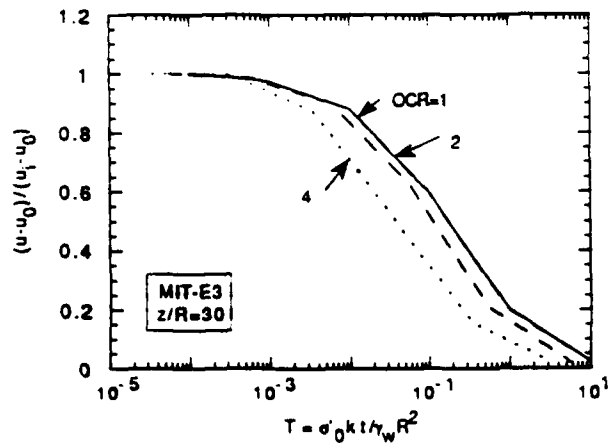
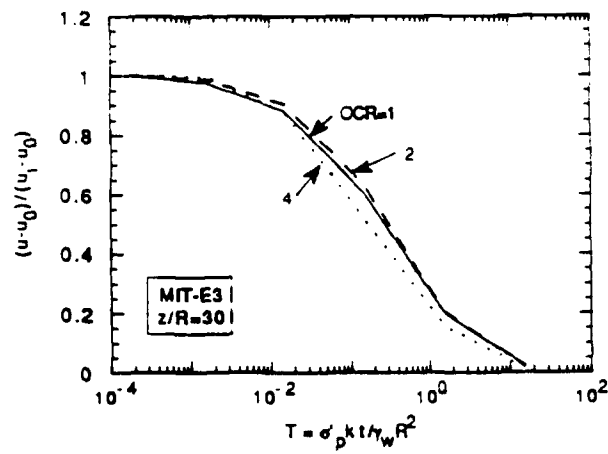


Figure 5.23a The Effect of Stress History on Pore Pressure Dissipation Curves - Shaft Pore Pressures (Non-linear, Coupled Analysis)

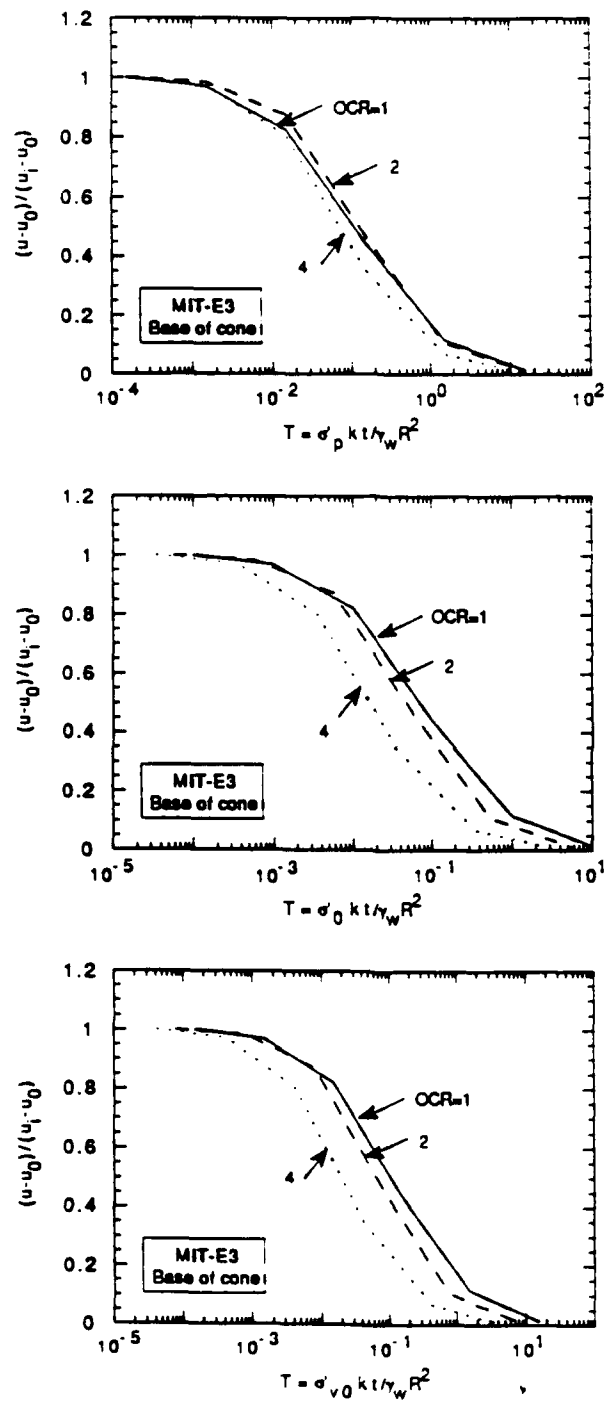


Figure 5.23b The Effect of Stress History on Pore Pressure Dissipation Curves - Base Pore Pressures (Non-linear, Coupled Analysis)

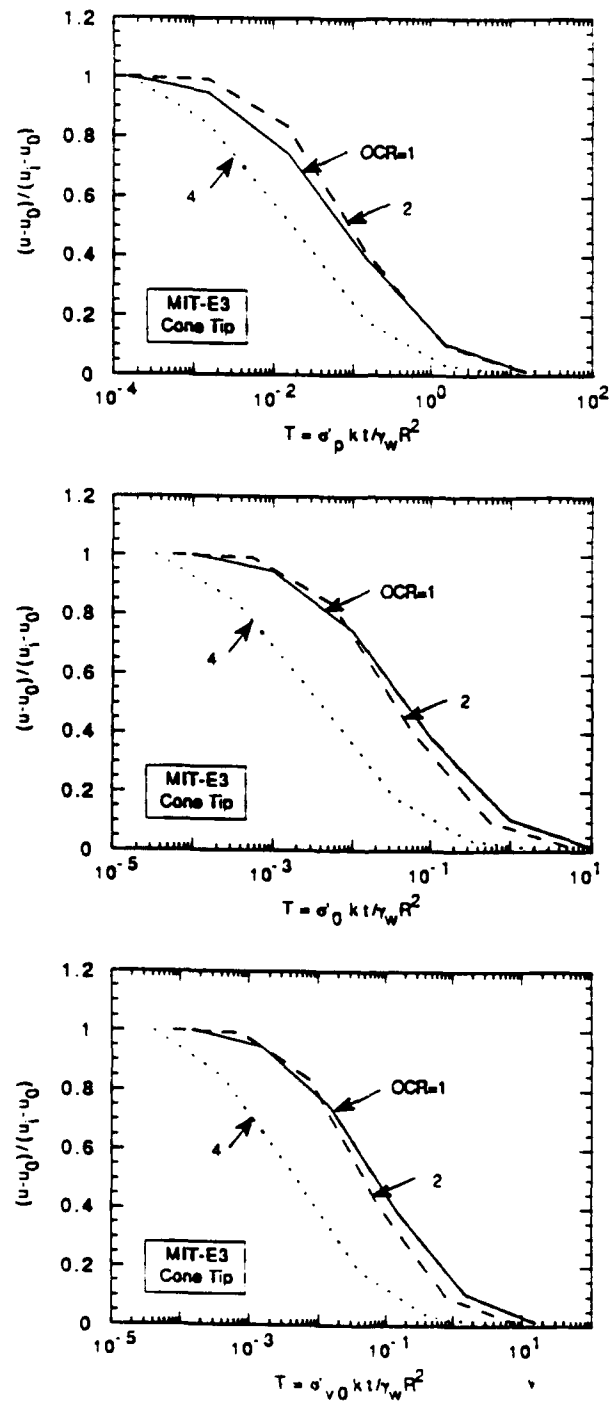
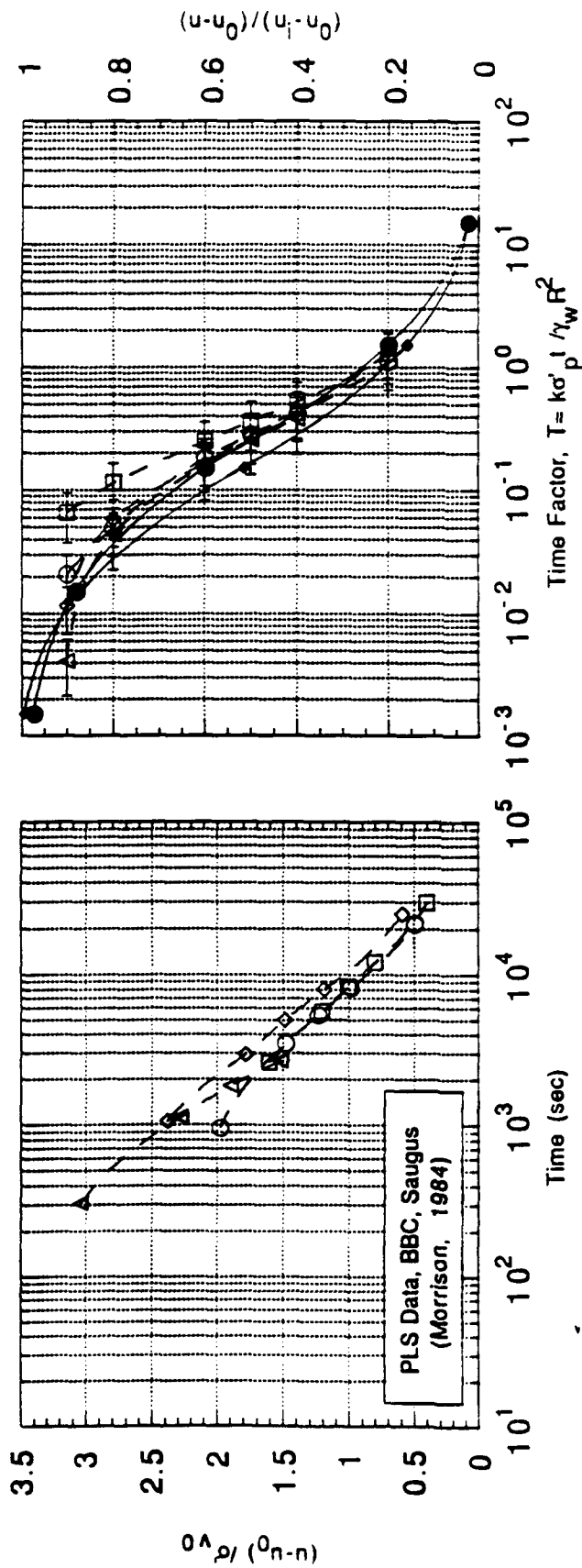


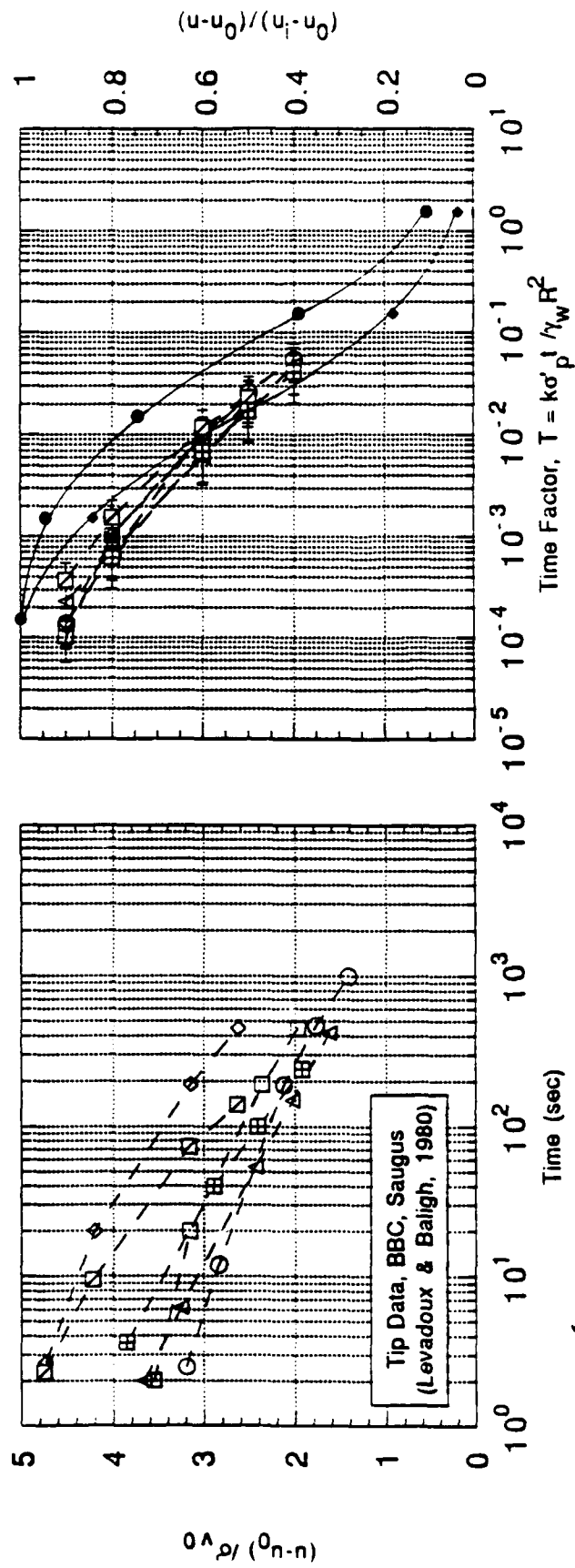
Figure 5.23c The Effect of Stress History on Pore Pressure Dissipation Curves - Tip Pore Pressures (Non-linear, Coupled Analysis)



Key	Hole	Depth (ft)	$\Delta u_i / \sigma'_v$	σ'_{v0} (ksc)	σ'_p (ksc)	k_h (10^{-8} cm/s)
Δ	1	44.5	3.80	1.00	3.0-3.9	9-20
\diamond	3	62.0	2.98	1.41	2.4-3.2	5-9
\square	1	84.5	2.01	1.93	2.3-2.9	4-8
\circ	5	107.5	2.22	2.47	2.8-3.4	4-8

MIT-E3 Predictions	
Key	OCR
\bullet	1
\circ	4

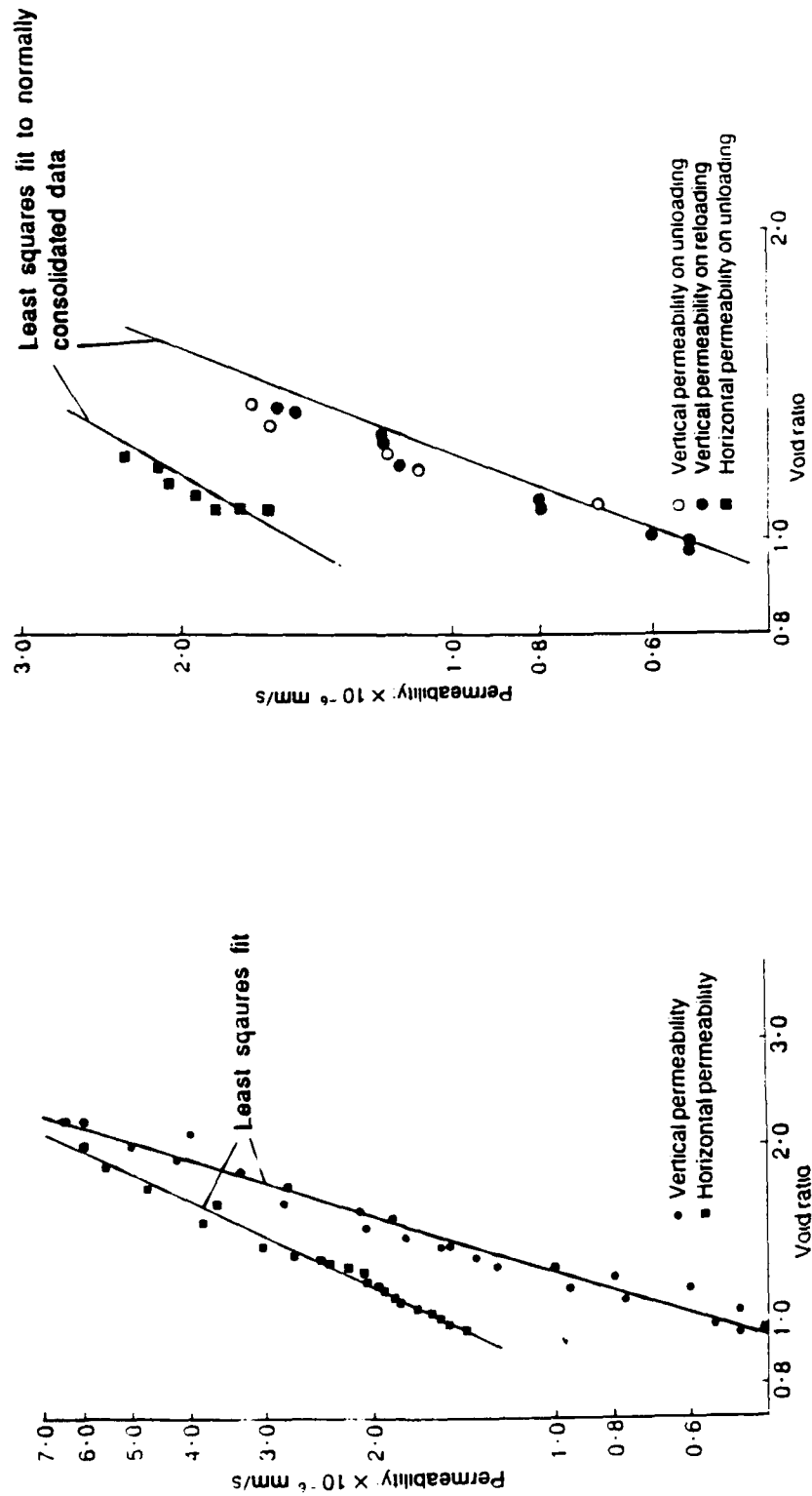
Figure 5.24 Comparison of MIT-E3 Predictions to Field Measurements Shaft Pore Pressures



Key	Hole	Depth (ft)	$\Delta u_i / \sigma'_{v0}$	σ'_{v0} (ksc)	σ'_p (ksc)	k_h (10^{-8} cm/s)
\boxplus	JPP3	42.0	4.82	0.94	3.0-3.9	9-21
\boxtimes	JPP3	44.0	5.28	0.99	3.0-3.8	9-20
Δ	8	50.0	4.07	1.13	2.7-3.6	7-15
\diamond	JPP3	67.5	5.26	1.54	2.3-3.0	4-8
\square	JPP3	82.5	3.95	1.89	2.3-3.9	4-8
\circ	8	95.9	3.55	2.20	2.6-3.1	4-8

MIT-E3 Predictions	
Key	OCR
\bullet	1
\diamond	4

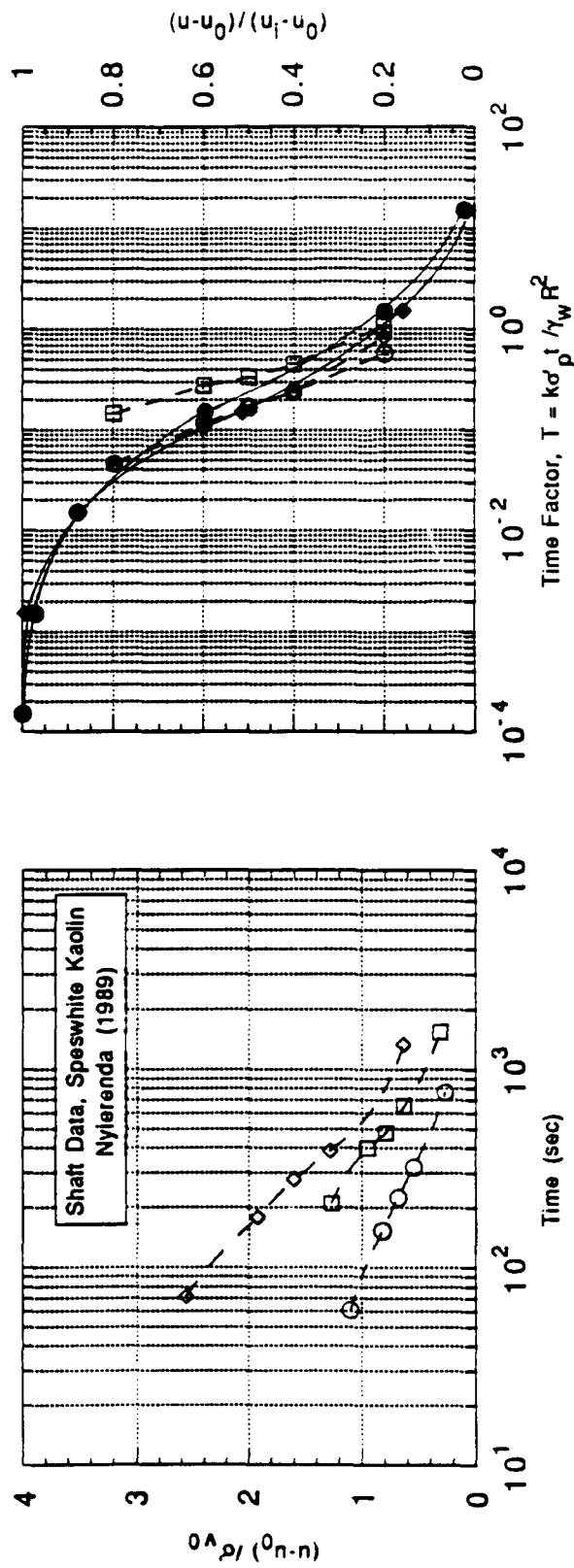
Figure 5.25 Comparison of MIT-E3 Predictions to Field Measurements of Tip Pore Pressures



b) Overconsolidated

a) Normally Consolidated

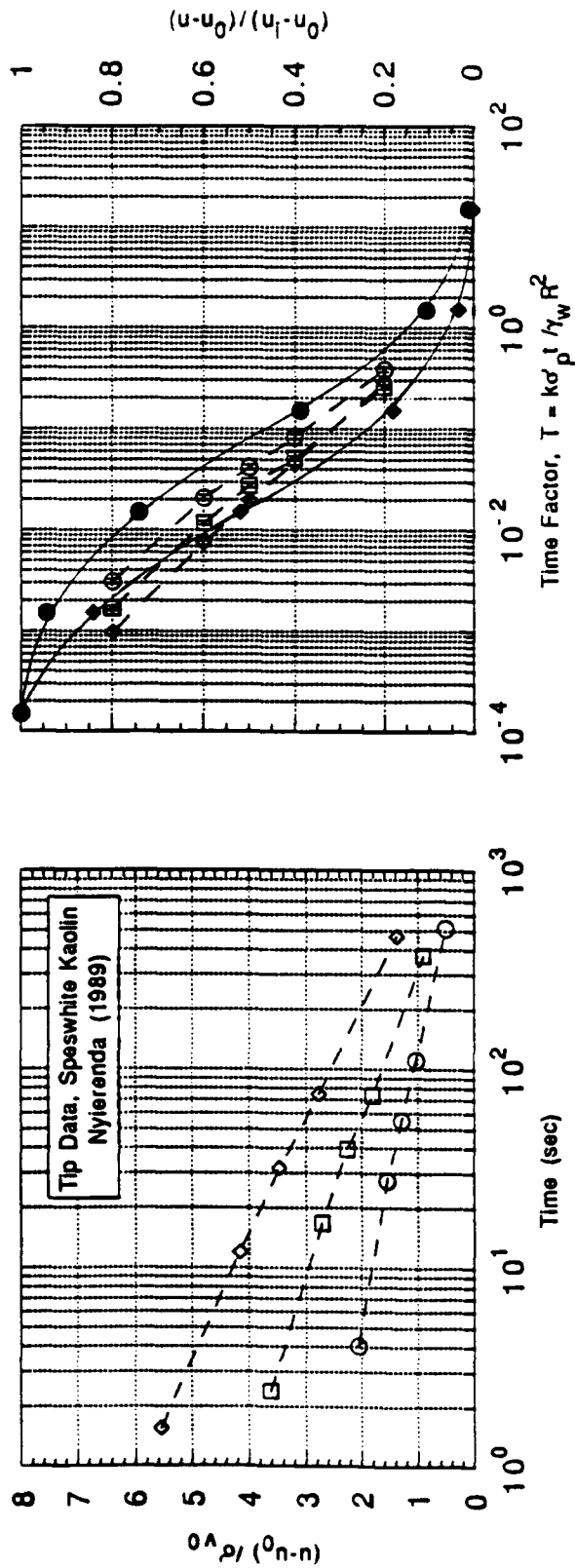
Figure 5.26 Permeability of Resedimented Speswhite Kaolin (Al-Tabaa and Wood, 1987)



Key	Cake No.	Void Ratio, e	k_h (10^{-7} cm/sec)	$\Delta u / \sigma'_{v0}$	σ'_p (ksc)	σ'_{v0} (ksc)
○	Z9C	1.00-1.06	1.49-1.67	1.38	7.7	5.9
□	Z12C	1.08-1.13	1.74-1.91	1.59	6.0	2.0
◇	Z4C	1.14-1.21	1.94-2.19	3.21	4.9	0.97

MIT-E3 Predictions	
Key	OCR
●	1
◆	4

Figure 5.27 Comparison of MIT-E3 Predictions to Consolidation Chamber Test Measurements of Shaft Dissipation in Resedimented Kaolin (data from Nyirenda, 1989)



Key	Cake No.	Void Ratio, e	k_h (10^{-7} cm/sec)	$\Delta u_i / \sigma'_{v0}$	σ'_p (ksc)	σ'_{v0} (ksc)
O	Z9C	1.00-1.06	1.49-1.67	2.59	7.7	5.9
□	Z12C	1.08-1.13	1.74-1.91	4.53	6.0	2.0
◇	Z4C	1.14-1.21	1.94-2.19	6.95	4.9	0.97

MIT-E3 Predictions	
Key	OCR
•	1
•	4

Figure 5.28 Comparison of MIT-E3 Predictions to Consolidation Chamber Test Measurements of Tip Dissipation Measurements in Resedimented Kaolin (data from Nyierenda, 1989)

6. PRESSUREMETER TESTING

6.1 INTRODUCTION

The original Ménard pressuremeter (Ménard, 1956) consisted of an expandable membrane mounted on a cylindrical probe which was lowered into a borehole. The pressuremeter expansion (MPMT) test was performed by monitoring the volume of water injected into the cell as a result of pressure increments applied at one minute intervals. The test procedure inevitably causes disturbance of the surrounding soil, and experience has shown that the measurements cannot be reliably correlated to engineering properties of the soil. The data are widely used in empirical design procedures for both deep and shallow foundations (Baguelin et al., 1978). In the early 1970's self-boring pressuremeters were developed independently in France and Britain (Baguelin et al., 1972; Wroth and Hughes, 1973). The objective of these devices is to minimize the disturbance associated with device installation, and hence enable the in-situ horizontal stress and shear stress-strain properties of the soil to be interpreted from cavity expansion theory (Bishop et al., 1945; Gibson and Anderson, 1961). In practice, two issues have hindered the subsequent development and usage of self-boring pressuremeters: 1) the equipment is complex, difficult to use and expensive compared to other in-situ penetration tests (e.g., Withers et al., 1986), and 2) extensive experience has shown that undrained shear strengths estimated from SBPMT's are often significantly larger than those obtained in conventional laboratory or other field tests (Jamiolkowski et al., 1985; Baguelin et al., 1978).

Recent developments in pressuremeter equipment have reverted to the concept that installation disturbance is inevitable, and have instead focused on developing more robust equipment. Specific devices of interest include a) the full-displacement pressuremeter (FDPMT) (Withers et al., 1986; Campanella et al., 1990) and b) the push-in pressuremeter (PIPMT) (Henderson et al., 1980; Huang and Haeferle, 1988). These are classified as displacement pressuremeters as no soil is removed during installation, and hence the volume of the penetrometer is accommodated entirely by deformations within the soil. There is very little data currently available in the literature for evaluating the performance of these devices.

This chapter uses the Strain Path Method to assess how installation disturbance affects the interpretation of undrained shear strength and in-situ horizontal stress from displacement (FDPMT, PIPMT) and self-boring (SBPMT) pressuremeter tests.

Section 6.2 provides extensive background information on pressuremeter tests including: a) description of equipment and test procedures; b) methods currently used to

interpret test data; c) previous analytical evaluations of factors affecting pressuremeter test measurements; and d) summary of previous field experience with pressuremeter tests. Section 6.3 studies how anisotropic stress-strain-strength properties affect the interpretation of ideal pressuremeter tests. Section 6.4 presents numerical predictions of pressuremeter tests in which installation is modelled using the Strain Path Method and generalized effective stress soil models. Engineering properties (K_0 , c_u) are then interpreted from the predictions using procedures described in Section 6.2.2 and are then compared to known in-situ properties. Section 6.5 compares these predictions with results from recent SBPMT tests at a site in South Boston (Ladd, 1991).

6.2 BACKGROUND

6.2.1 Equipment and Procedures

There is currently no standardization of procedures or device geometry for displacement or self-boring pressuremeters. The following sections describe typical devices.

6.2.1.1 Displacement Pressuremeters

Figure 6.1 shows a schematic diagram of a full-displacement pressuremeter (FDPMT), which comprises an expandable membrane located on the shaft of a cone penetrometer. Two prototype FDPMT devices have been presented in the literature:

1. Withers et al. (1986) use a standard Fugro piezocone ($A=15\text{cm}^2$) with a pressuremeter unit centered at an elevation $z/R=21$ above the cone tip. The design enables standard piezocone measurements (tip resistance, pore pressure on the cone face, and sleeve friction) to be made during steady penetration. When penetration is interrupted the pressuremeter membrane is inflated by gas or oil pressure. The radial expansion of the membrane is measured at mid-section by three strain sensing arms oriented at 120° .
2. Campanella et al. (1990) introduce a 'seismic cone pressuremeter' with a much shorter pressuremeter membrane ($L=220\text{mm}$; Figure 6.1). This device also records standard piezocone measurements during penetration. Campanella et al. (1990) report details of their test procedure which include: a) delay times (i.e., time intervals between installation and membrane expansion) ranging from $t_d=1.5$ to 13 mins; and b) strain controlled expansion rates, $dR/dt=5\text{-}10\%/min$. These procedures are not standardized, and their influence on field measurements has not been systematically studied.

Figure 6.2 shows a schematic diagram of a push-in pressuremeter (PIPMT), together with dimensions of two prototype devices. The 'stressprobe' (Henderson et al., 1980) was developed for offshore site investigations. Subsequent use of the probe has been

documented by Reid et al. (1982), Fyffe et al. (1986), and Lacasse et al. (1990). The probe is characterized by a cross-sectional width-to-thickness aspect ratio, $B/t \approx 10$, and has similar dimensions to a Shelby tube sampler. The pressuremeter membrane is located immediately above the cutting shoe. The stressprobe is installed from the bottom of a borehole with an approximate insertion stroke of 750mm (penetration rate is not specified). After installation there is a short time to allow the pressure to stabilize prior to membrane inflation. Membrane expansion is performed at an inflation rate $dR/dt = 1\%/min$. Huang and Haefele (1988) describe a PIPMT device with similar overall dimensions to the stressprobe (Figure 6.2). The cutting shoe is designed with a 7.7° inward taper in order to minimize disturbance of the surrounding soil¹ (according to the assumptions proposed by the authors). The bottom of the membrane is located at an elevation $z/R \approx 3.5$ above the cutting tip. The device is also inserted from the bottom of a borehole at an average penetration rate $U \approx 0.4\text{cm/sec}$ over a maximum stroke length of 700mm. The authors allow delay periods $t_d \leq 60$ mins following installation.

6.2.1.2 Self-Boring Pressuremeters

Self-boring pressuremeters attempt to minimize soil disturbance during insertion by removing a sufficient volume of soil to accommodate the volume of the pressuremeter. The soil is removed using a sharp cutting shoe and a rotating cutter, assisted by a water jet. Soil that enters the cutting shoe is ground into a slurry and flushed to the ground surface. The SBPMT was developed simultaneously at Cambridge University (Camkometer, Wroth and Hughes, 1973) and at École National Pont et Chaussées (PAFSOR, Baguelin et al., 1972; Baguelin et al., 1978). Figure 6.3 illustrates the designs of the original SBPMT devices, while Table 6.1a summarizes their typical dimensions. Primary differences in the design of SBPMT's relate to a) device diameter, B ; b) length to diameter aspect ratio of the pressuremeter membrane, and c) the instrumentation used to monitor the expansion of the membrane. It should also be noted that the Camkometer devices are generally equipped with a pore pressure transducer which can be used to measure pore water pressure during installation and throughout membrane expansion tests.

During penetration, the cutting tool configuration and rotation rate, the volume of wash water, and the force applied to the drill rods can all be varied. The above variables are established by experience at each new site. Reported penetration rates vary from $U = 1.5\text{--}2$

¹Henderson et al. (1980) also report an alternative procedure in which a 50mm diameter sample tube is pushed into the soil and extracted prior to insertion of the PIPMT. In this case, installation of PIPMT merely shaves off the remaining annulus of soil and does not closely simulate open-ended pile penetration. This procedure is not considered further in this chapter.

cm/min in Norwegian clays (Lacasse and Lunne, 1982) to $U=20$ cm/min in London Clay (Windle and Wroth, 1977).

Some test procedures (Lacasse and Lunne, 1982; Denby and Clough, 1980; Wroth and Hughes, 1973) require full dissipation of installation excess pore pressures prior to membrane expansion. In these cases, required delay times range from 30 to 1300 minutes. Alternately, a fixed delay is specified, typically $t_d \approx 30$ mins (Ladd et al., 1980; Ladd, 1991).

Membrane expansion is most commonly strain controlled, with a rate of radial expansion of 1% per minute. The maximum radial strain is typically between 10 and 20% (Windle and Wroth, 1977; Ladd et al., 1980; Campanella et al., 1990).

6.2.2. Pressuremeter Test Interpretation

This section summarizes methods which have been proposed for estimating for estimating 1) soil stress-strain-strength behavior and 2) in-situ total horizontal stress from pressuremeter measurements in cohesive soils.

6.2.2.1 Shear Stress-Strain-Strain Strength

The techniques discussed in this section all assume the following:

1. Pressuremeter expansion can be analyzed as a plane strain problem (i.e., assuming that the device produces a cylindrical cavity of infinite length, such that there are no soil displacements in the vertical direction).
2. The effective stress-strain relationship is unique for all locations in the soil mass (i.e., the soil is homogeneous and there is no disturbance in the stress state or soil properties due to device installation).
3. The membrane expansion occurs sufficiently rapidly that there is no migration of pore water within the soil mass. Thus the soil is subjected to undrained shearing.

Figure 6.4a shows the geometry considered in the analyses. Initially the pressuremeter has radius, R_0 , which increases to R during membrane expansion ($\Delta R = R - R_0$). Soil elements initially located at radial distance, r_0 , are displaced to new locations, r , during this process (the displacement $u_r = (r - r_0)$). The natural (Hencky) strains experienced by soil elements can be written:

$$\epsilon_{rr} = -\epsilon_{\theta\theta} = \log_e \left(\frac{r}{r_0} \right) \quad (6.1)$$

For undrained shearing, no volume change occurs in the soil; hence, volume must be conserved during the membrane expansion:

$$\pi (r^2 - R^2) = \pi (r_0^2 - R_0^2) \quad (6.2)$$

By combining these results, the strains can be expressed as functions of the membrane radius:

$$\epsilon_{rr} = -\epsilon_{\theta\theta} = -\frac{1}{2} \log_e \left\{ 1 - \frac{R^2 - R_0^2}{r^2} \right\} \quad (6.3)$$

and hence can be related to volume changes in the pressuremeter:

$$\epsilon_{rr} = -\epsilon_{\theta\theta} = -\frac{1}{2} \log_e \left\{ 1 - \frac{\Delta V}{V} \left(\frac{R}{r} \right)^2 \right\} \quad (6.4)$$

where $\Delta V/V$ is the 'current volumetric strain', $\Delta V = (V - V_0)$ is the volume of fluid injected into the pressuremeter, and V is the current volume.

Pressuremeter data are often reported in terms of a 'pressuremeter strain'², $\epsilon_0 = \Delta R/R_0$, which can be related directly to the current volumetric strain:

$$\left(\frac{\Delta V}{V} \right) = 1 - (1 + \epsilon_0)^{-2} \quad (6.5)$$

For situations where $(r/R) \gg (\Delta V/V)$, the expressions for natural strains (Equation 6.4) can be approximated by:

$$\epsilon_{rr} = -\epsilon_{\theta\theta} = \frac{1}{2} \frac{\Delta V}{V} \left(\frac{R}{r} \right)^2 \quad (6.6)$$

Windle and Wroth (1977) and Gibson and Anderson (1961) assume that the soil exhibits linearly elastic, perfectly plastic behavior. The Gibson and Anderson (1961) method applies to the Ménard pressuremeter and incorporates the effect of elastic unloading of the borehole prior to membrane expansion (see Section 6.2.3). Windle and Wroth (1977) adapted the Gibson-Anderson formulation for the self-boring pressuremeter, for which they assumed no change in the initial horizontal stress during installation.

²By convention ϵ_0 is positive in tension. All other soil strains are positive in compression.

In the initial expansion phase, soil elements remain elastic and solutions can be obtained using infinitesimal strain theory. In this case, the elastic shear modulus, G , can be determined from the slope of the measured expansion curve³:

$$P = P_0 + G \frac{\Delta V}{V}; \quad P \leq \sigma_{h0} + c_u \quad (6.7)$$

where P is the expansion pressure, P_0 is the initial pressure (at $R=R_0$) and V_0 is the initial volume of the pressuremeter. Usually it is assumed that $P_0 = \sigma_{h0}$, while $\Delta V/V_0 \Rightarrow \Delta V/V$ for small strains.

For continued membrane expansion, the shear strength of the soil is characterized by a Tresca failure criterion:

$$\left| \frac{\sigma_{rr} - \sigma_{\theta\theta}}{2} \right| = c_u \quad (6.8)$$

and hence equilibrium conditions in the plastic zone are described by:

$$\frac{d\sigma_{rr}}{dr} + \frac{2c_u}{r} = 0 \quad (6.9)$$

The expansion pressure is then estimated from Equation 6.9 using boundary conditions at the elasto-plastic boundary ($r=r_p$):

$$P = \sigma_{h0} + c_u \left\{ 1 + \log_e \left[\left(\frac{\Delta V}{V} \right) \left(\frac{G}{c_u} \right) \right] \right\} \quad (6.10)$$

At infinite expansion $\Delta V/V$ approaches unity, and the limit pressure P_L is obtained:

$$P_L = \sigma_{h0} + N_p c_u \quad (6.11)$$

where, $N_p = [1 + \log_e (G/c_u)]$. The undrained shear strength, c_u , is then estimated from the pressuremeter data in $p\text{-}\log_e(\Delta V/V)$ space:

$$P = P_L + c_u \log_e (\Delta V / V) \quad (6.12)$$

³ A more reliable procedure for estimating G is to measure the slope of the expansion curve during a small unload-reload cycle: $G = \Delta P / (\Delta V/V)$.

Baguelin, Palmer, and Ladanyi (PBL, 1972) independently⁴ developed methods for computing the shear stress-strain-strength of the clay from pressuremeter measurements. The authors assume that all points in a horizontal plane of the soil are initially at the same state of stress and exhibit homogeneous stress-strain properties. Baguelin et al. (1972) obtain the cavity shear stress $q_h(= (\sigma_{rr} - \sigma_{\theta\theta})/2)$ in the soil adjacent to the pressuremeter membrane using equilibrium and continuity conditions:

$$q_h(R) = \epsilon_0 (1 + \epsilon_0) \left(1 + \frac{\epsilon_0}{2}\right) \frac{dP}{d\epsilon_0} \quad (6.13)$$

where $\epsilon_0 = \Delta R/R_0$ is the circumferential strain at the membrane. For small strain conditions, $\epsilon_0 \ll 1$ and hence:

$$q_h(R) = \epsilon_0 \frac{dP}{d\epsilon_0} = \frac{dP}{d(\log_e \epsilon_0)} \quad (6.13a)$$

Equation 6.13 describes the complete stress-strain behavior of the soil ($q_h(R) - \epsilon_0$), and the shear strength is equated with $(q_h)_{\max}$. Palmer (1972) expresses equation 6.13 in the form:

$$q_h(R) = \frac{dP}{d(\log_e \frac{\Delta V}{V})} \quad (6.14)$$

For a perfectly plastic material, this result is identical to the solution of Gibson and Anderson (1961) in Equation 6.12.

The stress-strain behavior from the Baguelin-Palmer-Ladanyi approach (Equations 6.13 and 6.14) is obtained by numerical differentiation of experimental data. In practice the derived stress-strain curves are often unreliable due to scatter in the measured data. In order to overcome this difficulty, Baguelin et al. (1972) propose that an empirical function should be fitted to the measured data. They recommend:

$$P = P_0 + \frac{1}{2b} \left[a \log(1 + \epsilon_0^2) + \tan^{-1} \epsilon_0 \right] \quad (6.15)$$

where a and b are constants obtained by least-squares fitting methods. However, even with this approach, the interpreted stress-strain-strengths are highly sensitive to installation

⁴ Baguelin et al. (1972), Palmer (1972), Ladanyi (1972)

disturbances which affect the determination of the initial radial stress (σ_{h0}). Methods to estimate this 'lift-off' pressure are described in Section 6.2.2.3.

A number of authors have used empirical equations to describe the constitutive behavior during membrane expansion and then used the BPL analysis in order to estimate these functions from the expansion data:

a) Prévost and Hoeg (1975) introduce equations to describe 'strain-hardening' and 'strain-softening' soils⁵:

$$q_h = c_{u\infty} \left[\frac{\epsilon_h}{a + \epsilon_h} \right] \quad \text{Strain Hardening Soil} \quad (6.16a)$$

$$q_h = A \left[\frac{\epsilon_h (1 + B\epsilon_h)}{(1 + \epsilon_h^2)} \right] \quad \text{Strain Softening Soil} \quad (6.16b)$$

where a , A , and B are curve fitting parameters, $\epsilon_h = |\epsilon_{\theta\theta}|$ is the maximum shear strain in the horizontal plane, $c_{u\infty}$ and AB are the large strain and residual shear strengths, respectively.

Using Equations 6.16a, and b the pressuremeter expansion curve is then obtained analytically:

$$P = \sigma_{h0} + \frac{1}{\sqrt{3}} c_{u\infty} \log_e \left[1 + \frac{\epsilon_0}{a} \right] \quad \text{Hardening} \quad (6.17a)$$

$$P = \sigma_{h0} + \frac{A}{\sqrt{3}} \left[\frac{B}{2} \log_e (1 + \epsilon_0^2) + \tan^{-1} \epsilon_0 \right] \quad \text{Softening} \quad (6.17b)$$

The empirical constants are then determined by curve fitting to a measured expansion curve (P , ϵ_0).

b) Ladd et al. (1980) present a modified version of the Prévost-Hoeg equations for strain softening soil:

$$q_h = A \left[\frac{\epsilon_h (1 + B\epsilon_h)}{(1 + C \epsilon_h^2)} \right] \quad (6.16c)$$

where C is an additional, curve fitting constant. This equation describes soil behavior in which the peak shear strength occurs at small strain levels (typical of sensitive clays). The pressuremeter expansion curve is then obtained as:

⁵ Their formulation neglects elastic strain components.

$$P = \sigma_{h0} + \frac{A}{\sqrt{3} C} \left[\frac{B}{2} \log_e (1 + C \epsilon_h^2) + \tan^{-1} C \epsilon_0 \right] \quad (6.17c)$$

c) Denby and Clough (1980) also modify the Prévost-Hoeg equations for strain hardening soils using an hyperbolic-perfectly plastic model:

$$q_h = A \left[\frac{\epsilon_h}{\left(\frac{1}{2G_i} + \frac{R_f}{c_u} \epsilon_h \right)} \right] \quad (6.16d)$$

where c_u is the undrained shear strength, R_f controls the strain at failure, ϵ_{hf} (Figure 6.5a). The pressuremeter expansion curve is given by:

$$P = \sigma_{h0} + \frac{c_u}{R_f} \log_e \left[1 + \left(\frac{2G_i}{c_u} \right) R_f \epsilon_0 \right]; \quad \epsilon_0 \leq \epsilon_{hf} \quad (6.17d)$$

$$P = \sigma_{h0} + c_u \log_e \left[\left(\frac{2G_i}{c_u} \right) (1 - R_f) \epsilon_0 \right] + \frac{c_u}{R_f} \log_e \left(\frac{1}{1 - R_f} \right); \quad \epsilon_0 \geq \epsilon_{hf}$$

These results lead to the interpretation of the expansion curve shown in Figure 6.5b.

6.2.2.2 Effects of Installation Disturbance

The pressuremeter interpretation methods described in the previous section do not consider the effects of installation disturbance on soil stresses and properties. Hence, these methods are relevant only when installation procedures induce negligible disturbance, as is generally assumed for the self-boring pressuremeter test (this assumption is evaluated in Section 6.4.4). The same approaches cannot be used reliably for 'displacement type' pressuremeters.

However, the importance of installation disturbance has been appreciated since the first development of the Ménard pressuremeter. Indeed, the original Gibson and Anderson (1961) interpretation of the Ménard pressuremeter test includes elastic unloading of the borehole prior to membrane expansion (c.f. Equation 6.10):

$$P = \sigma_{h0} + c_u \left\{ 1 + \log_e \left[\left(\frac{\Delta V}{V} \right) \left(\frac{G}{c_u} \right) - \left(1 - \frac{\Delta V}{V} \right) \frac{\sigma_{h0}}{G} \right] \right\} \quad (6.18)$$

Baguelin et al. (1978) have studied the effects of disturbance on the interpretation of self-boring pressuremeter tests using a conceptual model (Figure 6.6a). The authors assume a two zone distribution of soil properties: i) for $r > r_1$ the soil is undisturbed, and the

shear stress $q_h = f(g)$ where g is the Green strain⁶; and ii) for $R \leq r \leq r_1$ the soil is disturbed with properties $q_h = f_1(g)$. The shear stresses derived from the hypothetical pressuremeter expansion (q_{ap}) can be expressed by:

$$q_{ap} = f(g_0/b) + f_1(g_0) - f_1(g_0/b) \quad (6.19)$$

where $b = (r_1/R)^2$ describes the extent of the zone of disturbance, and g_0 is the Green strain at the pressuremeter boundary. Figure 6.6b shows that the apparent stress-strain curve exhibits peak strength $c_{u(ap)}$ which exceeds the undisturbed (true) shear strength and has an initial modulus lower than that of the undisturbed soil.

These results are qualitatively in accordance with the behavior commonly interpreted from self-boring pressuremeter tests. However, the model is purely a conceptual representation of disturbance⁷ and cannot be used to modify quantitatively the interpretation of the measured data.

Houlsby and Withers (1988) are the first authors to present an analytical interpretation of the undrained shear strength from displacement-type pressuremeter data accounting explicitly for installation disturbance. Their method assumes 1) that the soil exhibits an elastic-perfectly plastic behavior (with shear strength given by Equation 6.8), and 2) changes in soil stresses due to installation can be modelled by the expansion of a cylindrical cavity (from $R=0$ to R_0 , where R_0 is the radius of the penetrometer shaft for the FDPMT). The authors analyze the contraction phase of the test after the pressuremeter is expanded to a maximum radius R_e (Figure 6.4b). The natural (Hencky) membrane strains during the contraction phase are defined by:

$$(\epsilon_0^e - \epsilon_0) = \log_e (R_e/R) \quad (6.20)$$

where R , ϵ_0 are the current radius and membrane strain, respectively, and ϵ_0^e is the membrane strain at R_e .

During the initial phases of cavity contraction, the soil behaves elastically, in which case, the shear modulus can be computed from the expression:

$$G = \frac{1}{2} \left(\frac{P_e - P}{\epsilon_0^e - \epsilon} \right) \quad (6.21)$$

⁶ The Green strain is related to the hoop strain $\epsilon_{\theta\theta}$ by the following: $g = (1/2)[(1 + \epsilon_{\theta\theta})^2 - 1]$.

⁷ The model does not account for stress changes in the soil due to installation.

where P_e is the pressure at R_e during the expansion phase.

When soil yielding occurs during cavity contraction, the authors obtain the undrained shear strength from:

$$c_u = \frac{(\epsilon_0^e - \epsilon)}{2f} \frac{dP}{d\epsilon_0} \quad (6.22)$$

where $f = (\epsilon_0^e - \epsilon_0) / \tanh(\epsilon_0^e - \epsilon_0)$. The authors show that $f \approx 1.0$ for $0.0 \leq (\epsilon_0^e - \epsilon_0) \leq 0.6$. Hence, the undrained shear strength c_u can be estimated directly from the slope of the contraction curve.

6.2.2.3 In-situ Horizontal Stress, σ_{h0}

Lacasse and Lunne (1982) describe eleven methods of estimating in-situ horizontal stress from SBPM tests (Table 6.2). These can be separated in two categories:

1. Lift-off pressure methods which equate the lift-off pressure P_0 to the in-situ horizontal stress, σ_{h0} . It is assumed that adequate time is allowed between installation and membrane expansion for stresses to 'relax' to their in-situ condition.
2. Methods based on the complete expansion curve. In this case the in-situ stress is estimated by extrapolating back to zero strain level. Differences in the proposed methods relate to the assumed stress-strain behavior (see Section 6.2.2.1) and the definition of the 'zero' strain (i.e., the method by which false initial strains are eliminated). Figure 6.7 illustrates the methods described by Lacasse and Lunne (1982).

A comprehensive comparison by Lacasse and Lunne (1982) of P_0 values estimated by various methods at the Onsøy and Drammen sites indicated that interpretation method can affect computed values by $\pm 25\%$. It also indicated that lift-off related methods tend to give lower estimates of P_0 values than methods which use the entire expansion curve. It is important to note that reported P_0 values involve considerable manipulation of the data and are not necessarily reliable indicators of the total horizontal stress σ_{π} acting on the pressuremeter membrane following installation. This is particularly true for those methods which place little weight on the small strain portion of the expansion curve by using the entire expansion curve.

6.2.3 Influence of Finite Membrane Length

Yeung and Carter (1990) performed finite element analyses to evaluate the influence of finite membrane length on the interpreted undrained shear strength from SBPMT's. Their analyses assume a) no disturbance due to installation; and b) the soil exhibits linearly-elastic perfectly-plastic behavior with shear strength described by a von Mises failure criterion. They report calculations for a membrane aspect ratio $L/B=6$ (Camkometer, Figure 6.3a) and soil rigidity $7.5 \leq G/c_u \leq 300$. Undrained shear strengths were back-calculated from the numerical pressuremeter expansion curves using the Gibson-Anderson method (Equation 6.12).

The analyses show that finite membrane length can cause overprediction of the actual shear strength by up to 40%. Overprediction is especially significant for soils with low rigidity ($G/c_u < 100$). They propose an empirical correction factor for pressuremeters with $L/B=6$:

$$c_u = [0.65 + 0.061 \log_{10} (G/c_u)] c_{uCEM} \quad (6.23)$$

where c_u is the true undrained shear strength and c_{uCEM} is the shear strength back-calculated from the expansion curve (assuming plane strain conditions).

6.2.5 Field Experience

This section summarizes previous field experience in evaluating factors affecting the interpretation of engineering properties from high quality pressuremeter tests in normally and lightly overconsolidated clays. Table 6.3 summarizes soil properties from six well-documented test sites discussed in this section. The data is reviewed to assess the following factors:

1. The influence of the method of interpretation on SBPMT undrained shear strength estimates (Sections 6.2.2.1 and 6.2.2.2).
2. The effect of membrane aspect ratio, L/B , on SBPMT strength estimates.
3. The relationship between stress changes during installation (as quantified by P_0/σ_{h0}) and c_u estimated from pressuremeter tests.
4. The effect of displacement versus self-boring installation on strength estimates.
5. The influence of SBPMT test procedures, including a) cutter position, b) cutter rotation rate, c) expansion rate, and d) oversizing of the cutting shoe.

Table 6.4 summarizes undrained shear strengths interpreted from SBPM tests at five sites. The tests include data from three different types of pressuremeter: a) PAFSOR with $L/B=2,4$ (Figure 6.3b) and b) Camkometer with $L/B=6$ (Figure 6.3a); and using four methods of interpretation (Gibson and Anderson, 1961; Windle and Wroth, 1977; Prévost

and Hoeg, 1975; and Denby and Clough, 1980). In general, these data show large differences in the performance of the different types of self-boring pressuremeter:

1. At the Onsøy and Drammen sites (Lacasse et al., 1981) the undrained shear strengths, c_{uPM}/σ'_{v0} , estimated from Camkometer data are not affected by the method of interpretation. The magnitudes of c_{uPM}/σ'_{v0} are consistently 30% higher than reference shear strengths (c_{uTC}/σ'_{v0}) measured in CK₀UC laboratory tests reconsolidated to the in-situ stress state.
2. At the Porto Tolle and Trieste sites (Ghionna et al., 1982), large differences in c_{uPM}/σ'_{v0} are reported between the two PAFSOR devices with aspect ratios $L/B=2, 4$. The data also show that the Gibson-Anderson method leads to lower estimates (up to 30% less) of the undrained shear strength than are obtained from the other three methods. Measurements from the $L/B=2$ pressuremeter give strength estimates which are significantly higher than those obtained for the $L/B=4$ device (differences are in the range $0.25\sigma'_{v0}$ to $0.50\sigma'_{v0}$), and there are correspondingly large deviations from the reference strength ratios in laboratory triaxial tests.
3. Data from the Haga site (Lacasse et al., 1990) strength estimates c_{uPM}/σ'_{v0} from expansion curves using the PAFSOR device range from 25% less to 50% greater than the reference triaxial shear strength. The method of interpretation was not reported for this data.

Ghionna et al. (1982) investigated the interrelationship between the measured lift-off pressure, P_0 , and the estimated undrained shear strength from the PAFSOR tests and the Porto Tolle site. In Figure 6.8 the lift-off pressures are computed using the graphical iteration procedure (Marsland and Randolph, 1977) and are normalized by the best estimate of the in-situ (total) horizontal stress, σ_{h0} . In the ideal SBPMT, $P_0/\sigma_{h0}=1$, and hence deviations from this condition can be classified as installation disturbance. The data show that there is a strong correlation between the contact pressure and the estimated shear strength. At this site the estimated lift-off pressures range from $P_0/\sigma_{h0}=0.8$ to 1.4 and are associated with a strength decrease $\Delta c_u \approx 0.13\sigma'_{v0} - 0.20\sigma'_{v0}$. Thus, installation disturbance⁸ is an important factor affecting the estimation of undrained shear strength from self-boring pressuremeter tests.

Benoît and Clough (1986) performed tests in the San Francisco Bay mud, using a pressuremeter similar to the 8 cm diameter Camkometer. Their study investigated the influence of the following parameters:

⁸ The data in Figure 6.8 also show that differences in shear strengths due to pressuremeter aspect ratio are not affected by changes in lift-off pressures.

1. The rate of applied pressure, $\dot{P} = 0.2$ to 4.5 kN/min compared to the standard rate $\dot{p} = 6.9$ kN/min in stress controlled expansion tests.
2. Position of the cutter inside the cutting shoe, ranging from tests with the cutter located flush with the tip to fully retracted tests with the cutter located 3.8 cm inside the shoe. The 'normal' cutting position is 2.5 cm inside the cutting shoe.
3. Rate of rotation of the cutter, with the cutter rotation rate being increased from a 'standard' rate of 60 rpm to 180 rpm.
4. Oversizing the borehole by means of a wide cutting shoe having a diameter 1.1% greater than the probe diameter.

Figure 6.9 compares the estimated values of P_0 and c_u obtained by varying these parameters with data obtained using standard test procedures. In-situ strengths were estimated from pressuremeter curves using the Baguelin-Palmer-Ladanyi (Section 6.2.2.1) approach, and P_0 was estimated by visual inspection. These results show the following:

1. Membrane expansion rate has practically no effect on the estimated in-situ lateral stress. However, it has a moderate effect on undrained shear strength estimates, with a 12% decrease in estimated strength for expansion rates less than normal and a 16% increase for expansion rates greater than normal.
2. Cutter position only affects the estimated undrained shear strength when the cutter is in the fully retracted position. In this case, they report erratic estimates of shear strength which they attribute to clogging of the cutting shoe.
3. Increasing the cutting rate has a significant influence on both contact pressure and estimated shear strengths. At the higher cutting rate (180 rpm) the estimated in-situ horizontal stress decreased by 45 - 50% , while the estimated shear strength increased by 80 - 150% . Similar behavior is observed using an oversized cutting shoe.

Lacasse et al. (1990) present the results comparing undrained shear strengths estimated from self-boring (Camkometer) and push-in (Stressprobe) pressuremeters at two sites (Haga and Onsøy). Figure 6.10 a and b summarize the shear strengths for the SBPMT and PIPMT together with reference strengths from CK_0UC and field vane tests at the Onsøy and Haga sites, respectively. The data show the following:

1. The undrained shear strengths estimated from SBPM tests are significantly higher than the reference shear strengths obtained from CK_0UC tests (typically 50 - 150% higher). These observations are consistent with observations at other sites (Table 6.4).
2. Average shear strengths from PIPM tests are similar in magnitude to the triaxial shear strengths at the Onsøy site. However, significant scatter in the PIPMT data (± 10 kPa) make the comparisons tentative. At the Haga site PIPM shear strengths are

significantly lower (typically 50%) than the reference c_{uTC} values with the notable exception of tests performed at depths of 3-5m.

The main conclusions on the interpretation of pressuremeter tests can be made from the above studies as follows:

1. Shear strengths estimated from SBPMT data in soft clays are typically 30-50% larger than shear strengths measured in laboratory triaxial compression tests.
2. Estimates of undrained shear strengths using the Baguelin-Palmer-Ladanyi, Windle and Wroth, and Denby (Section 6.2.2.1) approaches are very similar.
3. Low SBPM contact pressures (relative to the expected in-situ total horizontal stress) are associated with high estimates of shear strengths and vice-versa. This conclusion is supported by the data from Ghionna et al. (1982) and Benoît and Clough (1986).
4. Benoît and Clough (1986) show that the rate of soil extraction (cutting rate) and the size of the cutting shoe are important parameters affecting SBPMT data. For example at higher cutting rates, the measured lift-off pressure decreases and there is a corresponding increase in estimated shear strength. Other factors such as membrane expansion rate have a moderate influence on estimated shear strength (28% increase in estimated strength for a twenty-fold increase in expansion rate).
5. Displacement pressuremeters (PIPM) strength estimates are significantly lower than those obtained from SBPMT performed in the same soil. Limited experimental data suggest that the PIPM test strengths are smaller than c_{uTC} values in laboratory CK_0UC tests.
6. Shear strengths estimated from SBPM's with small membrane aspect ratios ($L/B=2$) are not reliable.

6.3 THE IDEAL PRESSUREMETER SHEAR MODE

In an ideal pressuremeter test: a) there is no disturbance caused by device installation and hence the surrounding soil exhibits homogeneous properties, with spatially uniform initial stresses acting at all locations; b) the device is infinitely long such that the mode of shearing corresponds exactly to a one-dimensional cylindrical cavity expansion; and c) there is no migration of pore water for a test performed in a low permeability clay. Model predictions of the ideal pressuremeter mode of shearing can be obtained using generalized effective stress models (MCC or MIT-E3) with input parameters corresponding to Boston Blue Clay (cf., Chapter 3). Table 6.5 and Figure 6.11 summarize the model predictions for ideal pressuremeter tests on BBC for $OCR=1, 2$, and 4 . The results show the following:

1. The MCC model has an isotropic failure criterion; therefore, shear strength is constant for all plane strain shear modes and depends on the generalization of the critical state failure condition. For a von Mises failure criterion $c_{uPM} = (2/\sqrt{3})c_{uTC}$.
2. The MIT-E3 model predicts an anisotropic response with the strength in a pressuremeter shearing mode c_{uPM} approximately equal to that in a direct simple shear mode c_{uDSS} and substantially less (approximately 40%) than the strength in a plane strain active shear mode c_{uPSA} . One source of uncertainty in the MIT-E3 predictions is the coefficient of earth pressure at rest in the normally consolidated stress state, K_{0NC} . MIT-E3 predictions for $K_{0NC} = 0.48$ to 0.53 are practically identical at $OCR = 1$ but can affect strength estimates by 10-20% in $OCR = 4$ (at $OCR = 1$ $K_0 = 0.75 - 1.00$).
3. The predicted stress-strain curves in a pressuremeter shear mode show almost perfect plastic behavior beyond peak shear resistance.
4. Shear-induced pore pressures $\Delta u_s / \sigma'_{v0}$ predicted from the two models are similar for normally consolidated BBC. However, for $OCR = 4$, the magnitude of $\Delta u_s / \sigma'_{v0}$ predicted from the MCC model is substantially greater (2-3 times) than that predicted from the MIT-E3 model, due to the assumption of linear elastic behavior beneath the yield surface during undrained shearing. The MCC model also predicts that shear-induced pore pressures begin to develop at much larger strains than those predicted by the MIT-E3 model.

The ideal pressuremeter test can be simulated in a laboratory element test using devices such as the True Triaxial Apparatus (TTA) or the Directional Shear Cell (Arthur et al., 1981; Germaine, 1982). Figure 6.12 illustrates the DSC test procedure, which includes the following steps: 1) the sample is consolidated one dimensionally (K_0 stress history) such that there are no lateral strains in the horizontal plane ($\epsilon_{xx} = \epsilon_{zz} = 0$; Figure 6.12a); 2) the sample is sheared undrained in the horizontal (x-z) plane ($\epsilon_{xx} = -\epsilon_{zz}$) by applying boundary tractions at various orientations, ψ (Figure 6.12b). Stage 1 is accomplished in a large-scale consolidation chamber (Germaine, 1982), after which the specimen is transferred to the DSC apparatus. In contrast, tests performed in the True Triaxial Apparatus can accomplish stages 1 and 2 without physical re-orientation of the specimen, but can only apply principal stresses at $\psi = 0$ and 90° . In principle, the soil exhibits isotropic properties in the horizontal plane, due to the K_0 -stress history and hence, the direction of shearing (ψ) should not affect the measured stress-strain response. Figure 6.13 shows the measured stress-strain response for pressuremeter element tests on K_0 -consolidated BBC at OCR's 1 and 4. The measured data show:

1. The undrained shear strength is mobilized at shear strains, $\gamma = 5\%$, and give no indication of post-peak strain softening.

2. Predictions of the MIT-E3 model match closely the measured behavior, especially the undrained strength at both OCR's, but tend to overestimate the material stiffness.
3. The summary of predicted and measured undrained strength ratios for a number of shearing modes presented in Table 6.5 shows that MIT-E3 predictions are consistent with measurements for all shear modes. The MCC predictions are consistent with measurements for the triaxial compression (TC) mode but significantly overestimate the strengths in other shearing modes.
4. The measured undrained strength ratios in a pressuremeter shear mode, c_{uPM}/σ'_{v0} , are similar to those measured in a DSS mode.

The above comparison of predictions to measurements show that that MIT-E3 soil model gives reasonable predictions of stress-strain-strength behavior in all shearing modes. Therefore, predictions of the effects of installation disturbance in pressuremeter test results to be presented subsequently in this chapter will rely primarily on the MIT-E3 model.

6.4 PREDICTIONS OF PRESSUREMETER TESTS WITH INSTALLATION DISTURBANCE

This section presents numerical predictions to investigate the effects of installation disturbance on the interpretation of pressuremeter measurements. The analyses predict the effects of: 1) the method of installation, 2) the time delay between installation and membrane expansion (dissipation of installation pore pressures), 3) membrane expansion versus contraction, and 4) the stress history of the clay. The analyses are restricted to pressuremeter tests in Boston Blue Clay, whose constitutive behavior is simulated using the MIT-E3 model (cf., Section 6.3). The predictions assess the effect of the above factors on two engineering properties commonly obtained from pressuremeter tests: the coefficient of earth pressure at-rest, K_0 ; and the undrained shear strength c_{uPM} .

6.4.1 Analytical Framework

The pressuremeter test predictions in this section assume the following:

1. Initial stress fields are one-dimensional (i.e., stress fields prior to membrane expansion vary only in the radial direction.)
2. The installation disturbances are estimated using the Strain Path Method and consider membrane expansion in a plane far above the cutting shoe.
3. An infinitely long, cylindrical pressuremeter membrane (i.e., plane strain geometry).
4. No drainage occurs during membrane expansion.

These assumptions enable the strains at any point in the surrounding soil to be determined independently from the shearing resistance of the soil. If the pressuremeter volume is increased at a rate \dot{V} per unit length, then the conservation of volume requirement implied from the third assumption requires that the current radial coordinate, r , at time, t , is:

$$r(t) = (r_0^2 + \frac{\dot{V}t}{\pi})^{1/2} \quad (8.26)$$

where r_0 is the initial coordinate of the point. Thus, the particle velocities can be defined by:

$$v_r = \frac{dr}{dt} = \frac{1}{r} \frac{\dot{V}}{2\pi} \quad (8.27)$$

and infinitesimal strain rates given by:

$$\dot{\epsilon}_{\pi} = -\frac{dv_r}{dr} = \frac{1}{r^2} \frac{\dot{V}}{2\pi} \quad (8.28a)$$

$$\dot{\epsilon}_{\theta\theta} = -\frac{v_r}{r} = -\frac{1}{r^2} \frac{\dot{V}}{2\pi} \quad (8.28b)$$

With the strain history⁹ completely defined at all points, the effective stress history can be computed using an appropriate generalized effective stress soil model.

The total radial stress at the membrane P_0 can then be computed from equilibrium considerations, that is

$$P_0 = \sigma_{h0} - \int_{r_0}^{r_{\infty}} \frac{\sigma'_{\pi} - \sigma'_{\theta\theta}}{r} dr \quad (8.29)$$

where σ_{h0} is the in-situ total horizontal stress in the far field.

6.4.2 Interpretation of Predictions

The interpretation of pressuremeter predictions includes the evaluation of the following parameters:

1. The lift-off pressure $(P_0 - u_0)/\sigma'_{v0}$ is equated with the total radial stress in excess of the in-situ pore pressure $(\sigma_{\pi} - u_0)/\sigma'_{v0}$ acting on the pressuremeter prior to membrane expansion (i.e., after installation and 'relaxation').

⁹ The relevant transformed strain components (cf., Appendix C) become:

$$\dot{E}_2 = \frac{1}{\sqrt{2}} (\dot{\epsilon}_{\theta\theta} - \dot{\epsilon}_{\pi}) = -\frac{\dot{V}}{\sqrt{2} r^2}; \dot{E}_1 = \dot{E}_3 = \dot{E}_4 = \dot{E}_5 = 0$$

2. The limit pressure at infinite membrane expansion $(P_L - u_0)/\sigma'_{v0}$ is evaluated using the method described by Ladd et al. (1980) in which the P versus $\log(\Delta V/V)$ curve is linearly extrapolated to $\Delta V/V=1$.
3. The undrained shear strength, c_{uPM} , from a pressuremeter expansion curve is evaluated using the BLP method (Section 6.2.2.1):

$$c_u = \left[\frac{dP}{d [\ln (\Delta V/V)]} \right]_{\max} \quad (8.30)$$

Undrained shear strengths from the pressuremeter contraction curve are evaluated using the formulation proposed by Houlsby and Withers (1988):

$$c_u = \frac{1}{2} \frac{dP}{d [\ln(\epsilon_0^e - \epsilon_0)]} \quad (8.31)$$

$$\epsilon_0^e - \epsilon_0 = \frac{1}{2} \ln(V_e/V)$$

where V_e is the pressuremeter volume at maximum expansion and V is the current pressuremeter volume.

4. Strength factor, N_p . The strength factor N_p is based on a theoretical relation derived by Bishop et al. (1945) for an elastic-perfectly-plastic material, and can be expressed in terms of the limit pressure P_L , the contact pressure P_0 and the undrained shear strength c_{uPM} :

$$N_p = \frac{P_L - P_0}{c_{uPM}} \quad (8.32)$$

6.4.3 Displacement Pressuremeter Predictions

This section presents predictions for displacement pressuremeters, which were discussed in Section 6.2.1.1. The analyses consider three penetrometer geometries: 1) the solid-section full-displacement or cone pressuremeter (FDPM), 2) the open-ended push-in pressuremeter (PIPM) with aspect ratio $B/t=12$ which corresponds approximately to the dimensions of the Stressprobe reported by Lacasse and Lunne (1982) and Fyffe (1986), and 3) a hypothetical thin-walled push-in device with $B/t=40$ ¹⁰. Loading conditions for the predictions entail: 1) 20% radial expansion of the membrane $\Delta R/R_0 = 20\%$ ($\Delta V/V_0=44\%$)¹¹, and 2) contraction to the original undeformed configuration of the pressuremeter.

¹⁰This is a similar aspect ratio to pipe piles used for offshore foundations.

¹¹This level of expansion represents a general upper bound of the values typically reported in the literature.

Strain Path predictions of installation disturbances for axisymmetric cone penetrometers have been described by Baligh (1986a,b), Whittle (1987), and Chapter 3. The results in Chapter 3 show that the simple pile provides a good approximation for the stress fields around a 60° cone penetrometer; thus, the simple pile is used to simulate installation disturbance for the full-displacement pressuremeter (Figure 6.14a). Predictions for the PIPM devices are based on solutions for a 'simple open-ended pile' (Chin, 1986), which is assumed to penetrate the soil in an unplugged mode. Contours of octahedral shear strain, E , corresponding to FDPM and standard PIPM penetration are shown in Figure 6.14, which indicates that the lateral extent of disturbance induced by the two devices is quite similar. However, the near-field strains are significantly larger for FDPM penetration.

6.4.3.1 No Drainage of Installation Pore Pressures

Installation stresses and pore pressures for FDPM and PIPM penetration in K_0 -normally consolidated BBC (based on MIT-E3 predictions) corresponding to conditions of no drainage are shown in Figure 6.15. This figure indicates that method of installation has minor effect on stresses and excess pore pressures following installation, with excess pore pressures and radial effective following PIPM installation being slightly smaller than those corresponding to FDPM installation.

The effect of installation disturbance on stress-strain behavior in a pressuremeter shearing mode for penetration in K_0 -normally consolidated BBC (with no drainage of installation pore pressures) is shown in Figures 6.16a and b, which show the strain behavior of a soil element adjacent to the pressuremeter boundary, and the radial distribution of available shear resistance after installation, respectively. These figures show:

1. The strength of the disturbed clay adjacent to the pressuremeter membrane is 25-30% of the undisturbed strength c_{uPM} .
2. The disturbed clay exhibits a non-linear elastic perfectly-plastic response (i.e. no hardening or softening) similar to the undisturbed clay for all geometries.
3. The available shear resistance in the soil after installation disturbance decreases markedly within $r/R \leq 5-6$ of the FDPM boundary and within $r/R = 2-3$ of the standard PIPM boundary.

Table 6.6 and Figures 6.17 and 6.18 present MIT-E3-pressuremeter predictions for the displacement pressuremeter tests¹² performed in normally consolidated Boston Blue Clay. The results in Figure 6.17 are reported in a dimensionless format relating the total net

¹²Assuming there is no time delay between device installation and membrane expansion.

membrane pressure, $(P-u_0)/\sigma'_{v0}$; excess pore pressure, $(u-u_0)/\sigma'_{v0}$; and radial effective stress σ'_r/σ'_{v0} to the volumetric strain $\Delta V/V_0$. The figure shows the following:

1. Pore pressure dominates the response during the expansion phase. For the undisturbed soil, the increase in pore pressure during the expansion phase slightly exceeds the increase in net membrane pressure (total radial stress), and hence, the effective radial stress decreases during membrane expansion. Installation disturbance causes large initial excess pore pressures, which account for over 90% of the net membrane pressure. During membrane expansion, increases in excess pore pressure account for 80-90% of the changes in net pressure.
2. During the contraction phase, $(P - u_0)/\sigma'_{v0}$ is less than the installation pore pressure $(u_i - u_0)/\sigma'_{v0}$ over a large portion of the curve for small changes ($\epsilon_0 - \epsilon_0^e \cong 0.4-.5\%$) in the volume of the pressuremeter¹³, and thus the effective radial stresses reduces to $\sigma'_r/\sigma'_{v0} \approx 0.1$.
3. Expansion curves in the disturbed soil are similar for the three pressuremeter geometries as expected from the predicted stress fields shown in Figure 6.15. The analyses show that the membrane pressure at the end of contraction increases with the level of installation disturbance (i.e., B/t ratio).

The undrained strength ratio, c_{uPM}/σ'_{v0} , can be estimated from the slope¹⁴ of the expansion curve plotted in Figure 6.18a, using the BLP method (Section 6.2.2.1). Alternately, shear strengths can be estimated using the Houlsby-Withers approach, using the membrane contraction curve shown in Figure 6.18b. Table 6.6b summarizes the predictions of undrained shear strength from Figure 6.18. The results show the following:

1. The net contact pressures, immediately after pressuremeter installation, range from $(P_0 - u_0)/\sigma'_{v0} = 1.1-1.3$ (Figure 6.18a; Table 6.6a), are significantly larger than the in-situ lateral stress ratio, $K_0=0.48$. This behavior can be attributed to the development of large excess pore pressures during installation (Figure 6.15).
2. For the undisturbed pressuremeter test, the expansion curve in figure 6.18a is approximately linear for $\Delta V/V > 1\%$, and the computed undrained shear strength matches the ideal, elemental behavior described in Figure 6.11. Installation disturbance introduces significant non-linearities in the expansion curves. The apparent peak shear

¹³For this condition, a gap between the membrane and the soil becomes possible, in which case a more realistic boundary condition might be $(p_0 - u_0)/\sigma'_{v0} = (u_i - u_0)/\sigma'_{v0}$.

¹⁴In this figure net membrane pressure is plotted versus $\log_{10} (\Delta V/V)$; hence, the apparent undrained strength ratio is 2.3 times the maximum slope of this curve.

strength is mobilized at large strains, and the curvature of the expansion curve makes reliable estimates of c_u/σ'_{v0} difficult to achieve.

3. The undrained strength ratios derived from the predicted expansion curves at $\Delta V/V_0=10$ and 40% are shown in Table 6.6b. These results illustrated the uncertainty in estimating c_u/σ'_{v0} from displacement pressuremeter expansion measurements. The FDPM expansion curve (Figure 6.18a) shows a maximum slope at small strains which falsely implies post-peak strain softening behavior.
4. Estimates of c_u/σ'_{v0} from FDPM expansion curves at large strains ($\Delta V/V_0=10-40\%$) underpredict the actual pressuremeter strength by 70 to 80%.
5. The predicted contraction curves reach an approximately linear range for $\ln(V_e/V) \approx .02$ for all displacement pressuremeters (Figure 6.18) and, hence, the peak shear resistance can be estimated unambiguously using the Houlsby-Withers approach (Table 6.6b). However, at this strain level, the net membrane pressure is less than the the installation pore pressure $\Delta u_i/\sigma'_{v0}$, introducing the possibility of a gap forming between the membrane and the soil, as discussed earlier.
6. As the aspect ratio, B/t , increases the contraction curves tend to match more closely the behavior of the undisturbed soil. The undrained strength ratios derived from the contraction curves are relatively insensitive to installation disturbance (Table 6.6b).

Figures 6.19 through 23 show the effect of stress history on predicted pressuremeter measurements. Figures 6.19a and 6.20a present the stress-strain behavior in a pressuremeter shearing mode for soil elements adjacent to the pressuremeter boundary and $OCR=2$ and 4, respectively; while Figures 6.19b and 6.20b show the corresponding radial distributions of available shear resistance:

1. The disturbance at $OCR=2$ causes a large reduction in the available shear resistance for soil elements adjacent to the pressuremeter similar to that predicted for disturbed normally consolidated soil. Furthermore, the predicted radial distribution of available shear resistance for the $OCR=2$ soil is very similar to that predicted at $OCR=1$ (cf., Figure 6.16).
2. The disturbed $OCR=4$ soil strength adjacent the pressuremeter boundary is comparable to the intact strength (within $\pm 20\%$). The radial distribution of available shear resistance also differs qualitatively from that predicted at $OCR=1$ and 2 soil. The available shear resistance in $OCR=4$ soil decreases with distance from the membrane in the zone $r/R \leq 2-3$.

The predicted contact pressures (total stress and pore pressures) during pressuremeter expansion and contraction in $OCR=2$ and 4 soils (Figures 6.21a and b) and the predicted pressuremeter curves plotted on semi-logarithmic scales (Figures 6.22a and b) show

qualitatively similar trends to those noted for the normally consolidated soil: 1) pore pressure dominates the response during membrane expansion and contraction, and 2) installation pressure P_0 substantially exceeds (by a factor of greater than 3) the in-situ horizontal stress σ_{h0} .

The undrained shear strengths derived from the predicted pressuremeter curves are summarized in Figure 6.23. The error bars shown in this figure represent the uncertainties in estimating undrained shear strength at large expansion strains. The derived shear strengths are compared with model predictions for the ideal pressuremeter behavior (c_{uPM}/σ'_{v0}) and with strengths from undrained plane strain active and triaxial extension shear modes. The results show the following:

1. Non-linearity of the disturbed pressuremeter expansion (on a semi-logarithmic plot) curves creates significant uncertainty ($\pm 50\%$) in strength estimates derived from expansion curves.
2. As the degree of disturbance (B/t ratio) decreases, strength estimates derived from expansion curves increase. Strengths derived from FDPM expansion curves severely underpredict (by 50-75%) c_{uPM} at all OCR's, while strengths derived from standard ($B/t=12$) PIPM expansion curves underestimate c_{uPM} by 10-70%. Average strengths derived from the hypothetical 'thin-walled' ($B/t=40$) PIPM are in good agreement with the ideal pressuremeter behavior. However, there is a large uncertainty in interpreting the strength from the predicted expansion curves.
3. The undrained shear strength interpreted from the contraction curve of the intact soil is up to 10% smaller than the c_{uPM} obtained in an ideal monotonic shear test. Peak strengths derived from contraction curves are relatively insensitive to installation disturbance, particularly those derived from the PIPM ($B/t=12$ and 40) contraction curves. The peak c_{uPM} estimates from the PIPM curves match closely the estimates obtained from pressuremeter contraction in an intact soil.

The limit pressures P_L and strength factors N_p derived from the pressuremeter predictions are listed in Table 6.6c. This table indicates:

1. The effect of installation disturbance on limit pressure $(P_L - u_0)/\sigma'_{v0}$ is less than 10%. As the B/t ratio of the penetrometer increases, the limit pressures tend to agree more closely with the undisturbed limit pressure.
2. The mean strength factor $N_p=6.8$ for undisturbed BBC and exhibits minor variation with OCR. This is in reasonable agreement with the estimate made by Ladd et al. (1980) that for most clays $N_p=6.0\pm 1.5$.
3. Strength factors from the disturbed soils underestimate N_p of the undisturbed soil by 40-65%.

4. Strength factors derived from pressuremeter curves in disturbed soil show more variability with varying OCR than those derived from undisturbed soils. Strength derived from the FDPMT show the highest degree of variability and lowest strength factors.
5. Examination of Table 6.6a suggests that the chief source of the discrepancy between N_p derived from disturbed versus undisturbed soils lies in the lift-off pressure P_0 . The results in Figures 6.18 and 6.22 show that disturbance has only a minor effect on the limit pressure P_L (<10%), but affects the contact pressures P_0 by up to 300%.

Overall, the predictions for displacement pressuremeter tests for which there is no dissipation of installation pore pressures suggest:

1. Effective radial stresses immediately following penetrometer installation bear no relation to the in-situ horizontal effective stress (K_0).
2. Undrained shear strength estimates based on pressuremeter expansion curves are strongly influenced by 1) level of disturbance and 2) strain level at which the strength is evaluated. In some instances the pressuremeter test results can falsely indicate strain softening behavior. Higher levels of installation disturbance (i.e., lower B/t ratios) tend to result in lower estimates of shear strength.
3. Undrained shear strength estimates based on pressuremeter contraction curves are insensitive to installation disturbance.

6.4.3.2 Drainage of Installation Pore Pressures

Conventional pressuremeter test procedures include a time delay between device installation and membrane expansion. For displacement pressuremeters, which induce large excess pore pressures during installation, the time delay can enable significant dissipation of excess pore pressure and concomitant changes in effective stresses to occur. In order to assess these effects, a parallel set of numerical predictions of displacement pressuremeter tests have been performed assuming full dissipation of installation pore pressures. Stresses at the end of consolidation were computed using the radial, non-linear, coupled finite element analysis described in Chapter 5.

Installation stresses and pore pressures for FDPM and PIPM penetration in K_0 -normally consolidated BBC (based on MIT-E3 predictions) with full drainage of installation excess pore pressures are shown in Figure 6.15. Comparison of stress conditions at the end of consolidation shows that penetrometer geometry has a modest effect on near field stresses (i.e.; σ'_r/σ'_{v0} at the PIPM boundary is 15-20% less than that at the FDPM boundary) and a negligible effect on far-field stresses.

Figure 6.24a shows the effect of penetrometer geometry (B/t ratio) on the shear stress-strain response for soil elements adjacent to the pressuremeter following penetration in normally consolidated BBC and full dissipation of excess pore pressures:

1. The pressuremeter geometry has a significant effect on the amount of shear strength recovery in the disturbed soil due to consolidation. For the FDPM device, the ratio of disturbed to undisturbed strength is approximately 75% after consolidation as compared to 30% immediately after installation. In contrast, for the thin-walled ($B/t=40$) PIPM, the ratio of disturbed to undisturbed strength is approximately 25% prior to consolidation and 40% after consolidation.
2. Differences in strength during loading and unloading become more significant when dissipation of installation pore pressures occurs. For tests performed immediately after installation, the ratio of unloading to loading shear strength is 60-70%. After full dissipation of pore pressures, this ratio reduces to 40-50%.
3. The strength recovery described above becomes less significant at higher OCR's.

Figures 6.25 and 6.26 show the pressuremeter predictions for tests performed in BBC at OCR's=1, 2, and 4, respectively, for the three displacement devices (FDPM, PIPM, and $B/t=40$) described previously. Table 6.7a summarizes the net membrane pressure at lift-off, which corresponds to the effective radial stress ratio, $K_c = \sigma'_r / \sigma'_{v0}$, acting on the pressuremeter prior to expansion. The tabulated values show the following:

1. The lateral stress ratio $K_c=0.26-0.38$ for normally consolidated BBC, which is less than the initial condition. In contrast, at OCR=4, $K_c=2.0-2.6K_0$. These results show that the installation disturbance causes a permanent (long-term) change in the lateral effective stress in the soil. Thus, the in-situ lateral earth pressure K_0 cannot be evaluated reliably from the contact pressures measured by displacement pressuremeters.
2. There are small differences in the predicted contact pressures for FDPM, PIPM and the thin-walled ($B/t=40$) pressuremeter geometries. The results consistently show that K_c for the FDPM device is approximately 10-15% less than that for the PIPM device.

Expansion curves showing the net membrane pressure $(P-u_0)/\sigma'_{v0}$ versus $\log(\Delta V/V)$ at OCR's 1, 2, and 4 are shown in Figure 6.26. Strength estimates derived from these curves are summarized in Tables 6.7b. The predictions show:

1. Although the expansion curves at OCR=1 show a consistent strength ratio $c_u/\sigma'_{v0}=0.22-0.24$, the expansion curves never reach a truly linear range (for $\Delta V/V_0 \leq 40\%$). Therefore, it is difficult to estimate reliably the undrained shear strength from these curves. Peak shear resistance generally occurs at large shear strains, except for the case of a FDPMT in OCR=4 soil, where the peak strength is predicted at $\Delta V/V=0.42\%$. Table 6.7b summarizes the uncertainties in the interpreted undrained shear strengths.

2. For normally consolidated BBC, the estimated strength ratios agree with the undisturbed strength to within 20% and are not affected significantly by penetrometer geometry. At higher OCR's (2 and 4), c_u/σ'_{v0} estimated from the expansion curves tends to underestimate the ideal pressuremeter shear strength. For example, at OCR=4 the interpreted strength from the PIPMT B/t=40 expansion curves underestimate the in-situ shear strength by 15-35% for the thin-walled PIPM (B/t=40), and by 50-90% for the FDPM device. The FDPM also indicates an apparent strain softening behavior which is not characteristic of the true material behavior (Figure 6.22).

Predicted contraction curves and estimates of undrained strength c_u/σ'_{v0} derived from these curves presented in Figures 6.26a, b, and c and Table 6.7b show:

1. All of the contraction curves indicate peak undrained shear strengths occurring at strains $\ln(V_0/V) = 0.02-0.07$. The curvature of the contraction curves imply a post-peak strain softening which is not characteristic of the elemental material behavior. Comparison with Table 6.7b (see Section 6.4.3.1) shows that when full dissipation of installation pore pressures occurs, the interpreted strength is more sensitive to the strain level at which the strength is evaluated, and there is more apparent strain softening.
2. Peak undrained shear strengths c_u computed from the contraction curves agree with the in-situ shear strength to within 10%, irrespective of penetrometer and stress history.

Strength factors N_p , back-calculated from pressuremeter predictions with full dissipation of installation pore pressures are shown in Table 6.7c. A comparison of these strength factors with those computed from tests immediately after installation (Table 6.6c) shows the following:

1. When full dissipation of pore pressures is permitted, the calculated strength factor N_p is generally greater than strength factors computed from pressuremeter curves from tests immediately after installation (one exception is the case of the PIPMT B/t=40 for OCR=4). This is due, in large part, to the reduction in contact pressure $(P_0 - u_0)/\sigma'_{v0}$ occurring after full dissipation.
2. Variability of strength factors, N_p , with OCR is substantially greater for the case of full dissipation.

Figure 6.27 compares the strengths derived from pressuremeter test predictions to the reference pressuremeter strength c_{uPM}/σ'_{v0} as well as for the plane strain active and triaxial extension strengths for $1 \leq \text{OCR} \leq 4$:

1. Strengths derived from the expansion curves show substantial scatter and tend to underestimate substantially the reference ideal pressuremeter strength c_{uPM}/σ'_{v0} .

2. Strengths derived from the contraction curves approximately match the reference pressuremeter strength c_{uPM}/σ'_{v0} . Strength estimates are relatively insensitive to the level of installation disturbance.

The predictions presented in this section show the following effects of installation disturbance with consolidation on the interpretation of displacement pressuremeter tests:

1. The contact pressure K_c is not a reliable indicator of the in-situ horizontal effective stress. The ratio K_c/K_0 ranges from 0.6 to 2.6 as OCR increases from 1 to 4..
2. Dissipation of installation pore pressures prior to membrane expansion does not improve significantly the estimates of undrained shear strength based on the membrane expansion curve. The estimated shear strengths are strongly dependent upon penetrometer geometry (FDPM, PIPM) and the strain level at which the strength estimate is computed. For OCR's greater than 1, estimates of c_u/σ'_{v0} significantly underestimate the actual strength ratio of the undisturbed clay.
3. Strength estimates obtained from the contraction curves are relatively insensitive to installation disturbance and match the undisturbed strengths to within 10%. In all the predictions performed the peak strengths occurred at pressures greater than the hydrostatic pore pressure. This result implies that the contraction curves can give reliable estimates of undrained shear strength if the pore pressures are allowed to dissipate fully.

6.4.4 Predictions for Self-Boring Pressuremeters

6.4.4.1 Simulation of Self-Boring Penetration

In contrast to displacement penetrometers, the installation of the self-boring pressuremeter (SBPM) extracts soil from the system to accommodate the volume of the device. In practice, this is accomplished by grinding or mixing the soil into a slurry and then flushing it to the surface. A comprehensive analysis of the process is currently not conceivable. An approximate analysis, which models the influence of soil extraction on strains in the outer soil is proposed in Figure 6.28. The analysis simulates soil extraction using a point sink centrally located at the tip of the cutting shoe. For steady penetration, the rate of soil extraction can be expressed by the ratio, $f=V^-/V^+$, where V^+ and V^- are the strengths of the source (which produces the tube geometry) and sink, respectively. Ideal self-boring occurs for $f=1$, when the rate of extraction exactly balances the displacement due to the pressuremeter tube. Appendix D describes in detail this Strain Path simulation of self-boring penetration. The analyses presented in this section consider values of f in the range $0 \leq f \leq 1$, which corresponds to the transition between PIPM and ideal SBPM tests.

Contours of octahedral strain, E , for standard ($B/t=12$, $f=0$) PIPM and ideal ($f=1$) SBPM penetration are presented in Figure 6.28. These results show that although self-boring greatly reduces the lateral extent of disturbances in the soil, significant shear strains do develop ahead of the cutting shoe.

6.4.4.2 Pressuremeter Test Predictions

Table 6.8a summarizes the predictions of installation stress conditions at the pressure membrane using the Strain Path simulations of self-boring penetration ($0 \leq f \leq 1$) for tests performed in K_0 -consolidated BBC ($OCR \leq 4$):

1. The lift-off pressure P_0 decreases with increasing rate of soil extraction f . The sharpest drop in P_0 occurs between $f=0.75$ and $f=1.0$. This also corresponds to the range of f at which final pressuremeter strains, E_2 , transition from negative (net expansion) to positive (net contraction) (see Appendix D). The lift-off pressure can either overestimate or underestimate the in-situ horizontal stress (K_0), depending on the magnitude of f .
2. Installation excess pore pressures $(u_i - u_0)/\sigma'_{v0}$ decrease with increasing f . For the ideal SBPM ($f=1$) at $OCR's=1$ and 2 $(u_i - u_0)/\sigma'_{v0} \geq 0$, while at $OCR=4$ $(u_i - u_0)/\sigma'_{v0} < 0$.

Predictions of net contact pressure during membrane expansion and contraction in normally consolidated BBC are shown in Figure 6.29 undisturbed and $f=1$ (ideal SBPM test). It can be seen that pore pressure accounts for 70-95% of the increase in membrane pressure during expansion. Effective radial stresses rapidly approach zero during membrane contraction.

Estimates of undrained shear strength c_u/σ'_{v0} from the SBPM expansion curves (Figure 6.30) are summarized in Table 6.8b. These predictions show:

1. Increasing the rate of soil extraction leads to an increase in the estimated undrained shear strength. For $0 \leq f \leq 0.875$, the pressuremeter expansion curves exhibit the same general characteristics of the PIPMT curves discussed in Section 6.4.3.1. In contrast, for $f > 0.875$, the net lift-off pressure is $(P_0 - u_0)/\sigma'_{v0} \leq K_0$ and the expansion curves indicate a peak shear resistance at $\Delta V/V = 1-2\%$. The interpreted shear strength in these tests are up to 60% larger than the true material behavior c_{uPM}/σ'_{v0} .
2. Strength estimates from the $f=1$ expansion indicate post-peak strain softening behavior, which corresponds to a 30-40% reduction in post-peak shear resistance. The shear strengths computed at large strains exceed the undisturbed strength by approximately 10%.

Strength estimates based on contraction curves (Figure 6.30) in Table 6.8b show:

1. As f increases from 0 to 1, the contraction curves tend to match more closely the behavior of the undisturbed soil.
2. Strength estimates from the contraction curves are relatively insensitive to soil extraction rate f during self-boring. The rate of soil extraction for $0 \leq f \leq 1$ has little effect on the calculated undrained shear strength ratio. Strength estimates at all values of f match the estimated strength obtained from a contraction curve in undisturbed soil to within 10%.

Figures 6.31 and 6.32 illustrate the influence of stress history on predicted pressuremeter curves for undisturbed and $f=1$ (ideal SBPM test). The predicted trends are qualitatively similar to those noted for SBPM predictions in normally consolidated BBC (Figures 6.29 and 6.30). Strength estimates derived from the expansion and contraction curves for $f=0$ and 1 (Figure 6.30) are presented in Figure 6.33. The arrows in this figure indicate the range between the apparent peak and ultimate strengths derived from the predicted pressuremeter curves, while the error bars indicate the uncertainties associated with evaluating the strengths at large strains. This figure indicates:

1. The ideal SBPM ($f=1$) strength estimates at all OCR's substantially exceed the reference pressuremeter strength (c_{uPM}/σ'_{v0}) and exhibit post-peak strength reductions of 20-40%. The possible range in strength estimates for $0 \leq f \leq 1$ illustrates the large uncertainties associated with strength derived from expansion curves.
2. Strength estimates derived from contraction curves are insensitive to extraction ratio and slightly underestimate the reference strength, c_{uPM}/σ'_{v0} .

The limit pressures and strength factors N_p derived from SBPM expansion curves are tabulated in Table 6.8c. This table indicates:

1. N_p increases by factors of 2.5 to 3.5 over the range $0 \leq f \leq 1$. For the ideal SBPM test ($f=1$) the expansion curve overestimates N_p of the undisturbed soil by 20-25%.
2. The variation in N_p with OCR decreases slightly with increasing f (from 0.083 to 0.064 over the range $0 \leq f \leq 1$). The variation for the $f=1$ case is comparable to the variation in N_p with OCR in the undisturbed soil.
3. As the rate of soil extraction f increases, the limit pressure P_L increases and tends to match more closely the undisturbed limit pressure. The overall effect of f on limit pressure amounts to less than 10% for $0 \leq f \leq 1$.

Overall, the SBPM predictions presented in this sections suggest the following conclusions:

1. Lift-off pressure $(P-u_0)/\sigma'_{v0}$ is strongly dependent on the extraction ratio, f , during self-boring. The fact that f is difficult to monitor and control in practice would suggest that lift-off pressures are highly susceptible to installation technique. The steep slope of

the predicted pressuremeter curve at small strains makes selection of the lift-off pressure by visual inspection unreliable.

2. The extraction ratio f has a very significant effect on prediction of undrained shear strength from expansion curves. At low f values the disturbance effect is similar to that occurring in a PIPMT and the estimated shear strengths are lower than the actual in-situ pressuremeter strength. In contrast, for ideal self-boring ($f=1$) the SBPM expansion curves overpredict significantly (by up to 60%) the actual in-situ strength. Large strain shear resistance from these tests estimated provide a more reasonable estimate of in-situ shear strength.
3. Peak strength estimates from contraction curves are insensitive to variations in extraction ratio, f . For ideal self-boring ($f=1$), the strength estimate is obtained at pressures higher than the installation pore pressure and should therefore be more reliable.

6.4.5 Finite Membrane Length Effects

The effects of finite membrane expansion was modelled by finite elements using the ABAQUS program described in Section 5.3. Equilibrium imbalances associated with Strain Path Method prediction of disturbance were treated by applying externally applied nodal equilibrating forces as described in Section 5.3. The analysis uses mixed elements with eight displacement nodes and four (corner) pore pressure nodes. These analyses should be considered to be tentative due to problems of mesh-locking associated with this element under conditions of undrained, axisymmetric shearing (Sloan, 1982). Predictions were performed for the following conditions:

1. A membrane having a length-to-diameter ratio, $L/B=6$, which corresponds to the standard Camkometer dimensions (Table 6.1a, Figure 6.3a). The membrane was assumed to be located far above the cutting shoe.
2. Pressuremeter testing in K_0 -normally consolidated BBC simulated using the MIT-E3 soil model.
3. Stress conditions prior to membrane expansion corresponding to conditions of a) no disturbance and b) ideal self-boring penetration ($f=1$).
4. The membrane was expanded under undrained conditions.

The mesh and used in the analyses are shown in Figure 6.34a, imposing the following boundary conditions:

1. The membrane boundary condition (OA) is stress controlled, with the horizontal total stress σ_{rr} set to the current level of membrane pressure, P .

2. Vertical displacements are zero in the horizontal plane passing through the center of the membrane (AB) and in a horizontal plane far below the membrane (CD).
3. The far-field (BC) horizontal stress σ_{π} is set to the in-situ horizontal stress, σ_{h0} .
4. Horizontal displacements are zero along the pressuremeter boundary outside of the membrane (DO).

The predicted membrane expansion curves presented in Figure 6.34b show:

1. In an intact soil, the finite length of the membrane ($L/B=6$) causes strength estimates derived from a pressuremeter curve to exceed the reference (intact) pressuremeter strength c_{uPM}/σ'_{v0} by 30%. This result is comparable to those obtained by Yeung and Carter (1990, Section 6.2.3), which predict strength overestimates of 24 to 40% (for rigidity indices $I_r=375$ and 50, respectively) for finite membrane ($L/B=6$) expansion in intact soil.
2. In a soil subject to disturbance caused by ideal self-boring penetration, the compound effect of the disturbance and the finite length of the membrane causes strength estimates derived from a pressuremeter curve to exceed the reference pressuremeter strength c_{uPM}/σ'_{v0} by over 150% and to exceed the reference triaxial compression strength $c_{uTC}/\sigma'_{v0}(=0.33)$ by approximately 50%.

6.5 FIELD MEASUREMENTS IN BOSTON BLUE CLAY

This section compares predictions to pressuremeter test data obtained from the South Boston Special Test Program for the Central Artery/Third Harbor Tunnel (CA/T) Project. A detailed description of the site is contained in Section 3.5. Eleven self-boring pressuremeter tests were conducted under the direction of Professor Jean Benoît of the University of New Hampshire (Benoît, 1991). The pressuremeter probe comprises a modified version of the Camkometer (Figure 6.3a) probe, with two additional sets of feeler arms located at the top and bottom quadrants of the membrane. Installation of the device is achieved using a non-standard jetting tip, shown in Figure 6.35. The test procedures include: a) delay periods following probe insertion ranging from 22 to 51 minutes, and b) stress controlled membrane expansion rates ranging from 28 to 55 kPa/min.

Comparisons of predicted to measured expansion and contraction curves for the middle feeler arms (M1, M2, and M3) for OCR=1 and 4 soils are shown in Figures 6.36a and b. These comparisons show:

1. Predictions of expansion curves in normally consolidated BBC significantly underpredict (by $\approx 30\%$) the overall magnitudes of the membrane pressures during expansion. For Arms 1 and 2 in Figure 6.36a, the lift-off pressures are comparable to

what would be expected during full-displacement penetration (Morrison, 1984), which places doubt on either the pressure measurements or the installation procedure. Predictions of contraction curves in normally consolidated BBC significantly underestimate the slope of the contraction curve. The source of these major discrepancies may be due to the following factors:

- a. The analyses apply to extraction ratios in the range, $f \leq 1$, while, in the field tests, overcutting ($f \geq 1$) may have occurred in the soft clays.
 - b. The simplified analyses of self-boring penetration do not accurately describe the boundary conditions around the pressuremeter. After penetration is interrupted, a stress-controlled boundary condition exists at the cutting shoe, with the vertical stress controlled by the weight of the slurry in the borehole. The Strain Path simulation of self-boring did not simulate this boundary condition.
2. Although there are significant initial differences in the $OCR = 4$ expansion curves measured by the three arms, the data coalesce for volumetric strains $\Delta V/V > 5\%$, and coincide with the predicted curves for the ideal SBPM test. The measurements for Arm 1 coincide with the idealized SBPM curve for $\Delta V/V > 1.5\%$ and show remarkable agreement with the subsequent curvature of the expansion curve. Differences in the simulated and measured expansion curves at low strains may indicate the importance of factors not considered in the analysis such as internal pressure inside the cutting shoe or consolidation prior to membrane expansion.

Peak and ultimate undrained shear strengths estimated from the expansion curves using the BLP formulation are shown in Table 6.9a. Similar estimates using the Houlsby and Withers (1986) interpretation of the contraction curves are shown in Table 6.9b.

Table 6.9a compares undrained shear strengths obtained from the measured expansion curves with reference properties from CK_0UC and CK_0UE tests:

1. Large variations in estimated strengths occur among the three sensing arms (up to 50%). Arm M1 estimates strengths which are up to 3 times greater than those from arms M2 and M3. In addition, arm M1 indicates that strain softening behavior (i.e., the maximum slope of the $P-\ln(\Delta V/V)$ curve occurs at small strains) in 7 of the nine tests, while arm M2 indicates strain softening behavior in only one test (SB2.7), and arm M3 never indicates strain softening behavior.
2. Ultimate strengths obtained from the individual sensing arms can either overestimate the reference triaxial compression strength by up to a factor of nearly 2 or underestimate it by nearly 30%. The mean of the three strengths obtained from the sensing arms also show no consistent pattern with respect to the reference strength, and they can either over- or under-estimate the reference triaxial compression strength. Stress history

(OCR) has no apparent influence on the differences between the reference strengths and the strengths estimated from the pressuremeter expansion curves.

3. Peak strengths obtained from the pressuremeter expansion curves severely overestimate the reference triaxial compression strengths (by up to a factor of 3).

The ultimate undrained shear strength estimates based on pressuremeter contraction curves shown in Table 6.9b show:

1. There is much less variability in strength estimates obtained from the three feeler arms when estimates are based on contraction curves rather than expansion curves. At a given elevation strength estimates from the pressuremeter contraction curves have a variability of less than 15% (as opposed to $\pm 50\%$ from expansion curves).
2. Strength estimates from the contraction curves severely overestimate the reference triaxial compression strength in the lower deposit of normally consolidated clay (by a factor of approximately 2). In the upper part of the deposit ($2 \leq \text{OCR} \leq 4$) the pressuremeter tests overestimate the reference strengths by somewhat smaller amounts (10-40%). Overall, the strength profile obtained from the pressuremeter contraction curves does not match the reference profile either in magnitude or in overall shape.

The relationship between initial lift-off pressure, P_0 ¹⁵, and undrained shear strength estimated from measured expansion curves is illustrated in Table 6.10 which shows:

1. The lift-off pressure, P_0 , varies substantially (by up to 70%) at a given elevation according to the measurement direction (M1, M2, or M3). While anisotropy of stress conditions in the horizontal plane is a possible explanation for this phenomenon, a more likely explanation is that disturbance during pressuremeter installation is not axisymmetric.
2. When lift-off pressures, P_0 , and estimated undrained shear strengths measured in the M1, M2, and M3 directions are compared at a given elevation, it can be seen that low lift-off pressures (relative to measurements in the other directions) are associated with a) high estimates of undrained shear strength (relative to strength estimates in the other directions), while high lift-off pressures are associated with a) low strength estimates.

With regard to the predictions made in Section 6.3, the following observations are pertinent to the measured South Boston BBC data presented in Tables 6.9 and 6.10:

1. The trends observed in Table 6.10 of low lift-off pressures being associated with high estimates of undrained shear strength, c_{uPM} , are similar to the predicted trends shown in Table 6.7. However, in the case of the predictions, the source of the variations in lift-off pressures was the rate of soil extraction during pressuremeter installation, f . For

¹⁵The lift-off pressures were estimated by visual inspection of P-log($\Delta V/V$) plots.

the South Boston measurements, the cause of variations in lift-off pressure with direction is not certain. A likely cause is that imperfections in alignment during penetration result in soil displacement (and consequently high lift-off pressures) in one direction and an overcoring effect (resulting in low lift-off pressures) in the other direction. Although the physical causes of the variations in lift-off pressure are different for the predictions in Table 6.7 and the measured data in Table 6.10, it appears that the impact on estimated shear strength is similar. Namely, horizontal stress reductions during penetration result in false indications of strain softening and high estimates of undrained shear strength, while horizontal stress increases during penetration result in low estimates of undrained shear strength. Both predictions and measurements indicate that strengths are quite sensitive to the lift-off pressure, and hence variability in lift-off pressure following penetration will result in substantial scatter in the strength estimates.

2. The relatively small scatter in strength estimates obtained from pressuremeter contraction curves at the South Boston site is consistent with the predictions in Section 6.3. The analyses show that strength estimates from pressuremeter contraction curves are insensitive to installation disturbance for a) displacement pressuremeters of varying geometries; and b) self-boring pressuremeters with varying extraction ratios, $0 \leq f \leq 1$. However, the predictions indicate that contraction curve strength estimates will slightly underestimate the undrained shear strength in a pressuremeter (or DSS) shearing mode, while the South Boston data shows that strength estimates from the contraction curve severely overestimate the reference triaxial compression strength. A possible reason for this discrepancy is that the predictions were based on expansion of an infinitely long cylindrical cavity while the actual pressuremeter has a finite length (length-to-diameter ratio, $L/B=6$).

Overall, the pressuremeter data measured at the South Boston site suggests the following conclusions:

1. Strength estimates from pressuremeter expansion curves is highly sensitive to the horizontal stress state following pressuremeter installation (lift-off pressure, P_0). Lift-off pressures can vary with the direction of measurement, probably due to imperfections in alignment during pressuremeter penetration, resulting in a wide scatter in strength estimates (variation by a factor of 2) based on measurements made in different directions.
2. No consistent trends can be identified between strengths estimated from pressuremeter expansion curves and reference triaxial compression or extension tests.

3. Peak strengths obtained from pressuremeter expansion curves are a consequence of stress reductions during probe installation and are not meaningful measures of the true soil properties.
4. Strength estimates obtained from pressuremeter contraction curves severely (by a factor of 2) overestimate reference triaxial compression strengths, hence such estimates cannot be used directly to estimate in-situ strength. However, contraction curve strength estimates appear to quite insensitive to stress changes due to installation disturbance. It may be possible to develop a correction factor to relate strengths from the contraction curve to laboratory shear strength. More field measurements of strength from contraction curves should be reviewed to assess the feasibility of this option.

6.6 SUMMARY AND CONCLUSIONS

This chapter has investigated the effects of the following factors on the performance of pressuremeter tests: 1) installation disturbance (displacement versus self-boring pressuremeters), 2) stress history, 3) dissipation of installation pore pressures, 4) membrane expansion versus contraction, and 5) finite membrane length. These factors were investigated by review of previously published field data, a comprehensive series of analytical predictions, and a review of pressuremeter data from the South Boston site. The study suggests the following conclusions:

1. Undrained strength estimates from pressuremeter expansion curves are strongly influenced by the horizontal stress (lift-off pressure) following probe insertion. High lift-off pressures (relative to the in-situ horizontal stress state) result in underprediction of in-situ strength, while low lift-off pressures result in overestimation of in-situ strength. Low lift-off pressures also result in pressuremeter expansion curves which indicate excessively high peak strengths and give false indications of material strain softening. Field data presented by Ghionna et al. (1982), Benoit and Clough (1986), and the Benoit (1991) data support the trends indicated from the predictions.
2. Predictions indicate that lift-off pressures around displacement pressuremeters (FDPM, PIPM) exceed the in-situ horizontal stress state and strength estimates derived from the pressuremeter expansion curves tend to underestimate in-situ strength. This effect occurs for both full-displacement pressuremeters and for push-in pressuremeters of varying tube diameter to wall thickness (B/t) ratios. The expansion curves are also non-linear (concave upward) over the practical range of significance for membrane expansions (up to $\Delta V/V_0=40\%$) and thus, it is difficult to estimate reliably the undrained shear strength from these measurements.

3. The predictions and field measurements from Benoît and Clough (1986) show that lift-off pressures around self-boring pressuremeters are strongly influenced by soil extraction rate during probe insertion. Increasing the rate of soil extraction (and overcoring) both result in reductions in lift-off pressures and consequently in overestimates of in-situ strength as described above. Measurements at the South Boston site show that measured lift-off pressure can also vary with direction of the feeler arms. Feeler arms which measure higher lift-off pressures exhibit expansion curves similar to those predicted for displacement pressuremeters ($f=0$); while those with low lift-off pressures are more comparable to predictions presented for ideal self-boring pressuremeters ($f=1$). This type of variability in measured lift-off pressures cannot be explained in terms of the predictive framework used in this chapter (assuming perfect axisymmetry) and cannot be ascribed to overcoring or soil extraction rate. Misalignment of the probe during penetration is the most likely cause of these directional variations.
4. Strength estimates derived from pressuremeter contraction curves are relatively insensitive to installation disturbance. Predictions indicate that this is true for a wide range of penetrometer geometries (B/t ratios) and soil extraction ratios, f . Data from the South Boston site show strength estimates from contraction curves are insensitive to the initial lift-off pressure and hence tend to support this conclusion. Predictions showing that strength estimates from pressuremeter contraction curves are in good agreement with the in-situ strength are not supported by the South Boston site data, which show overestimates of reference triaxial strengths (by up to a factor of 2). This discrepancy may be related in part to membrane length effects (cf., Section 6.4.5).
5. Predictions indicate that permitting full dissipation of excess pore pressures developed during pressuremeter installation does not improve strength estimates obtained from either expansion or contraction curves. Unfortunately no comprehensive field test programs have been performed to date which can verify this conclusion.
6. The predictions show a consistent trend between the volume of soil displaced during device installation and pressuremeter strength estimates. The displacement pressuremeter predictions showed a consistent increase in apparent strength with decreasing volume of soil displaced during pressuremeter installation; while the SBPM predictions showed similar trends with increasing extraction ratio, f . These predicted trends are in qualitative agreement with comparisons of displacement pressuremeter (PIPM) and SBPM measurements (Figure 6.10, Lacasse and Lunne, 1990), which show that SBPM strength estimates are substantially higher than PIPM estimates.

Device	Diameter B (mm)	Membrane L/B	Reference
Camkometer	39	2	Wroth and Hughes (1973)
Camkometer	63.5	6	Ladd et al. (1980)
Camkometer	80	6	Lacasse and Lunne (1982)
			Benoît and Clough (1986)
PAFSOR-72	132	2 or 4	Ladd et al. (1980)

Table 6.1a - Self-Boring Pressuremeter Characteristics

Penetration Rate (cm/min)	Relaxation Time (min)	Membrane Expansion Rate	Reference
	30	$d\epsilon_0/dt=1\%$ **	Ladd et al. (1980)
1.5-2	Up to 1300*	$d\epsilon_r/dt=1\%$ ***	Lacasse et al. (1982)
2.5-5	30-180*	7 kPa/min	Lacasse and Lunne (1982)
			Benoît and Clough (1986)
		6-9 kPa/min	Ladd et al. (1980)

*Full Dissipation of Excess Pore Pressure

** ϵ_0 =Circumferential Strain*** ϵ_r =Radial Strain

Table 6.1b - Typical SBPM Test Procedures

Method		Steps in Estimating σ_{h0}	Reference
Lift-off Related	a) Inspection	First movement of membrane or first break in p - ϵ_0 curve	Lacasse and Lunne (1982)
	b) Initial Development of Excess PWP	Inflation pressure at which PWP begin to develop	Wroth and Hughes (1974)
	c) Modified Lift-off	σ_{h0} corresponds to start of linear range in ϵ_{rr} vs. time curve	Lacasse et al. (1981)
	d) Log-Strain	σ_{h0} at first break in p vs. log strain curve	Law and Eden (1982)
	e) Inverse Volume	σ_{h0} at first break in p - $(1/\Delta V)$ curve	van Wanbeke and d'Hemricourt (1975)
Complete Expansion Curve	f) Graphical Iteration	Based on Gibson-Anderson (Eq. 8.18) 1. Assume p_0 2. Compute c_u for assumed p_0 3. Iterate until (p_0+c_u) coincides with yield point on PM expansion curve	Marsland and Randolph (1977)
	g) Hyperbolic-plastic modelling of expansion curve	1. Curve fit using hyperbolic-plastic soil model 2. Extrapolate back to zero strain 3. Correct σ_{h0} for false initial strain	Denby (1978)
	h) Double zero shift of hyperbolic expansion curve	1. Fit data points to hyperbolic expansion curve 2. Select p_0 on hyperbolic curve by inspection	Denby and Hughes (1982)
	i) Origin Adjustment	1. Assume initial strain 2. Compute expansion curve using Eq. 8.18 3. Repeat Steps 1&2 to create family of curves 4. Most linear curve corresponds to correct initial strain	Denby and Hughes (1982)

Table 6.2 Summary of Methods of Estimating In Situ Horizontal Stress from Pressuremeter Expansion Curves

Site	Soil Type	Plasticity Index I_p	OCR	Sensitivity S_r	c_u/σ'_{v0}			Reference
					CK ₀ UC	DSS	FV	
Porto Tolle	Silty Clay	30	1	2-3	0.31	0.26	0.29	Ghionna et al. (1982)
Trieste	Organic Clay	47	1	2-4	0.35	0.28	0.28	Ghionna et al. (1982)
Onsøy	Silty Clay	20-36	1-1.2	5-6	0.31	0.26-0.28	0.31	Lacasse et al. (1981)
Drammen	Plastic Clay Lean Clay	25-30 10-15	1.5 1.15	6-8 4-7	0.4	0.32 0.22	0.40 0.30	Lacasse et al. (1981)
Haga	Medium Clay	15	3-7		0.77 0.46		0.50 0.30	Lacasse et al. (1990)
S.F. Bay Mud	Medium Clay	45	1.1-1.3	6-8	0.35 ¹	0.32 ² 0.74 ³		Benoit and Clough (1986)

¹OCR=1.0 Bonaparte and Mitchell (1979)²OCR=1.5 DeGroot (1990)³OCR=4.1 DeGroot (1990)

Table 6.3 Data Summary at Six Pressuremeter Sites

Site	Porto Tolle	Trieste	Onsoy	Drammen	Haga
Reference	Ghionna et al. (1982)	Ghionna et al. (1982)	Lacasse et al. (1981)	Lacasse et al. (1981)	Lacasse et al. (1990)
OCR	1	1	1.1-1.3	1.5	2-30
L/B	2 4	2 4	6	6	2-4
Depth (m)	15 15	11 18	13	10	1-7
c_{uPM}/σ'_{v0}	Gibson-Anderson	0.36 0.20	0.54 0.17	0.41	0.50
	Windle-Wroth	0.49 0.24	0.80 0.23	0.41	0.75-1.15*
	Prévost-Hoeg	0.44 0.25	0.68 0.22	0.43	0.35-0.90
	Denby-Clough	0.48 0.23	0.71 0.24	0.42	0.51
		0.31	0.32	0.40	0.77 0.46
$\tilde{c}_{uTC}/\sigma'_{v0}$					
c_{uDSS}/σ'_{v0}	0.29	0.35	0.31	0.40	0.50 0.30
c_{uFV}/σ'_{v0}	0.26	0.28	0.26-0.28	0.32	

* Interpretation method not reported

Table 6.4 SBPMT Strength Estimates

OCR	1.0				4.0			
K_0	0.48-0.53				0.75-1.0			
Undrained Strength Ratio	MIT-E3	MCC	Measured BBC		MIT-E3	MCC	Measured BBC	
c_{uTC}/σ'_{v0}	0.33	0.32	0.33		1.16	1.05	1.04	
c_{uTE}/σ'_{v0}	0.15	0.32	0.14		0.40	1.05	0.52-0.60	
c_{uPSA}/σ'_{v0}	0.34	0.37	0.34		1.18	1.21	0.84-1.04	
c_{uPSP}/σ'_{v0}	0.18	0.37	0.16-0.19		0.44	1.21	0.52-0.60	
c_{uDSS}/σ'_{v0}	0.21	0.37	0.21		0.72	1.21	0.60-0.64	
c_{uPM}/σ'_{v0}	0.21-0.22	0.37	0.21		0.66-0.76	1.21	0.64-0.76	

Table 6.5 Undrained Shear Strength Ratios for Boston Blue Clay at OCR's 1 and 4

Disturbance	OCR	Lift-off Pressure $(P_0 - u_0)/\sigma'_{v0}$	Installation Pore Pressure $(u_i - u_0)/\sigma'_{v0}$	Effective Stress $(P_0 - u_i)/\sigma'_{v0}$
Intact	1	0.48	0	0.48
	2	0.57	0	0.57
	4	0.74	0	0.74
FDPM (B/t=2)	1	1.30	1.18	0.12
	2	1.89	1.66	0.23
	4	2.56	1.87	0.69
Standard PIPM (B/t=12)	1	1.22	1.15	0.07
	2	1.76	1.61	0.15
	4	2.45	1.81	0.64
Thin-Walled PIPM (B/t=40)	1	1.12	1.06	0.06
	2	1.60	1.48	0.12
	4	2.24	1.50	0.74

Table 6.6a Displacement Pressuremeters - No Drainage of Installation Pore Pressure
- Installation Conditions

Disturbance	OCR	c_u/σ'_{v0} from Expansion Curve BLP Interpretation		c_u/σ'_{v0} from Contraction Curve Houlsby-Withers Interpretation	
		$\Delta V/V_0=10\%$	$\Delta V/V_0=40\%$	Peak c_u/σ'_{v0}	$(\epsilon_{vc}-\epsilon)$ at Peak
Intact	1	0.20	0.20	0.21 ¹	---
	2	0.39	0.39	0.36 ¹	---
	4	0.66	0.66	0.61 ¹	---
FDPM (B/t=2)	1 ²	0.05	0.09	0.27	0.18
	2 ³	0.10	0.15	0.40	0.18
	4 ⁴	0.19	0.19	0.63	0.18
Standard PIPM (B/t=12)	1	0.07	0.19	0.21	0.03
	2	0.14	0.38	0.34	0.04
	4	0.22	0.61	0.57	0.02
Thin-walled PIPM (B/t=40)	1	0.13	0.21	0.21	0.03
	2	0.26	0.49	0.35	0.03
	4	0.43	0.86	0.59	0.01

¹Differences in expansion strengths are due to kinematic hardening in the MIT-E3 model.

²Peak strength $c_u/\sigma'_{v0}=0.70$ at $\Delta V/V=2\%$.

³Peak strength $c_u/\sigma'_{v0}=0.14$ at $\Delta V/V=3\%$.

⁴Peak strength $c_u/\sigma'_{v0}=0.56$ at $\Delta V/V=1\%$.

Table 6.6b Displacement Pressuremeters - No Dissipation of Installation Pore Pressures -
 c_u/σ'_{v0} from Predicted Pressuremeter Curves

Disturbance	OCR	$\frac{C_{uPM}}{\sigma'_{v0}}$	Limit Pressure, P_L		Strength Factor, N_p^2	
			$\Delta V/V_0$ =10% ¹	$\Delta V/V_0$ =40% ¹	$\Delta V/V_0$ =10%	$\Delta V/V_0$ =40%
Intact	1	0.20	1.97	1.97	7.24	7.24
	2	0.39	3.17	3.17	6.72	6.72
	4	0.66	5.00	5.00	6.49	6.49
					6.82	6.82
					5.5%	5.5%
FDPM (B/t=2)	1	0.20	1.73	1.77	2.08	2.33
	2	0.39	2.66	2.73	1.98	2.17
	4	0.66	4.66	4.65	3.20	3.19
	Mean				2.42	2.56
	Var. ³				23.6%	19.0%
Standard PIPM (B/t=12)	1	0.20	1.61	1.80	1.88	2.80
	2	0.39	2.51	2.93	1.90	2.99
	4	0.66	3.95	4.62	2.29	3.31
	Mean				2.02	3.03
	Var. ³				9.8%	8.4%
Thin-walled PIPM (B/t=40)	1	0.20	1.74	1.87	2.98	3.65
	2	0.39	2.78	3.20	3.03	4.12
	4	0.66	4.31	5.09	3.15	4.34
	Mean				3.05	4.04
	Var. ²				2.8%	8.6%

¹Limit Pressure computed by linearly extrapolating from this strain value to $\Delta V/V=100\%$.

² Strength Factor, $N_p = (P_L - P_0)/C_{uPM}$

³Variation = $\Delta x/2x$

$$\Delta x = x_{\max} - x_{\min}$$

$$x = (x_{\max} + x_{\min})/2$$

Table 6.6c Limit Pressures Predicted for Displacement Pressuremeters -
No Drainage of Installation Pore Pressures

Disturbance	OCR	Lift-off Pressure $(P_0 - u_0)/\sigma'_{v0} = K_c$
Intact	1	0.48
	2	0.57
	4	0.74
FDPM ($B/t=2$)	1	0.38
	2	0.63
	4	1.93
Standard PIPM ($B/t=12$)	1	0.32
	2	0.55
	4	1.60
Thin-Walled PIPM ($B/t=40$)	1	0.26
	2	0.46
	4	1.66

Table 6.7a Displacement Pressuremeters - Full Dissipation of Installation Pore Pressures - Installation Conditions

Disturbance	OCR	c_u/σ'_{v0} from Expansion Curve BLP Interpretation		c_u/σ'_{v0} from Contraction Curve Houlsby-Wihers Interpretation	
		$\Delta V/V_0=10\%$	$\Delta V/V_0=40\%$	Peak c_u/σ'_{v0}	$(\epsilon_{ve}-\epsilon)$ at Peak
Intact	1	0.20	0.20	0.21	
	2	0.39	0.39	0.36	
	4	0.66	0.66	0.61	
FDPM (B/t=2)	1	0.21	0.24	0.20	0.07
	2 ¹	0.17	0.22	0.33	0.03
	4 ²	0.11	0.08	0.68	0.04
Standard PIPM (B/t=12)	1	0.21	0.24	0.22	0.05
	2	0.20	0.35	0.39	0.02
	4	0.18	0.39	0.69	0.02
Thin-walled PIPM (B/t=40)	1	0.21	0.23	0.22	0.03
	2	0.29	0.42	0.40	0.02
	4	0.31	0.55	0.67	0.02

¹Peak Strength $c_u/\sigma'_{v0}=0.21$ at $\Delta V/V=1.0\%$

²Peak Strength $c_u/\sigma'_{v0}=0.33$ at $\Delta V/V=0.8\%$

Table 6.7b Displacement Pressuremeters - Full Dissipation of Installation Pore Pressures -
 c_u/σ'_{v0} from Predicted Pressuremeter Curves

Disturbance	OCR	$\frac{c_{uPM}}{\sigma'_{v0}}$	Limit Pressure, P_L		Strength Factor, N_p^2	
			$\Delta V/V_0$ =10% ¹	$\Delta V/V_0$ =40% ¹	$\Delta V/V_0$ =10%	$\Delta V/V_0$ =40%
Intact	1	0.20	1.97	1.97	7.24	7.24
	2	0.39	3.17	3.17	6.72	6.72
	4	0.66	5.00	5.00	6.49	6.49
					6.82	6.82
					5.5%	5.5%
FDPM (B/t=2)	1	0.20	1.77	1.82	5.94	6.20
	2	0.39	2.38	2.44	3.67	3.85
	4	0.66	4.24	4.15	3.52	3.39
	Mean				4.38	4.48
	Var. ²				25.6%	29.3%
Standard PIPM (B/t=12)	1	0.20	1.85	1.90	6.53	6.75
	2	0.39	2.31	2.57	3.66	4.34
	4	0.66	3.71	4.08	3.00	3.57
	Mean				4.40	4.89
	Var. ³				37.0%	30.8%
Thin-walled PIPM (B/t=40)	1	0.20	1.91	1.94	6.98	7.15
	2	0.39	2.50	2.74	4.29	4.89
	4	0.66	3.81	4.25	3.25	3.92
	Mean				4.84	5.32
	Var. ²				36.5%	29.2%

¹Limit Pressure computed by linearly extrapolating from this strain value to $\Delta V/V=100\%$.

²Strength Factor, $N_p = (P_L - P_0)/c_{uPM}$

³Variation = $\Delta x/2x$

$$\Delta x = x_{\max} - x_{\min}$$

$$x = (x_{\max} + x_{\min})/2$$

Table 6.7c Limit Pressures for Displacement Pressuremeters -
Full Drainage of Installation Pore Pressures

Disturbance	OCR	Lift-off Pressure $(P_0 - u_0)/\sigma'_{v0}$	Installation Pore Pressure $(u_i - u_0)/\sigma'_{v0}$	Effective Stress $(P_0 - u_i)/\sigma'_{v0}$
Intact	1	0.48	0	0.48
	2	0.57	0	0.57
	4	0.74	0	0.74
f=0 (PIPM)	1	1.22	1.15	0.07
	2	1.76	1.61	0.15
	4	2.45	1.81	0.64
f=0.50	1	1.09	0.87	0.22
f=0.75	1	0.90	0.76	0.14
f=0.875	1	0.64	0.53	0.11
f=0.95	1	0.39	0.36	0.03
f=0.99	1	0.23	0.19	0.04
f=1 Ideal SBPM	1	0.12	0.01	0.12
	2	0.12	0.02	0.11
	4	-0.05	0.49	0.44

Table 6.8a Self-Boring Pressuremeters - Installation and Limit Pressure Summary

Disturbance	OCR	c_u/σ'_{v0} from Expansion Curve BLP Interpretation				c_u/σ'_{v0} from Contraction Curve - Housby-Withers Interpretation	
		$\Delta V/N_0=10\%$	$\Delta V/N_0=40\%$	Peak	$\Delta V/N_0$ at Peak (%)	Peak	$(\epsilon_{ve}-\epsilon)$ at Peak
Intact	1	0.20	0.20			0.21	
	2	0.39	0.39			0.36	
	4	0.66	0.66			0.61	
f=0 (PIPM)	1	0.07	0.19			0.21	0.04
	2	0.14	0.38			0.34	0.04
	4	0.22	0.61			0.57	0.04
f=0.5	1	0.13	0.22			0.21	0.04
f=0.75	1	0.18	0.23			0.21	0.04
f=0.875	1	0.20	0.23			0.21	0.04
f=0.95	1	0.20	0.25	0.25	1.4	0.21	0.04
f=0.99	1	0.24	0.26	0.28	1.2	0.21	0.04
f=1 (Ideal SBPM)	1	0.23	0.24	0.32	0.7	0.22	0.04
	2	0.44	0.44	0.53	1.4	0.36	0.03
	4	0.72	0.63	1.01	1.4	0.64	0.07

Table 6.8b Self-Boring Pressuremeters - c_u/σ'_{v0} from Predicted Pressuremeter Curves

Disturbance	OCR	$\frac{c_{uPM}}{\sigma'_{v0}}$	Limit Pressure, P_L		Strength Factor, N_p^2	
			$\Delta V/V_0$ =10% ¹	$\Delta V/V_0$ =40% ¹	$\Delta V/V_0$ =10%	$\Delta V/V_0$ =10%
Intact	1	0.20	1.97	1.97	7.24	7.24
	2	0.39	3.17	3.17	6.72	6.72
	4	0.66	5.00	5.00	6.49	6.49
					6.82	6.82
					5.5%	5.5%
Standard PIPM (f=0)	1	0.20	1.61	1.80	1.88	2.80
	2	0.39	2.51	2.93	1.90	2.99
	4	0.66	3.95	4.62	2.29	3.31
	Mean				2.02	3.03
	Var. ³				9.8%	8.4%
Ideal SBPM (f=1)	1	0.20	1.98	1.99	9.05	9.08
	2	0.39	3.24	3.23	8.00	7.98
	4	0.66	5.42	5.24	8.33	8.06
	Mean				8.46	8.37
	Var. ²				6.2%	6.5%

¹Limit Pressure computed by linearly extrapolating from this strain value to $\Delta V/V=100\%$.

²Strength Factor, $N_p = (P_L - P_0)/c_{uPM}$

³ Variation = $\Delta x/2x$

$$\Delta x = x_{\max} - x_{\min}$$

$$x = (x_{\max} + x_{\min})/2$$

Table 6.8c Limit Pressures for Self-Boring Pressuremeters

Test No.	Elev. (ft)	OCR	SBPM Undrained Shear Strength Estimate, c_u/σ'_{v0}				Reference Strength (Ladd, 1991)	
			M1	M2	M3	Mean	Var. (%)*	$c_u TC/\sigma'_{v0}$ $c_u TE/\sigma'_{v0}$
SB2.1	67.9			0.77	0.76	0.77	0.7	
SB2.2	62.2	4.5	0.89	0.68	0.67	0.75	14.4	0.93 0.67
SB2.3	55.9	3.8	1.35	0.68	0.68	0.90	17.1	0.68 0.48
SB2.4	48.2	3.1	1.24	0.46	0.50	0.56	21.4	0.65 0.45
SB2.5	38.9	2.4	0.99	0.43	0.33	0.59	49.5	0.53 0.34
SB2.6	32.4	1.9	1.10	0.32	0.45	0.48	35.0	0.46 0.28
SB2.7	25.4	1.6	1.16	0.72	0.32	0.94	35.6	0.38 0.21
SB2.8	20.4	1.3	1.01	0.28	0.40	0.37	20.7	0.35 0.18
SB2.9	9.9	1.2	0.75	0.26	0.27	0.27	3.1	0.32 0.17
SB2.10	- 0.1	1.1	1.10	0.49	0.28	0.62	32.5	0.29 0.15

*Variation = $\frac{\Delta \bar{x}}{2\bar{x}} \cdot 100\%$; where $\Delta \bar{x} = x_{\max} - x_{\min}$; $\bar{x} = \frac{x_{\max} + x_{\min}}{2}$

Table 6.9a. Undrained Shear Strength from SBPMT Expansion Curves in BBC at South Boston Site (based SBPMT expansion curves from Benoit, 1991)

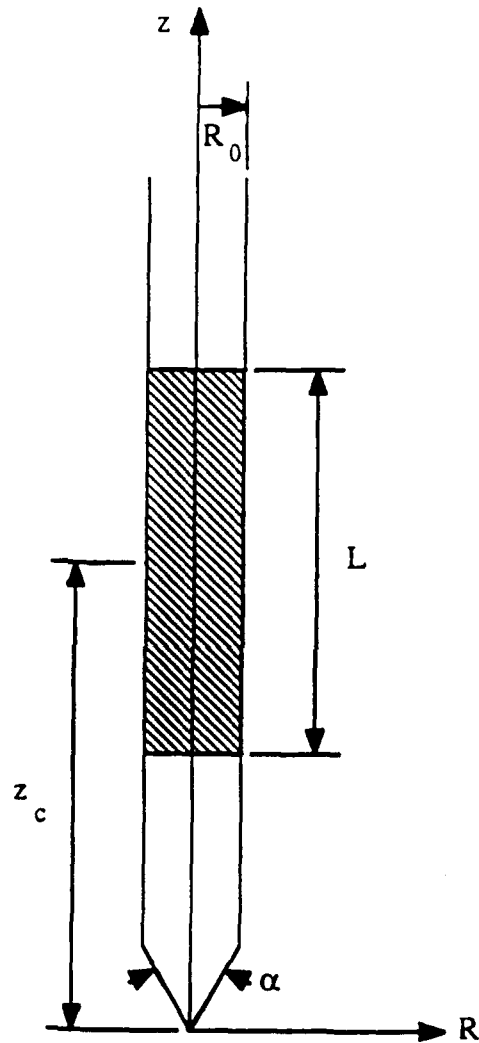
Test No.	Elev. (ft)	OCR	SBPM Undrained Shear Strength Estimate, c_u/σ'_{v0}					Reference Strength (Ladd, 1991)	
			M1	M2	M3	Mean	Var. (%) [*]	c_{uTC}/σ'_{v0}	c_{uTE}/σ'_{v0}
SB2.1	67.9		0.70	0.59	0.74	0.72	2.4		
SB2.2	62.2	4.5	1.0	1.08		1.04	3.7	0.93	0.67
SB2.3	55.9	3.8	0.94	0.99	0.94	0.96	5.4	0.68	0.48
SB2.4	48.2	3.1	0.87	0.96	0.87	0.90	8.8	0.65	0.45
SB2.5	38.9	2.4	0.76	0.63	0.72	0.71	4.3	0.53	0.34
SB2.6	32.4	1.9	0.75	0.69		0.72	12.9	0.46	0.28
SB2.7	25.4	1.6	0.59	0.76		0.67		0.38	0.21
SB2.8	20.4	1.3	0.65	0.65	0.72	0.68	5.3	0.35	0.18
SB2.9	9.9	1.2	0.53	0.63	0.63	0.60	9.4	0.32	0.17
SB2.10	- 0.1	1.1	0.54	0.54	0.54	0.54	0.0	0.29	0.15
SB2.11	-8.8	1.1				0.28	0.9	0.28	0.16

*Variation = $\frac{\Delta x}{\bar{x}} \cdot 100\%$; where $\Delta x = x_{max} - x_{min}$; $\bar{x} = \frac{x_{max} + x_{min}}{2}$

Table 6.9b. Undrained Shear Strength from SBPMT Contraction Curves in BBC at South Boston Site
(SBPMT data from Benoit, 1991)

Test No.	Elev. (ft)	OCR	M1		M2		M3	
			$\frac{(P_0-u_0)}{\sigma'_{v0}}$	$\frac{c_{uPM}}{c_{uTX}}$	$\frac{(P_0-u_0)}{\sigma'_{v0}}$	$\frac{c_{uPM}}{c_{uTX}}$	$\frac{(P_0-u_0)}{\sigma'_{v0}}$	$\frac{c_{uPM}}{c_{uTX}}$
SB2.3	55.9	3.8	2.21	1.99	2.81	1.0	2.90	1.0
SB2.4	48.2	3.1	2.19	1.90	3.25	0.71	2.91	0.77
SB2.5	38.9	2.4	2.22	1.87	2.48	0.81	3.26	0.62
SB2.6	32.4	1.9	1.75	2.39	2.63	0.70	2.31	0.98
SB2.7	25.4	1.6	1.98	3.05	1.77	1.89	3.26	0.84
SB2.8	20.4	1.3	2.00	2.89	3.11	0.80	3.10	1.14
SB2.9	9.9	1.2	1.76	2.34		0.81	2.94	0.84
SB2.10	- 0.1 -	1.1	1.65	3.79		1.69	2.70	0.97

Table 6.10. Relationship Between Undrained Shear Strength from SBPMT Expansion Curves and Contact Pressure in BBC at South Boston Site (based SBPMT expansion curves from Benoit, 1991)

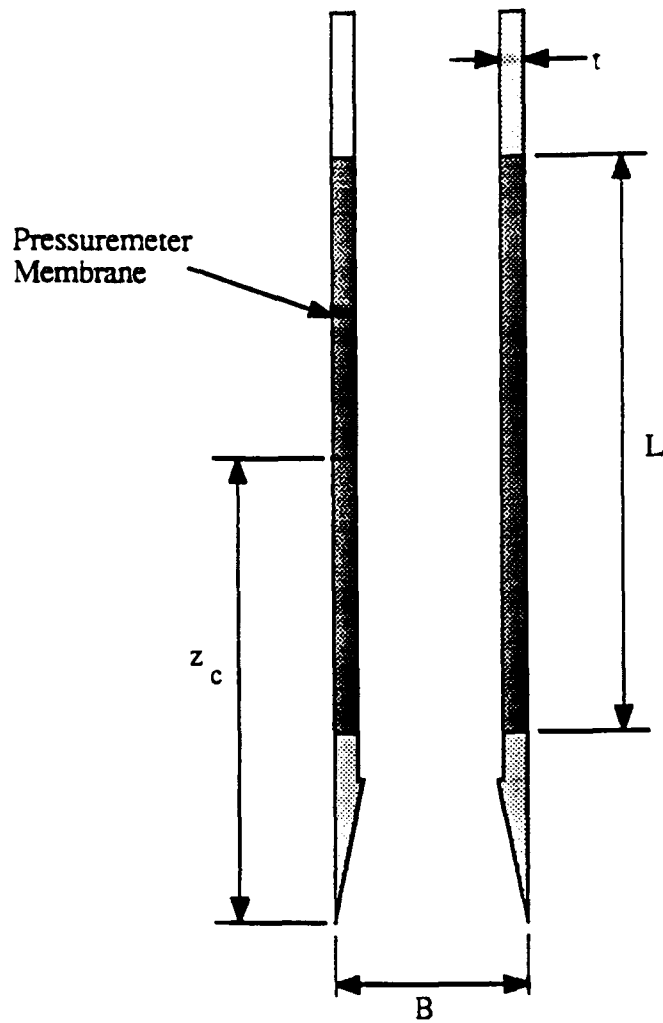


Reference	R_0 (mm)	L (mm)	z_c (mm)	α (°)	$\Delta R/R_0$	L/B	U^{**} (cm/s)
Withers et al. (1986)	22	448	930	60	50%	10	2
Campanella et al. (1990)	22	220	*	60	27%	5	2

*Located above standard friction sleeve, i.e., $z_c > 550$ mm.

**Assumed to be equal to standard piezocone penetration rate.

Figure 6.1 Full Displacement Pressuremeter Characteristics



Reference	B (mm)	L (mm)	t (mm)	z_c (mm)	L/B
Henderson et al. (1980)	78	330	8		4.2
Huang and Haeferle (1988)	78	360	8	310	4.6

Figure 6.2 Push-in Pressuremeter Characteristics

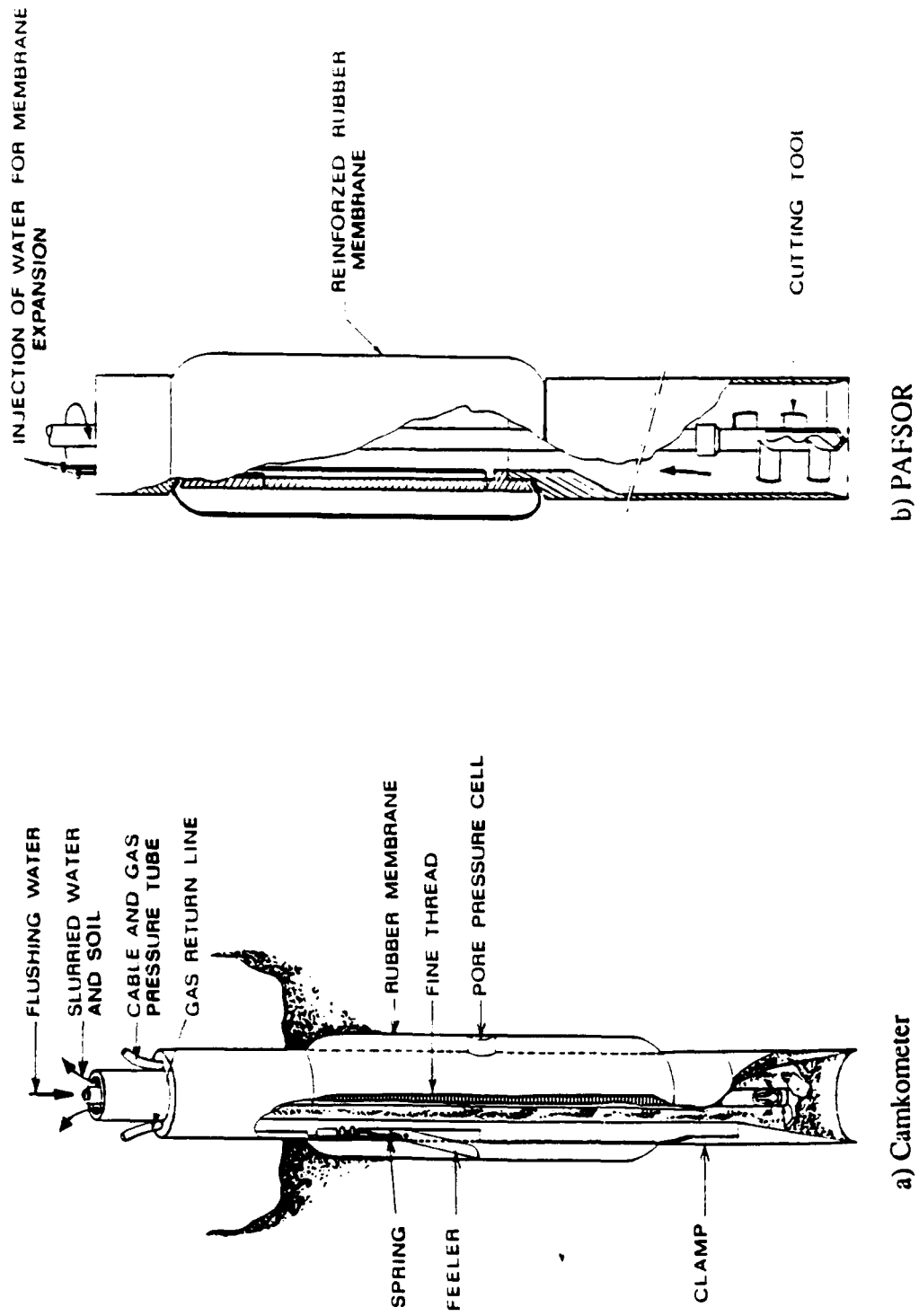
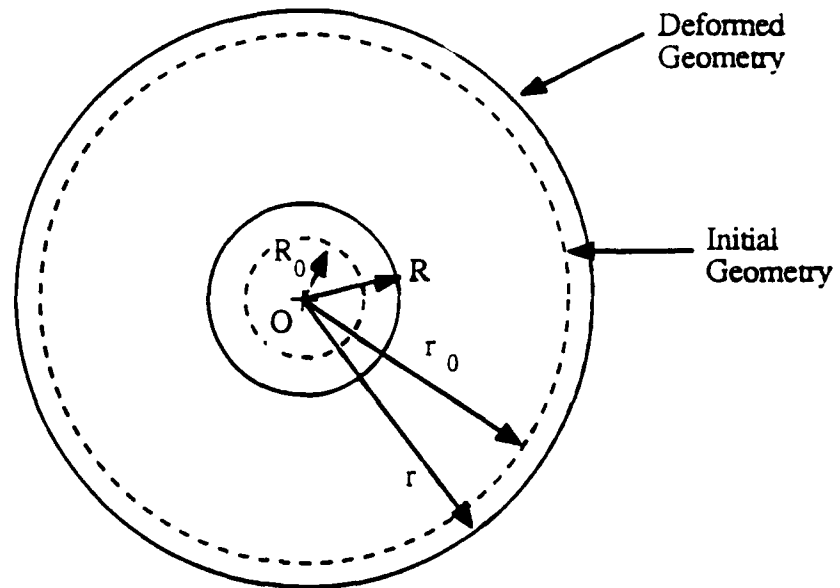
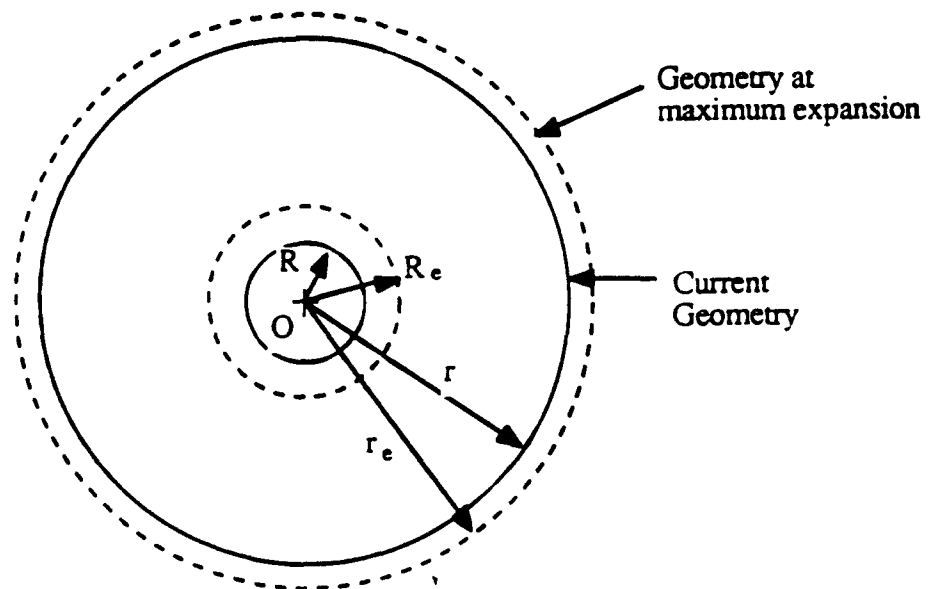


Figure 6.3 Self-Boring Pressuremeters

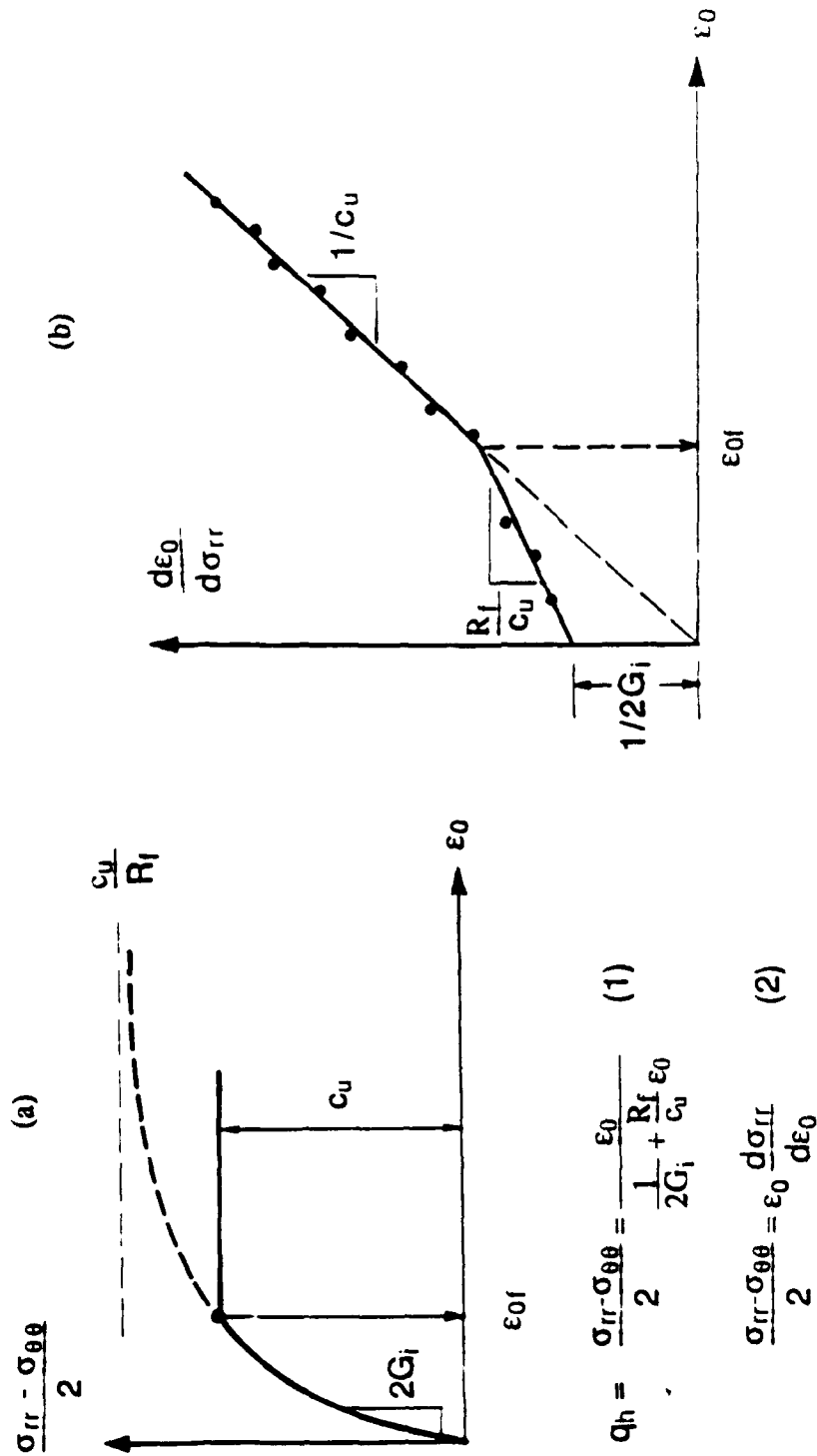


a) Expansion of an Existing Cavity



b) Contraction of a cavity

Figure 6.4 Cavity Expansion Definitions



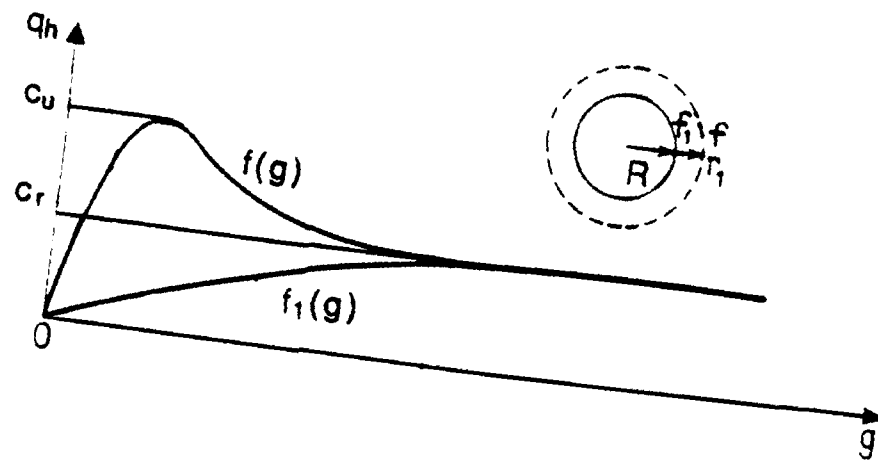
From (1) and (2)

$$\frac{d\epsilon_0}{d\sigma_{rr}} = \frac{1}{2G_i} + \frac{R_f}{c_u} \epsilon_0$$

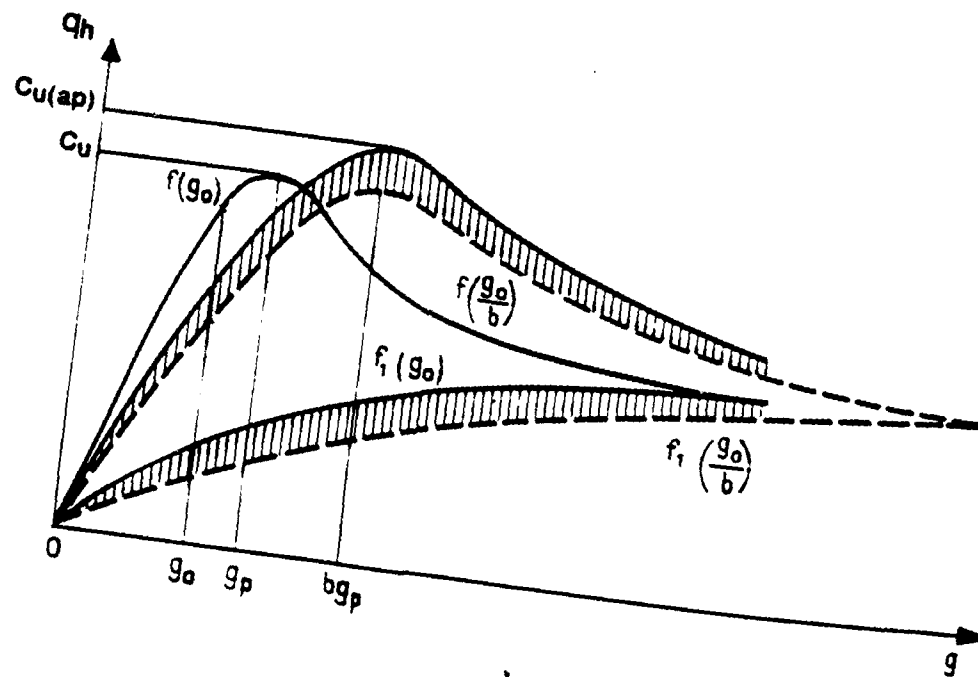
$$\frac{d\epsilon_0}{d\sigma_{rr}} = \frac{1}{2G_i} + \frac{R_f}{c_u} \epsilon_0$$

Figure 6.5 Undrained Strength from Pressuremeter Curve, Denby and Clough (1980)

(from Ghionna et al., 1982)



a) Assumed Effects of Disturbance



b) Apparent Stress-Strain Curve

Figure 6.6 Conceptual Model for Disturbance (Baguelin, 1978)

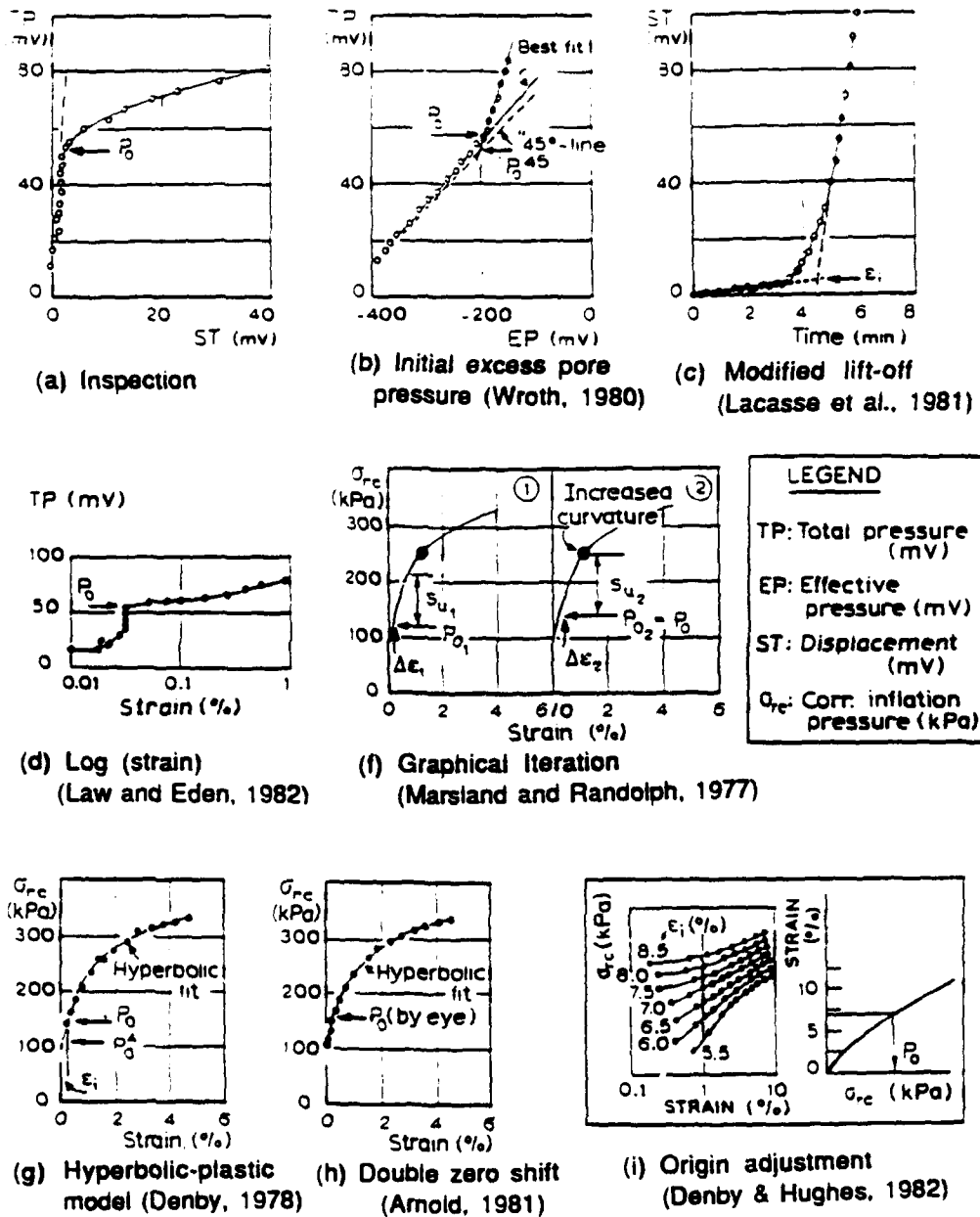
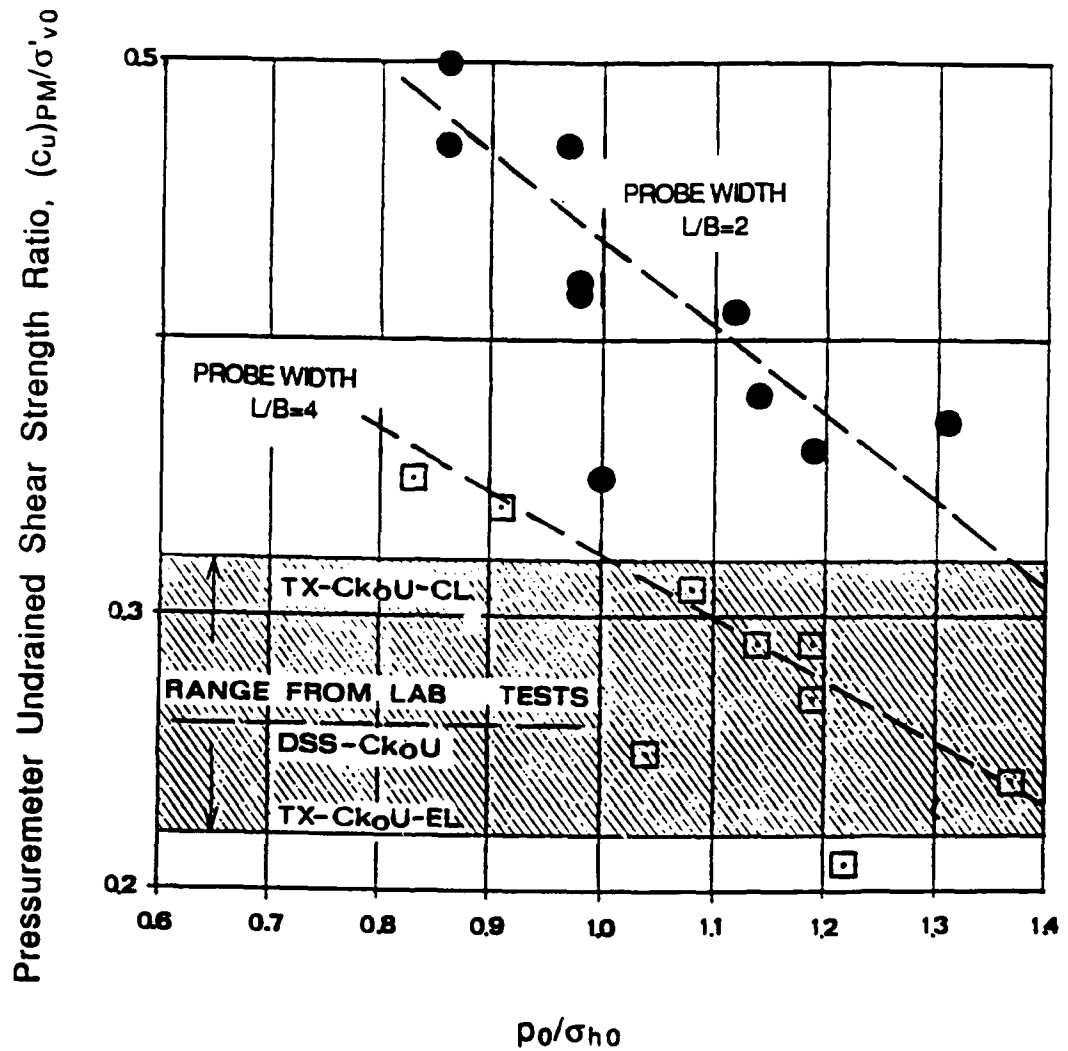
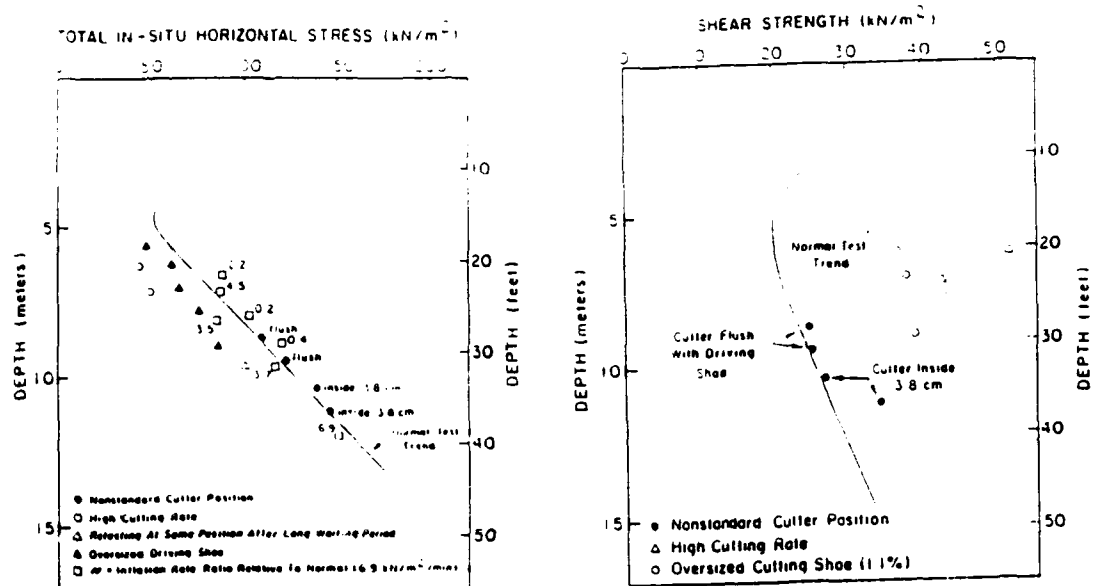


Figure 6.7 Methods of Estimating In Situ Horizontal Stress from SBPM Data, Lacasse and Lunne (1982)



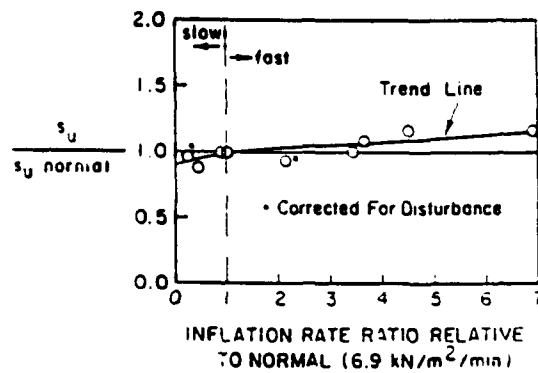
$(C_u)_{PM}/\sigma'_{v0}$ = Pressuremeter Undrained Shear Strength Ratio
 (Prevost and Hoeg method; Section 8.2.2.1)
 p_0 = Horizontal Pressure (Marsland and Randolph; Section 8.2.2.3)
 σ_{h0} = Estimated In Situ Horizontal Pressure

Figure 6.8 SBPM Contact Pressure versus Estimated Undrained Shear Strength (Ghionna et al., 1982)



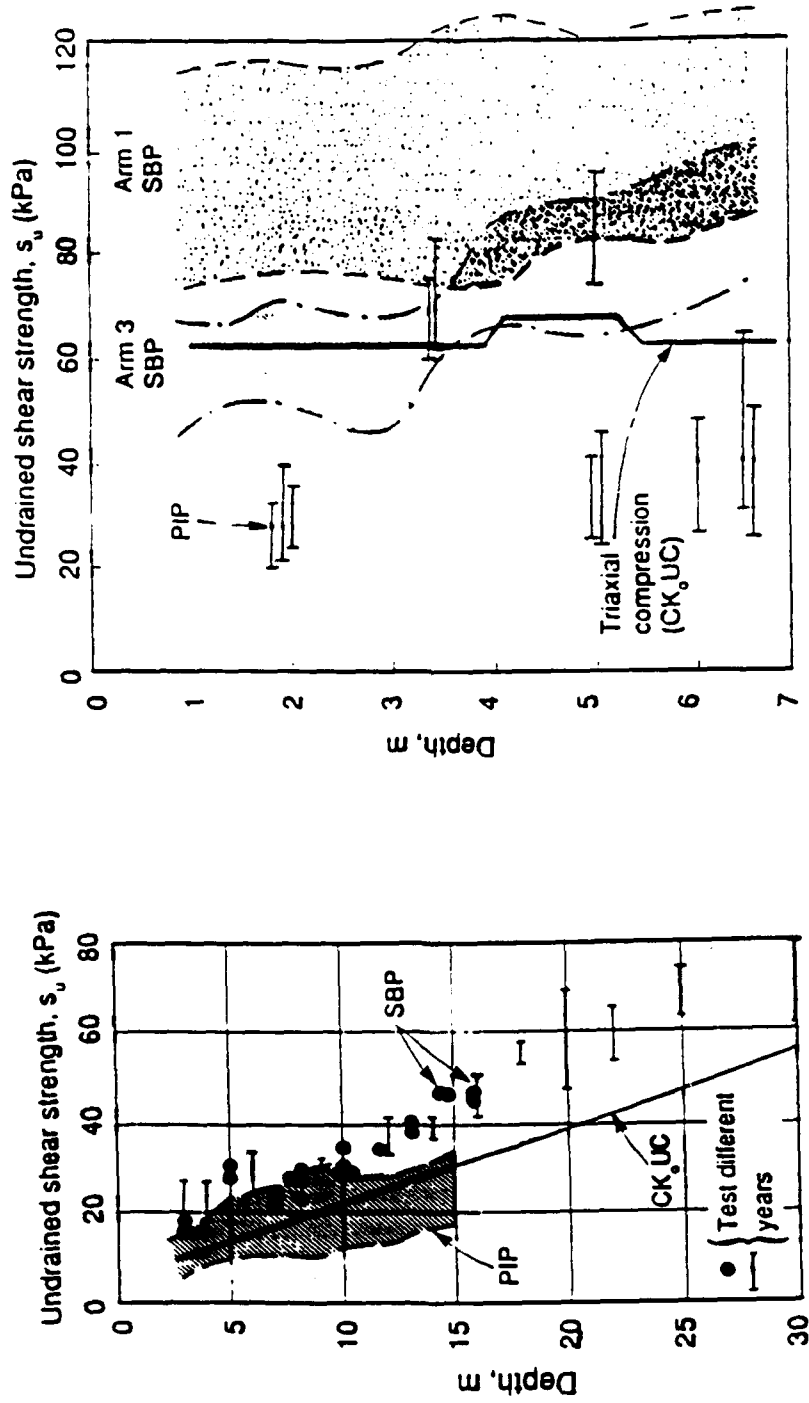
a) In Situ Horizontal Stress

b) Undrained Shear Strength



c) Effect of Membrane Expansion Rate

Figure 6.9 Influence of SBPM Test Procedures (Benoit and Clough, 1986)



a) Onsrøy

b) Haga

Figure 6.10 Strength Estimates from Pressuremeter Tests (Lacasse and Lunne, 1990)

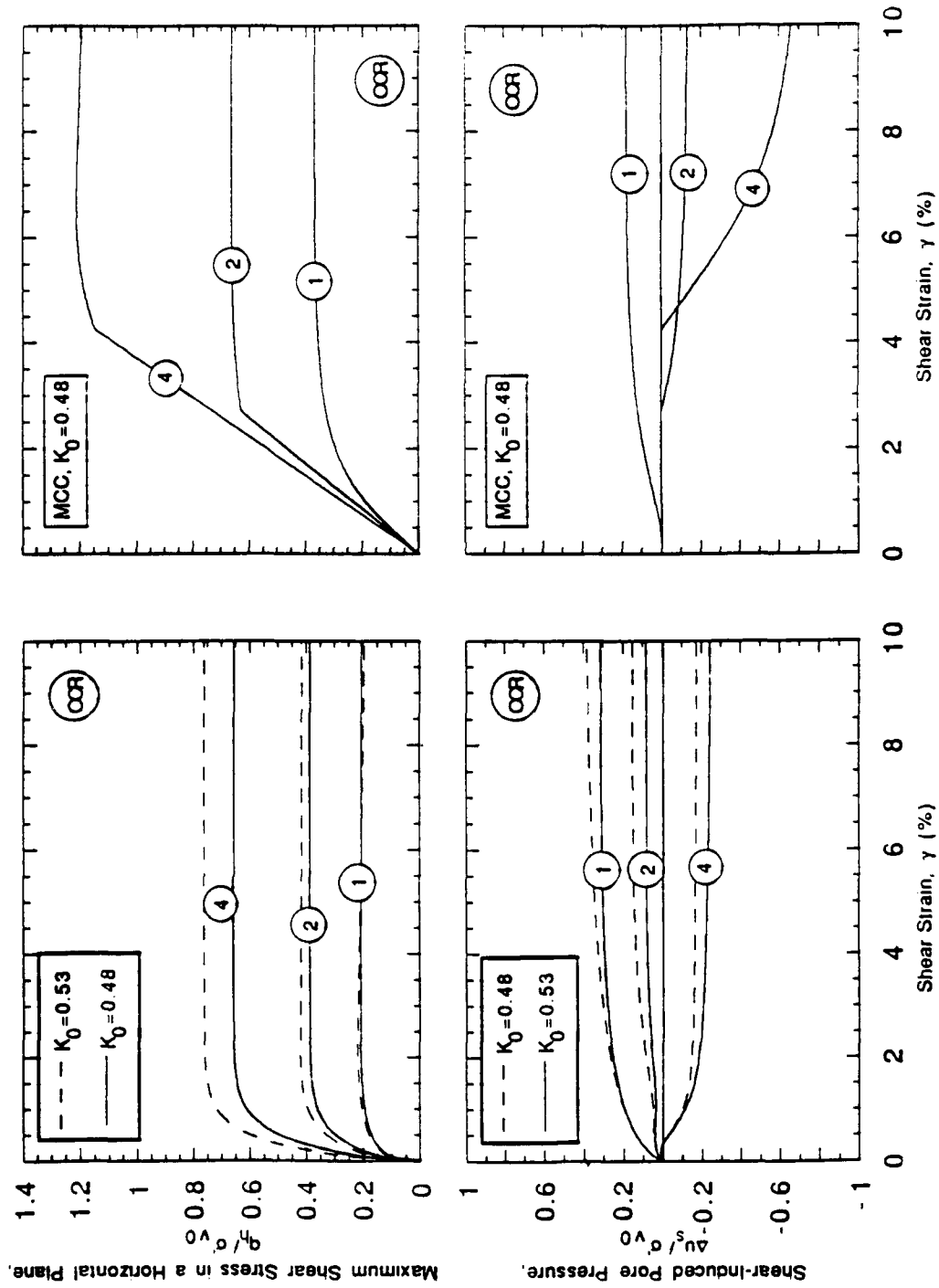
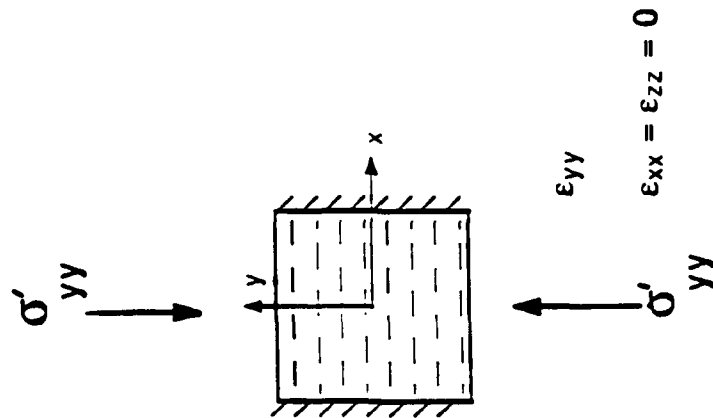


Figure 6.1.1 Model Predictions of Boston Blue Clay Behavior in a Pressuremeter Shear
Mode: a) MIT-E3; b) MCC

1. 1-D Consolidation



2. Undrained Shear

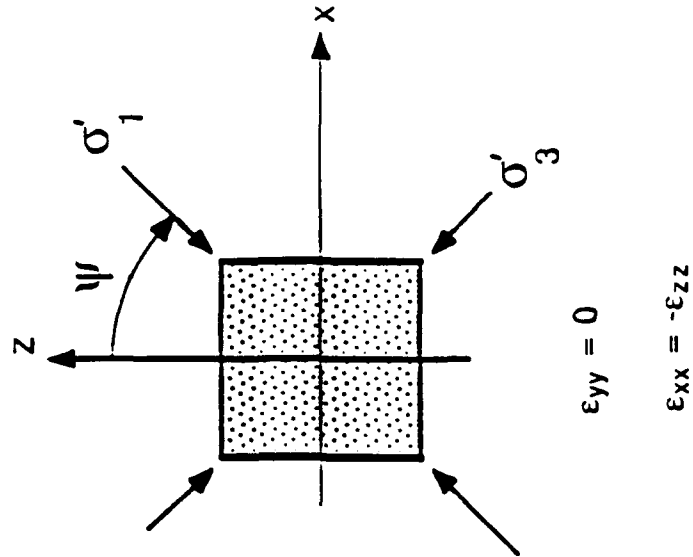


Figure 6.12 Element Stress and Strain History in the Directional Shear Cell (DSC) Test

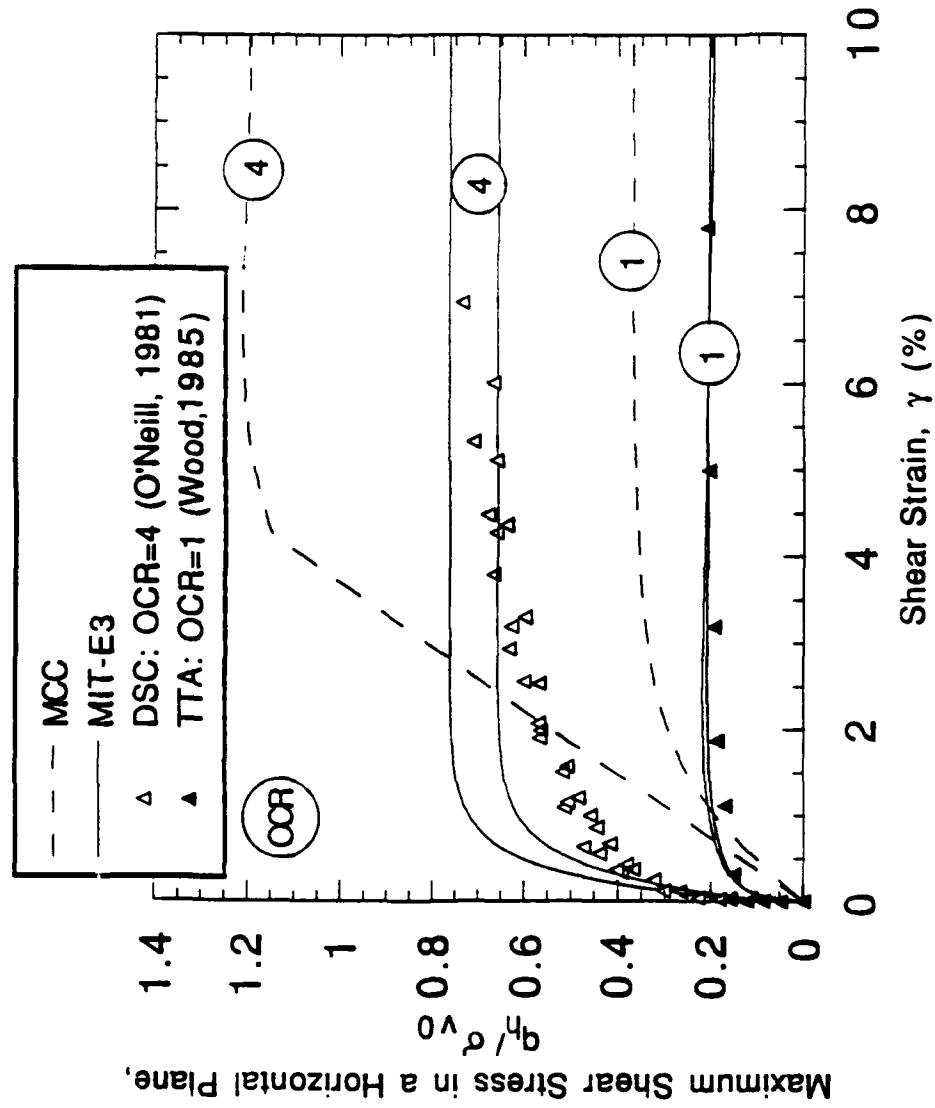


Figure 6.13 Comparison of Model Predictions and Measured Data for Stress-Strain Behavior of BBC at OCR=1 and 4 in the Isotropic (x-z) Plane

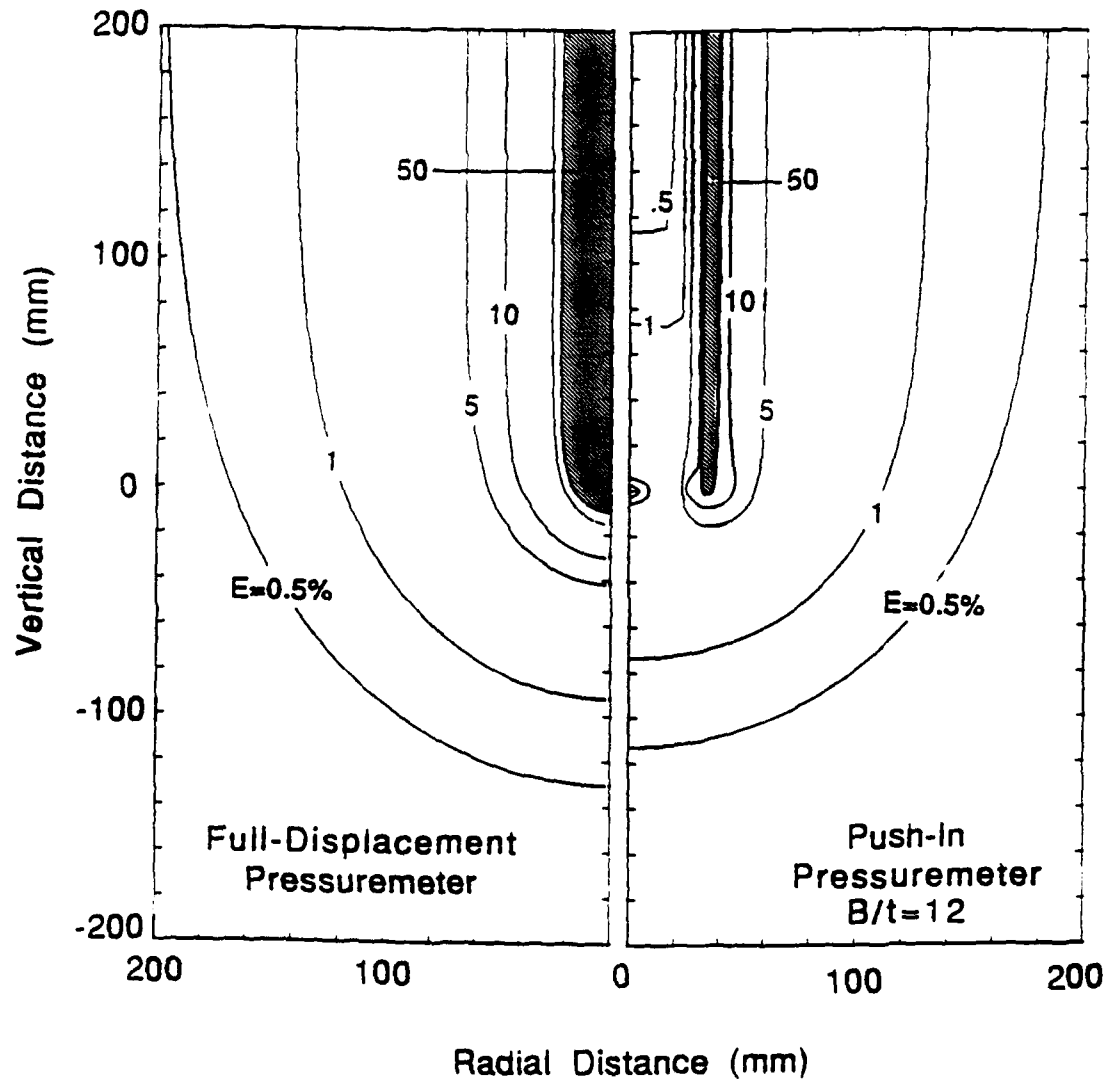


Figure 6.14 Contours of Octahedral Shear Strain, E , During Displacement Pressuremeter Installation

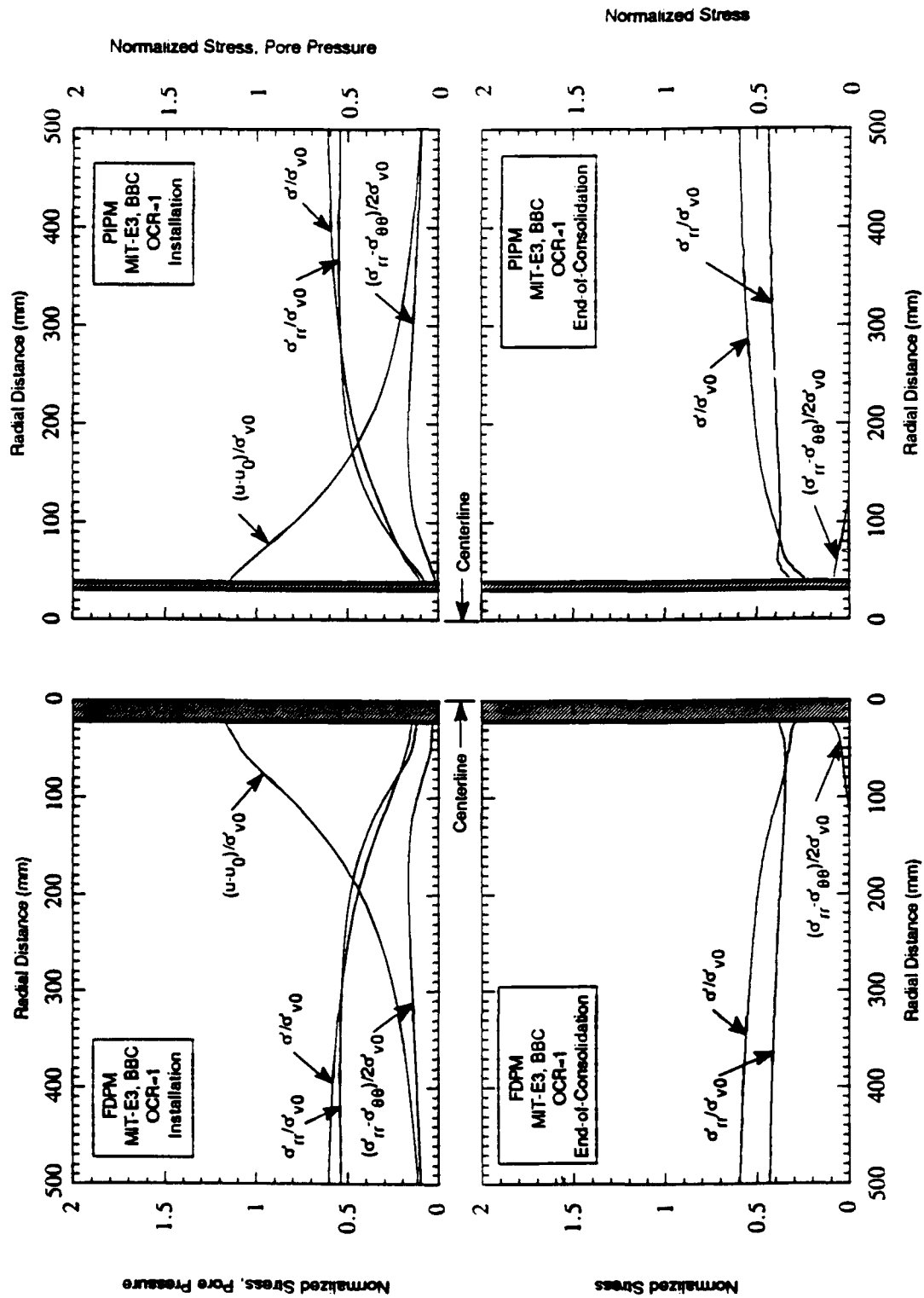
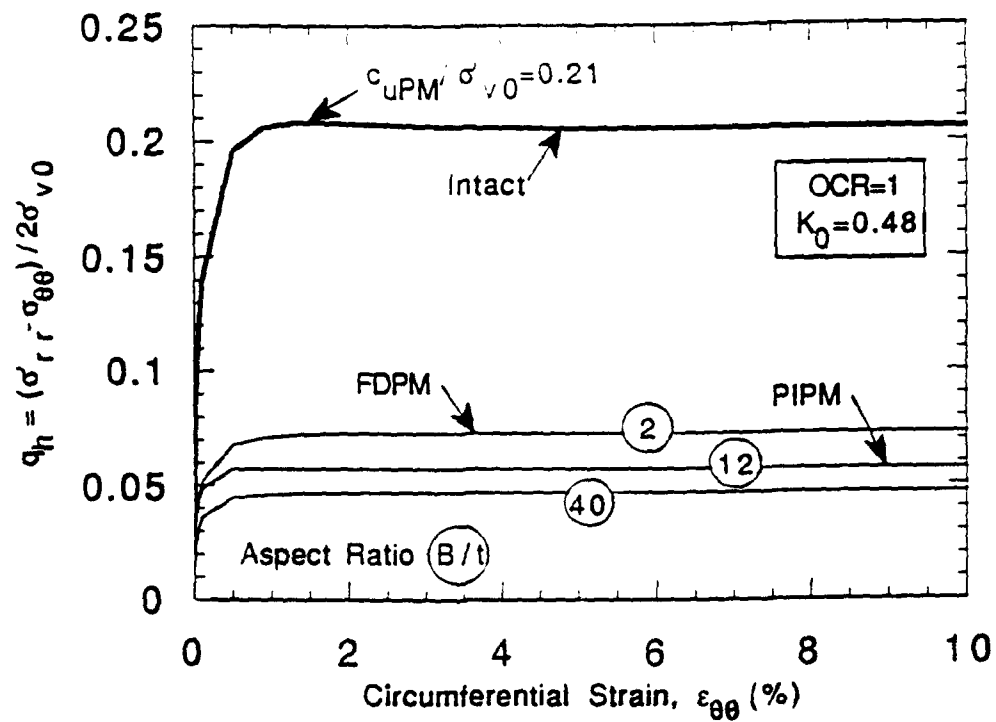
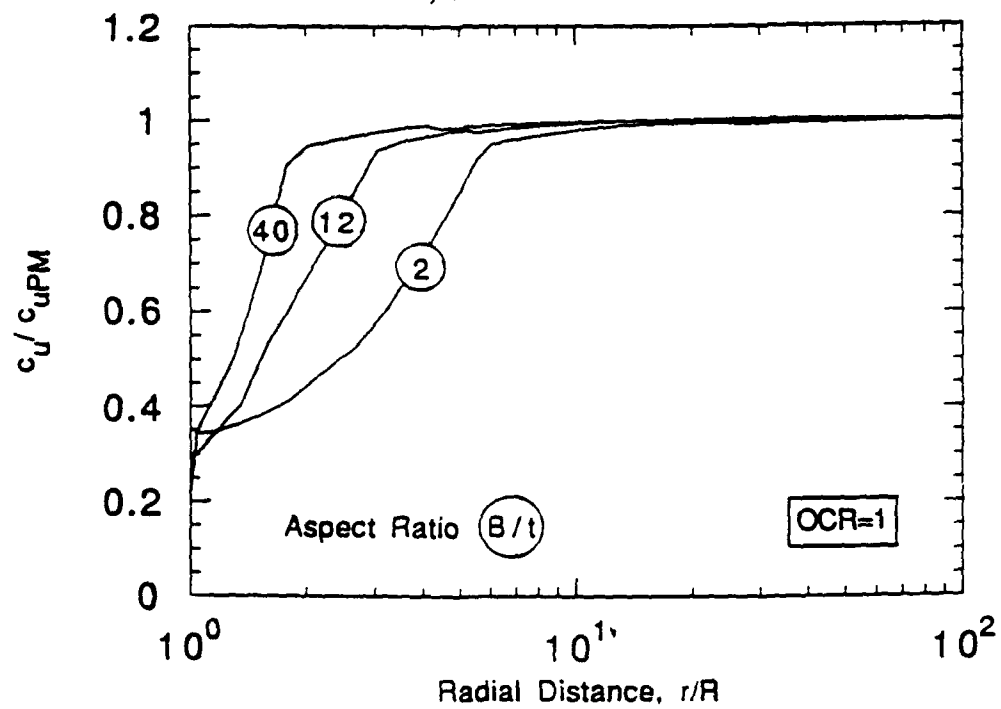


Figure 6.15 MIT-E3 Predictions of Displacement Pressurimeter Excess Pore Pressures and Stresses Immediately after Installation and at the End of Consolidation



a) Stress-Strain Behavior



b) Radial Distribution of Available Shear Strength

Figure 6.16 Influence of Disturbance on Stress-Strain Behavior in a Pressuremeter Shearing Mode - No Dissipation of Installation Pore Pressures:

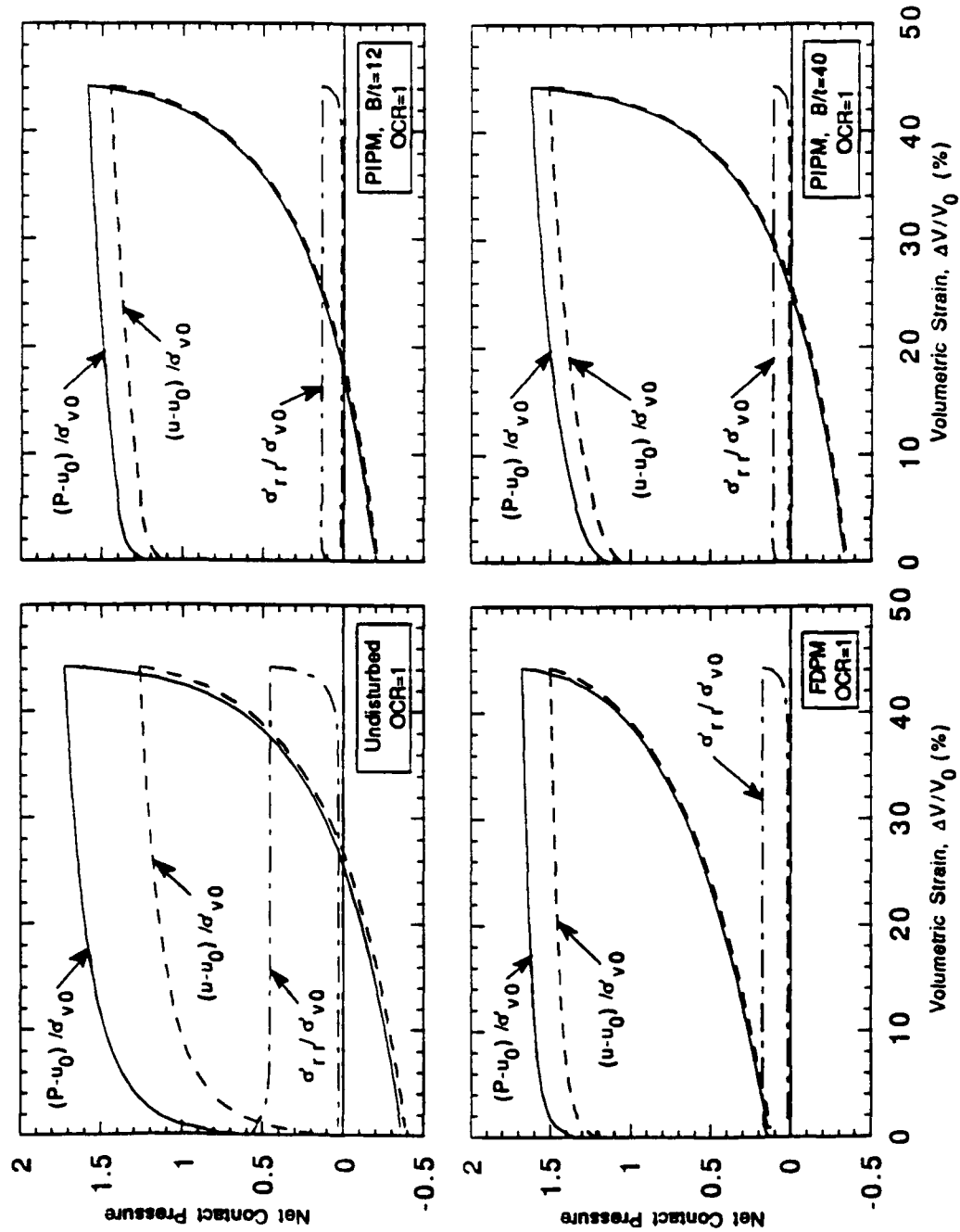


Figure 6.17 MIT-E3 Predictions of Total Radial Stress and Pore Pressure During Pressuremeter Expansion and Contraction In Normally Consolidated BBC- No Dissipation of Installation Pore Pressures

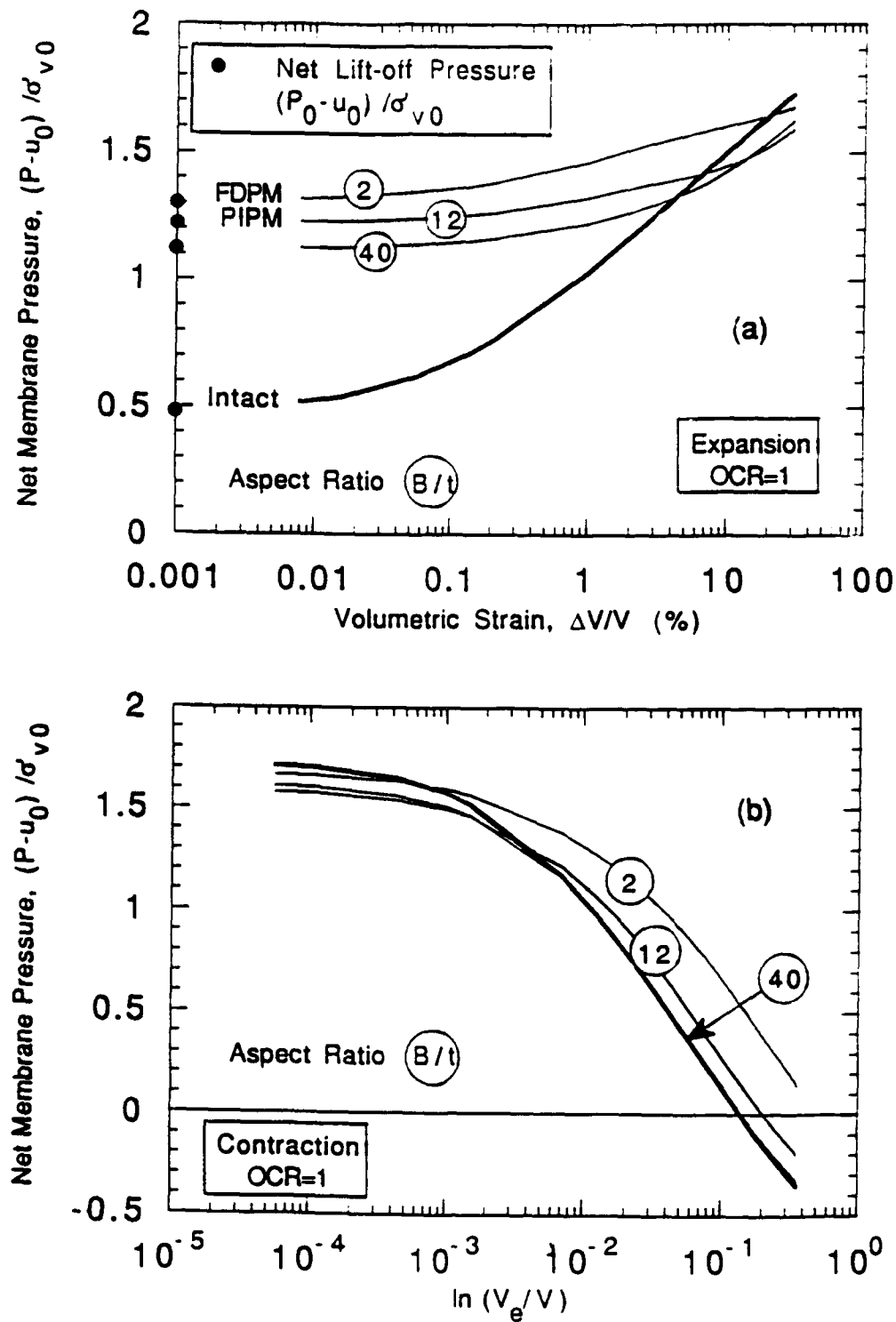
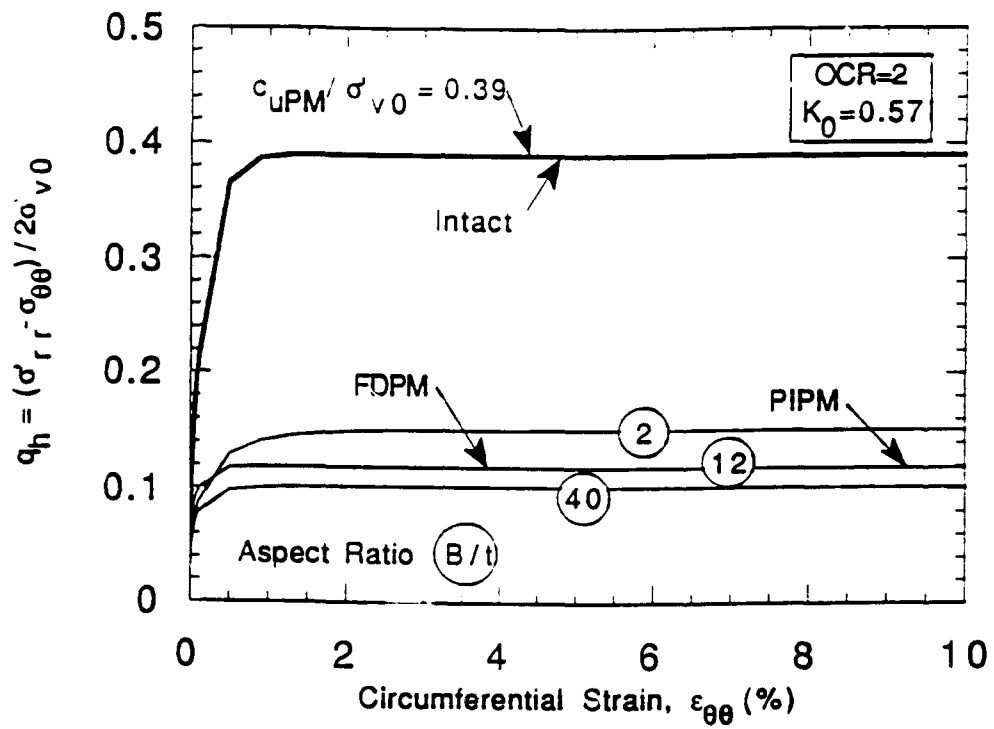
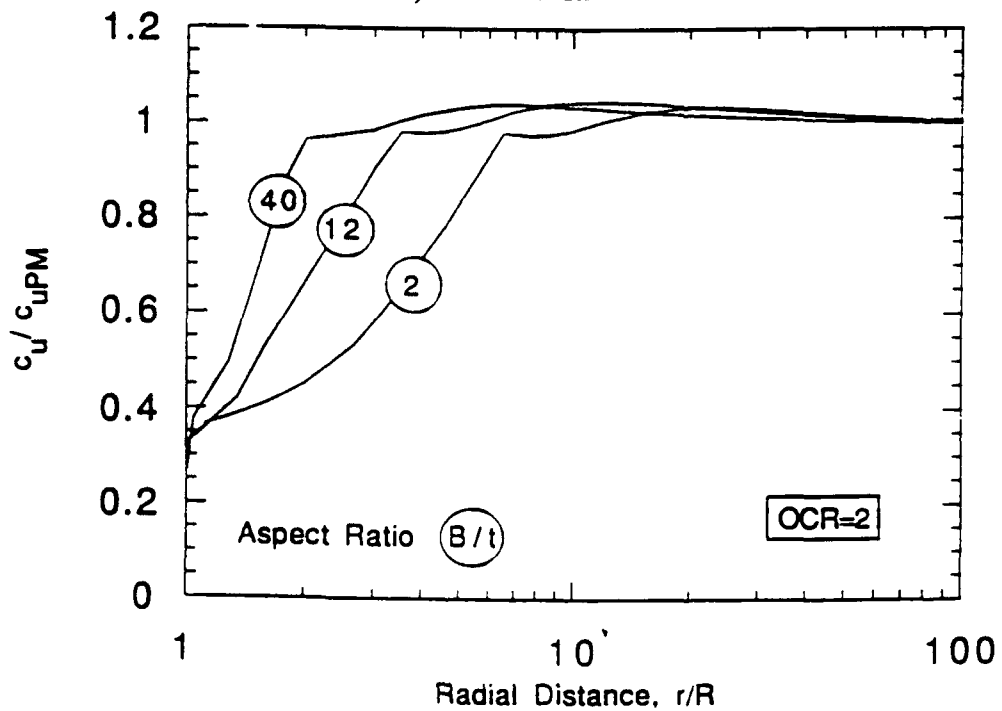


Figure 6.18 Predicted Expansion and Contraction Curves in Normally Consolidated BBC-
No Dissipation of Installation Pore Pressures

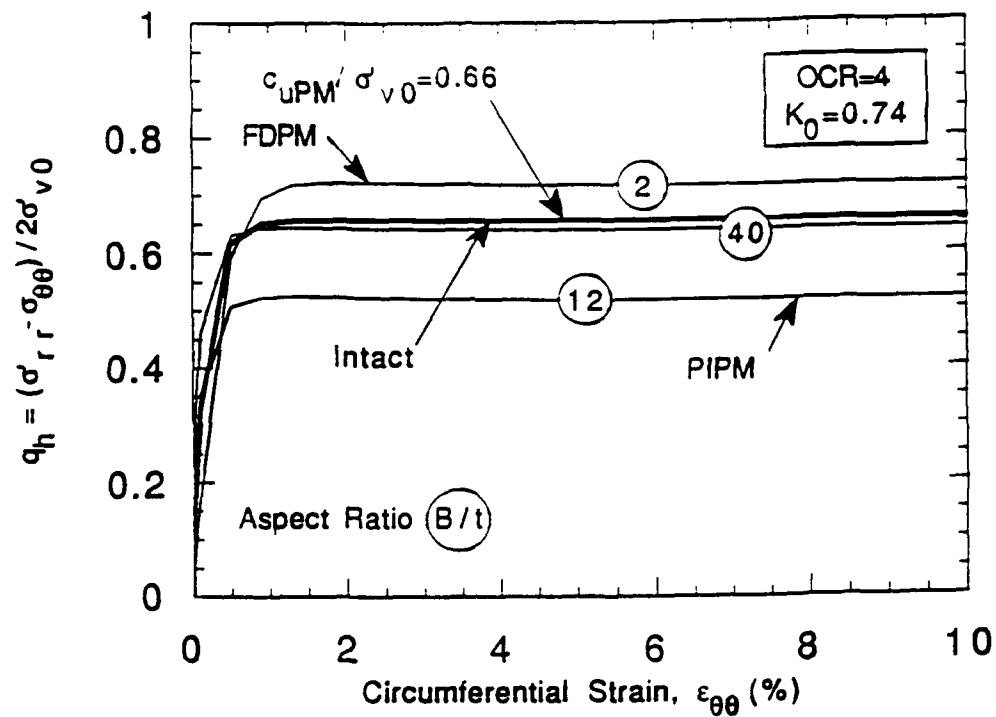


a) Stress-Strain Behavior

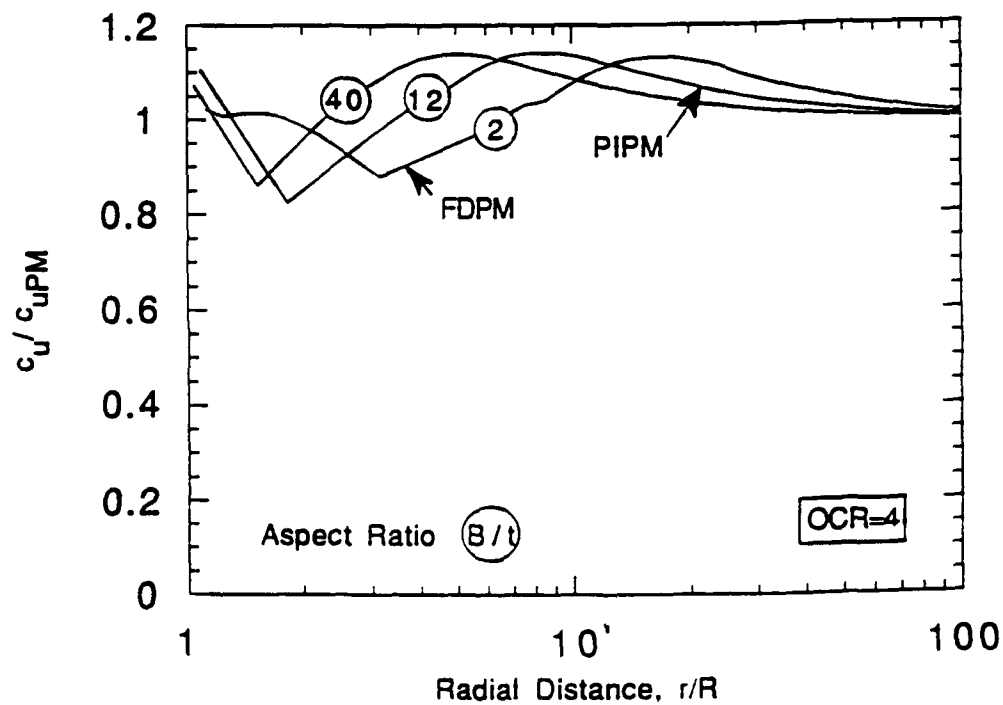


b) Radial Distribution of Available Shear Strength

Figure 6.19 Influence of Stress History on Disturbed Stress-Strain Behavior in a Pressuremeter Shearing Mode - No Dissipation of Installation Pore Pressures - OCR=2:



a) Stress-Strain Behavior



b) Radial Distribution of Available Shear Strength

Figure 6.20 Influence of Stress History on Disturbed Stress-Strain Behavior in a Pressuremeter Shearing Mode - No Dissipation of Installation Pore Pressures - OCR=4:

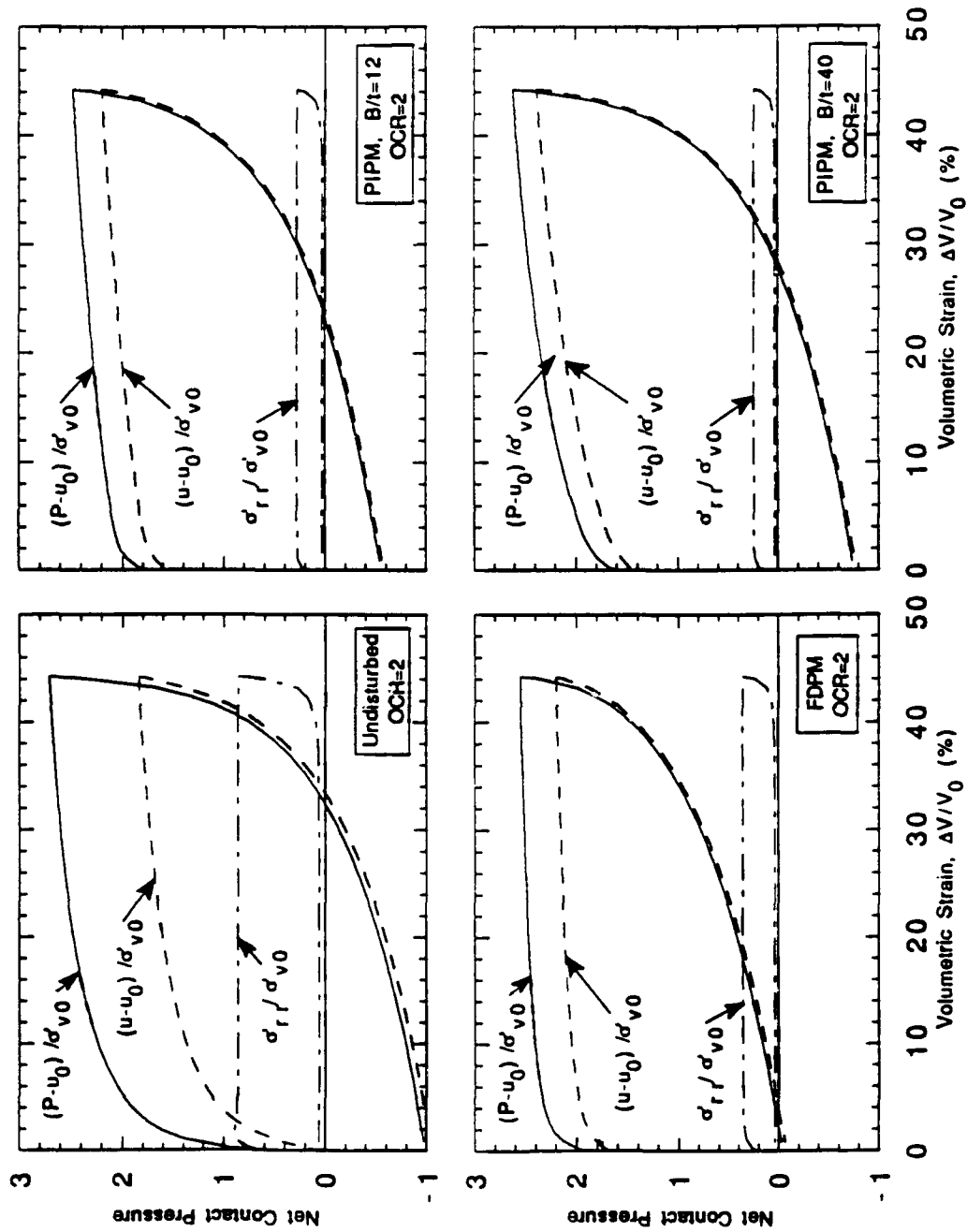


Figure 6.21 Influence of Stress History on Total Radial Stress and Pore Pressure During Pressuremeter Expansion and Contraction - No Dissipation of Installation
 Pore Pressures: a) OCR=2

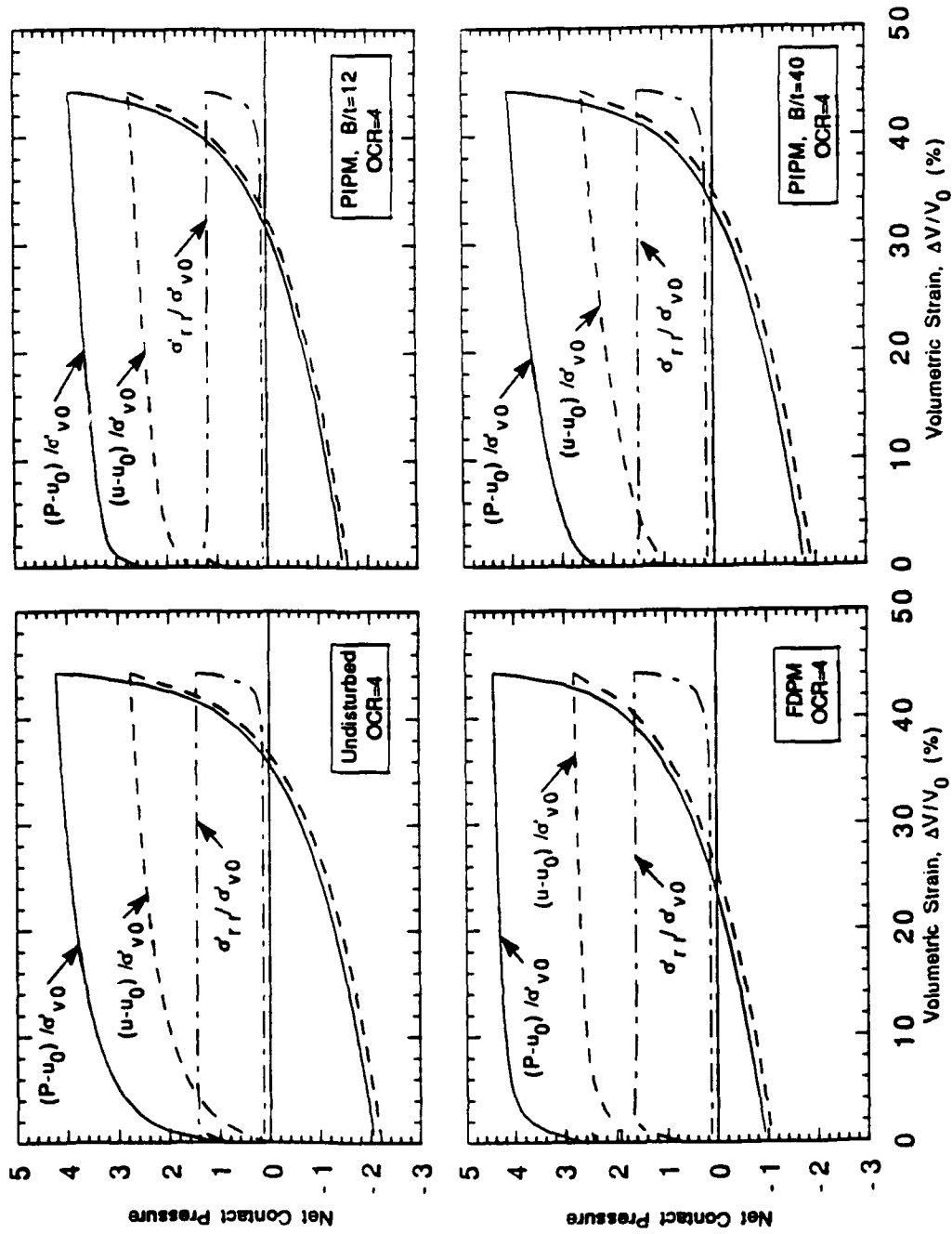


Figure 6.21 (contd.) Influence of Stress History on Total Radial Stress and Pore Pressure During Pressuremeter Expansion and Contraction - No Dissipation of Installation Pore Pressures: b) OCR=4

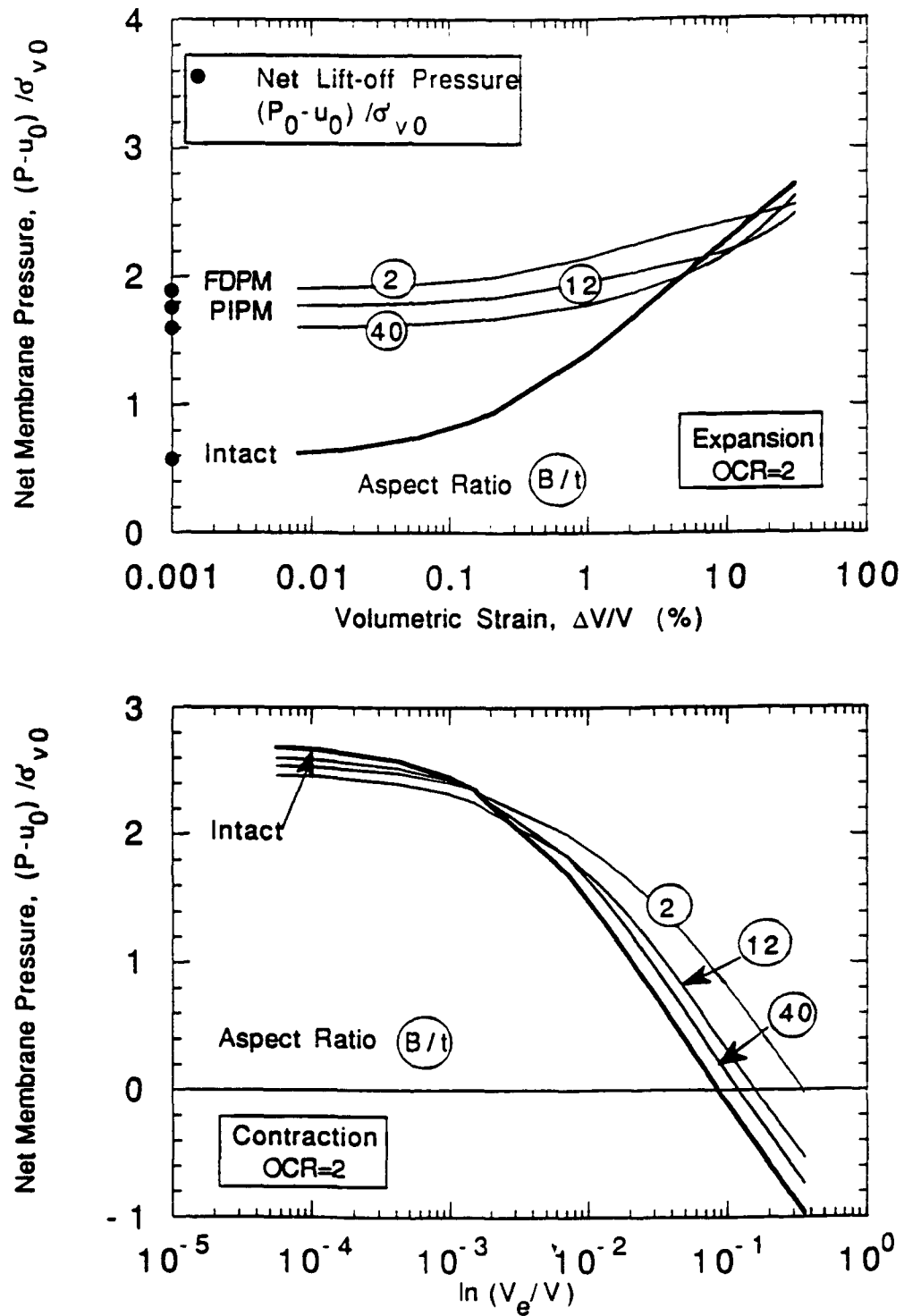


Figure 6.22 Influence of Stress History on Predicted Expansion and Contraction Curves - No Dissipation of Installation Pore Pressures: a) OCR=2

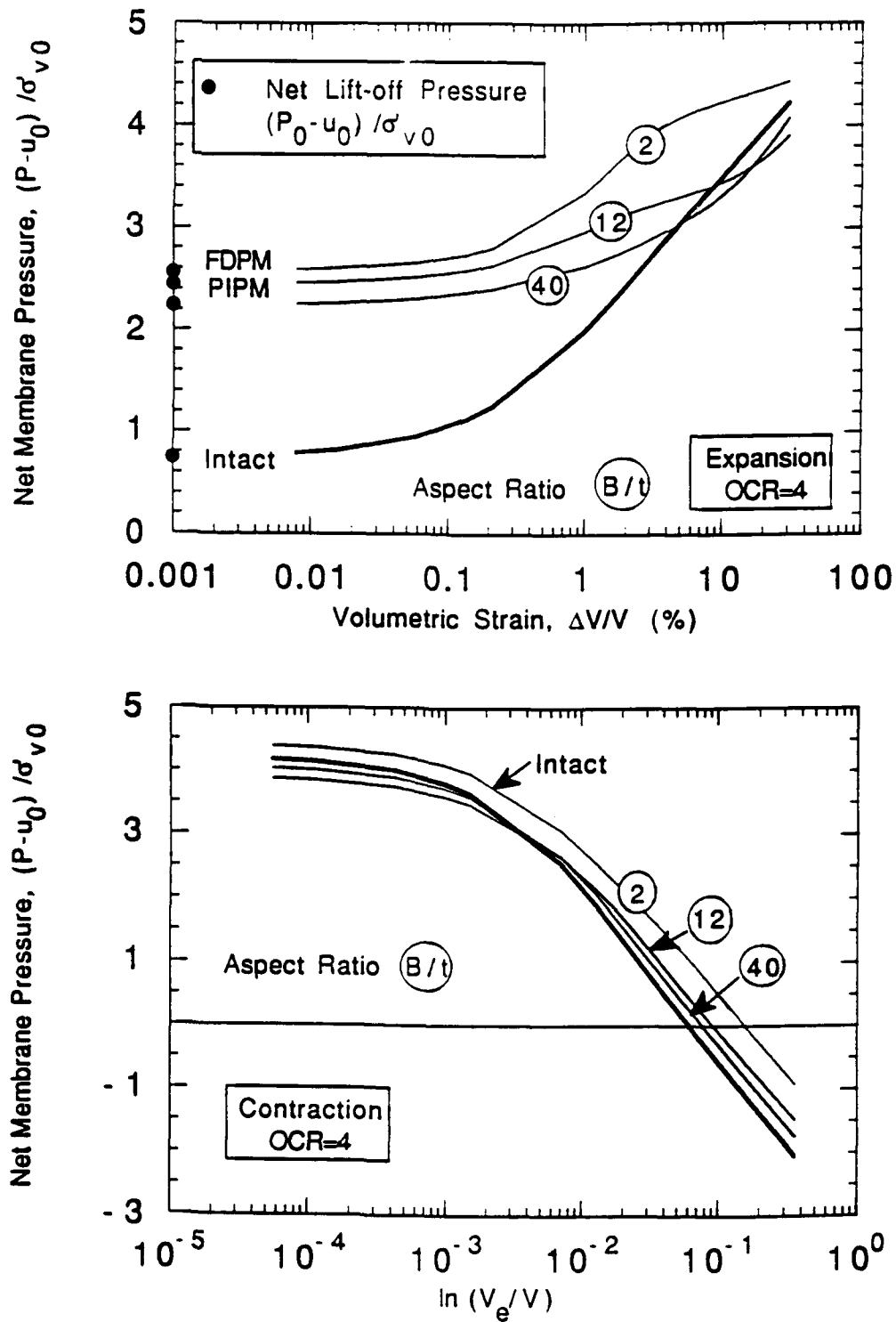


Figure 6.22 (contd.) Influence of Stress History on Predicted Expansion and Contraction Curves - No Dissipation of Installation Pore Pressures: b) OCR=4

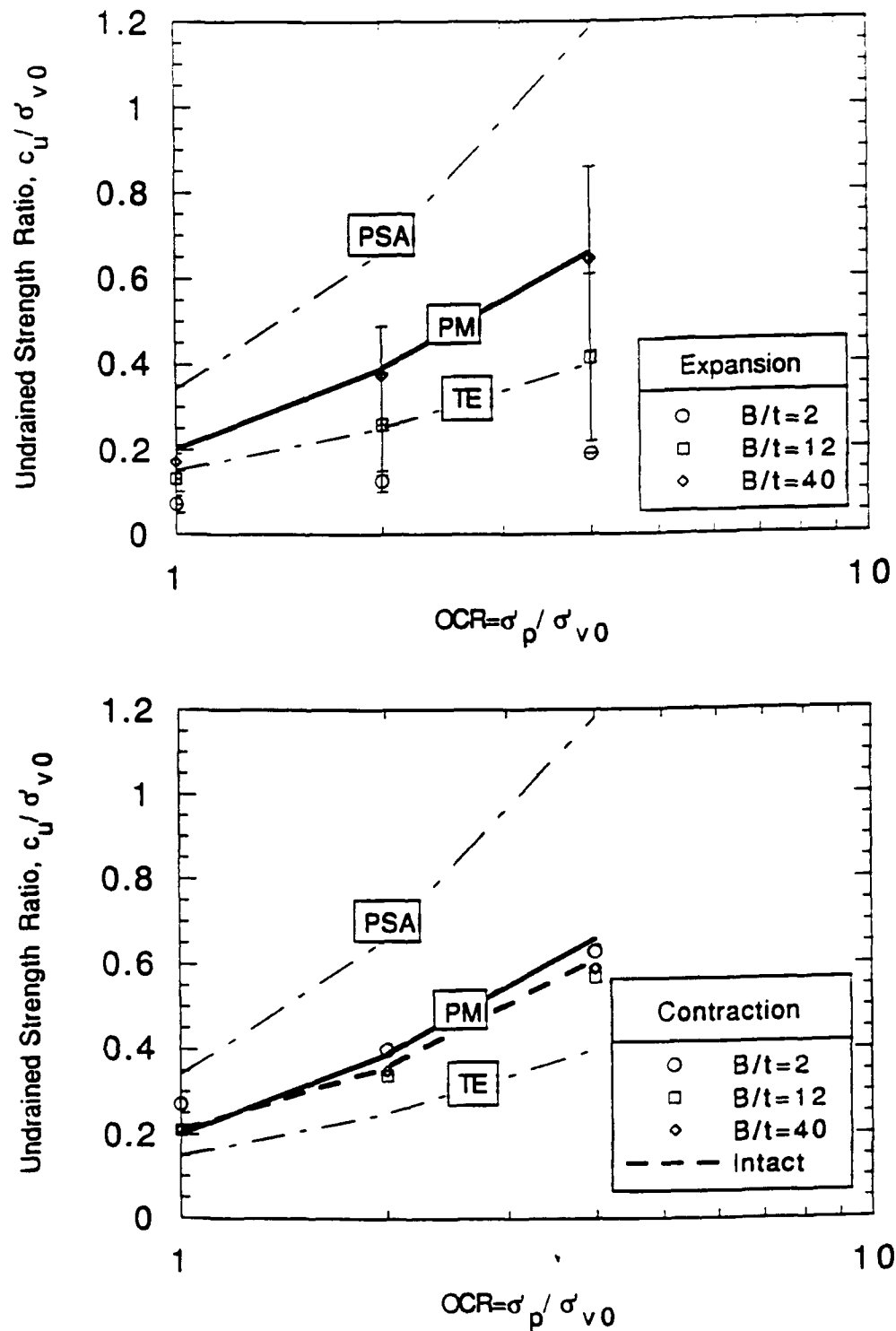


Figure 6.23 Influence of Stress History on Strength Estimates from Predicted Expansion and Contraction Curves - No Dissipation of Installation Pore Pressures

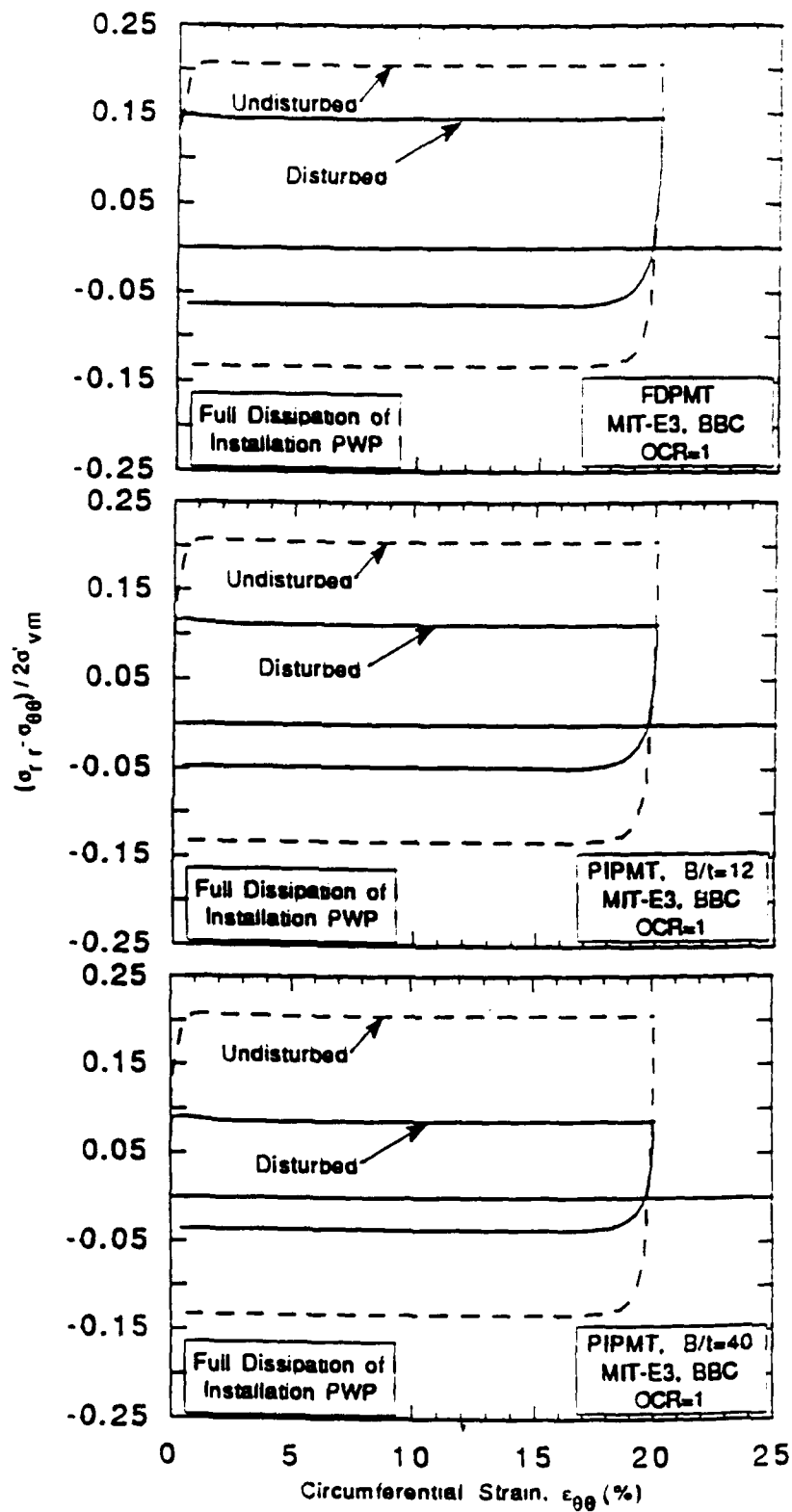


Figure 6.24 Influence of Disturbance on Stress-Strain Behavior- Full Dissipation of Installation Pore Pressure: a) Effect of B/t Ratio

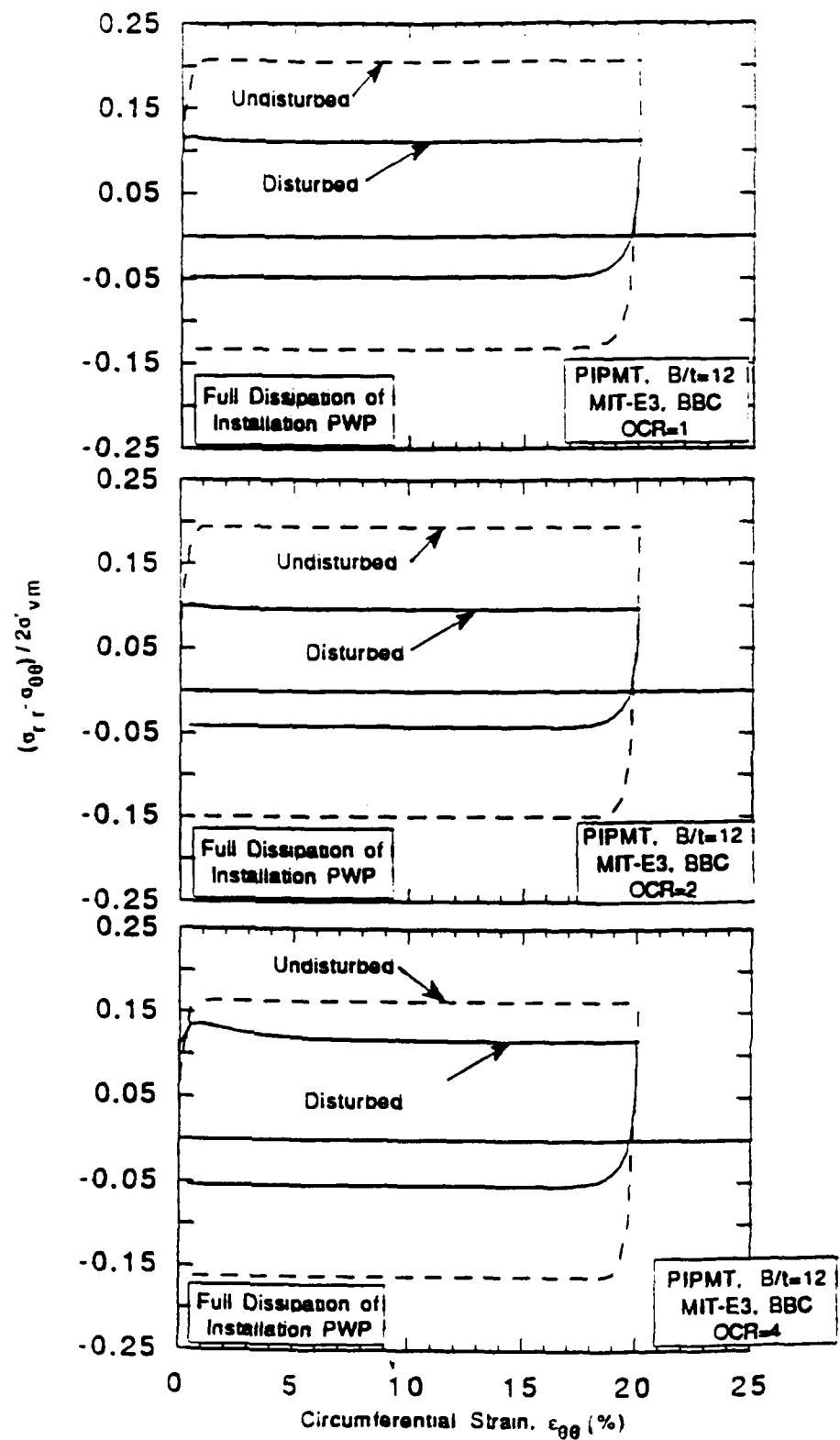


Figure 6.24 (contd.) Influence of Disturbance on Stress-Strain Behavior- Full Dissipation of Installation Pore Pressure: b) Effect of OCR

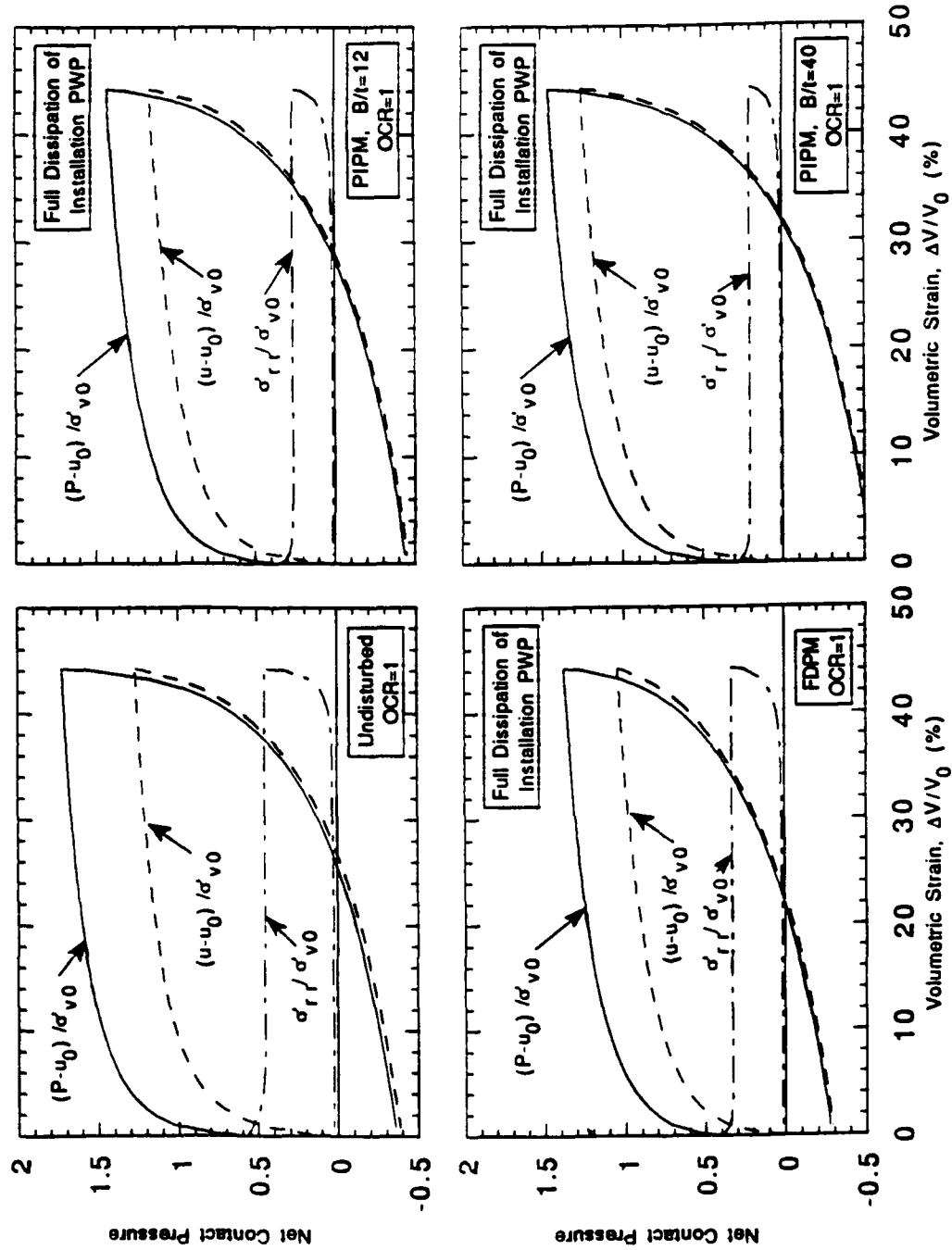


Figure 6.25 MIT-E3 Predictions of Total Radial Stress and Pore Pressure During Pressuremeter Expansion and Contraction - Full Dissipation of Installation Pore Pressures: a) $OCR=1$

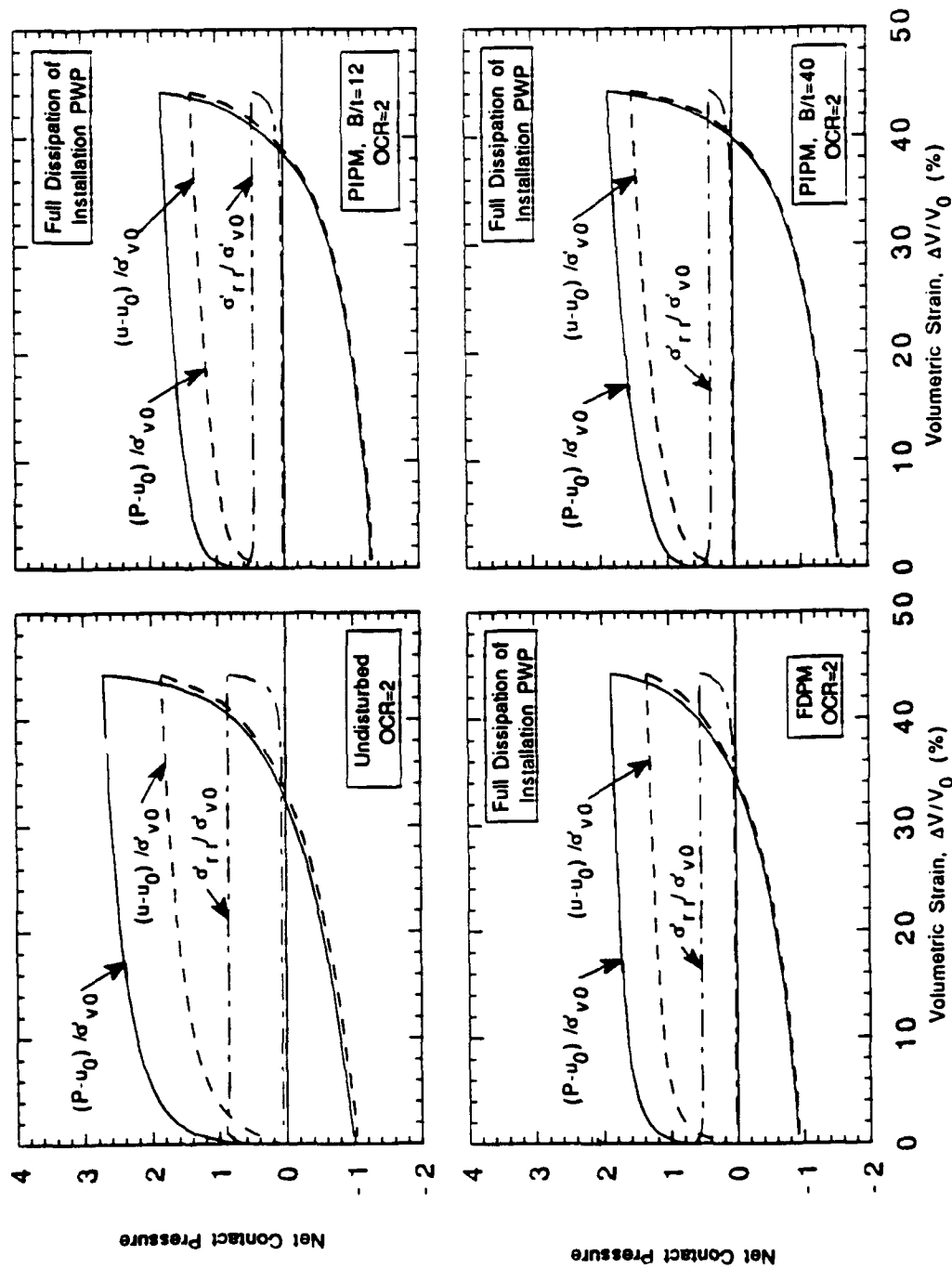


Figure 6.25 (contd.) MIT-E3 Predictions of Total Radial Stress and Pore Pressure During Pressuremeter Expansion and Contraction - Full Dissipation of Installation Pore Pressures: b) OCR=2

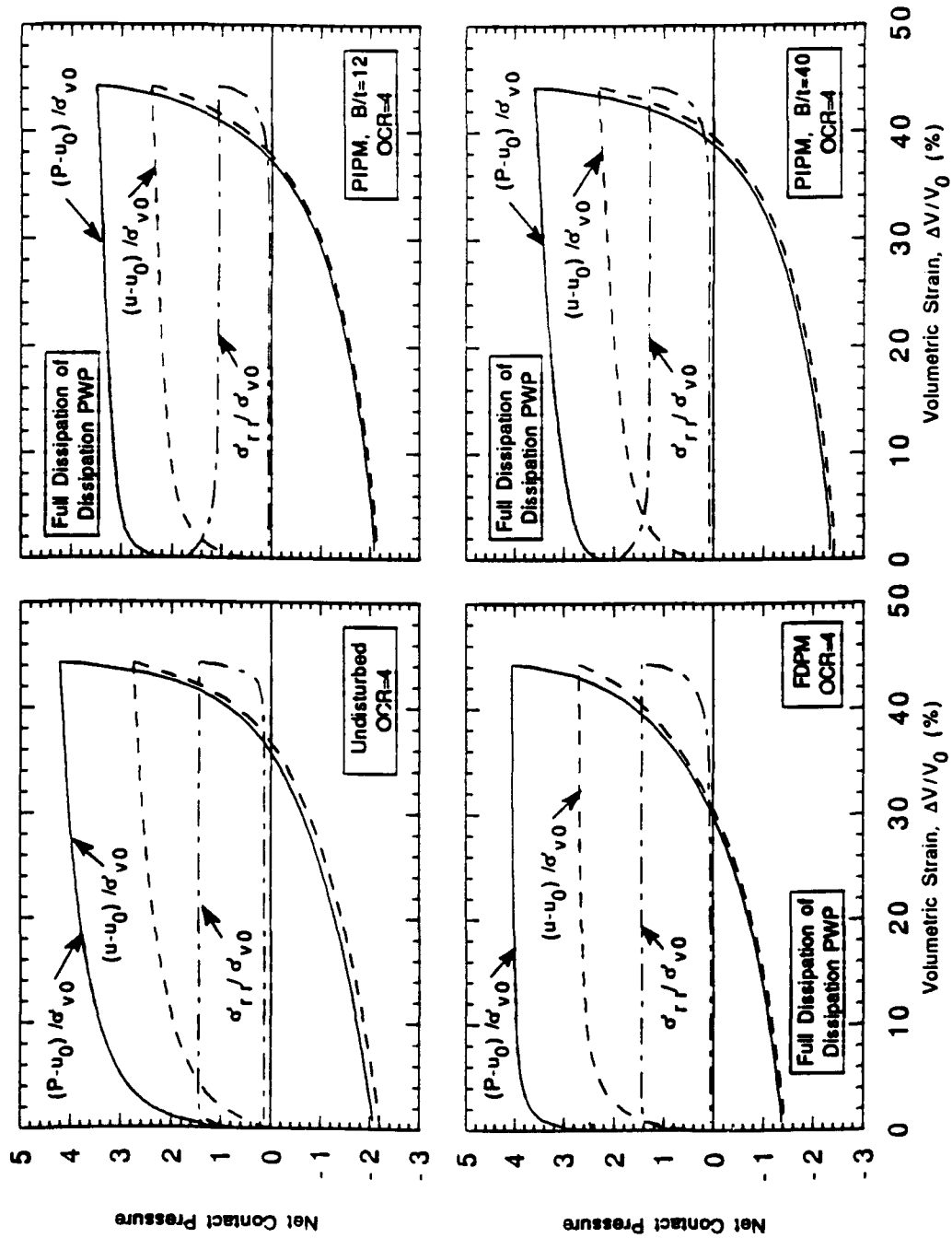


Figure 6.25 (contd.) MIT-E3 Predictions of Total Radial Stress and Pore Pressure During Pressuremeter Expansion and Contraction - Full Dissipation of Installation Pore Pressures: c) OCR=4

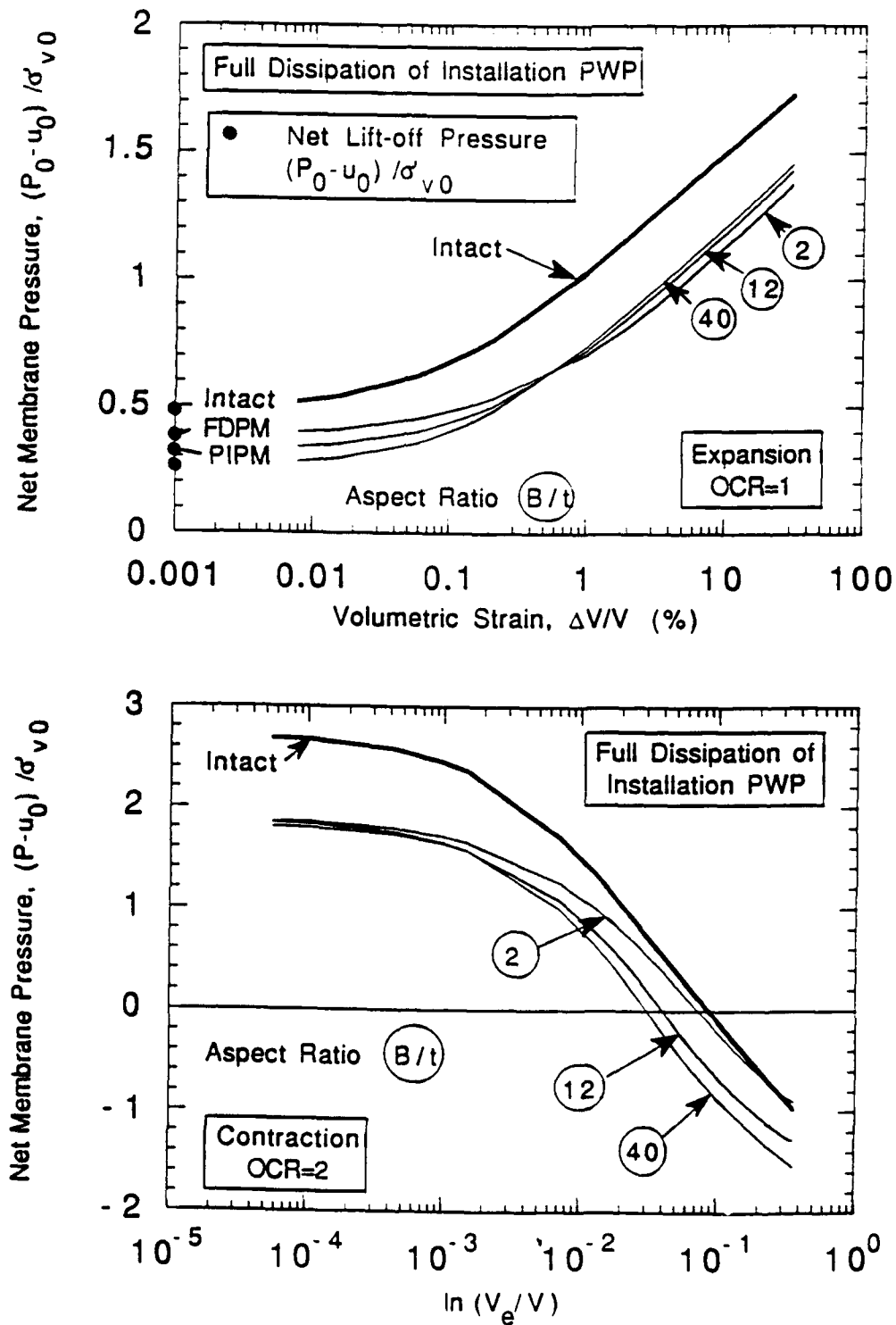


Figure 6.26 Predicted Expansion and Contraction Curves - Full Dissipation of Installation Pore Pressure: a) OCR=1

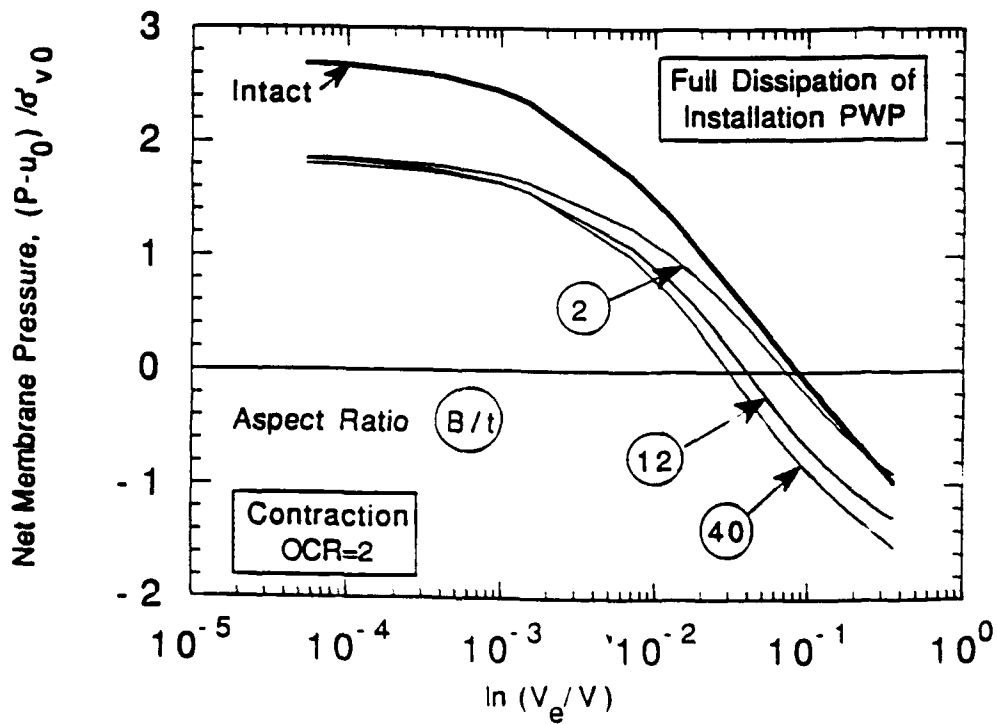
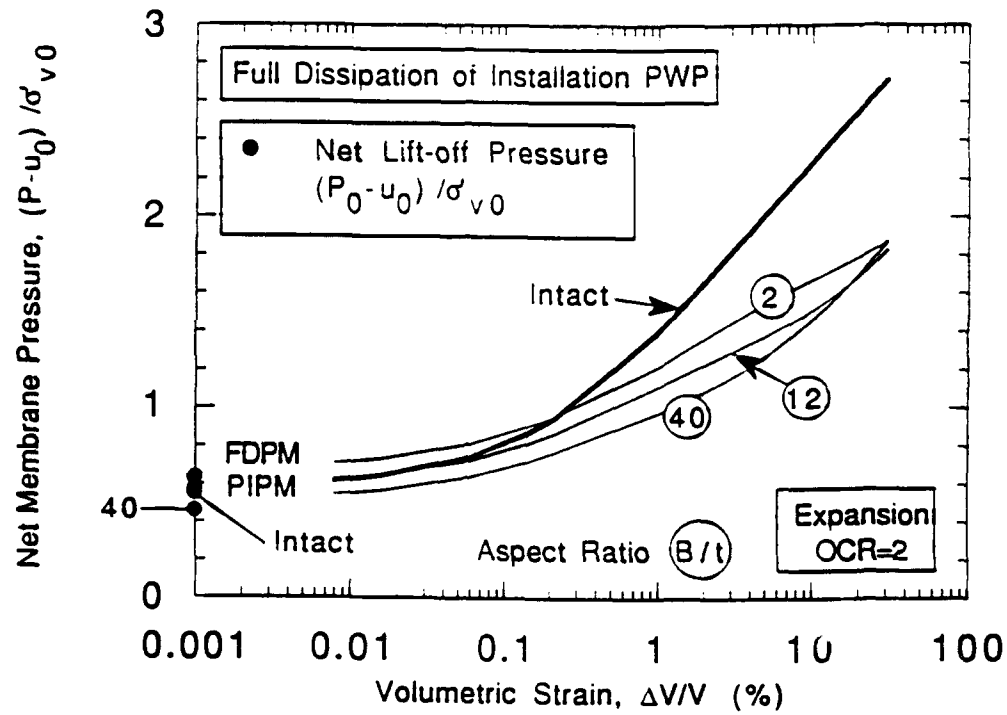


Figure 6.26 (contd.) Predicted Expansion and Contraction Curves - Full Dissipation of Installation Pore Pressure: b) OCR=2

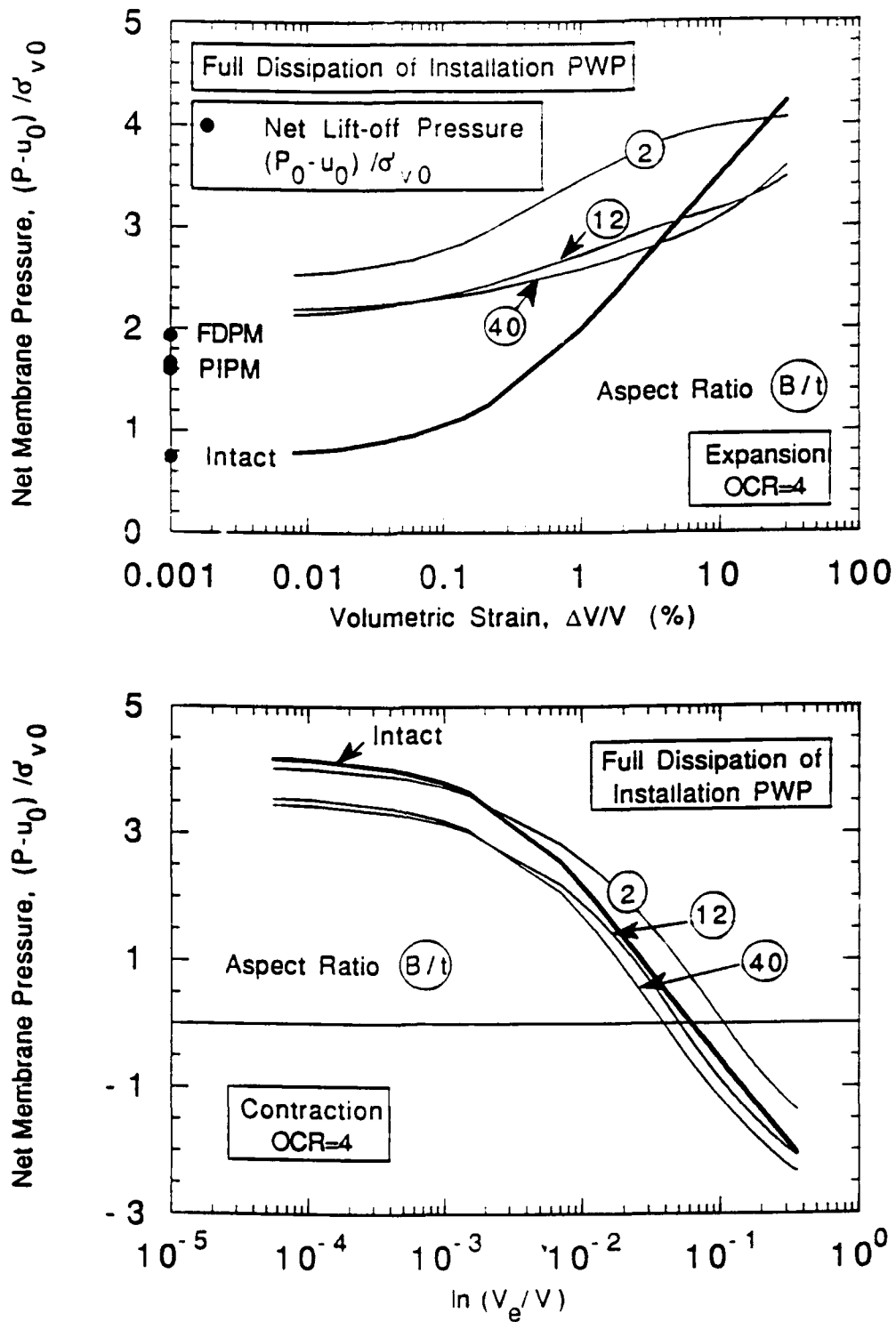


Figure 6.26 (contd.) Predicted Expansion and Contraction Curves - Full Dissipation of Installation Pore Pressure: c) OCR=4

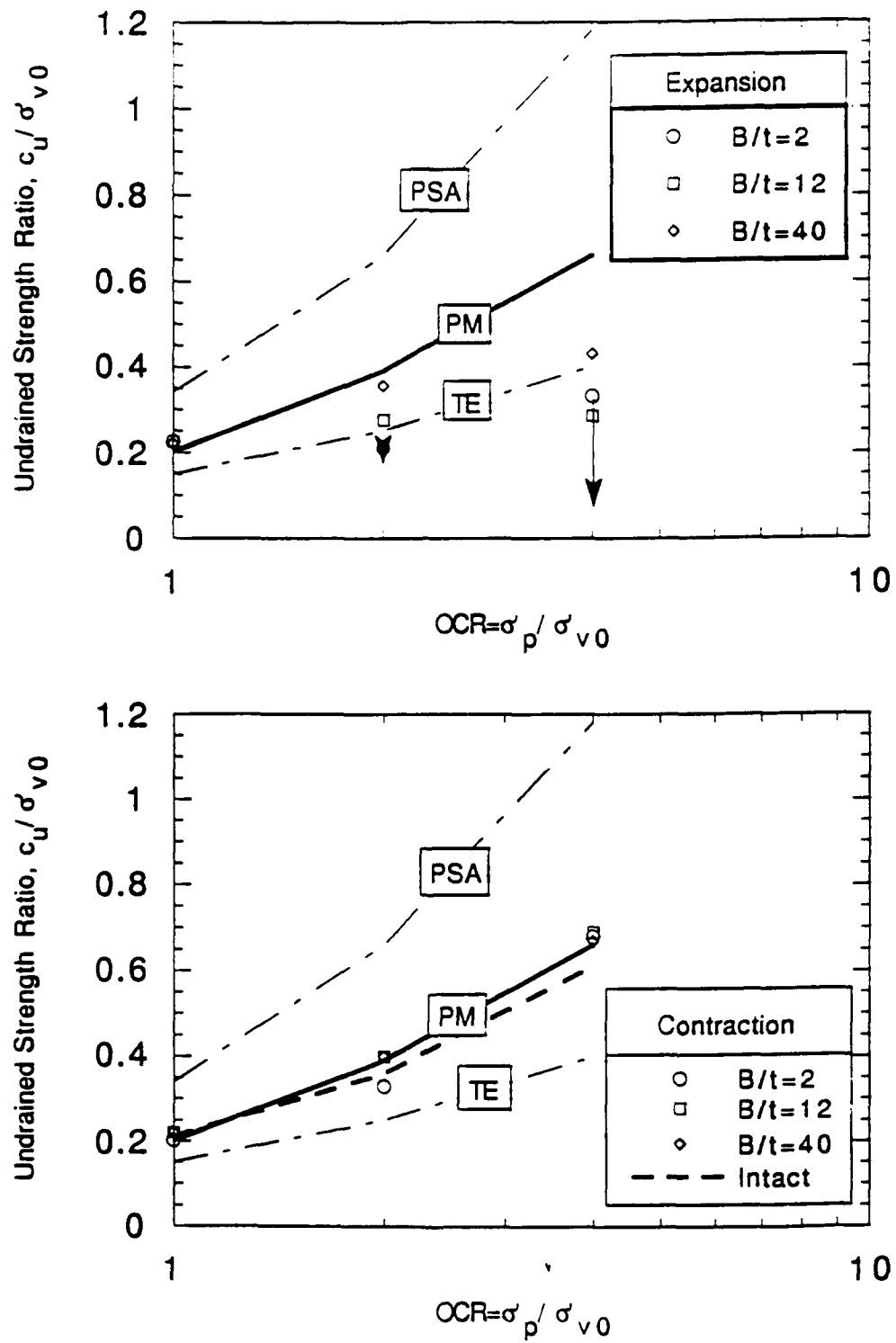
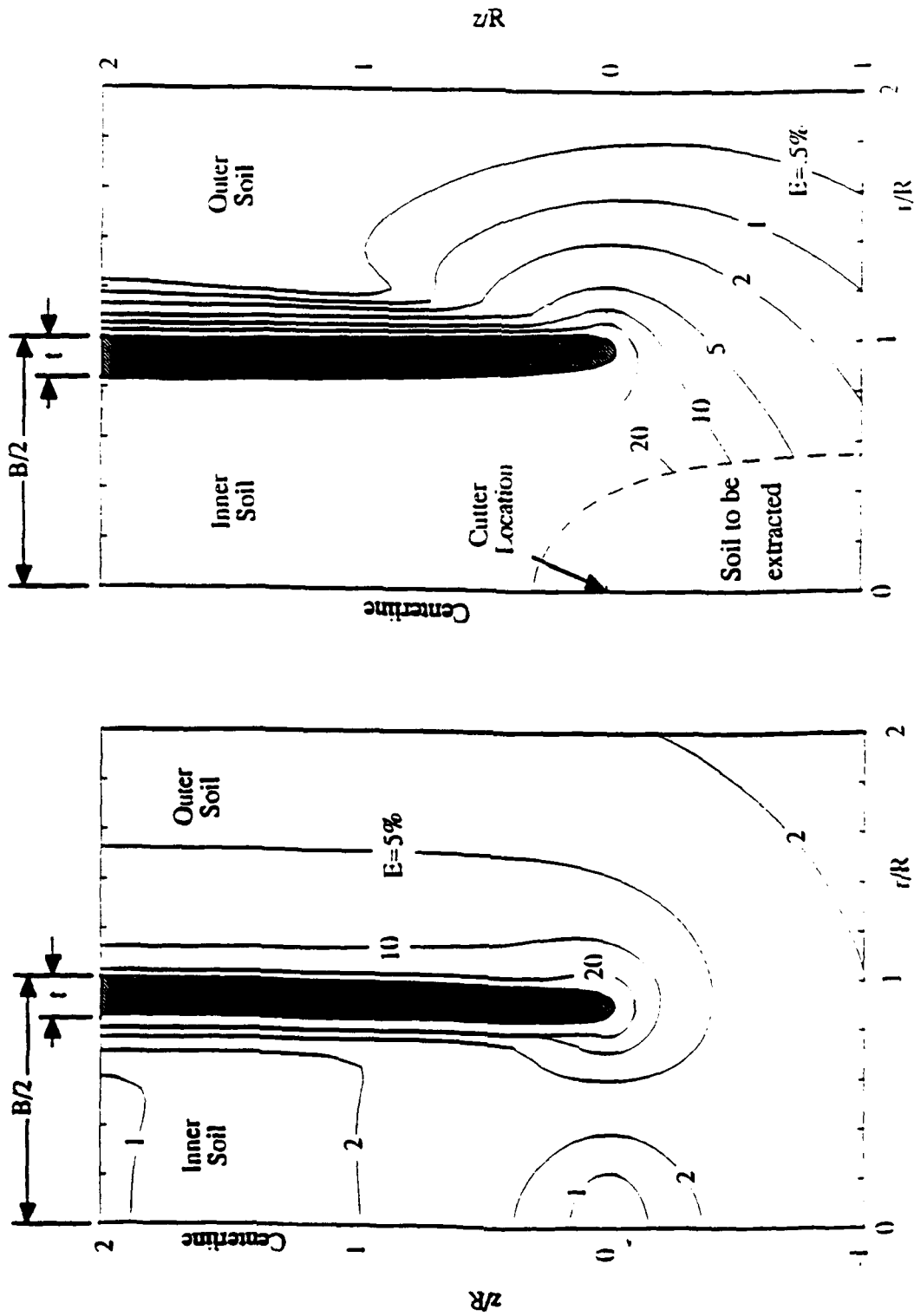


Figure 6.27 Influence of Stress History on Strength Estimates from Predicted Expansion and Contraction Curves - Full Dissipation of Installation Pore Pressures



b) Ideal Self-Boring Pressuremeter

a) Push-in Pressuremeter

Figure 6.28 Contours of Octahedral Shear Strain During Self-Boring Penetration:

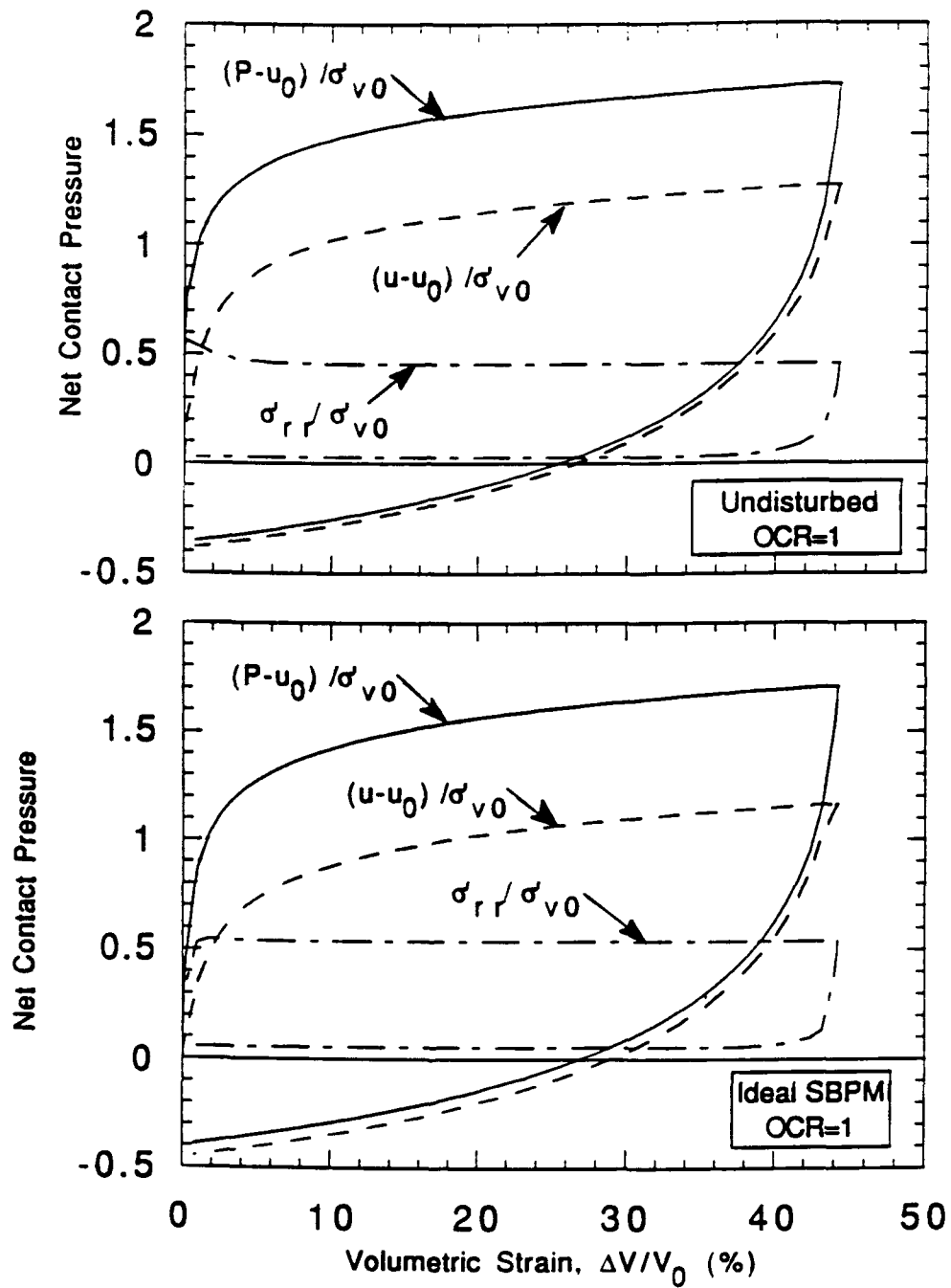


Figure 6.29 MIT-E3 Predictions of Total Radial Stress and Pore Pressure During Self-Boring Pressuremeter Expansion and Contraction in Normally Consolidated Boston Blue Clay

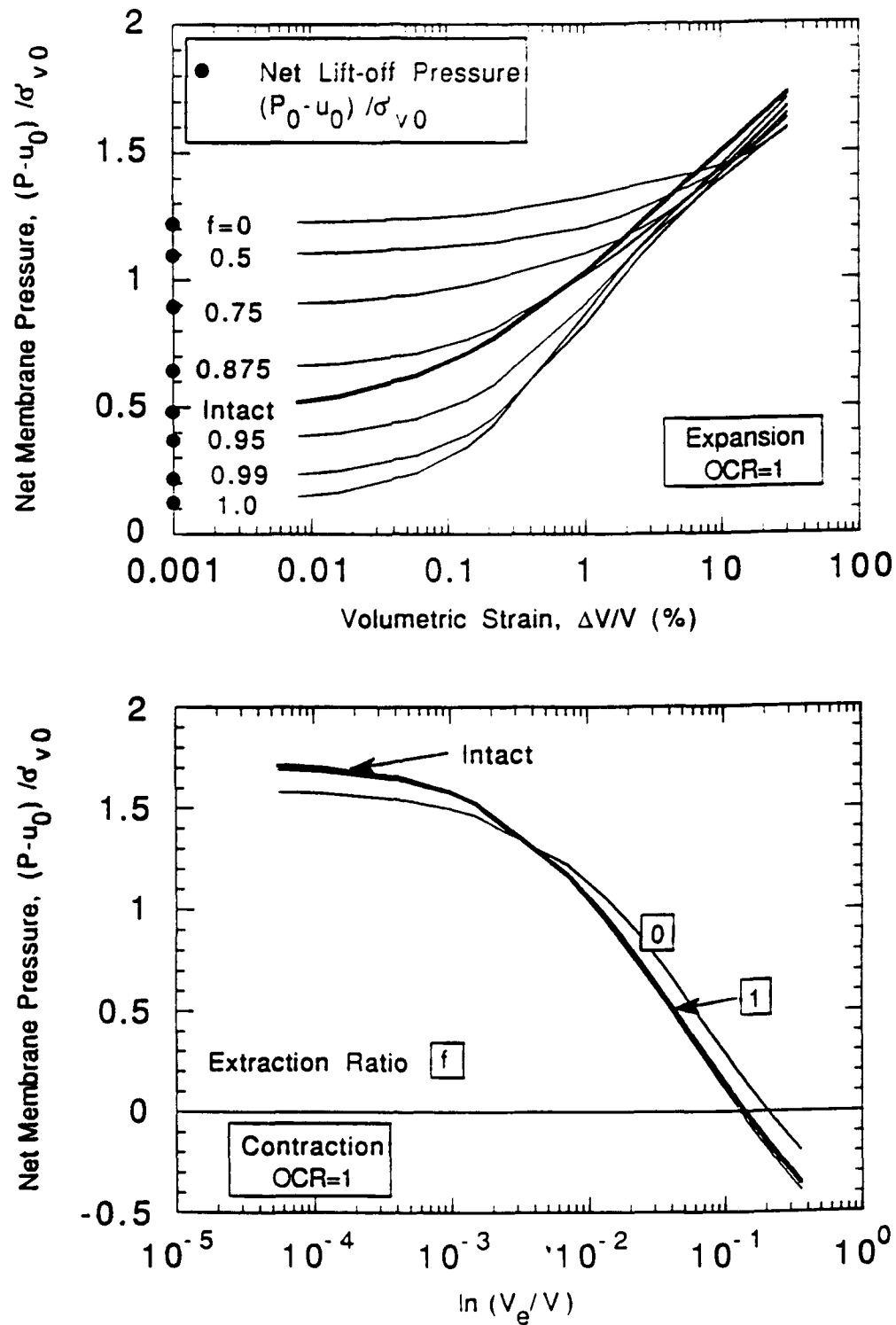


Figure 6.30 MIT-E3 Predictions of Self-Boring Pressuremeter Expansion and Contraction Curves in Normally Consolidated Boston Blue Clay

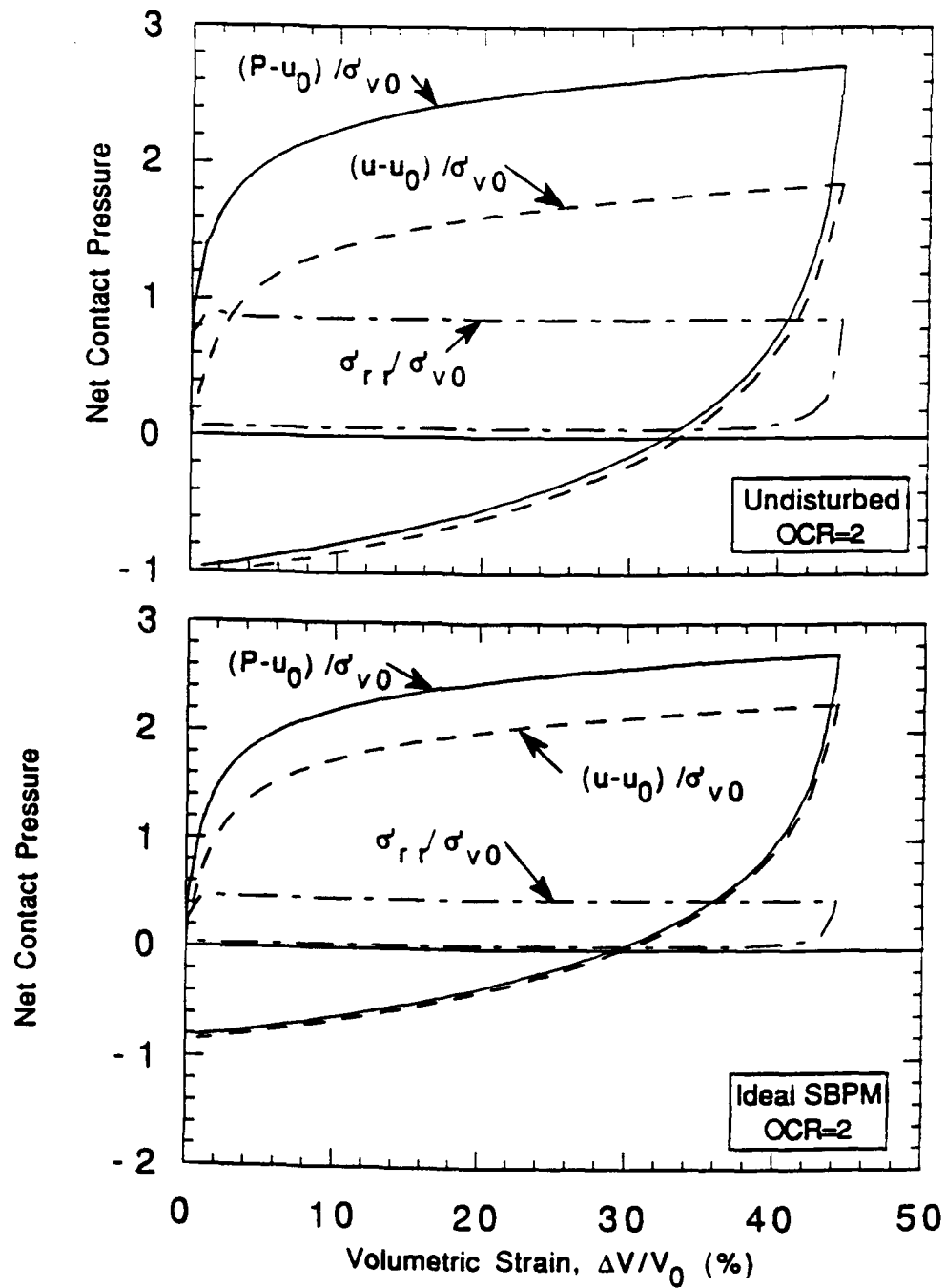


Figure 6.31 Influence of Stress History on Total Radial Stress and Pore Pressure During Self-Boring Pressuremeter Expansion and Contraction : a) OCR=2

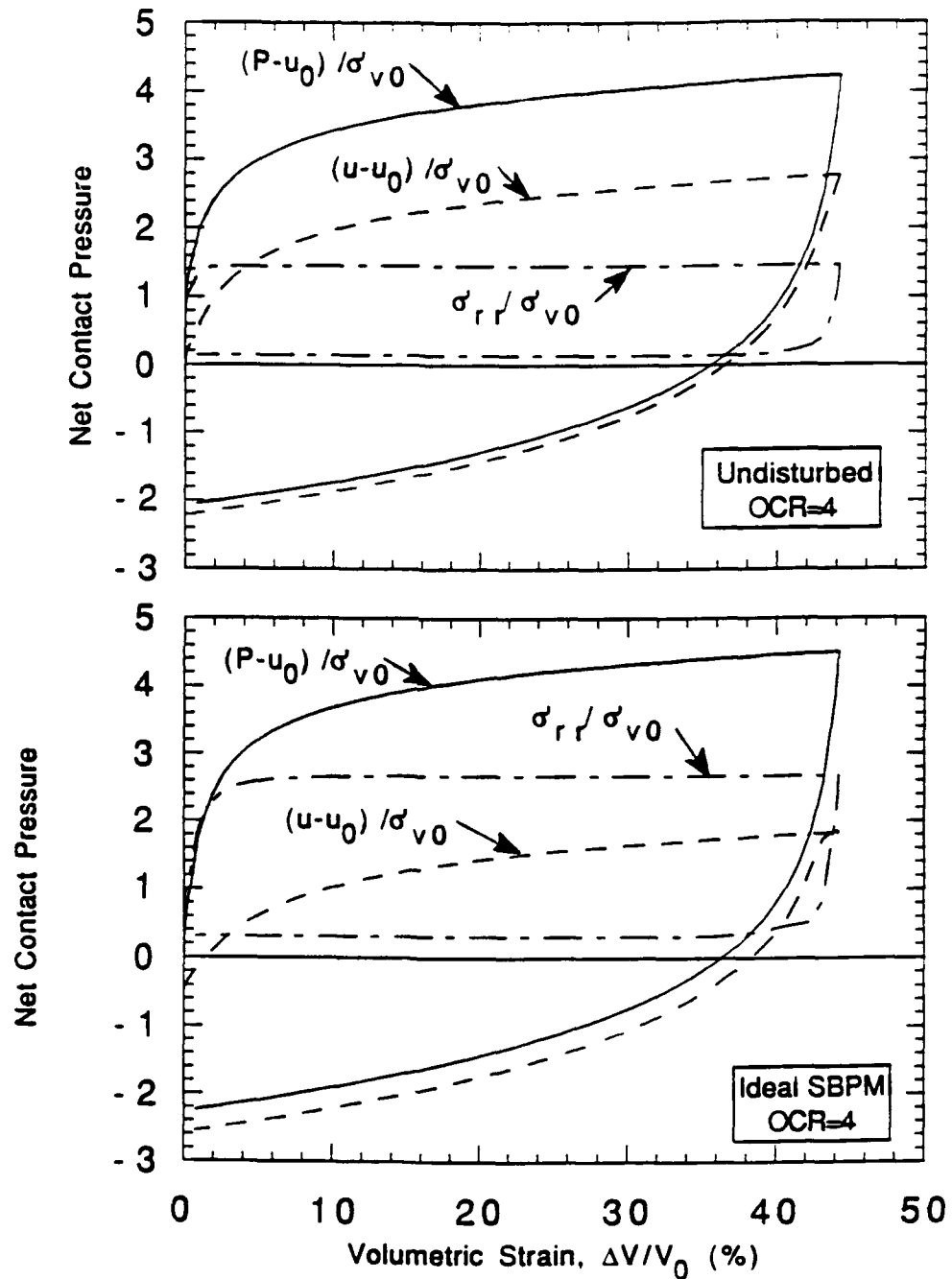


Figure 6.31 (contd.) Influence of Stress History on Total Radial Stress and Pore Pressure During Self-Boring Pressuremeter Expansion and Contraction : b) OCR=4

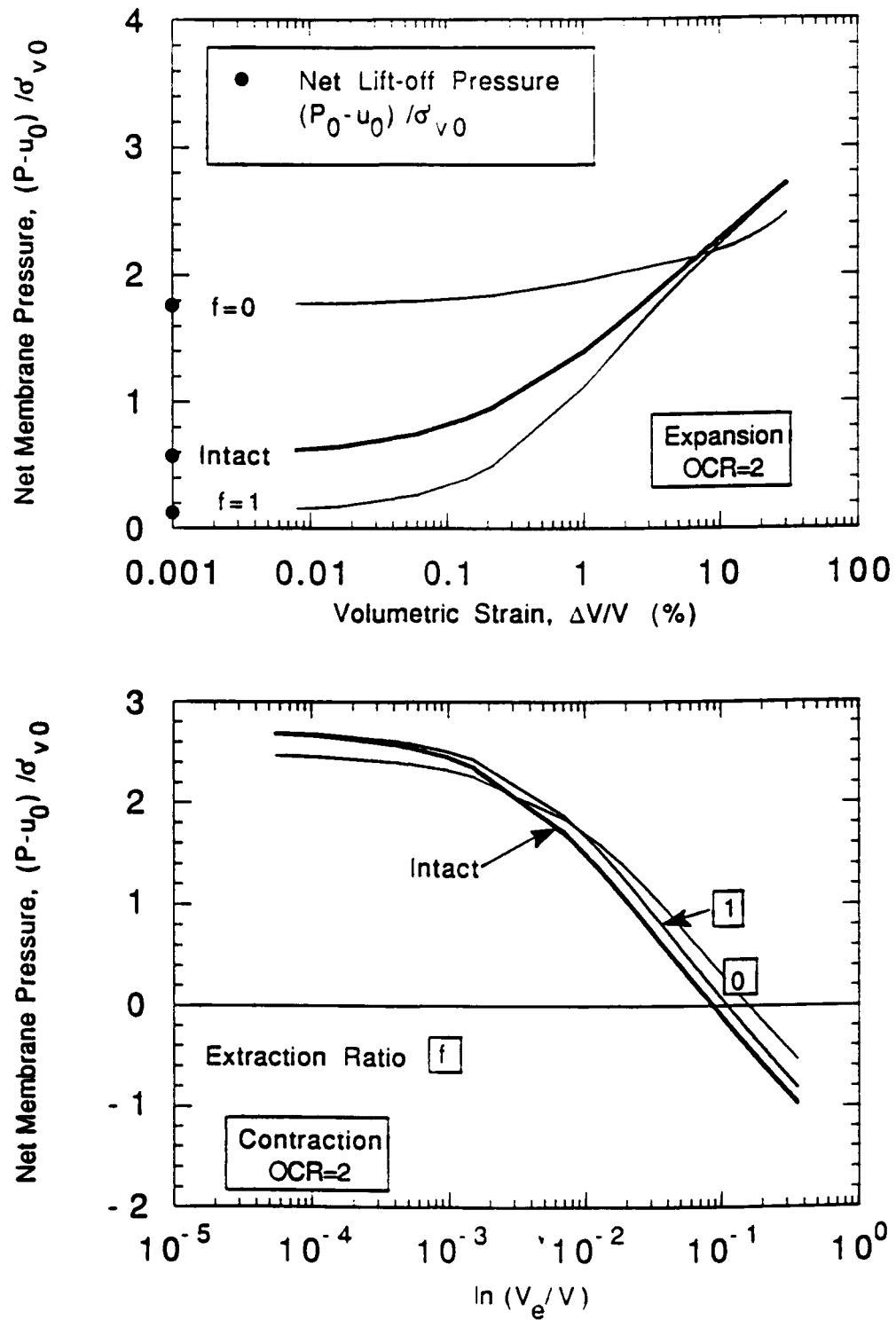


Figure 6.32 Influence of Stress History on Predicted Self-Boring Pressuremeter Expansion and Contraction Curves: a) OCR=2

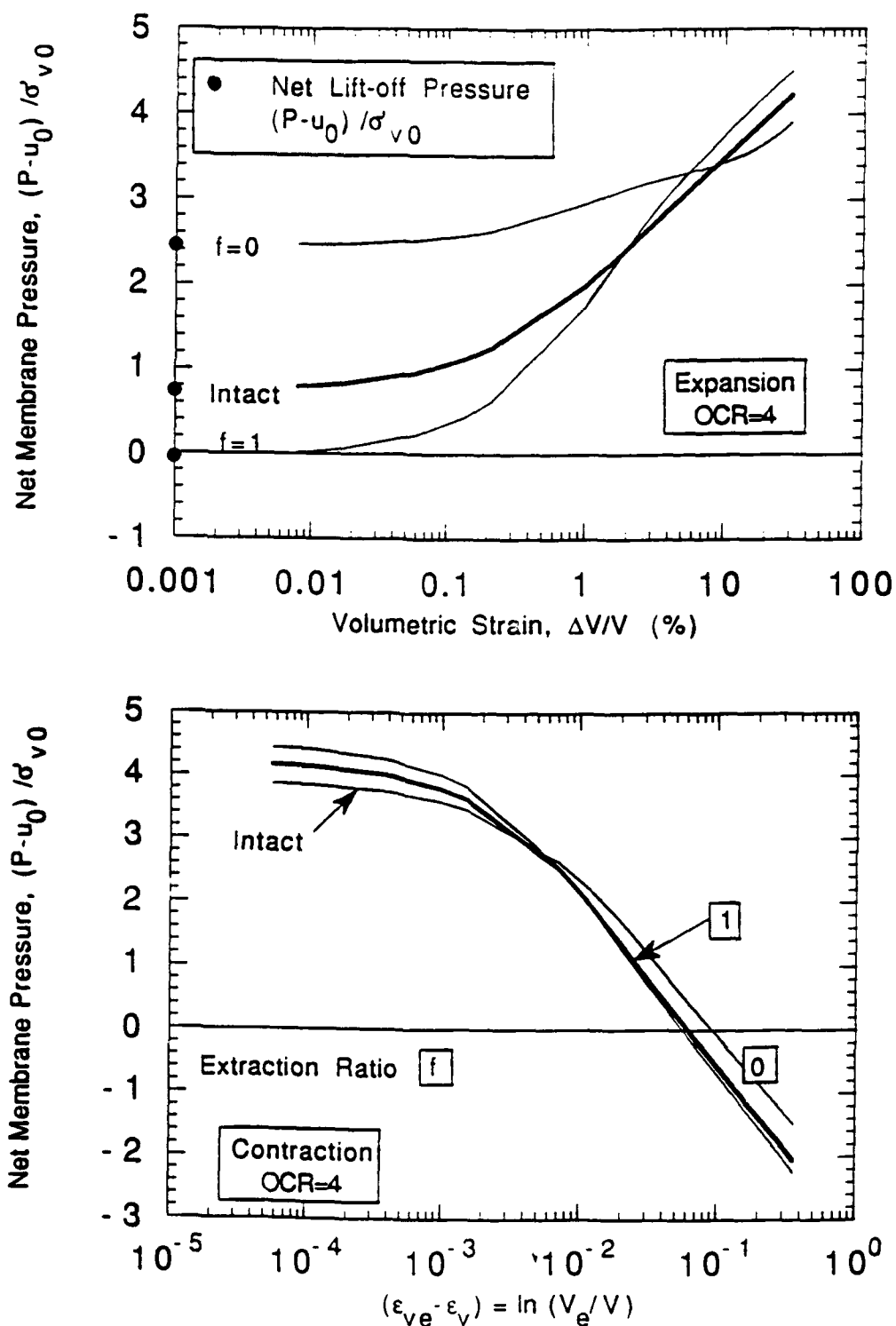


Figure 6.32 (contd.) Influence of Stress History on Predicted Self-Boring Pressuremeter Expansion and Contraction Curves: b) OCR=4

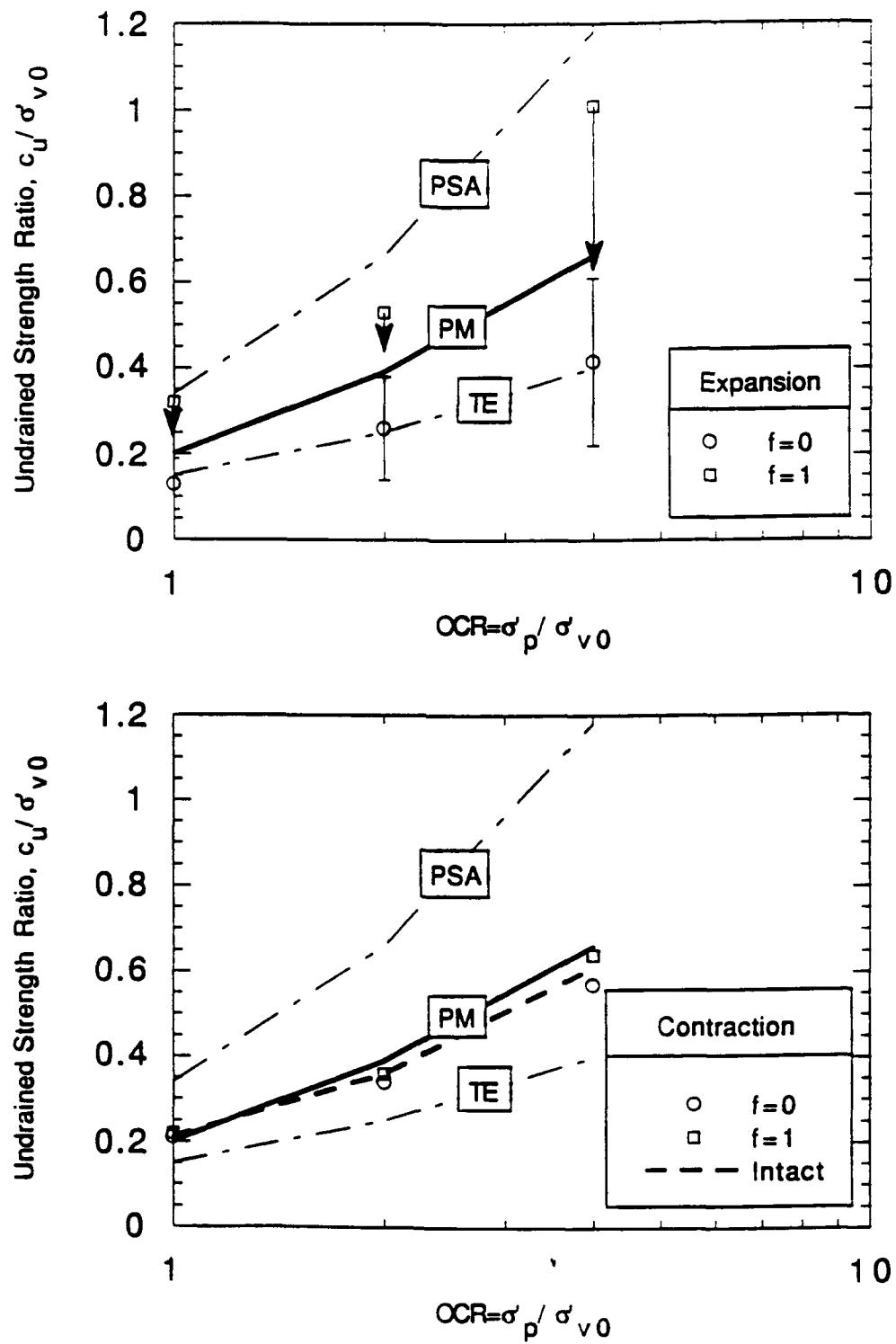


Figure 6.33 Influence of Stress History on Strength Estimates from Predicted Self-Boring Pressuremeter Expansion and Contraction Curves

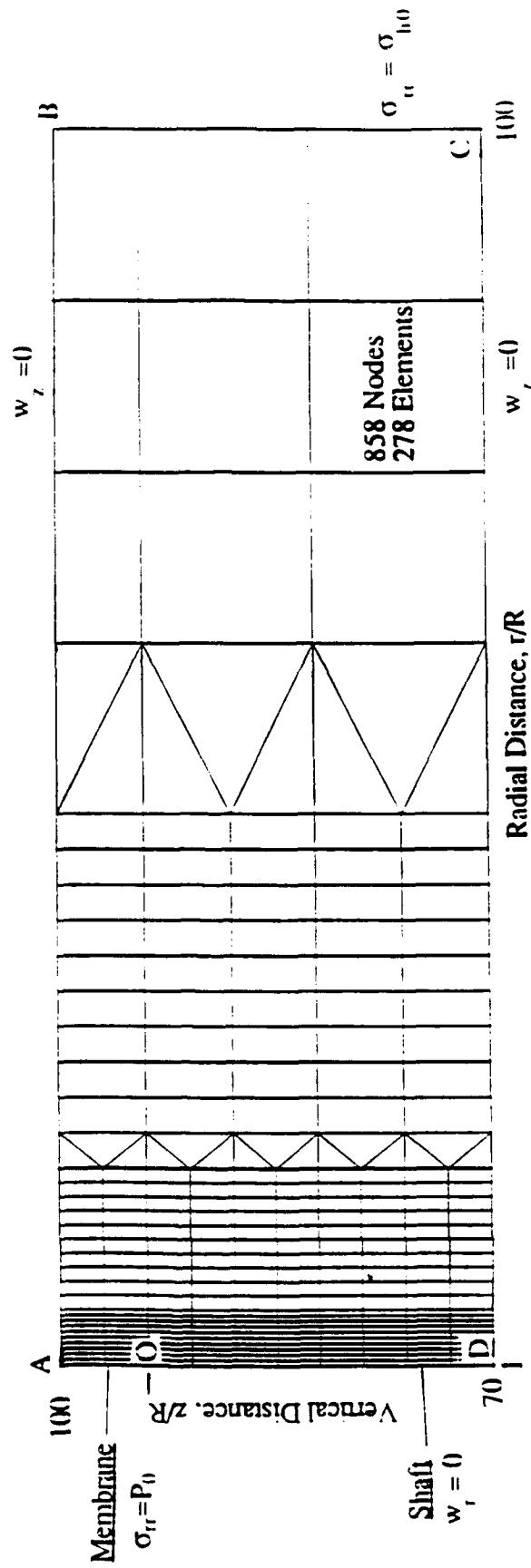


Figure 6.34a Finite Element Mesh and Boundary Conditions Used for Analysis of Finite Membrane Length Effects

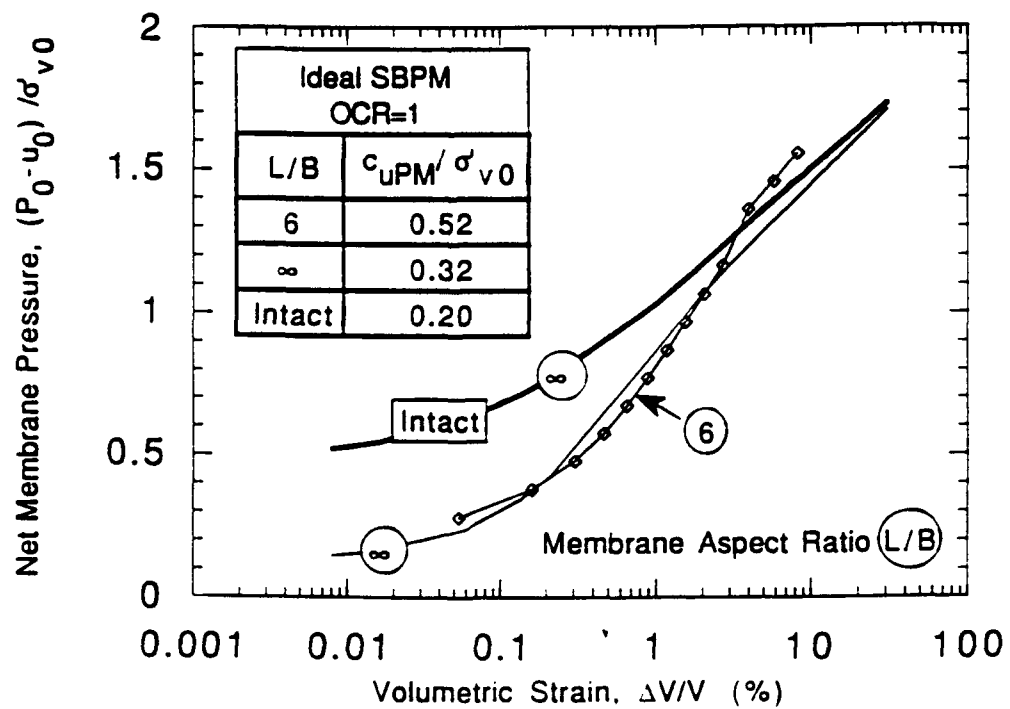
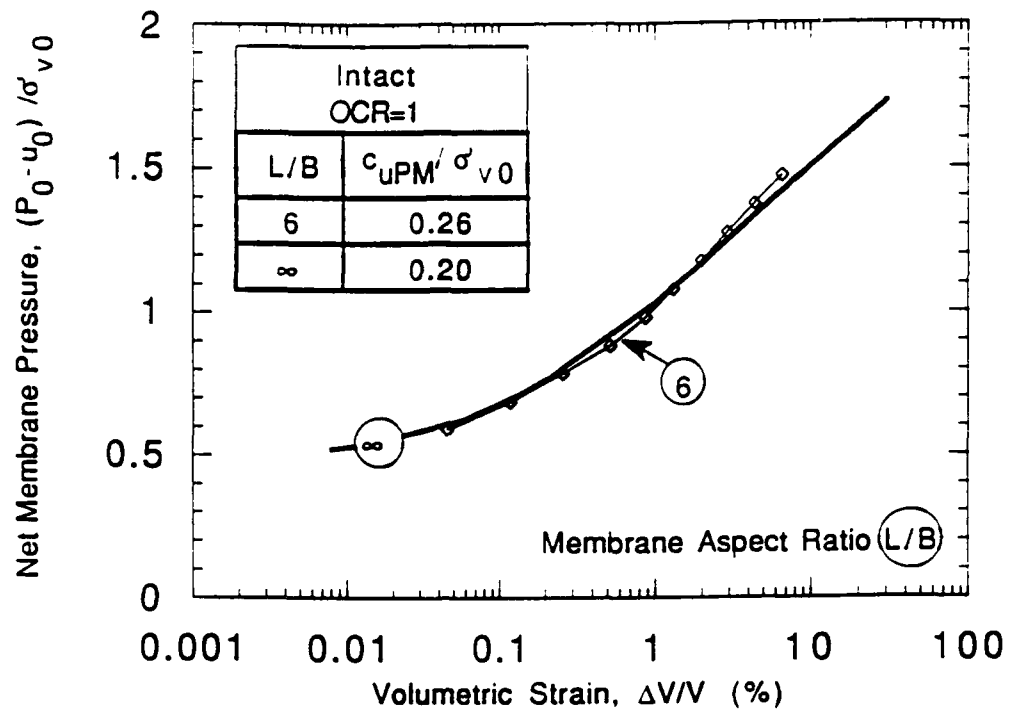


Figure 6.34b Influence of Finite Membrane Length on Predicted Pressuremeter Expansion Curves

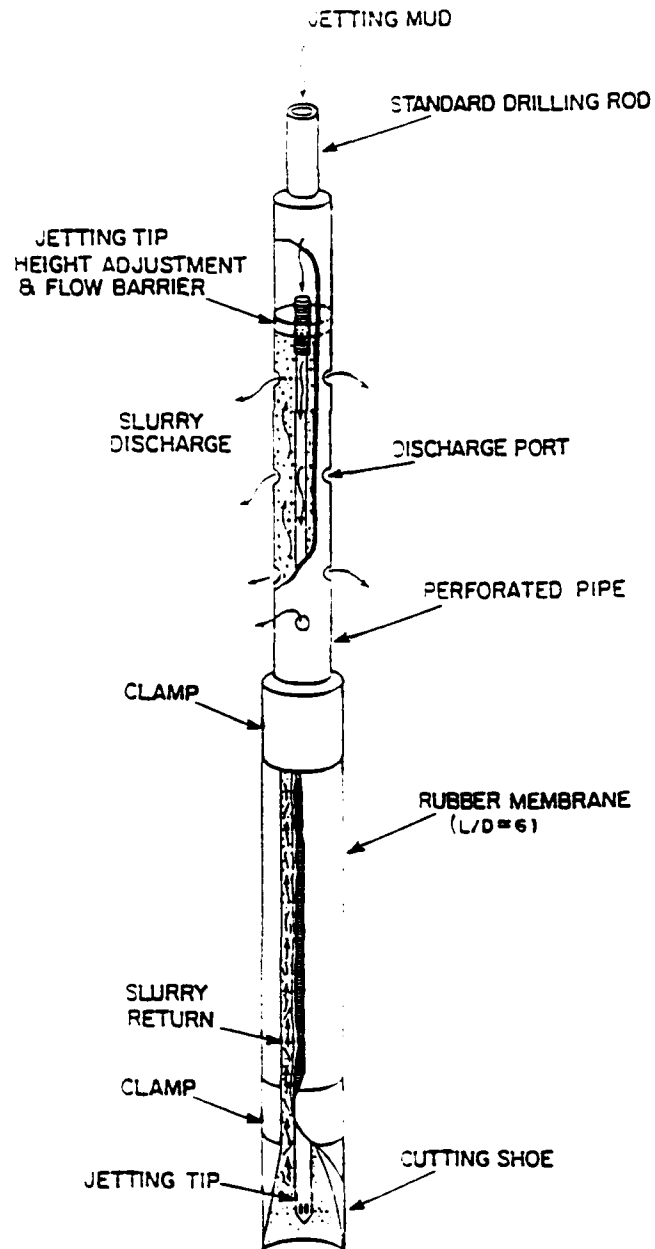


Figure 6.35 Modified Camkometer Used in South Boston Pressuremeter Special Test Program (after Benoit, 1991)

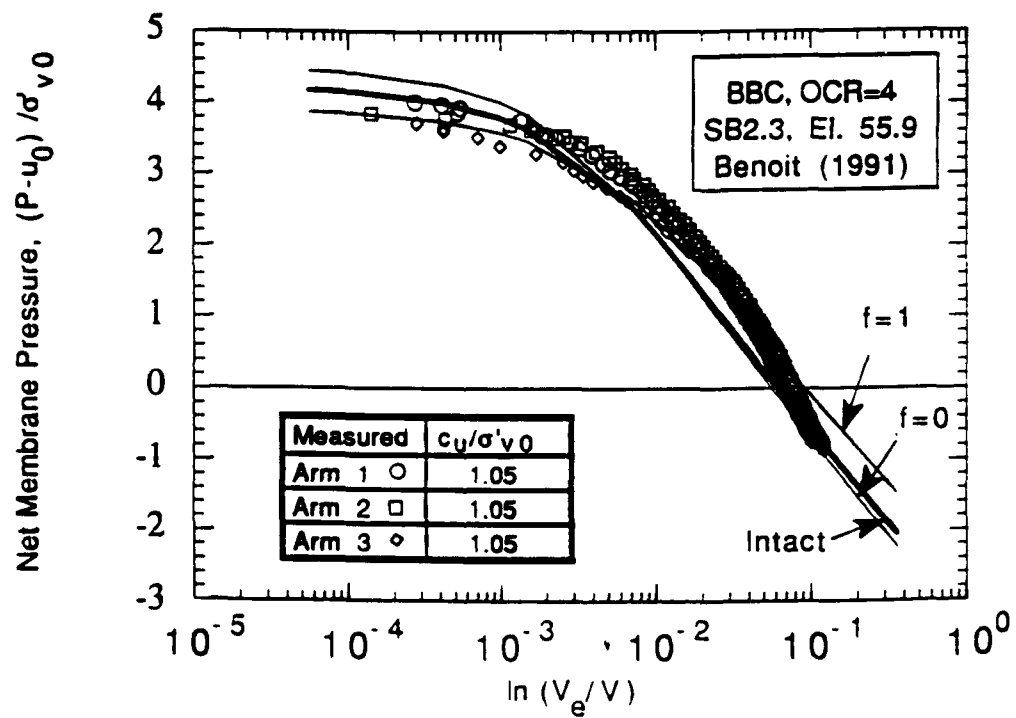
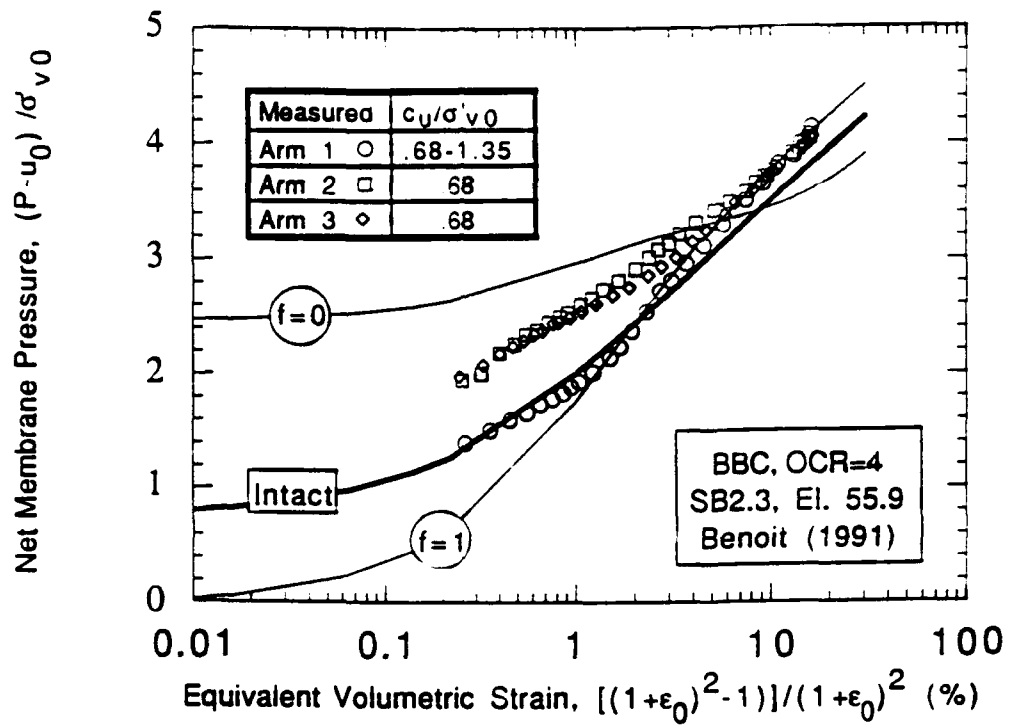


Figure 6.36 (contd.) Comparison of Predictions to Pressuremeter Measurements from South Boston Site: b) OCR=4

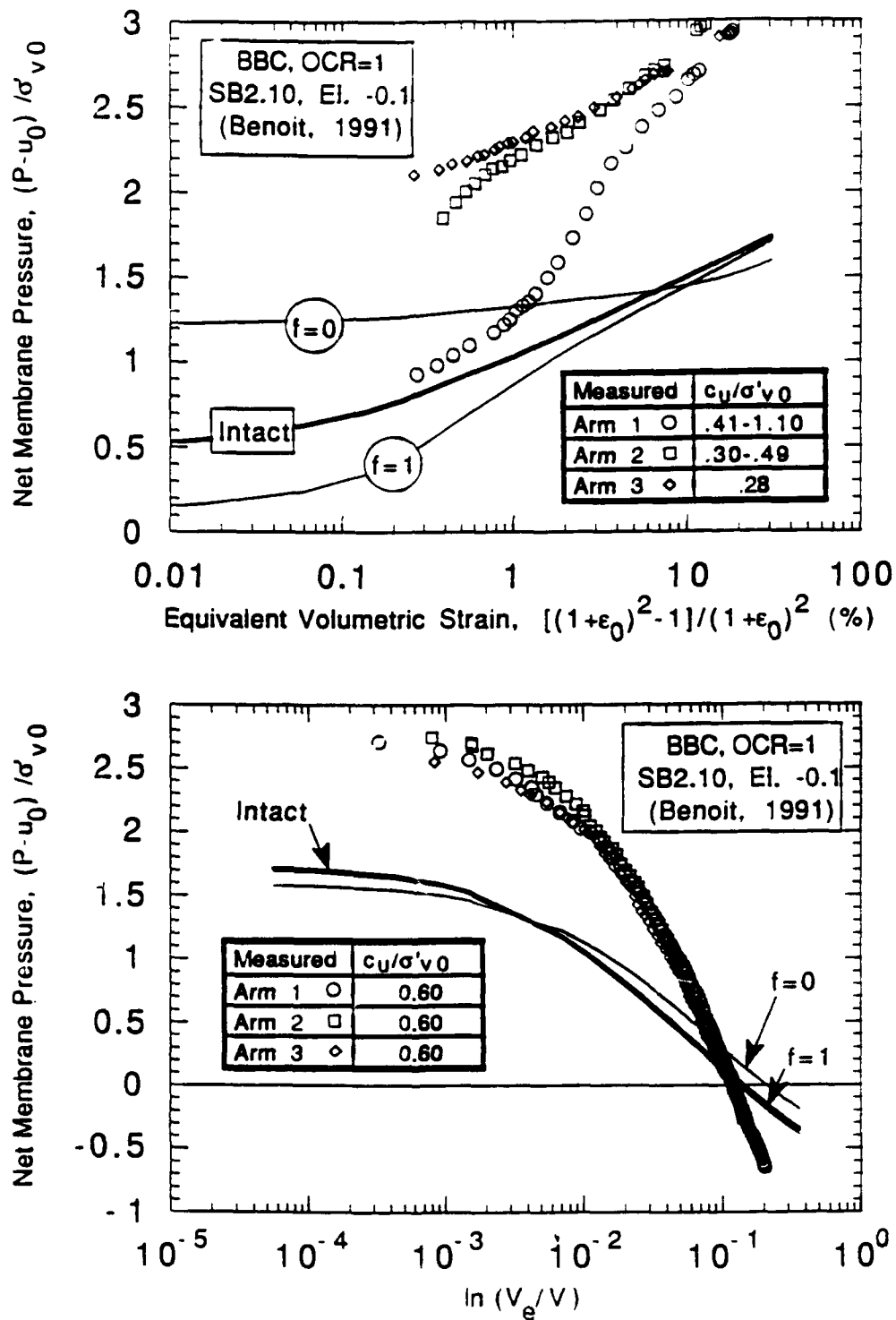


Figure 6.36 Comparison of Predictions to Pressuremeter Measurements from South Boston Site: a) OCR=1

7. SUMMARY, CONCLUSIONS, AND RECOMMENDATIONS

Existing methods for interpreting engineering properties from in-situ tests in clays are based primarily on empirical correlations. This situation has arisen, in large part, due to inherent limitations of in-situ tests (such as poorly defined boundary and drainage conditions) and to disturbances caused by the initial installation of the devices. This research has developed and applied a systematic analysis which predicts the in-situ measurements during both installation and in subsequent test procedures, based on a known set of soil properties. The predictive capabilities of the proposed analyses are evaluated through direct comparisons with field test data at well-documented test sites and are used to assess the reliability of correlations between the measurements and engineering properties of clay.

The research makes extensive use of two recent analytical developments at MIT: 1) the Strain Path Method (Baligh, 1985a), a comprehensive analytical framework which models quantitatively the disturbance effects caused by undrained deep penetration in clays; and 2) the MIT-E3 generalized effective stress soil model (Whittle, 1987, 1990), which describes realistically the non-linear, in-elastic, and anisotropic behavior of normally consolidated and lightly overconsolidated clays.

This report focuses on predictions of measurements obtained by three types of devices: a) piezocone, b) the flat plate dilatometer, and c) pressuremeters, using soil properties to describe the behavior of Boston Blue Clay. The following sections (7.1-7.5) describe the principal findings of the research, while Section 7.6 gives recommendations for further study.

7.1 EXCESS PORE PRESSURES DURING PENETRATION

Chapter 2 proposes a numerical scheme for computing an approximate field of excess pore pressures from the Strain Path Method by solving equilibrium equations in the form of a Poisson equation. This task is essential for predicting and interpreting in-situ test measurements for the following reasons:

1. Excess pore pressures dominate other soil stresses during deep penetration in normally to lightly overconsolidated clays and hence, represent an important component of the measured behavior during penetration.
2. Equilibrium conditions are not uniquely satisfied by the Strain Path Method. Previous applications of Strain Path analysis, which satisfy equilibrium in one direction only, are not reliable for estimating excess pore pressure distributions at all locations around the

penetrometer. The proposed method ameliorates the uncertainties in pore pressures and is especially useful for three-dimensional geometries.

Numerical implementation of the Poisson solution involves numerical differentiation of non-homogeneous stress fields, which presents a major difficulty for achieving accurate solutions. Section 2.4 presents a scheme which utilizes the divergence theorem to obtain reliable, robust solutions of the excess pore pressure fields.

Section 2.5 shows that for standard 60° cone penetration, the Poisson solution provides reasonable estimates of excess pore pressures (Figure 2.3b). However, for sharper tip angles (18°) the solution deteriorates in the vicinity of the cone face (Figure 2.3a). Section 2.6.2 shows that, for estimating excess pore pressure distribution in a horizontal plane far above the tip of a plate, the Poisson solution provides estimates of excess pore pressure which are an approximate 'average' of integration solutions in two orthogonal directions (Figure 2.9). For penetrometers with sharp tip geometries, the Poisson solution is modified to include only vertical equilibrium in the region ahead of the penetrometer tip (Figure 2.5). This Modified Poisson solution is used to predict the excess pore pressures in the vertical plane around plate penetrometers (Figure 2.7).

7.2 THE PIEZOCONE

Chapter 3 analyzes the measurements of tip resistance and excess pore pressures during steady piezocone penetration. A comprehensive series of Strain Path predictions for tests performed in BBC with $1 \leq OCR \leq 4$ were performed in order to assess the effects of: 1) tip shape (Figures 3.13 and 3.14); 2) stress history (Figure 3.15); and 3) soil model (Figures 3.16 and 3.17). The main results from these predictions can be summarized as follows:

1. Distributions of excess pore pressures around the 60° cone (standard piezocone) and the simple pile are very similar at all locations. The total vertical stress at the tip of a simple pile closely approximates the tip resistance of a 60° cone. These predictions a) justify the use of simple pile solutions to simulate penetration of the standard 60° cone and b) support the use of simple pile centerline solutions (Elghaib, 1989) for estimating cone tip resistance.
2. Tip shape (based on comparisons of the simple pile, 60° and 18° cones) has minimal ($\pm 10\%$) effect on predicted excess pore pressures on the shaft of the cone.
3. The predicted variation in excess pore pressure along the cone face (60° and 18°) is minor ($\pm 10\%$); hence, locating a pore pressure sensing element anywhere on the cone face should yield similar measurements. Sharp pore pressure gradients are predicted at

the cone base, indicating that pore pressure measurements will be sensitive to location of the pore pressure sensing element in this region.

4. Predicted tip and face excess pore pressures increase significantly with OCR (by a factor of 2.0 to 2.5 for an increase in OCR from 1 to 4), while the shaft and base excess pore pressures are less sensitive to changes in OCR. A practical implication of this set of predictions is that tip/face pore pressures measurements are more reliable indicators for profiling the stress history of a soil deposit.
5. Comparison of MCC and MIT-E3 predictions during simple penetration indicates that soil model has negligible influence on predictions of shaft excess pore pressures. This result is remarkable in view of the differences in the formulation of the two models. However, at the tip of the penetrometer, MIT-E3 predictions of excess pore pressures are significantly lower (up to 40%) than MCC predictions. This behavior can be explained in part by the strain softening behavior simulated by the MIT-E3 model.

A variety of predicted piezocone measurements and ratios of measurements were reviewed to assess their suitability for use as a basis for correlation to undrained shear strength, c_u , and stress history, OCR (Tables 3.5 and 3.6, respectively). The predictions indicated that the net tip resistance and the excess pore pressure at the cone tip are the most sensitive indicators of c_u and OCR.

Detailed analyses were performed to identify possible functional relationships between piezocone measurements and a) the reference undrained shear strength in triaxial compression, c_{uTC} (Table 3.5), and b) the preconsolidation pressure, σ'_p (Table 3.6). This study showed that undrained shear strength c_{uTC} can be correlated to either net tip resistance or tip excess pore pressure by a linear relationship.

The predictions were compared to field measurements in Boston Blue Clay at a well-documented site in South Boston (Figures 3.20 through 3.23). The comparisons showed that MIT-E3 predictions of net tip resistance are in excellent agreement with measurements. However, the predictions of excess pore pressures significantly underestimate the measurements by up to 30% at the base of the cone. Further comparisons with piezocone measurements in Boston Blue Clay at the Saugus site show significant differences from the South Boston site. These results can be attributed in part to differences in test procedures (tip correction factors, etc.) but may also indicate differences in soil properties at the two sites which require further validation.

Piezocone data at four additional well-documented sites reported in the literature were compiled and summarized in Figure 3.24. The data show significant scatter, indicating that piezocone measurements are influenced significantly by parameters other than OCR (e.g.; stress-strain behavior, sensitivity). Thus, universal correlations applicable to all soil types

are unlikely to be meaningful. Predictions and field measurements of various piezocone parameters indicate that the order of reliability for profiling OCR should be ranked as follows: 1) net normalized tip pore pressure $(u_1 - u_0)/\sigma'_{v0}$, 2) net normalized tip resistance $(q_t - \sigma_{v0})/\sigma'_{v0}$, 3) $B_q^2 = (u_2 - u_0)/(q_t - \sigma_{v0})$, 4) $B_q^1 = (u_1 - u_0)/(q_t - \sigma_{v0})$. Excess pore pressures at the base of the cone, $(u_1 - u_0)/\sigma'_{v0}$, and the factor $\beta = (u_2 - u_0)/(u_1 - u_0)$ are relatively insensitive to changes in OCR, and are therefore not suitable indicators of stress history.

Calibration chamber test measurements of the distribution of excess pore pressures during cone penetration in resedimented kaolin are in excellent agreement with predictions obtained using Boston Blue Clay parameters. These comparisons suggest that Strain Path analyses are capable of making realistic predictions of disturbance effects for deep penetration in other types of clays.

7.3 THE DILATOMETER

Chapter 4 presents a series of predictions of stresses and excess pore pressures which control the contact pressure $((p_0 - u_0)/\sigma'_{v0})$ measured by the Marchetti dilatometer. The analyses are based on the 'simple plate' geometry (Whittle et al., 1991). Figure 4.5 contrasts the effective stresses and excess pore pressures for cone and dilatometer penetration and shows that the disturbance effects corresponding to the two geometries are remarkably similar, when penetrometers of equal displaced volume are considered (i.e., normalizing by the equivalent radius, $R_{eq} = (4Bw/\pi)^{1/2}$). The lateral stresses acting on the dilatometer (Figure 4.6) vary slightly (20%) at different locations on the membrane.

Predictions of the 'contact pressure', p_0 , measured by a dilatometer were obtained for a range of stress histories ($1 \leq OCR \leq 4$) using the MCC and MIT-E3 soil models (Figure 4.7 and Table 4.1). A systematic study of predictions (Table 4.2) showed no simple correlation between dilatometer contact pressure, p_0 , and either the undrained shear strength, c_u , or the preconsolidation pressure, σ'_p . A similar conclusion applies to pore pressure measurements made at the center of the membrane. The dilatometer contact pressure is substantially less sensitive to variations in stress history than measurements of piezocone tip resistance or tip pore pressure (Table 3.4). Thus, the piezocone appears to be a superior device for profiling the stress history of a soil deposit.

Predicted dilatometer contact pressures, $(p_0 - u_0)/\sigma'_{v0}$, underestimate data in Boston Blue Clay at the South Boston site (Figure 4.10) for both the MIT-E3 and MCC soil models. This result is not unexpected, as experience with the piezocone shows that Strain Path analyses tend to underestimate the measured pore pressures (Figure 3.21). The South Boston measurements also show significant discrepancies with empirical correlations.

Dilatometer data from seven well-documented sites were compiled and summarized in Figure 4.12. These data indicate that a universal K_D -OCR correlation such as that proposed by Marchetti (1980) is not feasible and that even site-specific correlations are difficult to achieve.

Comparisons between dilatometer p_0 and cone measurements show: a) dilatometer contact pressure p_0 is comparable (usually slightly less than) to the total radial stress measured on the shaft of an axisymmetric penetrometer (Figure 4.14); b) p_0 is roughly comparable to the pore pressure measured at the base of the piezocone (Figure 4.15a); and c) p_0 is substantially less than (up to 60%) the pore pressure measured at the tip of the piezocone (Figure 4.15b).

7.4 PORE PRESSURE DISSIPATION AROUND PENETROMETERS

Measurements of pore pressure dissipation after piezocone penetration is interrupted are typically used to estimate consolidation and/or permeability properties of the soil. Chapter 5 presents solutions for non-linear, coupled, two-dimensional consolidation around a simple pile using the finite element code ABAQUS and generalized effective stress soil models (MCC and MIT-E3). Initial conditions are based on Strain Path estimates of installation excess pore pressures and effective stresses.

The analyses use an initial equilibration by applying external nodal forces which accommodate approximations in the Strain Path Method (Figures 5.11 through 5.13). The proposed equilibration method provides the most realistic solutions for predicted stress and excess pore pressures time histories at the tip of the cone and has little influence on the predicted behavior on the shaft of the penetrometer.

A comprehensive set of predictions were performed for dissipation tests in BBC using the MIT-E3 soil model for $1 \leq \text{OCR} \leq 4$ (Figures 5.17 through 5.20) and the MCC soil model for $\text{OCR}=1$ (Figure 5.14 and 5.15). The numerical accuracy of these solutions is verified by comparison to simpler one-dimensional solutions presented in Figure 5.17. The analyses assess the effect of: 1) non-linear coupling (Figure 5.16), 2) filter location (Figure 5.22) and 3) stress history (Figure 5.23).

The analyses show that non-linear coupling has little influence on the shape of dissipation curves for filters located far above the cone tip. However, coupling does have a noticeable effect on the characteristics of the pore pressure dissipation at the tip of the cone.

The effects of stress history on the pore pressure dissipation curve can be approximately normalized a dimensionless time factor, $T = \sigma'_{pkt}/\gamma_w R^2$. For filters located on the shaft, predictions indicate that a single dissipation curve can characterize dissipation

behavior for all stress histories in the range $1 \leq \text{OCR} \leq 4$, using this time factor. For a filter located at the tip, predictions indicate that for the range $1 \leq \text{OCR} \leq 4$, variations in OCR can affect the estimate of permeability by a factor of 5-6. Comparisons of dissipation curves at different filter locations confirmed the results of previous studies (Levadoux and Baligh, 1986) which indicate that dissipation at the tip occurs up to 10 times more rapidly than that on the shaft.

Field measurements of pore pressure dissipation in BBC (at the Saugus site) are in excellent agreement with predictions for filters located on the shaft (Figure 5.24b). Tip measurements are also in good agreement with predictions (Figure 5.25b), although the permeability computed from these data tend to overestimate the laboratory measurements (by up to a factor of 4). The predicted shaft and tip dissipation curves both give realistic predictions of the shape of the dissipation curve (i.e., evaluation of the permeability at a number of dissipation levels in the range $0.6 \geq \bar{u} \geq 0.4$ give consistent estimates of permeability).

Excellent agreement between predicted dissipation curves and measurements in resedimented kaolin (Figures 5.27 and 5.28) indicate that the proposed analyses can provide reasonable estimates of the permeability behavior for other types of clay. Overall, these comparisons indicate that the predicted dissipation behavior can provide a reliable basis for estimating permeability from measurements on either the tip or shaft of the piezocone. However, there is greater uncertainty associated with tip measurements. The pore pressure dissipation behavior is not strongly influenced by stress history or by soil type. Thus, the predictions for dissipation in BBC can provide a framework for estimating permeability in other types of soils.

7.5 PRESSUREMETERS

Pressuremeter tests were analyzed in order to assess how the computed undrained shear strength is affected by: 1) installation disturbance; 2) consolidation prior to membrane expansion; 3) stress history; 4) membrane expansion versus contraction; and 5) membrane length. Disturbance effects for full-displacement and push-in pressuremeters were simulated using simple pile and unplugged open-ended tube solutions, respectively (Figure 6.14). An approximate solution for disturbances due to self-boring was developed in this research (Section 6.4.4). This solution assumes that "ideal self-boring" represents a volume balance between soil displaced by the cutting shoe and that removed by the cutter itself (Figure 6.28). Predictions of the pressuremeter test were based on the MIT-E3 soil model, which simulates realistically shearing in an ideal cylindrical cavity expansion mode

(Figure 6.13). Strength estimates during membrane expansion were based on the formulation of Baguelin, Palmer, and Ladanyi (PBL, 1972), while estimates from the contraction curve were interpreted using the method proposed by Houlsby and Withers (1988).

The predictions indicate that installation disturbance caused by displacement pressuremeters (Figures 6.18, 6.22 and 6.23): a) generate lift-off pressures which exceed the in situ horizontal stress and b) causes the interpreted strength estimates from the expansion curve to underestimate the true c_{uPM} . Disturbance introduces significant non-linearity in the predicted expansion curve over the full range of expansion strains. Thus, the interpreted undrained shear strength is highly dependent on the strain level. The full-displacement pressuremeter gives the lowest interpreted shear strengths, while predictions for push-in pressuremeters show that the volume of displaced soil is directly related to the shear strength interpreted from the expansion curves. Similar trends are obtained for soils with $OCR \leq 4$. Undrained shear strengths interpreted from contraction curves are generally insensitive to the installation disturbance effects, although they generally tend to be slightly (10%) lower than the true soil strength. When full dissipation of installation excess pore pressures is permitted prior to membrane expansion (Figures 6.26 and 6.27), there is generally no improvement in the reliability of the interpreted undrained shear strengths.

The most crucial aspect of self-boring penetration which was considered in this work was the extraction of soil during the penetration process. Analyses were performed for a number of rates of soil extraction, ranging from no extraction (the push-in pressuremeter) to a soil extraction rate which exactly compensates for the pressuremeter volume (ideal self-boring). The predictions (Figures 6.30, 6.32, and 6.33) indicate that increasing the soil extraction rate has the following effects on the pressuremeter expansion curves: 1) the lift-off pressure decreases (at sufficiently high rates of soil extraction it can fall below the in situ horizontal stress); 2) the maximum slope (i.e., the apparent undrained strength) increases and can exceed the actual in situ undrained shear strength by up to 35%. These predictions imply that, depending on the rate of soil extraction during penetration, the self-boring pressuremeter tests can: 1) underestimate the in situ strength if the soil extraction rate is low and penetration approaches that of a displacement pressuremeter; or 2) overestimate the in situ strength if the soil extraction rate is great enough to cause the lift-off pressure to fall below the in situ horizontal stress. Predictions of contraction curves obtained from self-boring pressuremeter tests indicate that strength estimates are insensitive to soil extraction rate. This result also suggests that strength estimates can be more reliably interpreted from contraction measurements.

Field data from the South Boston site show that pressuremeter strengths estimated from contraction curves are insensitive to installation disturbance. However, the strengths derived were significantly higher than reference strengths measured in laboratory tests. Further studies are required to evaluate contraction measurements at other sites.

7.6 RECOMMENDATIONS

Further research on in-situ tests in cohesive soils should be pursued in three general areas: 1) development of the predictive framework; 2) applications of the predictive framework to investigate additional issues not covered in this work; and 3) further evaluation of predictions from field or laboratory measurements.

The predictive framework should be refined in the following areas:

1. The soil models used in this research have two significant limitations: a) their validity is restricted to lightly overconsolidated soils ($OCR \leq 8$); and b) they describe rate independent behavior. Interpretation of in-situ measurements in highly overconsolidated clays requires a soil model which can realistically simulate soil behavior at high OCR, while strain rate effects are a possible cause for the discrepancies between field measurements and Strain Path predictions of excess pore pressures on the penetrometer shaft. Strain Path analyses using a rate dependent soil model are an important first step in resolving this issue.
2. Equilibrium imbalance due to approximation in the Strain Path Method causes uncertainties in installation predictions which affect the analyses of subsequent activities (consolidation, undrained shearing). Correction of the Strain Path solutions to provide solutions which satisfy equilibrium would enhance the reliability of installation predictions and simplify the analysis of subsequent activities.
3. For the simplified analysis of self-boring used in Chapter 6, it is not possible to simulate overcutting of the soil. Further studies should be conducted to evaluate the effects of overcutting on strengths interpreted from pressuremeter tests.

Applications of the Strain Path Method to areas which were not fully covered in this research include:

1. The pressuremeter predictions in Chapter 6 were largely based on expansion and contraction of an infinitely long membrane. A comprehensive analysis of membrane length effects is needed to complete the study of pressuremeter tests. This work should be performed using higher order finite elements (e.g., a 15-node triangular element), which can alleviate the effects of mesh locking in incompressible analysis.

2. The influence of installation disturbance on the interpretation of field vane strength estimates can be investigated using the Strain Path and finite analyses (Whittle et al., 1991). A comprehensive study of the field vane should include predictions to assess the effects of : 1) no dissipation of installation excess pore pressures; 2) full dissipation of excess pore pressures; 3) stress history; and 4) soil model.

Evaluation of predictions is particularly important in the following areas:

1. Consolidation measurements around plates of various geometries, including time histories of excess pore pressures and lateral stresses, are required to evaluate the capability of earth pressures cells to measure in-situ lateral stress, σ_{h0} .
2. To evaluate fully the pressuremeter predictions presented in Chapter 6, the following types of pressuremeter measurements at well-documented sites are necessary: a) measurements for all methods of installation (full-displacement, push-in, and self-boring); b) complete expansion and contraction curves; c) excess pore pressure measurements during membrane expansion and contraction; d) data on excess pore pressure dissipation prior to membrane expansion. A series of tests for which no dissipation and full dissipation of installation excess pore pressures is also desirable.

REFERENCES

- Aas, G., Lacasse, S., Lunne, T. & Hoeg, K. (1986) "Use of in-situ tests for foundation design on clay," Proc. ASCE Specialty Conf. on Use of In Situ Tests in Geotechnical Engrg. (In-Situ '86), Vicksburg, VA., pp 1-30.
- Al-Tabaa, A. & Wood, D.M. (1987) "Some measurements of the permeability of kaolin," Géotechnique, Vol. 37, No. 4, pp. 499-503.
- Arnold, M. (1981) "An empirical evaluation of pressuremeter test data," Canadian Geotechnical Journal, Vol. 18, No. 3, pp. 455-459.
- Arthur, J.R.F., Bekenstein, S., Germaine, J.T., & Ladd, C.C. (1981) "Stress path tests with controlled rotation of the principal stress directions," Laboratory Shear Strength of Soil, ASTM STP 740, pp. 516-540.
- ASTM (1972) "Standard Test Method for Field Vane Shear Test in Cohesive Soil" ASTM Standard D 2573-72
- Atkinson, J.H. & Bransby, P.L. (1976) The Mechanics of Soils: An Introduction to Critical State Soil Mechanics, McGraw Hill, London, 375p.
- Azzouz, A.S., Baligh, M.M. & Ladd, C.C. (1982), "Cone penetration and engineering properties of soft Orinoco clay," MIT Sea Grant Report, MITSG-82-11, 53p.
- Azzouz, A.S. & Baligh, M.M. (1984) "Behavior of friction piles in plastic Empire clays," Research Report R84-14, Dept. of Civil Engrg., MIT, Cambridge, MA., 619p.
- Azzouz, A.S. & Lutz, D.G. (1986) "Shaft behavior of a model pile in plastic Empire clays," ASCE, Journal of Geotechnical Engrg., Vol. 112, No. GT4, pp. 389-406.
- Baguelin, F., Jézéquel, J.F., Mee, E.L. & Mehauté, A.L. (1972) "Expansion of cylindrical probes in cohesive soils," ASCE Journal of the Soil Mech. and Fdn. Engrg. Division, Vol. 98, SM11, pp 1129-1142.
- Baguelin, F., Jézéquel, J.F., & Shields, D.H. (1978) The Pressuremeter and Foundation Engineering, Trans Tech Publ., 617p.
- Baguelin, F.J. & Jézéquel, J.F. (1983) "The LPC pressiopenetrometer," Proc. ASCE Conf. on Geotechnical Practice in Offshore Engrg., Austin, TX, pp. 203-219.
- Baligh, M.M. (1975), "Cavity expansion in sands with curved envelopes," ASCE, Journal of Geotechnical Engrg., Vol. 102, GT11, pp. 1131-1146.
- Baligh, M.M. (1984), "The Strain Path Method in Geotechnical Engrg.," Research Report No. R84-01, Order No. 761, MIT, Department of Civil Engrg., Cambridge, MA.
- Baligh, M.M. (1985a), "Strain Path Method," ASCE, Journal of Geotechnical Engrg., Vol. 111, No. GT9, pp. 1108-1136.
- Baligh, M.M. (1985b), "Fundamentals of deep penetration, I: Shear stresses," MIT Report

- R85-9, Order No. 776, 64p.
- Baligh, M.M. (1985c), "Fundamentals of deep penetration, II: Pore pressures," MIT Report R85-10, Order No. 777, 78p.
- Baligh, M.M. (1985d) "Lecture 8: Interpretation of piezocone measurements after penetration," MIT Special Summer Course 1.60S: Recent Developments in Measurement and Modelling Clay Behavior for Foundation Design, Cambridge, MA.
- Baligh, M.M. (1986a) "Undrained deep penetration: 1. Shear stresses," Géotechnique, Vol. 36, No. 4, pp. 471-485.
- Baligh, M.M. (1986b) "Undrained deep penetration: II. Pore pressures," Géotechnique, Vol. 36, No. 4, pp. 487-501.
- Baligh, M.M. & Levadoux, J-N. (1980), "Pore pressure dissipation after cone penetration," MIT Report No. 80-11, Order No. 662, Dept. of Civil Engrg., MIT, Cambridge, MA.
- Baligh, M.M., Vivatrat, V. & Ladd, C.C. (1980) "Cone penetration in soil profiling," ASCE Journal of Geotechnical Engrg., Vol. 106, GT4, pp. 447-461.
- Baligh, M.M., Azzouz, A.S., Wissa, A.E.Z., Martin, R.T. & Morrison, M.J. (1981) "The Piezocone Penetrometer," Proc. Symp. on Cone Penetration Testing and Experience, ASCE Natl. Convention, St. Louis, MO., pp. 247-263.
- Baligh, M.M. & Levadoux, J-N (1986), "Consolidation after undrained piezocone penetration II: Interpretation," ASCE Journal of Geotechnical Engrg., Vol. 112, No. GT7, pp. 727-745.
- Bathe, K.J. (1982), Finite Element Procedures in Engineering Analysis, Prentice-Hall, N.J.
- Bathe, K.J. (1987) A Finite Element Program for Automatic Dynamic Incremental Nonlinear Analysis of Structures, Report ARD 87-2, ADINA R&D, Inc., Watertown, MA.
- Battaglio, M., Jamiolkowski, M., Lancelotta, R. & Maniscalco, R. (1981) "Piezometer probe test in cohesive deposits," Proc., Cone Penetration Testing and Experience, ASCE National Convention, St. Louis, MO, pp.264-302.
- Battaglio, M. & Maniscaldo, R. (1983) "Il piezocono: Esecuzione ed interpretazione," Report No. 607, Politecnico di Torino.
- Battaglio, M., Bruzzi, D., Jamiolkowski, M. & Lancellotta, R. (1986) "Interpretation of CPT's and CPTU's, 1st Part: undrained penetration of saturated clays," Proc. 4th Intl. Geotechnical Seminar on Field Instrumentation and in Situ Measurements, Singapore.

- Bennett, R.H., Li, H., Valent, P.J., Lipkin, J., & Esrig, M.I. (1985) "In-situ undrained shear strengths and permeabilities derived from piezometer measurements," Strength Testing of Marine Sediments: Laboratory and In-Situ Measurements, ASTM STP 883, R.C. Chaney and K.R. Demars, Ed., American Society for Testing and Materials, Philadelphia, pp. 83-100.
- Benoît, J. (1991) Self-boring pressuremeter testing, Central Artery (I-93)/Third Harbor Tunnel (I-90) Project, Haley & Aldrich Special Test Program, South Boston, Massachusetts, Department of Civil Engrg., College of Engrg. & Physical Sciences, University of New Hampshire, 122p.
- Benoît, J. & Clough, G.W. (1986) "Self-boring pressuremeter tests in soft clay," ASCE Journal of Geotechnical Engrg., Vol. 112, GT1, pp 60-78.
- Berg, A.P.v.d. (1982) "Latest development in static cone penetrometers and other soil testing equipment," Proc., 2nd European Symp. on Penetration Testing, Amsterdam, Vol. 2, pp. 447-455.
- Biot, M.A. (1935) "Le Probleme de la Consolidation des Matieres Argileuses sous une Charge," Annales de la Societe Scientifique de Bruxelles, Series B, 55, pp. 110-113.
- Bishop, R.F., Hill, R., Mott, N.F. (1945) "Theory of indentation and hardness tests," Proc. of the Physical Society, London, Vol. 57, No. 321, Part 3, May, pp. 147-159.
- Bjerrum, L. (1972) "Embankments on soft ground," Proc. ASCE Spec. Conf. on Performance of Earth and Earth Supported Structures, Lafayette, Ind., Vol. 2, pp. 1-54.
- Boghrat, A. (1982) "The design and construction of a piezoblade and evaluation of the Marchetti dilatometer in some Florida soils," PhD Thesis, Univ. of Florida, Gainesville, FL.
- Bonaparte, R., & Mitchell, J. (1979) The Properties of San Francisco Bay Mud at Hamilton Air Force Base, California, Dept. of Civil Engrg., Univ. of California, Berkeley.
- Bond, A.J. (1989) Behavior of Displacement Piles in Overconsolidated Clay, PhD Thesis, Imperial College, London, 725p.
- Borja, R.I. (1991) "Non-linear consolidation: linear multistep methods and iterative algorithms," Proc. of the 7th Int. Conf. on Computer Methods and Advances in Geomechanics, Cairns, Vol. 2, pp. 1111-1116.
- Briaud, J.L. & Shields, D. (1979) "A special pressuremeter and pressuremeter test for pavement evaluation and design," ASTM Geotechnical Testing Journal, Vol. 2,

- No. 3, pp. 143-151.
- Bromwell, L.G. & Lambe, T.W. (1968) "A comparison of laboratory and field values of c_v for Boston Blue Clay," Professional Paper P68-3, Soils Publication No. 205, Dept. of Civil Engrg., MIT, Cambridge, MA, Jan.
- Brooker, E.W. & Ireland, H.O. (1965) "Earth pressures at rest related to stress history," Canadian Geotechnical Journal, Vol. 2, No. 1, pp. 1-15.
- Burland, J.B. (1990) "On the compressibility and shear strength of natural clays," Géotechnique, Vol. 40, No.3, pp 329-378.
- Butterfield, R. & Bannerjee, P.K., (1970), "The effect of pore water pressure on the ultimate bearing capacity of driven piles," Proc., 2nd S.E. Asia Conf. on Soil Engrg., Singapore, pp 385-394.
- Cadling, L. & Odenstad, S. (1948) "The Vane Borer," Proc. Royal Swedish Geotechnical Institute, No. 2.
- Campanella, R.G., Gillespie, D. & Robertson, P.K. (1982), "Pore pressure during cone penetration," Proc., 2nd European Symp. on Penetration Testing, Amsterdam, Vol. 2, pp. 507-512.
- Campanella, R.G. & Robertson, P.K. (1988) "Current status of the piezocone test", Proc. 1st Int. Symp. on Penetration Testing, Orlando, FL., Vol. 1, pp. 93-117.
- Campanella, R.G., Howie, J.A., Hers, I., Sully, J.P. & Robertson, P.K. (1990) "Evaluation of cone pressuremeter tests in soft cohesive soils," Pressuremeters, Institution of Civil Engineers, London, pp 125-135.
- Carlson, L. (1948) "Determination in situ of the shear strength of undisturbed clay by means of a rotating auger," Proc. 2nd Intl. Conf. on Soil Mechs. & Fdn. Engrg., Vol. 1, pp 265-270.
- Chandler, R.J. (1988) "The in-situ measurement of the undrained shear strength of clays using the field vane", Vane Shear Testing in Soils: Field and Lab. Studies, ASTM STP 1014 (A.F. Richards ed.), pp. 13-44.
- Chin, C.T & Whittle, A.J. (1984) "The use of ADINAT to solve a Poisson equation: The solution of the octahedral stress field caused by penetration of a 2-D axisymmetric indenter," Unpublished Project, MIT, Cambridge, MA.
- Chin, C.T. (1986), "Open-ended pile penetration in saturated clays," PhD Thesis, MIT, Cambridge, MA, 296p.
- Clark, B.G., Carter, J.P., & Wroth, C.P. (1979) "In-situ determination of consolidation characteristics of clays," Proc., 7th European Conf. on Soil Mech. and Fdn. Engrg., Brighton, England, Vol. 2, pp. 207-213.
- Cleveland, W.S. (1979), "Robust locally weighted regresion and smoothing scatterplots",

- Journal of the American Statistical Association, Vol. 74, No. 368, Theory and Methods Section, pp 829-836.
- Dafalias, Y.F. & Hermann, L.R. (1980) "A generalized bounding surface constitutive model for clays," Symposium on Limit Equilibrium and Generalized Stress-Strain in Geotechnical Engrg., FL, pp.78-95.
- DeBorst, R. & Vermeer, P.A. (1982) "Finite element analysis of static penetration test," Proc. 2nd European Symp. on Penetration Testing, Amsterdam.
- DeGroot, D.J. (1989) "The MultiDirectional Simple Shear Apparatus with application to the design of offshore Arctic structures," PhD Thesis, MIT, Cambridge, MA.
- Denby, G.M. (1978) Self-Boring Pressuremeter Study of San Francisco Bay Mud, Ph.D. Thesis, Stanford University, Department of Civil Engrg., Technical Report, CE-232, 270p.
- Denby, G.M. & Clough, G.W. (1980) "Self-boring pressuremeter tests in clay," Journal of the Geotechnical Engrg. Division, ASCE, Vol. 106, no. GT12, pp 1369-1387.
- Denby, G.M. & Hughes, J.M.O. (1985) "Horizontal stress interpretation of pressuremeter tests," Proc. ASCE Conf. on Updating Subsurface Sampling of Soils and their In-Situ Testing, Santa Barbara, California, pp. 227-244.
- de Ruiter J. (1971) "Electric penetrometer for site investigation", ASCE Journal of the Soil Mech. and Fdn. Engrg. Division, Vol. 97, SM2, pp 457-472.
- de Ruiter J. (1981) "Current Penetrometer Practice", Proc. Symp. on Cone Penetration Testing and Experience, ASCE Natl. Convention, St. Louis, MO., pp. 1-48.
- de Ruiter J. (1982) "The static cone penetration test State-of-the-Art Report", Proc. 2nd European Symp. on Penetration, Vol. 2, Amsterdam, pp 389-405.
- Donald, I.B., Jordan, D.O., Parker, R.J. & Toh, C.T. (1977) "The Vane Test- A critical appraisal," Proc. 9th Intl. Conf. on Soil Mech. & Fdn. Engrg., Tokyo, Vol. 1, pp 81-88.
- Draپر. N., & Smith H. (1981), Applied Regression Analysis, John Wiley & Sons, New York.
- Durgunoglu, H.T. & Mitchell, J.K. (1975a) "Static penetration of soils: I-Analysis," Proc. ASCE Specialty Conf. In-Situ Measurement of Soil Properties, Raleigh, NC.
- Durgunoglu, H.T. & Mitchell, J.K. (1975b) "Static penetration of soils: II-Evaluation of theory and implications for practice," Proc. ASCE Specialty Conf. In-Situ Measurement of Soil Properties, Raleigh, NC.
- Elghaib, M.K. (1989), "Prediction and interpretation of piezocone tests in clays, sands and silts," PhD Thesis, MIT, Cambridge, MA, 404p.
- Foott, R., Kousoftsas, D.C., & Handfelt, L.D. (1987) "Test fill at Chek Lap Kok, Hong

- Kong," ASCE Journal of Geotechnical Engrg., Vol. 113, No. 2, pp. 106-126.
- Fyffe, S., Reid, W.M. & Summers, J.B. (1986) "The push-in pressuremeter: 5 years offshore experience," The Pressuremeter and its Marine Applications, 2nd Int. Symp.:ASTM STP 950, J.-L. Briaud and J.M.E. Audibert Eds., ASTM.
- Gens, A., & Potts, D.M. (1987) "Critical state models in computational geomechanics," Engrg. Comp., Vol. 5, Sept., pp. 178-197.
- Germaine, J.T. (1980) Evaluation of Self-Boring Pressuremeter Tests in Soft Cohesive Soils, SM Thesis, MIT, Cambridge, MA.
- Germaine, J.T. (1982) Development of the Directional Shear Cell for Measuring Cross-Anisotropic Clay Properties, Sc.D. Thesis, Dept. of Civil Engrg. Cambridge, MA, 530p.
- Ghionna, V., Jamiolkowski, M., Lancellota, R., Tordella, M.L., and Ladd, C.C. (1981), Performance of Self-Boring Pressuremeter Tests in Cohesive Deposits (Tech. Rep. DOT-FH-11-9264), U.S. Department of Transportation, Federal Highway Administration.
- Ghionna, V.N., Jamiolkowski, M., & Lancellotta, R. (1982) "Characteristics of saturated clays as obtained from SBP tests," Symp. on the Pressuremeter and its Marine Applications, Institut Français du Pétrol Laboratoires des Ponts et Chaussées, Paris pp. 165-185.
- Gibson, R.E. & Anderson, W.F. (1961) "In situ measurement of soil properties with the pressuremeter," Civil Engrg. Public Works Review, Vol. 56, No. 658, pp. 615-618.
- Gibson, R.E., Schiffman, R.L., Whitman, R.V. (1989) "On two definitions of excess pore pressure," Géotechnique, Vol. 39, No. 1, pp. 169-171.
- HKS (1989) "ABAQUS Version 4.8 User's Manual," Hibbit, Karlson, and Sorenson, Inc., Providence, R.I.
- Hashash, Y.M.A. (1992) "Analysis of Deep Excavations in Clay", Ph..D. Thesis, Dept. of Civil Engrg., MIT, Cambridge, MA, 337p.
- Hashiguchi, K, (1985) "Constitutive laws for soils: II Macrometric approaches-static intrinsically time-dependent," State-of-the-Art Report, Proc, XIth Int. Conf. Soil Mech. and Fnd. Engrg., SanFrancisco, CA, pp.25-65.
- Henkel, D.J. (1960) "The relationships between the effective stresses and water content in saturated clays," Géotechnique, Vol. 10, pp. 41-54.
- Henderson, G., Smith, P.D.K. & St.John, H.D. (1980) "The development of the push-in pressuremeter for offshore site investigations," Proc. of the Society for Underwater Technology Conf., Offshore Site Investigation, pp. 159-167.

- Hess, J.L. & Smith, A.M.O. (1962), "Calculation of non-lifting potential flow about arbitrary three dimensional bodies," Douglas Aircraft Company Report No. ES-40622.
- Hess, J.L. & Smith, A.M.O. (1964), "Calculation of non-lifting potential flow about arbitrary three dimensional bodies, Journal of Ship Research, Vol. 8, No. 2, pp. 22-44.
- Hight, D.W., Gens, A., & Symes, M.J. (1983) "The development of a new hollow cylinder apparatus for investigating the effects of principle stress rotation in soils," Géotechnique, Vol. 33 No. 4, pp. 385-396.
- Houlsby, G.T. & Withers, G.T. (1988) "Analysis of the cone pressuremeter test in clay", Géotechnique, Vol. 38, No.4, pp. 575-587.
- Huang, A.B. & Haeefe, K.C. (1988) "A push-in pressuremeter/ sampler," Proc. 1st Int. Symp. on Penetration Testing, Orlando, FL, Vol. 1, pp. 533-538.
- Huang, A-B. (1989), "Strain path analyses for arbitrary 3-D penetrometers", Intl J. for Anal. & Num. Meth. in Geomech., Vol. 13, No. 5, pp. 551-564
- Huang, A.B. & Haeefe, K.C. (1990) "Effects of penetration on pressuremeter tests in clays," Pressuremeters, Institution of Civil Engineers, pp. 299-308.
- Hueckel, T. & Nova, R. (1979) "Some hysteresis effects of the behavior of geologic media," Int. Journal of Solids and Structures, Vol. 15, pp. 625-642.
- Hughes, J.M.O, Erwin, M.C., Holden, J.C. & Harvey, R.J. (1980) "Determination of the engineering properties of the Coode Island silts using a self-boring pressuremeter," Proc. 3rd Australian-New Zealand Conf. on Soil Mech. and Fdn. Engrg., Wellington, Vol.1, pp.249-254.
- Jamiolkowski, M., Lancellotta, R., Tordella, L., & Battaglio, M. (1982), "Undrained Strength from CPT," Proc. 2nd European Symp. on Penetration Testing, Vol. 2, Amsterdam, pp. 599-606.
- Jamiolkowski, M., Lancellotta, R. & Wolski, W. (1983) "Precompression and speeding up consolidation, state of the art report," 8th European Conf. on Soil Mech. and Fdn. Engrg., Helsinki, pp 1201-1226.
- Jamiolkowski, M., Ladd, C.C., Germaine, J.T. & Lancellotta, R. (1985) "New developments in field and laboratory testing of soils, Theme Lecture 2," Proc. 11th Intl. Conf. on Soil Mechs. & Fdn. Engrg., San Fransisco, Vol. 1, pp. 57-153.
- Jamiolkowski, M., Battaglio, M. & Bruzzi, D. (1989) "Discussion, Session 3," Proc. Conf. on Penetration Testing in the UK, Birmingham, pp. 180-183.
- Janbu, N. & Senneset, K. (1974) " Effective stress interpretation of in-situ static penetration tests," Proc. 1st European Symp. on Penetration Testing, Stockholm,

- Vol. 2.2, pp. 181-193.
- Jardine, R.J. & Bond, A.J. (1989) "Behaviour of displacement piles in heavily overconsolidated clay," Proc. 12th Intl. Conf. on Soil Mechs. & Fdn. Engrg., Rio de Janeiro, Vol. 2, pp. 1147-1152.
- Jones, G.A. & Rust, E. (1982) "Piezometer penetration testing," Proc. ESOPT-II, Amsterdam, Vol. 2, pp. 607-613.
- Jones, G. A., Van Zyl, D. & Rust, E. (1981) "Mine tailings characterization by piezometer cone", Proc. Symposium on Cone Penetration Testing and Experience, ASCE Natl. Convention, St. Louis, MO., pp. 303-324.
- Kabir, M.G. & Luttengger, A.J. (1990) "In-situ estimation of the coefficient of consolidation in clays," Canadian Geotechnical Journal, Vol. 27, No. 1, pp 58-67.
- Karlsrud, K. & Haugen, T. (1984) "Cyclic loading of piles and pile anchors - Phase II final report," NGI Report 40018-11, July 31.
- Kavvasdas, M. (1982) Non-Linear Consolidation around Driven Piles in Clays, Ph.D. Thesis, Dept. of Civil Engrg., MIT, Cambridge, MA, 666p.
- Kjekstad, O., Lunne, T., and Clausen, C.J.F. (1978) "Comparison between in-situ cone resistance and laboratory strength for overconsolidated North Sea Clays", Marine Geotechnology, Vol. 3, No. 1, pp. 23-36.
- Konrad, J.M. & Law, K.T. (1987) "Preconsolidation pressure from piezocone tests in marine clays," Géotechnique, Vol. 37, No. 2, pp. 177-190.
- Lacasse, S. (1979) "Effect of load duration on undrained behaviour of clay and sand," NGI Internal Report, No. 40007-2.
- Lacasse, S., Jamiolkowski, M., Lancellotta, R., Lunne, T. (1981) "In situ characteristics of two Norwegian clays," Proc. 10th Intl. Conf. on Soil Mechs. & Fdn. Engrg., Stockholm, pp. 507-511.
- Lacasse, S. & Lunne, T. (1982) "Dilatometer tests in two soft marine clays," Proc. ASCE Conf. on Updating Subsurface Sampling of Soils and Rocks and their In-situ Testing, Santa Barbara, CA., 8p. (also NGI Report No. 146).
- Lacasse, S. & Lunne, T. (1982) "In-situ horizontal stress from pressuremeter tests," Symposium on the Pressuremeter and its Marine Applications, Paris, pp. 187-208.
- Lacasse, S., Berre, T., & Lefebvre, G. (1985) "Block sampling of sensitive clays," Proc. 11th Intl. Conf. on Soil Mechs. & Fdn. Engrg., San Francisco, Vol. 2, pp.887-892.
- Lacasse, S. & Lunne, T. (1988) "Calibration of dilatometer correlations," Proc. 1st Int. Symp. on Penetration Testing, Orlando, FL, Vol. 1, pp. 539-548.
- Lacasse, S., D'Orazio, T.B., Bandis, C. (1990) "Interpretation of self-boring and push-in

- pressuremeter tests," Pressuremeters, Institution of Civil Engineers, London, pp. 273-285.
- Ladanyi, B. & Eden, W.J. (1969) "Use of the deep penetration test in sensitive clays," Proc. 7th Intl. Conf. on Soil Mechs. & Fdn. Engrg., Mexico City, Vol. 1, pp. 225-230.
- Ladanyi, B. (1972) "In-situ determination of undrained stress-strain behavior of sensitive clays with the pressuremeter," Canadian Geotechnical Journal, Vol. 9, No. 3, pp. 313-319.
- Ladd, C.C. (1976) "Use of precompression and vertical sand drains for stabilization of foundation soils," Research Report R76-4, Order 541, Dept. of Civil Engrg., MIT, Cambridge, MA, June.
- Ladd, C.C. (1990) "Results of CA/T Special Test Program at South Boston," Presentation to Haley & Aldrich and Bechtel / Parsons Brincherhoff, Oct. (Unpublished)
- Ladd (1991) Personal communication.
- Ladd, C.C. & Foott, R. (1974) "New design procedure for stability of soft clays," ASCE Journal of Geotechnical Engrg., Vol. 100, No. GT7, pp. 763-786.
- Ladd, C.C. & Foott, R. (1977) "Foundation design of embankments constructed on varved clays," FHWA Report No. TS-77-214, US Dept of Transportation, 234p.
- Ladd, C.C., Foott, R., Ishihara, K., Schlosser, F. & Poulos, H.G. (1977) "Stress-deformation and strength characteristics, State-of-the-Art Paper," Proc. 9th Intl. Conf. on Soil. Mechs. & Fdn. Engrg., Tokyo, Vol. 2, pp. 421-494.
- Ladd, C.C., Germaine, J.T., Baligh, M.M., Lacasse, S. (1980) Evaluation of Self-Boring Pressuremeter Tests in Boston Blue Clay, Report No. FHWA/RD-80/052, Washington, Sept., 223p.
- LaRochelle, P., Roy, M. & Tavenas, F. (1973) "Field measurements of cohesion in Champlain clays," Proc. 8th Intl. Conf. on Soil Mechs. & Fdn. Engrg., Moscow, Vol. 1, pp. 229-236.
- Law, K.T., & Eden W.J. (1985) "Effects of soil disturbance in pressuremeter tests," Proc. ASCE Conf. Updating Subsurface Sampling of Soils and their In-Situ Testing, Santa Barbara, California, 1982, pp. 291-303.
- Levadoux, J-N. (1980) "Pore pressures in clays due to cone penetration," PhD Thesis, MIT, Cambridge, MA., 752p.
- Levadoux, J-N. & Baligh, M.M. (1980), "Pore pressures in clays due to cone penetration," Research Report R80-15, Order No. 666, Dept. of Civil Engrg., MIT, Cambridge, MA.
- Levadoux, J-N, Baligh, M.M. (1986a), "Consolidation after undrained piezocone

- penetration. I: Prediction", ASCE Journal of Geotechnical Engrg., Vol. 112, No. GT7, pp 707-726.
- Levadoux, J.-N. & Baligh, M.M. (1986b) "Consolidation after undrained piezocone penetration. II. Interpretation," ASCE Journal of Geotechnical Engrg., Vol. 112, No. 7, July, pp. 727-745.
- Lee, J.T. (1987) "A potential based panel method for the analysis of marine propellers in steady flow," PhD Thesis, MIT, Cambridge, MA.
- Lunne, T., Myrvoll, F., & Kjekstad, O. (1981) "Observed settlements of five North Sea gravity platforms, NGI Technical Report No. 52410/s-6.
- Lunne, T., Christoffersen, H.P., & Tjelta, T.I. (1985) "Engineering use of the piezocone test in North Sea Clays," Proc. 11th Intl. Conf. on Soil Mechs. & Fdn. Engrg., San Fransisco, Vol. 2, pp. 907-912.
- Lunne, T., Lacasse, S., Rad, N.S. & Decourt, L. (1989) "SPT, CPT, Pressuremeter testing and recent developments on in-situ testing: General Report Session 2," Proc. 12th Intl. Conf. on Soil Mechs. & Fdn. Engrg., Rio de Janeiro, 65p.
- Lutenegger, A.J. (1988) "Current status of the Marchetti dilatometer: Special Lecture," Proc. 1st Int. Symp. on Penetration Testing, Orlando, FL, Vol. 1, pp. 137-155.
- Lutenegger, A.J. & Kabir, M.G. (1988) "Dilatometer C-reading to help determine stratigraphy," Proc. 1st Int. Symp. on Penetration Testing, Orlando, FL., Vol. 1, pp. 549-554.
- Lutenegger, A.J. & Blanchard, K.C. (1990) "A comparison between full displacement pressuremeter tests and dilatometer tests in clay," Proc. 3rd Intl. Conf. on Pressuremeter Testing, Oxford, pp. 309-320.
- Lutenegger, A.J., Timian, D.A. (1986) "In-situ tests with K_0 -Stepped Blade," Proc. ASCE Conf. on Use of In-situ Tests in Geotechnical Engrg. (In-situ, '86), Blacksburg, VA, pp 730-751.
- Marchetti, S. (1980) "In-situ tests by flat dilatometer," ASCE Journal of Geotechnical Engrg., Vol. 106, No. GT3, pp. 299-321.
- Marchetti, S., Campanella, R.G., Robertson, P.K. & Taddei, B. (1986) "The DMT- σ_{hc} method for piles driven in clay," Proc. ASCE Conf. on Use of In Situ Tests in Geotechnical Engrg. In Situ '86, Blacksburg, VA, pp765-779.
- Marchetti, S., Totani, G., Campanella, R.G. & Robertson, P.K. (1986) "The DMT σ_{HC} method for piles driven in clay," Proc., ASCE Conf. on Use of In-Situ Tests in Geotechnical Engrg. In-Situ '86, Blacksburg, VA., pp. 765-779.
- Marchetti, S. & Totani, G. (1989) " C_h evaluations from DMTA dissipation curves," Proc. XII Int. Conf. on Soil Mech. and Fdn. Engrg., Rio de Janeiro, pp. 281-286.

- Marsland, A. & Randolph, M.F. (1977) "Comparisons of the results from pressuremeter tests and large in situ plate tests in London clay," Géotechnique, Vol. 27, No. 2, pp 217-243.
- Massarsch, K.R. (1979) "Lateral earth pressure in normally consolidated clay," Proc. 7th European Conf. on Soil Mech. and Fdn. Engrg., Brighton, Vol. 2, pp. 245-249.
- Matsui, T. & Abe, N. (1981) "Multi-dimensional elasto-plastic consolidation analysis by finite element method," Soils and Foundations, Vol. 21, No. 1, pp. 79-95.
- May, R.E. (1987) A Study of the Piezocone Penetrometer in Normally Consolidated Clay, Ph. D. Thesis, Oxford University.
- Mayne, P.W. (1986), "CPT indexing of in-situ OCR in clays," Proc., ASCE Conf. on Use of In-Situ Tests in Geotechnical Engrg., (In-Situ '86), Blacksburg, VA., pp. 780-793.
- Mayne, P.W. (1987) "Determining preconsolidation stress and penetration pore pressures from DMT contact pressures," ASTM Geotechnical Testing Journal, Vol. 10, No. 3, pp. 146-150.
- Mayne, P.W., Kulhawy, F.H. & Kay, J.N. (1990) "Observations on the development of pore-water stresses during piezocone penetration in clays," Canadian Geotechnical Journal, Vol. 27, pp. 418-428.
- Ménard, L. (1956) An Apparatus for Measuring the Strength of Soils in Place, M.Sc. Thesis, Dept. of Civil Engrg., Univ. of Illinois, Urbana.
- Menzies, B.K. & Merrifield, C.M. (1980) "Measurements of shear stress distribution on the edges of a shear vane blade" Géotechnique, Vol. 30, No. 2, pp. 314-318.
- Morino, L. & Kuo, C-C. (1974), "Subsonic aerodynamics for complex configurations," AIAA Journal, Vol. 12, No. 2, pp. 191-197.
- Morrison, M.J. (1984) "In situ measurements on a model pile in clay," PhD Thesis, MIT, Cambridge, MA., 700p.
- Myerhof, G.G. (1961) "The ultimate bearing capacity of wedge-shaped foundations," Proc. 5th Int. Conf. on Soil Mech. and Fdn. Engrg., Vol. 2, pp. 105-109.
- Newman, J.N. (1986) "Distributions of sources and normal dipoles over a quadrilateral panel," Journal of Engrg. Mathematics, Vol. 20, pp. 113-126.
- Nyirenda, Z.M. (1989) The Piezocone in Lightly Overconsolidated Clay, Ph. D. Thesis, Oxford University.
- Nyirenda, Z.M. & Sills, G.C. (1989) "Discussion, Session 3," Proc. Conf. on Penetration Testing in the UK, Birmingham, pp. 183-184.
- O'Neill, D.A. (1985) Undrained Strength Anisotropy of an Overconsolidated Thixotropic Clay, S.M. Thesis, Dept. of Civil Engrg., MIT, Cambridge, MA, 359p.

- Palmer, A.C. (1972) "Undrained plane-strain expansion of a cylindrical cavity in clay: a simple interpretation of the pressuremeter test," Géotechnique, Vol. 22, No. 3, pp. 451-457.
- Powell, J.J.M. & Uglow, I.M. (1988) "Marchetti dilatometer testing in UK soils," Proc. 1st Int. Symp. on Penetration Testing, Orlando, FL., Vol. 1, pp. 555-562.
- Prévost, J.H. & Hoeg, K. (1975) "Analysis of the pressuremeter in strain-softening soil," ASCE Journal of the Geotechnical Engrg. Division, Vol. 101, No. GT8, Proc Paper 11488, pp. 717-731.
- Rad, N. S. & Lunne, T. (1988) "Direct correlations between piezocone test results and undrained shear strength of clay," Proc. 1st Int. Symp. on Penetration Testing, Orlando, FL., Vol. 2, pp. 911-918.
- Rafalovich, A. (1991) The Mechanics of Plate Penetration in Clays, SM Thesis, MIT, Cambridge, MA, 259p.
- Randolph, M.F., Carter, J.P. & Wroth, C.P. (1978), "Driven piles in clay: Installation modelled as the expansion of a cylindrical cavity," University of Cambridge Research Report CUED/D-Soils TR53.
- Randolph, M.F. & Wroth, C.P. (1979), "Driven piles in clay: Effects of installation and subsequent consolidation," Géotechnique, Vol. 29, No. 4, pp. 361-393.
- Reid, W.M., St. John, H.D., Fyffe, S., Ridgen, W.J. (1982) "The push-in pressuremeter," Proc. of the Symp. on the Pressuremeter and its Marine Applications, Paris, pp. 247-261.
- Ridgen, W.J., Thorburn, S., Marsland, A. & Quartermain, R.S.T. (1982) "A dual load range cone penetrometer," Proc. ESOPT-II, Amsterdam, Vol. 2, pp. 787-796.
- Robertson, P.K. & Campanella, R.G. (1983), "Interpretation of cone penetration tests, II: Clays," Canadian Geotechnical Journal, Vol. 20, No. 4, pp. 734-745.
- Robertson, P.K., & Campanells, R.G. (1984) "Guidelines for use and interpretation of the electronic cone penetration test", Soil Mechanics Series No.69, Dept. of C.E., The University of British Columbia, Vancouver.
- Robertson, P.K., Campanella, R.G., Gillespie, D., & Greig, J. (1986) "Use of piezometer cone data" Proc. ASCE Conf. on Use of In-situ Tests in Geotechnical Engineering. (In-situ '86), Blacksburg, VA, pp. 1263-1280.
- Robertson, P.K., Campanella, R.G., Gillespie, D. & By, T. (1988) "Excess pore pressures and the flat dilatometer test," Proc. 1st Int. Symp. on Penetration Testing, Orlando, FL., Vol. 1, pp. 567-576.
- Robertson, P.K., Sully, J., Woeller, D.J., Lunne, T. & Powell, J.J.M. (1990) Guidelines for Interpretation of CPTU Test Data for Determination of Consolidation and

- Permeability Parameters of Soils, Vol. No. 1. - Report, Prepared for Energy, Mines and Resources, Nova Scotia, Contract No. 23420-9-M644/01-OSC, 50p.
- Roscoe, K.H., Burland, J.B. (1968) "On the generalized stress-strain behaviour of 'Wet' clay", Engineering Plasticity, Ed. J. Heyman and F.A. Leckie, Cambridge University Press, pp. 535-609.
- Rouse, H. (1959) Advanced Mech. of Fluids, Wiley & Sons, New York.
- Roy, M & Leblanc, A. (1988) "Factors affecting the measurement and interpretation of the vane strength in soft sensitive clays," Vane Shear Testing in Soils: Field and Lab Studies, ASTM STP 1014, pp. 117-130.
- Schaap, L.H.J. & Zuidberg, H.M. (1982) "Mechanical and electrical aspects of the electrical cone penetrometer tip," Proc. 2nd European Symp. on Penetration Testing, Amsterdam, Vol. 2, pp. 841-851.
- Schmertmann, J.H. (1982) "A method for determining the friction angle in sands from the Marchetti dilatometer test," Proc. 2nd European Symp. on Penetration Testing, Amsterdam, Vol. 1, pp. 853-861.
- Schmertmann, J. (1986) "Suggested method for performing the flat dilatometer test," ASTM Geotechnical Testing Journal, Vol. 9, No. 2, pp. 93-101.
- Schmidt, B. (1966) "Discussion on: Brooker, E.W. and H.O. Ireland, Earth pressure at rest related to stress history," Canadian Geotechnical Journal, Vol. 3, No. 4, pp. 239-242.
- Schofield, A.N. & Wroth, C.P. (1968) Critical State Soil Mechanics, McGraw Hill. London, 310p.
- Senneset, K., Janbu, N. & Svanø, G. (1982), "Strength and deformation parameters from cone penetration tests, " Proc., 2nd European Symp. on Penetration Testing, Amsterdam, Vol. 2, pp. 863-870.
- Senneset, K. & Sandven, R. (1988) "Piezocone test in silty soils," Proc. 1st Int. Symp. on Penetration Testing, Orlando FL, Vol. 2, pp. 955-966.
- Sills, G.C. (1975) "Some conditions under which Biot's equation of consolidation reduce to Terzaghi's Equation," Géotechnique, Vol. 25., No. 1, pp. 129-132.
- Sills, G.C., Almeida, M.S.S. & Danziger, F.A.B. (1988) "Coefficient of consolidation from piezocone dissipation in a very soft clay," Proc. 1st Int. Symp. on Penetration Testing, Orlando FL, Vol. 2, pp. 967-974.
- Skempton, A.W. (1954) "The pore pressure coefficients A and B," Géotechnique, No. 4.
- Sloan, S.W. & Randolph, M.F. (1982) "Numerical predictions of collapse loads using finite element methods," Int. Journal for Numerical and Analytical Methods in Geomechanics, Vol. 6, pp. 47-76.

- Smits, F.P. (1982) "Penetration pore pressure measured with piezometer cones", Proc. 2nd European Symp. on Penetration Testing, Amsterdam, Vol. 2, pp. 887-881.
- Suklje, L. & Majes, B. (1991) "Influence of the density of finite element networks on consolidation analysis," Technical Note, Géotechnique, Vol. 41, No. 1, pp-139-142.
- Sully, J.P., Campanella, R.G. & Robertson, P.K. (1988), "Overconsolidation ratio of clays from penetration pore pressures," ASCE, Journal of Geotechnical Engrg., Vol. 114, No. GT2, pp. 209-216.
- Tavenas, F., Blanchette, G., Leroueil, S., Roy, M. & LaRochelle, P. (1975) "Difficulties in the in-situ determination of K_0 in soft sensitive clays" Proc.: In-Situ Measurement of Soil Properties, Raleigh, NC, pp. 450-476.
- Tavenas, F., Leroueil, S., Roy, M. (1982) "The piezocone test in clays," Proc. of the 2nd European Symp. on Penetration Testing, Amsterdam, pp. 889-894.
- Tedd, P. & Charles, J.A. (1981) "In-situ measurement of horizontal stress in overconsolidated clay using push-in spade-shaped pressure cells," Géotechnique, Vol. 31, No. 4, pp. 554-558.
- Tedd, P., Powell, J.J., Charles, J.A., & Uglow, I.M. (1990) "In-situ measurements of earth pressures using push-in spade-shaped pressure cells - 10 years experience," Geotechnical Instrumentation in Practice, Institution of Civil Engineers, London, pp. 701-715.
- Teh, C-I (1987), "An analytical investigation of the cone penetration test," PhD Thesis, University of Oxford.
- Teh, C-I, Houlsby, G.T. (1987), "Undrained deep penetration, I. Shear stresses; Discussion of Paper by M.M. Baligh," Géotechnique, Vol. 37, No. 4, pp. 525-527.
- Teh, C-I & Houlsby, G.T. (1989) "An analytical study of the cone penetration test in clay," Oxford University Soil Mech. Report, No. OUEL 1800/89.
- Thornburn, S., Laird, C.L., & Reid, W.M., (1981) "The importance of stress histories of cohesive soils and the cone penetration test", The Structural Engineer, 59A, pp. 87-92.
- Torstensson, B.A. (1975) "Pore pressure sounding instrument," Proc. ASCE Specialty Conf. on In situ Measurement of Soil Properties, Raleigh, NC, Vol. 2, pp 48-54.
- Torstensson, B.A. (1977) "Time-dependent effects in the field vane test," Int. Symp. on Soft Clay, Bangkok, pp 387-397.
- Torstensson, B.A. (1982) "A combined pore pressure and point resistance probe," Proc., 2nd European Symp. on Penetration Testing, Amsterdam, Vol. 2, pp. 903-908.

- Tumay, M.T., Acar, Y.B., Cekirge, M. & Ramesh, N. (1985) "Flow field around cones in steady penetration," ASCE, Journal of Geotechnical Engrg., Vol. 111, No. GT2, pp. 325-342.
- Tumay, M.T. & Acar, Y.B. (1985) "Piezocone penetration testing in soft cohesive soils," Strength Testing of Marine Sediments: Laboratory and In-Situ Measurements, ASTM STP 883, R.C. Chaney and K.R. Demars, Eds., American Society for Testing and Materials, Philadelphia, pp 72-82.
- Vermeer, P.A. & Verruut, A. (1981) "An accuracy condition for consolidation by finite elements," Int. Journal for Numerical and Analytical Methods in Geomechanics, Vol. 5, pp. 1-14.
- Vivatrat, V. (1978) "Cone penetration in clays," PhD Thesis, MIT, Cambridge, MA., 427p.
- Wambeke, A. Van & d'Hemricourt, J. (1975) "Courbes pressiometriques inverses; methode d'interpretation de l'essai pressiometrique," Sols-Soils, Vol. 7, No. 25, pp 15-25.
- Weinstein, A. (1948) "On axially symmetric flows," Quarterly of Applied Mathematics, Vol. 5, No. 4, pp. 429-434.
- Whittle, A.J. (1987) A Constitutive Model for Overconsolidated Clays with Application to the Cyclic Loading of Friction Piles, ScD Thesis, MIT. 641 p.
- Whittle, A.J. (1990), A Constitutive Model for Overconsolidated Clays, MIT Sea Grant Report No. MITSG90-15.
- Whittle, A.J. (1992) "Evaluation of a constitutive model for overconsolidated clay," Géotechnique, to be published.
- Whittle, A.J., Ladd, C.C., Baligh, M.M. (1989) "Interpretation of in-situ testing of cohesive soils using rational methods", Annual Technical Report submitted to Air Force Office of Scientific Research Report, November.
- Whittle, A. J. & Baligh, M.M. (1990), "Prediction and evaluation of pile shaft behaviour in lightly overconsolidated clays," submitted for publication.
- Whittle, A.J. & Aubeny, C.P. (1991) "Pore pressure fields around piezocone penetrometers installed in clays," Proc. of the 7th Int. Conf. on Computer Methods and Advances in Geomechanics, Cairns.
- Williamson, A.E. (1989) "Use of a panel method to predict disturbance due to penetrometer installation in clays", SM Thesis, MIT, Cambridge, MA, 143p.
- Windle, D. & Wroth, C.P. (1977) "The use of a self-boring pressuremeter to determine the undrained properties of clays," Ground Engineering, Sept., pp. 37-46.
- Wissa, A.E.Z., Martin, R.T. & Garlanger, J.E. (1975) "The Piezometer Probe," Proc.

- ASCE Conf. on In-situ Measurement of Soil Properties, Rayleigh, NC, Vol. 2, pp. 536-545.
- Withers, N.J., Schapp, B.L., and Dalton C. (1986) "The development of the full displacement pressuremeter," The Pressuremeter and its Marine Applications, ASTM STP No. 950, pp. 38-56.
- Wood, D.M. (1981) "True triaxial tests on Boston Blue Clay," Proc. Xth Int. Conf. on Soil Mech. and Fnd. Engrg., Stockholm, pp. 825-830.
- Woodward-Clyde Consultants (1989) "Analysis of instrumentation data, Arthur C. Storz Expressway, Omaha, Nebraska," Final Report to HDR Engrs. Inc., 2 Vols.
- Wroth, C.P. (1980) "Cambridge in-situ probe," Proc. of the FHWA Symp. on Site Exploration in Soft Ground Using In Situ Techniques, Alexandria, VA, 1978, Report FHWA-TS-80-202, pp. 97-135.
- Wroth, C.P. (1984), "The interpretation of in-situ soil tests," Géotechnique, Vol. 34, No. 4, pp. 449-489.
- Wroth, C.P. & Hughes, J.M.O. (1973) "An instrument for the in-situ measurement of the properties of soft clays," Proc. of the 8th Intl. Conf. on Soil Mech. and Found. Engr., Moscow, Vol. 1.2, pp. 487-494.
- Wroth, C.P. & Hughes, J.M.O. (1974) "Development of a special instrument for the in situ measurement of the strength and stiffness of soils," ASCE, Specialty Conf. on Subsurface Exploration for Underground Excavation and Heavy Construction, Henniker, N.H., 1974, Proc., pp. 295-311.
- Yeung, K.S. & Carter, J.P. (1990) "Interpretation of the pressuremeter test in clay allowing for membrane end effects and material non-homogeneity," Pressuremeters, Institution of Civil Engineers, London, pp. 199-208.
- Zuidberg, H.M., Schapp, L.H.J., & F.L. Beringen (1982) "A penetrometer for simultaneous measuring of cone resistance, sleeve friction, and dynamic pore pressure," Proc., 2nd European Symp. on Penetration Testing, Amsterdam, Vol. 2, pp. 963-970.

A. GENERALIZED EFFECTIVE STRESS SOIL MODELS

A.1 INTRODUCTION

In the application of the Strain Path Method in this thesis, effective stresses, σ'_{ij} , are computed directly from the strain paths of individual elements using an effective stress model (Figure 2.1). This approach can be contrasted to total stress analyses (Baligh and Levadoux, 1980; Teh and Houlsby, 1991) which compute deviatoric stresses through a deviatoric stress-strain model and introduce a separate model for shear-induced pore pressures. The main advantage of the effective stress analysis is that the same model can be used to study stress changes after installation and throughout subsequent test procedures.

Although simple models of soil behavior provide useful physical insights into the mechanics of deep penetration in clays (e.g., Baligh, 1986a; Teh and Houlsby, 1991), more comprehensive constitutive equations are necessary to achieve reliable predictions of stress and pore pressure fields for real soils. The analyses presented in this thesis use two particular effective stress models to describe clay behavior: 1) Modified Cam Clay (Roscoe and Burland, 1968); and 2) MIT-E3 (Whittle, 1990, 1992). The following sections contain summaries of the formulation for these models extracted from Hashash (1992).

A.2 MODIFIED CAM CLAY FORMULATION (extracted from Hashash, 1992)

The Modified Cam Clay model (MCC; Roscoe and Burland, 1968) is the most widely used effective stress soil model for non-linear finite element analyses of practical geotechnical problems (c.f. Potts and Gens, 1988). The MCC model describes an idealized behavior of soils which is characterized by the framework of Critical State Soil Mechanics (Schofield and Wroth, 1968, Atkinson and Bransby, 1976). The model is formulated around two major observations of soil behavior:

1. It unifies observations of: a) 'volumetric behavior' of soils (characterized by relations between mean effective stress, σ' , and void ratio, e ; and b) shear behavior, relating σ' to the shear stress¹, S_1 . Normally consolidated states of soil form a unique state boundary surface, $\mathcal{S}(\sigma', S_1, e)=0$. Large irrecoverable plastic strains occur only for stress states located on the state boundary surface. Stress states $\mathcal{S}(\sigma', S_1, e)<0$ are

¹Where S_1 is the deviatoric stress in triaxial space, Table A.1.

referred to as overconsolidated and exhibit elastic, recoverable behavior.

2. When soils are sheared, under general drainage conditions, they tend asymptotically to a critical state, $h(\sigma', S_1, e)=0$, where continued shear distortions can occur at constant effective stress, σ' , with no further change in void ratio (i.e., no further volumetric strains).

The generalized constitutive equations of the MCC model can be summarized as follows:

1. The yield function has the form of an ellipsoid:

$$f\{\underline{\sigma}, \alpha'(e)\} = S_i S_i - c^2 \sigma' (2\alpha' - \sigma') = 0 \quad (\text{A.1})$$

where α is a hardening parameter describing the maximum hydrostatic pressure (hydrostatic pre-consolidation pressure), and c is the slope of the critical state line² (Figure A.1). Equation A.1 assumes a von Mises generalization of the yield function and critical state failure criterion (Whittle, 1987). The constant c is calculated from large strain frictional angle in triaxial compression shear tests, ϕ'_{TC} :

$$c = \sqrt{\frac{2}{3}} M = \sqrt{\frac{2}{3}} \frac{6 \sin \phi'_{TC}}{3 - \sin \phi'_{TC}} \quad (\text{A.2})$$

2. The plastic strains follow an associated flow rule:

$$P = Q = \frac{\partial f}{\partial \sigma'} = 2c^2 (\sigma' - \alpha') \quad (\text{A.3a})$$

$$P'_i = Q'_i = \frac{\partial f}{\partial S_i} = 2S_i \quad (\text{A.3b})$$

3. The elastic moduli are estimated from the slope of a 1-D swelling line, κ , in e - $\log_e \sigma$ space (Figure A.1):

$$K = \frac{\dot{\sigma}'}{\dot{\epsilon}} = \left(\frac{v_0}{\kappa} \right) \sigma' \quad (\text{A.4a})$$

where $v_0 = (1+e_0)$ is the initial specific volume.

In this version of the model, a constant Poisson's ratio, v' , is used and hence:

$$2G/K = 3(1-2v') / (1+v') = \text{constant}. \quad (\text{A.4b})$$

4. The yield surface exhibits density hardening which is proportional to the rate of plastic volumetric strain $\dot{\epsilon}^P$:

$$\dot{\alpha}' = \left(\frac{v_0}{\lambda - \kappa} \right) \dot{\epsilon}^P \quad (\text{A.5a})$$

where λ is the measured slope of the virgin consolidation line (VCL) in e - $\log_e \sigma'$

² c also describes the ratio of the major to minor semi-axes of the ellipsoid.

space (Figure A.1). It should be noted that changes in void ratio are controlled by the rate of volume change:

$$\dot{e} = -(1 + e_0) \dot{\epsilon} \quad (\text{A.5b})$$

5. Overall, the MCC model uses four input material constants (ϕ'_{TC} , κ , λ , $2G/K$) and two state variables (α' , e).

A.3 MIT-E3 MODEL FORMULATION³ (extracted from Hashash, 1992)

The MIT-E3 model was developed to describe the behavior of overconsolidated clays and clays under cyclic loading. The model is based on a simple conceptual framework which attempts to unify important aspects of non-linear, in-elastic and anisotropic behavior of overconsolidated clays.

Experimental data indicate that the unloading and reloading characteristics of a clay in drained shearing ($\sigma' = \text{constant}$) and hydrostatic compression exhibit similar features: a) much stiffer response than the primary loading curve; b) hysteretic stress-strain behavior; c) small irrecoverable deformations on completion of the unload-reload cycle; and d) reloading transition to the primary loading curve (normally consolidated condition). These observations are modelled in MIT-E3 using a simple mechanical model. Figure A.2 shows the conceptual framework used by the model for the hydrostatic unloading and reloading. It is assumed throughout that the soil can be modelled as a rate independent material (i.e., creep effects are not considered). The measured behavior of a clay is most closely described by A-B-C (Figure A.2b). For modelling purposes, MIT-E3 subdivides this behavior into two components:

1. A closed, symmetric, hysteresis loop (Figure A.2a) which matches the observed behavior during unloading. This response is referred to as 'Perfectly Hysteretic' and is described through a formulation similar to that proposed by Hueckel and Nova (1979).
2. For reloading, plastic (irrecoverable) strains are assumed to develop as the Virgin Consolidation Line (VCL) is approached, resulting in residual plastic strains, Δ^p , at A. The magnitude of plastic strains is determined by the proximity of the current stress state to the VCL. Thus the plasticity is conveniently described using a bounding surface (Dafalias and Herrmann, 1980) or subloading surface (Hashiguchi, 1980) model.

Within this subdivision, MIT-E3 implicitly contains a number of important

³For complete details of the model formulation refer to Whittle (1990).

assumptions concerning the behavior of overconsolidated clays:

1. The behavior of overconsolidated clays can not be fully described by the overconsolidation ratio (OCR) of the soil. Additional information of the loading history is also required to distinguish between 'unloading' and 'reloading' at a particular overconsolidated stress state, i.e., extra state variables must be included in the material description.
2. A load cycle in stress space always involves some plastic strains, so that there is no purely reversible (elastic) range of behavior.
3. Inclusion of plastic strains, using bounding surface plasticity, provides the means of coupling volumetric and shear behavior and is also the mechanism by which anisotropic properties are described for overconsolidated clays. Bounding surface plasticity also insures a smooth transition to normally consolidated behavior, so that 'yielding' is smoothed out (hence the classical role of the 'yield surface' is no longer of critical importance).

Finally, the generalized behavior of K_0 -normally consolidated clays is described using an elasto-plastic formulation (extending an earlier model developed by Kavvadas, 1982). This model describes; a) the anisotropic properties of K_0 -normally consolidated clays, and b) strain softening behavior which is observed experimentally for certain modes of deformation.

A.3.1 Normally Consolidated Clay

The mechanical behavior of soil elements normally consolidated along radial effective stress paths ($S/\sigma' = \text{constant}$) is described by a yield surface which is initially oriented along the direction of consolidation. The yield function is written (Kavvadas, 1982):

$$f = (S - \sigma' \mathbf{b}) : (S - \sigma' \mathbf{b}) - c^2 \sigma' (2\alpha' - \sigma') = 0 \quad (\text{A.6})$$

where, α' controls the size of the yield surface, \mathbf{b} is a second order tensor describing the orientation of the yield surface in effective stress space (σ' , S) and c is the ratio of the semi-axes of the ellipsoid (Figure A.3). For the case when $\mathbf{b}=\mathbf{0}$, the yield surface reduces to the same form as that used in the Modified Cam Clay model (MCC; Roscoe and Burland, 1968).

A 'virgin normally consolidated' soil element (i.e., one consolidated from a slurry along a radial effective stress path) is described by the stress state at the tip of the yield surface such that:

$$\begin{aligned} \sigma' &= 2 \alpha' \\ S &= 2 \alpha' \mathbf{b} \end{aligned} \quad (\text{A.7})$$

The load direction, \mathbf{Q} , for stress states located on the yield surface is given by the gradient of the yield surface:

$$\begin{aligned} Q &= 2 c^2 (\sigma' - \alpha') - 2 (S - \sigma' b) : b \\ Q'_i &= 2 (S_i - \sigma' b_i) \end{aligned} \quad (A.8)$$

Failure conditions are represented by an anisotropic failure criterion:

$$h = (S - \sigma' \underline{\xi}) : (S - \sigma' \underline{\xi}) - k^2 \sigma'^2 = 0 \quad (A.9)$$

where h describes a cone in effective stress space, with apex at the origin and axes along the direction $(\mathbf{I} + \underline{\xi})$ (Figure A.3).

In general, the components of $\underline{\xi}$ cannot be determined from standard laboratory tests. Instead, it is assumed that the orientation tensor is fully defined by the friction angles measured in triaxial compression and extension tests (ϕ'_{TC} and ϕ'_{TE} , respectively) at large strain conditions (typically $\epsilon_a \approx 10\%$ in undrained shear tests). The failure condition can then be written using the transformed stress measures (Tables A.1):

$$h = S_i S_i - 2 S_1 \sigma' \xi_1 + \sigma'^2 (\xi_1^2 - k^2) = 0 \quad (A.10)$$

where $\xi_1 = \frac{1}{2} (C_c - C_e) \quad k = \frac{1}{2} (C_c + C_e)$

$$C_c = \sqrt{\frac{2}{3}} \frac{6 \sin \phi_{TC}}{3 - \sin \phi_{TC}} \quad C_e = \sqrt{\frac{2}{3}} \frac{6 \sin \phi_{TE}}{3 + \sin \phi_{TE}}$$

The model assumes two hardening rules to describe changes in the size and orientation of the yield surface respectively:

$$\dot{\alpha}' = \alpha' \zeta \dot{\epsilon}^p \quad (A.11a)$$

$$\dot{\mathbf{b}} = \psi_0 \langle r_x \rangle \frac{1}{\alpha'} (S - \sigma \mathbf{b}) \dot{\epsilon}^p \quad (A.11b)$$

where ζ is a dimensionless function of the state variables which is obtained by invoking the consistency requirement ($\dot{f} = 0$), ψ_0 is a material constant controlling the rate of rotation of the yield surface, and r_x is a scalar which describes the relative orientation of the yield surface to the critical state cone (Figure A.3).

Equation A.11a corresponds to density hardening similar to that used by the MCC model, while Equation A.11b describes the rotational hardening of the yield surface and hence controls the rate of change of anisotropy of the clay. The general form of the equation is such that the principal axes of anisotropy rotate towards the principal stress axes. For the specific case when the principal axes of stress (σ) and anisotropy (\mathbf{b}) coincide, there are no further rotations of the principal directions of anisotropy ($\mathbf{b} = \mathbf{0}$). The variable r_x imposes limits on the principal directions of anisotropy. The form of r_x is selected such that a K_0 -normally consolidated material (i.e., a sample with anisotropic structure due to its consolidation history) changes its anisotropic structures more slowly than a hydrostatically consolidated sample (which is isotropic due to the stress history)

loaded under the same conditions.

A non-associated flow rule is used in order to generate: a) critical state failure conditions; and b) K_0 conditions for a 'virgin normally consolidated clay' (K_{0NC}). The flow rule is defined as follows:

$$\begin{aligned} P &= 2 c^2 \alpha' r_c \\ P' &= c^2 \times (Q' + \langle r_c \rangle S) \end{aligned} \quad (A.12)$$

where x is a constant which defines the K_{0NC} condition:

$$x = \left(\frac{\lambda}{\lambda - \kappa} \right) \left(\frac{1 + 2 K_{0NC}}{3 (1 - K_{0NC})} - \frac{K}{2G} \left(\frac{\kappa}{\lambda} \right) \right) \quad (A.13)$$

The parameter r_c is a scalar variable (Figure A.3) which describes the location of the current stress state relative to the failure surface.

The elasto-plastic modulus, H , is defined by detailed consideration of the behavior of K_0 -normally consolidated clays. The functional form of H is selected in order to describe: a) virgin consolidation lines (VCL) with slope λ in e - $\log_e \sigma'$ space for all radial consolidation paths in effective stress (σ', S) space; and b) strain hardening, peak strength, strain softening and critical state conditions for undrained shearing of K_0 -normally consolidated clays:

$$H = 2 c^2 \left(\frac{\kappa}{\lambda - \kappa} \right) K \left\{ \alpha' P - S_t 2 c^2 \alpha' x \langle r_c \rangle (Q' : b) \right\} \quad (A.14)$$

where S_t is a material constant.

Having selected the functional form of the elasto-plastic modulus, the model formulation is completed by invoking the consistency requirement that the stress state remains in contact with the yield surface for loading of a normally consolidated clay:

$$\dot{f} = \frac{\partial f}{\partial \sigma} : \dot{\sigma} + \frac{\partial f}{\partial \alpha'} : \dot{\alpha}' + \frac{\partial f}{\partial b} : \dot{b} \quad (A.15)$$

This equation can be satisfied by solving for the constant ζ (Equation A.11a) (Kavvasdas, 1982):

$$\zeta = \frac{1}{\alpha'} \left\{ \frac{1}{2 c^2 \alpha'} \frac{H}{P} - \psi_0 \langle r_x \rangle \frac{\sigma'}{\alpha'} (2 \alpha' - \sigma') \right\} \quad (A.16)$$

A.3.2 Hysteretic Model

For a load cycle in stress space, the perfectly hysteretic model describes a closed symmetric hysteresis loop in the stress-strain response of the material. This behavior is obtained using a formulation which is piecewise continuous (i.e., the moduli vary smoothly) between stress reversal points as suggested by Hueckel and Nova (1979). The model requires a) the definition of a 'stress reversal point', and b) the development of suitable expressions to describe the (secant or tangent) moduli relative to the stress reversal point.

It is assumed that the perfectly hysteretic response is based on the incremental isotropic relations between effective stress and elastic strain rates. Furthermore, the Poisson's ratio for the soil skeleton, ν' , is assumed to be constant, (i.e. $2G/K = \text{constant}$). Thus, there is no coupling between volumetric and shear behavior in the perfectly hysteretic equations. The perfectly hysteretic model is constructed by dimensionless distances (in stress space), which relate the current stress state to the stress reversal state:

$$\xi = \begin{cases} \sigma' / \sigma'_{rev} & \text{if } \sigma' > \sigma'_{rev} \\ \sigma'_{rev} / \sigma' & \text{if } \sigma' < \sigma'_{rev} \end{cases} \quad (A.17)$$

$$\xi_s = (\bar{\eta}_i \bar{\eta}_i)^{1/2}$$

where, σ'_{rev} is the mean effective stress at the stress reversal point, and $\bar{\eta}_i = \omega_i \times \eta_i = \omega_i \times \left(\frac{S_i}{\sigma'} - \frac{S_{i, rev}}{\sigma'_{rev}} \right)$ is the change in shear stress ratio from the last stress reversal state. The parameters ω_i are material constants. For K_0 -normally consolidated clays, values of ω_i can be obtained from triaxial shear data assuming that $\omega_1 = \omega$, $\omega_2 = \omega_3 = \omega_4 = \omega_5 = 10\omega_1$.

The volumetric response is described by a tangential bulk modulus:

$$K = \frac{1+e_0}{(1+\delta) \kappa_0} \sigma' \quad (A.18)$$

$$\delta = C n (\log_e \xi + \xi_s)^{n-1}$$

where e_0 is the void ratio, κ_0 defines the initial unloading slope in e - $\log_e \sigma'$ space, and C and n are material constants to describe non-linearity at small strain levels.

Equations A.17 and A.18 show that:

1. The variation of moduli are described using the two measures of stress amplitude ξ and ξ_s corresponding to volumetric and shear behavior. This takes advantage of the uncoupled nature of the incremental stress-strain relations.
2. The moduli are related to the most recent stress reversal state. This implies that the small strain behavior of an overconsolidated clay is controlled by the most recent stress history as suggested by Hight et al (1983).

The major assumption of the perfectly hysteretic model is that strains are only recovered in a stress cycle if the cycle begins from a stress reversal point. In this sense, the perfectly hysteretic model may be classed as a para-elastic constitutive law (Huekel and Nova, 1979). In the proposed formulation, the moduli are described relative to the most recent stress reversal point. Thus there is a strong similarity between the stress reversal point and the concept of unloading in plasticity. However for the perfectly hysteretic model, the effective stress (σ' , S) and strain rates ($\dot{\epsilon}$, \dot{E}) are proportional and the stress reversal point is defined in the direction of the strain rates. Hight et al. (1983)

present data which further suggest that the initiation of undrained shearing always involves high stiffness at small strain levels irrespective of the past consolidation (or strain) history. This implies that it may be more useful to separate the loading criterion into volumetric and deviatoric components and take advantage of the lack of coupling between volumetric and shear behavior in the perfectly hysteretic model. The definition of the load reversal point is achieved by introducing a scalar strain amplitude parameter which describes the strain history relative to (the strain state at) the most recent stress reversal point as follows:

$$\chi = \begin{cases} \Delta l_E & \text{for } \dot{\epsilon} \neq 0, \text{ Drained Behavior} \\ (\Delta l_E : \Delta l_E)^{1/2} & \text{for } \dot{\epsilon} = 0, \text{ Undrained Behavior} \end{cases} \quad (\text{A.19})$$

where, $\Delta l_E = \int_{rev} d\epsilon = \epsilon - \epsilon_{rev}$; and E are the deviatoric strains.

The implication of Equation A.19 is that the volumetric strains are predominantly important in determining the non-linearity of the soil. 'Loading' is then defined from the sign of the rate of the strain amplitude; $(\dot{\chi} = {}^{t+\Delta t}\chi - {}^t\chi)$.

A.3.3 Bounding Surface Plasticity

In the modelling of overconsolidated clays, the development of plastic strains plays a crucial role for three main reasons. Firstly, plastic strains introduce coupling between volumetric and shear behavior, so that shear induced pore pressures are obtained for undrained (monotonic and cyclic) shearing. Secondly, within the MIT-E3 formulation, plastic strains enable the incorporation of anisotropic response for overconsolidated clays and provide a smooth transition to the normally consolidated behavior. The bounding surface model (Dafalias and Herrmann, 1980) relates the plastic strains of overconsolidated clays to the plastic behavior previously defined for the normally consolidated material. Difficulties lie in the formulation of these mapping relations and the physical meaning of material constants to describe them.

In the proposed model, the bounding surface of normally consolidated clay behavior is described by the yield function (Equation A.6). For overconsolidated stress states, a radial mapping rule is used to define a unique image point in the bounding surface (Figure A.3). Plastic behavior at the current (overconsolidated) stress state, P, is linked to the plastic behavior at the image point, I. The occurrence of plastic strains at P is contingent on the loading condition defined as:

$$K Q_I \dot{\epsilon} + 2G (Q'_I : \dot{E}) \begin{cases} \geq 0 \text{ loading} \\ < 0 \text{ unloading} \end{cases} \quad (\text{A.20})$$

where, Q_I and Q'_I are the volumetric and deviatoric components of the gradient of the bounding surface at the image point I.

For stress states within the bounding surface, plastic strains are defined by specifying the elasto-plastic modulus, H , and flow direction, P , for loading at the current stress state. In the bounding surface formulation, functions are developed to relate H and P to the corresponding values at the current image point, H_I and P_I . The MIT-E3 model introduces separate mapping rules for the elasto-plastic modulus and the flow direction which can be expressed in general form:

$$\begin{aligned} P &= P_I + P_0 g_1 \\ H &= H_I + H_0 g_2 \end{aligned} \quad (A.21)$$

where P_0 , H_0 are the values of P and H at the first yield (i.e. at first loading for stress states within the bounding surface); and g_1 , g_2 are mapping functions described by the relative position of the current stress and image stress states.

The selection of suitable expressions for H_0 , P_0 , g_1 and g_2 is a difficult process, especially in view of the joint effects of the two mapping functions. However, this task can be achieved by observing clay behavior in a) hydrostatic unloading and reloading, and b) undrained triaxial shearing of overconsolidated clays. After a number of iterations, a consistent set of equations has been adopted as follows:

$$\begin{aligned} P_0 &= - \{ 2 c^2 \alpha' r_c + (\eta_I : Q'_I) \} \\ P'_0 &= 0 \\ g_1 &= \{ (\alpha' - \alpha'_{0i}) / (\alpha' - \alpha'_{0i}) \}^\gamma \\ H_0 &= \frac{1}{\kappa_0} (1+e_0) \{ (\alpha' - \alpha'_{0i}) h |Q_I| |P_I| \} \\ g_2 &= \{ (\alpha' - \alpha'_{0i}) / (\alpha'_{0i} - \alpha'_{0i}) \} \end{aligned} \quad (A.22)$$

In these equations, h, g are dimensionless material constants which are established from parametric studies; α'_{0i} is the size of the load surface at first yield.

A.3.4 Model Input Parameters

Table 3.2 summarizes the input parameters used by the MIT-E3 model together with their physical significance and proposed laboratory tests from which these properties can be determined (Whittle, 1990). In addition to these 15 material constants, the MIT-E3 model uses the following state variables:

1. The effective stress tensor (σ' , S).
2. The size and orientation of the bounding surface (α' , b).
3. Effective stresses at the most recent reversal state (σ'_{rev} , S_{rev}).
4. The strains accumulated since the last reversal state (Δl_E , Δl_F).
5. The size of the bounding surface at the last reversal state, α'_{rev} ; and the size of the load surface at first yield, α'_{0i} .

Initial values of these state variables must be specified at the start of an analysis:

1. For virgin K_0 -normally consolidated clays, the initial values can be defined unambiguously:

$$\sigma' = \frac{1}{3} (1 + 2 K_{0NC}) \sigma'_{v0}, \quad S_1 = \frac{2}{\sqrt{6}} (1 - K_{0NC}) \sigma'_{v0}, \quad S_2 = S_3 = S_4 = S_5 = 0$$

$$\alpha' = \frac{1}{2} \sigma',$$

$$b_1 = \frac{1}{2 \alpha'} S_1,$$

$$b_2 = b_3 = b_4 = b_5 = 0$$

$$\sigma'_{rev} = \sigma',$$

$$S_{rev} = S$$

$$\Delta l_E = \Delta l_E = 0,$$

$$\alpha'_{rev} = \alpha'_{0i} = \alpha'$$

Equations A.23

2. For overconsolidated clays, ambiguity can arise due to lack of information on the past stress history of the clay (Whittle, 1990). For practical calculations, this thesis assumes that the current (initial) stress state is a stress reversal state and hence:

$$\sigma' = \frac{1}{3} (1 + 2 K_0) \sigma'_{v0}, \quad S_1 = \frac{2}{\sqrt{6}} (1 - K_0) \sigma'_{v0}, \quad S_2 = S_3 = S_4 = S_5 = 0$$

$$\alpha' = \alpha'_{rev} = \frac{1}{6} (1 + 2 K_{0NC}) \sigma'_p, \quad b_1 = \frac{1}{\alpha' \sqrt{6}} (1 - K_{0NC}) \sigma'_p, \quad b_2 = b_3 = b_4 = b_5 = 0$$

$$\sigma'_{rev} = \sigma',$$

$$S_{rev} = S$$

$$\Delta l_E = \Delta l_E = 0,$$

$$\alpha'_{0i} = \frac{1}{2} \sigma'$$

Equations A.24

Effective Stress	Strain	Yield Surface Gradient	Plastic Flow Direction	Anisotropy
$\sigma = (\sigma', S)$	$\epsilon = (\epsilon, E)$	$Q = (Q, Q')$	$P = (P, P')$	$(1, b)$
$\sigma' = \frac{1}{3}(\sigma_x + \sigma_y + \sigma_z)$	$\epsilon = \epsilon_x + \epsilon_y + \epsilon_z$	$Q = Q_x + Q_y + Q_z$	$P = P_x + P_y + P_z$	1
$S_1 = \frac{1}{\sqrt{6}}(2\sigma_y - \sigma_x - \sigma_z)$	$E_1 = \frac{1}{\sqrt{6}}(2\epsilon_y - \epsilon_x - \epsilon_z)$	$Q'_1 = \frac{1}{\sqrt{6}}(2Q_y - Q_x - Q_z)$	$P'_1 = \frac{1}{\sqrt{6}}(2P_y - P_x - P_z)$	$b_1 = \frac{1}{\sqrt{6}}(2b_y - b_x - b_z)$
$S_2 = \frac{1}{\sqrt{2}}(\sigma_z - \sigma_x)$	$E_2 = \frac{1}{\sqrt{2}}(\epsilon_z - \epsilon_x)$	$Q'_2 = \frac{1}{\sqrt{2}}(Q_z - Q_x)$	$P'_2 = \frac{1}{\sqrt{2}}(P_z - P_x)$	$b_2 = \frac{1}{\sqrt{2}}(b_z - b_x)$
$S_3 = \sqrt{2}\sigma_{xy}$	$E_3 = \sqrt{2}\epsilon_{xy}$	$Q'_3 = \sqrt{2}Q_{xy}$	$P'_3 = \sqrt{2}P_{xy}$	$b_3 = \sqrt{2}b_{xy}$
$S_4 = \sqrt{2}\sigma_{yz}$	$E_4 = \sqrt{2}\epsilon_{yz}$	$Q'_4 = \sqrt{2}Q_{yz}$	$P'_4 = \sqrt{2}P_{yz}$	$b_4 = \sqrt{2}b_{yz}$
$S_5 = \sqrt{2}\sigma_{zx}$	$E_5 = \sqrt{2}\epsilon_{zx}$	$Q'_5 = \sqrt{2}Q_{zx}$	$P'_5 = \sqrt{2}P_{zx}$	$b_5 = \sqrt{2}b_{zx}$

Table A.1 Transformed Measures (Kavvas, 1982).

The Modified Cam Clay Model

(after Roscoe and Burland, 1968)

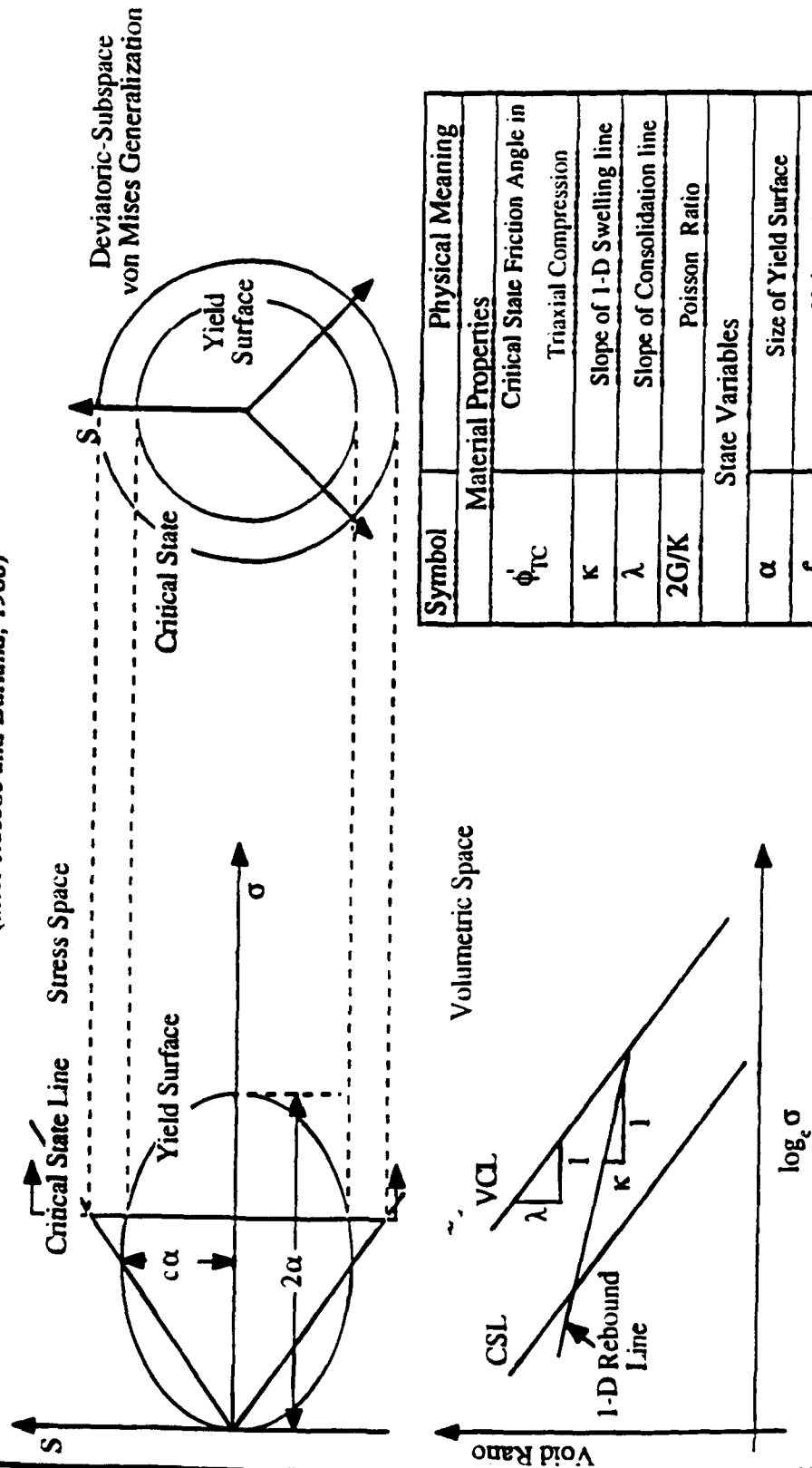
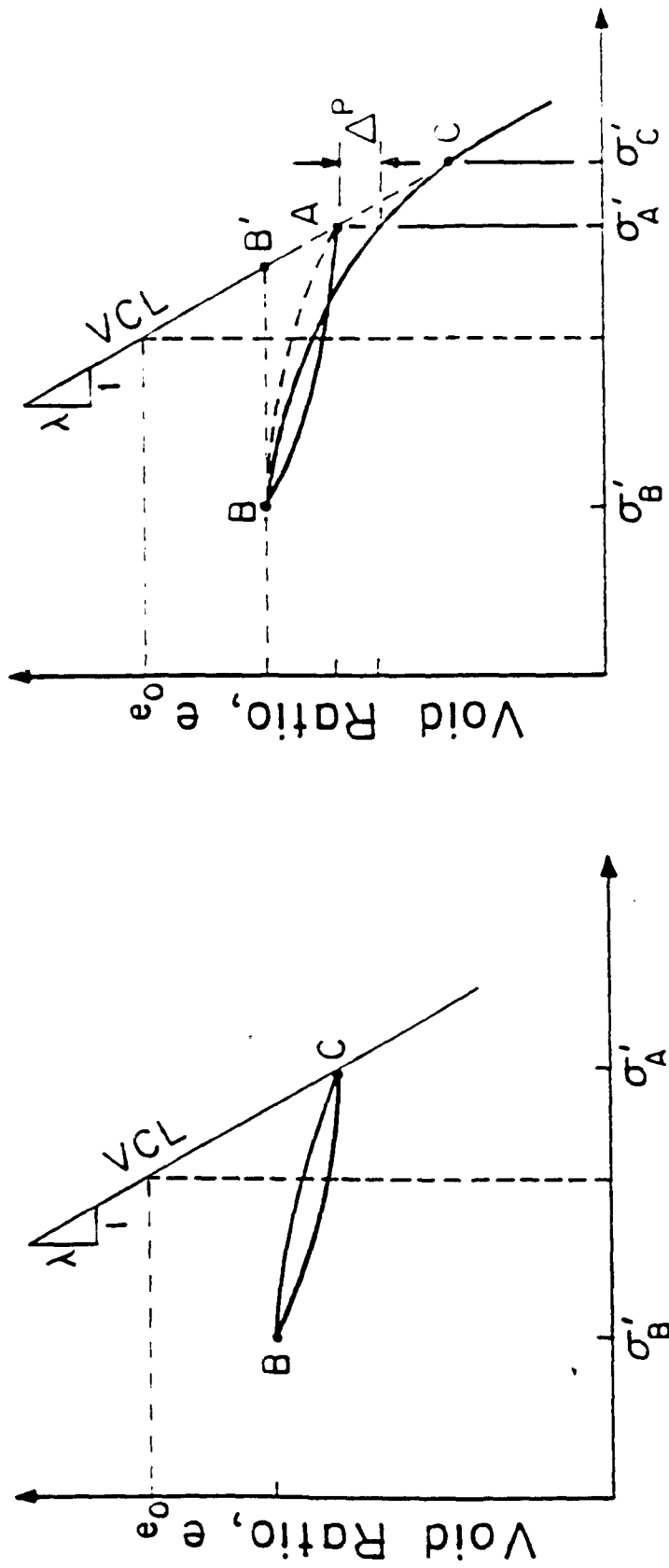


Figure A.1 The Modified Cam Clay Model



$\log_e(\text{mean effective stress}, \sigma')$

a) 'Perfect Hysteresis'

b) Hysteresis and Bounding Surface Plasticity

Figure A.2 Conceptual Model of Unload-Reload Used by MIT-E3 for Hydrostatic Compression (Whittle, 1990)

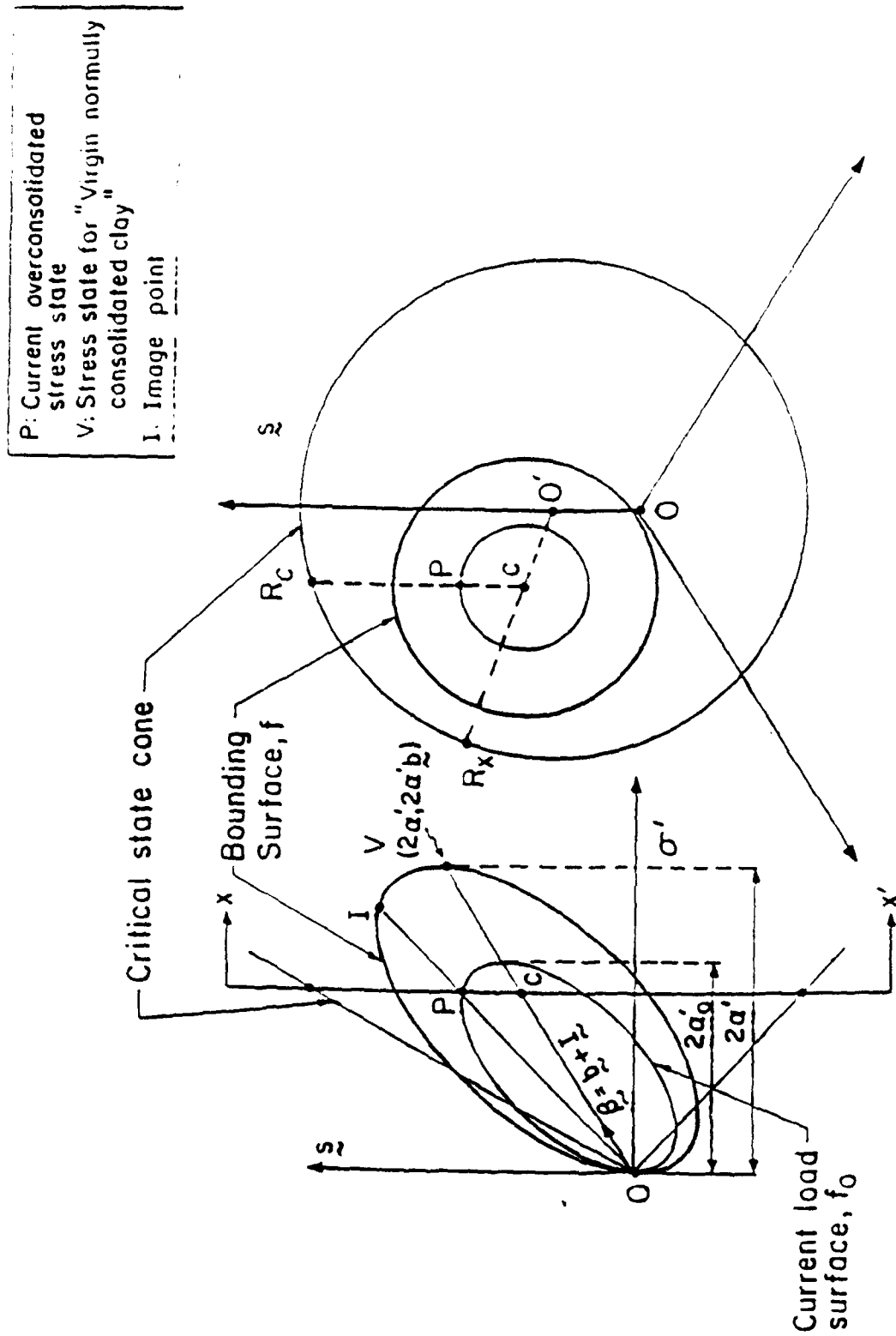


Figure A.3 Yield and Failure Surface for Normally Consolidated Clay (Whittle, 1990)

B. ISOPARAMETRIC INTERPOLATION FUNCTIONS

Implementation of the Poisson solution requires numerical differentiation of predicted stress fields using data points which are not located along a rectangular grid. This can be conveniently accomplished using isoparametric interpolation functions (Bathe, 1982). Computation of stress gradients in a vertical plane requires a higher degree of numerical accuracy due to rapidly changing conditions ahead of the penetrometer tip; hence, a second-order scheme employing 9-node elements (Figure B.1) is utilized, and the relevant interpolation functions are presented in Table B.1. In horizontal planes far above the penetrometer tip, gradients are less severe, and first-order differentiation of stress fields (Table B.2) was found to provide suitable accuracy.

i	h_i	$\frac{\partial h_i}{\partial s}$	$\frac{\partial h_i}{\partial t}$
1	$\frac{1}{4} st(1+s)(1+t)$	$\frac{1}{4} t(1+t)(1+2s)$	$\frac{1}{4} s(1+s)(1+2t)$
2	$-\frac{1}{4} st(1-s)(1+t)$	$-\frac{1}{4} t(1+t)(1-2s)$	$-\frac{1}{4} s(1-s)(1+2t)$
3	$\frac{1}{4} st(1-s)(1-t)$	$\frac{1}{4} t(1-t)(1-2s)$	$\frac{1}{4} s(1-s)(1-2t)$
4	$-\frac{1}{4} st(1+s)(1-t)$	$-\frac{1}{4} t(1-t)(1+2s)$	$-\frac{1}{4} s(1+s)(1-2t)$
5	$\frac{1}{2} t(1-s^2)(1+t)$	$-st(1+t)$	$\frac{1}{2} (1-s^2)(1+2t)$
6	$-\frac{1}{2} s(1-s)(1-t^2)$	$-\frac{1}{2} (1-t^2)(1-2s)$	$st(1-s)$
7	$-\frac{1}{2} t(1-s^2)(1-t)$	$st(1-t)$	$-\frac{1}{2} (1-s^2)(1-2t)$
8	$\frac{1}{2} s(1+s)(1-t^2)$	$\frac{1}{2} (1-t^2)(1+2s)$	$-st(1+s)$
9	$(1-s^2)(1-t^2)$	$-2s(1-t^2)$	$-2t(1-s^2)$

Table B.1 Isoparametric Interpolation Functions and Their Derivatives for 9-Node Isoparametric Element

Table B.2 Interpolation Functions and Their Derivatives for a Four-Node Isoparametric Element *

h_i	$\partial h_i / \partial s$	$\partial h_i / \partial t$
$(1+s)(1+t)/4$	$(1+t)/4$	$(1+s)/4$
$(1-s)(1+t)/4$	$-(1+t)/4$	$(1-s)/4$
$(1-s)(1-t)/4$	$-(1-t)/4$	$-(1-s)/4$
$(1+s)(1-t)/4$	$(1-t)/4$	$-(1+s)/4$

*Nodal point locations are illustrated in Figure B.1.

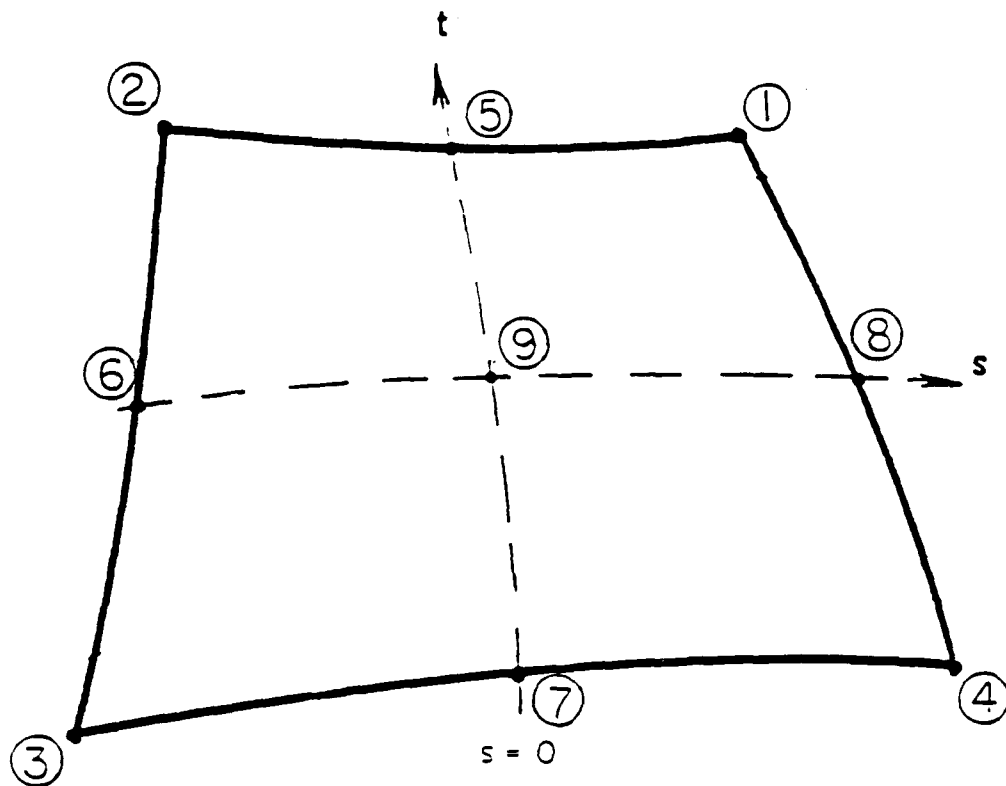


Figure B.1 Isoparametric Element Definition Sketch

C. THE SIMPLE PLATE

C.1 INTRODUCTION

A number of in-situ devices analyzed in this thesis are described by a flat plate geometry, including the Marchetti dilatometer (Chapter 4; Marchetti, 1980) and earth pressure cells (Tedd and Charles, 1981; Tavenas et al., 1975). For analysis of these devices by the Strain Path Method, estimates of velocities during penetration can be made using two possible approaches:

1. Numerical methods that model the surface geometry of the penetrometer. For three dimensional penetrometer geometries, boundary element formulations such as the panel method are widely used by aeronautical engineers and hydrodynamicists. The first use of the panel method within the framework of the strain path method was proposed by Huang (1989) using the formulation of Hess and Smith (1962, 1964). In previous work, Williamson (1989) (Whittle et al., 1989) also implemented a potential based panel method to study the disturbance due to dilatometer installation. However, due to the complexities associated with modeling real surface geometries, it is difficult to gain insight about the basic penetration mechanics. Williamson (1989) (Whittle et al., 1989) used a potential based panel method to study the strain paths due to dilatometer penetration. These studies showed that results from panel method computations require very careful evaluation in order to establish their reliability and accuracy for a given surface discretization.
2. Simple solutions using fundamental analytical solutions. This approach was used by Baligh (1986) to describe steady penetration of a solid circular penetrometer by considering the velocity field corresponding to a 3-dimensional point source superimposed onto a uniform flow field. The resulting 'simple pile' deformation grids and strain paths corresponding are shown in Figures C.1 and C.2, respectively. Additional fundamental solutions for other penetrometer shapes are summarized in Table C.1. These analyses provide considerable insight into the basic mechanics of penetration but do not closely model the surface geometry of a particular penetrometer.

This appendix describes the application of the latter approach for analysis of plate penetration.

C.2 THE SIMPLE PLATE [extracted from Whittle et al. (1990) and Rafalovich (1991)]

This section presents the 'simple plate' solution based on the solution for a semi-infinite

line source in a uniform flow field which was first presented by Whittle et al. (1989, 1990). The 'simple plate' geometry is characterized by the length of a finite line source, $2B$, and its strength, Q' (rate of volume discharged per unit length), superimposed in a uniform flowfield (of velocity, u_z). For the particular case when $B \rightarrow 0$, the simple plate reduces to a simple pile geometry (Baligh, 1985a), while for $B \rightarrow \infty$, the simple wall is obtained. The following sections describe the mechanics of flat plate penetration based on the simple plate geometry.

C.2.1 Fundamental Solution for a Finite Line Source

A single point source, discharging volume at a rate, V (volume per unit time), produces a velocity that acts radially away from the source (Figure C.3). Assuming that the emitted fluid occupies a spherical cavity, the radius of the cavity, $R(t)$, can be related to the rate of discharge by:

$$R(t) = \frac{3Vt}{4\pi} \quad (C.1a)$$

The radial location of a soil element, $r(t)$, is then related to its initial location, r_0 , by the incompressibility constraint:

$$\rho(t) = \left\{ \rho_0^3 + R^3(t) \right\}^{1/3} \quad (C.1b)$$

Hence, if the radius of the cavity is defined at time, t , all deformations and strains are fully determined. The velocity of soil elements due to a point source located at the origin of the reference coordinate frame can then be written:

$$v_p^0 = \frac{V}{4\pi\rho^2} \quad \text{Spherical} \quad (C.2a)$$

$$v_r^0 = \frac{V \sin \phi}{4\pi\rho^2} ; v_z^0 = \frac{V \cos \phi}{4\pi\rho^2} \quad \text{Cylindrical} \quad (C.2b)$$

$$v_x^0 = v_r^0 \cos \theta ; v_y^0 = v_r^0 \sin \theta \quad \text{Cartesian} \quad (C.2c)$$

where, $\rho = (x^2 + y^2 + z^2)^{1/2}$, $r = (x^2 + y^2)^{1/2}$, $\phi = \tan^{-1} \frac{r}{z}$ and $\theta = \tan^{-1} \frac{y}{x}$.

If the cartesian frame is translated (Figure C.3b) such that $x'=x$, $y'=y+x$, $z'=z$, then the velocity components (x', y', z') due to a source at $y'=x$ are given by:

$$\begin{aligned}
 v_x^0 &= \frac{V \sin \phi \cos \theta}{4\pi\rho^2} \\
 v_y^0 &= \frac{V \sin \phi \sin \theta}{4\pi\rho^2} \\
 v_z^0 &= \frac{V \cos \phi}{4\pi\rho^2}
 \end{aligned}
 \tag{C.2d}$$

where, $y = y' - x$.

If the point source is then treated as a line source of elemental length, dx ; then, $V = Q'dx$, where Q' is the source strength per unit length. Hence the velocity components for a line source of finite length ($x_1 \leq x \leq x_2$) can be obtained by direct integration:

$$v_i' = \int_{x_1}^{x_2} v_i^0(\xi) d\xi \tag{C.3}$$

where v_i^0 are the velocity components given by equation C.2d.

For the particular case of a semi-infinite line source ($0 \leq x \leq \infty$) (Figure C.3), the velocity components are given by:

$$\begin{aligned}
 v_x' &= \frac{Q' \cos \theta'}{4\pi r'} \left(1 + \frac{y'}{\rho'} \right) \\
 v_y' &= \frac{Q'}{4\pi \rho'} \\
 v_z' &= \frac{Q' \sin \theta'}{4\pi r'} \left(1 + \frac{y'}{\rho'} \right)
 \end{aligned}
 \tag{C.4}$$

where, $r' = (x'^2 + z'^2)^{1/2}$, $\rho' = (x'^2 + y'^2 + z'^2)^{1/2}$, and $\theta' = \tan^{-1} \frac{z'}{x'}$.

When the sign of the strength (Q') is negative, the results (Equation C.4) describe the flow field for a semi-infinite sink. Hence, the solution for a line source of finite length can be obtained by superposition using the fundamental solutions for a semi-infinite source.

The strain rate components of the flow field described by Equation C.5 are obtained by differentiating the velocities with respect to the spatial coordinates. This leads to the following expressions for the strain rates of a semi infinite line source:

$$\begin{aligned}
\dot{\epsilon}_{x'x'} &= \frac{Q'}{4\pi} \left\{ \frac{1}{r'^2} \left(1 + \frac{y'}{\rho'} \right) - \frac{2x'^2}{r'^4} \left(1 + \frac{y'}{\rho'} \right) - \frac{x'^2 y'}{r'^2 \rho'^3} \right\} \\
\dot{\epsilon}_{y'y'} &= -\frac{Q' y'}{4\pi \rho'^3} \\
\dot{\epsilon}_{z'z'} &= \frac{Q'}{4\pi} \left\{ \frac{1}{r'^2} \left(1 + \frac{y'}{\rho'} \right) - \frac{2z'^2}{r'^4} \left(1 + \frac{y'}{\rho'} \right) - \frac{z'^2 y'}{r'^2 \rho'^3} \right\} \\
\dot{\epsilon}_{x'y'} &= -\frac{Q' x'}{4\pi \rho'^3} \\
\dot{\epsilon}_{y'z'} &= -\frac{Q' z'}{4\pi \rho'^3} \\
\dot{\epsilon}_{x'z'} &= -\frac{Q'}{4\pi} \left\{ \frac{2x'z'}{r'^4} \left(1 + \frac{y'}{\rho'} \right) - \frac{x'y'z'}{r'^2 \rho'^3} \right\}
\end{aligned} \tag{C.5}$$

The 'simple plate' geometry is then obtained by superimposing a uniform flow of velocity, u_z , with the semi-infinite line source result. For example, the velocity field around a line source of finite length $2B$ can be written:

$$\begin{aligned}
v_x &= v_x(+Q'; 0, -B, 0) + v_x(-Q'; 0, +B, 0) \\
v_y &= v_y(+Q'; 0, -B, 0) + v_y(-Q'; 0, +B, 0) \\
v_z &= u_z + v_z(+Q'; 0, -B, 0) + v_z(-Q'; 0, +B, 0)
\end{aligned} \tag{C.6}$$

where, $v_i(Q'; x, y, z)$ describes the velocity component (v_x , v_y , or v_z) due to a semi-infinite source of strength Q' that originates at (x, y, z) and extends to (x, ∞, z) . The uniform flow velocity (u_z) is equivalent to the rate of penetration of the penetrometer. Applying Equation C.7 to Equation C.6 yields the following velocity field for a 'simple plate':

$$\begin{aligned}
v_x &= \frac{Q' \cos \theta}{4\pi r} \left\{ \frac{\rho_1(y-B) - \rho_2(y+B)}{\rho_1 \rho_2} \right\} \\
v_y &= \frac{Q'}{4\pi} \left\{ \frac{\rho_1 - \rho_2}{\rho_1 \rho_2} \right\} \\
v_z &= u_z + \frac{Q' \sin \theta}{4\pi r} \left\{ \frac{\rho_1(y-B) - \rho_2(y+B)}{\rho_1 \rho_2} \right\}
\end{aligned} \tag{C.7}$$

where, $\rho_1 = \{x^2 + (y+B)^2 + z^2\}^{1/2}$, and $\rho_2 = \{x^2 + (y-B)^2 + z^2\}^{1/2}$

Using similar superposition arguments, the strain rates for a 'simple plate' of length $2B$ are given by:

$$\begin{aligned}
\dot{\epsilon}_{xx} &= \frac{Q'}{4\pi} \left[\left(\frac{\rho_1(y-B) - \rho_2(y+B)}{\rho_1\rho_2} \right) \left(\frac{1}{r^2} - \frac{2x^2}{r^4} \right) - \frac{x^2}{r^2} \left(\frac{\rho_1^3(y-B) - \rho_2^3(y+B)}{\rho_1^3\rho_2^3} \right) \right] \\
\dot{\epsilon}_{yy} &= -\frac{Q'}{4\pi} \left(\frac{\rho_1^3(y-B) - \rho_2^3(y+B)}{\rho_1^3\rho_2^3} \right) \\
\dot{\epsilon}_{zz} &= \frac{Q'}{4\pi} \left[\left(\frac{\rho_1(y-B) - \rho_2(y+B)}{\rho_1\rho_2} \right) \left(\frac{1}{r^2} - \frac{2z^2}{r^4} \right) - \frac{z^2}{r^2} \left(\frac{\rho_1^3(y-B) - \rho_2^3(y+B)}{\rho_1^3\rho_2^3} \right) \right] \\
\dot{\epsilon}_{xy} &= -\frac{Q'x}{4\pi} \left(\frac{\rho_1^3 - \rho_2^3}{\rho_1^3\rho_2^3} \right) \\
\dot{\epsilon}_{yz} &= -\frac{Q'z}{4\pi} \left(\frac{\rho_1^3 - \rho_2^3}{\rho_1^3\rho_2^3} \right) \\
\dot{\epsilon}_{zx} &= -\frac{Q'}{4\pi} \left[\left(\frac{\rho_1(y-B) - \rho_2(y+B)}{\rho_1\rho_2} \right) \left(\frac{2xz}{r^4} \right) - \frac{xz}{r^2} \left(\frac{\rho_1^3(y-B) - \rho_2^3(y+B)}{\rho_1^3\rho_2^3} \right) \right]
\end{aligned} \tag{C.8}$$

Due to the condition of incompressibility, $(\dot{\epsilon}_{xx} + \dot{\epsilon}_{yy} + \dot{\epsilon}_{zz} = 0)$, there are five independent shear strain rate components. These are conveniently expressed by transformed measures of deviatoric strain rates:

$$\begin{aligned}
\dot{E}_1 &= \dot{\epsilon}_{zz}; \quad \dot{E}_2 = \frac{1}{\sqrt{3}}(\dot{\epsilon}_{xx} - \dot{\epsilon}_{yy}) \\
\dot{E}_3 &= \frac{2}{\sqrt{3}}\epsilon_{xy}; \quad \dot{E}_4 = \frac{2}{\sqrt{3}}\dot{\epsilon}_{yz}; \quad \dot{E}_5 = \frac{2}{\sqrt{3}}\dot{\epsilon}_{zx}
\end{aligned} \tag{C.9}$$

These measures are introduced to enable comparisons with axisymmetric penetrometers. The overall magnitude of shear strain in the soil is described by the second invariant of the deviatoric strain rates, \dot{E} :

$$\dot{E} = \frac{1}{\sqrt{2}} \sqrt{\dot{E}_1^2 + \dot{E}_2^2 + \dot{E}_3^2 + \dot{E}_4^2 + \dot{E}_5^2} \tag{C.10}$$

Using the fundamental solutions for velocity and strain rate components, the framework of the strain path method can then be invoked to determine the strain paths of soil elements due to steady penetration.

C.2.2 Simple Plate Geometry and Deformation Grids

The maximum thickness of the simple plate, $2w$, for a given length, $2B$, is controlled by the magnitude of the source strength Q' relative to the velocity of penetration, u_z . In

order to enable comparisons of simple plate solutions with those of the simple pile, the source strength is selected so that all dimensions of the problem can be normalized by the half thickness of the plate (w). Hence the geometry of the a simple plate can be fully described by the aspect ratio, B/w . Figure C.4 is a dimensionless plot that shows the relationship between source strength (Q') and plate aspect ratio (B/w).

Surface geometries of the simple plate, presented by Rafalovich (1991), are shown for three different aspect ratios in Figures C.5a-c. An aspect ratio, $B/w = 6.8$ was selected because of its similarity to a standard Marchetti dilatometer (Marchetti, 1980; chapter 4), while the plate with $B/w = 32.5$ closely resembles the standard dimensions of one blade of a field vane (Chandler, 1988). Penetrometer geometry and soil deformations are shown through three sections of each simple plate a) the longitudinal section ($x=0$ plane), b) the central or lateral section ($y=0$ plane), and c) a horizontal section far above the tip of the plates, which is subsequently referred to as the 'steady state' plane¹ (in this case $z/w=200$). The location of the line source is included to illustrate its relationship with the geometry of the solid body. The following aspects of the simple plate geometry should be noted:

1. The simple plate is symmetric about the $x=0$ and $y=0$ planes. Its surface exhibits a slight curvature in all directions. Soil elements that are initially located in the $y=0$ plane remain in that plane during shearing. Hence, these elements experience no out of plane straining and their strain histories can be described by a reduced set of 3 shear strains.
2. All of the plates exhibit actual aspect ratios (L/w) greater than the aspect ratio of the line source used to generate the plate, B/w . The ratio L/B varies as a function of B , as shown in Figures C.6a-c.

It is important to emphasize that the 'simple plate' geometry is introduced in order to elucidate basic disturbance mechanisms during flat blade penetration, but does not exactly model the physical geometry of an earth pressure cell or dilatometer. Namely, the simple plate will generally differ from actual penetrometers in the following respects:

1. It is infinitely long in the vertical direction, whereas actual plate penetrometers have a finite length.
2. The rounded tip and edges of the simple plate will not match the actual shape of real plate penetrometers.

C.2.3 Shear Strains around Simple Plates

¹The steady state plane is defined by the asymptotic condition that there are no further changes in the field variables (deformations, strains and stresses) with vertical elevation. The results in figure C.6 are shown at a nominal steady state condition, $z/w=200$.

Figures C.6a-c show contours of octahedral shear strain, $E = 1, 5, 10$ and 20% in the three cross sections of the simple plates. In the central ($y=0$) plane of the simple plates it can be seen that, for all of the plates, soil elements initially located at lateral distances $x_0/w < 3$ experience strain levels that are larger than those imposed in conventional laboratory tests ($E \approx 10\%$).

Previous results for the simple pile showed that all soil elements experienced monotonic increases in the level of octahedral shear strain, E , during steady penetration, and that contours of E were parallel to the shaft of the penetrometer (e.g. Figure 7 of Baligh, 1985b). In contrast, for the simple plates, Figure C.6 shows that in the central ($y=0$) plane there is a locus of maximum lateral extent for a given strain level. Hence, it can be seen that for soil elements initially located at $x_0/w < 10$, the octahedral shear strain level decreases when the element reaches this locus.

Figures C.7 and C.8 show the variation of the octahedral shear strain (E) with lateral distance (in the x and y directions) in the steady state (horizontal) plane². In Figure C.7, the lateral dimensions are normalized with respect to the half-thickness of the plate. The results show the following:

1. For soil elements located close to the plate interface, the simple plates with aspect ratios, $6.8 \leq B/w \leq 32.5$ all exhibit similar magnitudes of octahedral shear strain and strain levels that are less than those for the simple pile at a given lateral distance.
2. Further away from the plates the shear strain increases with B/w for a given lateral distance, indicating a greater zone of disturbance.

Figure C.8 shows the same results for E plotted against lateral distance normalized to the equivalent radius, R_{eq} , of the plate, where:

$$R_{eq} = \sqrt{\frac{4Bw}{\pi}} \quad (C.11)$$

i.e. R_{eq} is the equivalent radius of an axisymmetric simple pile that has the same cross-sectional area as the simple plate. Thus, the results in Figure C.8 compare the strain field for penetrometers with similar cross-sectional areas. The figure shows the following:

1. At lateral locations far from the penetrometer ($x/R_{eq} > 10-20$; $(y-B)/R_{eq} > 30-40$), the effects of penetrometer shape (B/w) are insignificant.
2. For soil elements close to the penetrometer, the disturbance (magnitude of E) at a given lateral location decreases as the aspect ratio increases.

² The distance necessary to achieve this "steady state" condition increases as the aspect ratio, B/w , increases. For $B/w = 6.8$, $z/w = 200$ was sufficient, while for $B/w = 20, 32.5$, the $z/w = 2000$ plane was used to ensure steady state conditions.

C.2.4 Strain Paths During Plate Installation

The strain paths of soil elements in the central plane ($y=0$) are shown in Figures C.9a, b and c for various initial locations, x_0/w . The strain history of these elements is fully described by the following transformed measures of strain ⁴:

$$E_1 = \epsilon_{zz}; E_2 = \frac{1}{\sqrt{3}}(\epsilon_{xx} - \epsilon_{yy}); E_3 = \frac{2}{\sqrt{3}}\epsilon_{zx} \quad (C.12)$$

For all three of the plates considered, soil elements initially located at lateral distances far away from the plate surface experience strain paths that are qualitatively similar to those of the simple pile (Figure C.2):

1. Ahead of the penetrometer, straining is primarily in the E_1 direction (vertical compression). As the element moves past the tip of the penetrometer, this component reverses in sign (vertical extension). The E_5 component (shear strain on the vertical plane) increases to a maximum close to the level of the penetrometer tip and then reverses direction. The E_2 component increases monotonically throughout the strain path and controls the magnitude of the shear strains behind the plate tip (where $E_5 \Rightarrow 0$ and $E_2 \Rightarrow 0$).
2. For a given x_0/w , soil elements close to the plate experience an increasing amount of negative E_2 straining as the B/w ratio increases. In fact, Whittle et al. (1989) show that for a plate with $B/w = 10$ and $x_0/w \leq 1$ the E_2 component remains negative during an element's entire strain path. This behavior is associated with a condition in which both the length, $2B$, and width, $2w$, affect the strain history of soil elements. Very similar results were reported previously for open-ended pile penetration (Chin, 1986).

For initial soil element locations that are not in the central plane the strain paths become very complex, and involve all five strain components. Figure C.10 shows one example of strain paths for a simple plate with $B/w = 6.8$ and soil elements initially located at $y_0/w = 6.8$ and $x_0/w = 0.5, 1, 3, 5$. The soil elements have three degrees of freedom (i.e., 3 components of displacement). It can be seen that, for the element furthest from the penetrometer ($x_0/w = 5$), the strain path is qualitatively similar to that described for the $y = 0$ plane (Figure C.9a) but includes additional shear components E_3 and E_4 . For the element closest to the plate ($x_0/w = 0.5$) the behavior is strongly influenced by the displacement out of the $y/w = 6.8$ plane. This causes a reversal in the sign of the E_2 , E_3 and E_5 strain

⁴ Note that in the central plane $\epsilon_{xy} = \epsilon_{yz} = 0$.

components. For intermediate soil elements, the strain paths reflect directly the distortion of the soil around the edge of the plate.

Singularity	Location of Singularity	Velocity Components	Geometry & Application
Point Source	$x=0; y=0; z=0$	$v_p = \frac{V}{4\pi \rho^2} \quad (\text{spherical})$ $v_r = \frac{V}{4\pi} \frac{\sin \phi}{\rho^2} \quad (\text{cylindrical})$ $v_z = \frac{V}{4\pi} \frac{\cos \phi}{\rho^2} \quad (\text{cylindrical})$ <p>where $\rho = (r^2 + z^2)^{1/2}$ and $\phi = \tan^{-1}(r/z)$</p>	<ul style="list-style-type: none"> Spherical cavity expansion (Vesic, 1972) with uniform flow: Simple Pile (Baligh, 1985)
Line Source	$x=0; -\infty \leq y \leq \infty; z=0$	$v_x = \frac{Q}{2\pi p} \sin \phi \quad (\text{cartesian})$ $v_z = \frac{V}{2\pi p} \cos \phi \quad (\text{cartesian})$ <p>where $\rho = (x^2 + z^2)^{1/2}$ and $\phi = \tan^{-1}(x/z)$</p>	<ul style="list-style-type: none"> Cylindrical cavity expansion with uniform flow: Simple Wall (Chin, 1986)
Ring Source	$r=R; z=0$	$v_r = \frac{V}{4\pi^2} \frac{1}{r\sqrt{z^2 + (r+R)^2}} \left[K(k) - 1 - \frac{2r(r-R)}{z^2 + (r-R)^2} E(k) \right] \quad (\text{cylindrical})$ $v_z = \frac{V}{4\pi^2} \frac{2z}{\sqrt{z^2 + (r+R)^2} [z^2 + (r-R)^2]} E(k) \quad (\text{cylindrical})$ <p>where $k = \frac{4rR}{z^2 + (r+R)^2}$ and $K(k), E(k)$ are complete elliptic integrals of the first and second kind</p>	<ul style="list-style-type: none"> with uniform flow: Simple open ended pile (Chin, 1986); Ideal Sampler (Baligh et al., 1987)
Semi-infinite Source	$x=0; 0 \leq y \leq \infty; z=0$	$v_x = \frac{Q}{4\pi} \sin \theta \left(1 + \frac{y}{r} \right) \quad (\text{cartesian})$ $v_y = \frac{Q}{4\pi} \frac{1}{r} \quad (\text{cartesian})$ $v_z = \frac{Q}{4\pi} \frac{\cos \theta}{r} \left(1 + \frac{y}{r} \right) \quad (\text{cartesian})$ <p>where $r = (x^2 + z^2)^{1/2}$, $\rho = (x^2 + y^2 + z^2)^{1/2}$ and $\phi = \tan^{-1}(z/x)$</p>	<ul style="list-style-type: none"> Superposition; simple wall field vane etc. (this report)

Table C.1 Fundamental Analytical Solutions Used in the Strain Path Method

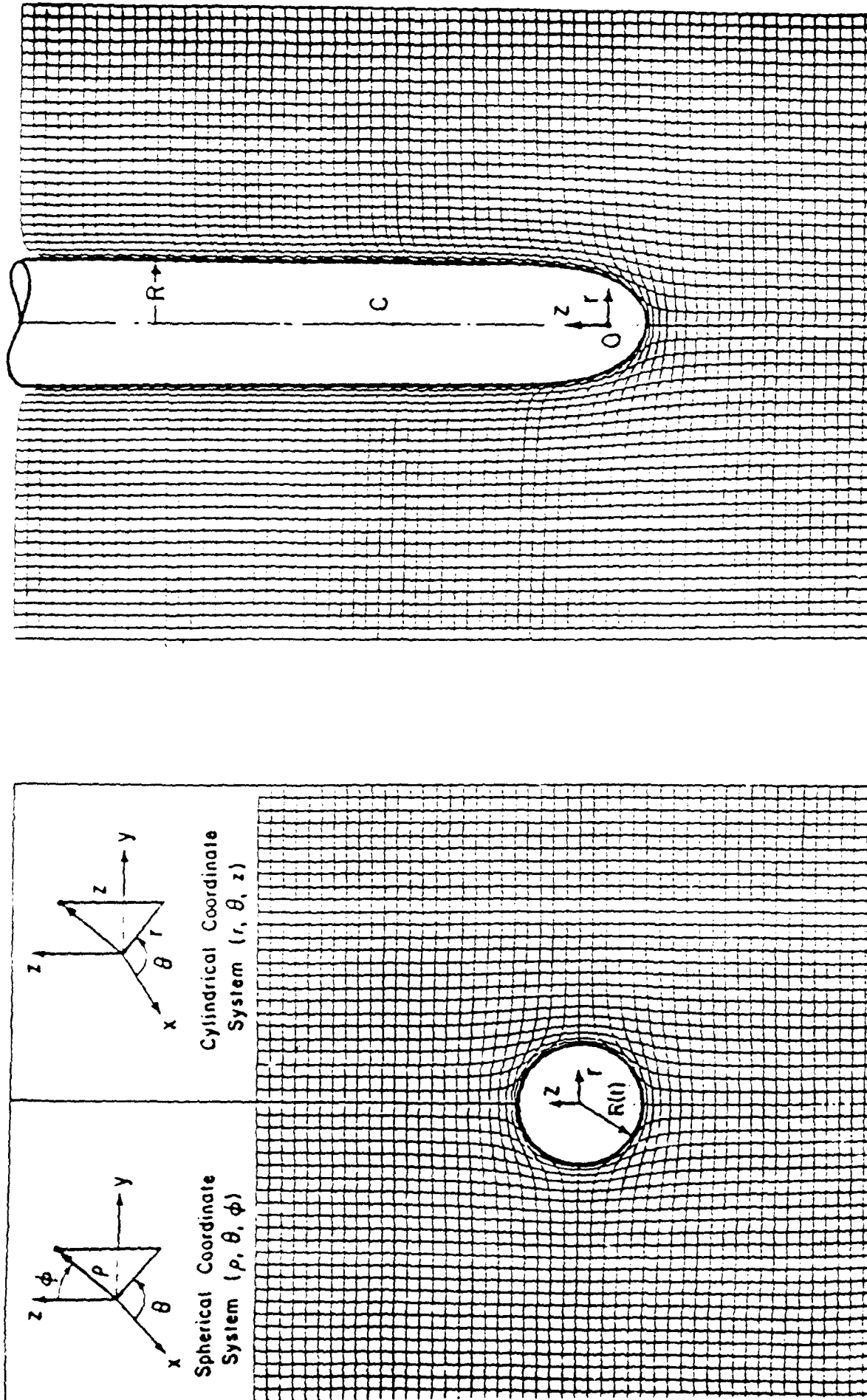


Figure C.1 Deformation fields for a) Spherical Cavity Expansion and b) Simple Pile (Baligh, 1985)

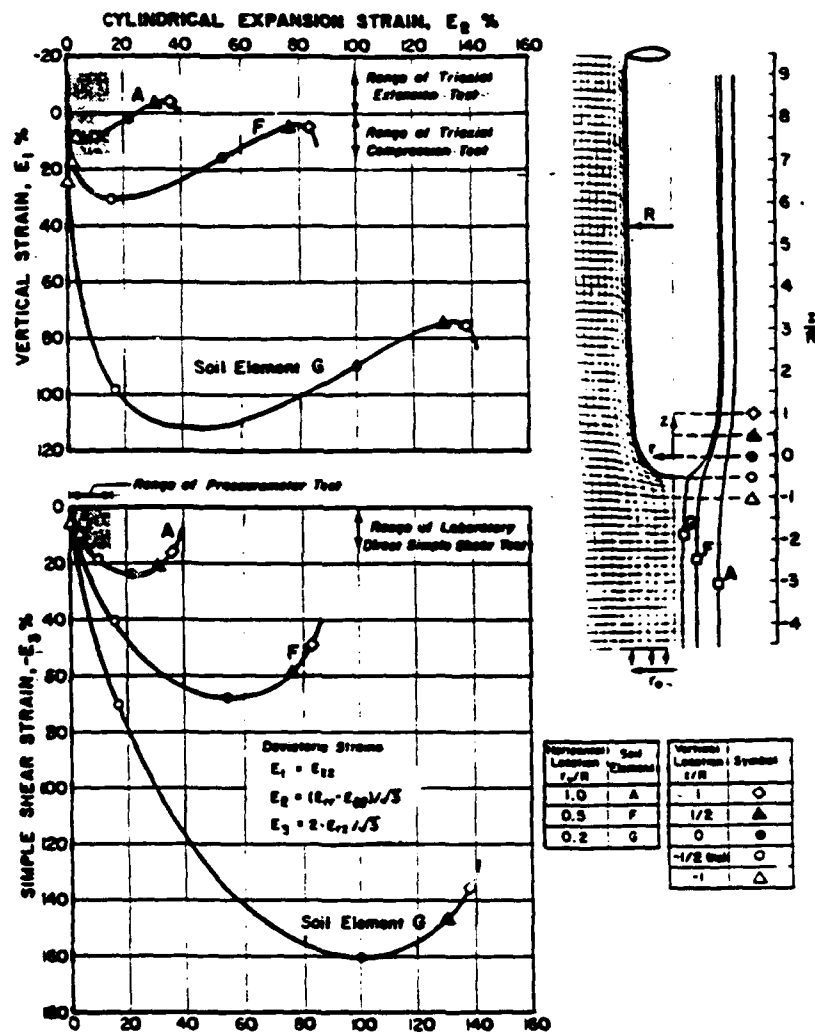


Figure C.2 Strain paths for axisymmetric penetrometers: Simple Pile

a) Point Source Located at Origin

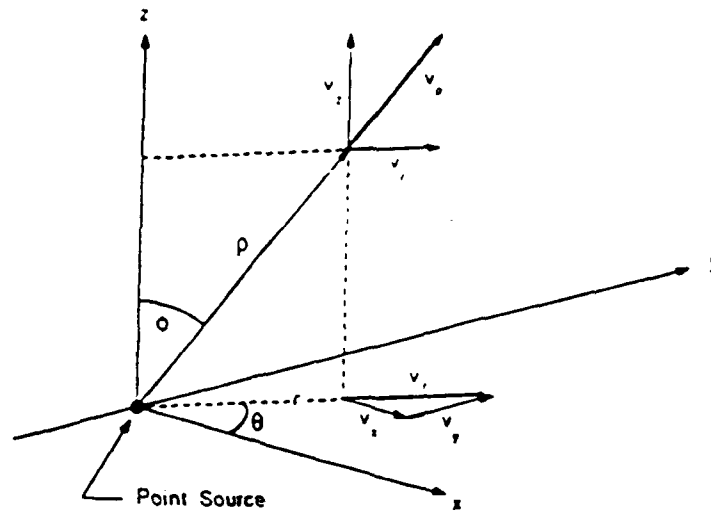
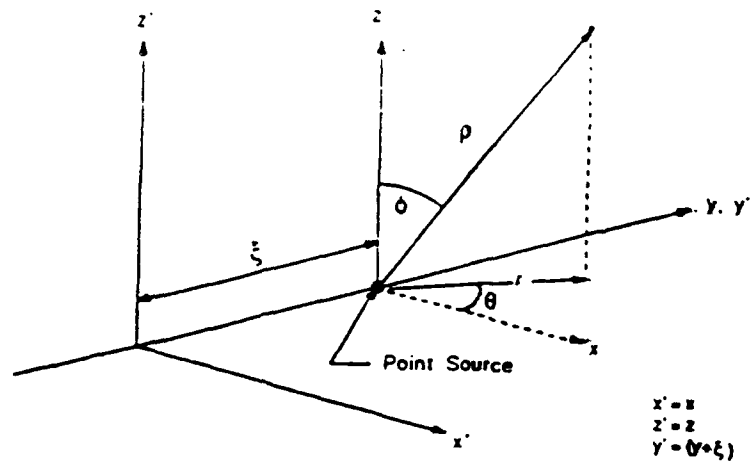
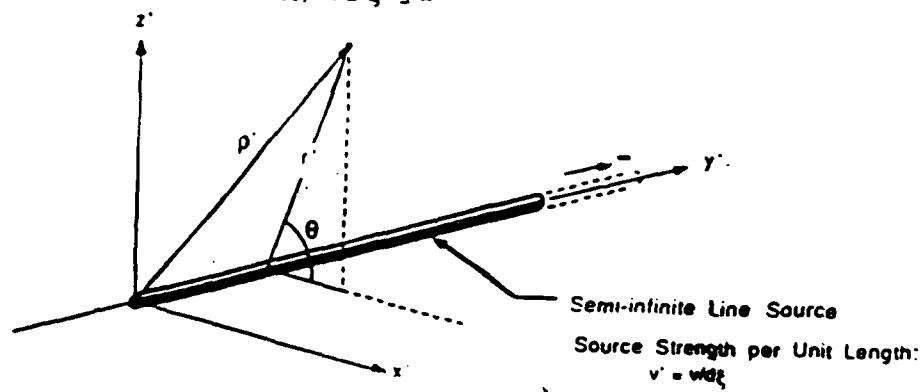
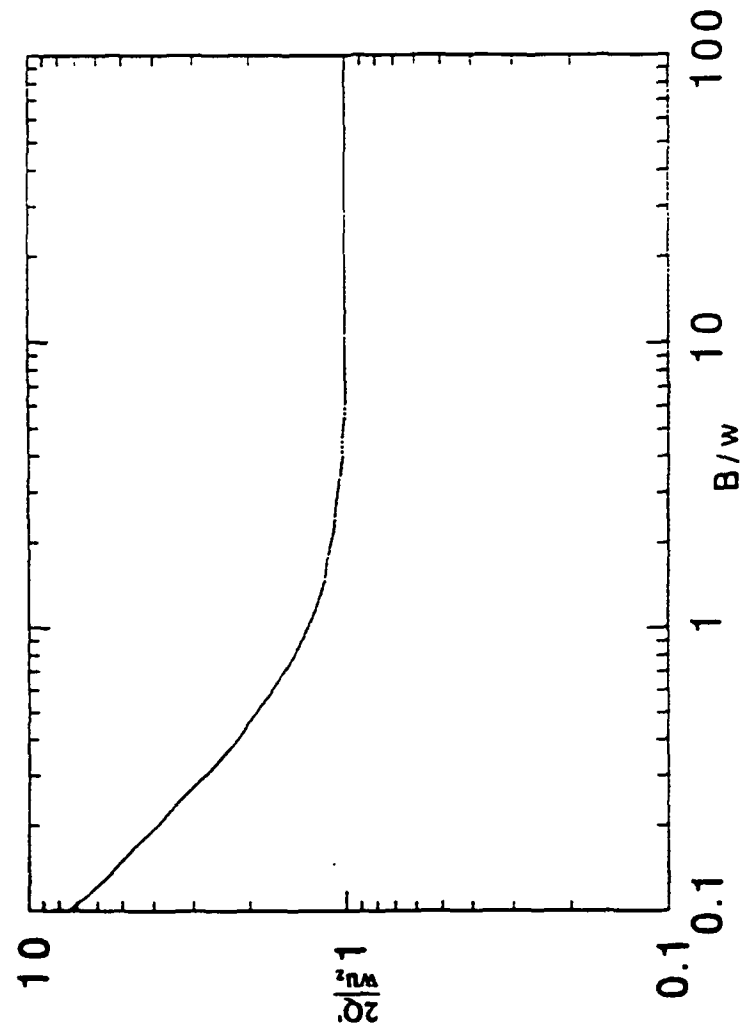
b) Point Source Located at $y' = \xi$ c) Semi-infinite Line Source, $0 \leq \xi \leq \infty$ 

Figure C.3. Coordinate system for the semi-infinite line source (Whittle et al. 1989)



Aspect Ratio (B/w)	2Q'/w u_z
1	1.346
3	1.087
10	1.013
30	1.000
100	1.000

Figure C.4 Source strength used for Simple Plate geometry

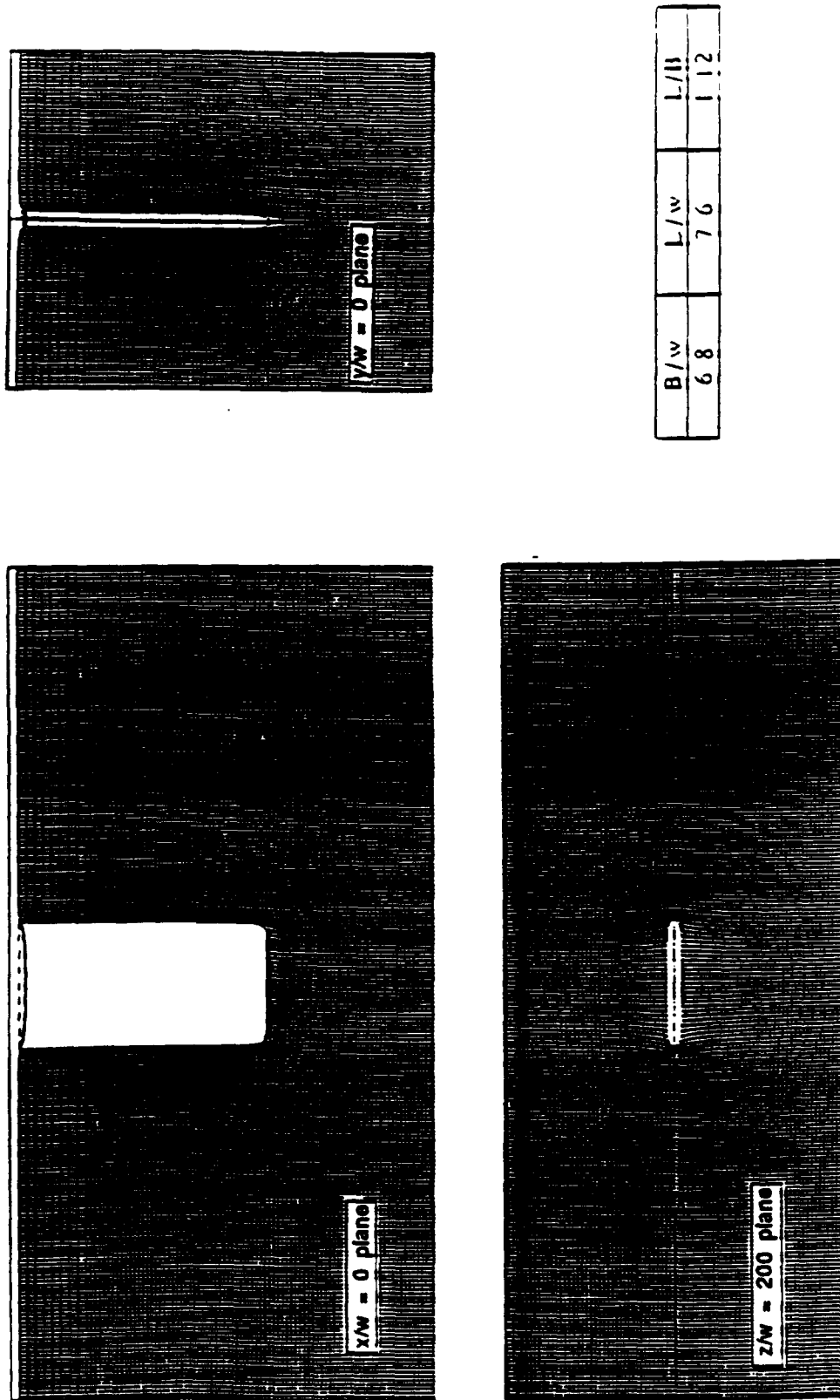


Figure C.5a Predicted deformation pattern around a simple plate, $B/w=6.8$
(Rafalovich, 1991)

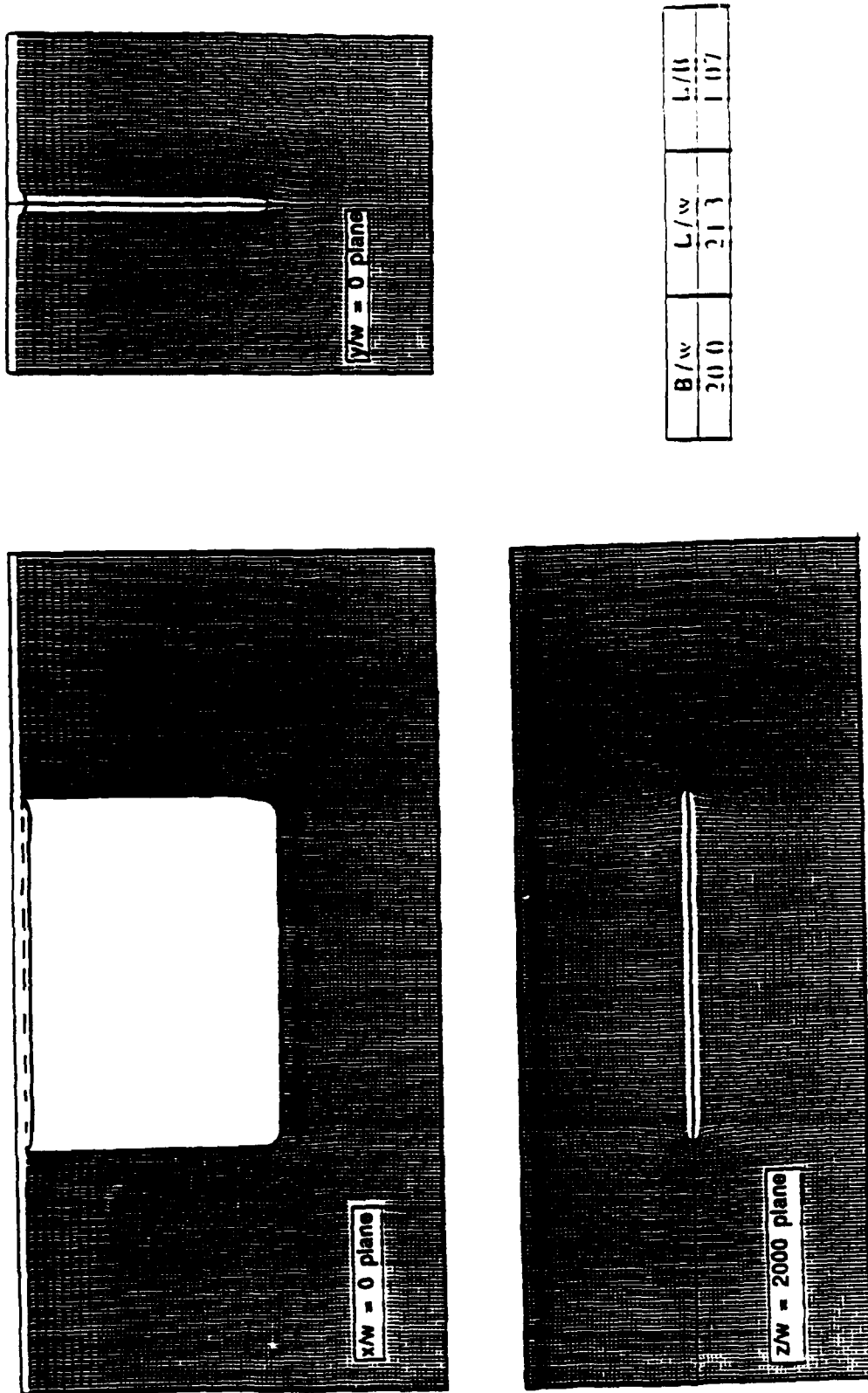


Figure C.5b Predicted deformation pattern around a simple plate, $B/w=20$
(Rafalovich, 1991)

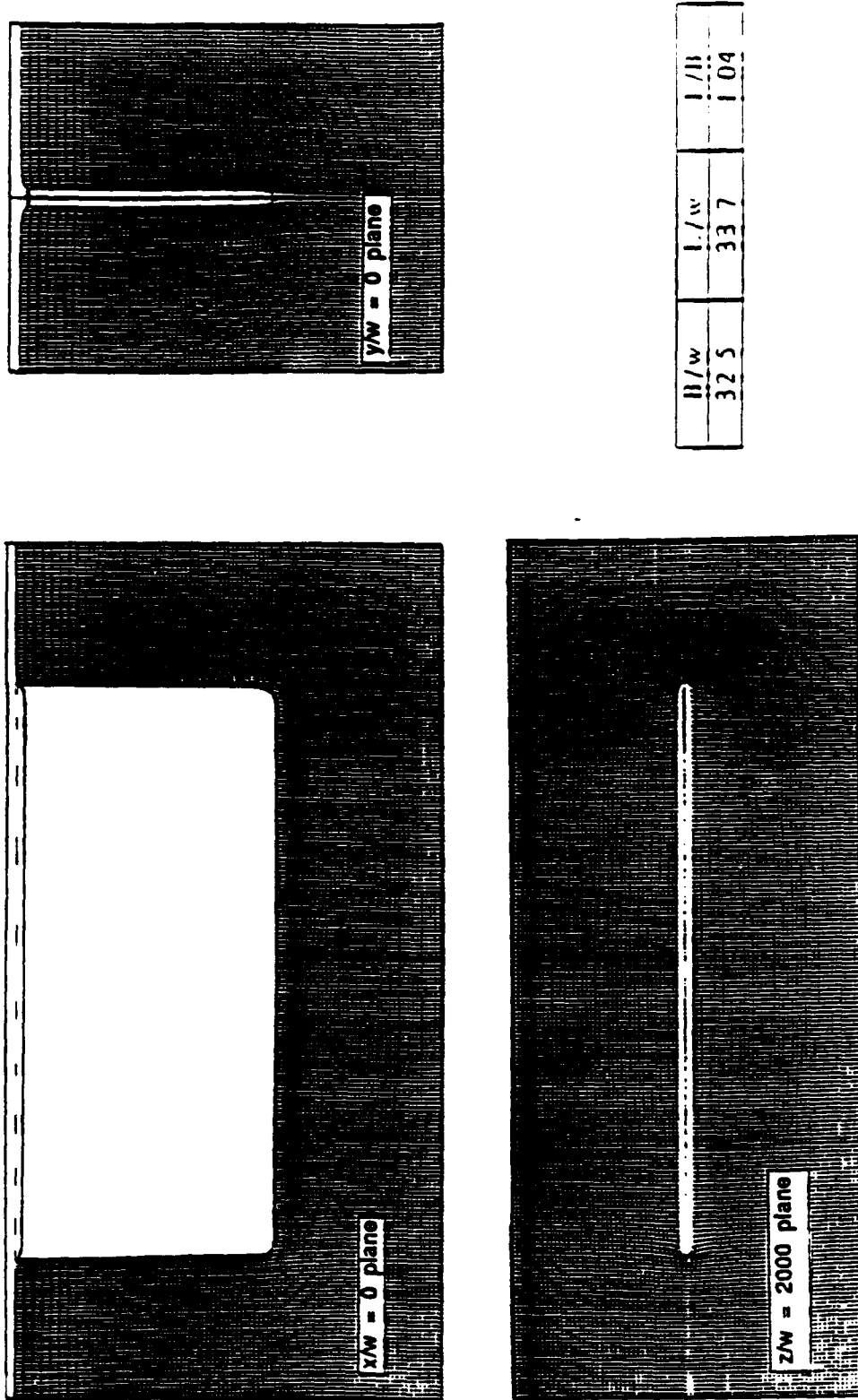
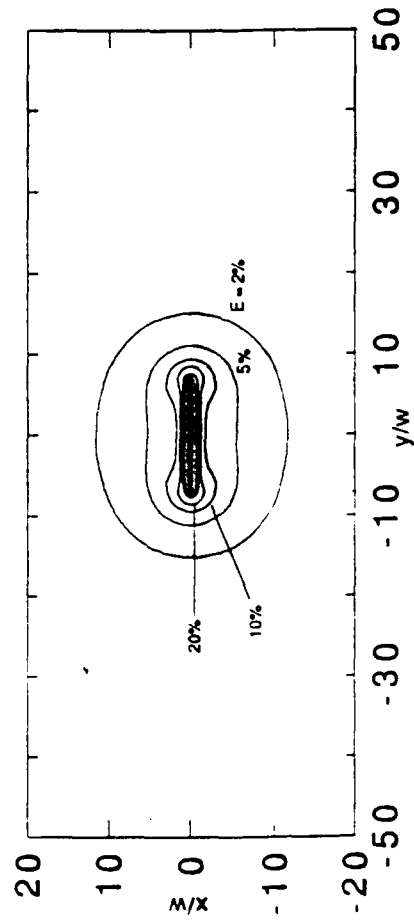
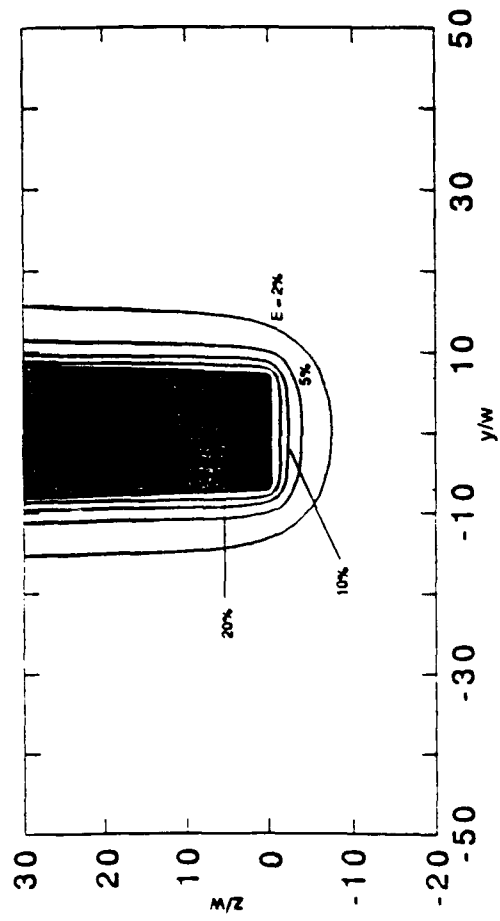
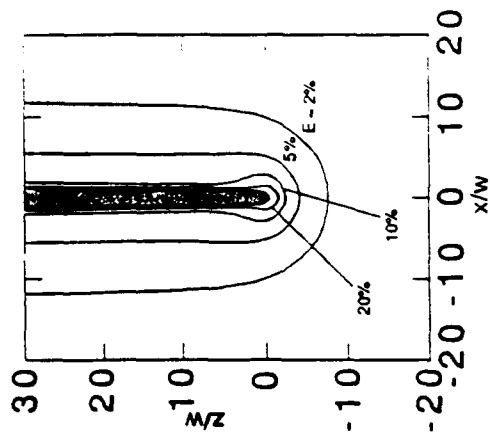
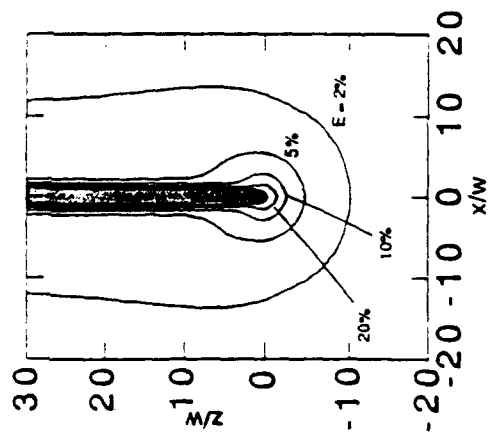


Figure C.5c Predicted deformation pattern around a simple plate, $B/w=32.5$
(Rafalovich, 1991)



B/w	L/w	L/B
6.8	7.6	1.12

Figure C.6a Simple Plate with aspect ratio, $B/w = 6.8$



B/w	L/w	L/B
20.0	21.3	1.07

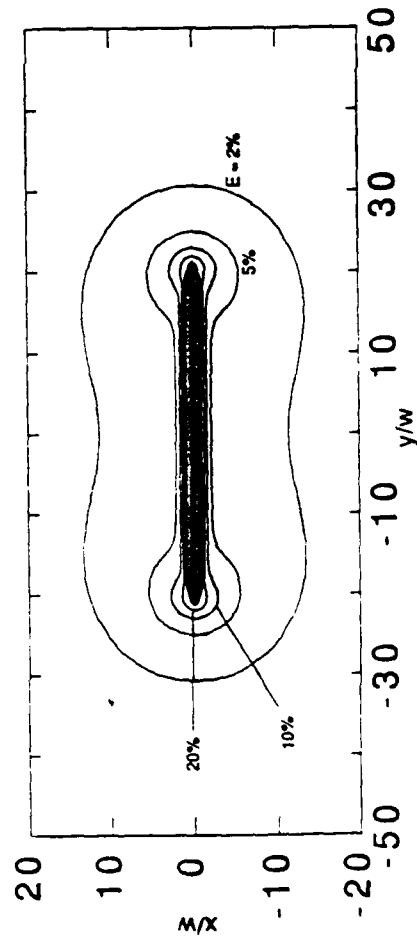
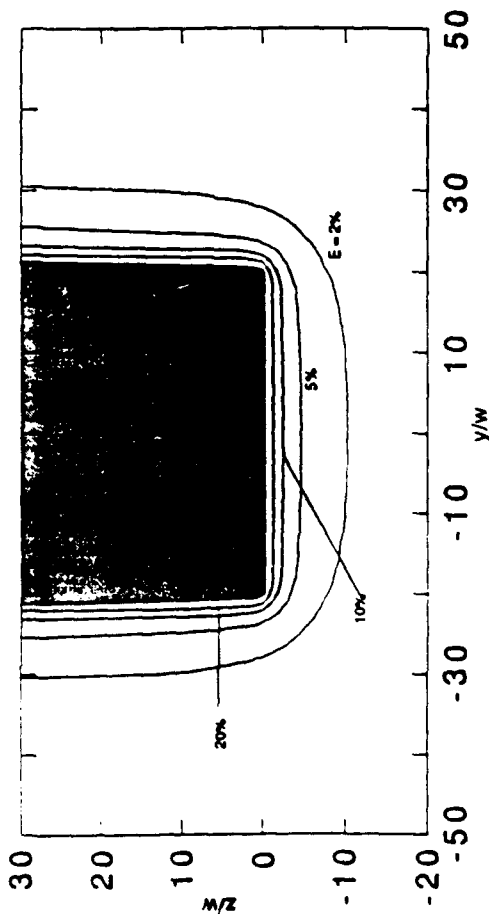
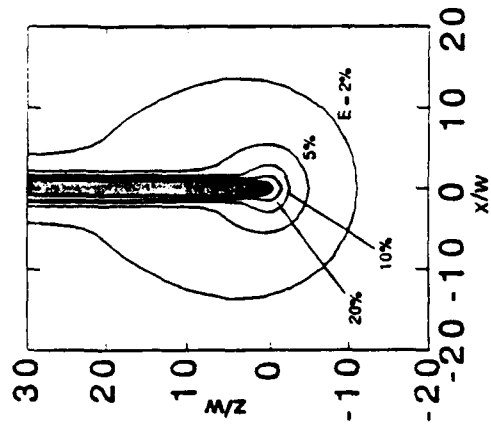


Figure C.6b Simple Plate with aspect ratio, $B/w = 20$



B/w	L/w	L/B
32.5	33.7	1.04

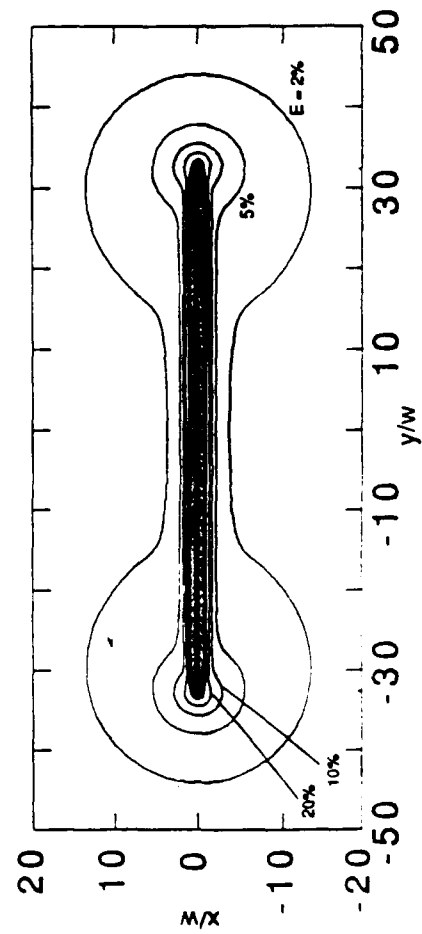
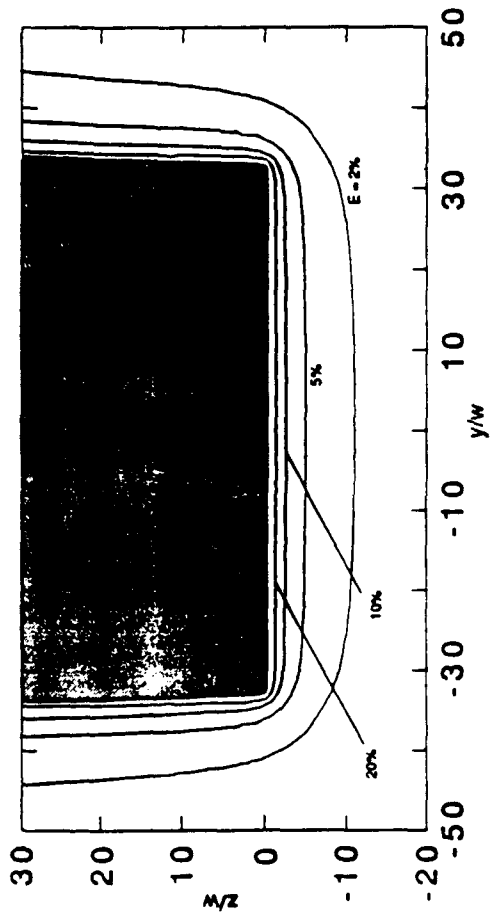


Figure C.6c Simple Plate with aspect ratio, $B/w = 32.5$

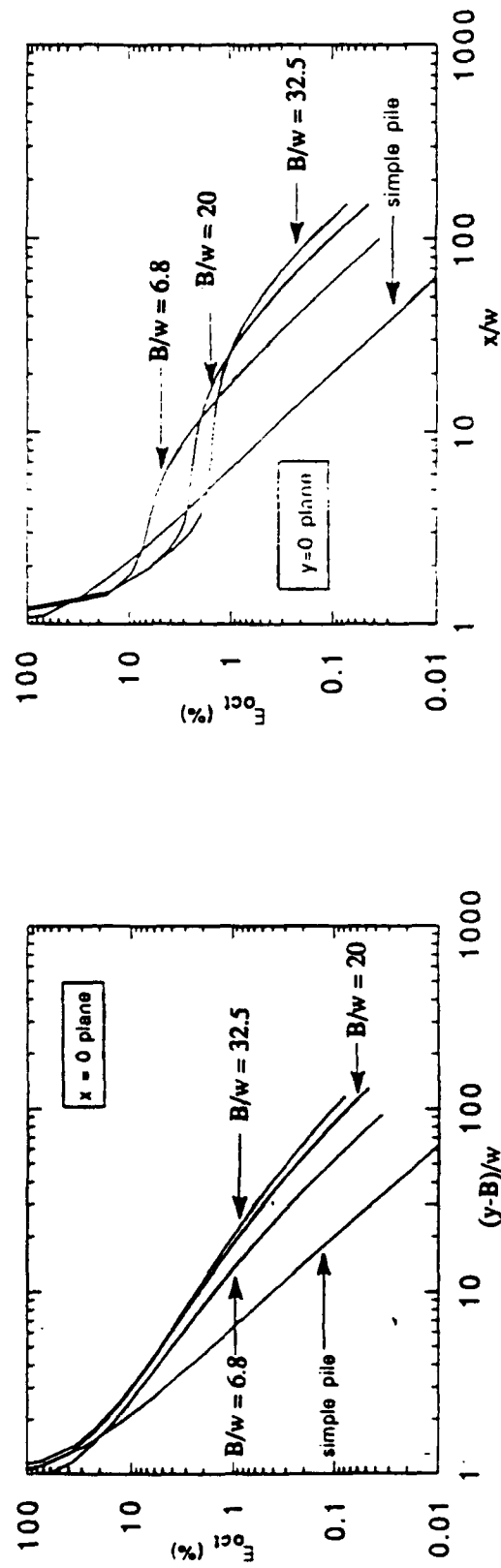


Figure C.7 Octahedral shear strain around Simple Plates

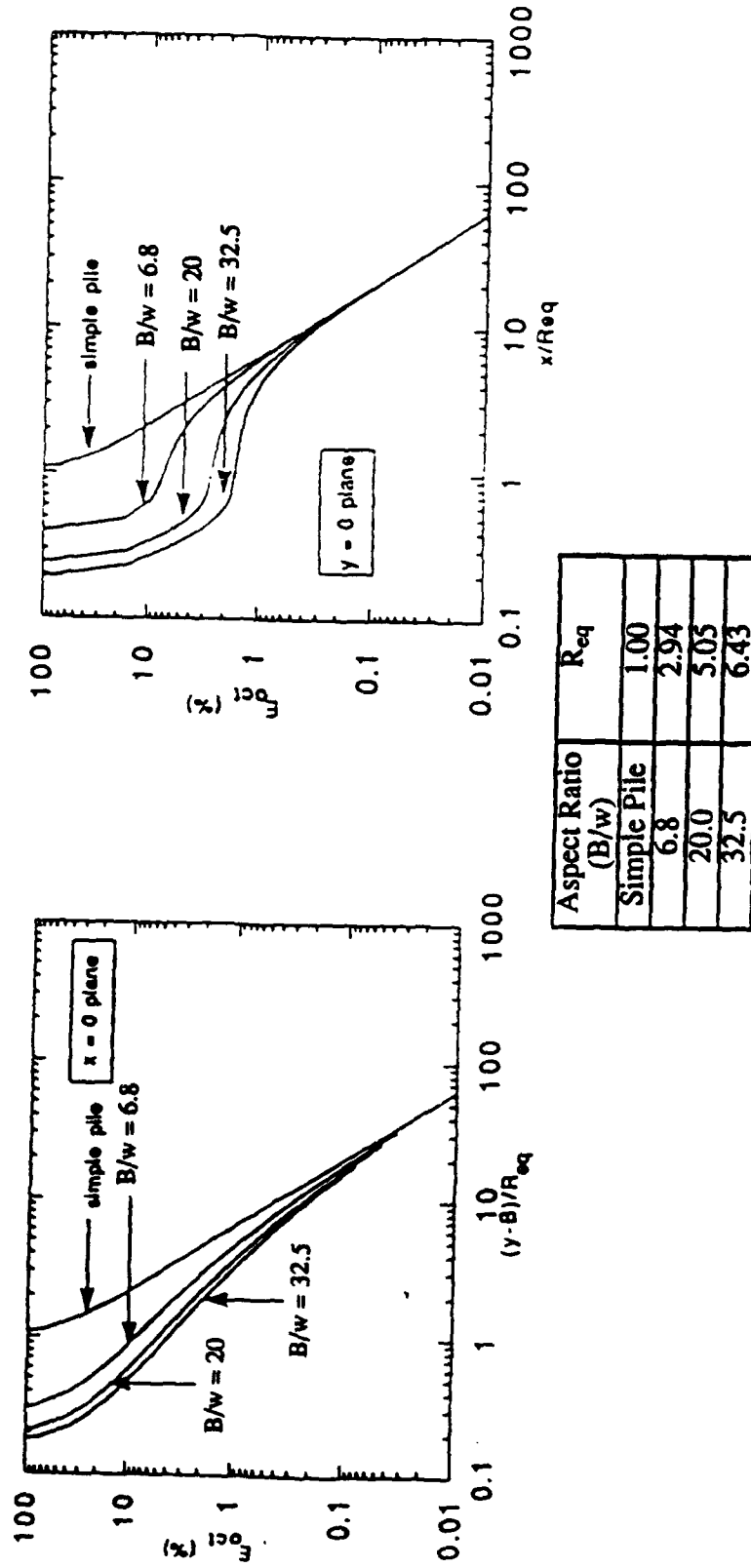
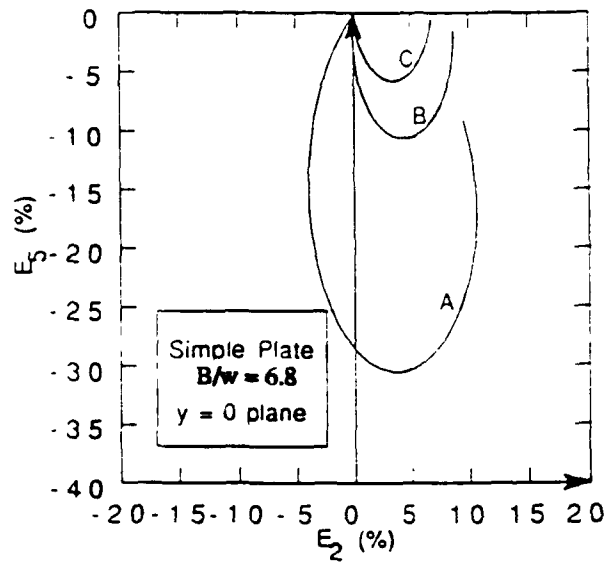


Figure C.8 Octahedral shear strain around Simple Plates using R_{eq} normalization



	A	B	C
x_0/w	1.0	3.0	5.0

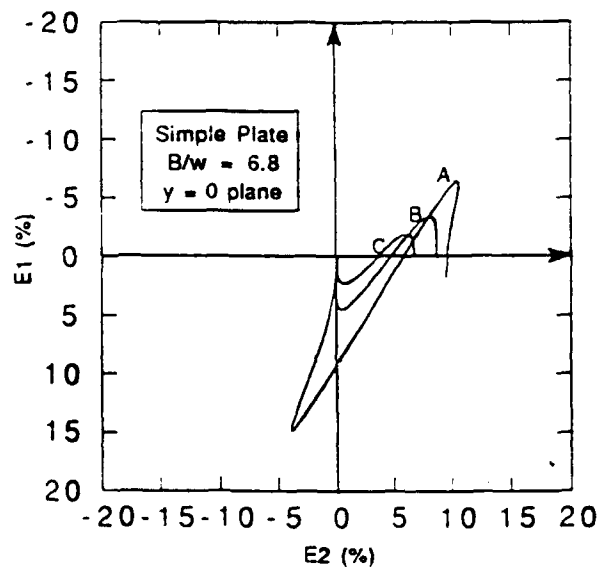
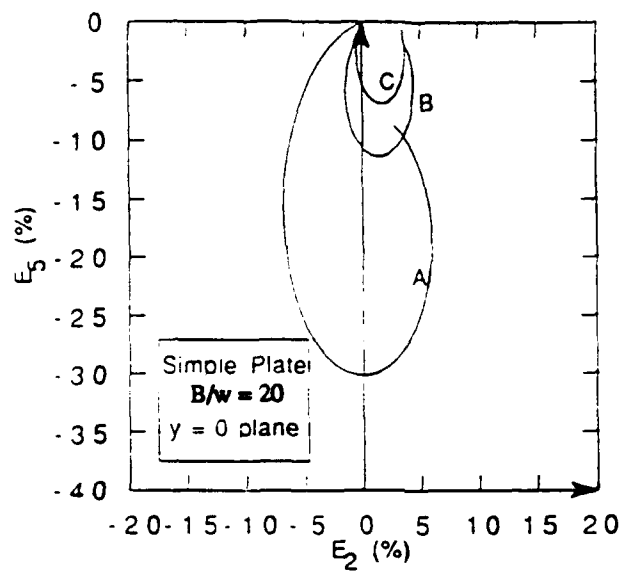


Figure C.9a Strain paths of soil elements around Simple Plate in the $y/w = 0$ plane, $B/w=6.8$



	A	B	C
x_0/w	1.0	3.0	5.0

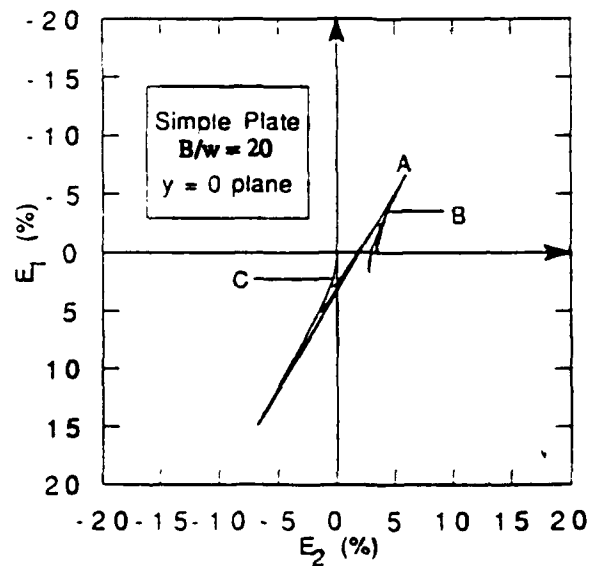
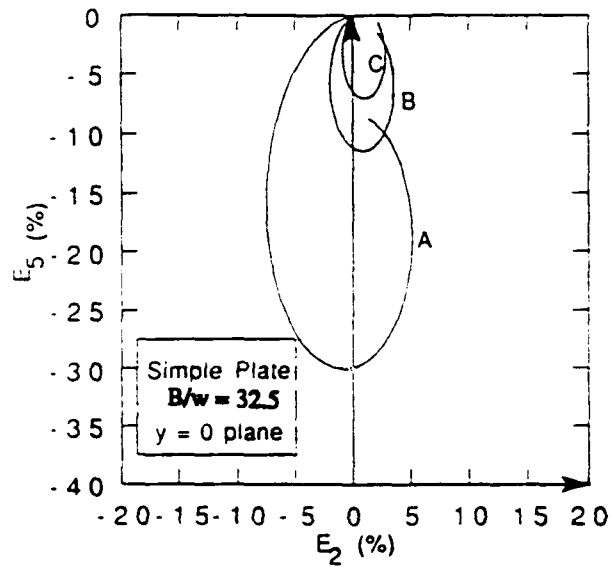


Figure C.9b Strain paths of soil elements around Simple Plate in the $y/w = 0$ plane, $B/w=20$



	A	B	C
x_0/w	1.0	3.0	5.0

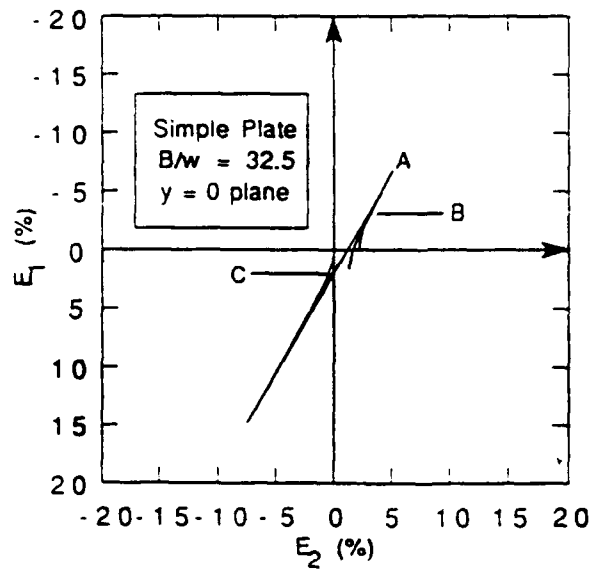
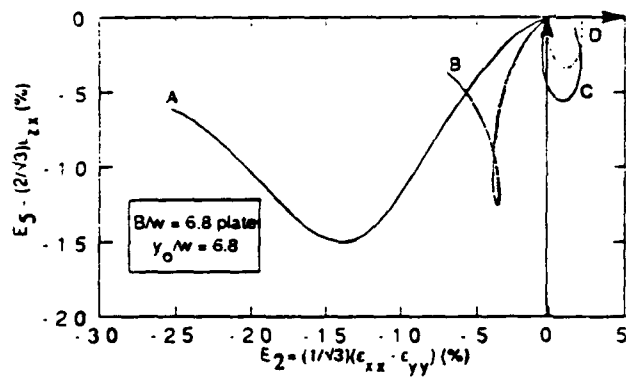
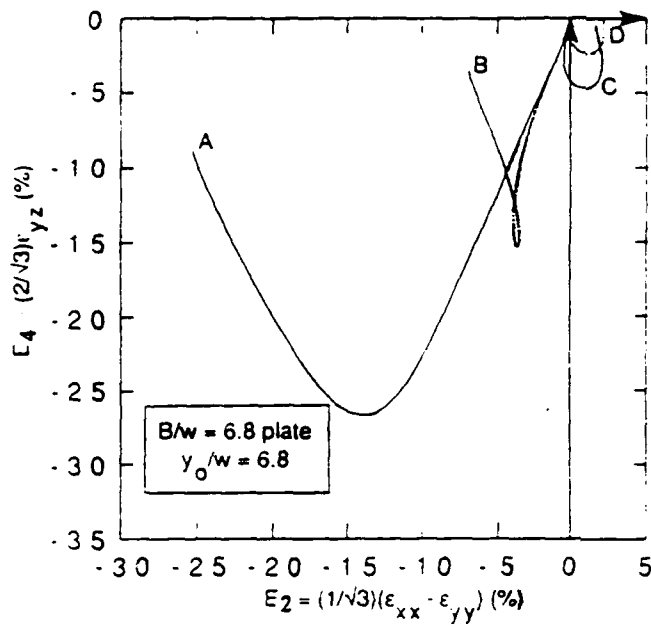


Figure C.9c Strain paths of soil elements around Simple Plate in the $y/w = 0$ plane, $B/w=32.5$



	A	B	C	D
x_0/w	5	1	3	5

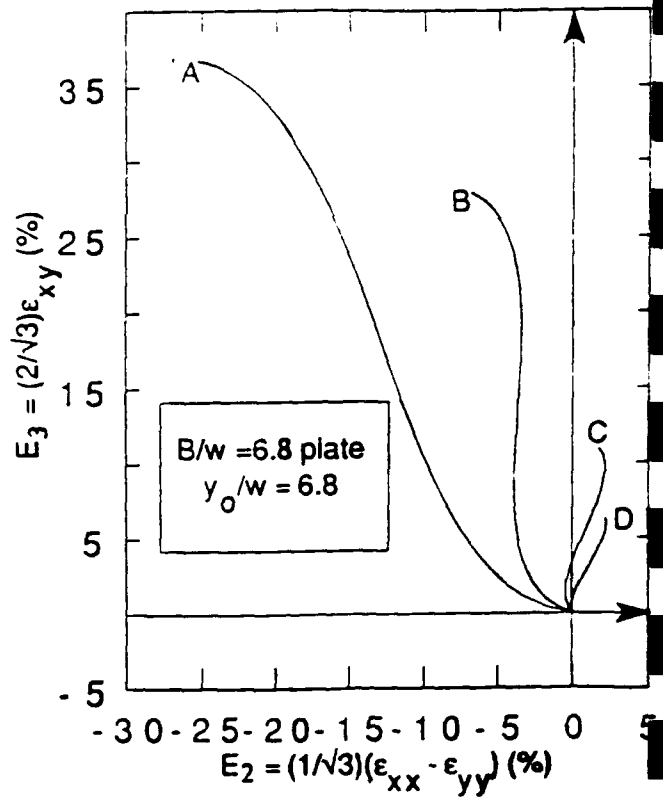
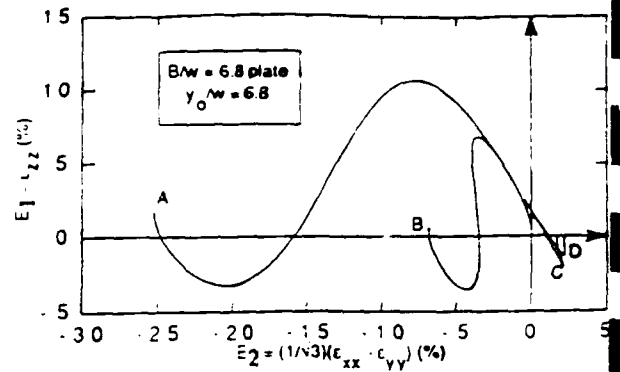


Figure C.10 Example strain paths for soil elements around Simple Plate, $B/w = 6.8$, with $y_0/w = 6.8$.

D. DEFORMATIONS, STRAINS, AND STRESSES DURING SELF-BORING PENETRATION

D.1 INTRODUCTION

For the piezocone, flat plate dilatometer, and displacement pressuremeters (FDPM, PIPM), the volume of the penetrometer is ultimately accommodated by lateral displacement of the soil. In contrast, self-boring penetration involves extraction of soil during the penetration process. In general, the volume of the soil can be either greater or less than the volume of the penetrometer. Actual self-boring penetration generally entails a complex process of soil being chopped by a rotating cutter and then jetted to the surface. A detailed analytical or numerical simulation of such a process is currently not conceivable; however, an approximate approach is possible using the Strain Path Method and combining: a) simulation of the tube geometry using a ring source in a uniform flow field; and b) superposing a sink(s) to model the removal of soil during penetration. As a first step in understanding the basic mechanisms of self-boring penetration, a single point sink is located at the center of the ring source. Three parameters are required to describe this simplified model of self-boring penetration:

1. An aspect ratio, $B/t=12$, to characterize the geometry of the penetrometer and to facilitate comparisons with penetration of a 'standard' push-in pressuremeter (PIPM, Section 6.4.3) .
2. The rate of soil extraction can be conveniently expressed as a fraction of the rate of volume displaced by the penetrometer, $f=V_{\text{sink}}/V_{\text{source}}$, where V_{source} is the ring source strength and V_{sink} is the point sink strength corresponding to the soil extraction process. Since the rate of soil extraction during self-boring cannot be accurately determined, a parametric study was performed using $f=0, 0.5, 0.75$, and 1.0 , where $f=0$ corresponds to the push-in pressuremeter geometry and $f=1$ represents "ideal" self-boring.
3. The sink is located at $z/R=0$ in order to represent the standard cutter geometry of the real self-boring devices.

D.2 DEFORMATION GRIDS AND PENETROMETER GEOMETRY

Deformation grids and penetrometer geometries for $f=0$ and $f=1$ are shown in Figure D.1, and Table D.1 summarizes of the device geometry for these two solutions. These results show the following features:

1. An inner stagnation streamline of radius $r = \sqrt{\dot{V}_{\text{sink}}/\pi U}$ at $z = -\infty$ defines boundary the zone of soil absorbed by the point sink. A second stagnation streamline separates the soil entering the tube from that moving outside the tube. At $f=1$, the radius of this stagnation line is greater than the tube radius far above the tip, indicating a net inward movement of the outer soil toward the penetrometer during penetration.
2. At $f=1$, the tip of the penetrometer becomes slightly flared (i.e., the outer radius is largest at the tip of the penetrometer). Table D.1b indicates that this "overcoring" is nearly 3% for $f=1$. Therefore, the simple single ring source-single point sink solution will reflect the effects of both soil removal and "overcoring". Assessing the effects of these factors individually will require more complex superposition solutions.

D.3 STRAINS

Figure D.2 shows strain paths describing the shear strain components E_1 , E_2 , and E_3 (Equation C.12). Note that E_1 represents a triaxial mode of shearing with compression being positive, while E_2 represents a pressuremeter mode of shearing with contraction being positive. In this figure, r_f refers to the radial coordinate of a material point far above the penetrometer tip. This figure indicates:

1. Increasing the sink strength causes a tendency for the soil particles to contract inward, as indicated by an overall shift of the strain paths to the right with increasing f . For $f \leq 0.75$, E_2 far above the tip is always negative, indicating a net outward movement (cavity expansion) of the soil during penetration. In comparison, when $f=1$, E_2 the net cavity shear strain is positive, indicating a net contraction of the outer soil during penetration.
2. For $f=0$ E_3 is always negative, while for $f>0$, E_3 is initially positive and then reverses direction. The minimum E_3 experienced by the soil particles increases with increasing f . The effect of f on E_3 far above the penetrometer tip is minimal.
3. The influence of f on E_1 is minor. For example, the maximum E_1 experienced by point A is 37% for $f=0$ and decreases to 33% for $f=1$. Similarly, point A experiences a minimum E_1 value of -3% for $f=0$ versus -5% for $f=1$.

Contours of deviatoric strain $E = \sqrt{1/2 E_i E_i}$ for $f=0$ and $f=1$ are shown in Figure 6.18, which shows:

1. Overall magnitudes of E in the vicinity of the penetrometer are similar for both $f=0$ and $f=1$. However, the lateral extent of the shear strains is greatly reduced in the outer soil for $f=1$.
2. Reversals in the magnitude of E are much more significant for $f=1$ than for $f=0$. For

example, for $f=1$, a soil particle on a streamline initially located at a radial distance $r_0/R \approx 1.2$ experiences a maximum deviatoric strain, E , of approximately 5% compared to a steady-state (i.e., far above the tip) deviatoric strain of 2%. Examination of E contours for the $f=0$ case indicates substantially smaller reversals in E for soil particles in the outer soil.

D.4 STRESSES AND PORE PRESSURES

Figure D.3a shows MCC predictions of the lateral distribution of excess pore pressures and stresses far above the penetrometer tip as a function of the rate of soil extraction f for penetration in K_0 -normally consolidated BBC. This figure shows:

1. Excess pore pressures at the penetrometer boundary decrease substantially with increasing f , with $\Delta u/\sigma'_{v0}$ being slightly negative for $f=1$. The shape of the pore pressure distribution curve is also affected by f . For $f \leq 0.5$, the excess pore pressure decreases monotonically with increasing radius, while for $f > 0.5$, the peak excess pore pressure occurs a small distance ($r/R < 1.5$) away from the penetrometer boundary. The lateral extent of positive excess pore pressures decreases substantially with increasing f (i.e., excess pore pressures begin to develop at $r/R \approx 6$ for $f=0$ versus $r/R \approx 1.5$ for $f=1$).
2. The predicted lateral distribution of mean effective stress, σ'/σ'_{v0} , shows that a critical state condition occurs at successively smaller radii as f is increased. This is consistent with the strain level predictions presented in Section D.3 showing that, as f is increased, the magnitude of the octahedral shear strain E at a given radial location decreases.
3. Predicted lateral distributions of the radial effective stress, σ'_r/σ'_{v0} , and the cavity shear stress, $q_h = (\sigma'_r - \sigma'_{\theta\theta})/2\sigma'_{v0}$, show the far field distribution of these stresses are qualitatively similar for $f \leq 0.75$, but the radial location of the peak stress moves inward with increasing f . The maximum value of these stress components are essentially unaffected by f . The far field distribution of these stress components for $f=1$ is markedly different from the stress distribution corresponding to smaller f values, with the both σ'_r/σ'_{v0} and q_h showing little variation throughout the far field. As noted earlier, $f=1$ differs from the other cases in that there is a net inward movement of the outer soil during penetration.
4. Radial effective stresses, σ'_r/σ'_{v0} , at the penetrometer boundary exhibit a complex pattern of decreasing (from 0.31 to 0.14) as f is increased from 0 to 0.5 and then increasing (from 0.14 to 0.25) as f is increased from 0.75 to 1.0.
5. The cavity shear stress, q_h , at the penetrometer boundary is nearly zero when $f=0$. As f

is increased, q_h decreases substantially to $q_h \approx -0.22$ for $f \geq 0.75$ (the critical state strength in this shearing mode is 0.37). Thus, subsequent shearing during pressuremeter expansion will begin at cavity shear stress values which deviate substantially from zero.

The MIT-E3 predictions shown in Figure D.3b show that the influence of f on predicted stress fields is qualitatively similar to the trends noted for the MCC predictions. The most notable differences between the MCC and MIT-E3 predictions are: a) the predicted lateral extent of disturbance at a given extraction ratio, f , is greater for the MIT-E3 model; and b) the mean stress, σ'/σ'_{v0} , predicted from the MCC model decreases to the critical state value and is constant within $r/R \leq 0.5-1$, while mean stresses predicted from the MIT-E3 model decrease significantly in the vicinity of the shaft.

Table D.1a Initial Radii of Stagnation Lines for Various Sink Strengths During Self-Boring Penetration, $B/t=12$

$f=V_{\text{sink}}/V_{\text{source}}$	Radius of Inner Stagnation Line at $z=-\infty$	Radius of Outer Stagnation Line at $z=-\infty$
0	-----	0.850
0.5	0.391	0.932
0.75	0.479	0.970
1.0	0.553	1.007

Table D.1b Penetrometer Characteristics for Various Sink Strengths During Self-Boring Penetration, $B/t=12$

$f=V_{\text{sink}}/V_{\text{source}}$	$R_{\text{max}}/R_{z=-\infty}$	z/R at R_{max}
0	1.000	-----
0.5	1.000	-----
0.75	1.011	.255
1.0	1.026	.194

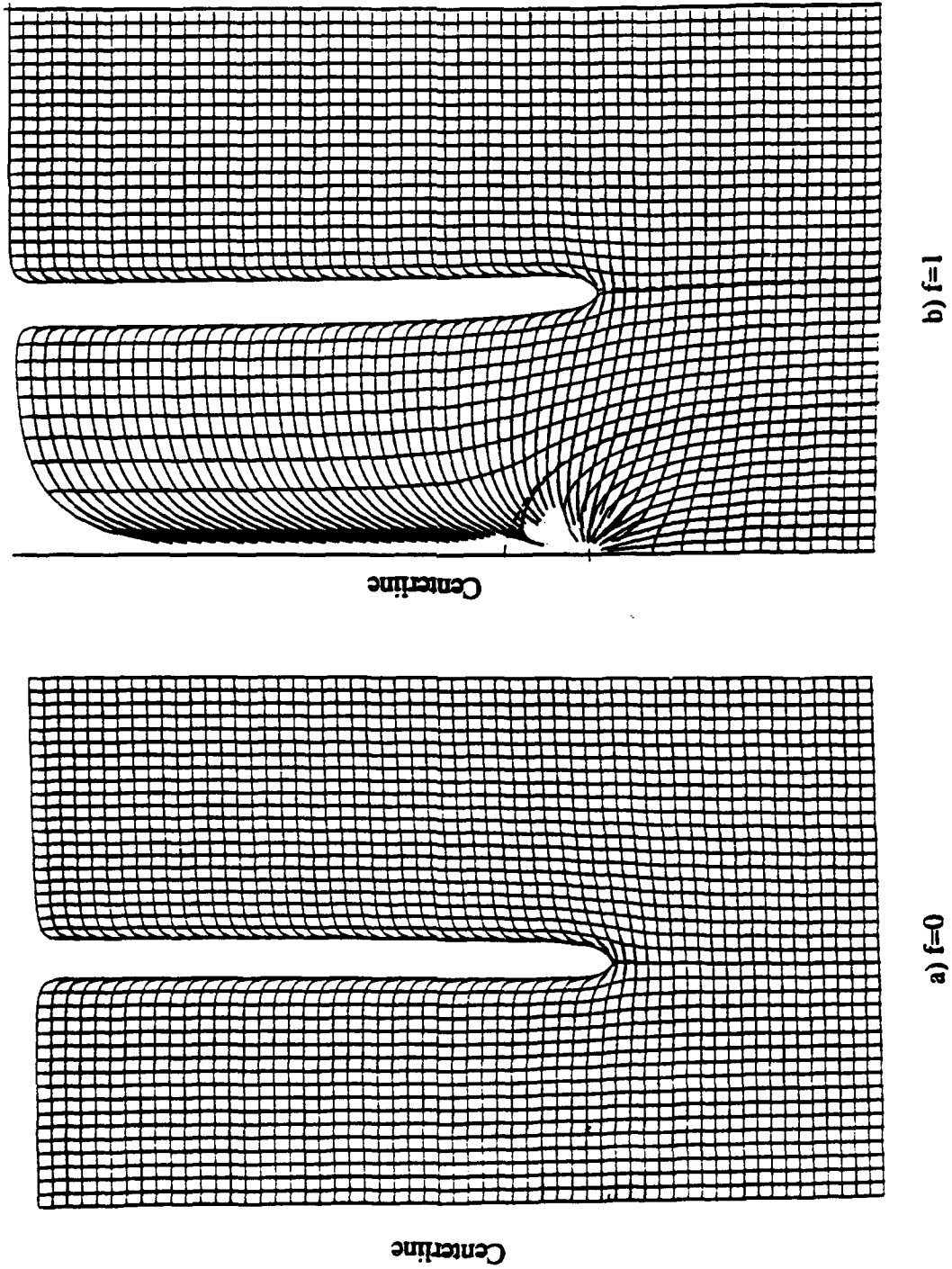
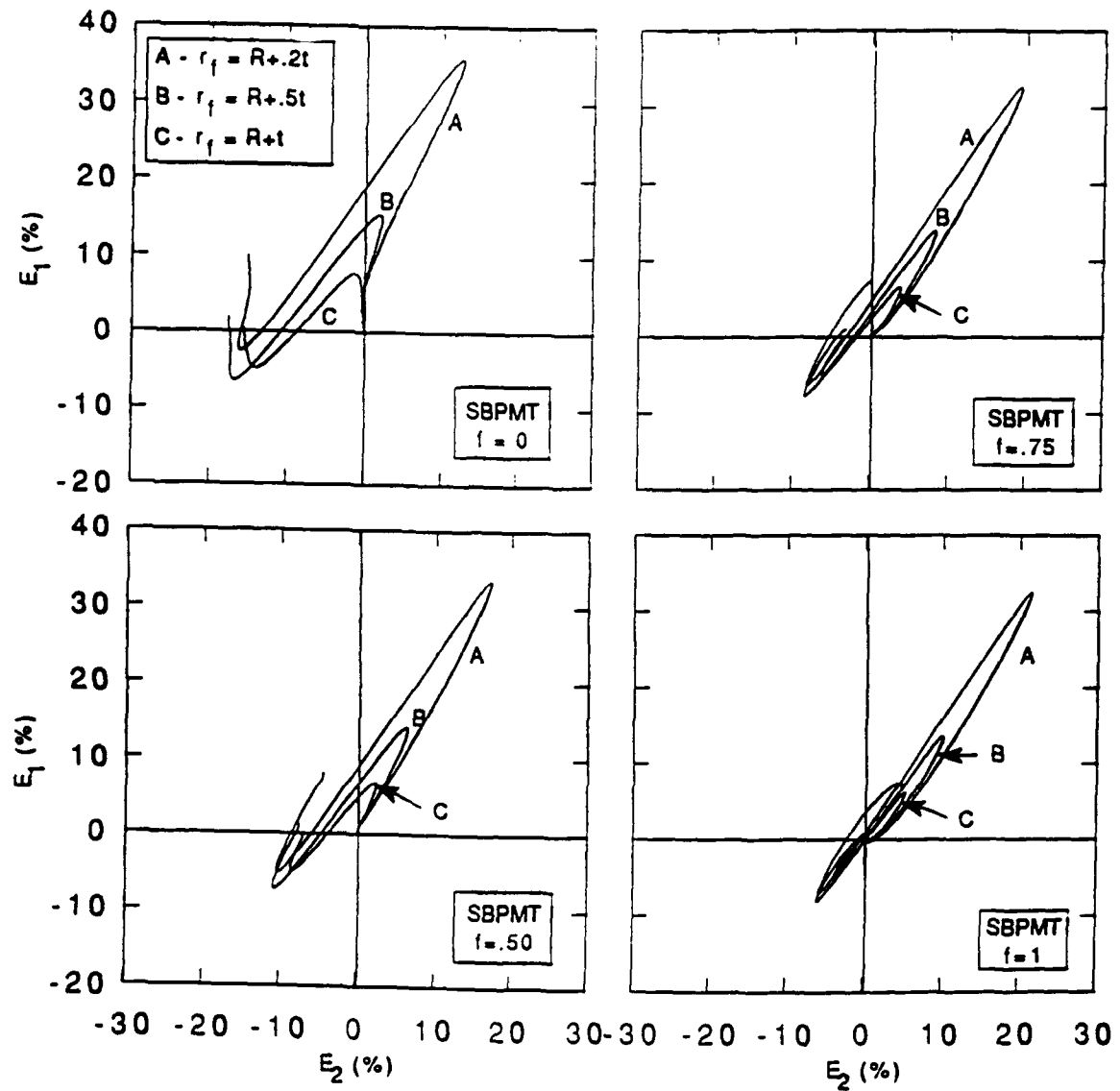
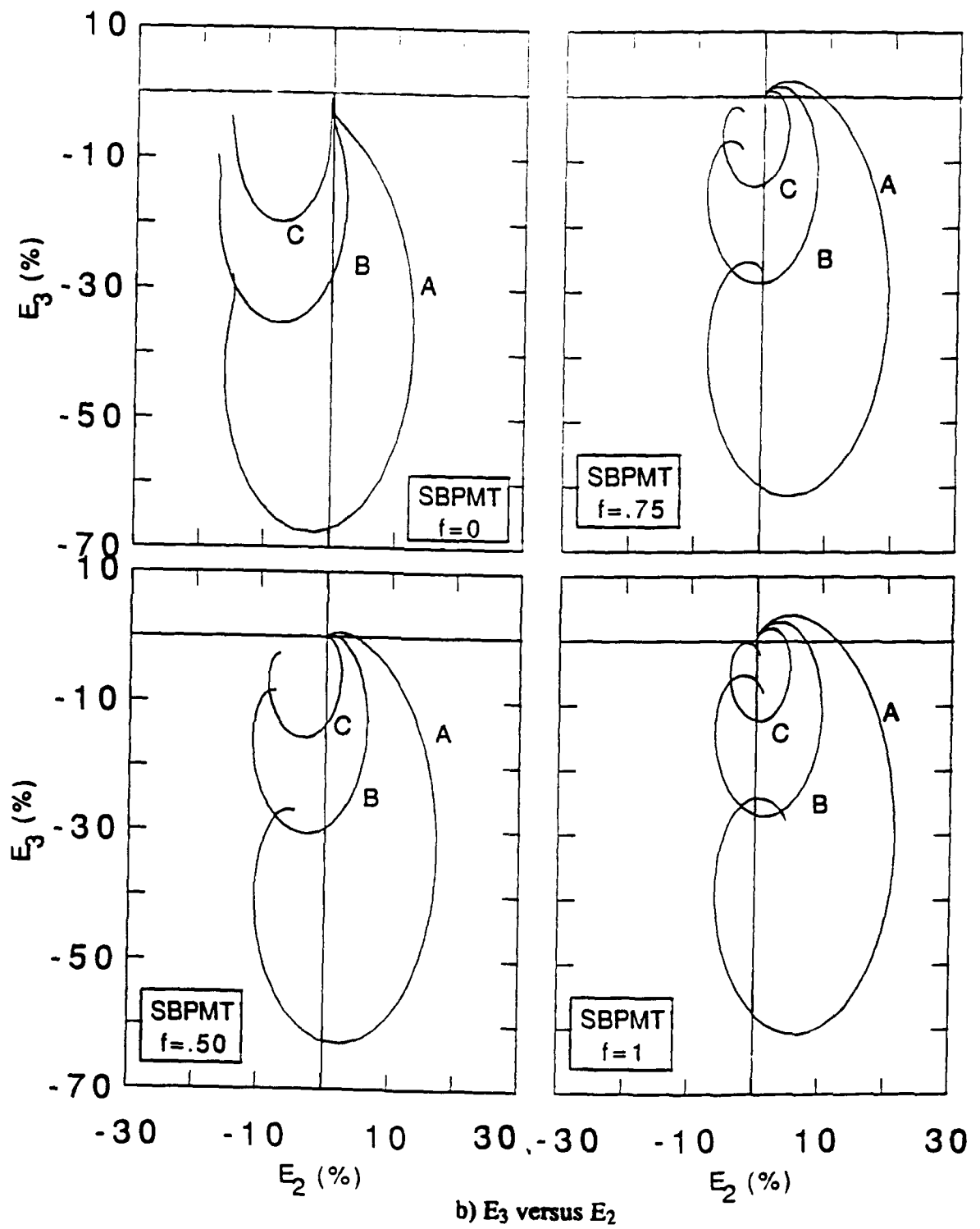


Figure D.1 Deformation Grids during Self-boring Penetration, $B/t=12$

a) E_1 versus E_2 Figure D.2 Strain Paths during Self-Boring Penetration, $B/t=12$

Figure D.2 Strain Paths during Self-Boring Penetration. $B/t=12$

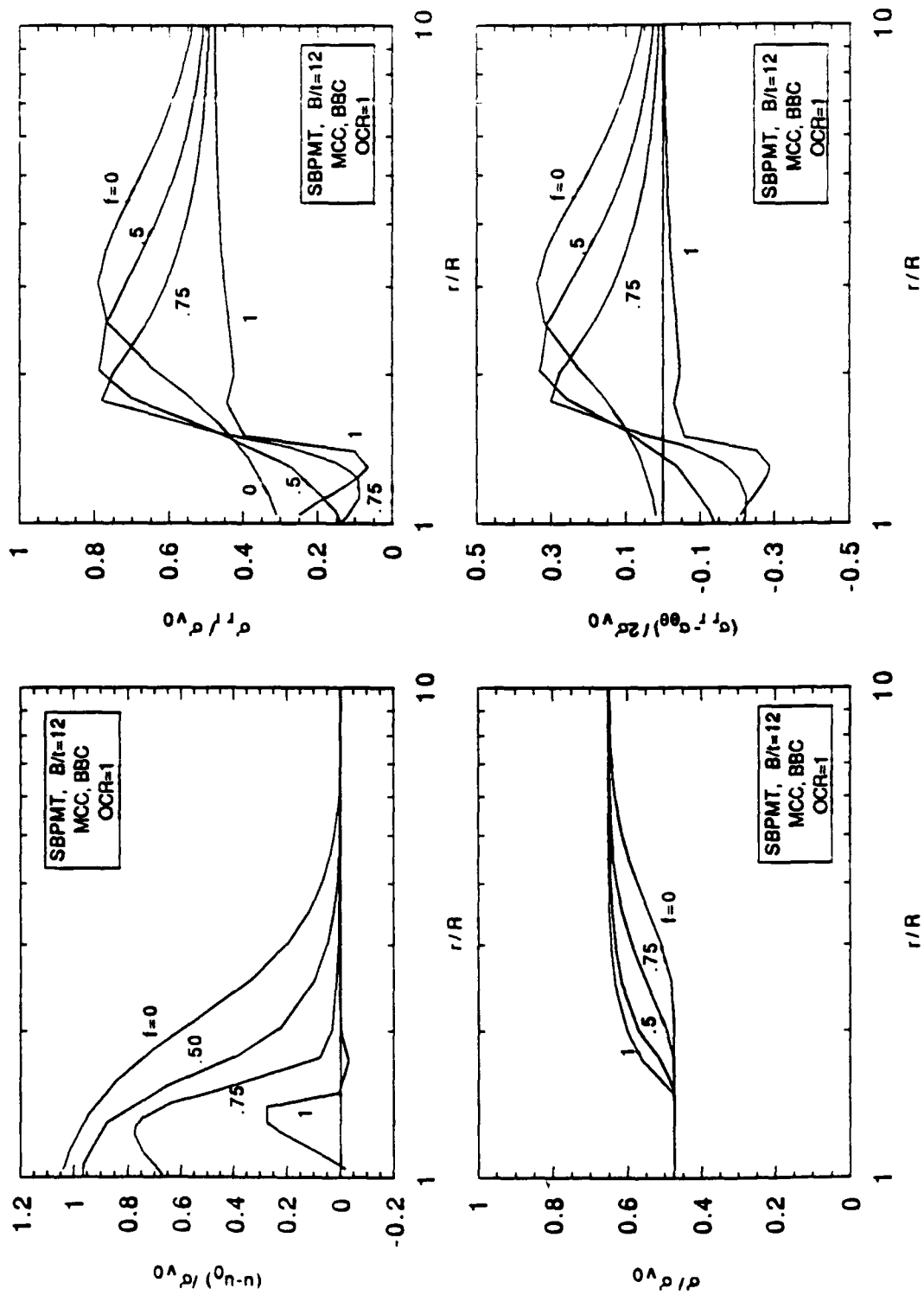


Figure D.3a Lateral Distribution of Stresses and Pore Pressures far above Penetrometer Tip during Self-Boring Penetration: MCC

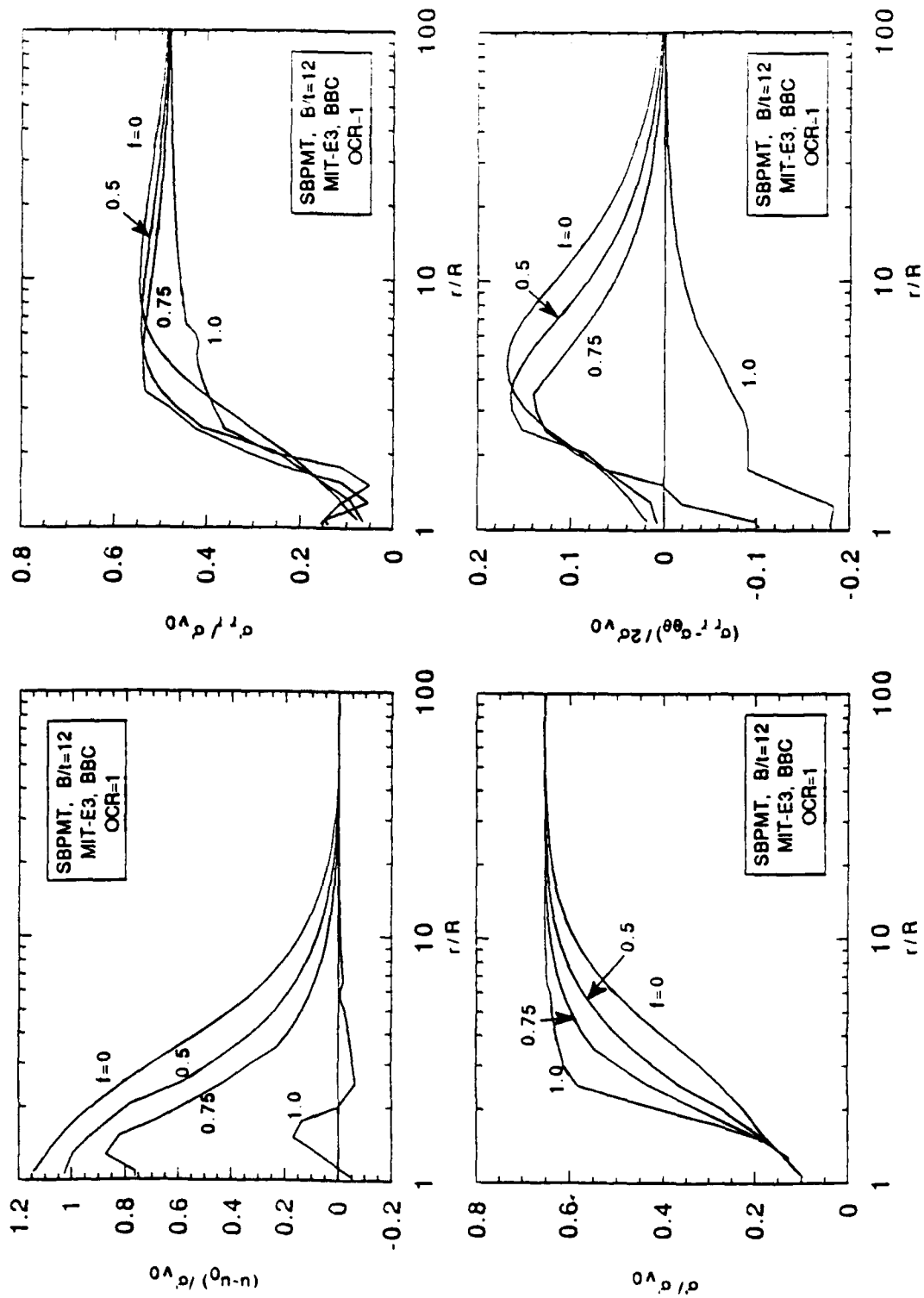


Figure D.3b Lateral Distribution of Stresses and Pore Pressures far above Penetrometer Tip during Self-Boring Penetration: MIT-E3